

**TELLURITE AND FLUOROTELLURITE  
GLASSES FOR ACTIVE AND PASSIVE  
FIBROPTIC WAVEGUIDES**



Matthew O'Donnell, MEng

Thesis submitted to the University of Nottingham  
for the degree of Doctor of Philosophy

December 2004

## **Acknowledgements**

I would like to thank the following:

The University of Nottingham and EPSRC for funding the work.

Prof. A. B. Seddon, Dr. D. Furniss and my other colleagues in the Novel Photonic Glasses Research Group, and Materials Engineering at the University of Nottingham.

My family and Amanda for their support.

## Abstract

Glasses systems based on  $\text{TeO}_2\text{-ZnO-Na}_2\text{O}$  (TZN),  $\text{TeO}_2\text{-WO}_3$ , and  $\text{TeO}_2\text{-Na}_2\text{O-ZnF}_2$  are reported here, with a number of other components added ( $\text{PbO}$ ,  $\text{GeO}_2$ ,  $\text{Nb}_2\text{O}_5$ ,  $\text{Bi}_2\text{O}_3$ ,  $\text{Er}_2\text{O}_3$ ,  $\text{Yb}_2\text{O}_3$ ,  $\text{PbF}_2$ , and  $\text{ErF}_3$ ).

Glass formation was shown for the first time, to this author's knowledge, in the ternary system  $(90-x)\text{TeO}_2\text{-}10\text{Na}_2\text{O-xZnF}_2$  for  $5 \leq x \leq 30$  mol. %. Glass stability ( $T_x\text{-}T_g$ ) was found to increase with  $\text{ZnF}_2$  addition, reaching a plateau of around  $161^\circ\text{C}$  at  $x = 25$  mol. %. This could be due to competition of various phases to crystallise ( $\text{NaZnF}_3$  and  $\text{Zn}_2\text{Te}_3\text{O}_8$ ) as the eutectic is approached, with fluoride addition. These glasses are the most stable  $\text{ZnF}_2$  containing tellurite compositions reported to date, to the author's knowledge.

As-received  $\text{ZnF}_2$  batch material was shown to contain a significant proportion of  $\text{Zn(OH)F}$ , identified by XRD. The as-received  $\text{ZnF}_2$  was fluorinated with  $(\text{NH}_4)\text{HF}_2$ , which produced a substantially more phase pure powder, with oxygen levels reduced from around 13.2 to 3.1 at. % from XPS spectra. By calculation from the O1s XPS peaks, the proportion of  $\text{Zn(OH)F}$  was reduced in the powders from 39.7 to 9.4 mol. %.

A number of absorption bands in the infrared were identified by FTIR for the  $\text{TeO}_2\text{-ZnO-Na}_2\text{O}$  glasses due to intrinsic lattice vibrations (visible in a 0.2 mm sample), and extrinsic impurity absorption, including: free OH ( $\approx 3.0 \mu\text{m} \equiv 3300 \text{ cm}^{-1}$ ), weakly hydrogen-bonded OH ( $\approx 3.3 \mu\text{m} \equiv 3060 \text{ cm}^{-1}$ ), and strongly hydrogen-bonded OH ( $\approx 4.8 \mu\text{m} \equiv 2090 \text{ cm}^{-1}$ ).

For the series  $(90-x)\text{TeO}_2-10\text{Na}_2\text{O}-x\text{ZnF}_2$ , mol. %,  $5 \leq x \leq 30$  mol. % melted for 2 hours as bulk glasses, OH bands at  $2900 \text{ cm}^{-1}$  were reduced in intensity with  $\text{ZnF}_2$  addition due to self drying of the melt, from around  $0.12 \text{ cm}^{-1}$  ( $120 \text{ dB.m}^{-1}$ ) for  $x = 5$  mol. %, to around  $0.02 \text{ cm}^{-1}$  ( $20 \text{ dB.m}^{-1}$ ) for  $x \geq 15$  mol. %. Melting time also had a significant effect on drying of this series, with the loss at  $2900 \text{ cm}^{-1}$  reduced by two orders of magnitude when increased from 1 hour ( $0.705 \text{ cm}^{-1} \equiv 705 \text{ dB.m}^{-1}$ ) to 2 hours ( $0.01 \text{ cm}^{-1} \equiv 10 \text{ dB.m}^{-1}$ ). Refractive index of the series  $(90-x)\text{TeO}_2-10\text{Na}_2\text{O}-x\text{ZnF}_2$ , mol. %,  $5 \leq x \leq 30$  mol. % decreased linearly with  $\text{ZnF}_2$  addition, from 2.02 ( $x = 5$  mol. %) to 1.85 ( $x = 30$  mol. %), as the fluoride and zinc are less polarisable than oxygen and tellurium.

Cohen-Grest viscosity modelling was used to predict the fibre drawing temperature ( $T_\eta \approx 330^\circ\text{C}$  corresponding to a viscosity of  $10^{4.5}$  Pa.s), and fragility of the fluorotellurite core / clad pair (20 / 25 mol. %  $\text{ZnF}_2$ ), occurring at least  $60^\circ\text{C} < T_x$ . Fragility of these glasses was predicted to lie between oxide tellurite glasses (stronger) and fluorozirconate glasses (more fragile).

Increasing melting time and fluorination resulted in a significant decrease in OH bands in the 700 nm to  $2.5 \mu\text{m}$  region for unstructured  $70\text{TeO}_2-10\text{Na}_2\text{O}-20\text{ZnF}_2$  mol. % fibre, from around 40 to  $4 \text{ dB.m}^{-1}$  at  $2.5 \mu\text{m}$  as melting time was increased from 3 to 10 hours. Fibre optical loss for the 10 hour melt was relatively flat ( $\leq 5 \text{ dB.m}^{-1}$ ) over the entire 700 nm to  $2.5 \mu\text{m}$  region.

# Contents

<b>Contents</b>	<b>i</b>
<b>Glossary</b>	<b>v</b>
<b>1. Introduction</b>	<b>1</b>
1.1. Fibreoptic technology	1
1.2. The role of novel glass compositions	3
1.3. Aims and objectives of this study	4
1.4. Thesis structure	6
1.5. References	7
<b>2. Literature review</b>	<b>9</b>
2.1. The nature of glass	9
2.1.1. The behaviour of glass-forming materials on melt-cooling	9
2.2. The structure of glass	12
2.2.1. Atomic structure	12
2.2.2. Structural theories of glass formation	13
2.2.2.1. Early structural theories	13
2.2.2.2. Goldschmidt's radius ratio criterion	14
2.2.2.3. Zachariassen's random network theory	15
2.2.2.4. Dietzel and field strength	17
2.2.3. Kinetic theory of glass formation	18
2.3. Tellurite glasses	20
2.3.1. Early studies	20
2.3.2. Structure	23
2.3.2.1. TeO <sub>2</sub>	24
2.3.2.2. TeO <sub>2</sub> -ZnO	26
2.3.2.3. TeO <sub>2</sub> -Na <sub>2</sub> O	29
2.3.2.4. TeO <sub>2</sub> -ZnF <sub>2</sub>	32
2.4. Impact of fibreoptics	33
2.4.1. Infrared fibreoptics and potential applications	36
2.4.2. Optical loss mechanisms	38
2.4.3. Non-linear properties	42
2.5. Tellurite and fluorotellurite glasses for infrared (IR) waveguide applications	45
2.5.1. TeO <sub>2</sub> -ZnO-Na <sub>2</sub> O (TZN) glasses	45
2.5.1.1. Optical, mechanical and thermal properties	45
2.5.1.2. Er <sup>+3</sup> -doping of TZN glasses	53
2.5.2. Fluorotellurite glasses	55
2.5.2.1. TeO <sub>2</sub> -ZnF <sub>2</sub> glasses reported in the literature	56
2.5.2.2. Thermal properties	57
2.5.2.3. Optical properties	58
2.5.2.4. Mechanical properties	60
2.6. References	60
<b>3. Glass batching &amp; melting</b>	<b>66</b>
3.1. Glass compositions used in this study	66
3.2. Glass batching	66

3.3. Glass melting	72
3.4. Fluorination of ZnF <sub>2</sub>	78
3.5. References	80
<b>4. Thermal properties and glass stability</b>	<b>82</b>
4.1. Experimental	83
4.1.1. Method, instrumentation and theory of operation	83
4.1.1.1. DTA	83
4.1.1.2. DSC	85
4.1.2. Identification of transformations	86
4.1.3. Modelling transformation kinetics	91
4.1.4. Experimental considerations	96
4.1.5. Time-temperature-transformation (TTT) experiments	98
4.2. Results	100
4.2.1. DTA traces of oxide glasses	100
4.2.2. DTA traces of fluorotellurite glasses	104
4.3. Discussion	114
4.4. Summary	128
4.5. References	129
<b>5. Crystallisation studies</b>	<b>134</b>
5.1. Experimental	134
5.1.1. X-ray diffraction (XRD)	134
5.1.1.1. Method and instrumentation	134
5.1.1.2. Theory of operation	135
5.2. Results	139
5.2.1. XRD	139
5.2.1.1. XRD of batch materials	139
5.2.1.2. XRD of deposits from glass melting and fluorination	146
5.2.1.3. XRD of glasses which crystallised during processing and characterisation	149
5.2.1.4. Heat treated Er <sup>+3</sup> -doped compositions	152
5.3. Discussion	154
5.3.1. XRD	154
5.3.1.1. XRD of batch materials	154
5.3.1.2. XRD of deposits from glass melting and fluorination	156
5.3.1.3. XRD of glasses which crystallised during processing and characterisation	159
5.3.1.4. Heat treated Er <sup>+3</sup> -doped compositions	162
5.4. Summary	163
5.5. References	163
<b>6. Optical properties</b>	<b>165</b>
6.1. Experimental	165
6.1.1. Infrared (IR) absorption spectroscopy	165
6.1.1.1. Method and instrumentation	165
6.1.1.2. Theory of operation	166
6.1.2. Ellipsometry	180

6.1.2.1. Method and instrumentation	180
6.1.2.2. Theory of operation	180
6.2. Results	183
6.2.1. Infrared spectroscopy	183
6.2.1.1. Infrared spectroscopy of oxide tellurite glasses	183
6.2.1.2. Infrared spectroscopy of fluorotellurite glasses	202
6.2.1.3. Spectroscopy of Er <sup>+3</sup> -doped compositions	216
6.2.2. Refractive index (ellipsometry)	220
6.2.2.1. Refractive index of oxide tellurite glasses	220
6.2.2.2. Refractive index of fluorotellurite glasses	221
6.3. Discussion	223
6.3.1. Infrared spectroscopy	224
6.3.1.1. Infrared spectroscopy of oxide tellurite glasses	224
6.3.1.2. Infrared spectroscopy of fluorotellurite glasses	236
6.3.1.3. Spectroscopy of Er <sup>+3</sup> -doped compositions	240
6.3.2. Refractive index (ellipsometry)	243
6.3.2.1. Refractive index of oxide tellurite glasses	243
6.3.2.2. Refractive index of fluorotellurite glasses	243
6.4. Summary	244
6.5. References	245
<b>7. Surface properties</b>	<b>249</b>
7.1. Experimental	250
7.1.1. X-ray photoelectron spectroscopy (XPS)	250
7.1.1.1. Method and instrumentation	250
7.1.1.2. Theory of operation	252
7.1.2. Chemical and environmental durability	256
7.1.2.1. Method	256
7.1.3. Ion exchange	258
7.1.3.1. Method and instrumentation	258
7.1.3.2. Environmental scanning electron microscopy (ESEM)	259
7.2. Results	272
7.2.1. X-ray photoelectron spectroscopy (XPS)	272
7.2.1.1. XPS of ZnF <sub>2</sub> powder	272
7.2.1.2. XPS of oxide tellurite glasses	274
7.2.1.3. XPS of fluorotellurite glasses	278
7.2.2. Chemical and environmental durability	289
7.2.2.1. Durability of oxide tellurite glasses	289
7.2.2.2. Durability of fluorotellurite glasses	296
7.2.3. Ion exchange	304
7.3. Discussion	306
7.3.1. X-ray photoelectron spectroscopy (XPS)	306
7.3.1.1. XPS of ZnF <sub>2</sub> powder	306
7.3.1.2. XPS of oxide tellurite glasses	308
7.3.1.3. XPS of fluorotellurite glasses	310
7.3.2. Chemical and environmental durability	314
7.3.2.1. Durability of oxide tellurite glasses	314
7.3.2.2. Durability of fluorotellurite glasses	316
7.3.3. Ion exchange	320

7.4. Summary	326
7.5. References	327
<b>8. Fibre drawing</b>	<b>330</b>
8.1. Experimental	330
8.1.1. Thermal mechanical analysis (TMA)	330
8.1.2. Preform manufacture	332
8.1.3. Fibre drawing	335
8.1.4. Optical loss measurements – cut-back method	338
8.2. Results	339
8.2.1. Viscosity (TMA)	339
8.2.3. Crystals in drawn fibre	341
8.2.4. Optical loss of fluorotellurite fibre	352
8.3. Discussion	353
8.3.1. Stress in a proposed core / clad pair	353
8.3.2. Viscosity (TMA)	355
8.3.3. ESEM of crystallised fibre	360
8.3.4. Optical loss of fluorotellurite fibre	367
8.4. Summary	371
8.5. References	372
<b>9. Conclusions</b>	<b>375</b>
9.1. Thermal properties and glass stability (Chapter 4)	375
9.2. Crystallisation studies (Chapter 5)	377
9.3. Optical properties (Chapter 6)	380
9.4. Surface properties (Chapter 6)	384
9.5. Fibre drawing (Chapter 7)	388
9.6. Overall conclusions and recommendations	390
9.7. References	391
<b>10. Future work</b>	<b>393</b>
10.1. References	397

## Glossary

- $a_M$  = partial refractivity of component  $M_mO_n$   
 $A$  = materials constant (viscosity and optical loss)  
 $[A]$  = concentration of acid / alkali species  $A$  in solution  
 $AES$  = Auger electron spectroscopy  
 $\alpha$  = absorption coefficient
- $B$  = materials constant (viscosity)  
 $BE$  = binding energy  
 $BO$  = bridging oxygen  
 $BSE$  = Backscattered electron  
 $\beta$  = isothermal compressibility
- $c$  = velocity of light in a vacuum ( $2.998 \times 10^8 \text{ m.s}^{-1}$ )  
 $C$  = materials constant (viscosity and optical loss)  
 $CCD$  = charge coupled device  
 $CG$  = Cohen-Grest (viscosity model)  
 $CN$  = coordination number  
 $C_0$  = current of electron beam leaving tungsten filament in SEM  
 $C_I$  = current of electron beam striking sample surface in SEM  
 $C_p$  = molar heat capacity at constant temperature  
 $cps$  = counts per second  
 $CRT$  = cathode ray tube  
 $\chi_n$  =  $n^{\text{th}}$  order non-linear susceptibility
- $d$  = atomic plane  $d$ -spacing used in XRD  
 $d_f$  = optical fibre diameter  
 $d_n$  = nearest neighbour bond length  
 $D$  = diffusion coefficient  
 $\overline{D}_e$  = dissociation energy of a molecule  
 $DOF$  = depth of field in SEM  
 $DSC$  = differential scanning calorimetry  
 $DTA$  = differential thermal analysis  
 $DTGS$  = deuterated triglycine sulphate  
 $\delta$  = phase difference  
 $\Delta$  = related to phase of reflected light in ellipsometry calculation
- $e$  = charge of electron ( $1.602 \times 10^{-19} \text{ C}$ )  
 $E$  = energy  
 $\mathbf{E}$  = electromagnetic field strength  
 $E_0$  = ground energy state of molecule  
 $E_a$  = activation energy  
 $E_B$  = binding energy of an electron  
 $E_d$  = depth of potential well  
 $EDFA$  = erbium doped fibre amplifier  
 $EDX$  = energy dispersive X-ray (analysis)  
 $E_g$  = electronic band gap energy  
 $E_{kin}$  = kinetic energy of an ejected electron  
 $EM$  = electromagnetic  
 $EMI$  = electromagnetic interference  
 $E_p$  = potential energy  
 $erf$  = error function  
 $erfc$  = complimentary error function  
 $E_s$  = Sellmeier gap energy

$E_v$  = energy of quantum level  $v$

*ESEM* = environmental *SEM*

$E_\eta$  = activation energy for viscous flow

$\varepsilon$  = extinction coefficient

$\varepsilon_0$  = dielectric permeability

$f$  = frequency

$f_c$  = threshold frequency for ejection of photoelectrons

$\tilde{f}$  = wavenumber

$F$  = force

*FOG* = fibre-on-glass<sup>1</sup>

$F_s$  = cation field strength

$F_t$  = fraction of glass crystallised

*FTIR* = Fourier transform infrared (spectroscopy)

$\phi$  = angle

$\gamma$  = absorbance

$\Gamma$  = work function

$h$  = Planck's constant ( $6.62608 \times 10^{-34}$  J.s)

$H$  = enthalpy

*hkl* = Miller indices

*HMO* = heavy metal oxide

$h_s$  = sample height

$H_v$  = Vicker's hardness

$\eta$  = viscosity

$\eta_n$  = kinetic energy dependent spectrometer transmission of species  $n$  in XPS

$i$  = crystal nucleation frequency

$I$  = intensity

$I_0$  = initial intensity

$I_{n\sigma}$  = intensity of  $n^{\text{th}}$  harmonic

$I_n$  = area of XPS peak of species  $n$

*IR* = infrared

$j$  = electron angular momentum

$[J]$  = molar concentration of absorbing species  $J$

*JCPDS* = Joint Committee on Powder Diffraction Standards

$\varphi$  = transmittance

$k$  = bond force constant

$k$  = Boltzmann's constant ( $1.38 \times 10^{-23}$  J.K<sup>-1</sup>)

$k_0$  = pre-exponential crystallisation rate constant

$K_b$  = bulk modulus

$k_c$  = crystallisation rate constant

$k_e$  = anharmonic force constant

$k_{tc}$  = thermal conductivity

$K_H$  = Hurby's thermal stability parameter

$K_I$  = stress intensity factor

$\kappa$  = curvature of bottom of potential well

$\kappa_d$  = thermal diffusivity

$l$  = length

---

<sup>1</sup> Idea conceived by Prof. P. Sewell, School of Electrical and Electronic Engineering, Nottingham University

$\lambda$  = wavelength

$\lambda_n$  = the mean free-path in species  $n$

$A$  = optical basicity

$m$  = crystallisation mechanism constant

$M$  = cation

$MCA$  = multi-channel analyser

$m_g$  = *SEM* magnification

$ML$  = Macedo-Litovitz (viscosity model)

$\mu$  = reduced mass of bonding atoms

$\mu_p$  = Poisson's ratio

$n$  = linear refractive index

$n_2$  = non-linear refractive index

$N$  = exchanged ion concentration

$N_0$  = surface exchanged ion concentration

$NA$  = numerical aperture of waveguide

$NBO$  = non-bridging oxygen

$n_{cl}$  = refractive index of optical fibre cladding

$n_{co}$  = refractive index of optical fibre core

$NIST$  = National Institute of Standards and Technology

$N_M$  = number of atoms of  $M$  per atom of oxygen

$NMR$  = nuclear magnetic resonance

$p$  = average photoelastic constant

$P$  = induced polarisation / dipole

$PLA$  = pressure limiting aperture

$PS$  = pixel size in *SEM*

$\pi_{ion}$  = electronic polarisability of cation

$q$  = distance between bonding atoms  $\pm r_e$

$Q_m^n$  = structural unit  $Q$ , with  $m$  oxygens, bonded to a central cation,  $n$  of which oxygens are bridging

$\theta$  = critical angle for total internal reflection ( $2\theta$  angle used in XRD for miller indices reflections of crystal)

$r$  = radius

$R$  = gas constant ( $8.314 \text{ J.K}^{-1} \text{ mol}^{-1}$ )

$r_{co}$  = radius of optical fibre core

$r_{of}$  = outer radius of optical fibre

$R_f$  = Fresnel reflection coefficient

$R_p$  = Fresnel reflection coefficient of  $p$  polarised light

$R_s$  = Fresnel reflection coefficient of  $s$  polarised light

$\rho$  = density

$r_a$  = anion radius

$RAM$  = relative atomic mass

$RAP$  = reactive atmosphere processing

$r_{b-s}$  = Bragg-Slater radius

$r_c$  = cation radius

$r_{cov}$  = covalent radius

$r_e$  = equilibrium radius between two bonding atoms

$r_{ion}$  = ionic radius

$RMM$  = relative molecular mass

$r_{vdw}$  = Van der Waals radius

$\rho$  = density

- $SD$  = standard deviation  
 $SE$  = secondary electron  
 $SEM$  = scanning electron microscopy  
 $\sigma$  = stress  
 $\sigma_n$  = photoelectric cross-section of species  $n$
- $t$  = time  
 $T$  = temperature  
 $T_0$  = temperature parameter for viscosity modelling  
 $tbp$  = trigonal bipyramid  
 $T_c$  = peak crystallisation temperature  
 $TEC$  = thermal expansion coefficient  
 $TEM$  = transmission electron microscope  
 $T_f$  = fictive temperature  
 $T_g$  = glass transition temperature  
 $T_l$  = liquidus temperature  
 $T_m$  = melting temperature  
 $TMA$  = thermal mechanical analysis  
 $t_n$  = time on the TTT nose  
 $T_n$  = corresponding temperature to  $t_n$  on the TTT nose  
 $T_{nd}$  = preform neck down temperature  
 $tp$  = trigonal pyramid  
 $T_s$  = solidus temperature  
 $T_{ss}$  = steady state fibre drawing temperature  
 $TTT$  = time-temperature-transformation (diagram / plot)  
 $T_x$  = onset of crystallisation temperature  
 $TZN$  =  $TeO_2$ - $Na_2O$ - $ZnO$   
 $T_\eta$  = temperature corresponding to a viscosity of  $10^{4.5}$  Pa.s  
 $\tau_c$  = cation valence
- $u$  = crystal growth rate  
 $UV$  = ultraviolet  
 $v$  = quantum number
- $v$  = crack velocity  
 $V$  = volume  
 $V_A$  = volume of acid / alkali species in solution  
 $V_{total}$  = total volume of acid / alkali solution  
 $V_{dws}$  = volume of distilled water in an acid / alkali solution  
 $V_0$  = volume of glass containing 1 g.atom of oxygen  
 $VFT$  = Vogel-Fulcher-Tamman (viscosity model)  
 $\omega$  = fundamental frequency
- $W_d$  = working distance in SEM  
 $WDM$  = wavelength division multiplexing  
 $\omega$  = angular frequency
- $x$  = depth  
 $XRD$  = X-ray diffraction  
 $XRF$  = X-ray fluorescence  
 $XPS$  = X-ray photoelectron spectroscopy
- $Y$  = Young's modulus

$\Psi$  = complex dielectric function relating to the ellipticity of reflected light in ellipsometry calculation

$Z$  = atomic number

$\zeta_n$  = fraction of photoelectric events which take place without intrinsic plasmon excitation in species  $n$

# 1. Introduction

## 1.1. Fibreoptic technology

The idea of guiding light, confined within a medium of higher refractive index than air (e.g. water, glass rods), or contained in reflective pipes, has existed since the 1800s [1, 2]. The major breakthrough came in the 1950s, when silica ( $\text{SiO}_2$ ) glass fibre was clad with a lower refractive index glass, guiding launched light by total internal reflection [3]. A large number of these fibres bundled together coherently (arranged in identical positions relative to one another where light enters and leaves the fibre) were shown to transmit an image; incoherently arranged fibres could be used to deliver light [2].

Early fibres absorbed a large proportion of the light which was launched into them, with only around 1 % remaining after 20 m (attenuation or loss of  $1 \text{ dB.m}^{-1}$ ). In 1966, Kao and Hockman published their seminal paper suggesting that most of this loss was extrinsic [4, 5], which should be eliminated by careful processing, to around 10 % transmission over 500 m ( $0.02 \text{ dB.m}^{-1} \equiv 20 \text{ dB.km}^{-1}$ ). This prediction was conservative, as in 1979 10 % transmission was demonstrated over 50 km ( $0.02 \text{ dB.km}^{-1}$ ) in laboratory experiments [2], and now in commercial systems attenuation in the field is  $\approx 0.18 \text{ dB.km}^{-1}$ , with spacing of amplifiers  $\approx 200 \text{ km}$  [6]. Significantly, the first laser was demonstrated in 1960 [7], and these are an intrinsic part of commercial systems.

Fibreoptic communication systems have proved advantageous over other methods of sending and receiving electromagnetic (EM) radiation for a number of reasons. Electronic

communication systems operate by passing electrons through wires. Microwave ( $\lambda \approx 10^{-4}$  to  $10^{-1}$  m) and radio ( $\lambda \approx 10^{-1}$  to  $10^3$  m) systems function by sending EM waves through open space, including satellite systems, and fibreoptic systems by the transmission of light ( $\lambda \approx 10^{-8}$  to  $10^{-3}$  m) through transparent materials. The final application probably determines the choice of medium for a communications system [2]. For example, radio-frequency appears suited for non-directional transmission, such as radio, but for a cellular-phone network, local airborne systems are most appropriate. For physical links between two or more fixed points, such as telephone and cable television, cable systems are appropriate.

The separate types of systems have very different data carrying characteristics and physical utility. The capacity a cable can carry (data transfer rate or bandwidth, measured in  $\text{Mbit.s}^{-1}$ ), and the distance the information must go, and hence loss, are the most important considerations. Simple metal wiring can carry a low speed signal; coaxial cable can carry high speed signals over short distances, however optical fibre can carry data at high speeds over long distances. Transatlantic fibreoptic links have around 100 times the capacity of coaxial cables [2]. Optical fibre systems have the advantage of not being affected by electromagnetic interference (EMI), and hence the signal cannot be eavesdropped, important for secure links. Optical fibres are also flexible, light, and small, compared to coaxial cable [2].

Focussing now on fibreoptic telecommunications systems, their operation wavelengths are defined by residual impurity hydroxyl (OH) which manifest as extrinsic absorption bands in the transparent window of the silica glass optical fibre. The first short, low speed systems used GaAs / GaAlAs sources emitting in the 750 to 900 nm region. Long

distance systems operate at 1.3 and 1.55  $\mu\text{m}$  using InGaAsP sources, where losses and pulse dispersion are lowered. 1.55  $\mu\text{m}$  operation can incorporate all optical amplifiers; erbium doped fibre amplifiers (EDFAs), with erbium (III) -  $\text{Er}^{+3}$ , doped into the silica glass [2]. These are fast, and the signal no longer has to be transduced to electronics for amplification (hence all optical). EDFAs can transmit data at  $2.4 \text{ Gbit.s}^{-1}$  over a distance of 21,000 km [8], with efficiencies around  $50,000 \text{ Gbit.km.s}^{-1}$  [9], without the need for a repeater, and performance of these devices has since increased further due to wavelength division multiplexing (WDM) [6]. WDM currently allows the simultaneous transmission of around 100 different wavelengths along one fibre, to increase signal capacity, and is at present limited by the flatness of gain of the EDFA.

## **1.2. The role of novel glass compositions**

Novel glass compositions made from constituents other than  $\text{SiO}_2$ , such as fluorides, chalcogenides, and heavy-metal oxides, are more optically flexible than silica, having a wide range of transparent windows, linear and non-linear refractive indices, and lower phonon energies, for more efficient rare-earth luminescence [10]. This lower phonon energy than silica, results in substantially increased rare-earth lifetimes in the glass host (and possibly shifted and broadened emission bands), as de-population of excited states is statistically less likely by non-radiative processes. Rare-earth solubility is often higher in novel glass hosts [11]. These are important considerations for developing the next generation of low loss broadband, flat gain fibre amplifiers.

Infrared transmission is useful for spectroscopic sensing of chemicals / organic groups, whose fundamental absorption bands occur in the mid-IR region. Bandwidth, and hence information carrying capacity is maximised at zero dispersion ( $d^2n/d\lambda^2=0$ , occurring at 1.3  $\mu\text{m}$  for silica, and at longer wavelengths for infrared transmitting materials), and intrinsic scattering losses fall with increasing wavelength [10].

A high linear refractive index generally results in higher non-linearity than silica, with the possibility for use in high-speed switching and high power delivery devices. Glasses with an induced second-order non-linearity can be used for second harmonic generation. The third-order non-linearity can be utilised in devices to boost the transmitted signal with solitons, and the bandwidth increased with all-optical processing [12]. Raman amplification is another way of amplifying the signal carried by the fibre, and is an intrinsic non-linear property of the material. Novel glasses have been shown to exhibit Raman gain much higher than silica [13].

### **1.3. Aims and objectives of this study**

The glasses studied here, tellurite and fluorotellurite ( $\text{TeO}_2$ -based), exhibit many of the desirable properties listed in section 1.2, and therefore show potential in a number of devices and applications. However, there is not much published work to date, particularly on fluorotellurite glasses. Useful properties include transmission from the visible (400 nm) to the mid-IR (6  $\mu\text{m}$ ) [11], high refractive index ( $\approx 2$ , compared to  $\approx 1.5$  of silica [14]), large non-linearity (non-linear refractive index two orders of magnitude greater than silica [12]), with broad, long erbium (III) lifetimes [15], and Raman gain around 30

times that of silica [13]. The performance of these materials in any device will be affected by the optical loss of the glass due to extrinsic factors. As these novel compositions cannot be prepared by vapour deposition routes [16], extrinsic absorption losses must be reduced using more conventional methods.

The processing (melting and fibre drawing), thermal, optical, and surface properties of these glasses were studied here. Therefore, the overall aim of this study was to investigate suitable compositions and processing routes of tellurite and fluorotellurite glasses for future passive and active photonic devices and applications. The objectives were to:

- Characterise the properties of suitable tellurite and fluorotellurite glass compositions for preform making and fibre drawing. Properties to include:
  - characteristic temperatures,
  - viscosity-temperature behaviour,
  - thermal expansion coefficients,
  - chemical durability, and
  - refractive indices.
- Optimise the processing routes of glass preforms and fibre, to minimise extrinsic losses, particularly OH.
- Fabricate suitable glasses into preforms and fibre, and characterise the fibre.

## 1.4. Thesis structure

A literature review (chapter 2) will follow this introductory section, outlining tellurite and fluorotellurite glass research most relevant to the compositions studied here. Background to glass formation, and optical loss mechanisms will also be discussed. Chapters 3 to 8, inclusively, individually containing experimental, results, discussion, and summary sections based on the work undertaken. Chapter 3 will detail the glass batching and melting procedures used, with a tabulated list of all compositions studied. Chapter 4 looks at the characteristic temperatures of these glasses, obtained by differential thermal analysis (DTA). Crystal structure of batch materials, products of melting, and devitrified glasses were then examined, using X-ray diffraction (XRD), presented in chapter 5. The infrared spectra and refractive indices of a number of compositions are then evaluated in chapter 6, by FTIR- spectroscopy, and ellipsometry respectively. Chapter 7 shows some of the surface properties of the tellurite and fluorotellurite glasses: X-ray photoelectron spectroscopy (XPS), chemical and environmental durability, and ion-exchange. Finally chapter 8 presents the optical fibre drawing process, viscosity-temperature behaviour, defects in the fibres, and fibre loss, measured by cut-back. The conclusions chapter (9) summarises the main points from chapters 3 to 8 inclusive, and the thesis ends with future work (chapter 10). References will be listed at the end of each chapter.

## 1.5. References

- [1] J. Tyndall, *Notes of a course of nine lectures on Light, delivered at the Royal Institution of Great Britain, April 8-June 3, 1869*. London: Longmans, Green and Co., 1870.
- [2] J. Hecht, *Understanding fiber optics*, 2nd ed. Indianapolis: Sams Publishing, 1993.
- [3] A. C. S. van Heel, "A new method of transporting optical images without aberrations," *Nature*, vol. 173, pp. 39, 1954.
- [4] K. C. Kao and G. A. Hockman, "Dielectric-fibre surface waveguides for optical frequencies," *Proceedings of the IEE*, vol. 113, pp. 1151-1158, 1966.
- [5] C. K. Kao, *Optical fibre*. London: Peter Peregrinus Ltd., 1988.
- [6] L. Solymar and D. Walsh, *Electrical properties of materials*, 6th ed. Oxford: Oxford University Press, 1998.
- [7] T. H. Maiman, "Stimulated optical radiation in ruby," *Nature*, vol. 187, pp. 493-494, 1960.
- [8] N. S. Bergano, J. Aspell, C. R. Davidson, P. R. Trischitta, B. M. Nyman, and F. W. Kerfoot, "Feasibility demonstration of transoceanic EDFA transmission," *Proceedings of SPIE*, vol. 1581, pp. 182-187, 1995.
- [9] M. Suyamaa, H. Iwatab, N. Shimojohc, S. Harasawaa, and T. Naitoc, "Transoceanic WDM system with more than 100 Gb/s capacity," *Optical Fiber Technology*, vol. 3, pp. 309-319, 1997.
- [10] J. M. Parker and A. B. Seddon, "Infrared-transmitting optical fibres," in *High-Performance Glasses*, M. Cable and J. M. Parker, Eds. London: Blackie, 1992, pp. 252-286.
- [11] J. Wang, E. Vogel, and E. Snitzer, "Tellurite glass: a new candidate for fiber devices," *Optical Materials*, vol. 3, pp. 187-203, 1994.
- [12] J. S. Aitchison, J. D. Prohaska, and E. M. Vogel, "The nonlinear optical properties of glass," *Metals Materials and Processes*, vol. 8, pp. 277-290, 1997.
- [13] R. Stegeman, L. Jankovic, H. Kim, C. Rivero, G. Stegeman, K. Richardson, and P. Delfyett, "Tellurite glasses with peak absolute Raman gain coefficients up to 30 times that of fused silica," *Optics Letters*, vol. 28, pp. 1126-1128, 2003.

- [14] J. E. Shelby, *Introduction to glass science and technology*. Cambridge: RSC Paperbacks, 1997.
- [15] S. Shen, A. Jha, E. Zhang, and S. J. Wilson, "Compositional effects and spectroscopy of rare earths ( $\text{Er}^{3+}$ ,  $\text{Tm}^{3+}$ , and  $\text{Nd}^{3+}$ ) in tellurite glasses," *Comptes Rendus Chimie*, vol. 5, pp. 921-938, 2002.
- [16] W. Vogel, *Glass chemistry*, 2nd ed. New York: Springer-Verlag, 1994.

## **2. Literature review**

In this chapter, the main points relating to the glasses studied here (tellurite and flurotellurite) will be outlined. It will begin with a brief outline of the glass transition, then the general theories, structural and kinetic, of glass formation will be summarised. Important results from early studies on tellurite glasses will subsequently be reviewed, followed by the structure of tellurite glasses. Finally, the impact of fibre optics will be presented, concluding with research in that area on tellurite and fluorotellurite glasses.

### **2.1. The nature of glass**

#### **2.1.1. Behaviour of ‘typical’ glass-forming materials on melt-cooling**

Many inorganic elements and compounds (e.g. Zn, LiCl, Fe, CdBr<sub>2</sub> and Na) melt to form liquids with a viscosity of the order of magnitude as water ( $\approx 10^{-4}$  to  $10^{-3}$  Pa.s) [1]. When these types of liquids are cooled, rapid crystallisation occurs at the melting point. Even when the cooling is fast, in general, crystallisation cannot be avoided. In some cases, small droplets of these types of materials may be supercooled far below the freezing point, but cooling cannot be carried out indefinitely without crystallisation occurring, although theoretically any liquid can be cooled to form a glass if quenching is rapid enough. However, a number of materials exist which melt to form very viscous liquids, of the order of  $\approx 10^4$  to  $10^6$  Pa.s (e.g. SiO<sub>2</sub>, BeF<sub>2</sub>, B<sub>2</sub>O<sub>3</sub>, As<sub>2</sub>O<sub>3</sub>, P<sub>2</sub>O<sub>5</sub>, and GeO<sub>2</sub>) [1]. If

one of these liquids is held at a temperature just below the freezing point, it will slowly crystallise, as the crystalline form is thermodynamically more stable than the liquid state. However, if the liquid is continuously cooled from above the freezing point, crystallisation may, or may not occur, depending on the rate of cooling<sup>1</sup>. If the rate of cooling is slow, the material will more than likely crystallise to some extent, but at high cooling rates, it is possible to avoid crystallisation altogether. During this cooling process, the viscosity of the liquid increases to such a degree that atomic rearrangement becomes difficult and the material has become a solid without long-range periodic order, but with a structure closer to the liquid state. This metastable solid is called a glass. This phenomena is not limited to inorganic materials, there are many examples of organic glasses, and glasses do not necessarily have to be formed from rapid melt cooling; sol-gel glasses are prepared using organic-precursors and heat treated at conditions close to ambient. The relatively recent achievement of cooling rates of the order of  $10^6$  K.sec.<sup>-1</sup> and greater has resulted in the formation of low volume wires or ribbons of glasses formed from very fluid metal melts, i.e. metallic glasses [2].

A better appreciation of the relationship between the liquid, crystalline and glassy forms of a material from melt-cooling can be gained by considering the volume-temperature relationship of a glass-forming substance as shown in fig. (2.1) [1].

---

<sup>1</sup> It is possible to form glass relatively easily from some systems, such as fluorozirconates (e.g. ZBLAN), which have viscosities of the order of water ( $\approx 10^{-2}$  Pa.s) at their melting points; this phenomenon will be addressed in section 2.2.3, on the kinetic theory of glass formation.

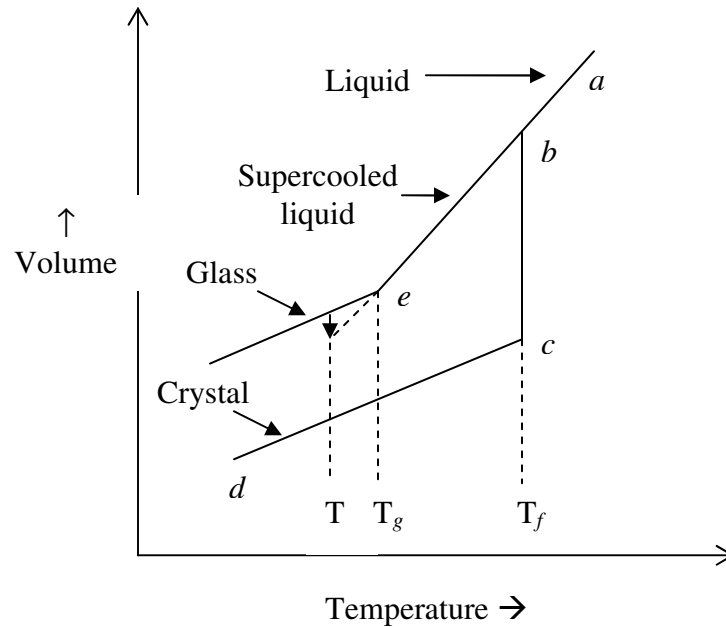


Fig. (2.1): Variation in volume with temperature for a glassy and crystalline solid [1].

On cooling from the melt along the line  $ab$ , the volume of the liquid decreases at a steady rate. If cooling is slow enough and nuclei are present in the melt, the liquid will crystallise at temperature  $T_f$ , with an abrupt change in volume represented by the line  $bc$ . When cooled further the crystalline material contracts along the line  $cd$ . However, if the rate of cooling is high enough, crystallisation does not occur at  $T_f$ , and the volume of the supercooled liquid decreases along  $be$ , which is a continuation of  $ab$ . At the temperature,  $T_g$ , the glass transition temperature, the volume-temperature curve undergoes a change in gradient and continues almost parallel to the curve of the crystalline form of the material. Only below  $T_g$  is it correct to describe the material as a glass, and at this point the viscosity is extremely high,  $\approx 10^{12}$  Pa.s. Between  $T_g$  and  $T_f$  (line  $be$ ) the material is a supercooled liquid. If the glass is held at temperature  $T$ , just below  $T_g$ , the volume will decrease along the vertical arrow, until it reaches a point which is a continuation of the

supercooled liquid contraction line, *be*. Other properties of the glass also change with time in the region of the glass-transition temperature, a process known as ‘stabilisation’. Above  $T_g$ , no such time-dependent changes are observed as the supercooled liquid cannot reach a more stable state without crystallising. A glass on the other hand, at a temperature well below  $T_g$  could theoretically achieve a more stable (glassy) state, given long enough. Due to these stabilisation effects, the properties of glasses depend to a certain degree on the rate of cooling, particularly in the temperature range near  $T_g$ . The exact value of  $T_g$  depends on the rate of cooling (being higher, the higher the rate of cooling used) [1].

## **2.2. The structure of glass**

### **2.2.1. Atomic structure**

The discontinuity on cooling which occurs at  $T_g$  (see point e on fig. (2.1)) is related to the failure of the material to adjust itself to the changing temperature, i.e. crystallise. Therefore, it would be expected to find a similar structure between the liquid and glassy forms of a material. X-ray diffraction (XRD) patterns of the glassy and liquid states show broad diffuse diffraction rings (or an amorphous ‘halo’) at approximately the same positions. This is in contrast to the sharply defined rings characteristic of the crystalline form. This is due to the lack of long range periodic order in the glass and liquid, as opposed to the systematic repetition over (relatively) long distances of atoms in unit cells found in crystals. Crystalline materials, when finely divided also show broad diffuse XRD patterns, which led Randall *et al.* [3] to believe glasses consisted of a random

structure of tiny ‘crystallites’. However, if this were the case the crystallites would be approximately the size of a unit cell (of the order  $1 \text{ \AA} \rightarrow 10^{-10} \text{ m}$ ), and on this scale the idea of crystallinity has little meaning [4].

## **2.2.2. Structural theories of glass formation**

Various theories have been proposed as to how the arrangement of atoms in space, and the nature of the bonds between the atoms are related to glass formation, known as the structural theories of glass formation. The kinetic theory of glass formation, which disregards any structural factors and deals only with the kinetic of crystallisation below the melting temperature, is also an important consideration (see section 2.2.3). Both theories are important when trying to understand the phenomena of glass formation, and a satisfactory explanation is not possible by considering either alone.

### **2.2.2.1. Early structural theories**

Tammann first investigated the constitution of glasses and regarded them as strongly undercooled liquids, which to a certain extent agreed with later XRD interpretations. This general theory of a ‘frozen-in’ liquid-type structure was fairly general, but a good start for the future direction of thinking [2].

### 2.2.2.2. Goldschmidt's radius ratio criterion

Goldschmidt's theory as to the structure of inorganic oxide glasses in 1926 led to the development of all other modern structural theories of glass formation [1]. Goldschmidt, who is also considered the father of modern crystal chemistry, derived empirical rules for glass formation [2]. His general observation was: for a simple oxide of formula  $M_mO_n$  ( $M \rightarrow$  cation), that glass formation is only possible when the ratio of atomic radii,  $r_a/r_c$  (where  $c$  denotes cation, and  $a$  anion), falls between 0.2 to 0.4 [1]. This condition is met for oxides  $SiO_2$ ,  $B_2O_3$  and  $P_2O_5$ . Later, after publication of this theory, it was also found glass-formers  $GeO_2$  and  $BeF_2$  (if F is substituted for O) also satisfied the criterion [2].

In crystal chemistry, the cation / anion ratio determines how many anions can be packed around a given cation, i.e. the co-ordination number of the compound. Most crystals with a cation / anion radius ratio of 0.2 to 0.4 have a co-ordination number (CN) of 4 with anions at the corners of a tetrahedron. Therefore Goldschmidt was led to believe that tetrahedral arrangement of oxygen ions around a cation  $M$  was necessary for glass formation [1]. It is important to note once again that these observations were purely empirical, and no attempt was made to try and explain why this should be so. Also, by considering the radius ratio of the ions and co-ordination number, it is assumed the oxide is purely ionic. This is not strictly correct as many glass-forming oxides have covalent character (e.g.  $SiO_2$ ), which must be kept in mind [1].

### 2.2.2.3. Zachariasen's random network theory

Zachariasen did not agree with the crystallite theory proposed by Randall *et al.* [5] as assumptions in the theory<sup>2</sup> led to discrepancies between observed and calculated densities of silica glass. Diffraction patterns and thermal properties observed were also not in accordance [6].

Over large temperature ranges the mechanical properties of glasses are comparable (superior in some cases) to those of crystalline materials. Because of this Zachariasen proposed that the forces in glasses are essentially the same as those in a crystal, with atoms oscillating about definite equilibrium positions forming an extended three-dimensional network [6]. X-ray diffraction data had shown this network was not periodic and symmetrical, but not entirely random, as inter-nuclear distances do not fall below a minimum value. Therefore, all inter-nuclear distances are not equally probable which results in the diffraction patterns seen [6].

It can be said that the glass network is characterized by an infinitely large unit cell containing an infinite number of atoms. Due to a lack of periodicity, no two atoms are structurally equivalent [6]. The isotropic nature of glass is a direct consequence of this lack of symmetry, as the atomic arrangement is statistically equivalent in all dimensions. As all atoms are not structurally equivalent, the energy needed to detach an atom from the network will be different for each atom. This means with increasing temperature an increasing number of detached atoms would be expected, so the network breaks down continuously, as opposed to a crystalline material where the breakdown is an abrupt

---

<sup>2</sup> These assumptions were: (i) the average linear dimensions of the cristobalite crystallites were of the order of 15Å, and (ii) lattice constants were 6.6% larger than in cristobalite crystals.

phenomenon [6]. As a result of this the supercooled liquid  $\leftrightarrow$  glass transition occurs over a range of temperatures.

Zachariasen outlined a set of 'rules' for glass formation from compounds such as  $\text{SiO}_2$ ,  $\text{B}_2\text{O}_3$ ,  $\text{P}_2\text{O}_5$ ,  $\text{GeO}_2$ ,  $\text{As}_2\text{S}_3$ , and  $\text{BeF}_2$  [2]:

- The compound will tend to form a glass if it easily forms polyhedral units as the smallest structural units.
- Polyhedra should not share more than one corner.
- Anions ( $\text{O}^{2-}$ ,  $\text{S}^{2-}$ ,  $\text{F}^-$ ) should not link more than two central cations of the polyhedra.
- The number of corners of the polyhedra must be less than six.
- At least three corners of the polyhedra must link with other polyhedra.

Cations in the glass were categorised by Zachariasen according to their role in the glass network [2].

- Network-formers:  $\text{Si}^{4+}$ ,  $\text{B}^{3+}$ ,  $\text{P}^{5+}$ ,  $\text{Ge}^{4+}$ ,  $\text{As}^{3+}$ ,  $\text{Be}^{2+}$ , with CN of 3 or 4.
- Network-modifiers:  $\text{Na}^+$ ,  $\text{K}^+$ ,  $\text{Ca}^{2+}$ ,  $\text{Ba}^{2+}$ , with  $\text{CN} \geq 6$ .
- Intermediates, which may reinforce ( $\text{CN} = 4$ ) or loosen the network further ( $\text{CN} 6$  to 8).

The Zachariasen random network theory can be used to explain many properties of conventional glasses, such as viscosity-temperature behaviour, and electrical

conductivity. However, it cannot explain all phenomena, such as property effects thought to be due to short range ordering, and the glass formation in some novel systems also contradict the criteria of this theory. The kinetic theory of glass formation provides a more satisfactory explanation of glass formation of known systems, but the structural theories are still valid and widely used [2].

#### 2.2.2.4. Dietzel and field strength

By extending Goldschmidt's original consideration of glass formation to radius and charge of the constituent atoms / ions, Dietzel classified elements according to their field strength,  $F_s$ . This considers the forces (attraction / repulsion) between cations and anions in the glass [2].

$$F_s = \frac{\tau_c}{(r_a + r_c)^2} \quad (2.1)$$

where  $\tau_c$  is the valence of the cation,  $r$  the ionic radius of the cation (c) or anion (a). Using Zachariassen's classification, ions can be categorised into three field strength groups,  $F_s = 0.1$  to  $0.4$  (network modifiers),  $F_s = 0.5$  to  $1$  (intermediates), and  $F_s = 1.4$  to  $2$  (network formers) [2].

On cooling a binary melt with cations of approximately the same field strength, phase separation or crystallisation of the pure oxide phases is normally seen (e.g.  $\text{SiO}_2\text{-P}_2\text{O}_5$ ,  $\text{SiO}_2\text{-B}_2\text{O}_3$ ,  $\text{B}_2\text{O}_3\text{-P}_2\text{O}_5$ ). To form a single stable crystalline compound normally requires  $\Delta F_s > 0.3$ . As  $\Delta F_s$  increases, so does the number of possible stable compounds, and the

tendency to form a glass. For a binary system, glass formation is likely for  $\Delta F_s > 1.33$  [2]. Again, this theory can usefully categorise glass forming ability in conventional systems, but not universally.

### 2.2.3. Kinetic theory of glass formation

Glass formation has been shown in materials of a wide variety of compositional, bonding, and structural types. Therefore, considering how rapidly a vapour or liquid must be cooled to avoid a detectable volume fraction of crystallisation ( $10^{-6} \rightarrow 0.0001\%$ ) can be a useful way of characterising its glass forming ability [2]. If nucleation frequencies,  $i$  (in  $\text{s}^{-1}$ ), and growth rates,  $u$  (in  $\text{cm}\cdot\text{s}^{-1}$ ), are known as functions of temperature, equation (2.2) can be used to plot a time-temperature-transformation (TTT) diagram.

$$10^{-6} = \frac{\pi}{3} i u^3 t^4 \quad (2.2)$$

where  $it$  is the frequency of nucleation with time, and  $u^3 t^3$  the growth in three dimensions with time [2]. However, it is important to note that current theories of homogeneous nucleation in glasses are not able to predict accurately the observed homogeneous rates, and can be many orders of magnitude disparate [7]. From the measured TTT plot, it is possible to obtain the time at each temperature before a significant fraction of the undercooled melt has devitrified. These plots have a ‘nose’ shape with the temperature at the apex of the nose where crystallisation is most rapid. This nose shape arises, as the tendency for crystallisation will be initially enhanced thermodynamically on melt

cooling, reaching its peak at the apex of the nose. Below this temperature, crystallisation is suppressed due to the rising viscosity of the supercooled liquid [2].

The critical cooling rate,  $[dT/dt]_c$  to avoid 0.0001 % volume crystallisation can be approximately obtained from the TTT diagram, at any temperature on the nose,  $T_n$ , and corresponding time,  $t_n$ .

$$\left[ \frac{dT}{dt} \right]_c \approx \frac{T_l - T_n}{t_n} \quad (2.3)$$

where  $T_l$  is the liquidus temperature [2].

Heterogeneous nucleation has a strong influence on this critical cooling rate, compared to homogeneous nucleation, resulting in a  $[dT/dt]_c$  value 5 to 10 times slower for homogeneous nucleation. As the contact angle of the heterogeneous nuclei decreases, so does  $[dT/dt]_c$ . Complex compositions, and those close to eutectics can hinder nucleation processes (see below). Ideally a glass melt should have a high viscosity at  $T_l$ , or rapidly increasing below  $T_l$  on cooling [2], as seen with ‘typical’ glass formers in section 2.1.1.

However, many low viscosity melts, such fluorozirconates (ZBLAN –  $ZrF_4$ - $BaF_2$ - $LaF_3$ - $AlF_3$ - $NaF$ ), can be quenched to form a glass relatively easily. These ‘novel’ glass systems have viscosities of the order of water ( $10^{-2}$  Pa.s) around their melting temperatures. Seddon *et al.* [8] showed that the most stable ZBLAN compositions occurred at the interface between two crystalline phases on the phase diagram ( $LaF_3$ - $2ZrF_4$  and  $NaF$ - $BaF_2$ - $2ZrF_2$ ). Therefore, it is believed that in the undercooled melt,

crystallisation was suppressed due to the competition between these two phases. This idea might be extended to other novel glasses which have a low viscosity at the liquidus.

## 2.3. Tellurite glasses

### 2.3.1. Early studies

The trioxide of tellurium ( $\text{TeO}_3$ ) decomposes when heated to dull redness with the formation of the dioxide ( $\text{TeO}_2$ ). Tellurium dioxide, is a white crystalline solid which can be melted at  $733^\circ\text{C}$ , without the gain or loss of oxygen [9]. Melts of pure  $\text{TeO}_2$  do not solidify to form a glass [2], but glass formation has been shown with systems of more than 90 mol. %  $\text{TeO}_2$  (eutectic region of  $\text{TeO}_2$ -rich area of the phase diagram) and no other glass former present [2]. Since the early work of Berzelius in 1834 [10], very little was contributed to work on tellurite compounds, until Lenher *et al.* in 1913 [11] studied the chemistry of the so-named metallic tellurites, and observed that sodium di- and tetra-tellurite fuse below red heat to form a clear glass. In this work sodium tellurite was also found to be readily soluble in water (important when considering glass durability). In 1952, Stanworth [12, 13] performed the first major systematic studies on tellurite glasses on the basis  $\text{Te}^{4+}$  has an electronegativity in the range of other good glass forming oxides (1.7 to 2.1) as shown in table (2.1) with some network formers for comparison. This is known as Stanworth's electronegativity criterion [1].

Table (2.1): Electronegativities of good glass forming oxides and network modifiers [14].

Element	Pauling electronegativity
<i>Glass network formers</i>	
Te	2.1
B	2.0
Si	1.8
P	2.1
Ge	1.7
As	2.0
Sb	1.8
<i>Glass network modifiers</i>	
Li	1.0
Na	0.9
K	0.8

These glass formers bond to oxygen in the network with a substantial covalent nature, with a more or less random distribution of other atoms of lower electronegativity forming bonds to oxygen of a more ionic nature. This prediction of glass formation based on electronegativity proved useful as, according to Zachariasen rules for glass formation, cations in a good glass former should be surrounded by 3 or 4 anions and most of the anions are bonded to two cations (see section 2.2.2.3).  $\alpha$ -TeO<sub>2</sub> has a structure similar to tin oxide in which six oxygen atoms surround each cation, although two of the oxygen atoms are nearer to the cation than the other four. So the structure may be regarded a collection of TeO<sub>2</sub> groups (see the next section for a more detailed discussion of TeO<sub>2</sub> structure, and its relation to the glass network). Therefore, the Zachariasen rules would not lead one to expect easy glass formation from TeO<sub>2</sub>. Also, the radius of the Te<sup>4+</sup> ion (97 pm [15]) would appear too great for tetrahedral coordination in the pure oxide. Using equation (2.1), Dietzel's field strength, gives  $F = 0.71$  for TeO<sub>2</sub>, i.e. falling into the category of an intermediate. In spite of these unfavourable circumstances (according to

the Zachariasen and Dietzel) highly thermally stable glasses can result from tellurite systems. Stanworth [13] also predicted some tellurite glass properties from knowledge of the chemical bonding in  $\text{TeO}_2$ . Equation (2.4) can be used to roughly calculate the contribution of oxide  $\text{M}_m\text{O}_n$  to the refractive index ( $n$ ) of the glass:

$$(n - 1)V_0 = \sum a_M N_M \quad (2.4)$$

where  $a_M$  is the partial refractivity of component  $\text{M}_m\text{O}_n$ ,  $V_0$  the volume of the glass containing 1 g.atom of oxygen and  $N_M$  the number of atoms of  $M$  in the glass per atom of oxygen. Using this equation, Stanworth predicted the contribution of tellurium dioxide to the refractive index of the glass is,  $a_M \approx 1.93$  (wavelength not stated) [13]. Stanworth also predicted that tellurite glasses would have softening points well below silicates due to their much lower melting temperatures and the lower Te-O bond strength compared to Si-O. Softening points were in the range of 250 to 400°C [13].

Furthermore, Stanworth melted the first fluorotellurite glasses, based on the ternary system  $\text{TeO}_2\text{-PbO-ZnF}_2$  [14]. Glass formation was shown from 8.2 to 33.2 mol. %  $\text{ZnF}_2$ , for glasses melted in a zirconia crucible. These compositions were shown to have improved infrared transmission (extinction coefficient  $< 0.5$  from 1.5 to 5  $\mu\text{m}$ ), compared to the oxide compositions studied ( $\text{TeO}_2$  with  $\text{PbO}$ , or  $\text{BaO}$ , and one of the following:  $\text{SO}_3$ ,  $\text{Li}_2\text{O}$ ,  $\text{Na}_2\text{O}$ ,  $\text{B}_2\text{O}_3$ ,  $\text{Nb}_2\text{O}_5$ ,  $\text{P}_2\text{O}_5$ ,  $\text{MoO}_3$ ,  $\text{WO}_3$ ,  $\text{V}_2\text{O}_5$ ,  $\text{MgO}$ ,  $\text{CdO}$ ,  $\text{TiO}_2$ ,  $\text{GeO}_2$ ,  $\text{ThO}_2$ ,  $\text{Ta}_2\text{O}_5$ ,  $\text{La}_2\text{O}_3$ ). Absorption bands at around 3.2 and 4.5  $\mu\text{m}$  due to OH [16, 17] were significantly reduced with  $\text{ZnF}_2$  addition [14], due to self drying during glass melting.

Thermal expansion coefficients for these systems were 20 to  $40 \times 10^{-6} \text{ }^\circ\text{C}^{-1}$  over the 100 to  $200^\circ\text{C}$  region, and refractive indices  $> 2.1$  for  $\text{TeO}_2\text{-PbO}$  and  $\text{TeO}_2\text{-PbO-}\text{SeO}_2$  glasses (at 578 nm) [14]. All glasses were found to be durable to the laboratory atmosphere. Glasses which contained  $\text{BaO}$ ,  $\text{Na}_2\text{O}$ ,  $\text{Li}_2\text{O}$ , and  $\text{B}_2\text{O}_3$  were least durable when exposed to an atmosphere saturated with water vapour at around 50 to  $55^\circ\text{C}$ . All glasses were slightly attacked by citric acid, and sodium carbonate solution. However, heavy attack of the alkali was shown by the binary  $\text{TeO}_2\text{-PbO}$  glasses, and the ternary lead tellurite glasses containing  $\text{P}_2\text{O}_5$ ,  $\text{ZnF}_2$ ,  $\text{BaO}$ ,  $\text{Li}_2\text{O}$  and  $\text{Na}_2\text{O}$ , as well as the  $\text{TeO}_2\text{-BaO-As}_2\text{O}_5$  glass. Glasses containing d-block oxides:  $\text{MoO}_3$ ,  $\text{WO}_3$  and  $\text{Nb}_2\text{O}_5$  showed the best overall resistance to acid, alkali and water [14].

The next early study of note, by Redman *et al.* in 1967 [18], was on zinc tellurite glasses. These glasses had a Knoop hardness of around 270, much lower than silica (540). The transmission of these glasses was from around 380 nm to  $6.6 \mu\text{m}$ , with OH absorption bands at 3.35 and  $4.5 \mu\text{m}$ . Increasing  $\text{TeO}_2$  content shifted the electronic absorption edge to longer wavelengths, and good rare-earth solubility was shown (1 mol. %  $\text{Nd}_2\text{O}_3$ ), showing promise for a host glass for stimulated emission. Optical surfaces showed resistance to attack of cold water, with slight attack from boiling water and dilute acid, and strong attack from concentrated acids and dilute alkali [18].

### 2.3.2. Structure

In this section the structure of the four main constituents in the glasses studied here will be summarised:  $\text{TeO}_2$ ,  $\text{ZnO}$ ,  $\text{Na}_2\text{O}$ , and  $\text{ZnF}_2$ .

### 2.3.2.1. $\text{TeO}_2$

$\alpha$ - $\text{TeO}_2$ , or paratellurite, is tetragonal (space group  $P4_32_12$ ) [2]. Early work suggested the network in tellurite glasses consisted of strongly deformed  $[\text{TeO}_6]$  units, analogous in structure to rhombic  $\beta$ - $\text{TeO}_2$  (tellurite, space group  $Pbca$ ), where  $\text{Te}^{+4}$  is coordinated to four oxygens. Fig. (2.2) shows the crystal structure of  $\alpha$ - and  $\beta$ - $\text{TeO}_2$ .

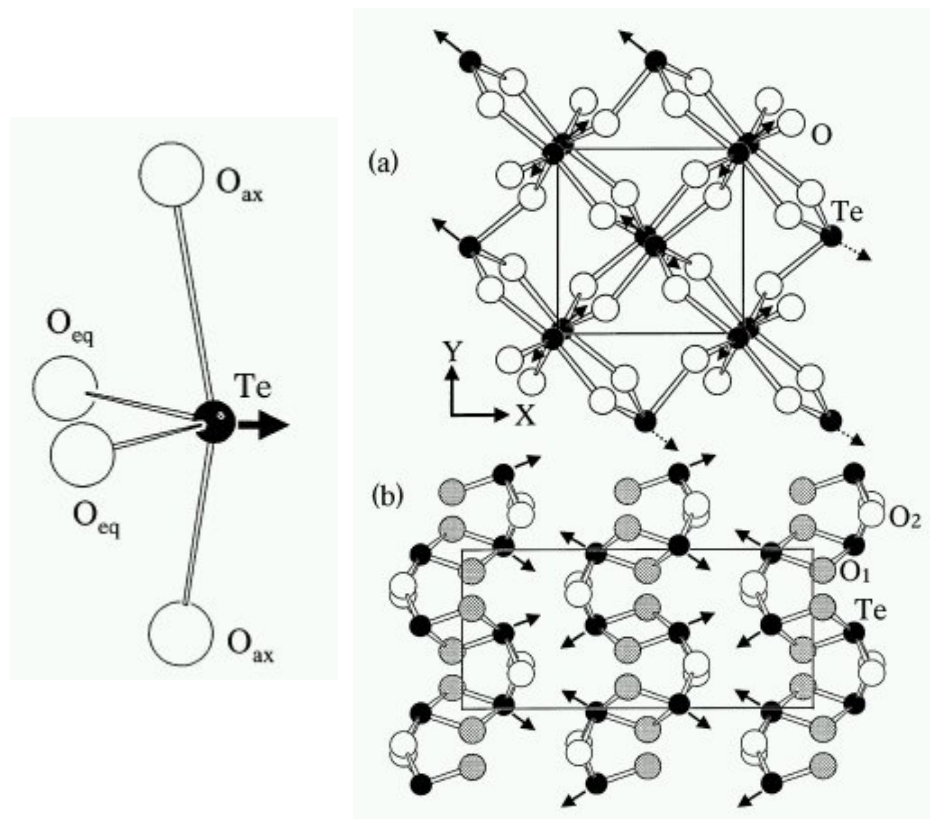


Fig. (2.2): Structure of  $\text{TeO}_2$ : (a)  $\alpha$ - $\text{TeO}_2$ , and (b)  $\beta$ - $\text{TeO}_2$  (arrows represent the Te 5s electron lone-pair) [19].

However, later work proved that in tellurite minerals and glasses, a number of polyhedra are formed, of  $\text{Te}^{+4}$  coordination: 3, 3+1 and 4. In the glasses this variety of coordination is due to the presence of network modifiers and intermediates [2]. Table (2.2) summarises

the two extreme cases of coordination in both forms of crystalline  $\text{TeO}_2$ :  $\alpha\text{-TeO}_2$  and  $\beta\text{-TeO}_2$  and coordination in tellurite glasses.

Table (2.2): Coordination of both forms of crystalline  $\text{TeO}_2$ : paratellurite ( $\alpha\text{-TeO}_2$ ) and tellurite ( $\beta\text{-TeO}_2$ ) and tellurite glasses [2].

	Coordination	Structure	Te-O bond distance / pm	Te-O-Te bond angle / °
<b>Crystal</b>	3	Trigonal pyramid (tp)	195	95
	4	Trigonal bipyramid (tbp)	200	120 ± 20 (equatorial) 180 ± 30 (axial)
<b>Glass</b>	3, 3+1 and 4	tp and tbp	209 (equatorial) 191 (axial)	92.1 ± 6.6 (equatorial) 162.6 (axial)

Recent work on the structure of tellurite glasses has concluded that the network more closely resembles paratellurite ( $\alpha\text{-TeO}_2$ ), where  $[\text{TeO}_4]$  units are only linked at their corners [2]. Combining  $\text{TeO}_2$  with network modifiers (such as  $\text{Na}_2\text{O}$ ) and intermediates (such as  $\text{ZnO}$ ) results in structural modification to chain like structures. Similar structures are seen in tellurite minerals such as zinc tellurite ( $\text{Zn}_2\text{Te}_3\text{O}_8$ ), and increase the tendency of glass formation from melt cooling [2]. However, the corner sharing structure seen in tellurite glasses would not necessarily lead to the conclusion of easy glass formation. Pauling's third rule states that the stability of ionic tetrahedra (i.e. ionic bond strength) decreases across the series: corner-sharing  $\rightarrow$  edge-sharing  $\rightarrow$  face-sharing [20]. As the distance between cations across this series decreases, the covalent interaction increases [20]. Therefore, it could be concluded that melts with a higher proportion of corner-sharing tetrahedra will have a higher viscosity (due to increased ionic interaction) than edge- and face-sharing melts. On rapid quenching, crystallisation can be avoided as viscosity will rise relatively rapidly, possibly inhibiting atomic rearrangement.

Champarnaud-Mesjard *et al.* [19, 21] have recently found evidence of  $\gamma$ - and  $\delta$ -TeO<sub>2</sub> phases in crystalline and glassy samples.  $\gamma$ -TeO<sub>2</sub> was formed by heat treating binary TeO<sub>2</sub> glasses which contain WO<sub>3</sub>, Nb<sub>2</sub>O<sub>5</sub> or PbO (5-10 mol. %). The glasses were slowly heated to 440°C and held at this temperature for 60 hours. The crystal structure of this phase was determined by XRD to be orthorhombic, space group P2<sub>1</sub>2<sub>1</sub>2<sub>1</sub>. A band at 430 cm<sup>-1</sup> in the Raman spectra of these glasses corresponded to a similar structural unit to  $\gamma$ -TeO<sub>2</sub> [21].

$\delta$ -TeO<sub>2</sub> is thought to be an intermediate phase between the crystalline and glassy state (an ‘antiglass’) [19]. This phase was formed by annealing TeO<sub>2</sub>-WO<sub>3</sub> compositions (5-10 mol. %) for 25 hours at 340°C.  $\delta$ -TeO<sub>2</sub> was determined by XRD to be a metastable fluorite-related cubic structure, space group Fm  $\bar{3}$  m [19].

### 2.3.2.2. TeO<sub>2</sub>-ZnO

The ZnO crystal structure is hexagonal, space group P6<sub>3</sub>mc, analogous to wurtzite (ZnS). Oxygen anions are hexagonally close packed (hcp) with alternate tetrahedral voids filled with zinc cations [20]. Both zinc and oxygen are four coordinated to one another, therefore the structure can be thought of as interpenetrating hcp sublattices of Zn and O [20].

Kozhukharov studied the structure of 80TeO<sub>2</sub>-20ZnO mol. % glass with neutron diffraction [22]. This study showed that the structural units in the glass ([TeO<sub>4</sub>], [TeO<sub>3</sub>] and [ZnO<sub>6</sub>]) are similar to those in  $\alpha$ -TeO<sub>2</sub>, and Zn<sub>2</sub>Te<sub>3</sub>O<sub>8</sub>, but predominantly the latter. The average coordination number of tellurium was found to be 3.35. Interatomic (Te-O,

and Zn-O) distances are also preserved in the glass from crystalline  $\alpha$ -TeO<sub>2</sub> and zinc tellurite [22]. One of the axial (Te-O<sub>ax</sub>) bonds can elongate in the [TeO<sub>4</sub>] units with second component addition due to lack of central symmetry, forming [TeO<sub>3+1</sub>]. This elongation can be so extreme, such as in K<sub>2</sub>TeO<sub>3</sub>·3H<sub>2</sub>O with three Te-O bonds of 1.85 Å and a fourth of 3.87 Å that the structural unit should be considered [TeO<sub>3</sub>]. The zinc tellurite glass was found to be composed of 35 % [TeO<sub>4</sub>], and 65 % [TeO<sub>3</sub>] / [TeO<sub>3+1</sub>] [22].

Neutron diffraction peaks > 3 Å were thought to be due to weak cation bonds (Te-Te and Te-Zn via oxygen atoms) between chains in the glass. Distances between chains were not preserved from crystalline materials on glass formation due to incorporation in between chains of [ZnO<sub>4+1+1</sub>] polyhedra [22]. These zinc structural units can link the  $\alpha$ -TeO<sub>2</sub> like chains, terminate chains, or bond onto the side of chains sitting in the channel in between chains.

ZnO enters tellurite glass network as [ZnO<sub>5</sub>] and [ZnO<sub>6</sub>] units as opposed to [ZnO<sub>4</sub>] units, which make up crystalline ZnO. This type of coordination in TeO<sub>2</sub>-ZnO containing glasses bears a closer resemblance to the structure of crystalline ZnTeO<sub>3</sub> (orthorhombic) and Zn<sub>2</sub>Te<sub>3</sub>O<sub>8</sub> (monoclinic) than to ZnO [23]. The TeO<sub>2</sub>-ZnO system contains a eutectic point at 21 % ZnO at a temperature of 590°C [22].

Smimizugawa *et al.* [23] studied the structure of a series of TeO<sub>2</sub>-ZnO glasses by EXAFS.  $\alpha$ -TeO<sub>2</sub> is composed of deformed [TeO<sub>6</sub>] octahedral rather than [TeO<sub>4</sub>] as in the glass. This 6-coordination of TeO<sub>2</sub> with two remaining weak Te-O in the pure form is what prevents glass formation [23]. The presence of a second component lowers the CN to 3 or 4, and Te<sup>+4</sup> satisfies the criteria for a network former after Zachariasen [6]. With

the addition of ZnO, structural units change from  $[\text{TeO}_4]$  tbp to  $[\text{TeO}_3]$  tp via  $[\text{TeO}_{3+1}]$  polyhedra, as shown by fig. (2.3).

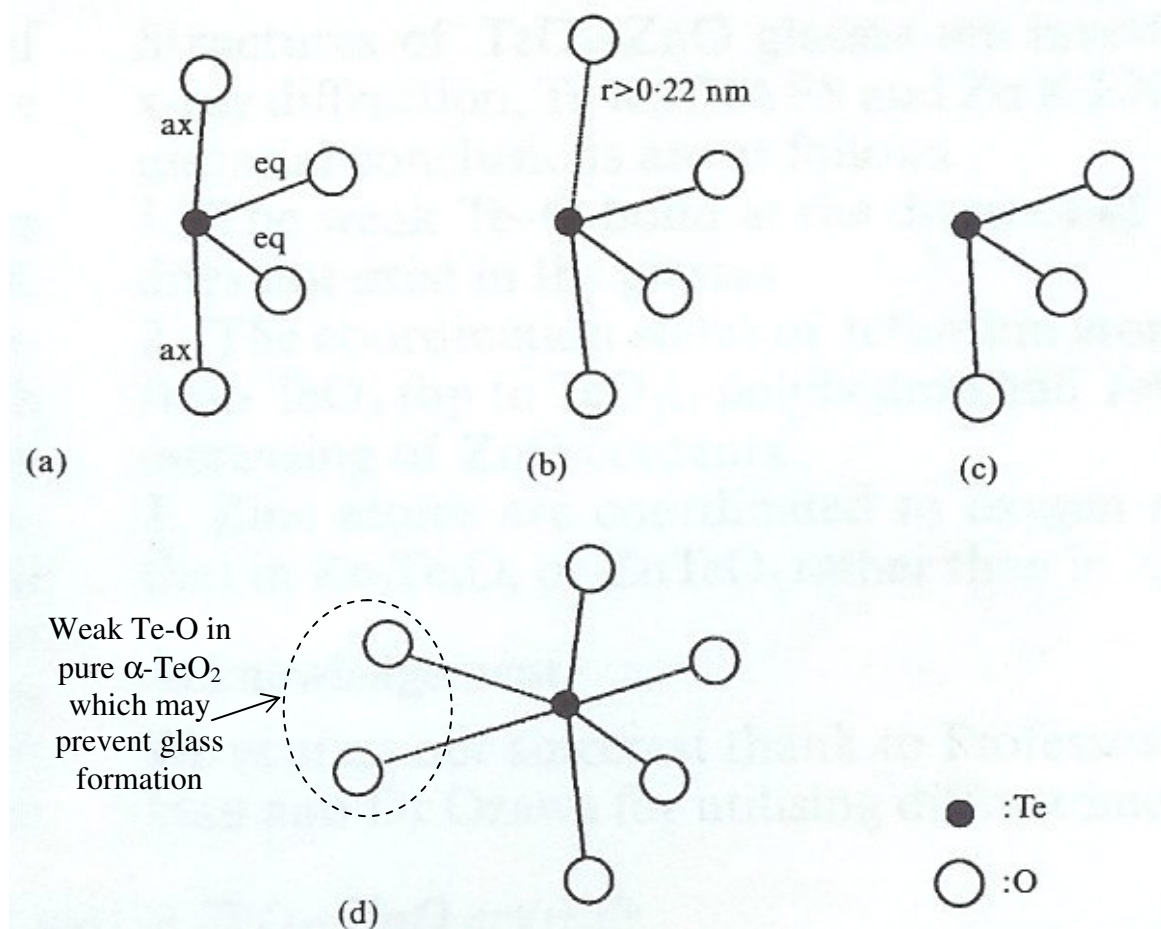


Fig. (2.3): Structural units in  $\text{TeO}_2$ -ZnO glasses: (a)  $[\text{TeO}_4]$  tbp, (b)  $[\text{TeO}_{3+1}]$  polyhedra, (c)  $[\text{TeO}_3]$  tp, and (d)  $[\text{TeO}_6]$  in  $\alpha\text{-TeO}_2$  [23]

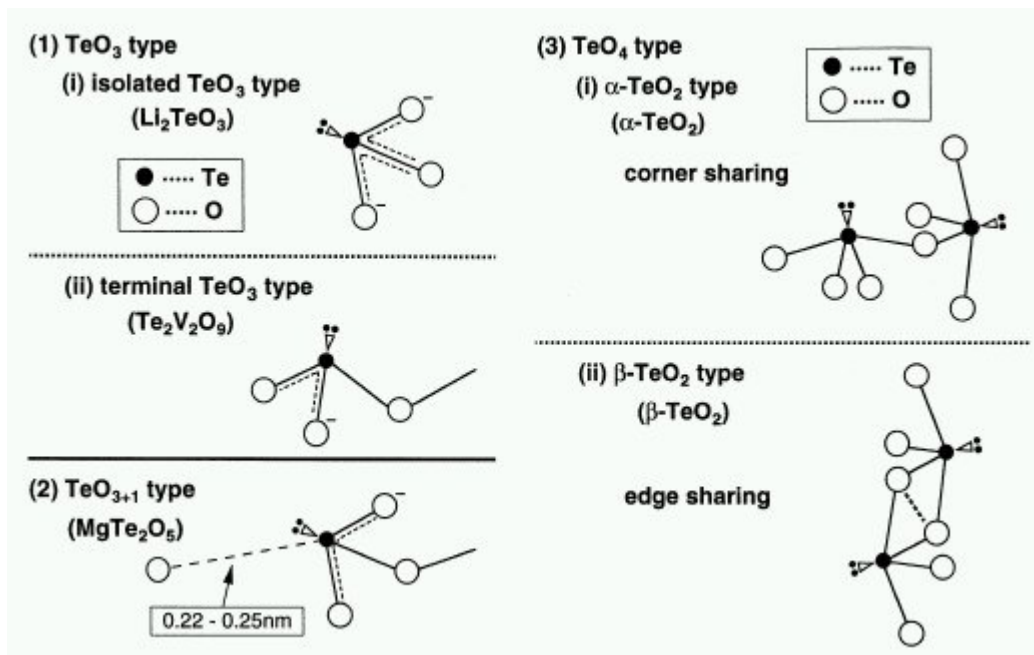
Zinc atoms in the glass occupy  $[\text{ZnO}_6]$  sites as in  $\text{Zn}_2\text{Te}_3\text{O}_8$ , and  $[\text{ZnO}_5]$  as in  $\text{ZnTeO}_3$ , but not tetrahedral  $[\text{ZnO}_4]$  sites as in ZnO [23].

### 2.3.2.3. TeO<sub>2</sub>-Na<sub>2</sub>O

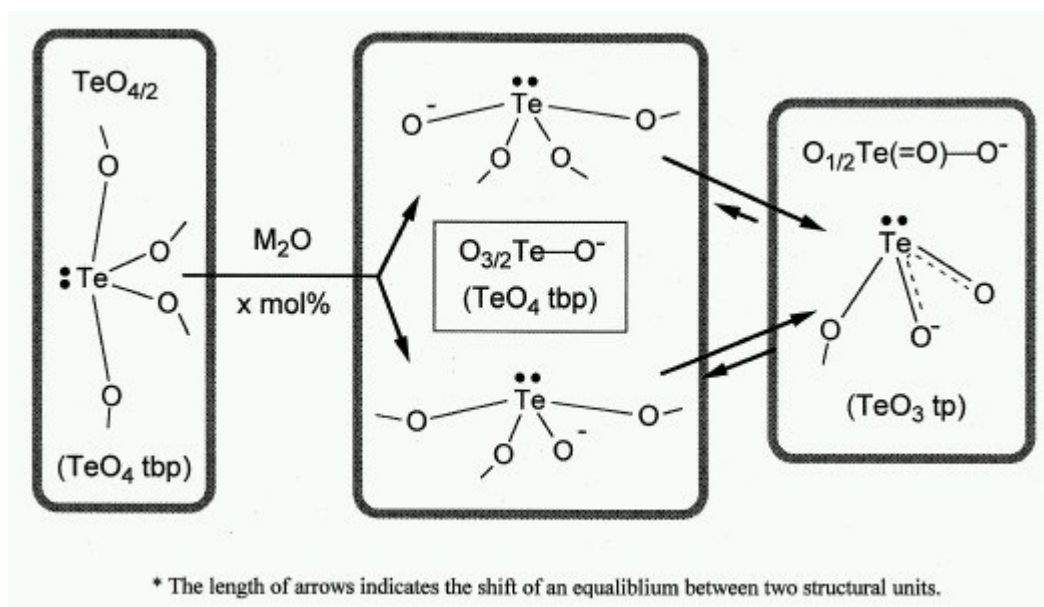
Addition of Na<sub>2</sub>O, a network modifier, to TeO<sub>2</sub> glasses results in more significant depolymerisation than ZnO, as sodium is monovalent, and will terminate network linkages wherever bonded to oxygen. Himei *et al.* [24] studied the structure of alkali (Li, Na, K, Rb, and Cs) tellurite glasses with X-ray photoelectron spectroscopy (XPS). The valence band spectra (0 to 30 eV) showed a change in structure from [TeO<sub>4</sub>] tbp to [TeO<sub>3</sub>] tp with alkali addition. The [TeO<sub>4</sub>] tbp has a lone pair of electrons at one of the equatorial sites of the tellurium sp<sup>3</sup>d hybrid orbital and [TeO<sub>3</sub>] sp<sup>3</sup> [24].

Zwanziger *et al.* [25] probed the sodium distribution in TeO<sub>2</sub>-Na<sub>2</sub>O glasses by spin-echo NMR. Maximum stability has been shown to occur at 20 mol. % Na<sub>2</sub>O. Na-Na distances in the glass were shown to be much closer than the random distribution expected around the 20 mol. % Na<sub>2</sub>O composition, and sodium was shown to reside in different sites to crystalline Na<sub>2</sub>Te<sub>4</sub>O<sub>9</sub>. This difference in structure which occurs at maximum glass stability could provide a high enough energy barrier to prevent structural rearrangement, and hence inhibit crystallisation [25].

Sakida *et al.* [26] studied the structure of alkali-metal tellurite (Li, Na, K, Rb, and Cs) glasses by NMR. Fig. (2.4) shows (a) the range of structural units seen in the glasses, and (b) mechanisms for M<sub>2</sub>O entering the glass network.



(a)



(b)

Fig. (2.4): (a) Range of structural units seen in the glasses, and (b) mechanisms for  $\text{M}_2\text{O}$  entering the glass network [26].

[TeO<sub>4</sub>] and [TeO<sub>3</sub>] units with non-bridging oxygens (NBOs) were shown to increase in the glass with alkali addition at the expense of [TeO<sub>4</sub>] units with no NBOs [26].

McLaughlin *et al.* [27, 28] showed by neutron diffraction, XRD, and NMR that all five polyhedra shown in fig. (2.5) are present in TeO<sub>2</sub>-Na<sub>2</sub>O glasses.

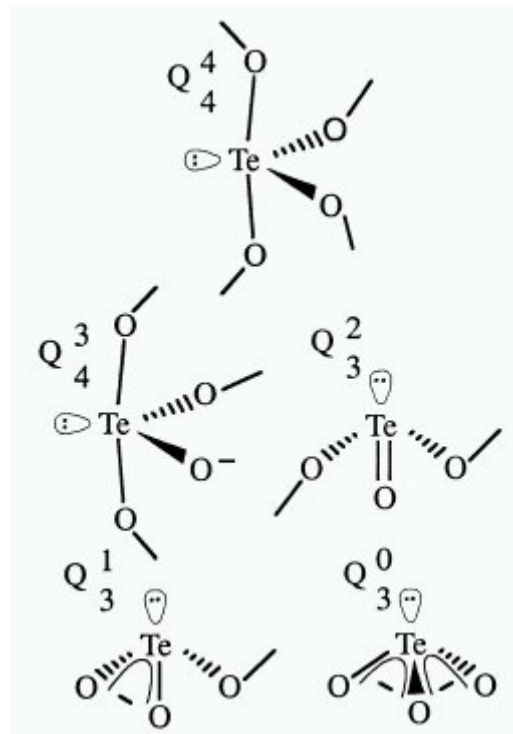


Fig. (2.5): Variety of polyhedra present in TeO<sub>2</sub>-Na<sub>2</sub>O glasses, where  $Q_m^n$  denotes the structural unit  $Q$ , with  $m$  oxygens bonded to a central tellurium atom,  $n$  of which oxygens are bridging [27].

A continuous cleavage of the TeO<sub>2</sub> network occurs with Na<sub>2</sub>O addition, with an equilibrium population and type of polyhedra depending on composition, frozen in from the liquid [27]. In crystalline sodium tellurites, dimers linked by four member rings are seen. However, in TeO<sub>2</sub>-Na<sub>2</sub>O glasses, only a few percent of the tellurium atoms engage in this type of ring structure (around 3 %). This again points to a high degree of structural rearrangement needed for devitrification, and may explain glass stability. This study also

showed clustering of sodium cations around the eutectic (20 mol. % Na<sub>2</sub>O) composition in the glass [27].

#### 2.3.2.4. TeO<sub>2</sub>-ZnF<sub>2</sub>

The tetragonal phase ZnF<sub>2</sub> (space group P4<sub>2</sub>/mnm) has an analogous structure to rutile (TiO<sub>2</sub>). The zinc cations sit in octahedral holes, between the fluorine anions. Each zinc ion is surrounded by six fluorine ions, with each fluorine surrounded by three zinc ions [20]. This suggests that in tellurite glasses, [ZnF<sub>6</sub>] units will enter the glassy network, and a number of structural units could exist in the series [ZnF<sub>6-x</sub>O<sub>x</sub>], for 1 ≤ x ≤ 6. This substitution is possible due to the similar ionic radius of F<sup>-</sup> and O<sup>2-</sup>, and the six-coordination of zinc to both anions. Therefore, ZnF<sub>2</sub> can be substituted for ZnO in tellurite glasses, resulting in compositions with stability equal to, and exceeding those of pure oxide compositions.

Sidebottom *et al.* [29] studied the Raman spectra of the ternary glass system TeO<sub>2</sub>-ZnO-ZnF<sub>2</sub>. The Raman bands due to symmetric stretching modes of TeO<sub>2</sub> structural units ([TeO<sub>4</sub>], [TeO<sub>3+1</sub>] and [TeO<sub>3</sub>]) in the 650-750 cm<sup>-1</sup> region were unaffected by fluoride addition. However, the bending mode at 420 cm<sup>-1</sup> increased in intensity with increasing ZnF<sub>2</sub> content. This indicates that fluorine is readily incorporated into the glassy network, directly replacing oxygen, without depolymerising the network further [29]. In this glass system, the increase in bending mode intensity at 420 cm<sup>-1</sup> is due to the conversion of [TeO<sub>3</sub>] units to [Te(O,F)<sub>3+1</sub>], with increasing fluoride content [29]. However,

depolymerisation will occur with addition, as was shown with ZnO [22], although it will not be as significant as with Na<sub>2</sub>O addition.

Nazabal *et al.* [30, 31] showed for the TeO<sub>2</sub>-ZnO-ZnF<sub>2</sub> system, that ZnF<sub>2</sub> addition increases the amount of [TeO<sub>3</sub>] in the glass at the expense of [TeO<sub>4</sub>] via [TeO<sub>3+1</sub>], much like ZnO and to a lesser extent than Na<sub>2</sub>O.

## 2.4. The impact of fibreoptics

The transmission of light along a curved dielectric cylinder was the subject of a spectacular lecture demonstration by John Tyndall in 1854 [32]. His light pipe was a stream of water emerging from a hole in the side of a tank which contained a bright light. The light followed the stream by total internal reflection at the surface of the water. Light pipes made of flexible bundles of glass are now used to illuminate internal organs in surgical operations in the endoscope which also transmits the image back to the surgeon. As already introduced in chapter 1, the overwhelming use of glass fibres is, however, to transmit modulated light over large distances at high speeds with low loss for communications, first shown by van Heel in 1954 [33]. Unlike coaxial cable, optical fibre loss does not depend on frequency in the 10 MHz to 1 GHz region [34].

Electrical communication cables and radio have largely been replaced by optical fibre in long-distance terrestrial communications. Hundreds of thousands of kilometres of fibre optic cables are now in use, carrying light modulated at high frequencies, providing the large communication bandwidths needed for television and data transmission. The techniques which made this possible include the manufacture of glass with very low

absorption of light, the development of light emitters and detectors which can handle high modulation rates, and fabrication of very thin fibres which preserve the waveform of very short light pulses. An essential development has been the cladding of fibres with a glass of lower refractive index, which prevents the leakage of light from the surface.

Optical fibres are also useful in short communication links, especially where electrical connections are undesirable. They also offer remarkable opportunities in computer technology and laboratory instrumentation such as interferometers and a variety of optical fibre sensors.

### *Total internal reflection*

The transmission of light over long lengths of glass optical fibre, is possible by cladding a core glass of refractive index  $n_{co}$ , with a higher index glass of refractive index  $n_{cl}$ . Fig. (2.6) illustrates this principle.

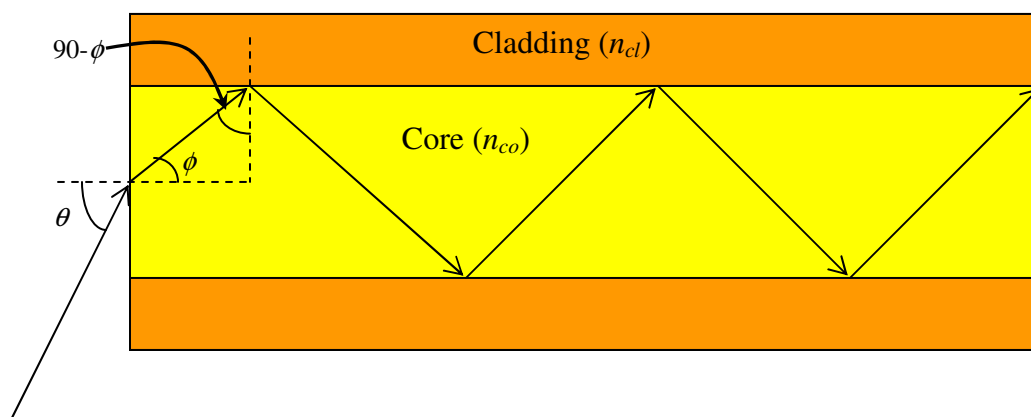


Fig. (2.6): Total internal reflection of light along a glass optical fibre with a core of refractive index  $n_{co}$ , and cladding index  $n_{cl}$  [35].

For total internal reflection, there is a limit on the angle, below which incident light will be trapped in the core and propagate. This is known as the critical angle,  $\theta$ . Incident light of angles  $> \theta$ , and  $< 90^\circ$ , will ‘leak’ into the cladding, and may not result in a guided mode. Equation (2.5) relates the geometry in fig. (2.5) to the numerical aperture,  $NA$ , of the fibre, the sine of  $\theta$  [35]. ‘Leaky’ modes can result from this condition, and over short lengths (e.g. 2 m), the  $NA$  of the fibre can appear larger than that calculated, due to modes just outside of  $\theta$ , propagated in the cladding. If the  $NA$  is measured over, say 1 km, the  $NA$  will be close to the calculated value [34].

$$NA = \sin \theta = n_{co} \sin \phi = n_{co} \left[ 1 - \left( \frac{n_{cl}}{n_{co}} \right)^2 \right]^{1/2} = (n_{co}^2 - n_{cl}^2)^{1/2} \quad (2.5)$$

The higher the refractive index contrast ( $\Delta n$ ), the closer  $NA$  will be to 1, and more light can be launched into the fibre.

### *Mode propagation*

Note, that  $NA$  does not depend on fibre dimensions, only the refractive indices of the core and clad glasses. However, fibre dimensions, and the refractive index profile of the fibre will govern the number of modes which will be guided. Large core, thin cladding fibres with a step index, are known as multimode, as incident light can propagate along a number of paths through the fibre [35]. This type of fibre, can be used for sensing, imaging, or power delivery, but is inappropriate for telecommunication applications, as a

sharp signal launched into the fibre will spread out in space and time, resulting in a distorted, noisy signal at the receiver. To overcome this, a very small core (of the order of the wavelength of the light) can be used so only one mode propagates (single mode fibre), or a complex refractive index profile (e.g. parabolic graded index fibres) can be utilised, so essentially all modes propagate at the same speed [35].

### **2.4.1. Infrared (IR) fibre optics and potential applications**

With the current interest in an efficient broadband, flat gain fibre optic amplifier and low-loss infrared (IR) optical fibre, a number of ‘novel’ glass systems have received considerable attention in the last 10 years, the three major groups include: chalcogenides (anionic moiety in glass is sulphur, tellurium and / or selenium), fluorides and heavy metal oxides (HMOs). Tellurite ( $\text{TeO}_2$ ) glasses, studied here, belong to the HMO group. Advantages of tellurite glasses include [36]:

- reasonably wide transmission range, from visible to mid-IR ( $\approx 400 \text{ nm}$  to  $6 \mu\text{m}$ );
- good glass stability, strength and corrosion resistance;
- relatively low phonon energy for an oxide glass ( $\approx 800 \text{ cm}^{-1}$ ) for amplification applications;
- high refractive index ( $\approx 2$ ) for non-linear applications; and
- ease of fabrication due to presence of oxide.

Non-silica based glass hosts typically exhibit higher rare-earth solubility, and lower phonon energies, which results in longer excited state lifetimes of transitions in the glass. Emission bands of rare-earths may also be shifted and broadened in these glasses, compared to silica. Some novel glass groups have recently been investigated as Raman amplifiers, such as tellurite glasses which exhibit Raman gain around 30 times that of silica [37]. As well as amplification, infrared fibres find a number of other possible applications in telecommunications such as switching and multiplexing [35].

The fundamental absorption bands for many organic groups lie beyond 2  $\mu\text{m}$  (attenuation in silica increases exponentially beyond 1.55  $\mu\text{m}$ ), therefore IR spectroscopic sensing is a potential application for these materials. Fundamental frequencies of organic groups will also be of much higher intensity than the overtone bands which silica can transmit. Sensing of explosive materials, where the presence of an electric current may be catastrophic, gives fibre optic sensors a distinct advantage [35]. Remote sensing 'in the field' is another benefit of these devices, as spectroscopy can be carried out without collecting samples which may degrade on transportation to a laboratory, or are toxic / radioactive [38]. Fibre can be implanted in a medium, such as a resin or a biological sample, and detect the chemical changes in the medium by spectroscopy of the evanescent wave traveling in the cladding which interacts with the sample [35]. These materials can be used for radiometric temperature sensing, and thermal imaging. Their increased transmission range gives them a distinct advantage over silica, as very hot sources, such as engine exhausts produce radiation in the 2 to 6  $\mu\text{m}$  region (e.g. missile countermeasures on a fighter jet [38]). Room temperature objects however emit further into the infrared region: 8 to 12  $\mu\text{m}$  [35]. Infrared fibres can also be used for scanning

near field spectroscopy, by etching a tip on the end of the fibre (e.g. sub-cellular spectroscopy) [38].

Laser power delivery in the infrared is also another possible usage for these materials. Welding and surgical lasers are the two main applications in this field. The use of optical fibre to deliver the beam would significantly reduce the size of current systems [35]. Surgical lasers operate at the resonant frequencies of organic groups present in tissue, such as OH (2.94  $\mu\text{m}$ ), or for cleaner incisions, proteins (6.45  $\mu\text{m}$ ) [38]. Surgical fibres must lack toxicity, have relatively low loss at the laser wavelengths ( $< 1 \text{ dB}\cdot\text{m}^{-1}$ ), be resistant to damage from high laser power, and possess a small bend radius to enable easy manipulation [35].

#### **2.4.2. Optical loss mechanisms**

Attenuation in an optical fibre can be categorised by absorption or scattering losses. The source of these losses can be either intrinsic to the material, or extrinsic, and in theory the latter reduced significantly, or eliminated with careful processing. The multiphonon and electronic absorption edges are intrinsic to the constituent atoms / ions present in the glass, and can be shifted with composition.

Transition metals, such as Fe, Cr, Mo, and Co, exhibit absorption bands in the near-IR, but contribute to attenuation less than the scattering component, in parts per billion concentration (loss depends on valence, and coordination of ions in the glass host). However, OH contributes significantly to loss, even at parts per billion levels [39], and is much more difficult to eliminate from the glass.

Extrinsic scattering centres in the glass include crystals, undissolved batch, bubbles, and refractory material. In the optical fibre, imperfections at the core / clad boundary can also result in losses [35]. In fibre optic networks, splicing the fibre together is often necessary. This will result in some degree of loss, as well as misalignment of spliced cores [34]. As light passes from one medium to the fibre (e.g. air to fibre, or other material of dissimilar refractive index to fibre), losses will result, due to Fresnel reflection at the boundary [34] (see section 6.1.2.2.).

The electronic absorption edge is a result of electronic transitions in the glass, and known as the Urbach edge, its position defined by,  $\alpha_{UV}$ .

$$\alpha_{UV} = A \exp \left[ \frac{E - E_g}{hf} \right] \quad (2.6)$$

where  $A$  is a constant,  $E$  the energy of the incident photons,  $E_g$  the photon energy corresponding to the electronic band gap of the material,  $h$  Planck's constant ( $6.62608 \times 10^{-34}$  J.sec), and  $f$  the frequency of the incident photons [35].

The infrared-edge and other absorption bands in multicomponent inorganic glasses are due to the vibrational modes of bonds in structural units in the glass. The infrared edge corresponds to the low frequency cut-off of transmission. This absorption edge tails off to higher frequencies exponentially. The absorption coefficient,  $\alpha_{IR}$ , is given by equation (2.7) [40].

$$\ln \alpha_{IR}(f) = B - Af \quad (2.7)$$

where  $f$  = frequency, and  $A$  and  $B$  are materials constants. Multiphonon absorption occurs when a transverse optical mode couples weakly with a high energy phonon [40]. This mode decays into two or more lower energy phonons of frequencies which corresponds to fundamental vibrations in the glass [40].

As the position of the infrared edge is dependent on lattice vibrations, the masses of the atoms / ions present and the strength of the forces between the atoms / ions define the position of this edge [35]. The frequency of the edge,  $f$ , is given by equation (2.8), known as the Szigeti relationship [35].

$$f = \frac{1}{c} \sqrt{\frac{k}{\mu}} \quad (2.8)$$

where  $c$  is the velocity of light in a vacuum ( $2.998 \times 10^8 \text{ m.s}^{-1}$ ),  $k$  the bond force constant, and  $\mu$  the reduced mass of the bonding atoms (see section 6.1.1.2). Therefore, for a glass system to transmit further in the infrared than  $\text{SiO}_2$  ( $\approx 1.55 \text{ }\mu\text{m}$ ), would require [35]:

- Replacement of Si by heavier cations (increase  $\mu$ ).
- Replacement of Si by cations with a higher charge (decrease  $k$ ).
- Replacement of O by heavier anions (increase  $\mu$ ).
- Replacement of O by monovalent anions (decrease  $k$ ).

One advantage of working in the infrared, is that Rayleigh scattering losses are proportional to  $A_0/\lambda^4$  [35]. Therefore they are greatly reduced at longer wavelengths (Mie

scattering due to microinhomogeneities is proportional to  $1/\lambda^2$ ).  $A_0$  is a constant [41-44], which depends on local variations in electron density, refractive index, and composition, frozen in from the melt.  $A_0$  will be defined in the next section in relation to tellurite glasses. Raman and Brillouin scattering result from optical and acoustic phonons causing density perturbations, which inelastically scatter incident photons [35].

Loss in an optical fibre can be calculated by the ratio of the intensity of the light leaving the fibre,  $I_t$ , to the intensity entering the fibre,  $I_i$ , over length  $\Delta l$ , measured in m.

$$\text{Loss (dB.m}^{-1}\text{)} = -\frac{10\log_{10}\left(\frac{I_t}{I_i}\right)}{\Delta l} \quad (2.9)$$

The benefit of a logarithmic scale is that losses from different sources are additive [35]. A loss of  $0.1 \text{ dB.m}^{-1}$  corresponds to 98 % transmission over 1 m,  $1 \text{ dB.m}^{-1}$  to 79 %,  $10 \text{ dB.m}^{-1}$  to 10 %,  $20 \text{ dB.m}^{-1}$  to 1 %, etc. Fig. (2.7) illustrates this relationship.

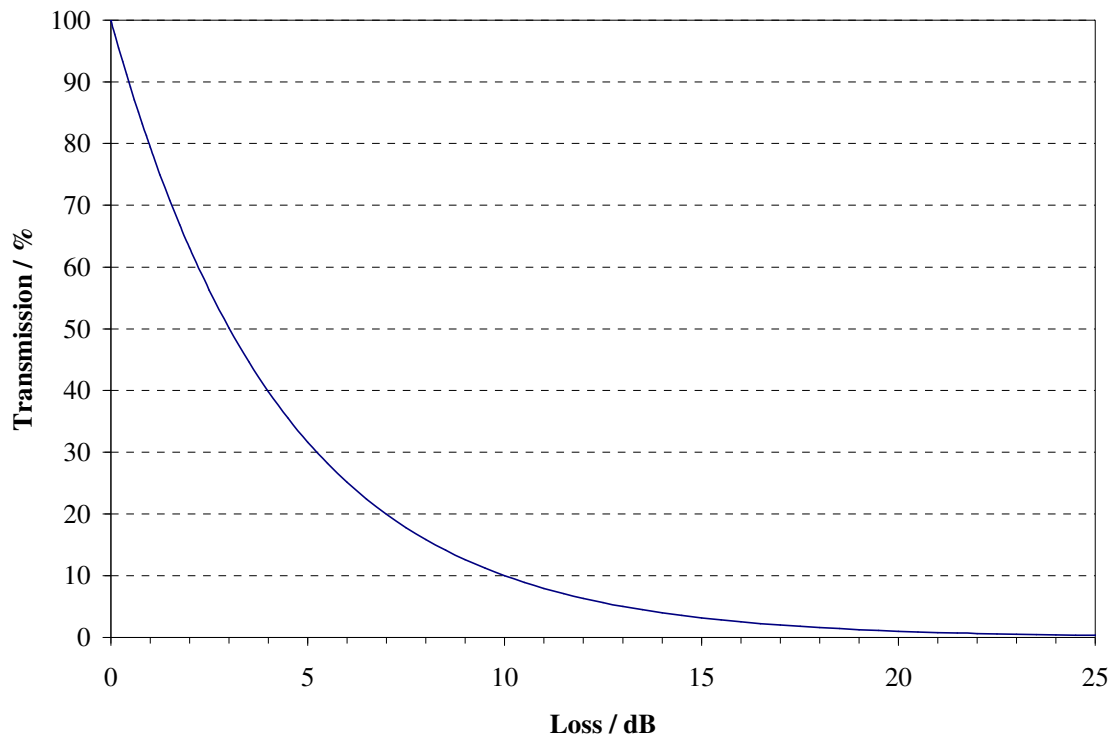


Fig. (2.7): Relationship between optical fibre attenuation (in dB) and % transmission.

### 2.4.3. Non-linear properties

Glasses with high non-linearity have received much attention recently for uses as high speed switches, and Raman amplification. By utilising the third-order non-linearity of the glass, signal transmission can be improved using solitons, and bandwidth increased using all-optical processing [45]. Second-order non-linearity, not normally seen in isotropic materials such as glasses, has been shown by photo-induction, and electric field poling [45].

The second-order non-linearity is a result of anharmonicity of electron motion. The induced polarisation,  $P$ , in a material by an incident electromagnetic field,  $\mathbf{E}$ , can be described by the  $n^{\text{th}}$  order non-linear susceptibility,  $\chi_n$ .

$$P = \varepsilon_0 (\chi_1 \mathbf{E} + \chi_2 \mathbf{E}^2 + \chi_3 \mathbf{E}^3 + \dots) \quad (2.10)$$

where  $\varepsilon_0$  is the dielectric permeability [45]. Due to a lack of symmetry, glasses normally have  $\chi_2 = 0$ . The glass structure can however be treated, inducing structural changes which cause second-order non-linear effects.

Efficient second harmonic generation (SHG) requires  $\chi_2 > 0$ , and phase matching between the fundamental (incident) wave, and the generated second harmonic (SH). The intensity of the SH,  $I_{2\omega}$ , is given by equation (2.11).

$$I_{2\omega} = l^2 \chi_2^2 \left[ \frac{\sin\left(\frac{l\Delta\delta}{2}\right)}{\Delta\delta/2} \right]^2 I_{\omega}^2 \quad (2.11)$$

where  $l$  is the path length,  $\Delta\delta$  the phase mismatch, and  $I_{\omega}$  the fundamental intensity [45]. SHG has been shown in Ge-doped silica optical fibres, after exposure to a 20 kW Nd-YAG laser. This SHG was thought to be due to formation of a dipole colour centre grating in the fibre core. Some models have suggested that an alternating  $\chi_2$  forms by defects aligning with the DC field produced by  $\chi_3$  effects. There is some contention if  $\chi_2$

originates from charge separation, or orientation, however, experimental evidence indicates the former [45].

Electric field poling of glasses at elevated temperatures has induced non-zero  $\chi_2$  in a number of systems such as silicates and tellurites. Similar effects have been observed using corona poling, electron bombardment, and UV laser exposure. This is thought to be due to space charge left behind after mobile species, such as alkali or hydrogen ions, have moved out of the poled region [45].

If the incident beam is non-resonant, i.e. detuned from any fundamental frequency of components in the glass, third-order non-linear effects will dominate. Equation (2.12) shows the relation between the non-linear refractive index,  $n_2$ , to the real part of  $\chi_3$  [45].

$$n_2 = \frac{12\pi}{n} \text{Re } \chi_3(1111)(-\omega, \omega, \omega, -\omega) \quad (2.12)$$

where  $n$  is the linear refractive index. This phenomena results in intensity dependent self-focusing. These non-linearities are electronic in origin, and due to fluctuations in electron cloud density, with sub-ps ( $10^{-12}$  s) response times [45]. The non-linear refractive index can be approximated by equation (2.13).

$$n_2 = \frac{\left(\frac{n^2 + 2}{3}\right)(n^2 - 1)d_n^2}{nE_s^2} \quad (2.13)$$

where  $d_n$  is nearest neighbour bond length, and  $E_s$  the Sellmeier gap [45]. Tellurite glasses have been shown to possess  $n_2$  values around two orders of magnitude greater than silica, 210 and  $2.7 \times 10^{-20} \text{ m}^2 \cdot \text{W}^{-1}$  respectively [45].

## **2.5. Tellurite and fluorotellurite glasses for infrared (IR) waveguide applications**

### **2.5.1 Tellurite $\text{TeO}_2$ -ZnO- $\text{Na}_2\text{O}$ (TZN) glasses**

#### **2.5.1.1. Optical, mechanical and thermal properties**

Wang *et al.* [36] first reported the properties of the ternary glass system  $\text{TeO}_2$ - $\text{Na}_2\text{O}$ -ZnO (good durability, thermally stable to crystallisation, and high rare-earth solubility) making these compositions ideal for optical fibre devices. In this study the thermal and optical properties of the glass (mol. %) 75 $\text{TeO}_2$ -5 $\text{Na}_2\text{O}$ -20ZnO were looked at. The viscosity-temperature behaviour (important when considering fibre-drawing) of the soda zinc tellurite glass was intermediate in behaviour between a silicate glass (strong) and ZBLAN (fragile) [46, 47]. DTA of this glass composition gave characteristic temperatures as:  $T_g = 299^\circ\text{C}$  and  $T_x = 417^\circ\text{C}$ , which gives a  $T_x - T_g$  value of  $118^\circ\text{C}$ , around three times as much as the soda tellurite composition also studied by Wang *et al.* [36] showing the stability of the ternary system. Also in this study fibre loss was measured on the soda zinc tellurite glass manufactured by the rod-in-tube preform method. This loss was calculated by generating a V-curve with equation (2.14) [43, 44]:

$$\alpha_t = A_0(1/\lambda^4) + B_0 \exp(B_1/\lambda) + C_0 \exp(-C_1\lambda) \quad (2.14)$$

where  $A_0$ ,  $B_0$ ,  $B_1$ ,  $C_0$  and  $C_1$  are constants and  $\lambda$  is the wavelength of the light. The first term indicates loss due to light scattering from microscopic density and composition fluctuations in the material. These effects rapidly decrease with increasing wavelength. The second and third terms describe, respectively, losses due to ultraviolet absorption from the electronic band edge (Urbach tail) and infrared edge losses due to multiphonon absorption. With an assumption of a single component tellurite glass, the first term could be calculated by equation (2.15) [41-44]:

$$A_0 = \frac{8}{3} \pi^3 n^8 p^2 \beta k T_g \approx \frac{8}{3} \pi^3 (n^2 - 1)^2 \beta k T_g \quad (2.15)$$

where  $n$  is the refractive index,  $p$  is the average photoelastic constant,  $\beta$  is the isothermal compressibility,  $T_g$  is the glass transition temperature and  $k$  is Boltzmann's constant ( $1.38 \times 10^{-23}$  J.K<sup>-1</sup>). This expression becomes more complicated, when considering multicomponent glasses, due to compositional fluctuations [35]. As  $T_g$  increases with quenching rate from the melt, so do scattering losses [39]. The second and third terms of equation (2.14) are used to fit experimental data on the UV and IR spectra of fibres, bulk glass and films. The fitting parameters for tellurite glasses are, for the first term (Rayleigh scattering loss)  $0.29/\lambda^4$  dB.km<sup>-1</sup>, the second term (UV absorption loss)  $6.47 \times 10^{-6} \cdot \exp(9.84/\lambda)$  dB.km<sup>-1</sup>, and the third term (IR absorption loss)

$5.75 \times 10^{15} \cdot \exp(-126.67/\lambda)$  dB.km<sup>-1</sup> [36]. Fig. (2.8) shows the theoretical minimum loss spectrum of TeO<sub>2</sub>-Na<sub>2</sub>O-ZnO glass. Line 1 is the UV edge, 2 the IR edge with OH, 3 IR edge without OH, and 4 Rayleigh scattering.

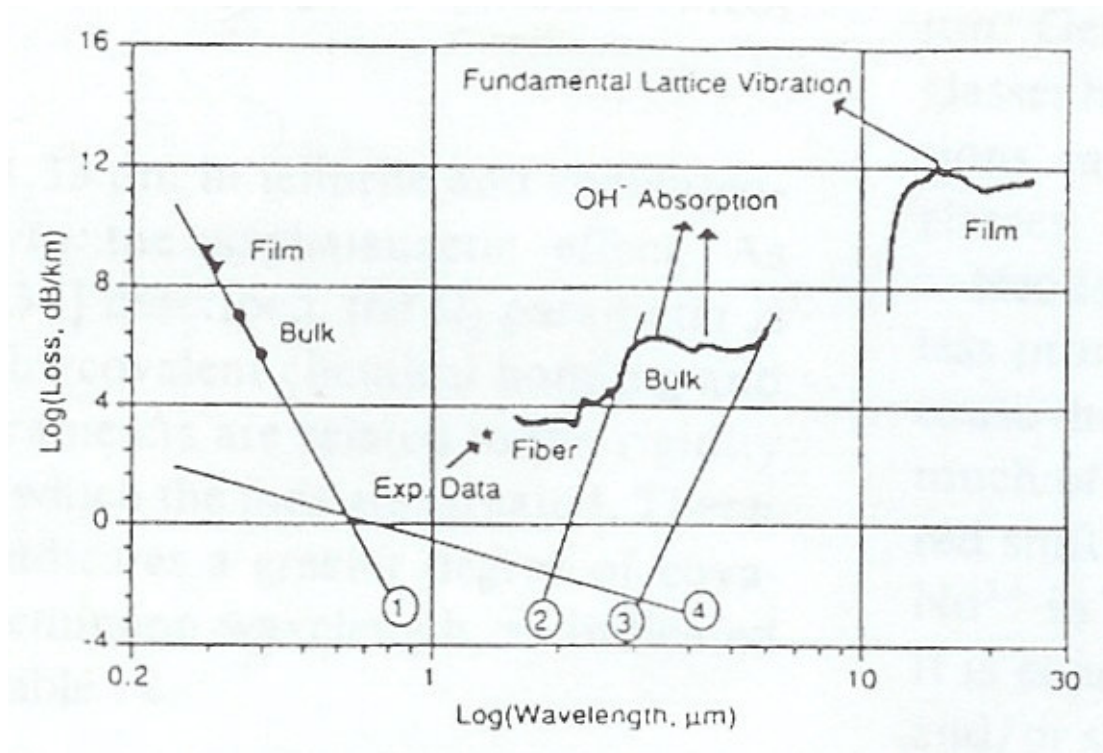


Fig. (2.8): Theoretical minimum loss spectrum of TeO<sub>2</sub>-Na<sub>2</sub>O-ZnO glass. Line 1 - UV edge, 2 - IR edge with OH, 3 - IR edge without OH, and 4 - Rayleigh scattering [36].

The calculated minimum intrinsic loss for tellurite glass fibre was  $3.6 \times 10^{-3}$  dB.km<sup>-1</sup> at 3.02 μm [36]. Due to extrinsic OH absorption bands (at 2.86 and 3.33 μm), this is pragmatically shifted to  $1.8 \times 10^{-2}$  dB.km<sup>-1</sup> at 1.9 μm [36]. Actual losses of fibre reported by Wang are around 900 dB.km<sup>-1</sup> at ≈ 1.35 μm [36]. This is likely to be due to other extrinsic factors such as scattering centres in the glass (undissolved batch material, crystals etc.), defects in the core/clad structure, and absorbing species (OH, crucible contamination).

Braglia *et al.* [48] performed a detailed thermal stability and viscosity-temperature study of a series of glasses which are shown in table (2.3) with their characteristic temperatures measured by DSC.

Table (2.3): Characteristic temperatures of  $\text{TeO}_2$ -ZnO- $\text{Na}_2\text{O}$  glasses [48].

$\text{TeO}_2$ /mol. %	ZnO /mol. %	$\text{Na}_2\text{O}$ /mol. %	$\text{Er}_2\text{O}_3$ /ppmw	$T_g/^\circ\text{C}$	$T_x/^\circ\text{C}$	$(T_x-T_g)/^\circ\text{C}$
76.58	20.42	3	1,000	313	452	139
75.00	20.00	5	1,000	302	440	138
74.00	20.00	6	1,000	302	456	154
72.63	19.37	8	-	297	472	175
71.05	18.95	10	1,000	298	474	176

From table (2.3), addition of  $\text{Na}_2\text{O}$  decreases  $T_g$  as expected and opens up the  $T_x-T_g$  gap (i.e. increases glass stability). The glass (mol. %) 74 $\text{TeO}_2$ -20ZnO-6 $\text{Na}_2\text{O}$  (with 1,000 ppmw  $\text{Er}_2\text{O}_3$ ) was subsequently heat treated at  $T_x$  (456 $^\circ\text{C}$ , time not stated) to crystallise the sample, and analysed by X-ray diffraction (XRD). Fig. (2.9) shows the XRD trace of this sample.

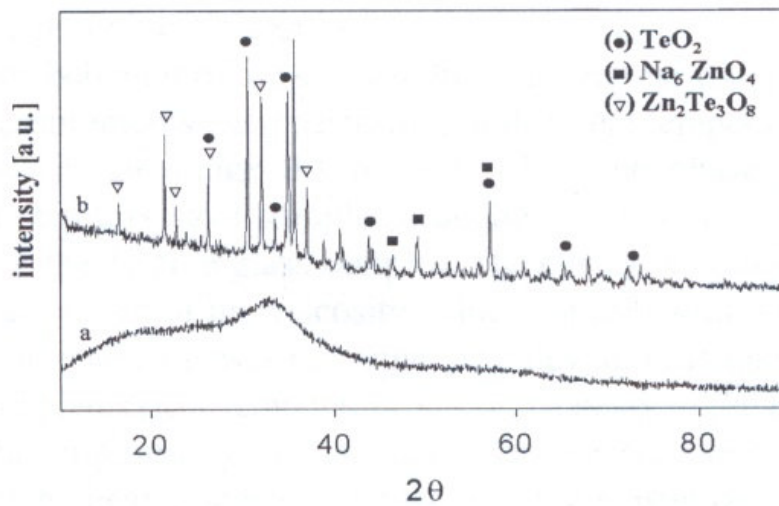


Fig. (2.9): XRD trace of glass 74 $\text{TeO}_2$ -20ZnO-6 $\text{Na}_2\text{O}$  (with 1,000 ppmw  $\text{Er}_2\text{O}_3$ ), before and after heat treatment at 456 $^\circ\text{C}$  (time not stated) [48].

From fig. (2.9), all major peaks were identified as  $\text{TeO}_2$ ,  $\text{Na}_6\text{ZnO}_4$  or  $\text{Zn}_2\text{Te}_3\text{O}_8$ . The viscosity-temperature study concluded that the tellurite melts are Newtonian fluids (i.e. viscosity depends only on temperature and during fibre-drawing, draw speed should not affect viscosity) and that the glass forming liquids can be drawn into fibres at temperatures around 370 to 400°C, which corresponds to a viscosity of around  $10^4$  Pa.s. It can be seen from table (2.3) that this is 50 to 100°C below the crystallisation exotherm of these glasses, so devitrification should not be a problem during fibre-drawing.

Yoshida *et al.* [49] investigated the crack growth behaviour of zinc tellurite glasses with and without sodium oxide (compositions (mol. %): 70 $\text{TeO}_2$ -30 $\text{ZnO}$  and 70 $\text{TeO}_2$ -20 $\text{ZnO}$ -10 $\text{Na}_2\text{O}$ ). Fig. (2.10) shows the stress intensity factor-crack velocity ( $K_I$ - $v$ ) curves for the two tellurite compositions:

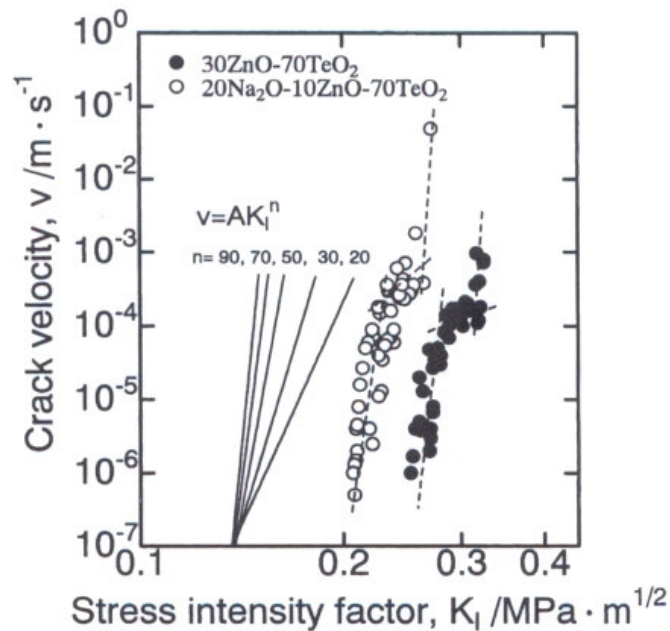


Fig. (2.10):  $K_I$ - $v$  curves for zinc tellurite glasses with and without  $\text{Na}_2\text{O}$  [49].

It can be seen the curves are shifted to much lower stress intensity factors for tellurite glasses compared to silicates (silicates have  $K_{IC}$  values around  $0.8 \text{ MPa}\cdot\text{m}^{1/2}$ ). This indicates tellurite glass is far more brittle than silicate glass. The substitution of ZnO by  $\text{Na}_2\text{O}$  shifts the curve to lower stress intensity due to the decrease in bond strength because of the introduction of weak non-bridging Na-O bonds. The slopes of tellurite glass  $K_I$ - $v$  curves are larger as there is a relatively small contribution of stress corrosion reaction (compared to silicates [50]) to subcritical crack growth, the stress corrosion mechanism being based upon a stress enhanced chemical reaction between water and the chemical bonds in the glass. This is possibly due to the lack of ring structure in tellurite glasses which is seen in silicates. A chain like structure is seen in zinc tellurite glasses which may not permit the strained bonds [49].

Watanabe *et al.* [51] studied the Vickers' hardness ( $H_v$ ) of a glass of composition (mol. %)  $70\text{TeO}_2$ - $15\text{ZnO}$ - $15\text{Na}_2\text{O}$  ( $H_v = 2.6 \text{ GPa}$  at room temperature) around its glass transition region ( $T_g = 264^\circ\text{C}$ ). There was a sharp decrease in hardness of this glass at around  $T/T_g = 0.9$  to  $1.0$ . This can be attributed to the 'fragile' [46, 47] nature of  $\text{TeO}_2$ -based glasses, so the breaking of atomic bonds and atomic rearrangement occur easily around  $T_g$ .

Aida *et al.* [52] studied the thermal stability of the compositions (mol. %)  $80\text{TeO}_2$ - $10\text{ZnO}$ - $10\text{Na}_2\text{O}$  and  $70\text{TeO}_2$ - $15\text{ZnO}$ - $15\text{Na}_2\text{O}$  as well as many other ternaries. Fig. (2.11) shows DTA traces of some alkali-containing zinc tellurite glasses.

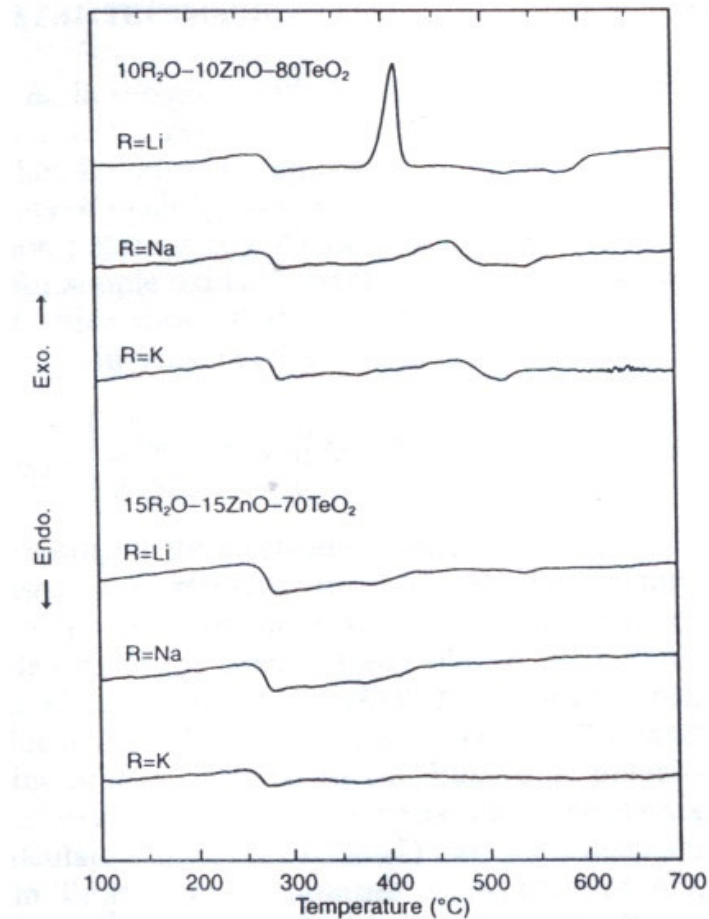


Fig. (2.11): DTA traces of some alkali-containing zinc tellurite glasses [52].

From fig. (2.11), soda zinc tellurite glasses are exceptionally stable, the composition containing 10 mol. % ZnO and 10 mol. % Na<sub>2</sub>O exhibiting a weak crystallisation exotherm and the composition containing 15 mol. % ZnO and 15 mol. % Na<sub>2</sub>O, showing no sign of devitrification. This study related the optical basicity of the oxides (numerical expression of the average electron donor power of the oxide species) to the thermal stability. The combination of a high optical basicity alkali metal oxide (Na<sub>2</sub>O – 1.15) and a low optical basicity metal oxide (ZnO – 0.95) causes a strong interaction in the glass

and suppresses the movement of  $\text{Na}^+$  and  $\text{Zn}^{2+}$  ions resulting in a high resistance to crystallisation [52].

Feng *et al.* [53] studied hydroxyl absorption of glasses in the system  $\text{TeO}_2\text{-Na}_2\text{O-ZnO-GeO}_2\text{-Y}_2\text{O}_3\text{-Er}_2\text{O}_3$ . Two absorption bands due to OH were prominent in these glasses, one at  $3500\text{ cm}^{-1}$  ( $2.86\text{ }\mu\text{m}$ ) attributed to free OH and one at  $2300\text{ cm}^{-1}$  ( $4.35\text{ }\mu\text{m}$ ) attributed to hydrogen bonded OH (the stronger the association the longer the wavelength of absorption). Bubbling  $\text{CCl}_4$  through the molten glass reduced the intensity of both absorption bands as OH was removed from the glass as  $\text{HCl}$ . Fig. (2.12) illustrates this showing the infrared spectra of an untreated (A: melted at  $950^\circ\text{C}$  in air for 2 hours), and treated melt (E: melted at  $950^\circ\text{C}$  in air for 1.5 hours, and bubbled with dry air and  $\text{CCl}_4$  for 30 min.).

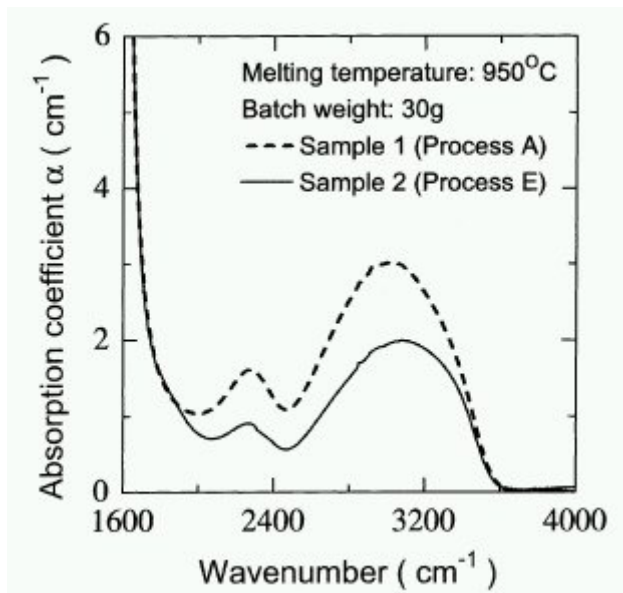


Fig. (2.12): Infrared spectra of  $\text{TeO}_2\text{-Na}_2\text{O-ZnO-GeO}_2\text{-Y}_2\text{O}_3\text{-Er}_2\text{O}_3$  glass untreated (A: melted at  $950^\circ\text{C}$  in air for 2 hours), and treated melt (E: melted at  $950^\circ\text{C}$  in air for 1.5 hours, and bubbled with dry air and  $\text{CCl}_4$  for 30 min.) [53].

Addition of  $\text{GeO}_2$  increased the intensity of the free OH band, but did not affect the hydrogen bonded band. Addition of  $\text{Y}_2\text{O}_3$  did not affect either the free or H-bonded bands, and  $\text{Na}_2\text{O}$  slightly reduced the free OH band only.

### 2.5.1.2. $\text{Er}^{3+}$ -doping of TZN glasses

Tellurite glasses have a lower phonon energy than silica (800 and 1000  $\text{cm}^{-1}$  respectively), which is important for efficient fluorescence of rare-earth transitions, as high phonon energy results in increased probability of non-radiative decay, with energy lost to the host lattice as heat. The erbium (III) 1.55  $\mu\text{m}$  transition has received much attention, for use as an amplifier in that particular telecommunications window.

Wang *et al.* [36] showed the addition of rare-earths, including erbium (III), generally increased the stability of TZN glasses. Table (2.4) summarises some of these results.

Table (2.4): Effect of erbium (III) on the characteristic temperatures of some tellurite glasses [36].

Glass / mol. % (+ wt. % $\text{Er}_2\text{O}_3$ )	$T_g /$ $^{\circ}\text{C}$	$T_x /$ $^{\circ}\text{C}$	$T_x - T_g /$ $^{\circ}\text{C}$
72 $\text{TeO}_2$ -28 $\text{ZnO}$	324	420	96
" (1)	330	425	95
75 $\text{TeO}_2$ -20 $\text{ZnO}$ -5 $\text{Na}_2\text{O}$	299	417	118
" (1)	304	432	128
" (3.9)	311	447	136
" (7.5)	324	443	119

It can be seen, in the ternary system 75 $\text{TeO}_2$ -20 $\text{ZnO}$ -5 $\text{Na}_2\text{O}$  mol. %, glass stability can be increased up to at least 4 wt. %  $\text{Er}_2\text{O}_3$ . The emission width for erbium (III) was shown to

be broader and flatter than for silicate based glasses (1530 to 1640 nm and 1520 to 1600 nm respectively) [36].

Feng *et al.* [54] showed that addition of  $\text{GeO}_2$  and  $\text{Y}_2\text{O}_3$  to erbium (III) doped  $\text{TeO}_2$ - $\text{GeO}_2$ - $\text{ZnO}$ - $\text{Na}_2\text{O}$ - $\text{Y}_2\text{O}_3$  glasses, increased glass stability and the lifetime of  $^4\text{I}_{13/2}$  level of the  $\text{Er}^{+3}$  ion.

Shen *et al.* [55] showed that the replacement of  $\text{ZnO}$  and  $\text{TeO}_2$  with  $\text{Na}_2\text{O}$  results in a narrowing of the emission band of erbium (III). The lifetime of erbium (III) in  $\text{TeO}_2$ - $\text{Na}_2\text{O}$ - $\text{ZnO}$  glasses reaches a maximum at 11000 ppmw  $\text{Er}^{+3}$ . Broadening of the  $1.55 \mu\text{m}$  emission also occurs with increasing  $\text{Er}_2\text{O}_3$  content. High OH content decreases the lifetimes of the  $^4\text{I}_{13/2} \rightarrow ^4\text{I}_{15/2}$  transition significantly [55]. Fibre drawn from this glass exhibited minimum loss of around  $0.5 \text{ dB}\cdot\text{m}^{-1}$  at  $1.3 \mu\text{m}$ , however, losses increases rapidly at lower and higher wavelengths. Fig. (2.13) shows the fibre loss spectra, with an inset of the theoretical intrinsic loss curve.

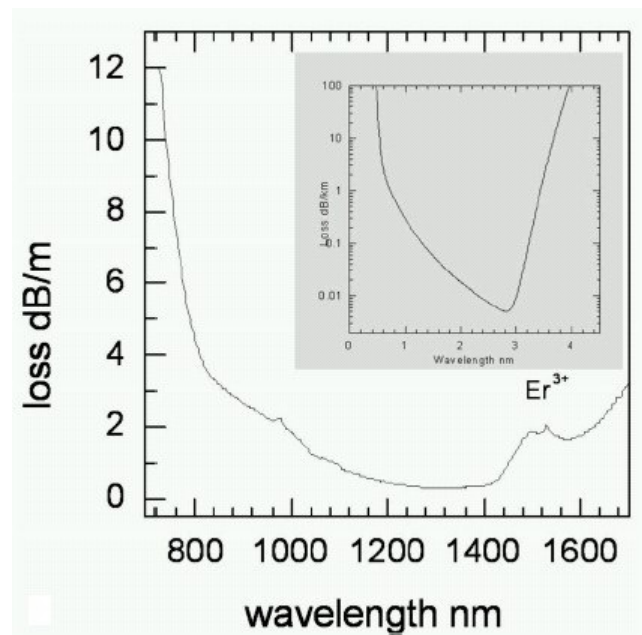
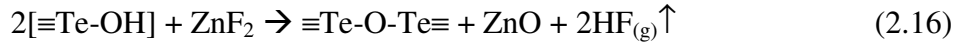


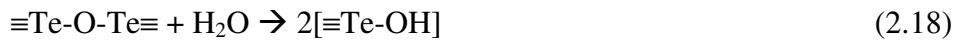
Fig. (2.13): Loss spectra of  $\text{Er}^{+3}$ -doped  $\text{TeO}_2$ - $\text{Na}_2\text{O}$ - $\text{ZnO}$  fibre (inset shows theoretical intrinsic loss curve) [55].

### 2.5.2. Fluorotellurite glasses

With conventional melting procedures, oxide-tellurite glasses cannot be prepared OH (hydroxyl) free without an elaborate set-up (e.g. bubbling drying chemicals such as carbon tetrachloride through the molten glass with platinum tubing [53]). This is problematic as OH exhibits two fundamental absorption bands in the mid-IR. A simpler way of removing the OH from the glass during melting is to add a metal fluoride to the batch and the fluoride will liberate hydrogen species from the melt ('drying' the glass) [56, 57]. For example, in the ternary glass system  $\text{TeO}_2\text{-ZnO-Na}_2\text{O}$ , which is known to be a good glass-former [36],  $\text{ZnF}_2$  can be added partially or completely replacing  $\text{ZnO}$ , and will react with accessible OH according to equation (2.16):



In addition, adventitious water in the glass melting atmosphere can be removed (equation (2.17)) to prevent hydrolysis of the melt (equation (2.18)):



Fluorotellurite compositions and properties reported in the literature are summarised in the next section (2.5.2.1).

### 2.5.2.1. TeO<sub>2</sub>-ZnF<sub>2</sub> glasses reported in the literature

Table (2.5) summarises the ZnF<sub>2</sub> containing fluorotellurite compositions found in the literature, and the melting procedures used:

Table (2.5): Fluorotellurite glasses reported in the literature and melting procedures used ( $T$  = melting temperature and  $t$  = melting time)

Composition	Mol. % ZnF <sub>2</sub>	Crucible Material	$T / ^\circ\text{C}$	$t / \text{min.}$	Ref.
9TeO <sub>2</sub> -2PbO-1ZnF <sub>2</sub> 4TeO <sub>2</sub> -1PbO-1ZnF <sub>2</sub> 7TeO <sub>2</sub> -2PbO-3ZnF <sub>2</sub> 3TeO <sub>2</sub> -1PbO-2ZnF <sub>2</sub>	8.20 16.40 24.80 33.20	Fused silica and zirconia	950 to 1000	N/A	[13]
75.9TeO <sub>2</sub> -9.13PbO-15.17ZnF <sub>2</sub> 63.29TeO <sub>2</sub> -7.99PbO-28.72ZnF <sub>2</sub> 52.14TeO <sub>2</sub> -6.93PbO-40.91ZnF <sub>2</sub> 42.79TeO <sub>2</sub> -5.4PbO-51.81ZnF <sub>2</sub>	15.17 28.72 40.91 51.81	N/A <sup>3</sup>	750	15	[56]
64TeO <sub>2</sub> -24ZnO-12ZnF <sub>2</sub> 65TeO <sub>2</sub> -13ZnO-22ZnF <sub>2</sub> 65TeO <sub>2</sub> -2ZnO-33ZnF <sub>2</sub>	12.00 22.00 33.00	Alumina	650	N/A	[29]
45.4TeO <sub>2</sub> -9PbO-45ZnF <sub>2</sub> -0.6PrF <sub>3</sub>	45.00	Platinum	600	30	[58]
63.3TeO <sub>2</sub> -8PbO-28.7ZnF <sub>2</sub> 52.1TeO <sub>2</sub> -7PbO-40.9ZnF <sub>2</sub> 42.1TeO <sub>2</sub> -6PbO-51.9ZnF <sub>2</sub> 37.7TeO <sub>2</sub> -5.3PbO-57ZnF <sub>2</sub>	28.70 40.90 51.90 57.00	N/A	N/A	N/A	[59]
61.7TeO <sub>2</sub> -14.9ZnO-23.4ZnF <sub>2</sub> 44.9TeO <sub>2</sub> -17.3ZnO-37.8ZnF <sub>2</sub>	23.40 37.80	Silica	650	60	[60]
68TeO <sub>2</sub> -12PbO-20ZnF <sub>2</sub> 59TeO <sub>2</sub> -11PbO-30ZnF <sub>2</sub> 50TeO <sub>2</sub> -10PbO-40ZnF <sub>2</sub> 46TeO <sub>2</sub> -9PbO-45ZnF <sub>2</sub>	20.00 30.00 40.00 45.00	Platinum	600	30	[61]
50TeO <sub>2</sub> -9.6As <sub>2</sub> O <sub>3</sub> -40ZnF <sub>2</sub> -0.4Cr <sub>2</sub> O <sub>3</sub> 50TeO <sub>2</sub> -9.6Bi <sub>2</sub> O <sub>3</sub> -40ZnF <sub>2</sub> -0.4Cr <sub>2</sub> O <sub>3</sub> 50TeO <sub>2</sub> -9.6P <sub>2</sub> O <sub>5</sub> -40ZnF <sub>2</sub> -0.4Cr <sub>2</sub> O <sub>3</sub>	40.00 40.00 40.00	N/A	N/A	N/A	[62]
74.7TeO <sub>2</sub> -18.3ZnO-7.1ZnF <sub>2</sub> 74.6TeO <sub>2</sub> -8.8ZnO-16.6ZnF <sub>2</sub> 69TeO <sub>2</sub> -9.3ZnO-21.7ZnF <sub>2</sub> 60.5TeO <sub>2</sub> -12ZnO-27.5ZnF <sub>2</sub> 46.6TeO <sub>2</sub> -18.2ZnO-35.2ZnF <sub>2</sub>	7.10 16.60 21.70 27.50 35.20	Platinum	650-800	20	[30, 31]

<sup>3</sup> No data given in reference.

A number of the compositions series in table (2.5) were melted in ceramic crucibles (silica, alumina or zirconia) which will inadvertently improve glass stability as some unwanted oxide will be taken into solution in the glass melt, but will affect optical properties (the IR-edge will be blue-shifted).

### 2.5.2.2. Thermal properties

The properties of fluorotellurite glasses in the early work by Stanworth [14] were reported in section 2.3.1.

Table (2.6) summarises the characteristic temperatures and Hruby's thermal stability parameter ( $K_H$ ) [63] of the glasses reported by Durga *et al.* [62].

Table (2.6): Thermal properties of the  $\text{Cr}^{3+}$  doped  $\text{ZnF}_2$ -MO- $\text{TeO}_2$  (MO =  $\text{P}_2\text{O}_5$ ,  $\text{Bi}_2\text{O}_3$  or  $\text{As}_2\text{O}_3$ ) glasses [62].

Glass (mol. %)	$T_g/^\circ\text{C}$	$T_c/^\circ\text{C}$	$T_m/^\circ\text{C}$	$T_c-T_g/^\circ\text{C}$	$K_H$
50 $\text{TeO}_2$ -9.6 $\text{As}_2\text{O}_3$ -40 $\text{ZnF}_2$ -0.4 $\text{Cr}_2\text{O}_3$	617	721	1081	104	0.289
50 $\text{TeO}_2$ -9.6 $\text{Bi}_2\text{O}_3$ -40 $\text{ZnF}_2$ -0.4 $\text{Cr}_2\text{O}_3$	595	679	1126	84	0.188
50 $\text{TeO}_2$ -9.6 $\text{P}_2\text{O}_5$ -40 $\text{ZnF}_2$ -0.4 $\text{Cr}_2\text{O}_3$	625	695	1145	70	0.155

The glass containing  $\text{As}_2\text{O}_3$  was the most thermally stable of the three.

Nazabal *et al.* [30] showed that thermal stability increased initially with  $\text{ZnF}_2$  addition to  $\text{TeO}_2$ - $\text{ZnO}$  glasses, however, further increases in stability with  $\text{ZnF}_2$  were not significant and within the errors of the DTA experiments. Table (2.7) summarises these characteristic temperatures, with glass density ( $\rho$ ), and electronic absorption edge ( $\lambda_c$ ).

Table (2.7): Characteristic temperatures, glass transition,  $T_g$ , onset of crystallisation,  $T_x$ , and peak crystallisation,  $T_c$ , with glass density ( $\rho$ ), and electric absorption edge ( $\lambda_c$ ) for  $\text{TeO}_2\text{-ZnO-ZnF}_2$  glasses [30].

Matrix	$T_g \pm 5 \text{ }^\circ\text{C}$	$T_x \pm 5 \text{ }^\circ\text{C}$	$T_c \pm 5 \text{ }^\circ\text{C}$	$T_x - T_g \text{ (}^\circ\text{C)}$	$\rho \pm 0.01 \text{ g/cm}^3$	$\lambda_c \text{ (nm)}$
75TeO <sub>2</sub> -25ZnO	315	404	420	89	5.53	357
75TeO <sub>2</sub> -18ZnO-7ZnF <sub>2</sub>	278	398	417	120	5.49	343
75TeO <sub>2</sub> -9ZnO-16ZnF <sub>2</sub>	261	380	398	119	5.45	331
69TeO <sub>2</sub> -9ZnO-22ZnF <sub>2</sub>	258	378	395	120	5.43	322
61TeO <sub>2</sub> -12ZnO-27ZnF <sub>2</sub>	257	374	389	117	5.37	311
47TeO <sub>2</sub> -18ZnO-35ZnF <sub>2</sub>	256	368	387	112	5.33	305

### 2.5.2.3. Optical properties

Adams [56] measured the IR-spectra of glasses in the system  $\text{TeO}_2\text{-PbO-ZnF}_2$  as shown in fig. (2.14). Trace (a) 15.17 mol. %  $\text{ZnF}_2$ , (b) 28.92 mol. %  $\text{ZnF}_2$ , (c) 40.91 mol. %  $\text{ZnF}_2$ , and (d) 51.81 mol. %  $\text{ZnF}_2$ .

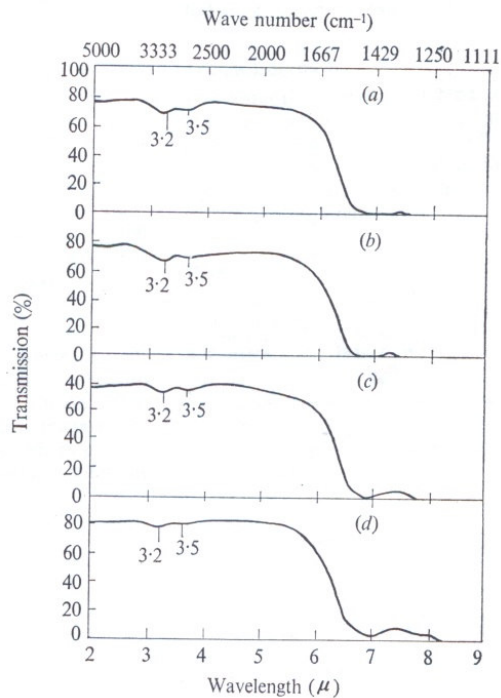


Fig. (2.14): IR-spectra of glasses in the system  $\text{TeO}_2\text{-PbO-ZnF}_2$  [56].

The glasses exhibited two absorption bands attributed to 'water', with maxima around 3.2 and 3.5  $\mu\text{m}$ . Both bands are broad and overlap, but are of low intensity, and are practically non-existent in the glass with 51.81 mol. %  $\text{ZnF}_2$ , due to chemical reactions which take place during melting as shown by equation (2.16) to (2.18).

Nazabal *et al.* [30] showed a decrease in OH bands with increasing  $\text{ZnF}_2$  content in the glass as shown by fig. (2.15).

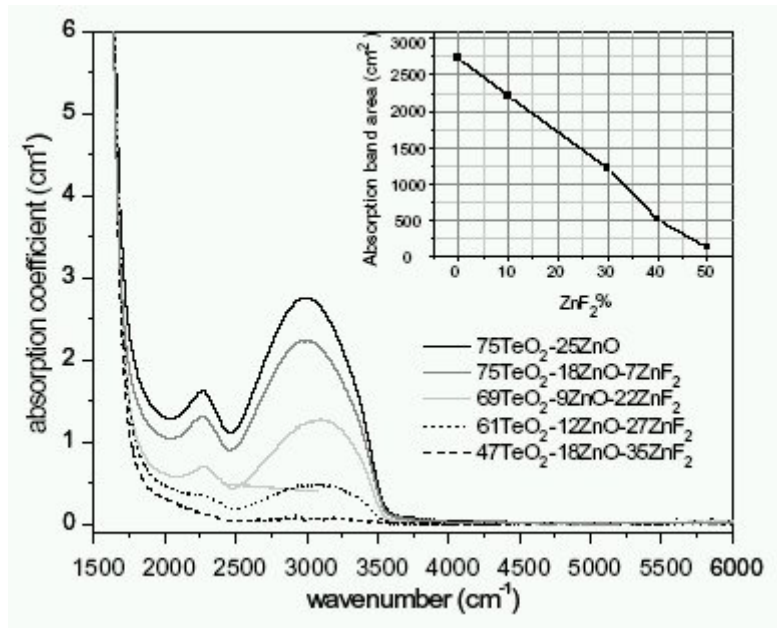


Fig. (2.15): Infrared spectra of  $\text{TeO}_2\text{-ZnO-ZnF}_2$  glasses [30].

It can be seen the OH bands were reduced by self-drying during melting as described by equations (2.16) to (2.18). Erbium (III) bands at around 1.55  $\mu\text{m}$  in these glasses were shown to slightly broaden, and  $^4\text{I}_{11/2}$  and  $^4\text{I}_{13/2}$  lifetimes significantly increase (from 0.4 to 2.2 ms and 3 to 7 ms respectively, for 0 to 35 mol. %  $\text{ZnF}_2$ ) with fluorine content. This was thought to be due to a combination of a change in ion-host field strengths, and reduction in OH content with fluorine addition [31].

### 2.5.2.4. Mechanical properties

Kumar *et al.* [59] studied the mechanical properties of TeO<sub>2</sub>-PbO-ZnF<sub>2</sub> glasses, shown in table (2.8).

Table (2.8): Mechanical properties of glasses (mol. %) A: 68TeO<sub>2</sub>-12PbO-20ZnF<sub>2</sub>, B: 59TeO<sub>2</sub>-11PbO-30ZnF<sub>2</sub>, C: 50TeO<sub>2</sub>-10PbO-40ZnF<sub>2</sub>, and D: 46TeO<sub>2</sub>-9PbO-45ZnF<sub>2</sub> [59].

Glass	Young's modulus $Y$ (kbar)	Shear modulus $\eta$ (kbar)	Poisson's ratio $\sigma$	Microhardness $H$ (kbar)
A	545	239	0.140	57.34
B	547	240	0.138	58.01
C	551	245	0.124	59.09
D	557	249	0.119	63.18

It can be seen, as the ZnF<sub>2</sub> content was increased, and PbO decreased, the elastic coefficients of the glass increased. This was thought to be due to depolymerisation of the network with increasing PbO content, which the authors believe had a stronger effect than ZnF<sub>2</sub> [59].

## 2.6. References

- [1] H. Rawson, *Inorganic glass-forming systems*, vol. 2, 1st ed. London: Academic Press, 1967.
- [2] W. Vogel, *Glass chemistry*, 2nd ed. New York: Springer-Verlag, 1994.
- [3] J. T. Randall, H. P. Rooksby, and B. S. Cooper, *Journal of the Society of Glass Technology*, vol. 14, pp. 219-229, 1930.
- [4] B. E. Warren, *Journal of Applied Physics*, vol. 8, pp. 645-654, 1937.

- [5] J. T. Randall, H. P. Rooksby, and B. S. Cooper, "The structure of glasses; the evidence of X-ray diffraction," *Journal of the Society of Glass Technology*, vol. 14, pp. 219-229, 1930.
- [6] W. H. Zachariasen, "The atomic arrangement in glass," *Journal of the American Chemical Society*, vol. 54, pp. 3841-3851, 1932.
- [7] E. Zanotto, "Private communication," 2004.
- [8] A. B. Seddon, W. A. Shah, A. G. Clare, and J. M. Parker, "The effect of NaF on the crystallisation of ZBLAN glasses," *Materials Science Forum*, vol. 19&20, pp. 465-474, 1987.
- [9] K. W. Bagnall, *The Chemistry of Selenium, Tellurium and Polonium*. London: Elsevier, 1966.
- [10] J. Berzelius, *Annalen der Physik und Chemie*, vol. 32, pp. 577, 1834.
- [11] V. Lenher and E. Wolessky, "A study of the metallic tellurites," *Journal of the American Chemical Society*, vol. 35, pp. 718-733, 1913.
- [12] J. E. Stanworth, "Tellurite glasses," *Nature*, vol. 169, pp. 581-582, 1952.
- [13] J. Stanworth, "Tellurite Glasses," *Journal of the Society of Glass Technology*, vol. 36, pp. 217-241, 1952.
- [14] J. E. Stanworth, "Tellurite glasses," *Journal of the Society of Glass Technology*, vol. 36, pp. 217-241, 1952.
- [15] N. N. Greenwood and A. Earnshaw, *Chemistry of the elements*. Oxford: Butterworth-Heinemann, 1995.
- [16] R. Adams, "Infra-red absorption due to water in glasses," *Physics and Chemistry of Glasses*, vol. 2, pp. 39-49, 1961.
- [17] M. D. O'Donnell, C. A. Miller, D. Furniss, V. K. Tikhomirov, and A. B. Seddon, "Fluorotellurite glasses with improved mid-infrared transmission," *Journal of Non-Crystalline Solids*, vol. 331, pp. 48-57, 2003.
- [18] M. Redman and J. Chen, "Zinc tellurite glasses," *Journal of the American Ceramic Society*, vol. 50, pp. 523-525, 1967.
- [19] A. P. Mirgorodsky, T. Merle-Mejean, J. C. Champarnaud, P. Thomas, and B. Frit, "Dynamics and structure of TeO<sub>2</sub> polymorphs: model treatment of paratellurite and tellurite; Raman scattering evidence for new gamma- and delta-phases," *Journal of Physics and Chemistry of Solids*, vol. 61, pp. 501-509, 2000.

- [20] J. A. K. Tareen and T. R. N. Kutty, *A basic course in crystallography*. Bangalore: Universities Press, 2001.
- [21] J. C. Champarnaud-Mesjard, S. Blanchandin, P. Thomas, A. Mirgorodsky, T. Merle-Mejean, and B. Frit, "Crystal structure, Raman spectrum and lattice dynamics of a new metastable form of tellurium dioxide: gamma-TeO<sub>2</sub>," *Journal of Physics and Chemistry of Solids*, vol. 61, pp. 1499-1507, 2000.
- [22] V. Kozhukharov, H. Burger, S. Neov, and B. Sidzhimov, "Atomic arrangement of a zinc-tellurite glass," *Polyhedron*, vol. 5, pp. 771-777, 1986.
- [23] Y. Shimizugawa, T. Maeseto, S. Inoue, and A. Nukui, "Structure of TeO<sub>2</sub>.ZnO glasses by RDF and Te, Zn K EXAFS," *Physics and Chemistry of Glasses*, vol. 38, pp. 201-205, 1997.
- [24] Y. Himei, Y. Miura, T. Nanba, and A. Osaka, "X-ray photoelectron spectroscopy of alkali tellurite glasses," *Journal of Non-Crystalline Solids*, vol. 211, pp. 64-71, 1997.
- [25] J. W. Zwanziger, J. C. McLaughlin, and S. L. Tagg, "Sodium distribution in sodium tellurite glasses probed with spin-echo NMR," *Physical Review B*, vol. 56, pp. 5243-5249, 1997.
- [26] S. Sakida, S. Hayakawa, and T. Yoko, "Part 2. Te-125 NMR study of M<sub>2</sub>O-TeO<sub>2</sub> (M = Li, Na, K, Rb and Cs) glasses," *Journal of Non-Crystalline Solids*, vol. 243, pp. 13-25, 1999.
- [27] J. C. McLaughlin, S. L. Tagg, J. W. Zwanziger, D. R. Haeffner, and S. D. Shastri, "The structure of tellurite glass: a combined NMR, neutron diffraction, and X-ray diffraction study," *Journal of Non-Crystalline Solids*, vol. 274, pp. 1-8, 2000.
- [28] J. C. McLaughlin, S. L. Tagg, and J. W. Zwanziger, "The structure of alkali tellurite glasses," *Journal of Physical Chemistry B*, vol. 105, pp. 67-75, 2001.
- [29] D. L. Sidebottom, M. A. Hruschka, B. G. Potter, and R. K. Brow, "Increased radiative lifetime of rare earth-doped zinc oxyhalide tellurite glasses," *Applied Physics Letters*, vol. 71, pp. 1963-1965, 1997.
- [30] V. Nazabal, S. Todoroki, A. Nukui, T. Matsumoto, S. Suehara, T. Hondo, T. Araki, S. Inoue, C. Rivero, and T. Cardinal, "Oxyfluoride tellurite glasses doped by erbium: thermal analysis, structural organization and spectral properties," *Journal of Non-Crystalline Solids*, vol. 325, pp. 85-102, 2003.
- [31] V. Nazabal, S. Todoroki, S. Inoue, T. Matsumoto, S. Suehara, T. Hondo, T. Araki, and T. Cardinal, "Spectral properties of Er<sup>3+</sup> doped oxyfluoride tellurite glasses," *Journal of Non-Crystalline Solids*, vol. 326-327, pp. 359-363, 2003.
- [32] J. Tyndall, *Proceedings of the Royal Institution*, vol. 6, pp. 189, 1870.

- [33] A. C. S. van Heel, "A new method of transporting optical images without aberrations," *Nature*, vol. 173, pp. 39, 1954.
- [34] J. Hecht, *Understanding fiber optics*, 2nd ed. Indianapolis: Sams Publishing, 1993.
- [35] J. M. Parker and A. B. Seddon, "Infrared-transmitting optical fibres," in *High-Performance Glasses*, M. Cable and J. M. Parker, Eds. London: Blackie, 1992, pp. 252-286.
- [36] J. Wang, E. Vogel, and E. Snitzer, "Tellurite glass: a new candidate for fiber devices," *Optical Materials*, vol. 3, pp. 187-203, 1994.
- [37] R. Stegeman, L. Jankovic, H. Kim, C. Rivero, G. Stegeman, K. Richardson, and P. Delfyett, "Tellurite glasses with peak absolute Raman gain coefficients up to 30 times that of fused silica," *Optics Letters*, vol. 28, pp. 1126-1128, 2003.
- [38] J. S. Sanghera, B. Shaw, L. Busse, P. Thielen, V. Nguyen, P. Pureza, F. Kung, D. Gibson, S. Bayya, and I. Aggarwal, "Chalcogenide glass optical fiber applications," presented at Glass and Optical Materials Fall 2004 Meeting incorporating the XIVth International Symposium on Non-Oxide and Novel Optical Glasses, Cape Canaveral, Florida, USA, 2004.
- [39] C. K. Kao, *Optical fibre*. London: Peter Peregrinus Ltd., 1988.
- [40] G. Fuxi, *Optical and spectroscopic properties of glass*, 1st ed. London: Springer-Verlag, 1992.
- [41] M. E. Lines, "Scattering losses in optical fiber materials. I. A new parameterization," *Journal of Applied Physics*, vol. 55, pp. 4052-4057, 1984.
- [42] M. E. Lines, "Scattering losses in optical fiber materials. II. Numerical estimates," *Journal of Applied Physics*, vol. 55, pp. 4058-4063, 1984.
- [43] D. W. Pinnow, T. C. Rich, F. W. Ostermayer, and M. DiDomenico, "Fundamental optical attenuation limits in the liquid and glassy state with application to fiber optic waveguide materials," *Applied Physics Letters*, vol. 22, pp. 527-529, 1973.
- [44] S. Shibata, M. Horiguchi, M. Jinguji, S. Mitachi, T. Kanamori, and T. Manabe, "Prediction of loss minima in infra-red optical fibres," *Electronics Letters*, vol. 17, pp. 775-777, 1981.
- [45] J. S. Aitchison, J. D. Prohaska, and E. M. Vogel, "The nonlinear optical properties of glass," *Metals Materials and Processes*, vol. 8, pp. 277-290, 1997.
- [46] C. A. Angell, "Spectroscopy simulation and scattering, and the medium range order problem in glass," *Journal of Non-Crystalline Solids*, vol. 73, pp. 1-17, 1985.

- [47] S. W. Martin and C. A. Angell, "On the glass transition and viscosity of  $P_2O_5$ ," *Journal of Physical Chemistry*, vol. 90, pp. 6736-6740, 1986.
- [48] M. Braglia, S. Mosso, G. Dai, E. Billi, L. Bonelli, M. Baricco, and L. Battezzati, "Rheology of tellurite glasses," *Materials Research Bulletin*, vol. 35, pp. 2343-2351, 2000.
- [49] S. Yoshida, J. Matsuoka, and N. Soga, "Crack growth behavior of zinc tellurite glass with or without sodium oxide," *Journal of Non-Crystalline Solids*, vol. 279, pp. 44-50, 2001.
- [50] R. J. Charles, "Dynamic fatigue of glass," *Journal of Applied Physics*, vol. 29, pp. 1657-1662, 1958.
- [51] T. Watanabe, Y. Benino, and T. Komatsu, "Change in Vickers hardness at the glass transition region for fragile and strong glasses," *Journal of Non-Crystalline Solids*, vol. 286, pp. 141-145, 2001.
- [52] K. Aida, T. Komatsu, and V. Dimitrov, "Thermal stability, electronic polarisability and optical basicity of ternary tellurite glasses," *Physics and Chemistry of Glasses*, vol. 42, pp. 103-111, 2001.
- [53] X. Feng, S. Tanabe, and T. Hanada, "Hydroxyl groups in erbium-doped germanotellurite glasses," *Journal of Non-Crystalline Solids*, vol. 281, pp. 48-54, 2001.
- [54] X. Feng, S. Tanabe, and T. Hanada, "Spectroscopic properties and thermal stability of  $Er^{3+}$ -doped germanotellurite glasses for broadband fiber amplifiers," *Journal of the American Ceramic Society*, vol. 84, pp. 165-171, 2001.
- [55] S. Shen, A. Jha, E. Zhang, and S. J. Wilson, "Compositional effects and spectroscopy of rare earths ( $Er^{3+}$ ,  $Tm^{3+}$ , and  $Nd^{3+}$ ) in tellurite glasses," *Comptes Rendus Chimie*, vol. 5, pp. 921-938, 2002.
- [56] R. Adams, "Some experiments on the removal of water from glasses," *Physics and Chemistry of Glasses*, vol. 2, pp. 50-54, 1961.
- [57] K. Kobayashi and H. Sasaki, "Visible rays cutoff and infrared transmission properties of  $TeO_2$ - $GeO_2$ - $V_2O_5$ - $PbF_2$  glass systems," *Journal of the European Ceramic Society*, vol. 19, pp. 637-639, 1999.
- [58] V. R. Kumar, N. Veeraiah, and B. A. Rao, "Optical absorption and photoluminescence properties of  $Pr^{3+}$ -doped  $ZnF_2$ - $PbO$ - $TeO_2$  glasses," *Journal of Luminescence*, vol. 75, pp. 57-62, 1997.
- [59] V. R. Kumar and N. Veeraiah, "Infrared spectral investigations on  $ZnF_2$ - $PbO$ - $TeO_2$  glasses," *Journal of Materials Science Letters*, vol. 16, pp. 1816-1818, 1997.

- [60] D. L. Sidebottom, M. A. Hruschka, B. G. Potter, and R. K. Brow, "Structure and optical properties of rare earth-doped zinc oxyhalide tellurite glasses," *Journal of Non-Crystalline Solids*, vol. 222, pp. 282-289, 1997.
- [61] V. R. Kumar and N. Veeraiah, "Dielectric properties of  $\text{ZnF}_2\text{-PbO-TeO}_2$  glasses," *Journal of Physics and Chemistry of Solids*, vol. 59, pp. 91-97, 1998.
- [62] D. K. Durga, P. Yadagiri Reddy, and N. Veeraiah, "Optical absorption and thermoluminescence properties of  $\text{ZnF}_2\text{-MO-TeO}_2$  (MO =  $\text{As}_2\text{O}_3$ ,  $\text{Bi}_2\text{O}_3$  and  $\text{P}_2\text{O}_5$ ) glasses doped with chromium ions," *Journal of Luminescence*, vol. 99, pp. 53-60, 2002.
- [63] A. Hruby, "Evaluation of glass-forming tendency by means of DTA," *Czechoslovak Journal of Physics Section B*, vol. 22, pp. 1187, 1972.

## 3. Glass batching and melting

### 3.1. Glass compositions used in this study

A wide range of oxide and oxyfluoride tellurite glass compositions was synthesised and characterised in this study to choose suitable core / cladding compositions for fibre drawing. Table (3.1) shows the oxide compositions melted and table (3.2) shows the fluorotellurite compositions (bulk samples for characterisation and fiberoptic preforms).

### 3.2. Glass batching

Glass properties are in general strongly dependent on composition so it is important to be able to predict final glass compositions as accurately as possible before melting. Due to volatilisation during glass melting, especially of fluoride compounds, there will have been some degree of error in the batch calculation, but with carefully controlled melting conditions these errors could be minimised. Table (3.3) shows the chemicals used to batch glasses in this study. Further purification of the batch is described later in section (3.4).

Batch calculations were performed using a program developed in house by Dr. D. Furniss, called *Batch*. Fig. (3.1) shows the input window of this programme.

Table (3.1): Multicomponent oxide tellurite glass compositions melted in this study.

<b>MOD ID</b>	<b>TeO<sub>2</sub> / mol. %</b>	<b>ZnO / mol. %</b>	<b>Na<sub>2</sub>O / mol. %</b>	<b>PbO / mol. %</b>	<b>GeO<sub>2</sub> / mol. %</b>	<b>WO<sub>3</sub> / mol. %</b>	<b>Nb<sub>2</sub>O<sub>5</sub> / mol. %</b>	<b>Bi<sub>2</sub>O<sub>3</sub> / mol. %</b>	<b>Er<sub>2</sub>O<sub>3</sub> / mol. %</b>	<b>Yb<sub>2</sub>O<sub>3</sub> / mol. %</b>	<b>La<sub>2</sub>O<sub>3</sub> / mol. %</b>
<b>T08</b>	80.00	9.00	10.00	-	-	-	-	-	1.00	-	-
<b>ST08</b>	79.00	5.00	10.00	5.00	-	-	-	-	-	1.00	-
<b>001</b>	79.00	-	10.00	10.00	-	-	-	-	-	1.00	-
<b>002</b>	78.21	4.95	9.90	4.95	-	-	-	-	0.99	0.99	-
<b>003</b>	82.29	5.21	10.42	-	-	-	-	-	1.04	1.04	-
<b>004</b>	80.00	10.00	9.00	-	-	-	-	-	-	-	1.00
<b>005</b>	78.00	10.00	5.00	5.00	-	-	-	-	1.00	1.00	-
<b>006</b>	77.00	10.00	10.00	3.00	-	-	-	-	-	-	-
<b>007</b>	78.00	12.00	10.00	-	-	-	-	-	-	-	-
<b>008</b>	74.00	12.00	10.00	3.00	-	-	-	-	-	1.00	-
<b>009</b>	77.00	12.00	10.00	-	-	-	-	-	-	1.00	-
<b>010</b>	75.00	10.00	10.00	5.00	-	-	-	-	-	-	-
<b>011</b>	70.00	10.00	10.00	10.00	-	-	-	-	-	-	-
<b>012</b>	75.00	10.00	10.00	-	5.00	-	-	-	-	-	-
<b>013</b>	80.00	10.00	10.00	-	-	-	-	-	-	-	-
<b>014</b>	90.00	-	-	-	-	5.00	5.00	-	-	-	-
<b>015</b>	82.50	-	-	-	-	7.50	10.00	-	-	-	-
<b>016</b>	70.00	-	-	-	-	25.00	-	5.00	-	-	-

Table (3.2): Fluorotellurite glass compositions melted in this study.

<b>MOF ID</b>	<b>TeO<sub>2</sub> / mol. %</b>	<b>Na<sub>2</sub>O / mol. %</b>	<b>ZnF<sub>2</sub> / mol. %</b>	<b>ZnO / mol. %</b>	<b>PbF<sub>2</sub> / mol. %</b>	<b>WO<sub>3</sub> / mol. %</b>	<b>Er<sub>2</sub>O<sub>3</sub> / mol. %</b>	<b>ErF<sub>3</sub> / mol. %</b>
001	65.00	10.00	25.00	-	-	-	-	-
002	70.00	10.00	10.00	-	10.00	-	-	-
003	65.00	10.00	20.00	-	5.00	-	-	-
004	60.00	10.00	30.00	-	-	-	-	-
005	70.00	10.00	20.00	-	-	-	-	-
006	75.00	10.00	15.00	-	-	-	-	-
007	80.00	10.00	10.00	-	-	-	-	-
008	85.00	10.00	5.00	-	-	-	-	-
009	65.00	10.00	20.00	5.00	-	-	-	-
010	65.00	10.00	15.00	10.00	-	-	-	-
011	65.00	10.00	10.00	15.00	-	-	-	-
012	65.00	10.00	5.00	20.00	-	-	-	-
013	65.00	10.00	-	25.00	-	-	-	-
014	65.00	10.00	-	-	-	25.00	-	-
015	69.30	9.90	19.80	-	-	-	1.00	-
016	69.93	9.99	19.98	-	-	-	0.10	-
017	69.86	9.98	19.96	-	-	-	-	0.20
018	69.98	10.00	20.00	-	-	-	-	0.02



In the first column of the input window (see fig. (3.1)) the required oxide and fluoride components in the final glass were selected from an alphabetical drop down menu. A different chemical had sometimes to be batched from the required chemical in the final glass, for example due to decomposition during melting (e.g.  $\text{Na}_2\text{CO}_3 \rightarrow \text{Na}_2\text{O} + \text{CO}_2\uparrow$  [1]). If applicable this different chemical was selected from a drop down menu in the third column. The molar % of each component required in the final glass was entered into the fifth column and finally the mass of the final glass required was entered at the bottom of the window in grams. The ‘Calc from Mole%’ button was then pressed and the weight % and weight in grams of each component were calculated. A description of the glass could be entered and the complete table printed off for reference when batching.

An example batch calculation will now be shown for the composition MOF001 shown in fig. (3.1). The calculation was for 10g of glass of composition 65TeO<sub>2</sub>-10Na<sub>2</sub>O-25ZnF<sub>2</sub> (mol. %). The ratio (by weight) of one mole Na<sub>2</sub>CO<sub>3</sub> needed to produce one mole of Na<sub>2</sub>O in the final glass is shown by equation (3.1), where  $RAM_x$  is the relative atomic mass of compound  $x$ :

$$\frac{[RAM_{\text{Na}_2\text{CO}_3}]}{[RAM_{\text{Na}_2\text{O}}]} = \frac{105.99}{61.98} = 1.71 \quad (3.1)$$

Equation (3.2) shows the weight % of TeO<sub>2</sub>, where  $Wt.\%_x$  is the weight % of compound  $x$  in the glass, and  $mol.\%_x$  is the molar % of compound  $x$  in the glass:

$$Wt.\%_{\text{TeO}_2} = \frac{mol.\%_{\text{TeO}_2} \times RAM_{\text{TeO}_2}}{(mol.\%_{\text{TeO}_2} \times RAM_{\text{TeO}_2}) + (mol.\%_{\text{Na}_2\text{O}} \times RAM_{\text{Na}_2\text{O}}) + (mol.\%_{\text{ZnF}_2} \times RAM_{\text{ZnF}_2})} \times 100$$

$$= \frac{65 \times 159.60}{(65 \times 159.60) + (10 \times 61.98) + (25 \times 103.37)} \times 100 = 76.40\% \quad (3.2)$$

Thus for 10g of glass  $0.7640 \times 10 = 7.64\text{g}$  of  $\text{TeO}_2$  was batched. Equation (3.3) shows the weight %  $\text{ZnF}_2$ :

$$\begin{aligned} \text{Wt.}\%_{\text{ZnF}_2} &= \frac{\text{mol.}\%_{\text{ZnF}_2} \times \text{RAM}_{\text{ZnF}_2}}{(\text{mol.}\%_{\text{TeO}_2} \times \text{RAM}_{\text{TeO}_2}) + (\text{mol.}\%_{\text{Na}_2\text{O}} \times \text{RAM}_{\text{Na}_2\text{O}}) + (\text{mol.}\%_{\text{ZnF}_2} \times \text{RAM}_{\text{ZnF}_2})} \times 100 \\ &= \frac{25 \times 103.37}{(65 \times 159.60) + (10 \times 61.98) + (25 \times 103.37)} \times 100 = 19.03\% \quad (3.3) \end{aligned}$$

Thus for 10g of glass  $0.1903 \times 10 = 1.90\text{g}$  of  $\text{ZnF}_2$  was batched. Equation (3.4) shows the weight % of  $\text{Na}_2\text{O}$ :

$$\begin{aligned} \text{Wt.}\%_{\text{Na}_2\text{O}} &= \frac{\text{mol.}\%_{\text{Na}_2\text{O}} \times \text{RAM}_{\text{Na}_2\text{O}}}{(\text{mol.}\%_{\text{TeO}_2} \times \text{RAM}_{\text{TeO}_2}) + (\text{mol.}\%_{\text{Na}_2\text{O}} \times \text{RAM}_{\text{Na}_2\text{O}}) + (\text{mol.}\%_{\text{ZnF}_2} \times \text{RAM}_{\text{ZnF}_2})} \times 100 \\ &= \frac{10 \times 61.98}{(65 \times 159.60) + (10 \times 61.98) + (25 \times 103.37)} \times 100 = 4.57\% \quad (3.4) \end{aligned}$$

Thus for 10g of glass  $0.0457 \times 10 \times 1.71 = 0.78\text{g}$  of  $\text{Na}_2\text{CO}_3$  was batched.

These calculations are summarised in Table (3.4).

Table (3.4): Summary of batch calculation above for 10g of glass MOF001 (65TeO<sub>2</sub>-10Na<sub>2</sub>O-25ZnF<sub>2</sub> mol. %).

Compound in glass	RAM / g.mol <sup>-1</sup>	Batch as	RAM / g.mol <sup>-1</sup>	Ratio	Mol. %	Wt. %	Mass / g
TeO <sub>2</sub>	159.60	TeO <sub>2</sub>	159.60	1.00	65	76.40	7.64
Na <sub>2</sub> O	61.98	Na <sub>2</sub> CO <sub>3</sub>	105.99	1.71	10	4.57	0.78
ZnF <sub>2</sub>	103.37	ZnF <sub>2</sub>	103.37	1.00	25	19.03	1.90
<b>Total:</b>					100	100.00	10.32

Glasses were batched into a gold or platinum crucible on electronic scales (Sartorius BP211D), which nominally read to five decimal places (i.e. to the nearest  $1 \times 10^{-5}$  g). The chemicals were weighed out accurately to three decimal places (i.e. to the nearest  $1 \times 10^{-3}$  g or 1 mg) from the batch calculation using clean stainless steel spatulas (Fisher), washed with acetone (Fisher analytical reagent grade) before batching and cleaned with non-shedding tissues (Fisher) between batching each chemical. The amount of glass batched depended on the use of the final glass; for instance in order to carry out thermal analysis and optical spectroscopy, typically just over 10g of material was batched yielding around 10g of final glass (see Table (3.4)). In order to produce an unstructured glass preform for fibre-drawing, typically just over 30g of material was batched yielding around 30g of final glass.

### 3.3. Glass Melting

Glasses were melted in a resistance furnace (Instron TF105/4.5/1ZF using an Instron C130011100 power supply containing a Eurotherm 2408 controller) housed in a stainless steel lined fume cupboard in a lidded platinum or gold crucible (height = 40 mm, base diameter = 23 mm, top diameter = 40 mm). The crucibles were cleaned by soaking in Fisher 48% HCl acid, diluted to 3M with distilled water, between each

melt for at least 24 hours, then rinsed with distilled water and acetone and placed in a drying oven at 100°C for at least 1 hour prior to melting. Melting was carried out inside a silica liner (Multilab, height = 300 mm, diameter = 80 mm, wall thickness = 2.5 mm), through which dry air (BOC, < 1ppm water), was flowed ( $1 \text{ l.min.}^{-1}$ ) through the silica lid (Multilab, diameter = 100 mm, thickness = 3 mm), dried by passage through an A4 molecular sieve (regenerated every 6 months by heating via an internal heater attached to a vacuum pump). The crucible was placed in, and removed from the furnace using a ceramic cradle (alumina, height = 31 mm, diameter 48 mm, wall thickness = 3 mm) equipped with a platinum wire as a handle. The crucibles were removed from the furnace using a brass hooked rod and were handled during casting with stainless steel tweezers (Fisher). Fig. (3.2) shows the melting set-up.

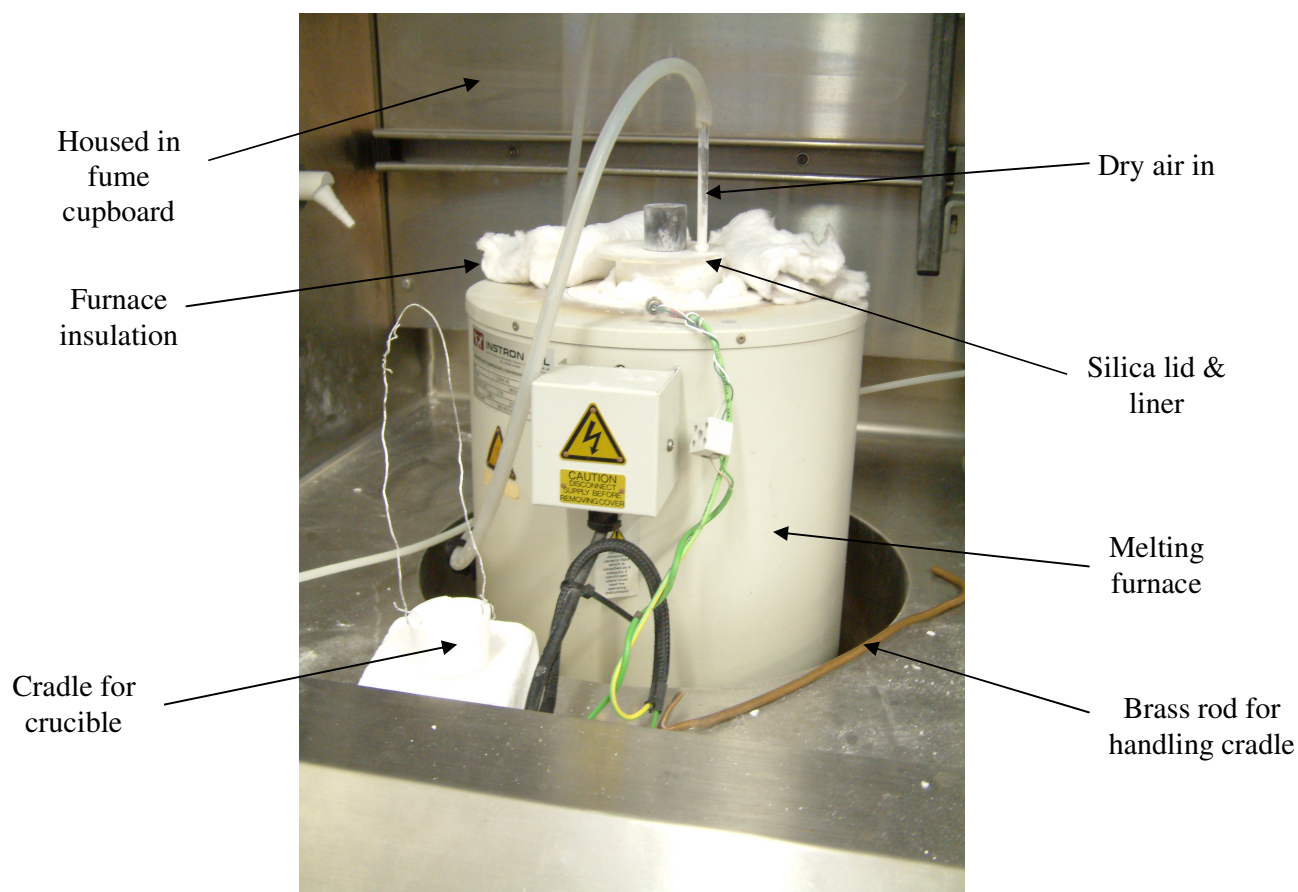


Fig. (3.2): Glass melting set-up.

Fig. (3.3) shows a typical temperature profile of the melting and annealing furnace (Instron TF105/4.5/1ZF using an Instron C130011100 power supply containing a Eurotherm 2408 controller) at 400°C. The furnace was left to equilibrate for 1 hour, with laboratory air.

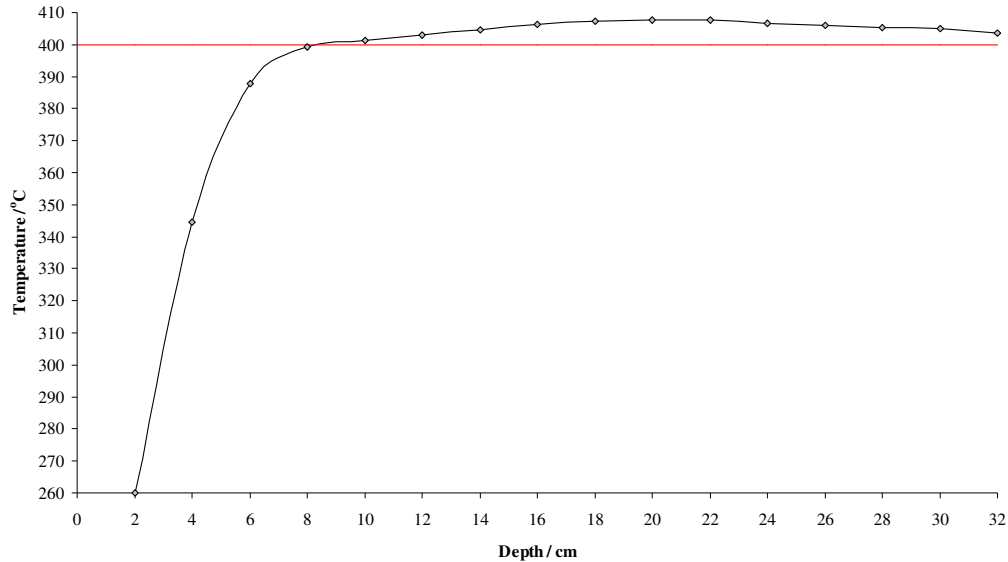


Fig. (3.3): Temperature profile of melting and annealing furnace at 400°C.

After melting the glasses were cast into preheated (to around 10°C below  $T_g$ ) brass or aluminium moulds (size and shape depending on the desired end product) and annealed for an hour just below the glass transition temperature ( $\approx T_g - 10^\circ\text{C}$ ) then slowly cooled to room temperature at around  $10^\circ\text{C}\cdot\text{hr}^{-1}$ . Between melts the inner surfaces of the moulds were cleaned with acetone. In this study three moulds were used, a small aluminium mould (SA: internal dimensions  $3 \times 20 \times 60$  mm, wall thickness = 5 mm), a large brass mould (LB: internal dimensions  $8 \times 40 \times 50$  mm, wall thickness = 10 mm), and a cylindrical brass mould (CB: internal diameter = 10mm, length = 110 mm, wall thickness = 4 mm). Fig. (3.4) shows these moulds.



Fig. (3.4): Moulds used for casting glasses in this study (from left to right): large brass (LB), small aluminium (SA) and cylindrical brass (CB).

The oxide glasses listed in table (3.1) were melted at 800°C (in a preheated furnace), with the duration depending on the size of the batch (see table (3.5)). In general, a larger batch weight required a longer melting time, to ensure the end glass was completely homogeneous and all the batch materials had fully melted. The glass also self-dried to some degree during melting, however, not to the extent of fluoride containing glasses. The fluorotellurite glasses listed in table (3.2) were held at 800°C for half the total melting time, and cooled to 670°C for the remainder of the melt due to strong mould adherence if they were cast at temperatures exceeding 700°C. Again,

the duration of melting depended on the size of the batch to ensure complete melting, homogenisation, and sufficient drying occurred (see table (3.6)).

Table (3.5): Melting details for oxide tellurite glasses melted in this study.

MOD ID	Stage 1 <sup>1</sup>		Stage 2 <sup>2</sup>		Weight / g	Mould <sup>3</sup>	Wt. % Volatilisation	Crystallisation
	Temp. / °C	Time / hr.	Temp. / °C	Time / hr.				
<b>T08</b>	830	1.0	250	1.0	10	LB	-	N
<b>ST08</b>	830	1.0	250	1.0	10	LB	-	N
<b>001</b>	830	1.0	250	1.0	10	LB	-	Y
<b>002</b>	830	1.0	250	1.0	10	LB	0.26	N <sup>1</sup>
<b>003</b>	830	1.0	250	1.0	10	LB	0.24	N <sup>4</sup>
<b>004</b>	830	1.0	250	1.0	10	SA	0.18	N
<b>005</b>	830	1.0	250	1.0	10	SA	0.58	Y
<b>006</b>	800	1.0	250	1.0	10	SA	-	N
<b>007</b>	800	1.0	250	1.0	10	SA	-	N
<b>008</b>	800	1.0	250	1.0	10	SA	0.52	N
<b>009</b>	800	1.0	250	1.0	10	SA	0.24	N
<b>010i</b>	800	2.0	250	1.0	30	CB	0.16	N
<b>010ii</b>	800	1.0	250	1.0	10	SA	0.25	N
<b>011</b>	800	1.0	250	1.0	10	SA	0.08	N <sup>1</sup>
<b>012</b>	800	1.0	250	1.0	10	SA	0.91	N
<b>013</b>	800	1.0	250	1.0	10	SA	0.43	N
<b>014i</b>	850	1.0	320	1.0	10	SA	0.20	N
<b>014ii</b>	850	1.0	335	1.0	18	LB	0.07	N
<b>015</b>	850	1.0	320	1.0	10	SA	0.15	N
<b>016</b>	820	1.0	350	1.0	10	SA	0.06	N

<sup>1</sup> Stage 1 was the melting stage

<sup>2</sup> Stage 2 was the annealing stage

<sup>3</sup> LB = large brass, SA = small aluminium, CB = cylindrical brass

<sup>4</sup> Partial

Table (3.6): Melting details for fluoride containing tellurite glasses melted in this study.

MOF ID	Stage 1 <sup>5</sup>		Stage 2 <sup>6</sup>		Stage 3 <sup>7</sup>		Weight / g	Mould <sup>8</sup>	Wt. % Volatilisation	Crystallisation
	Temp. / °C	Time / hr.	Temp. / °C	Time / hr.	Temp. / °C	Time / hr.				
001i	700	1.00	-	-	250	1.00	10	SA	-	N
001ii	750	1.00	-	-	230	1.00	10	SA	-	N
001iii	750	1.00	600	0.75	225	1.00	10	SA	5.84	N
001iv	750	1.00	650	0.75	230	1.00	10	SA	6.19	N
001v	800 <sup>9</sup>	1.00	670	1.00	230	1.00	10	SA	-	N
001vi	800	1.00	670	1.00	230	1.00	30	CB	-	N
002	750	1.00	-	-	250	1.00	10	SA	-	N
003	750	1.00	650	0.75	225	1.00	10	SA	1.77	N
004i	750	1.00	650	0.75	232	1.00	10	SA	10.06	N
004ii	800	1.00	670	1.00	230	1.00	30	CB	2.99	N
004iii	800	1.50	670	1.50	230	1.00	30	CB	3.05	N
004iv	800	1.50	670	1.50	230	1.00	30	CB	2.96	N
005i	750	1.00	650	0.75	234	1.00	10	SA	4.34	N
005ii	800	1.00	670	1.00	230	1.00	30	CB	2.03	N
005iii	800	1.00	670	1.00	230	1.00	30	CB	2.02	N
005iv	800	1.50	670	1.50	230	1.00	30	CB	2.44	N
005v	800	2.00	670	2.00	230	1.00	30	CB	2.83	N
005vi	800 <sup>9</sup>	2.50	670	2.50	230	1.00	30	CB	1.90	N
005vii	800 <sup>9</sup>	5.00	670	5.00	230	1.00	30	CB	5.53	N
005viii	800 <sup>9</sup>	6.00	670	6.00	230	1.00	30	CB	6.27	N
005ix <sup>10</sup>	800 <sup>9</sup>	12	-	-	230	1.00	30	CA	-	N
005x <sup>10</sup>	800 <sup>9</sup>	12	-	-	230	1.00	30	CA	-	N
006	750	1.00	650	0.75	230	1.00	10	SA	3.53	N
007	750	1.00	650	0.75	230	1.00	10	SA	2.32	N <sup>11</sup>
008	800	1.00	650	0.75	240	1.00	10	SA	0.68	N <sup>10</sup>
009	800	1.00	670	1.00	235	1.00	10	SA	4.50	N
010	800	1.00	670	1.00	235	1.00	10	SA	4.03	N
011	800	1.00	670	1.00	240	1.00	10	SA	0.33	N
012	800	1.00	670	1.00	240	1.00	10	SA	1.78	N
013	800	1.00	670	1.00	240	1.00	10	SA	0.33	N
014	850	1.00	700	1.00	250	1.00	10	SA	14.97	N
015	800 <sup>9</sup>	2.00	670	2.00	230	1.00	10	LB	-	Y
016	800 <sup>9</sup>	2.50	670	2.50	230	1.00	15	LB	-	Y
017i	800 <sup>9</sup>	2.50	670	2.50	230	1.00	15	LB	-	Y
017ii	800 <sup>9</sup>	2.50	670	2.50	230	1.00	10	SA	7.61	N
018i	800 <sup>9</sup>	1.50	670	1.50	230	1.00	6	SA	-	N
018ii	800 <sup>9</sup>	2.50	670	2.50	230	1.00	10	SA	7.90	N

<sup>5</sup> Stage 1 was the first stage of melting<sup>6</sup> Stage 2 was the second stage of melting<sup>7</sup> Stage 3 was the annealing stage<sup>8</sup> LB = large brass, SA = small aluminium, CB = cylindrical brass<sup>9</sup> Used fluorinated ZnF<sub>2</sub><sup>10</sup> Melted in glovebox, with 2:1 ration of dry N<sub>2</sub>:O<sub>2</sub><sup>11</sup> Partial

### 3.4. Fluorination of ZnF<sub>2</sub>

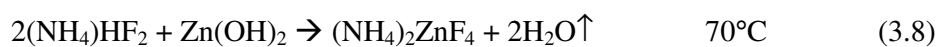
To ensure batch materials were as dry as possible, the ZnF<sub>2</sub> was fluorinated before melting, as the as-received chemicals were not phase pure (see chapter 5). The OH group can readily substitute with the F<sup>-</sup> ion in a number of compounds due to similar ionic radii (140 and ≈ 131 pm respectively [2]). The fluorination reaction was based on TGA (thermogravimetric analysis) results obtained by Sanghera *et al.* [3, 4]. This type of pre-melt drying has been employed for halide glasses for a number of years [5]. Equation (3.5) and (3.6) summarise the reactions which are believed to take place during fluorination. Saito *et al.* [6] are the only group, to the current authors knowledge, to describe the reaction between similar compounds to those used in this study (Zn(OH)F and NH<sub>4</sub>F) in any detail (a patent by Watanabe *et al.* [7] does briefly mention the fluorination reaction). From this work, and the work of Sanghera *et al.* [3, 4] which describes the drying of compounds used to synthesise ZBLAN glasses with (NH<sub>4</sub>)HF<sub>2</sub>, the following chemical reactions are proposed.



From XRD patterns obtained (see chapter 5), it was assumed that the as-received ZnF<sub>2</sub> was of average composition Zn(OH)F (i.e. batch composed of ZnF<sub>2</sub>, Zn(OH)F and Zn(OH)<sub>2</sub>). Therefore for each gram of fluoride, 0.56 g of (NH<sub>4</sub>)HF<sub>2</sub> was needed for complete fluorination to ZnF<sub>2</sub>, although the amount of (NH<sub>4</sub>)HF<sub>2</sub> was likely to have been excessive (see section 5). Therefore, for each fluorination, 8.4 g of (NH<sub>4</sub>)HF<sub>2</sub>

were added to 15 g of fluoride, which were mixed in a platinum crucible. This lidded crucible was then placed in the melting furnace, inside a silica liner, as described in section (3.3) and ramped from room temperature to 70°C, and held there for 17.5 hours. This stage was followed by a ramp to 400°C for 1 hour then cooled to room temperature (a heating / cooling rate of 300°C.hr.<sup>-1</sup> was used for all stages) [8]. The same heating procedure was also used for fluorination in the glovebox, however, a nitrogen rich atmosphere was used.

In the work on the fluorination of ZrF<sub>4</sub>.H<sub>2</sub>O described by Sanghera *et al.* [3, 4] the mixture of ‘wet’ fluoride and ammonium hydrogen difluoride was held at around 70°C for around 18 hours to allow the (NH<sub>4</sub>)HF<sub>2</sub> sufficient time to react with the fluoride. An intermediate fluoride compound (identified by TGA and XRD) was formed at this temperature, ammonium heptafluorozirconate ((NH<sub>4</sub>)<sub>3</sub>ZrF<sub>7</sub>), while drying the fluoride. As the temperature was increased to around 400°C this compound decomposed to the pure fluoride compound ZrF<sub>4</sub>. According to Sanghera *et al.* [3, 4], in the first stage of fluorination (70°C in this study), if the temperature was too low (e.g. 30°C), the reaction of (NH<sub>4</sub>)HF<sub>2</sub> with the ‘wet’ fluoride was too slow, and if the temperature was too high (e.g. 90°C) decomposition of the (NH<sub>4</sub>)HF<sub>2</sub> occurred too fast to enable the formation of the intermediate metal ammonium fluoride. In the fluorination of ‘wet’ ZnF<sub>2</sub>, the intermediate compound formed is (NH<sub>4</sub>)<sub>2</sub>ZnF<sub>4</sub> [7]. Equations (3.7) to (3.10) illustrate the proposed analogous decomposition reactions.



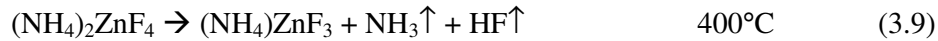


Fig. (3.5) summarises the stages of this drying and decomposition:

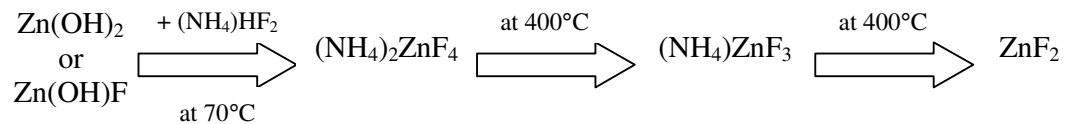


Fig. (3.5): Proposed drying and decomposition reactions of 'wet' ZnF<sub>2</sub>.

### 3.5. References

- [1] M. Cable, *The calculation of glass and batch compositions*, 5th ed. Sheffield: University of Sheffield, 1996.
- [2] J. E. Huheey, *Inorganic chemistry: principles of structure and reactivity*, S.I. Units ed. London: Harper & Row, 1975.
- [3] K. J. Ewing, J. S. Sanghera, R. E. Miklos, M. G. Sachon, L. Peitersen, P. Hart, and I. Aggarwal, "Reaction of Zirconium Fluoride Monohydrate and Ammonium Bifluoride - Its Effect on Fluoride Glass Preparation and Quality," *Journal of the American Ceramic Society*, vol. 72, pp. 1441-1443, 1989.
- [4] J. S. Sanghera, P. Hart, M. G. Sachon, K. J. Ewing, and I. Aggarwal, "New Fluorination Reactions of Ammonium Bifluoride," *Journal of the American Ceramic Society*, vol. 73, pp. 1339-1346, 1990.
- [5] M. Poulain, "Halide Glasses," *Journal of Non-Crystalline Solids*, vol. 56, pp. 1-14, 1983.
- [6] N. Saito, H. Haneda, W. S. Seo, and K. Koumoto, "Selective deposition of ZnF(OH) on self-assembled monolayers in Zn-NH<sub>4</sub>F aqueous solutions for micropatterning of zinc oxide," *Langmuir*, vol. 17, pp. 1461-1469, 2001.
- [7] M. Watanabe and S. Nishimura, "Process for producing fluorides of metals," in *U.S. Patent 4,741,893*. Japan: Solex Research Corporation of Japan, 1988.

- [8] M. D. O'Donnell, D. Furniss, V. K. Tikhomirov, and A. B. Seddon, "Low loss infrared fluorotellurite optical fibre," *Physics and Chemistry of Glasses*, in press.

## 4. Thermal properties and glass stability

*Characteristic temperatures – differential thermal analysis (DTA) and differential scanning calorimetry (DSC)*

Differential Thermal Analysis (DTA) and Differential Scanning Calorimetry (DSC) are techniques which can be used to determine temperatures at which changes of phase or state (e.g. glass  $\leftrightarrow$  supercooled liquid, around the glass transition temperature,  $T_g$ ) occur in a material. These techniques are particularly important to the glass technologist, as key characteristic temperatures can be accurately obtained, such as  $T_g$ , the onset of crystallisation ( $T_x$ ), the liquidus ( $T_l$ , the lowest temperature at normal pressure at which the system is entirely in the liquid state) and the solidus ( $T_s$ , the highest temperature at normal pressure at which the system is entirely in the solid state). From this information the  $T_x-T_g$  gap can be calculated, which is a rough estimate of glass stability on reheating, and an important consideration for fibredrawing, as this is the temperature region of greatest stability against crystallisation. For fibredrawing, a low enough viscosity ( $\approx 10^{4.5}$  Pa.s) must be exhibited in this temperature region. Therefore, this gap should be maximised so the fibredrawing viscosity occurs as far below  $T_x$  as possible, as even a small degree of crystallinity in the glass will result in optical absorption and scattering losses over long optical pathlengths. However, for a glass to have a fibredrawing viscosity as far below  $T_x$  as possible, and a large  $T_x-T_g$  gap, would usually require a shallow viscosity-temperature relationship, i.e. a non-fragile glass-forming liquid [1, 2].

## 4.1. Experimental

### 4.1.1. Method, instrumentation and theory of operation

#### 4.1.1.1. DTA

In this study, Perkin Elmer DTA7 equipment was used with unlidded platinum crucibles and holders. The DTA curves were recorded under a flowing BOC argon atmosphere (20 ml.min.<sup>-1</sup>) at heating rates of 10°C.min.<sup>-1</sup> (unless stated) on glass chips of around 2mm in diameter with a mass of around 35mg. The extrapolated onset glass transition temperature ( $T_g$ ) was measured with a repeatability of  $\pm 3^\circ\text{C}$ , onset of the first crystallisation above  $T_g$  ( $T_x$ )  $\pm 1^\circ\text{C}$ , and stability ( $T_x - T_g$ )  $\pm 4^\circ\text{C}$ . Characteristic temperatures were obtained using Perkin Elmer software (see later in this section for further details). DTA measures the difference in temperature between a sample and reference which are subjected to the same heating schedule by symmetrically arranging them in relation to the furnace of the equipment [3]. The reference can be any material with approximately the same thermal mass as the sample, which undergoes no transformations in the range of temperatures being measured. In this study an empty platinum crucible was used as the reference. A baseline run, measured using empty platinum sample and reference crucibles, was subtracted from the data obtained for each DTA run. The temperature of the sample and sample crucible will have differed slightly with respect to the empty reference crucible, due to the difference in thermal mass, and hence heat capacity; this

will have manifested as an offset in the baseline. Fig. (4.1) shows a schematic of the DTA cell and how the DTA curve is formed from the data recorded.

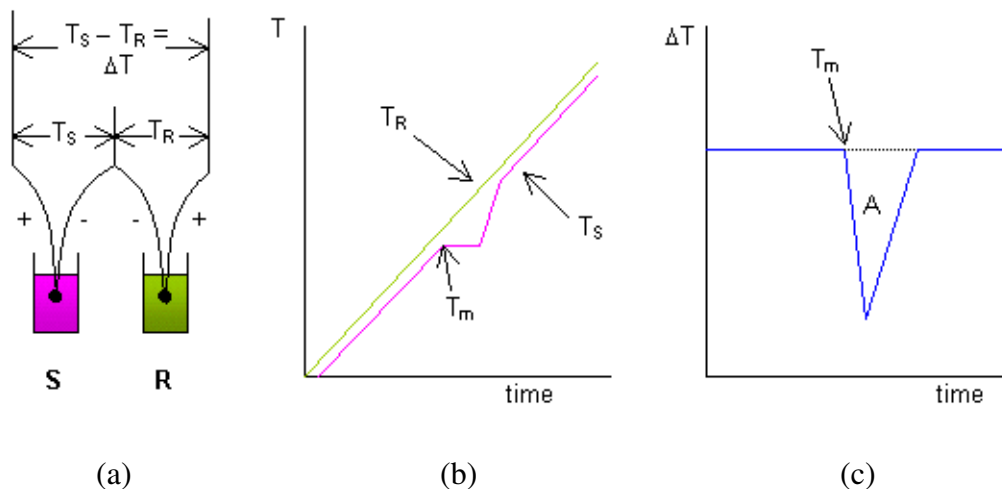


Fig. (4.1): (a) Schematic of DTA cell (S = sample, R = reference), (b) data recorded by equipment, and (c) to form the DTA trace.

The temperature difference ( $\Delta T$ ) between the sample ( $T_S$ ) and the reference ( $T_R$ ) is measured using a differential thermocouple, where one junction is in contact with the bottom of the sample crucible and the other is in contact with the bottom of the reference crucible. When the sample undergoes a transformation it either absorbs (endothermic) or gives out (exothermic) heat. The DTA detects if the sample is cooler or hotter than the reference and displays an exotherm or an endotherm on the trace of  $\Delta T$  versus time (or temperature if the heating rate is constant, as is the case in this study). Fig. (4.1b) shows the temperature of the sample and reference increasing with time. The reference temperature increases linearly ( $T_R$ ), however the sample temperature ( $T_S$ ) undergoes a melting transition at  $T_m$ . As melting phenomena are endothermic, the sample takes in heat from the surroundings and the temperature plateaus for some time until melting is

complete. The samples temperature of the sample then equilibrates with the surroundings and increases with a similar gradient to the reference as before. The difference ( $\Delta T$ ) between curves  $T_R$  and  $T_s$  are plotted in fig. (4.1c) which forms the DTA trace.

#### 4.1.1.2. DSC

The DSC used in this study was a power-compensated Perkin Elmer Pyris1 DSC with a water recirculating chiller at 12°C and an argon flow rate of 30 ml/min. The instrument was calibrated using the melting point of zinc ( $T_m = 419.5^\circ\text{C}$ ). Glass chips of around 20 mg were sealed in gold pans in a glovebox under a nitrogen atmosphere (<0.1 ppm  $\text{O}_2$  and <0.1 ppm water) using a Perkin Elmer DSC-pan press. An empty gold reference crucible was used and a baseline of empty sample chambers was subtracted from each DSC run. The output trace of the DSC looks very similar to that of the DTA, however the principle of operation is different. The instrument has separate containers for sample and reference, and these containers have individual heating elements as well as temperature measuring devices associated with them [3]. Both cells are surrounded by a water cooled block to allow rapid cooling. Perkin Elmer carries the patent for true DSC operation.

The sample and reference chambers are heated equally until a transformation occurs in the sample. As the sample temperature infinitesimally deviates from the reference, the DSC detects this and reduces the heat input to one cell while adding heat to the other to maintain a zero temperature difference between the sample and reference [3]. The quantity of electrical energy per unit time which must be applied to the heating elements (in addition to the normal programmed thermal schedule), in order to maintain zero

temperature difference, is assumed to be proportional to the heat released per unit time of the sample. Therefore, the y-axis of the DSC trace is expressed in terms of energy per unit time (i.e. Watts) [3].

The DSC has two control cycle portions, one to maintain zero temperature difference and one to keep the average temperature of the sample and the reference at the set point. These processes switch back and forth quickly to maintain both simultaneously [3].

#### 4.1.2. Identification of transformations

The following methods of identifying transformations were performed using automatic fitting functions in the Perkin Elmer Pyris software. Fig. (4.2) shows a typical DTA trace of glass MOF005 ( $70\text{TeO}_2\text{-}10\text{Na}_2\text{O-}20\text{ZnF}_2$  (mol. %)) to illustrate how the characteristic temperatures were obtained in this study.

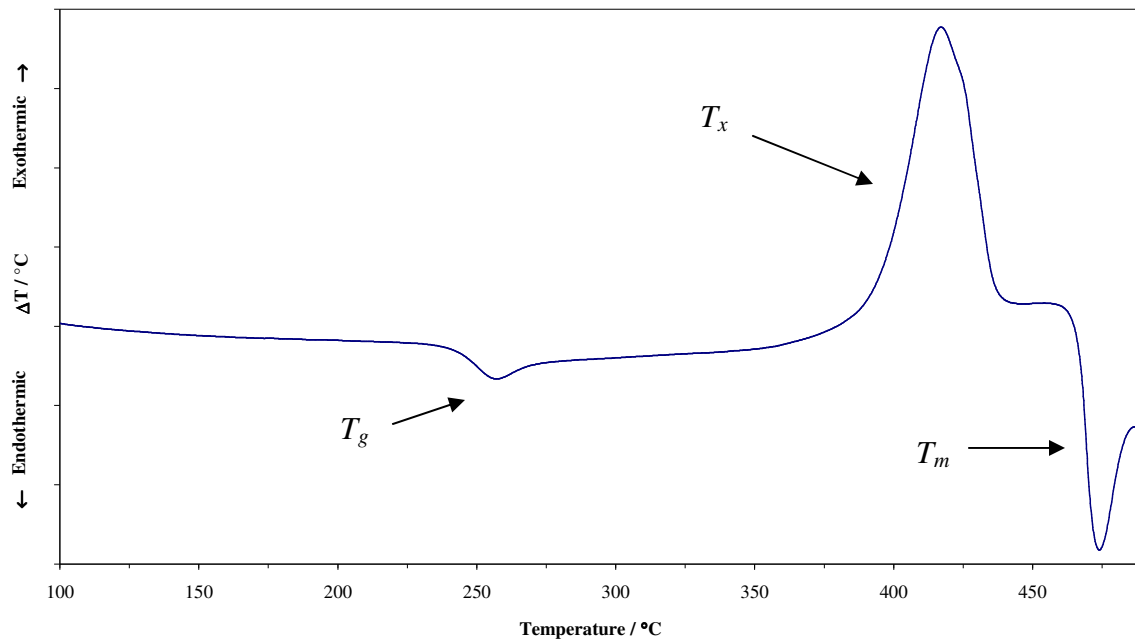


Fig. (4.2) DTA trace of glass MOF005 ( $70\text{TeO}_2\text{-}10\text{Na}_2\text{O-}20\text{ZnF}_2$  (mol. %)).

The first endotherm at around 250°C is the glass transition temperature ( $T_g$ ). The onset of this temperature was obtained by interpolating the straight line just before the transition and the straight line which occurs after the initial change in gradient as shown in fig. (4.3)<sup>1</sup>.

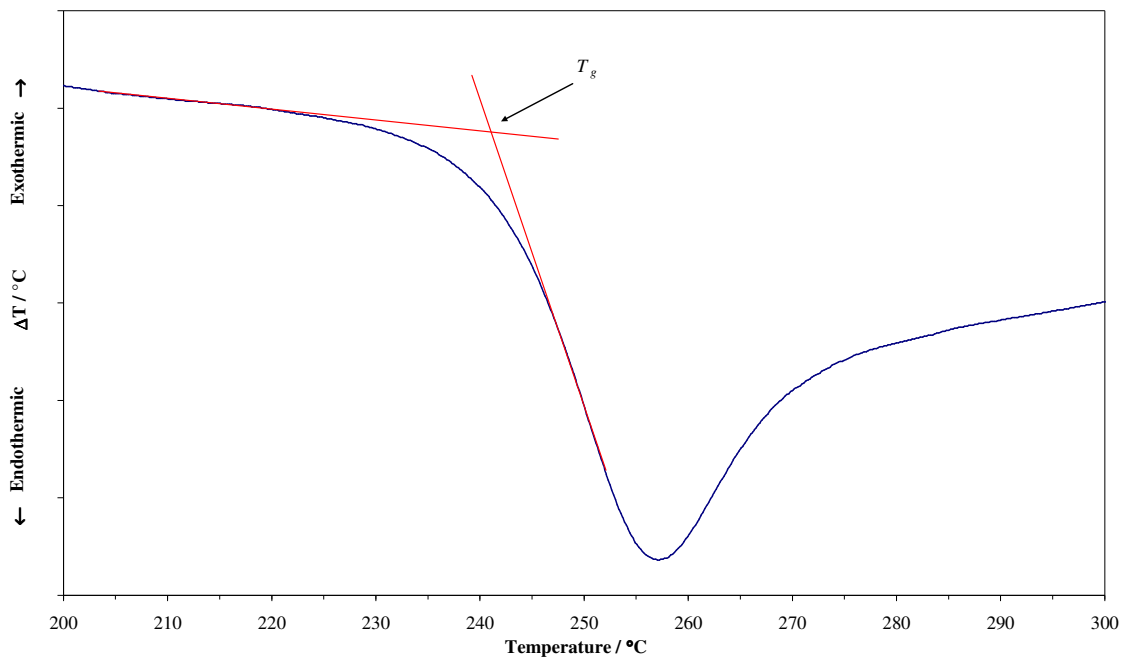


Fig. (4.3): DTA trace of glass MOF005 (70TeO<sub>2</sub>-10Na<sub>2</sub>O-20ZnF<sub>2</sub> (mol. %)), showing interpolation of the onset of the glass transition temperature,  $T_g$ .

The first exotherm on fig. (4.2) at around 425°C was due to crystallization event in the glass. The onset of crystallization,  $T_x$ , was obtained by plotting the ‘lift-off’ point from the baseline before the crystallisation event. Fig. (4.4) illustrates this. With  $T_x$  and  $T_g$  known, a crude measure of glass stability can be calculated:  $T_x - T_g$ .

<sup>1</sup> Transformations obtained using the DSC were identified using the same methods described here.

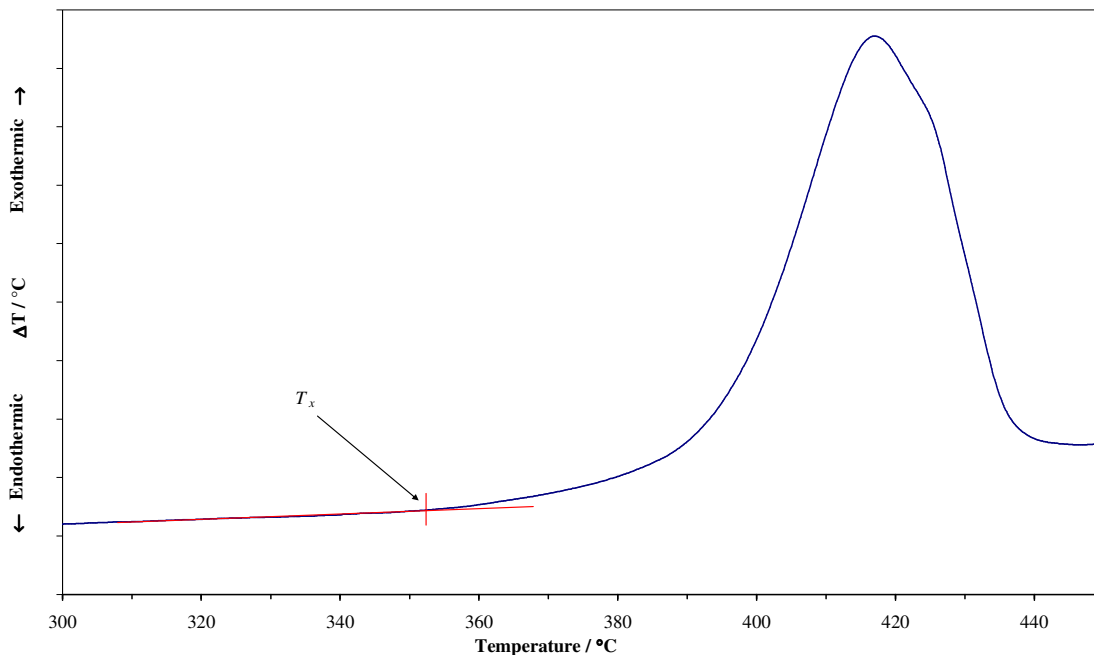


Fig. (4.4): DTA trace of glass MOF005 (70TeO<sub>2</sub>-10Na<sub>2</sub>O-20ZnF<sub>2</sub> (mol. %)), showing the 'lift-off' point ( $T_x$ ) from the baseline before the crystallisation event.

Irreversible transformations are those in which reactants do not reform from products on cooling. Here one of the reactants is a metastable state (i.e. glass) and only requires heat to raise it above  $T_g$  to the undercooled liquid state to initiate the transformation. Devitrification of glass is a classic example of an irreversible transformation. In these types of reactions the sample temperature will not remain constant during the transformation. As glass devitrification proceeds, heat released at the glass-crystal interface raises the temperature of the sample. The rates of such transformations generally have an exponential temperature dependence, causing them to proceed more rapidly, which in turn causes a more rapid temperature rise, and so on. Therefore, these 'self-feeding' reactions show irregular temperature-time profiles when heated at a constant rate [3]. This is why the peak crystallisation temperature on a DTA or DSC trace

has no fundamental meaning. The solidus and liquidus temperatures ( $T_s$  and  $T_l$  respectively) were obtained by the same interpolation method as  $T_g$  described above. Fig. (4.5) illustrates this.

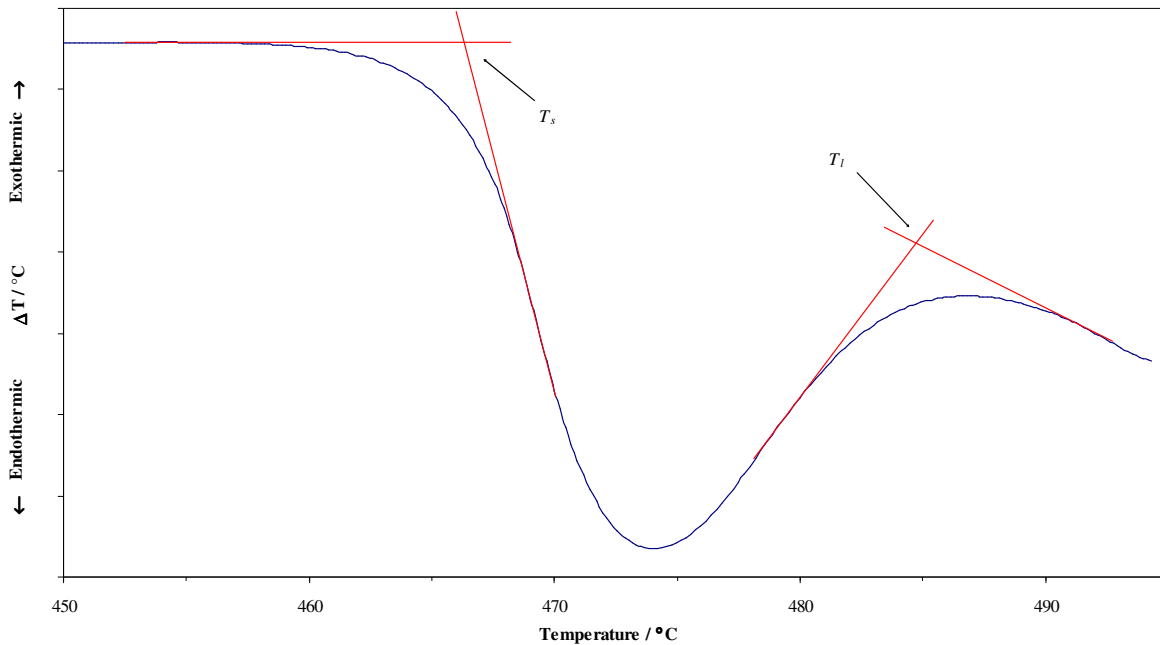


Fig. (4.5): DTA trace of glass MOF005 ( $70\text{TeO}_2\text{-}10\text{Na}_2\text{O-}20\text{ZnF}_2$  (mol. %)), showing interpolation of the solidus temperature,  $T_s$ , and liquidus temperature,  $T_l$ .

Transformations of this kind (melting) are reversible and obey Le Chatelier's principle [4] which implies, for example, that ice-water will stay at  $0^\circ\text{C}$  until it fully transforms to ice or water. Any heat added to the system contributes to the phase change rather than a change in temperature, as long as both phases exist. For this reason melting transformations have a distinct shape in DTA traces.

In a DTA scan at constant heating rate, where a solid sample fuses, the reference sample increases in temperature at the preprogrammed heating rate, while the sample temperature remains at the melting temperature until the transformation is complete. Therefore, when  $\Delta T$  vs. reference temperature is plotted, a linear deviation from the

baseline is seen on the leading edge of the endotherm. The peak of the endotherm represents the temperature at which melting terminates and the transformation is complete. At this point the sample is at a lower temperature than its surroundings and it heats at an accelerated rate, returning to the temperature of its surroundings. This is seen on the DTA curve as a return to the baseline. The return portion of the curve follows an exponential decay, where the sample initially rapidly catches up with its surroundings and then more slowly as the sample and surroundings temperatures approach one another. Fig. (4.6) shows the difference in melting endotherm if reference or sample (ideal and actual) temperature is plotted on the  $x$ -axis against  $\Delta T$ .

Ideally the melting portion of the DTA curve of a single solid phase would correspond to a vertical line, as the sample temperature would not change until melting is complete. For thermocouple junctions immersed within the sample, this ideal case is observed. Most contemporary DTAs however (including the one used in this study), are designed with the thermocouple junction in contact with the sample holder, and this holder tends to increase in temperature to a certain degree under the influence of the surroundings, which are rising in temperature. For this set-up the DTA curve of the sample has a sharper rising slope and broader exponential drop-off than that of the reference.

An important point to note is that although melting is complete at the peak of the endotherm, it is still the entire area under the peak which represents the latent heat of fusion. The enthalpy ( $H$ ) of the reference increases during the time of the transformation since the reference temperature increases ( $\Delta H = \int_0^T C_p dT$ , where  $T$  is the temperature and  $C_p$  is the molar heat capacity at constant pressure) as dictated by the heating rate. However, during sample melting there is no enthalpy change for the sample due to

temperature increase, simply because there is no increase in temperature. Only after completion of the transformation does the sample catch up with the reference which corresponds to the exponential decay portion of the endotherm. This part of the peak needs to be included in the integral so sample and reference both show the same contribution to enthalpy change due to the temperature increase [3].

### **4.1.3. Modelling transformation kinetics**

#### *Form of DTA transformation peaks*

Transformation kinetics can be modelled using data from the DTA. If it is assumed that the heat released per unit time is proportional to the rate of reaction, then the partial area swept under the peak divided by the entire peak area is equal to the fraction transformed [3]. For example, the crystallisation peak shown in fig. (4.4), was integrated and the resulting curve shows the fraction of the glass which has crystallised at any particular temperature. This integration was performed using Microcal Origin software. The background was first removed by manually generating a suitable equation, so only the area under the peak was integrated. Fig. (4.7) shows the crystallisation peak with background removed and integration results.

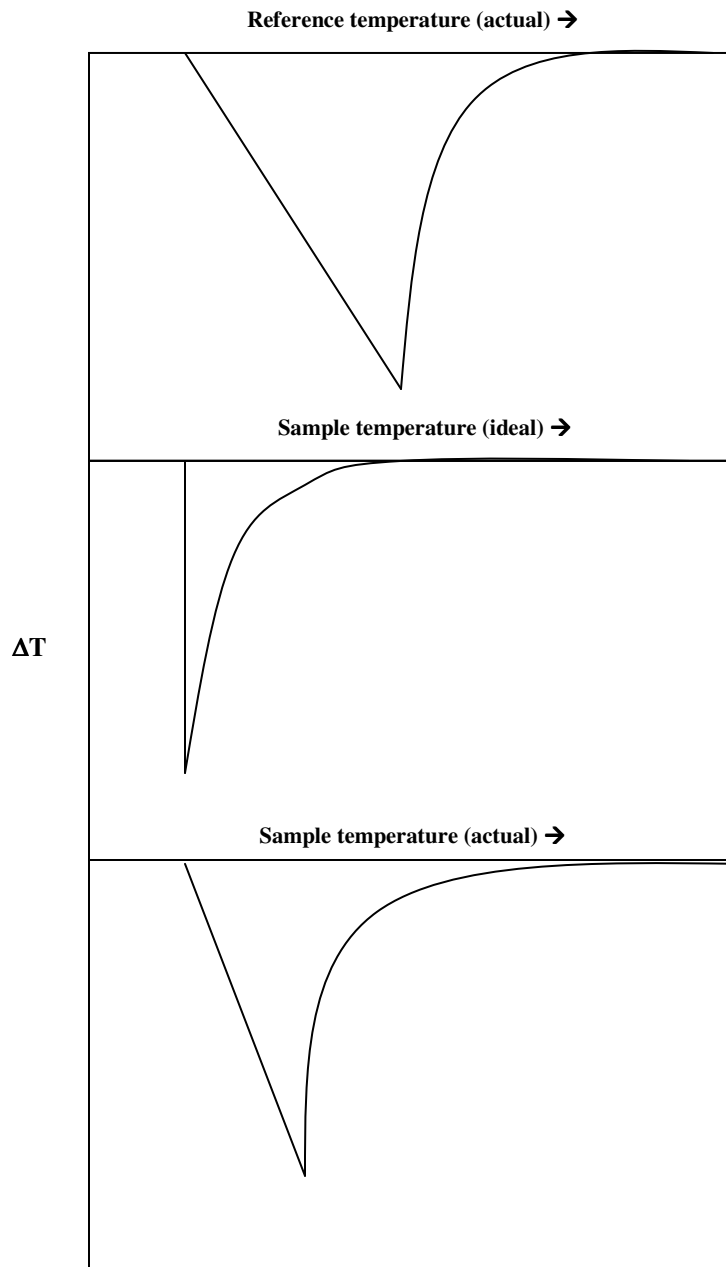


Fig. (4.6): Difference in melting endotherm on DTA trace if reference or sample (ideal and actual) temperature is plotted on the  $x$ -axis against  $\Delta T$ .

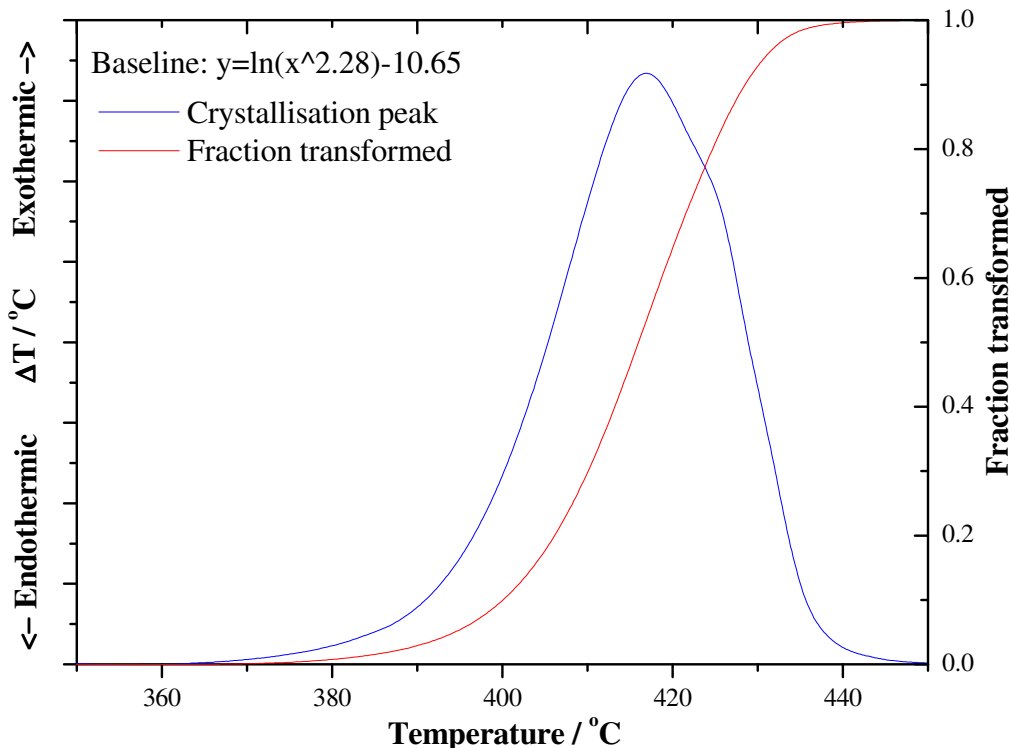


Fig. (4.7): DTA curve of glass MOF005 ( $70\text{TeO}_2\text{-}10\text{Na}_2\text{O-}20\text{ZnF}_2$  (mol. %)) showing the crystallisation peak with background removed and integration results.

Peaks from the DTA curves which are asymmetric are often composed of more than one transformation which overlap. Microcal Origin software was used to deconvolute these multiple peaks into individual Gaussian curves. For example, the curve shown in fig. (4.4) is clearly asymmetric, showing a higher temperature shoulder. The number of peaks, approximate peak positions and widths is entered into the software, which generates the fit. Data for the fitted peak are provided such as peak positions, widths, heights and areas. Values of  $\chi^2$  (is related to the iteration calculation performed by the software, and tends to zero as the iteration approaches a successful solution) and  $R^2$  (is the square of the correlation coefficient) are also calculated by the software, which

indicate the degree of fit between the generated peaks and the data (the closer  $\chi^2$  is to 0 and  $R^2$  to 1, the better the Gaussian fit correlates with the data). Fig. (4.8) illustrates this.

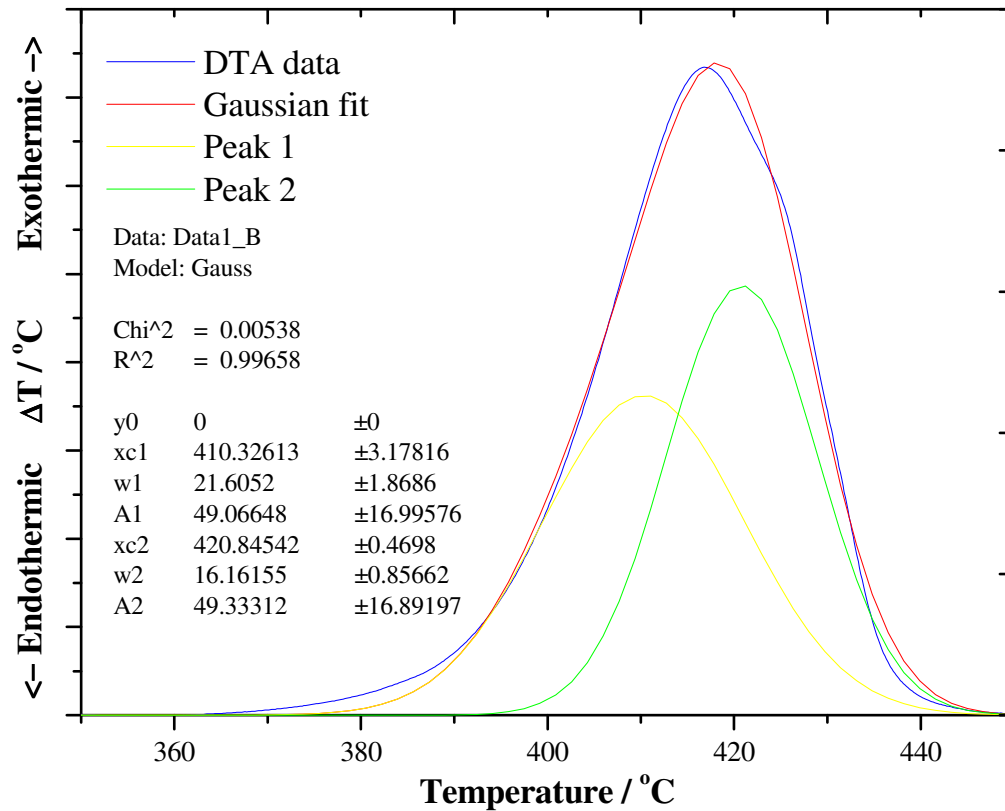


Fig. (4.8): DTA trace of glass MOF005 (70TeO<sub>2</sub>-10Na<sub>2</sub>O-20ZnF<sub>2</sub> (mol. %)) showing the crystallisation peak with background removed and Gaussian deconvolution performed (where  $xc_n$  is the position of peak  $n$ ,  $w_n$  the half width of peak  $n$ , and  $A_n$  the area of peak  $n$ , with 100% confidence limits displayed).

### Modelling equations

Nucleation and growth processes, such as glass devitrification, generally follow the Johnson-Mehl-Avrami (JMA) equation [3]:

$$F_t = 1 - \exp(-k_c t^m) \quad (4.1)$$

where  $F_t$  = fraction transformed,  $k_c$  = time independent, temperature dependent rate constant, and  $m$  = mechanism constant. If we assume homogeneous nucleation (i.e. no impurity surfaces) and that crystalline regions grow as spheres,  $m = 4$ . For different assumptions,  $m$  can vary from 1 to 4. Therefore, we can fit experimental data to the model and statements can be made about the crystallisation mechanism. However homogeneous nucleation is unusual in glasses, and heterogeneous nucleation typically occurs at the glass / crucible interface in the DTA. When DTA runs are performed on glass lumps and compared to traces run on powdered samples (higher surface area) of the same composition and thermal history, if homogeneous nucleation is occurring, then the crystallisation exotherm will move to a lower temperature in the powdered sample.

Glass samples can be held at a series of isothermal temperatures in the DTA around the crystallisation region and the fraction transformed calculated by the method described above. Equation (4.1) can be rearranged:

$$\ln(1 - F_t) = -k_c t^m \quad (4.2)$$

$$\ln(-\ln(1 - F_t)) = \ln k_c + m \ln t \quad (4.3)$$

A plot of  $\ln(-\ln(1 - F_t))$  vs.  $\ln t$ , should take the form of a straight line and  $k_c$  and  $m$  can be obtained for each temperature ( $y = mx + c$ , where  $m \equiv m = \text{gradient}$  and  $c \equiv \ln k_c = \text{y-axis intercept}$ ). The gradients (and hence  $m$ ) should be identical for each isothermal temperature, presuming the crystallisation mechanism does not change. The rate constant is generally taken to have Arrhenius temperature dependence [3]:

$$k_c = k_0 \exp\left(\frac{-E_a}{RT}\right) \quad (4.4)$$

where  $k_0$  is the pre-exponential rate constant and  $E_a$  the activation energy. If natural logs are taken on both sides:

$$\ln k_c = \ln k_0 - \frac{E_a}{RT} \quad (4.5)$$

Values of  $\ln k_c$  (obtained from isothermal experiments) can be plotted against  $1/T$  and the slope of this straight line is equal to  $-E_a/R$ . Therefore,  $E_a$ , the activation energy for crystallisation, for a particular glass composition can be calculated.

#### 4.1.4. Experimental considerations

Good mechanical contact between the sample and the bottom of the crucible will improve instrument sensitivity to transformations. Surface contact can be optimised by crushing granules finely (of equal particle size for reproducible results), however with glasses this can result in the crystal nucleation and growth mechanism changing from the bulk to the surface due to the increased surface energy [3]. Also, gas entrapment may result in poor heat transfer when using a powder compared to a single particle. The particle size also affects the rate of glass crystallisation. For spherical particles the surface to volume ratio decreases by  $3/r$  ( $r$  = particle radius) with increasing particle size. Heat flow from the surroundings to the interior of the larger particles is relatively suppressed due to reduced

access. This results in a time delay in the onset of transformation of these large particles [3]. The heat released from transformations within more massive particles would also be more insulated from escape, further delaying detection of the transformation. The latent heat of the transformation would then tend to increase the temperature of the large particle than small particles. The greater temperature rise accelerates the reaction rate resulting in early termination of the reaction in large particles. Therefore, for a fixed overall sample mass, samples composed of one large piece (as opposed to powder) will tend to transform initially more sluggishly, but ultimately more quickly for irreversible transformations such as crystallisation [3]. The distance heat penetrates a particle,  $x$ , is proportional to the square root of the product of thermal diffusivity,  $\kappa_d$  ( $\kappa_d = k_{tc} / (C_p \rho)$  where  $k_{tc}$  = thermal conductivity,  $C_p$  = heat capacity and  $\rho$  = density) and time ( $x = \sqrt{(\kappa_d t)}$ ).

The effect of heating rate on sample transitions such as melting in the DTA is significant. The onset of a transformation occurs at a higher temperature with increasing heating rate due to a lag from the sample interior compared to the thermocouple [3]. Peak intensity also increases with increasing heating rate as the reference temperature increase is more rapid (therefore  $\Delta T$  larger) whilst the sample attempts to remain at melting temperature. Melting also exhibits a broader temperature range for increasing heating rates since less time is allowed per degree of temperature increase for the reaction to proceed [3].

However, low heating rates more accurately represent the onset temperature of a transformation and reduce the accelerating effects of 'self-feeding' reactions. Also, transformations which are very close in temperature-range may be more clearly resolved with slower rates [3]. Ultimately, to obtain true thermodynamic data, experiments should

be conducted infinitely slowly, but the sensitivity of detection is then an issue. Thus, the DTA / DSC methods are a compromise.

#### **4.1.5. Time-temperature-transformation (TTT) experiments (using DSC)**

TTT (time-temperature-transformation) experiments were performed in this study using a DSC with conditions and sample preparation as described in section 4.1.1.1 unless otherwise stated. A number of groups has performed these experiments on various glass compositions such as aluminosilicates [5], borosilicates [6], heavy-metal-fluorides [7], Ga-La-S [8] and tellurites [9]. The glass samples here were quenched in the DSC from the molten state (600°C) at a rate of 300°C/min., to various temperatures between the glass transition and the melting point to study crystallisation kinetics. The samples were quenched from 600°C and isothermally held for 10 min. at 5°C intervals from 270 to 450°C. After each hold the sample was taken back up to 600°C and held there for 10 min. to ensure complete remelting. The TTT diagrams were constructed by integrating the crystallisation peak obtained from the isothermal steps using Microcal Origin software. The time corresponding to 50% area of the integrated crystallisation isotherm was taken as the time plotted on the TTT diagram for each isothermal temperature [7]. Fig. (4.9) illustrates this for an isothermal hold of glass MOF005 (70TeO<sub>2</sub>-10Na<sub>2</sub>O-20ZnF<sub>2</sub> mol. %) at 325°C.

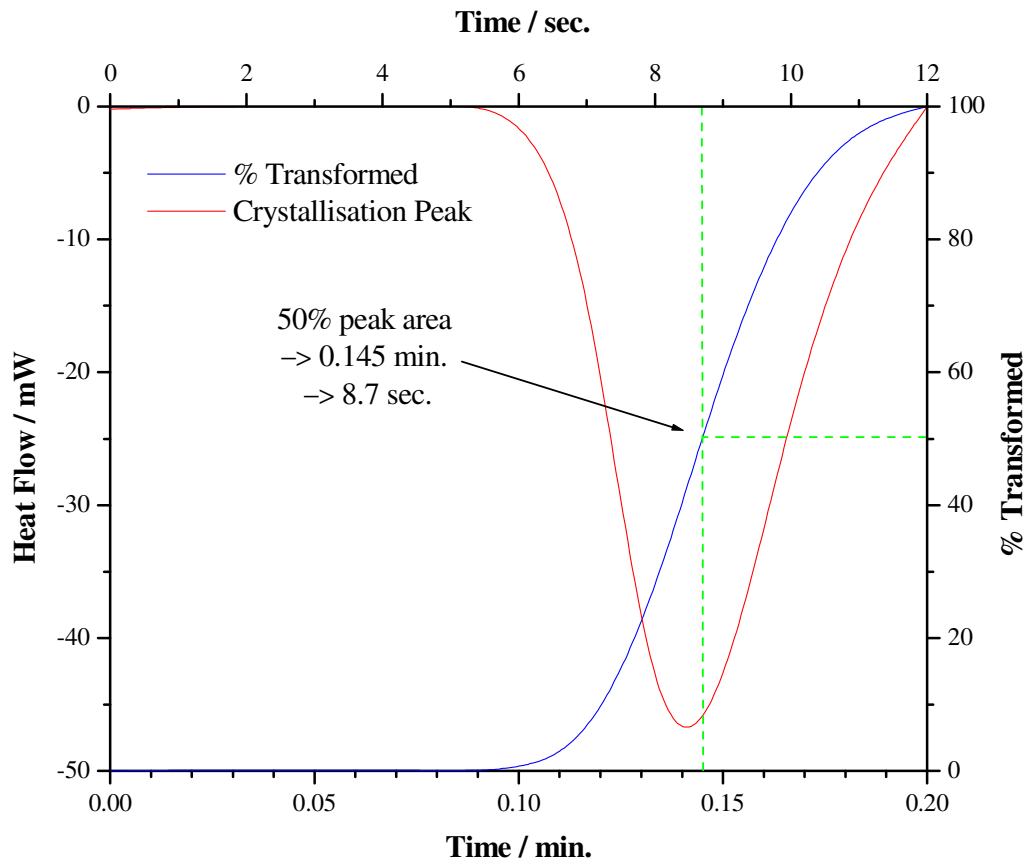


Fig. (4.9): Method of obtaining time values for TTT plot for isothermal hold of glass MOF005 (70TeO<sub>2</sub>-10Na<sub>2</sub>O-20ZnF<sub>2</sub> mol. %) at 325°C.

Time of the onset of crystallisation was also used to plot TTT diagrams, which is a more conservative estimate of the kinetics of devitrification.

## 4.2. Results

### 4.2.1. DTA traces of oxide tellurite glasses

#### *Effect of rare-earth and lead oxide addition*

Fig. (4.10) shows DTA traces of glasses MOD001 (79TeO<sub>2</sub>-10Na<sub>2</sub>O-10PbO-1Yb<sub>2</sub>O<sub>3</sub> mol. %) and MOD002 (78.21TeO<sub>2</sub>-4.95ZnO-9.9Na<sub>2</sub>O-4.95PbO-0.99Yb<sub>2</sub>O<sub>3</sub>-0.99Er<sub>2</sub>O<sub>3</sub> mol. %).

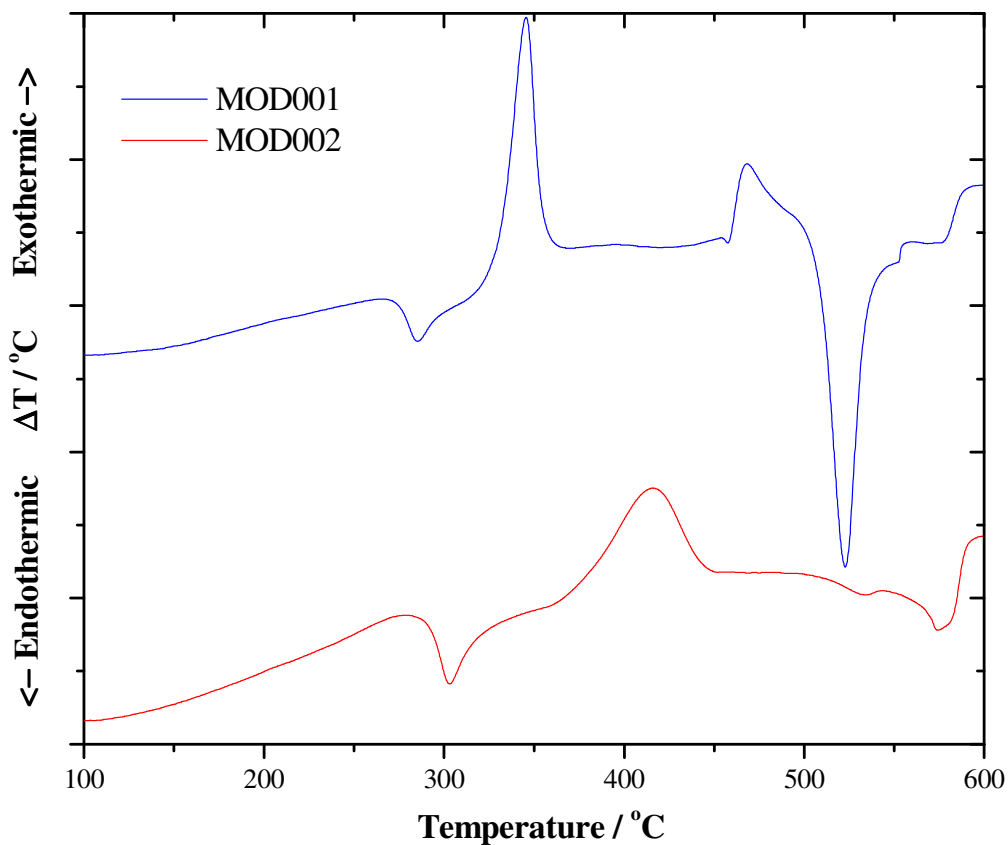


Fig. (4.10): DTA traces of glasses MOD001 (79TeO<sub>2</sub>-10Na<sub>2</sub>O-10PbO-1Yb<sub>2</sub>O<sub>3</sub> mol. %) and MOD002 (78.21TeO<sub>2</sub>-4.95ZnO-9.9Na<sub>2</sub>O-4.95PbO-0.99Yb<sub>2</sub>O<sub>3</sub>-0.99Er<sub>2</sub>O<sub>3</sub> mol. %).

Both glasses exhibited a typical DTA trace, showing endotherms for the glass transition ( $T_g$ ) temperature and melting events ( $T_s$  and  $T_l$ ) and exotherms for devitrification ( $T_x$ ).  $T_g$  occurred at 274°C and 288°C, and  $T_x$  329°C and 373°C for MOD001 and MOD002, respectively. This gives a  $T_x-T_g$  value of 55°C for MOD001 and 85°C for MOD002.

#### *TeO<sub>2</sub>-ZnO-Na<sub>2</sub>O (TZN) compositions*

Fig. (4.11) shows DTA traces for glasses MOD006 (77TeO<sub>2</sub>-10ZnO-10Na<sub>2</sub>O-3PbO mol. %), MOD007 (78TeO<sub>2</sub>-12ZnO-10Na<sub>2</sub>O mol. %), MOD008 (74TeO<sub>2</sub>-12ZnO-10Na<sub>2</sub>O-3PbO-1Yb<sub>2</sub>O<sub>3</sub> mol. %) and MOD009 (77TeO<sub>2</sub>-12ZnO-10Na<sub>2</sub>O-1Yb<sub>2</sub>O<sub>3</sub> mol. %).

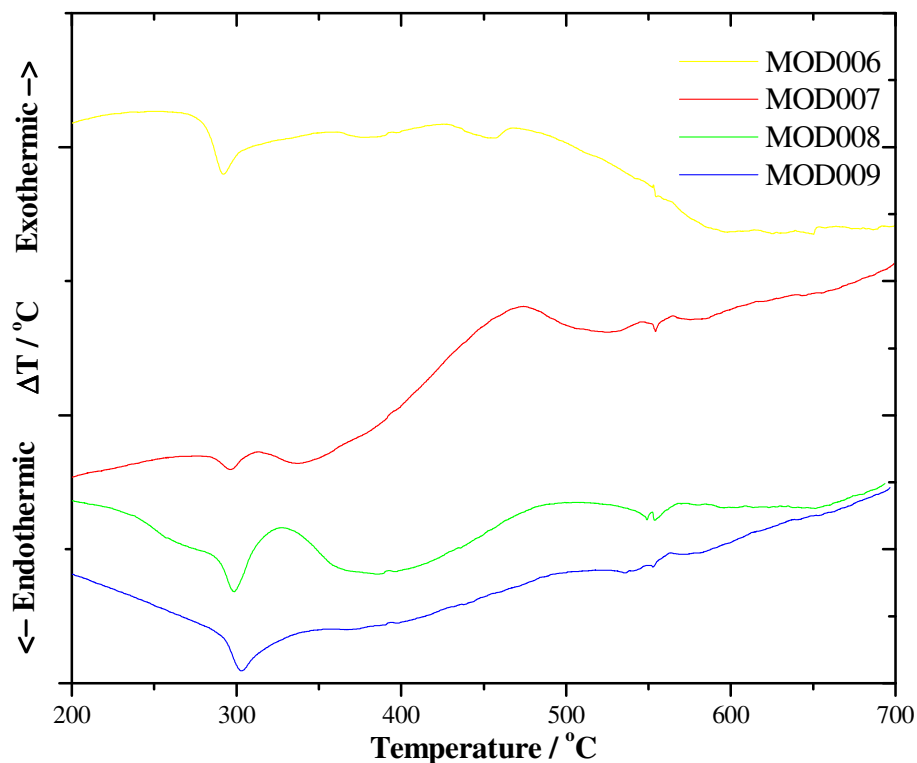


Fig. (4.11): DTA traces for glasses MOD006 (77TeO<sub>2</sub>-10ZnO-10Na<sub>2</sub>O-3PbO mol. %), MOD007 (78TeO<sub>2</sub>-12ZnO-10Na<sub>2</sub>O mol. %), MOD008 (74TeO<sub>2</sub>-12ZnO-10Na<sub>2</sub>O-3PbO-1Yb<sub>2</sub>O<sub>3</sub> mol. %) and MOD009 (77TeO<sub>2</sub>-12ZnO-10Na<sub>2</sub>O-1Yb<sub>2</sub>O<sub>3</sub> mol. %).

Crystallisation and melting peaks were not as clearly discernable for these compositions compared to glasses MOD001 and MOD002 due to increased glass stability.  $T_g$  occurred at 282°C, 286°C, 289°C and 292°C for MOD006 to MOD009 respectively. The only prominent crystallisation peak can be seen for MOD007 at 447°C, giving this glass a  $T_x$ - $T_g$  of 161°C.

Fig. (4.12) shows DTA traces for glasses MOD010 (75TeO<sub>2</sub>-10ZnO-10Na<sub>2</sub>O-5PbO mol. %), MOD011 (70TeO<sub>2</sub>-10ZnO-10Na<sub>2</sub>O-10PbO mol. %), MOD012 (75TeO<sub>2</sub>-10ZnO-10Na<sub>2</sub>O-5GeO<sub>2</sub> mol. %) and MOD013 (80TeO<sub>2</sub>-10ZnO-10Na<sub>2</sub>O mol. %).

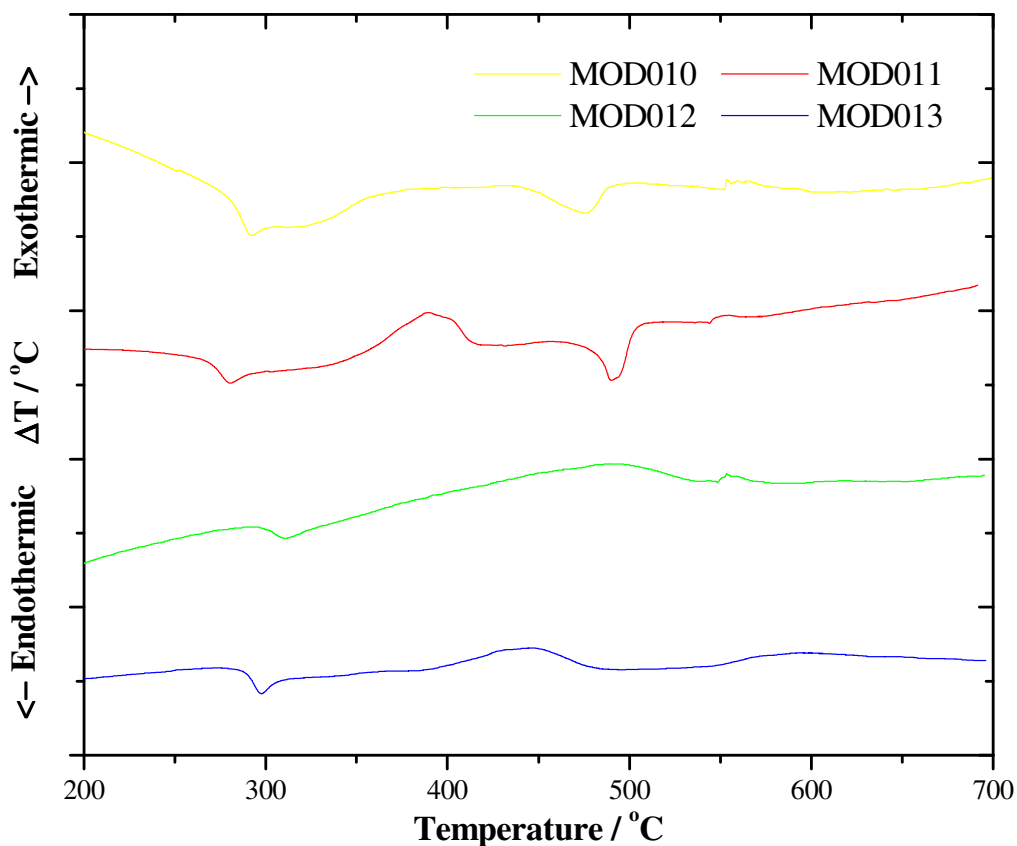


Fig. (4.12): DTA traces for glasses MOD010 (75TeO<sub>2</sub>-10ZnO-10Na<sub>2</sub>O-5PbO mol. %), MOD011 (70TeO<sub>2</sub>-10ZnO-10Na<sub>2</sub>O-10PbO mol. %), MOD012 (75TeO<sub>2</sub>-10ZnO-10Na<sub>2</sub>O-5GeO<sub>2</sub> mol. %) and MOD013 (80TeO<sub>2</sub>-10ZnO-10Na<sub>2</sub>O mol. %).

Again these glasses were relatively stable and exhibited  $T_g$  around 281°C, 266°C, 296°C and 281°C for glasses MOD010 to MOD013 respectively. Crystallisation peaks can be seen at 343°C, 460°C and 389°C for glasses MOD011 to MOD013, respectively, resulting in  $T_x-T_g$  values of 77°C, 164°C and 108°C.

*Effect of  $WO_3$ ,  $Nb_2O_5$  and  $Bi_2O_3$*

Fig. (4.13) shows DTA traces for glasses MOD014 (90TeO<sub>2</sub>-5WO<sub>3</sub>-5Nb<sub>2</sub>O<sub>5</sub> mol. %), MOD015 (82.5TeO<sub>2</sub>-7.5WO<sub>3</sub>-10Nb<sub>2</sub>O<sub>5</sub> mol. %) and MOD016 (70TeO<sub>2</sub>-25WO<sub>3</sub>-5Bi<sub>2</sub>O<sub>3</sub> mol. %).

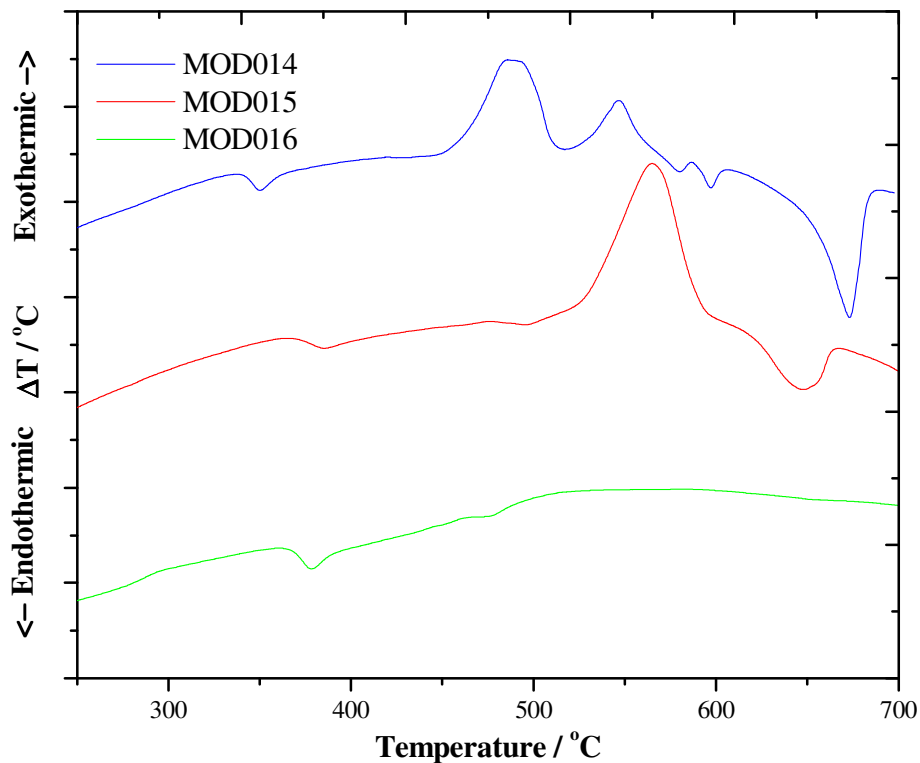


Fig. (4.13): DTA traces for glasses MOD014 (90TeO<sub>2</sub>-5WO<sub>3</sub>-5Nb<sub>2</sub>O<sub>5</sub> mol. %), MOD015 (82.5TeO<sub>2</sub>-7.5WO<sub>3</sub>-10Nb<sub>2</sub>O<sub>5</sub> mol. %) and MOD016 (70TeO<sub>2</sub>-25WO<sub>3</sub>-5Bi<sub>2</sub>O<sub>3</sub> mol. %).

These compositions showed  $T_g$  values at 337°C, 367°C and 366°C for glasses MOD014 to MOD015 respectively. Glasses MOD014 and MOD015 also exhibit crystallisation peaks at 456°C and 526°C respectively giving  $T_x-T_g$  values of 119°C and 159°C.

Table (4.1) summarises the characteristic temperatures of melts MOD001, 002, 006 to MOD016, inclusively.

Table (4.1): Characteristic temperatures for oxide tellurite glasses (see table (3.1)).

MOD ID	$T_g / ^\circ\text{C}$	$T_x / ^\circ\text{C}$	$(T_x-T_g) / ^\circ\text{C}$
001	274	329	55
002	288	373	85
006	282	-	-
007	286	447	161
008	289	-	-
009	292	-	-
010	281	-	-
011	266	343	77
012	296	460	164
013	281	389	108
014	337	456	119
015	367	526	159
016	366	-	-

#### 4.2.2. DTA traces of fluorotellurite glasses

*Effect of  $\text{ZnF}_2$  on the series  $(90-x)\text{TeO}_2 \cdot x\text{ZnF}_2 \cdot 10\text{Na}_2\text{O}$  (mol. %), for  $5 \leq x \leq 30$*

Fig. (4.14) shows DTA traces of glasses MOF001 (65TeO<sub>2</sub>-10Na<sub>2</sub>O-25ZnF<sub>2</sub> mol. %), MOF004 (60TeO<sub>2</sub>-10Na<sub>2</sub>O-30ZnF<sub>2</sub> mol. %), MOF005 (70TeO<sub>2</sub>-10Na<sub>2</sub>O-20ZnF<sub>2</sub> mol. %), MOF006 (75TeO<sub>2</sub>-10Na<sub>2</sub>O-15ZnF<sub>2</sub> mol. %), MOF007 (80TeO<sub>2</sub>-10Na<sub>2</sub>O-10ZnF<sub>2</sub>

mol. %) and MOF008 (85TeO<sub>2</sub>-10Na<sub>2</sub>O-5ZnF<sub>2</sub> mol. %) This glass melting series obeys the composition rule (90-x)TeO<sub>2</sub>.xZnF<sub>2</sub>.10Na<sub>2</sub>O (mol. %), for 5 ≤ x ≤ 30.

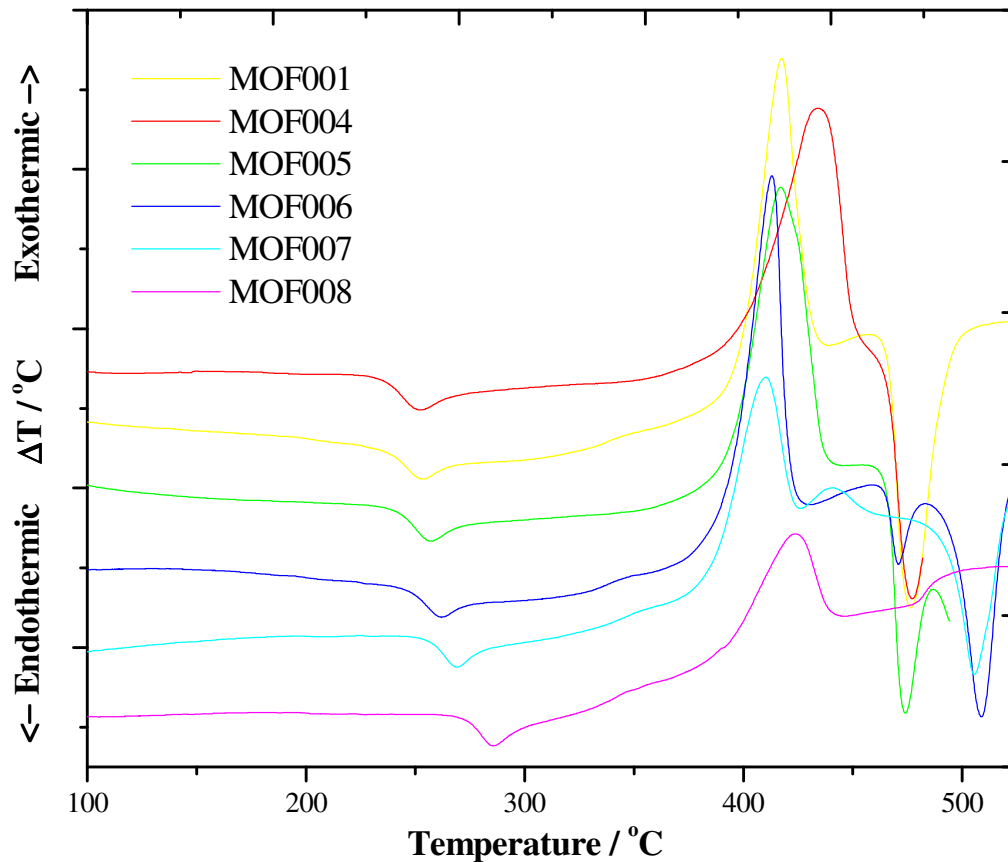


Fig (4.14): DTA traces of glasses MOF001 (65TeO<sub>2</sub>-10Na<sub>2</sub>O-25ZnF<sub>2</sub> mol. %), MOF004 (60TeO<sub>2</sub>-10Na<sub>2</sub>O-30ZnF<sub>2</sub> mol. %), MOF005 (70TeO<sub>2</sub>-10Na<sub>2</sub>O-20ZnF<sub>2</sub> mol. %), MOF006 (75TeO<sub>2</sub>-10Na<sub>2</sub>O-15ZnF<sub>2</sub> mol. %), MOF007 (80TeO<sub>2</sub>-10Na<sub>2</sub>O-10ZnF<sub>2</sub> mol. %) and MOF008 (85TeO<sub>2</sub>-10Na<sub>2</sub>O-5ZnF<sub>2</sub> mol. %) [10].

It can be seen from these curves that the glass transition temperature falls with increasing fluoride and the  $T_x$ - $T_g$  gap widens, thus the glass becomes more stable. Fig. (4.15) illustrates this.

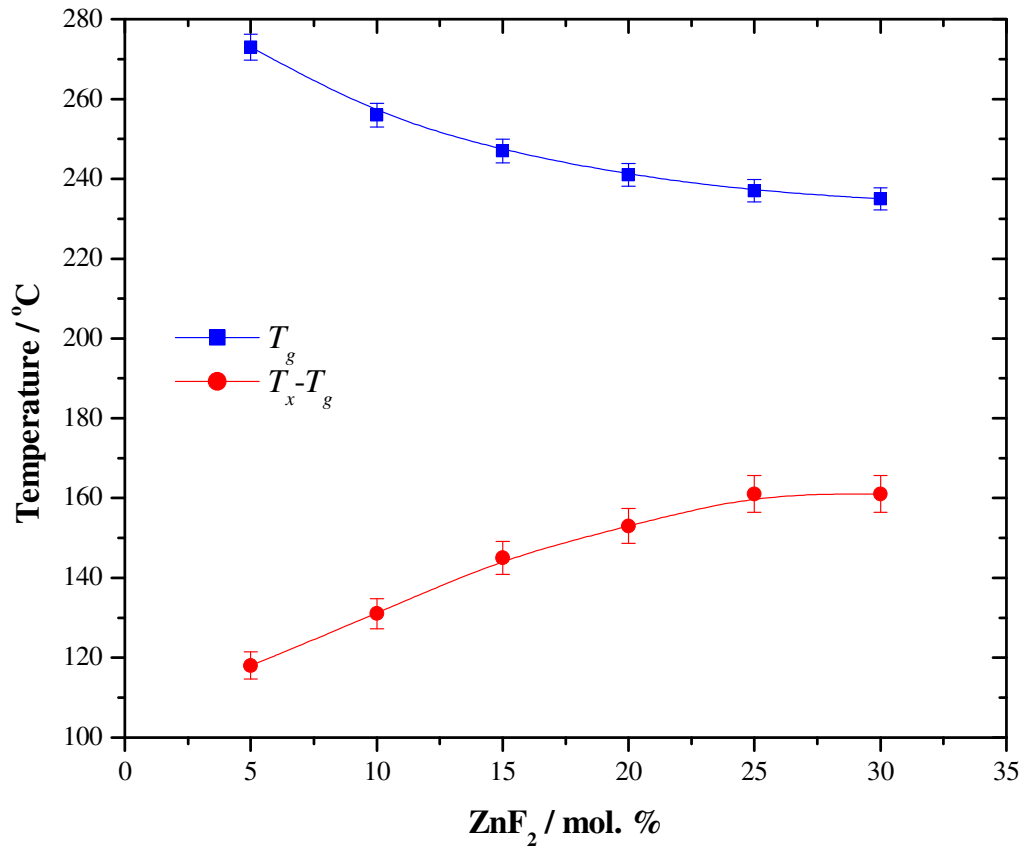


Fig. (4.15): Variation in  $T_g$  and  $T_x - T_g$  with increasing  $ZnF_2$  content from fig (4.14).

#### *Effect of $PbF_2$ and $WO_3$*

Fig. (4.16) shows DTA traces for glasses MOF002 (70TeO<sub>2</sub>-10Na<sub>2</sub>O-10ZnF<sub>2</sub>-10PbF<sub>2</sub> mol. %), MOF003 (65TeO<sub>2</sub>-10Na<sub>2</sub>O-20ZnF<sub>2</sub>-5PbF<sub>2</sub> mol. %) and MOF014 (65TeO<sub>2</sub>-10WO<sub>3</sub>-25 ZnF<sub>2</sub> mol. %).

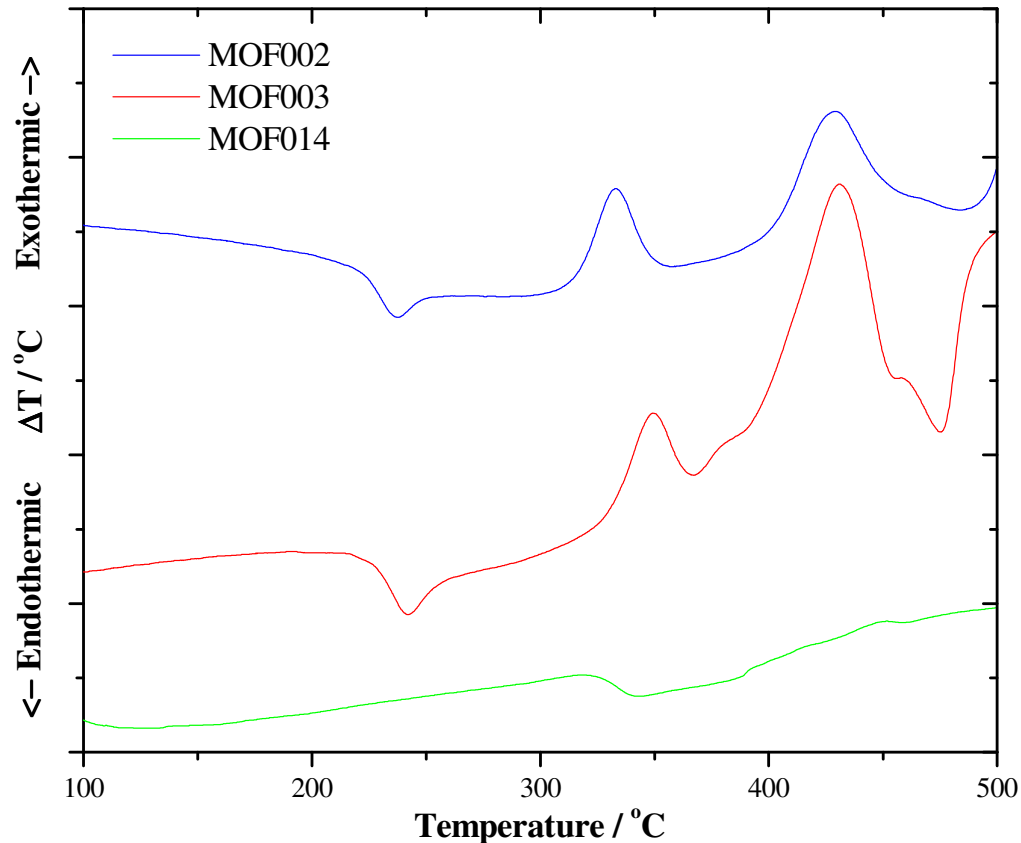


Fig. (4.16): DTA traces of glasses MOF002 (70TeO<sub>2</sub>-10Na<sub>2</sub>O-10ZnF<sub>2</sub>-10PbF<sub>2</sub> mol. %), MOF003 (65TeO<sub>2</sub>-10Na<sub>2</sub>O-20ZnF<sub>2</sub>-5PbF<sub>2</sub> mol. %) and MOF014 (65TeO<sub>2</sub>-10WO<sub>3</sub>-25 ZnF<sub>2</sub> mol. %).

The glass transition occurred at 215°C, 224°C and 324°C for MOF002, MOF003 and MOF014 respectively. The WO<sub>3</sub> containing compositions (MOF014) glass transition temperature is exceptionally high for a fluoride containing glass, comparable to the oxide compositions in section 4.1.2.1. The PbF<sub>2</sub> containing compositions exhibit multiple crystallisation peaks, the first occurring at 315°C and 331°C for MOF002 and MOF003 respectively. MOF014 did not exhibit a crystallisation peak over the temperature region recorded, indicating the ternary 65TeO<sub>2</sub>-10WO<sub>3</sub>-25 ZnF<sub>2</sub> forms a highly stable glass.

*Effect of ZnO:ZnF<sub>2</sub> ratio on the series 65TeO<sub>2</sub>·(25-x)ZnO·xZnF<sub>2</sub>·10Na<sub>2</sub>O (mol. %), for 0 ≤ x ≤ 20*

Fig. (4.17) shows DTA traces of glasses MOF009 (65TeO<sub>2</sub>-10Na<sub>2</sub>O-20ZnF<sub>2</sub>-5ZnO mol. %), MOF010 (65TeO<sub>2</sub>-10Na<sub>2</sub>O-15ZnF<sub>2</sub>-10ZnO mol. %), MOF011 (65TeO<sub>2</sub>-10Na<sub>2</sub>O-10ZnF<sub>2</sub>-15ZnO mol. %), MOF012 (65TeO<sub>2</sub>-10Na<sub>2</sub>O-5ZnF<sub>2</sub>-20ZnO mol. %) and MOF013 (65TeO<sub>2</sub>-10Na<sub>2</sub>O-25ZnO mol. %). This glass melting series obeys the composition rule 65TeO<sub>2</sub>·(25-x)ZnO·xZnF<sub>2</sub>·10Na<sub>2</sub>O (mol. %), for 0 ≤ x ≤ 20.

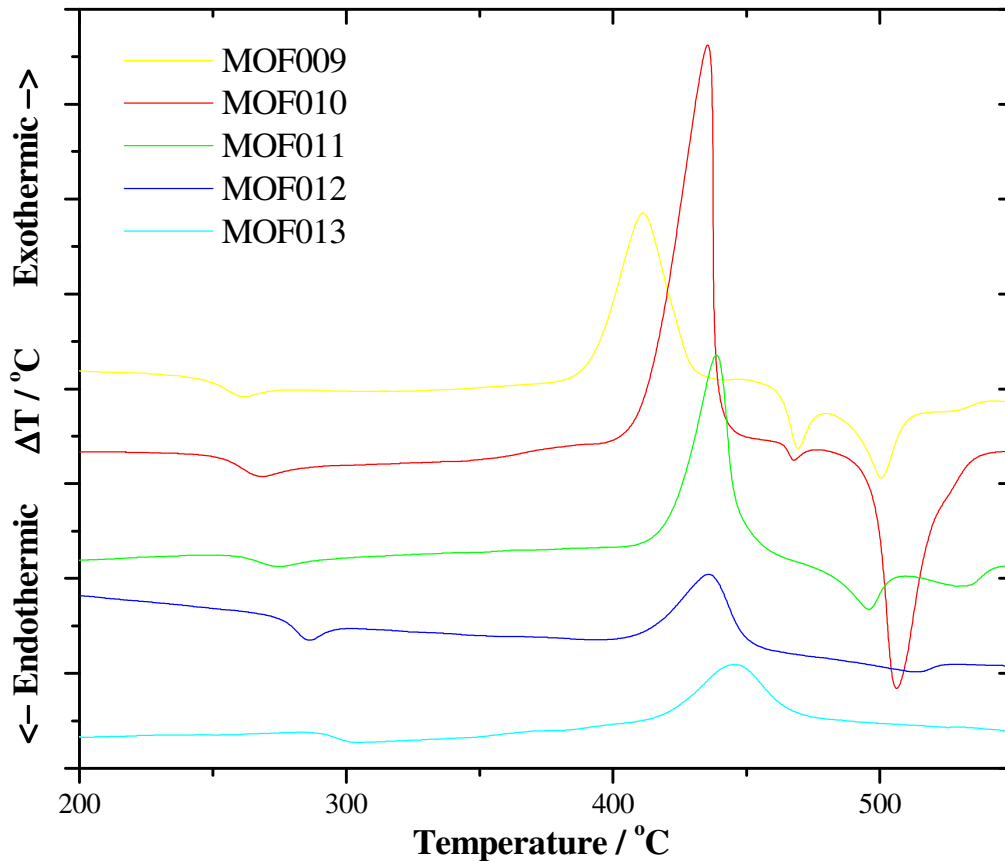


Fig. (4.17): DTA traces of glasses MOF009 (65TeO<sub>2</sub>-10Na<sub>2</sub>O-20ZnF<sub>2</sub>-5ZnO mol. %), MOF010 (65TeO<sub>2</sub>-10Na<sub>2</sub>O-15ZnF<sub>2</sub>-10ZnO mol. %), MOF011 (65TeO<sub>2</sub>-10Na<sub>2</sub>O-10ZnF<sub>2</sub>-15ZnO mol. %), MOF012 (65TeO<sub>2</sub>-10Na<sub>2</sub>O-5ZnF<sub>2</sub>-20ZnO mol. %) and MOF013 (65TeO<sub>2</sub>-10Na<sub>2</sub>O-25ZnO mol. %).

It can be seen from these curves that the glass transition temperature increases as the molar ratio of ZnO to ZnF<sub>2</sub> increases. Fig. (4.18) illustrates this trend along with  $T_x$  and  $T_x - T_g$ . Data for glass MOF001: 65TeO<sub>2</sub>-10Na<sub>2</sub>O-25ZnF<sub>2</sub> (ZnO:ZnF<sub>2</sub> = 0 =  $x$ ) was added to this figure.

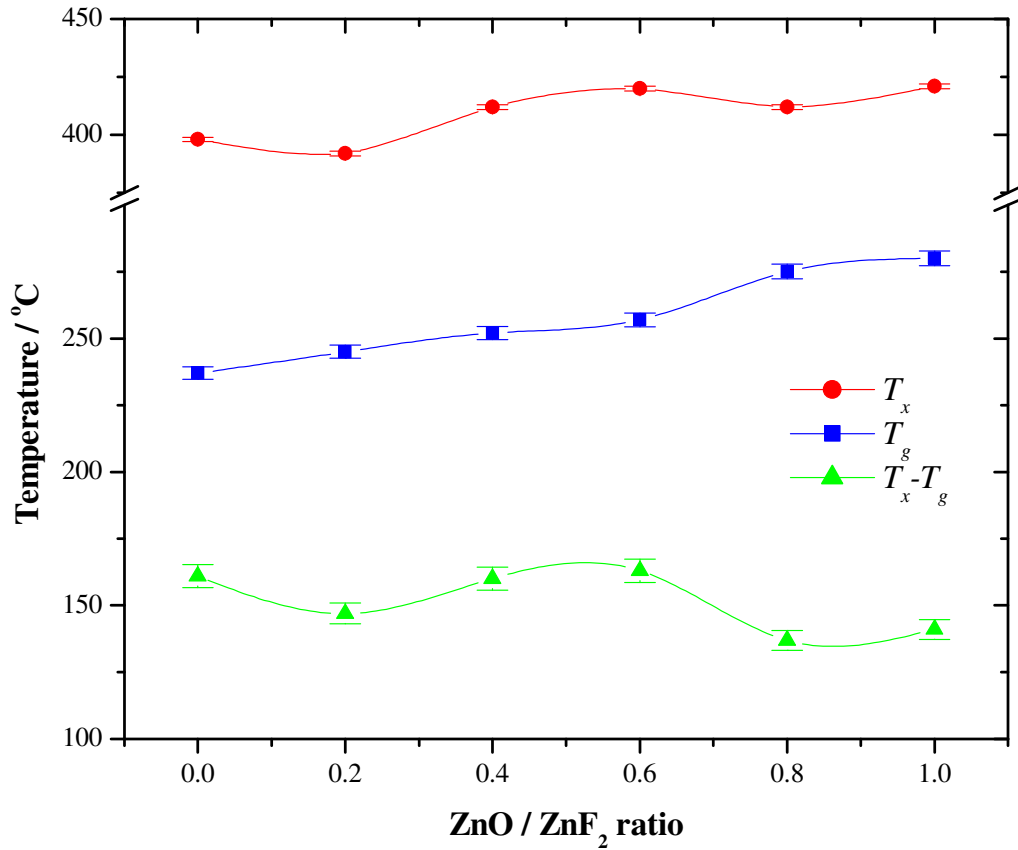


Fig. (4.18): Variation in  $T_g$ ,  $T_x$  and  $T_x - T_g$  with ZnO / ZnF<sub>2</sub> ratio for series 65TeO<sub>2</sub>.(25- $x$ )ZnO. $x$ ZnF<sub>2</sub>.10Na<sub>2</sub>O (mol. %), for  $0 \leq x \leq 20$  from fig. (4.17).

The irregular trend which  $T_x$  and  $T_x - T_g$  exhibit is likely to be due to an underlying structural change or two opposing effects in the glass.

*Effect of Er<sup>+3</sup> doping*

Fig. (4.19) shows DTA traces of glasses MOF015 to MOF018. The ratio of TeO<sub>2</sub>:ZnF<sub>2</sub>:Na<sub>2</sub>O were kept at 70:20:10 for this compositional series MOF015 (69.3TeO<sub>2</sub>-9.9Na<sub>2</sub>O-19.8ZnF<sub>2</sub>-1Er<sub>2</sub>O<sub>3</sub> mol. %), MOF016 (69.93TeO<sub>2</sub>-9.99Na<sub>2</sub>O-19.98ZnF<sub>2</sub>-0.1Er<sub>2</sub>O<sub>3</sub> mol. %), MOF017 (69.86TeO<sub>2</sub>-9.98Na<sub>2</sub>O-19.96ZnF<sub>2</sub>-0.2ErF<sub>3</sub> mol. %) and MOF018 (69.98TeO<sub>2</sub>-10Na<sub>2</sub>O-20ZnF<sub>2</sub>-0.02ErF<sub>3</sub> mol. %).

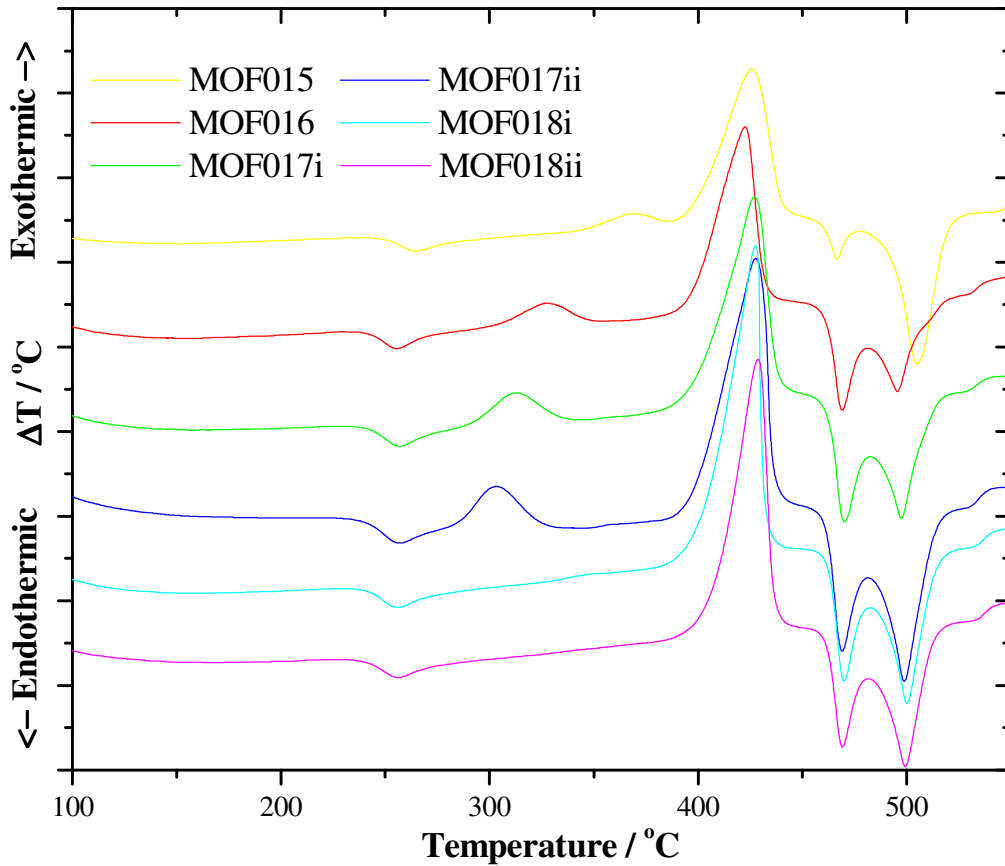


Fig. (4.19): DTA traces for glasses MOF015 (69.3TeO<sub>2</sub>-9.9Na<sub>2</sub>O-19.8ZnF<sub>2</sub>-1Er<sub>2</sub>O<sub>3</sub> mol. %), MOF016 (69.93TeO<sub>2</sub>-9.99Na<sub>2</sub>O-19.98ZnF<sub>2</sub>-0.1Er<sub>2</sub>O<sub>3</sub> mol. %), MOF017 (69.86TeO<sub>2</sub>-9.98Na<sub>2</sub>O-19.96ZnF<sub>2</sub>-0.2ErF<sub>3</sub> mol. %) and MOF018 (69.98TeO<sub>2</sub>-10Na<sub>2</sub>O-20ZnF<sub>2</sub>-0.02ErF<sub>3</sub> mol. %).

It can be seen the glasses containing  $\text{Er}_2\text{O}_3$  (0.1 and 1 mol. %) and higher levels of  $\text{ErF}_3$  (0.2 mol. %) were relatively unstable, exhibiting multiple crystallisation exotherms, with  $T_x-T_g$  values  $\approx 50^\circ\text{C}$  for MOF017. However, incorporating an order of magnitude lower dopant level of the fluoride (0.02 mol. %) resulted in high stability glass, with a  $T_x-T_g$  value ( $\approx 160^\circ\text{C}$ ) similar to the parent glass, MOF005 ( $70\text{TeO}_2-10\text{Na}_2\text{O}-20\text{ZnF}_2$ ).

*Effect of melting time for glass  $70\text{TeO}_2-10\text{Na}_2\text{O}-20\text{ZnF}_2$  mol. %*

Fig. (4.20) shows the variation in DTA trace with increasing melting time for samples taken from glass preforms MOF005vi, vii and viii which were all  $70\text{TeO}_2-10\text{Na}_2\text{O}-20\text{ZnF}_2$  mol. %.

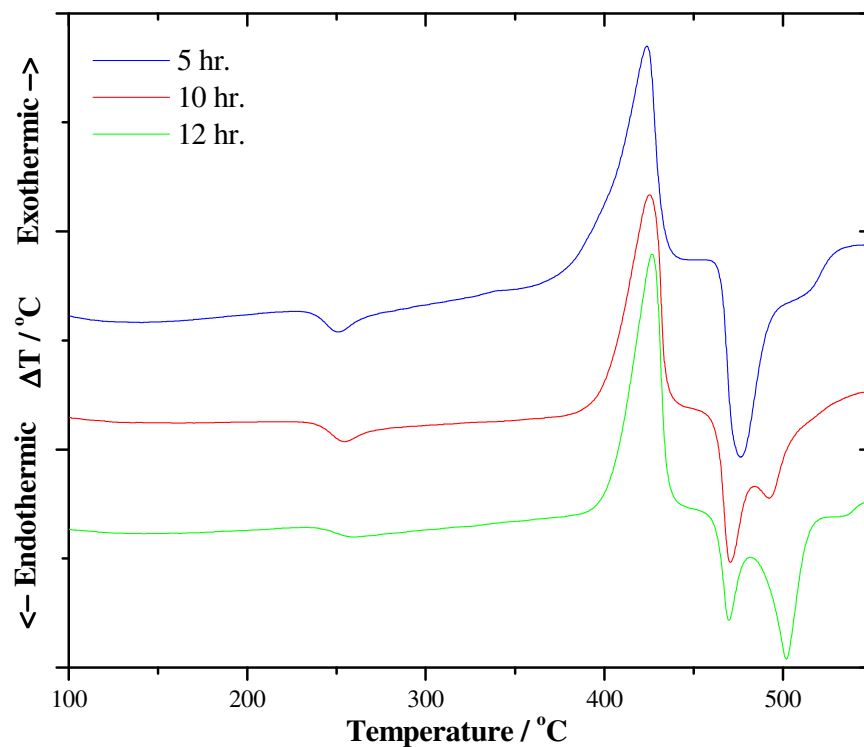


Fig. (4.20): DTA traces of glass preforms MOF005vi, vii and viii ( $70\text{TeO}_2-10\text{Na}_2\text{O}-20\text{ZnF}_2$  mol. %) with increasing melting time.

Fig. (4.21) shows variation of  $T_g$  and  $T_x - T_g$  with melting time for glass preforms MOF005vi, vii and viii. These glasses were melted in a gold crucible, calculated to give a 30g batch, for half the melting time at 800°C, the remainder at 670°C, then cast into a cylindrical brass mould (ID = 1 cm) and annealed for 1 hour at 230°C (see chapter 3).

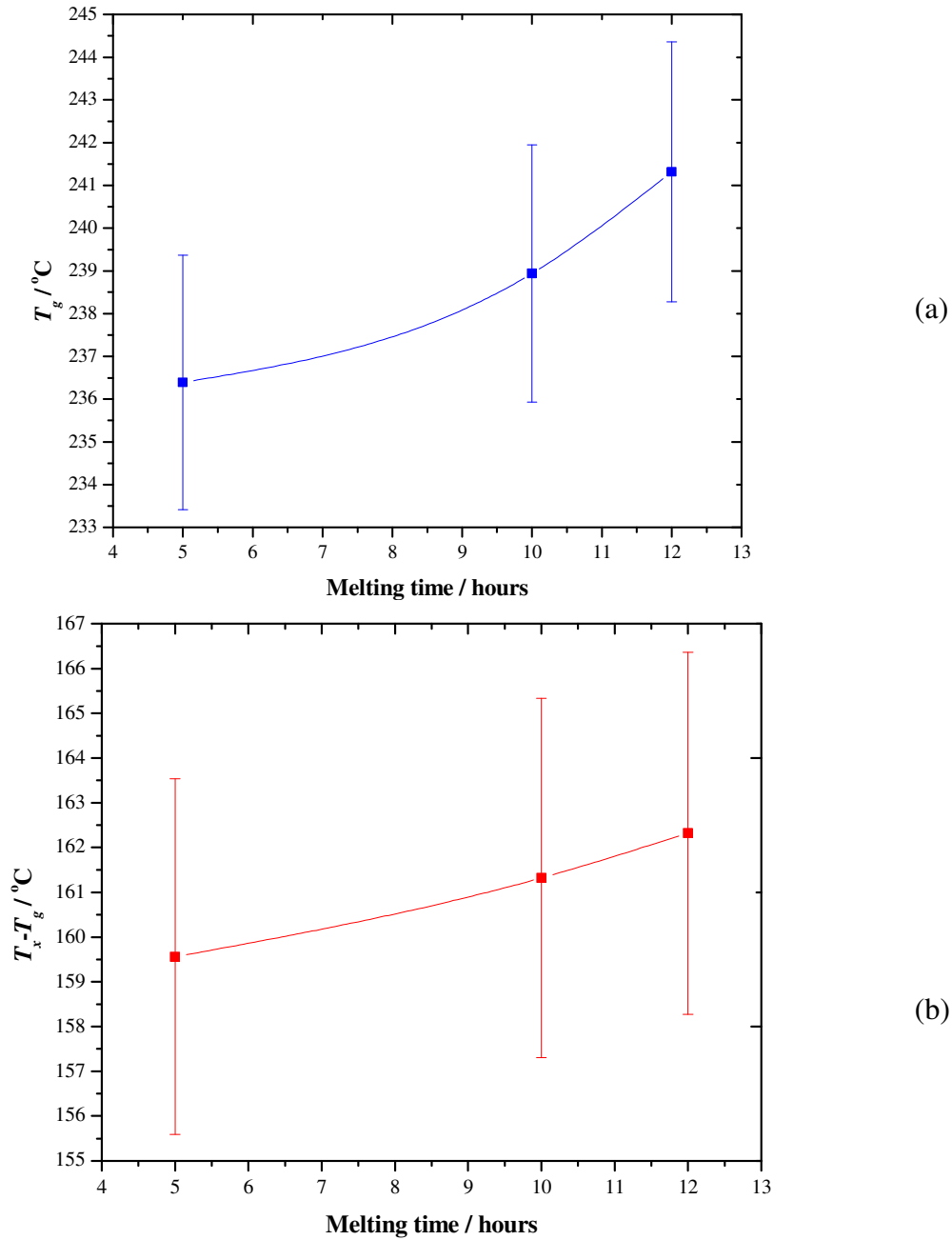


Fig. (4.21): Variation in (a)  $T_g$  and (b)  $T_x - T_g$  with melting time for glass preforms MOF005vi, vii and viii (70TeO<sub>2</sub>-10Na<sub>2</sub>O-20ZnF<sub>2</sub> mol. %).

Table (4.2) summarises the characteristic temperatures of melts MOF001 to MOF018, inclusively.

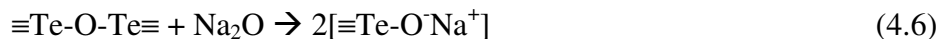
Table (4.2): Characteristic temperatures for fluorotellurite glasses (see table (3.2)).

<b>MOF ID</b>	<b><math>T_g / ^\circ\text{C}</math></b>	<b><math>T_x / ^\circ\text{C}</math></b>	<b><math>T_x - T_g / ^\circ\text{C}</math></b>
001	237	398	161
002	215	315	100
003	224	331	107
004	235	396	161
005i	241	394	153
005vi	236	396	160
005vii	239	400	161
005viii	241	404	162
006	247	392	145
007	256	387	131
008	273	391	118
009	245	392	147
010	252	412	160
011	257	420	163
012	275	412	137
013	289	421	132
014	324	-	-
015	248	344	96
016	241	304	63
017i	241	292	51
017ii	240	286	46
018i	241	401	160
018ii	239	407	168

### 4.3. Discussion

#### *Effect of rare-earth and lead oxide addition*

Glass MOD001, 79TeO<sub>2</sub>-10Na<sub>2</sub>O-10PbO-1Yb<sub>2</sub>O<sub>3</sub> mol. %, (fig. (4.10)) was rather unstable; thus  $T_x-T_g = 55^\circ\text{C}$ , compared with other glasses investigated in this study, with  $T_x-T_g > 150^\circ\text{C}$ . The binary system TeO<sub>2</sub>-Na<sub>2</sub>O has been reported to form stable glasses over a wide compositional range: 5.5 to 37.8 mol. % Na<sub>2</sub>O [11] with maximum stability occurring at 20 mol. % Na<sub>2</sub>O, for which  $T_x-T_g > 120^\circ\text{C}$  [12, 13]. This binary glass corresponds to the eutectic composition on the equilibrium phase diagram, and the phase Na<sub>2</sub>Te<sub>4</sub>O<sub>9</sub> [12]. Sodium oxide is a network modifier, i.e. it breaks up the covalent TeO<sub>2</sub> network by forming ionic bonds with non-bridging oxygens (NBOs), as illustrated by equation (4.6):



Thus addition of Na<sub>2</sub>O to TeO<sub>2</sub> results in a decrease in  $T_g$  and opens up the  $T_x-T_g$  gap. TeO<sub>2</sub> does not form a glass without the addition of at least one component (oxide or halide), however a glass can be formed with small additions of these second components [11]. The structure of pure TeO<sub>2</sub> at ambient temperature and pressure is based on [TeO<sub>4</sub>] trigonal bipyramids (tbp), which transform to [TeO<sub>3</sub>] trigonal pyramids (tp) with increasing alkali metal oxide addition. This range of structural units (see section 2) is

denoted by  $Q_m^n$  [11, 12, 14-18]. Due to this range of polyhedra present in the  $\text{TeO}_2\text{-Na}_2\text{O}$  glass, for crystallisation to occur, significant structural rearrangement would need to take place. This energy barrier, and slow kinetics around  $T_g$  result in a stable glass [12, 14, 15].

$\text{TeO}_2\text{-PbO}$  glasses form over a much narrower compositional range: 13.6 to 21.8 mol. % PbO [11], and are far less stable than  $\text{TeO}_2\text{-Na}_2\text{O}$  glasses, with  $T_x\text{-}T_g < 50^\circ\text{C}$  [19]. Stanworth [20] reported glass formation in the binary system  $\text{TeO}_2\text{-PbO}$  over a wide compositional range (15-85 wt. % PbO), however these glasses were melted in silica, alumina and zirconia crucibles, which this author suggests would have dissolved substantially into the glasses which therefore perhaps cannot be truly called binary compositions. Lead (II) oxide enters the glass as an intermediate, forming  $\text{-O-Pb-O-}$  linkages composed of  $[\text{PbO}_6]$  octahedra and  $[\text{PbO}_4]$  tetrahedra [21]. PbO addition also changes the proportion of  $[\text{TeO}_4]$  tbp and  $[\text{TeO}_3]$  tp present in the glass [19]; hence in this study addition of PbO to the  $\text{TeO}_2\text{-Na}_2\text{O}$  system has upset the stabilisation caused by  $\text{Na}_2\text{O}$  and reduced the  $T_x\text{-}T_g$  gap expected from the binary  $\text{TeO}_2\text{-Na}_2\text{O}$  ( $T_x\text{-}T_g$  of  $55^\circ\text{C}$  compared to  $> 120^\circ\text{C}$  [12, 13]). As only 1 mol. %  $\text{Yb}_2\text{O}_3$  was added to MOD001, the effect on destabilisation is likely to be insignificant compared to that of PbO, and oxide tellurite glass stability is relatively tolerant to rare-earth additions of this magnitude [22] (i.e. 0 to 5 mol. %).

Glass MOD002, 78.21 $\text{TeO}_2\text{-}4.95\text{ZnO-}9.9\text{Na}_2\text{O-}4.95\text{PbO-}0.99\text{Yb}_2\text{O}_3\text{-}0.99\text{Er}_2\text{O}_3$  mol. % (fig. 4.10), was slightly more stable ( $T_x\text{-}T_g = 85^\circ\text{C}$ ) than MOD001 ( $T_x\text{-}T_g = 85^\circ\text{C}$  compared to  $55^\circ\text{C}$ ) due to the presence of ZnO and  $\text{Na}_2\text{O}$  in the former glass. The

---

<sup>2</sup> where  $n$  = the number of bridging oxygens in the structural unit, and  $m$  = co-ordination of Te in the structural unit

structure and properties of zinc-tellurite glasses have been studied for some time [23-27]. Like lead (II) oxide, zinc oxide enters the glass network as an intermediate.  $[\text{ZnO}_6]$  polyhedra enter the network of Te-O chains breaking them in places, but weakly linking parallel chains in others [24]. However, unlike alkali metal oxide addition, there is not the same range of polyhedra present;  $[\text{TeO}_4]$ ,  $[\text{TeO}_3]$  and  $[\text{ZnO}_6]$  interatomic distances are preserved (see section 2) in the  $\text{TeO}_2$ -ZnO glasses [24]. This is likely to be due to the covalent nature of ZnO, which will enter the network with less disruption than the more ionic  $\text{Na}_2\text{O}$ . The ternary system  $\text{TeO}_2$ - $\text{Na}_2\text{O}$ -ZnO has been shown to be highly stable [22, 28, 29]. Aida *et al.* [28] explained this stability using the theory of optical basicity which was developed by Duffy [30] and has been used by other groups to help to explain the properties of oxide glasses [31-33]. Optical basicity is a numerical expression of the average electron donor power of the oxide species. Combining a high optical basicity alkali metal oxide ( $\text{Na}_2\text{O} - 1.15$ ) and a low optical basicity metal oxide ( $\text{ZnO} - 1.03$ ) causes strong interaction in the glass, and suppresses the movement of  $\text{Na}^+$  and  $\text{Zn}^{2+}$  ions, resulting in high resistance to crystallisation [28].  $\text{TeO}_2$  also has a similar optical basicity (0.99) to ZnO, which would indicate that addition of ZnO would result in less disruption to the glassy network compared to  $\text{Na}_2\text{O}$ .

#### *TeO<sub>2</sub>-ZnO-Na<sub>2</sub>O (TZN) compositions*

Fig. (4.11) shows the DTA trace of glass MOD006, 77 $\text{TeO}_2$ -10 $\text{ZnO}$ -10 $\text{Na}_2\text{O}$ -3 $\text{PbO}$  mol. %. This composition was far more stable than glass MOD002 (78.21 $\text{TeO}_2$ -4.95 $\text{ZnO}$ -9.9 $\text{Na}_2\text{O}$ -4.95 $\text{PbO}$ -0.99 $\text{Yb}_2\text{O}_3$ -0.99 $\text{Er}_2\text{O}_3$  mol. %, with  $T_x - T_g = 85^\circ\text{C}$ ), as it did not exhibit

a crystallisation peak. Glass MOD006 contained slightly less PbO than MOD002, no rare-earth oxide ( $\text{Er}^{3+}$  and  $\text{Yb}^{3+}$ ), and contained 1:1 molar ratio of  $\text{ZnO}:\text{Na}_2\text{O}$ . Aida *et al.* [28] found that ternary tellurite glass compositions with a 1:1 molar ratio of  $\text{R}_2\text{O}:\text{R}'\text{O}$  (where R is an alkali metal ion, e.g.  $\text{Na}^+$ ,  $\text{Li}^+$ ,  $\text{K}^+$ ; and R' is a metal ion, e.g.  $\text{Zn}^{+2}$ ,  $\text{Mg}^{+2}$ ,  $\text{Ba}^{+2}$ ) have a high resistance to crystallisation, particularly 10 to 15 mol. %  $\text{R}_2\text{O}$  and  $\text{R}'\text{O}$ .

The DTA trace of glass MOD007 (fig. (4.11)),  $78\text{TeO}_2\text{-}12\text{ZnO-}10\text{Na}_2\text{O}$  mol. %, showed a broad, low intensity crystallisation peak. This ternary composition  $78\text{TeO}_2\text{-}12\text{ZnO-}10\text{Na}_2\text{O}$  (MOD007) contained a 1.2:1.0 molar ratio of  $\text{ZnO}:\text{Na}_2\text{O}$  (close to a 1:1 molar ratio of  $\text{ZnO}:\text{Na}_2\text{O}$  [28]) and was far more stable than glasses MOD001 and 002 ( $T_x\text{-}T_g = 161^\circ\text{C}$  compared to  $55^\circ\text{C}$  and  $85^\circ\text{C}$  respectively).

Glasses MOD008 and 009 ( $74\text{TeO}_2\text{-}12\text{ZnO-}10\text{Na}_2\text{O-}3\text{PbO-}1\text{Yb}_2\text{O}_3$  and  $77\text{TeO}_2\text{-}12\text{ZnO-}10\text{Na}_2\text{O-}1\text{Yb}_2\text{O}_3$  mol. %), were also thermally stable. These compositions had the same molar ratio of  $\text{ZnO}:\text{Na}_2\text{O}$  (1.2:1.0) as MOD007, but some of the  $\text{TeO}_2$  was substituted by  $\text{PbO}$  and  $\text{Yb}_2\text{O}_3$  (3 and 1 mol. % respectively for MOD008) and  $\text{Yb}_2\text{O}_3$  (1 mol. % for MOD009). These substitutions improved the stability of the glasses in both cases compared to that of MOD007. No crystallisation exotherm was observed for MOD008 and 009, as opposed to MOD007 which had  $T_x\text{-}T_g$  value of  $161^\circ\text{C}$ .

Fig. (4.12) depicts the DTA trace of glass MOD010,  $75\text{TeO}_2\text{-}10\text{ZnO-}10\text{Na}_2\text{O-}5\text{PbO}$  mol. %, which was highly thermally stable. This composition had a 1:1 molar ratio of  $\text{ZnO}:\text{Na}_2\text{O}$  and 5 mol. %  $\text{PbO}$ . This glass would be suitable for the core of an optical fibre as it was thermally stable (no  $T_x$  peak on the DTA trace) and the addition of  $\text{PbO}$  would tend to increase the refractive index from the ternary composition  $80\text{TeO}_2\text{-}$

10Na<sub>2</sub>O-10ZnO mol. % ( $n = 2.046$  [28]) as Pb<sup>+2</sup> has a higher polarisability than Te<sup>+4</sup> [32].

Glass MOD011, 70TeO<sub>2</sub>-10ZnO-10Na<sub>2</sub>O-10PbO mol. %, which contained 10 mol. % PbO was less stable than MOD010 ( $T_x-T_g = 77^\circ\text{C}$  compared to no observable  $T_x$ ), indicating higher levels of PbO in the glass resulted in destabilisation. MOD001, which contained 10 mol. % PbO was also unstable ( $55^\circ\text{C}$ ), however compositions with 3 to 5 mol. % PbO (MOD002, 6, 8 and 10) showed greater resistance to devitrification ( $T_x-T_g$  of  $85^\circ\text{C}$  for MOD002 and no observable  $T_x$  for MOD006, 008 and 010).

Glass MOD012 (75TeO<sub>2</sub>-10ZnO-10Na<sub>2</sub>O-5GeO<sub>2</sub> mol. %) was identical to MOD010, but the PbO was substituted with GeO<sub>2</sub>. Glass MOD012 was also highly stable ( $T_x-T_g = 164^\circ\text{C}$ ), which is expected as GeO<sub>2</sub> is a glass former and will reinforce the covalent glassy network. Composition MOD012 would be suitable for the cladding in an optical fibre as it is thermally stable and GeO<sub>2</sub> would tend to lower the refractive index of the ternary composition 80TeO<sub>2</sub>-10Na<sub>2</sub>O-10ZnO, as Ge<sup>+4</sup> has a lower polarisability than Te<sup>+4</sup> [32]. Glass MOD013, 80TeO<sub>2</sub>-10ZnO-10Na<sub>2</sub>O mol. %, is stable ( $T_x-T_g = 108^\circ\text{C}$ ), as expected for a ternary composition with a 1:1 molar ratio of ZnO:Na<sub>2</sub>O [28].

#### *Effect of WO<sub>3</sub>, Nb<sub>2</sub>O<sub>5</sub> and Bi<sub>2</sub>O<sub>3</sub>*

Glasses MOD014 to 16 inclusively (fig. (4.13)), 90TeO<sub>2</sub>-5WO<sub>3</sub>-5Nb<sub>2</sub>O<sub>5</sub>, 82.5TeO<sub>2</sub>-7.5WO<sub>3</sub>-10Nb<sub>2</sub>O<sub>5</sub> and 70TeO<sub>2</sub>-25WO<sub>3</sub>-5Bi<sub>2</sub>O<sub>3</sub> mol. %, contained WO<sub>3</sub> and were all relatively thermally stable, with  $T_x-T_g$  values  $>110^\circ\text{C}$ ; moreover, glass MOD016 did not display a crystallisation exotherm over the region recorded (50 to 700°C). Several

workers have studied the structure and thermal properties of binary and ternary  $\text{WO}_3$ -containing glasses [34-39]. Shaltout *et al.* [38] studied the thermal properties by DSC and structure of a series of binary  $\text{TeO}_2$ - $\text{WO}_3$  glasses by Raman spectroscopy. Glasses were formed over a wide compositional range *viz.*: 5 to 50 mol. %  $\text{WO}_3$ .  $T_g$ ,  $T_x$  and  $T_x-T_g$  increased to a maximum at 27.5 mol. %  $\text{WO}_3$ . Around this composition is where the maximum population of  $[\text{WO}_4]$  tetrahedra occurred in the glass series. For concentrations of  $\text{WO}_3 > 27.5$  mol. %, the  $\text{W}^{+6}$  ions were found to exist in an increasing number of six-fold coordination:  $[\text{WO}_6]$  octahedra. Compositions MOD014 to 016, inclusive, which are shown in fig. (4.13) contained  $< 27.5$  mol. %  $\text{WO}_3$ , indicating the co-ordination of the  $\text{W}^{+6}$  ions was predominantly tetrahedral  $[\text{WO}_4]$ , which resulted in more stable glasses than for compositions with  $\text{WO}_3 > 27.5$  mol. %.

Champarnaud-Mesjard *et al.* [35] studied a wide range of compositions in the ternary system  $\text{TeO}_2$ - $\text{WO}_3$ - $\text{Bi}_2\text{O}_3$ . Glass formation was found to occur in the  $\text{TeO}_2$  rich region of the ternary phase diagram, and this region increased in size as the temperature the glass was quenched from was increased (650, 700 and 800°C). The most stable composition in the  $\text{TeO}_2$ - $\text{WO}_3$ - $\text{Bi}_2\text{O}_3$  series studied here was 70 $\text{TeO}_2$ -25 $\text{WO}_3$ -5 $\text{Bi}_2\text{O}_3$  (MOD016) with a  $T_x-T_g$  gap of 152°C [35].

Feng *et al.* [39] looked at glass formation in the ternary system  $\text{TeO}_2$ - $\text{WO}_3$ - $\text{Nb}_2\text{O}_5$  and found the most stable compositions to be 90 $\text{TeO}_2$ -5 $\text{WO}_3$ -5 $\text{Nb}_2\text{O}_5$  (equivalent to MOD014) and 82.5 $\text{TeO}_2$ -7.5 $\text{WO}_3$ -10 $\text{Nb}_2\text{O}_5$  (equivalent to MOD015) with  $T_x-T_g$  gaps of 173 and 171°C, respectively [39]. Unlike the glasses which contain alkali metal oxides [28], there is a wide range of ternary compositions of the series  $\text{TeO}_2$ - $\text{WO}_3$ -MO (where

MO is either Nb<sub>2</sub>O<sub>5</sub> or Bi<sub>2</sub>O<sub>3</sub>) which are reported to form highly stable glasses with the ratio of WO<sub>3</sub>:MO = 1 and WO<sub>3</sub>:MO ≠ 1 [35, 39].

Na<sub>2</sub>O disrupts the glassy network of TeO<sub>2</sub>, forming a range of at least five distinct polyhedra (see section 2), whereas other oxides such WO<sub>3</sub> cause less disruption (only forming two distinct structural units ([WO<sub>4</sub>] and [WO<sub>6</sub>])). W<sup>6+</sup>, Nb<sup>5+</sup> and Zn<sup>2+</sup> oxides have similar electronic polarisability ( $\pi_{ion}$ ), optical basicity ( $\mathcal{A}$ ) and bonding to Te<sup>2+</sup> in the oxide form [32]; these properties are summarized in table (4.3) for oxides used in this study.

Table (4.3): Optical basicity ( $\mathcal{A}$ ), electronic polarisability of cation ( $\pi_{ion}$ ) and bonding in oxides used in this study [32].

Oxide	$\mathcal{A}$	$\pi_{ion} / \text{\AA}^3$	Bonding type	Bonding details
GeO <sub>2</sub>	≈ 0.3 – 0.7	≈ 0.002 – 0.2	Semi-covalent or semi-ionic (acidic)	Large overlap between O 2p and metal valence orbitals
TeO <sub>2</sub> ZnO Nb <sub>2</sub> O <sub>5</sub> WO <sub>3</sub>	≈ 0.8 – 1.1	≈ 0.2 – 0.8	Ionic (basic)	Smaller overlap between O 2p and metal valence orbitals
Na <sub>2</sub> O PbO Bi <sub>2</sub> O <sub>3</sub>	> 1.1	≈ 0.8 – 3.7	Very ionic (very basic)	Small overlap between O 2p and metal valence orbitals

*Effect of ZnF<sub>2</sub> on the series (90-x)TeO<sub>2</sub>.xZnF<sub>2</sub>.10Na<sub>2</sub>O (mol. %), for 5 ≤ x ≤ 30*

A number of researchers has investigated fluoride-containing tellurite glasses, particularly PbF<sub>2</sub> and ZnF<sub>2</sub> containing compositions [10, 20, 40-52]. Ternary systems

such as  $\text{TeO}_2\text{-PbO-PbF}_2$  [48],  $\text{TeO}_2\text{-PbO-ZnF}_2$  [20, 44-46] and  $\text{TeO}_2\text{-ZnO-ZnF}_2$  [40, 41] have been studied; however the ternary  $\text{TeO}_2\text{-Na}_2\text{O-ZnF}_2$  has not been reported in the literature, except for work published from this study to the author's knowledge [10].

Fig. (4.14) shows DTA traces of glasses MOF001, MOF004 to 008 inclusively, of the composition series  $(90-x)\text{TeO}_2.10\text{Na}_2\text{O}.x\text{ZnF}_2$  ( $x = 5, 10, 15, 20, 25$  and  $30$  mol. %). The DTA traces show  $T_g$  decreased with increasing batched zinc fluoride in the glasses (see fig. (4.15)). At 5 mol. % added  $\text{ZnF}_2$ ,  $T_g$  was around  $273^\circ\text{C}$ , and it decreased to  $235^\circ\text{C}$  at 30 mol. %  $\text{ZnF}_2$ . This is to be expected as fluoride tends to break up the strong  $\text{TeO}_2$  covalent network of the glass by forming ionic, non-bridging M-F bonds (where M is a cation), enabling the glass-forming liquid to flow more easily at lower temperatures; hence isoviscous points occur at lower temperatures as fluoride increases. Fig. (4.15) shows that the glass stability on reheating, expressed as  $T_x - T_g$ , increased to a maximum of around  $161^\circ\text{C}$  at 25 mol. %  $\text{ZnF}_2$ , making glasses around this composition favourable for fibre drawing as the tendency for devitrification will be suppressed. This stability increase with increasing  $\text{ZnF}_2$  addition may have occurred because the more fluoride added, the more competition there is between different phases to crystallise, which would tend to stabilise the glass. Also, as the eutectic composition is approached across the notional fluoride/oxide tie-line, glass forming ability should be enhanced. It should also be noted here that the batched amount of fluoride was not equal to the retained fluoride in the glass, however, around 95 atomic % F was retained in the glass after melting, calculated from the weight % of the batch which volatilised. The glasses reported here are the most stable  $\text{ZnF}_2$ -containing reported in the literature to this author's knowledge, with  $T_x - T_g$  gaps exceeding  $160^\circ\text{C}$  (MOF001 and 4). Durga *et al.* [47] reported a glass of

composition, 50TeO<sub>2</sub>-40ZnF<sub>2</sub>-9.6As<sub>2</sub>O<sub>3</sub>-0.4Cr<sub>2</sub>O<sub>3</sub> mol. %, with a  $T_x-T_g$  gap of 104°C (see table (2.6)). Nazbal *et al.* [42] reported two compositions, 75TeO<sub>2</sub>-18ZnO-7ZnF<sub>2</sub> and 69TeO<sub>2</sub>-9ZnO-22ZnF<sub>2</sub> mol. %, with  $T_x-T_g$  gaps of 120°C (see table (2.7)). The inclusion of 10 mol. % Na<sub>2</sub>O in the glass series, (90- $x$ )TeO<sub>2</sub>. $x$ ZnF<sub>2</sub>.10Na<sub>2</sub>O (mol. %), resulted in resistance to devitrification over a wide compositional range, with  $T_x-T_g$  gaps > 110°C for  $5 \leq x \leq 30$  mol. % ZnF<sub>2</sub>.

#### *Effect of PbF<sub>2</sub> and WO<sub>3</sub>*

Fig. (4.16) shows DTA traces of MOF002 and 003, 70TeO<sub>2</sub>-10Na<sub>2</sub>O-10ZnF<sub>2</sub>-10PbF<sub>2</sub> and 65TeO<sub>2</sub>-10Na<sub>2</sub>O-20ZnF<sub>2</sub>-5PbF<sub>2</sub> mol. %, which contained PbF<sub>2</sub>. Both compositions formed glasses but exhibited two distinguishable crystallisation exotherms and were less stable than the ternary series (90- $x$ )TeO<sub>2</sub>. $x$ ZnF<sub>2</sub>.10Na<sub>2</sub>O (mol. %) for  $5 \leq x \leq 30$  mol. % ZnF<sub>2</sub> (i.e. MOF001, 004 to 008). However MOF002 and 003 had  $T_x-T_g$  gaps > 100°C, which is comparable to some of the stable oxide glasses reported in section 4.1.2.1. (e.g. MOD013, 80TeO<sub>2</sub>-10Na<sub>2</sub>O-10ZnO,  $T_x-T_g = 108^\circ\text{C}$ ). Table (4.4) shows van der Waals ( $r_{\text{vdw}}$ ), ionic ( $r_{\text{ion}}$ ), covalent ( $r_{\text{cov}}$ ) and Bragg-Slater ( $r_{\text{b-s}}$ ) ionic radii of elements used in this study [53, 54].

Table (4.4): Van der Waals ( $r_{vdw}$ ), ionic ( $r_{ion}$ ), covalent ( $r_{cov}$ ) and Bragg-Slater ( $r_{b-s}$ ) radii of elements used in this study [53, 54].

Element	Radius / pm			
	$r_{vdw}$	$r_{ion}$	$r_{cov}$	$r_{b-s}^{(3)}$
O <sup>-2</sup>	150	140	73	60
F <sup>-</sup>	150-160	133	71	50
Na <sup>+</sup>	230	102	154	180
Zn <sup>+2</sup>	140	74	120	135
Ge <sup>+4</sup>	-	53	122	125
Nb <sup>+5</sup>	-	64	-	145
Te <sup>+4</sup>	210	97	135	140
La <sup>+3</sup>	-	103	-	195
Er <sup>+3</sup>	-	89	-	-
Yb <sup>+3</sup>	-	87	-	-
W <sup>+6</sup>	-	60	-	-
Pb <sup>+2</sup>	200	119	-	-
Bi <sup>+3</sup>	-	103	-	160

Zn<sup>+2</sup> has a slightly lower ionic radii compared to Te<sup>+4</sup> (97 and 74 pm respectively [54]), therefore Zn<sup>+2</sup> can be introduced into the glass network with less disruption. Pb<sup>+2</sup> has a higher radius (119 pm) [54] and will disrupt the network more easily. Na<sup>+</sup> has a similar radius to tellurium (102 pm) [54], however it does not enter the glass as an intermediate like Zn<sup>+2</sup> and Pb<sup>+2</sup>. As discussed earlier, sodium oxide enters the glass as a network modifier and forms a range of polyhedra which stabilise the glass by means of providing a higher energy barrier for atomic and molecular rearrangement.

It is interesting to note that F<sup>-</sup> has a similar ionic radius to O<sup>-2</sup> (133 and 140 pm respectively) [54], so oxide batch materials should be readily substituted by fluoride batch materials and stable compositions could result, e.g. stable glasses were produced here from the oxide ternary TeO<sub>2</sub>-Na<sub>2</sub>O-ZnO and also the analogous oxyfluoride ternary TeO<sub>2</sub>-Na<sub>2</sub>O-ZnF<sub>2</sub>.

<sup>(3)</sup> Bragg-Slater radii roughly represents the size of the inner core of electrons

The DTA trace of glass MOF014, 65TeO<sub>2</sub>-10WO<sub>3</sub>-25ZnF<sub>2</sub> mol. % (fig. (4.16)), shows the WO<sub>3</sub>-containing composition to be highly stable, without exhibiting a significant crystallisation exotherm over the temperature range recorded (50 to 600°C). It can be seen from table (4.4) that W<sup>+6</sup> has a similar radius to Zn<sup>+2</sup>, lower than Te<sup>+4</sup> (60, 74 and 97 pm respectively) [53], therefore tungsten oxide will enter the network as an intermediate with less disruption than lead oxide, for example.

*Effect of ZnO:ZnF<sub>2</sub> ratio on the series 65TeO<sub>2</sub>.(25-x)ZnO.xZnF<sub>2</sub>.10Na<sub>2</sub>O (mol. %), for 0 ≤ x ≤ 20*

Fig. (4.17) shows DTA traces of glasses MOF009 to 13, which obeyed the compositional formula 65TeO<sub>2</sub>.(25-x)ZnO.xZnF<sub>2</sub>.10Na<sub>2</sub>O (mol. %), for 0 ≤ x ≤ 20. The effect of the molar ratio of ZnO:ZnF<sub>2</sub> in this series on T<sub>g</sub> and T<sub>x</sub>-T<sub>g</sub> is shown in fig. (4.18). As expected, T<sub>g</sub> fell with increasing fluoride in the glass as fluorine tends to break up the network due to its ionic character, enabling the glass to flow more easily at lower temperatures. Stability increased with addition of fluoride and then increased to a maximum of 168°C at around ZnO:ZnF<sub>2</sub> = 0.55, which corresponds to an interpolated composition of 65TeO<sub>2</sub>-10Na<sub>2</sub>O-13.75ZnO-11.25ZnF<sub>2</sub> (mol. %). Stability significantly decreased when the molar ratio of ZnO:ZnF<sub>2</sub> was > 0.6. The gradient of T<sub>g</sub> versus ZnO:ZnF<sub>2</sub> ratio also showed a marked increase here (fig. (4.18)), indicating some sort of structural change possibly occurred in the glass, perhaps a change of co-ordination of the Zn<sup>+2</sup> ions due to the change in the surrounding anionic environment (i.e. population and position of O<sup>-2</sup> and F<sup>-</sup> ions). Rao *et al.* [55] found that in the binary system PbO-PbF<sub>2</sub>,

depending on the proportion of PbO and PbF<sub>2</sub> in the glass, four distinct structural units occurred. These are illustrated in fig. (4.22).

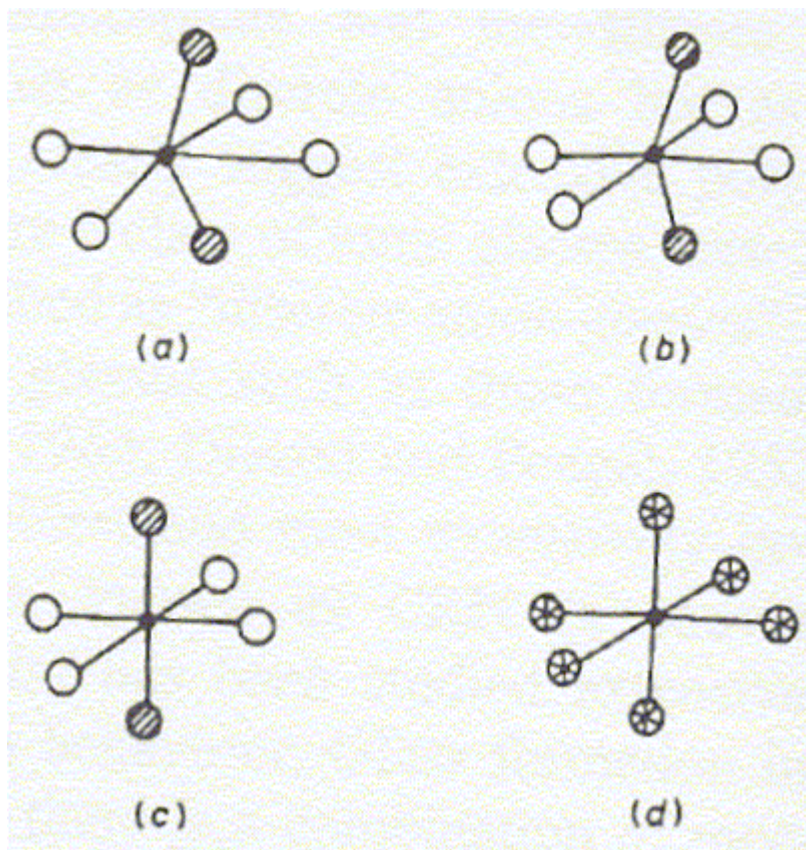


Fig. (4.22): Structural units in the PbO-PbF<sub>2</sub> glass system, with increasing PbO (a) to (d), where • = lead, ⊗ = oxygen, O = fluorine [55].

PbO is a covalent solid, whilst PbF<sub>2</sub> is highly ionic. In the PbO-PbF<sub>2</sub> glass system, distorted octahedral [PbO<sub>2</sub>F<sub>4</sub>] units are connected by oxygens which are coordinated to four lead atoms with a bond length of 220 pm [55]. In order to form octahedral units lead is sp<sup>3</sup>d<sup>2</sup> hybridised. Also, as PbF<sub>2</sub> content in the glass increases, so does the ionicity of the Pb-O bond. The PbO-PbF<sub>2</sub> glass system behaves very differently to conventional oxide glass systems; thus when halides are introduced into phosphates, they do not become part of the phosphate coordination polyhedra in the network [55]. A number of

structural units could exist in the series  $[\text{ZnF}_{6-x}\text{O}_x]$ , for  $1 \leq x \leq 6$ . This substitution is possible due to the similar ionic radius of  $\text{F}^-$  and  $\text{O}^{2-}$ , and the six-coordination of zinc to both anions. Therefore,  $\text{ZnF}_2$  can be substituted for  $\text{ZnO}$  in tellurite glasses, resulting in compositions with stability equal to, and exceeding those of pure oxide compositions. Sidebottom *et al.* [40] studied the Raman spectra of the ternary glass system  $\text{TeO}_2$ - $\text{ZnO}$ - $\text{ZnF}_2$ . The Raman bands due to symmetric stretching modes of  $\text{TeO}_2$  structural units ( $[\text{TeO}_4]$ ,  $[\text{TeO}_{3+1}]$  and  $[\text{TeO}_3]$ ) in the  $650\text{-}750\text{ cm}^{-1}$  region were unaffected by fluoride addition. However, the bending mode at  $420\text{ cm}^{-1}$  increased in intensity with increasing  $\text{ZnF}_2$  content. This indicates that fluorine was readily incorporated into the glassy network, directly replacing oxygen, without depolymerising the network [40]. In this glass system, the increase in bending mode intensity at  $420\text{ cm}^{-1}$  is due to the conversion of  $[\text{TeO}_3]$  units to  $[\text{Te}(\text{O},\text{F})_{3+1}]$ , with increasing fluoride content [40]. This author would propose a similar structural effect could occur in glasses MOF009 to 013, as zinc is divalent, like lead, and typically six-coordinated; however some depolymerisation will occur, as viscosity behaviour of these glasses becomes more fragile with  $\text{ZnF}_2$  addition (see chapter 8). When added to  $\text{TeO}_2$  glasses  $\text{ZnO}$  is known to form network linkages in places, but break the network in others [23, 24], therefore it would be reasonable to assume  $\text{ZnF}_2$  would have a similar effect, as zinc will bond to fluorine and oxygen in the final glass (although  $\text{ZnF}_2$  introduces two F anions into the glass per zinc cation, as opposed to  $\text{ZnO}$  which only introduces one anion).

*Effect of Er<sup>+3</sup> doping*

Fig. (4.19) shows DTA traces of the Er<sup>+3</sup> containing oxyfluoride glasses (MOF015 to 18), where Er<sub>2</sub>O<sub>3</sub> and ErF<sub>3</sub> was added in various amounts to the base ternary composition 70TeO<sub>2</sub>-10Na<sub>2</sub>O-20ZnF<sub>2</sub> (mol. %): 69.3TeO<sub>2</sub>-9.9Na<sub>2</sub>O-19.8ZnF<sub>2</sub>-1Er<sub>2</sub>O<sub>3</sub>, 69.93TeO<sub>2</sub>-9.99Na<sub>2</sub>O-19.98ZnF<sub>2</sub>-0.1Er<sub>2</sub>O<sub>3</sub>, 69.86TeO<sub>2</sub>-9.98Na<sub>2</sub>O-19.96ZnF<sub>2</sub>-0.2ErF<sub>3</sub> and 69.98TeO<sub>2</sub>-10Na<sub>2</sub>O-20ZnF<sub>2</sub>-0.02ErF<sub>3</sub> mol. %. All compositions showed a lower temperature crystallisation exotherm in addition to the single peak the undoped ternary 70TeO<sub>2</sub>-10Na<sub>2</sub>O-20ZnF<sub>2</sub> (mol. %) exhibited (see fig. (4.14)), except the composition containing 0.02 mol. % ErF<sub>3</sub> (MOF018). Erbium (III) is similar in size to tellurium (89 and 97 pm, respectively), however ErF<sub>3</sub> is 8-coordinate bicapped trigonal prismatic [54]. Er<sup>3+</sup> in oxide tellurite glasses is 6- or 7-coordinated [56], and has been shown to enhance the stability of TeO<sub>2</sub>-ZnO-Na<sub>2</sub>O glasses [22]. Therefore, this instability when added to fluorotellurite compositions could arise from the increase in coordination of erbium (III) in the presence of fluorine, making the glass network less tolerant to its addition, only resulting in stable glass for low dopant levels. The lower temperature crystallisation peak is likely to be an erbium rich phase (see section 5), indicating these compositions could be used to produce nano-glass-ceramics for photonic devices, with further compositional development. Hirano *et al.* [57] found that in the ternary glass 70TeO<sub>2</sub>-15K<sub>2</sub>O-15Nb<sub>2</sub>O<sub>5</sub>, when doped with around 1 mol. % rare-earth (Eu<sup>+3</sup>, Gd<sup>+3</sup>, Er<sup>+3</sup>, Tm<sup>+3</sup> and Yb<sup>+3</sup>) and heat treated after forming a glass from quenching, a rare-earth rich phase formed in nano-crystals (diameter = 20 nm). This phase resulted in an additional lower temperature

crystallisation exotherm on DTA traces and was identified as cubic in structure by XRD [57].

#### *Effect of melting time for glass 70TeO<sub>2</sub>-10Na<sub>2</sub>O-20ZnF<sub>2</sub>*

Fig. (4.20) shows the change in DTA trace with increasing melting time if glass MOF005, 70TeO<sub>2</sub>-10Na<sub>2</sub>O-20ZnF<sub>2</sub> mol. %.  $T_g$  and  $T_x-T_g$  were plotted against melting time in fig. (4.21). With increasing melting time, the fluorine content of the glass will be reduced, due to increased volatilisation, resulting in a more rigid oxide network, hence as expected  $T_g$  increased. Glass stability also increased with increasing melting time, indicating lower fluorine containing compositions are more stable, or OH in the glass results in destabilisation, providing sites for nucleation. The latter would seem more plausible as fig. (4.15) shows lower fluoride containing compositions are less stable; for the compositional series (90- $x$ )TeO<sub>2</sub>. $x$ ZnF<sub>2</sub>.10Na<sub>2</sub>O (mol. %),  $T_x-T_g = 118^\circ\text{C}$  for  $x = 5$  increasing to  $T_x-T_g = 161^\circ\text{C}$  for  $x = 30$ . It is also interesting to note that as the glass melting time increases, a higher temperature shoulder to the melting endotherm becomes more distinguishable, most likely due to the presence of more oxide fraction in the glass.

## **4.4. Summary**

The ternary system TeO<sub>2</sub>-ZnO-Na<sub>2</sub>O (TZN) can be melted to form a range of stable glasses, and doped with additions such as PbO to increase the refractive index, GeO<sub>2</sub> to lower the index, and rare-earths (La<sup>+3</sup>, Er<sup>+3</sup>, Yb<sup>+3</sup>) for active applications. These additions

did not adversely affect glass stability. Stable ternary tungsten-tellurite glasses (+ Nb<sub>2</sub>O<sub>5</sub> or Bi<sub>2</sub>O<sub>3</sub>) with high  $T_g$  values, were prepared which also show promise for infrared waveguides, due to their improved durability over TZN glasses, and higher refractive indices. Glass formation was shown for the first time in the system TeO<sub>2</sub>-Na<sub>2</sub>O-ZnF<sub>2</sub>, with stability increasing and  $T_g$  decreasing with ZnF<sub>2</sub> addition [10].

## 4.5. References

- [1] S. W. Martin and C. A. Angell, "On the glass transition and viscosity of P<sub>2</sub>O<sub>5</sub>," *Journal of Physical Chemistry*, vol. 90, pp. 6736-6740, 1986.
- [2] C. A. Angell, "Spectroscopy simulation and scattering, and the medium range order problem in glass," *Journal of Non-Crystalline Solids*, vol. 73, pp. 1-17, 1985.
- [3] R. F. Speyer, *Thermal analysis of materials*. New York: Marcel Dekker, 1994.
- [4] P. W. Atkins, *Physical Chemistry*, 5th ed. Oxford: Oxford University Press, 1994.
- [5] P. Rocabois, J. N. Pontoire, J. Lehmann, and H. Gaye, "Crystallization kinetics of Al<sub>2</sub>O<sub>3</sub>-CaO-SiO<sub>2</sub> based oxide inclusions," *Journal of Non-Crystalline Solids*, vol. 282, pp. 98-109, 2001.
- [6] K. Nakashima, K. Noda, and K. Mori, "Time-temperature-transformation diagrams for borosilicate glasses and preparation of chemically durable porous glasses," *Journal of the American Ceramic Society*, vol. 80, pp. 1101-1110, 1997.
- [7] L. E. Busse, G. Lu, D. C. Tran, and G. H. Sigel, "A combined DSC/optical microscopy study of crystallization in fluorozirconate glasses upon cooling from the melt," *Materials Science Forum*, vol. 5, pp. 219-228, 1985.
- [8] H. Takebe, D. J. Brady, D. W. Hewak, and K. Morinaga, "Thermal properties of Ga<sub>2</sub>S<sub>3</sub>-based glass and their consideration during fiber drawing," *Journal of Non-Crystalline Solids*, vol. 258, pp. 239-243, 1999.
- [9] S. X. Shen, M. Naftaly, and A. Jha, "Crystallization kinetics of tellurite glasses studied by DSC and DTA," *Glass Science and Technology-Glastechnische Berichte*, vol. 73, pp. 111-118, 2000.

- [10] M. D. O'Donnell, C. A. Miller, D. Furniss, V. K. Tikhomirov, and A. B. Seddon, "Fluorotellurite glasses with improved mid-infrared transmission," *Journal of Non-Crystalline Solids*, vol. 331, pp. 48-57, 2003.
- [11] W. Vogel, *Glass chemistry*, 2nd ed. New York: Springer-Verlag, 1994.
- [12] J. W. Zwanziger, J. C. McLaughlin, and S. L. Tagg, "Sodium distribution in sodium tellurite glasses probed with spin-echo NMR," *Physical Review B*, vol. 56, pp. 5243-5249, 1997.
- [13] D. M. Zhu, C. S. Ray, W. C. Zhou, and D. E. Day, "Glass transition and fragility of Na<sub>2</sub>O-TeO<sub>2</sub> glasses," *Journal of Non-Crystalline Solids*, vol. 319, pp. 247-256, 2003.
- [14] J. C. McLaughlin, S. L. Tagg, and J. W. Zwanziger, "The structure of alkali tellurite glasses," *Journal of Physical Chemistry B*, vol. 105, pp. 67-75, 2001.
- [15] J. C. McLaughlin, S. L. Tagg, J. W. Zwanziger, D. R. Haeffner, and S. D. Shastri, "The structure of tellurite glass: a combined NMR, neutron diffraction, and X-ray diffraction study," *Journal of Non-Crystalline Solids*, vol. 274, pp. 1-8, 2000.
- [16] Y. Himei, Y. Miura, T. Nanba, and A. Osaka, "X-ray photoelectron spectroscopy of alkali tellurite glasses," *Journal of Non-Crystalline Solids*, vol. 211, pp. 64-71, 1997.
- [17] S. Sakida, S. Hayakawa, and T. Yoko, "Part 2. Te-125 NMR study of M<sub>2</sub>O-TeO<sub>2</sub> (M = Li, Na, K, Rb and Cs) glasses," *Journal of Non-Crystalline Solids*, vol. 243, pp. 13-25, 1999.
- [18] S. Sakida, S. Hayakawa, and T. Yoko, "Part 1. Te-125 NMR study of tellurite crystals," *Journal of Non-Crystalline Solids*, vol. 243, pp. 1-12, 1999.
- [19] M. A. P. Silva, Y. Messaddeq, S. J. L. Ribeiro, M. Poulain, F. Villain, and V. Briois, "Structural studies on TeO<sub>2</sub>-PbO glasses," *Journal of Physics and Chemistry of Solids*, vol. 62, pp. 1055-1060, 2001.
- [20] J. E. Stanworth, "Tellurite glasses," *Journal of the Society of Glass Technology*, vol. 36, pp. 217-241, 1952.
- [21] M. Vithal, P. Nachimuthu, T. Banu, and R. Jagannathan, "Optical and electrical properties of PbO-TiO<sub>2</sub>, PbO-TeO<sub>2</sub>, and PbO-CdO glass systems," *Journal of Applied Physics*, vol. 81, pp. 7922-7926, 1997.
- [22] J. Wang, E. Vogel, and E. Snitzer, "Tellurite glass: a new candidate for fiber devices," *Optical Materials*, vol. 3, pp. 187-203, 1994.
- [23] M. Redman and J. Chen, "Zinc tellurite glasses," *Journal of the American Ceramic Society*, vol. 50, pp. 523-525, 1967.

- [24] V. Kozhukharov, H. Burger, S. Neov, and B. Sidzhimov, "Atomic arrangement of a zinc-tellurite glass," *Polyhedron*, vol. 5, pp. 771-777, 1986.
- [25] Y. Shimizugawa, T. Maeseto, S. Inoue, and A. Nukui, "Structure of  $\text{TeO}_2\text{-ZnO}$  glasses by RDF and Te, Zn K EXAFS," *Physics and Chemistry of Glasses*, vol. 38, pp. 201-205, 1997.
- [26] A. Nukui, T. Taniguchi, and M. Miyata, "In situ high-temperature X-ray observation of structural changes of tellurite glasses with p-block oxides;  $\text{ZnO-TeO}_2$  glasses," *Journal of Non-Crystalline Solids*, vol. 293, pp. 255-260, 2001.
- [27] G. D. Khattak and M. A. Salim, "X-ray photoelectron spectroscopic studies of zinc-tellurite glasses," *Journal of Electron Spectroscopy and Related Phenomena*, vol. 123, pp. 47-55, 2002.
- [28] K. Aida, T. Komatsu, and V. Dimitrov, "Thermal stability, electronic polarisability and optical basicity of ternary tellurite glasses," *Physics and Chemistry of Glasses*, vol. 42, pp. 103-111, 2001.
- [29] M. Braglia, S. Mosso, G. Dai, E. Billi, L. Bonelli, M. Baricco, and L. Battezzati, "Rheology of tellurite glasses," *Materials Research Bulletin*, vol. 35, pp. 2343-2351, 2000.
- [30] J. A. Duffy, "Optical basicity: A practical acid-base theory for oxides and oxyanions," *Journal of Chemical Education*, vol. 73, pp. 1138-1142, 1996.
- [31] V. Dimitrov and T. Komatsu, "Electronic polarizability, optical basicity and non-linear optical properties of oxide glasses," *Journal of Non-Crystalline Solids*, vol. 249, pp. 160-179, 1999.
- [32] V. Dimitrov and T. Komatsu, "Classification of simple oxides: A polarizability approach," *Journal of Solid State Chemistry*, vol. 163, pp. 100-112, 2002.
- [33] R. R. Reddy, Y. N. Ahammed, P. A. Azeem, K. R. Gopal, and T. V. R. Rao, "Electronic polarizability and optical basicity properties of oxide glasses through average electronegativity," *Journal of Non-Crystalline Solids*, vol. 286, pp. 169-180, 2001.
- [34] S. Blanchandin, P. Marchet, P. Thomas, J. C. Champarnaud-Mesjard, B. Frit, and A. Chagraoui, "New investigations within the  $\text{TeO}_2\text{-WO}_3$  system: phase equilibrium diagram and glass crystallization," *Journal of Materials Science*, vol. 34, pp. 4285-4292, 1999.
- [35] J. C. Champarnaud-Mesjard, P. Thomas, P. Marchet, B. Frit, A. Chagraoui, and A. Tairi, "Glass formation study in the  $\text{Bi}_2\text{O}_3\text{-TeO}_2\text{-WO}_3$  system," *Annales De Chimie-Science Des Materiaux*, vol. 23, pp. 289-292, 1998.

- [36] S. Blanchandin, P. Thomas, P. Marchet, J. C. Champarnaud-Mesjard, and B. Frit, "New heavy metal oxide glasses: investigations within the  $\text{TeO}_2$ - $\text{Nb}_2\text{O}_5$ - $\text{Bi}_2\text{O}_3$  system," *Journal of Alloys and Compounds*, vol. 347, pp. 206-212, 2002.
- [37] N. V. Ovcharenko and T. V. Smirnova, "High refractive index and magneto-optical glasses in the systems  $\text{TeO}_2$ - $\text{WO}_3$ - $\text{Bi}_2\text{O}_3$  and  $\text{TeO}_2$ - $\text{WO}_3$ - $\text{PbO}$ ," *Journal of Non-Crystalline Solids*, vol. 291, pp. 121-126, 2001.
- [38] I. Shaltout, Y. Tang, R. Braunstein, and A. M. Abuelazm, "Structural Studies of Tungstate Tellurite Glasses by Raman- Spectroscopy and Differential Scanning Calorimetry," *Journal of Physics and Chemistry of Solids*, vol. 56, pp. 141-150, 1995.
- [39] X. Feng, C. H. Qi, F. Y. Lin, and H. F. Hu, "Tungsten-tellurite glass: a new candidate medium for  $\text{Yb}^{3+}$ - doping," *Journal of Non-Crystalline Solids*, vol. 257, pp. 372-377, 1999.
- [40] D. L. Sidebottom, M. A. Hruschka, B. G. Potter, and R. K. Brow, "Increased radiative lifetime of rare earth-doped zinc oxyhalide tellurite glasses," *Applied Physics Letters*, vol. 71, pp. 1963-1965, 1997.
- [41] D. L. Sidebottom, M. A. Hruschka, B. G. Potter, and R. K. Brow, "Structure and optical properties of rare earth-doped zinc oxyhalide tellurite glasses," *Journal of Non-Crystalline Solids*, vol. 222, pp. 282-289, 1997.
- [42] V. Nazabal, S. Todoroki, A. Nukui, T. Matsumoto, S. Suehara, T. Hondo, T. Araki, S. Inoue, C. Rivero, and T. Cardinal, "Oxyfluoride tellurite glasses doped by erbium: thermal analysis, structural organization and spectral properties," *Journal of Non-Crystalline Solids*, vol. 325, pp. 85-102, 2003.
- [43] V. Nazabal, S. Todoroki, S. Inoue, T. Matsumoto, S. Suehara, T. Hondo, T. Araki, and T. Cardinal, "Spectral properties of  $\text{Er}^{3+}$  doped oxyfluoride tellurite glasses," *Journal of Non-Crystalline Solids*, vol. 326-327, pp. 359-363, 2003.
- [44] V. R. Kumar and N. Veeraiah, "Infrared spectral investigations on  $\text{ZnF}_2$ - $\text{PbO}$ - $\text{TeO}_2$  glasses," *Journal of Materials Science Letters*, vol. 16, pp. 1816-1818, 1997.
- [45] V. R. Kumar and N. Veeraiah, "Dielectric properties of  $\text{ZnF}_2$ - $\text{PbO}$ - $\text{TeO}_2$  glasses," *Journal of Physics and Chemistry of Solids*, vol. 59, pp. 91-97, 1998.
- [46] V. R. Kumar, N. Veeraiah, and B. A. Rao, "Optical absorption and photoluminescence properties of  $\text{Pr}^{3+}$ - doped  $\text{ZnF}_2$ - $\text{PbO}$ - $\text{TeO}_2$  glasses," *Journal of Luminescence*, vol. 75, pp. 57-62, 1997.
- [47] D. K. Durga, P. Yadagiri Reddy, and N. Veeraiah, "Optical absorption and thermoluminescence properties of  $\text{ZnF}_2$ - $\text{MO}$ - $\text{TeO}_2$  ( $\text{MO} = \text{As}_2\text{O}_3, \text{Bi}_2\text{O}_3$  and

- P<sub>2</sub>O<sub>5</sub>) glasses doped with chromium ions," *Journal of Luminescence*, vol. 99, pp. 53-60, 2002.
- [48] G. El-Damrawi, "Transport behavior of PbO-PbF<sub>2</sub>-TeO<sub>2</sub> glasses," *Physica Status Solidi a-Applied Research*, vol. 177, pp. 385-392, 2000.
- [49] K. Kobayashi, "Development of infrared transmitting glasses," *Journal of Non-Crystalline Solids*, vol. 316, pp. 403-406, 2003.
- [50] K. Kobayashi and H. Sasaki, "Visible rays cutoff and infrared transmission properties of TeO<sub>2</sub>-GeO<sub>2</sub>-V<sub>2</sub>O<sub>5</sub>-PbF<sub>2</sub> glass systems," *Journal of the European Ceramic Society*, vol. 19, pp. 637-639, 1999.
- [51] M. A. P. Silva, Y. Messaddeq, V. Briois, M. Poulain, F. Villain, and S. J. L. Ribeiro, "Synthesis and structural investigations on TeO<sub>2</sub>-PbF<sub>2</sub>-CdF<sub>2</sub> glasses and transparent glass-ceramics," *Journal of Physics and Chemistry of Solids*, vol. 63, pp. 605-612, 2002.
- [52] H. Burger, W. Vogel, and V. Kozhukharov, "IR transmission and properties of glasses in the TeO<sub>2</sub>-R<sub>n</sub>O<sub>m</sub>, R<sub>n</sub>X<sub>m</sub>, R<sub>n</sub>(SO<sub>4</sub>)<sub>m</sub>, R<sub>n</sub>(PO<sub>3</sub>)<sub>m</sub> and B<sub>2</sub>O<sub>3</sub> systems," *Infrared Physics*, vol. 25, pp. 395-409, 1985.
- [53] J. E. Huheey, *Inorganic chemistry: principles of structure and reactivity*, S.I. Units ed. London: Harper & Row, 1975.
- [54] N. N. Greenwood and A. Earnshaw, *Chemistry of the elements*. Oxford: Butterworth-Heinemann, 1995.
- [55] K. J. Rao, *Structural chemistry of glasses*. London: Elsevier, 2002.
- [56] A. Jha, S. Shen, and M. Naftaly, "Structural origin of spectral broadening of 1.5 micron emission in Er<sup>3+</sup>-doped tellurite glasses," *Physical Review B*, vol. 62, pp. 6215-6227, 2000.
- [57] K. Hirano, Y. Benino, and T. Komatsu, "Rare earth doping into optical nonlinear nanocrystalline phase in transparent TeO<sub>2</sub>-based glass-ceramics," *Journal of Physics and Chemistry of Solids*, vol. 62, pp. 2075-2082, 2001.

## 5. Crystallisation studies

The aims of this chapter are: to use X-ray diffraction (XRD) to assist the monitoring and optimisation of the purification procedures for glass batch precursors; to use knowledge of the crystal structures of precursors materials to gain further insight into the structure of tellurite and fluorotellurite glasses; and to use XRD to investigate the nature of crystalline phases formed in devitrification of glasses during processing and characterisation.

### 5.1. Experimental

#### 5.1.1. X-ray diffraction (XRD)

##### 5.1.1.1. Method and instrumentation

X-ray diffraction (XRD) was performed in this study using a Siemens D500 powder diffractometer. All traces were recorded using  $\text{CuK}\alpha$  radiation at  $1.5418 \text{ \AA}$ , scanning from  $10$  to  $100^\circ 2\theta$  with a step size of  $0.02^\circ 2\theta$  every  $1 \text{ s}$  (i.e. each trace took  $75 \text{ min.}$  to run), at ambient temperature, in air. Samples were ground to a fine powder using a pestle and mortar, and mounted in a Perspex / aluminium sample holder by compacting the powder into a circular disc ( $1$  to  $2 \text{ mm}$  thick) with a glass slide. Fig. (5.1) illustrates this holder.

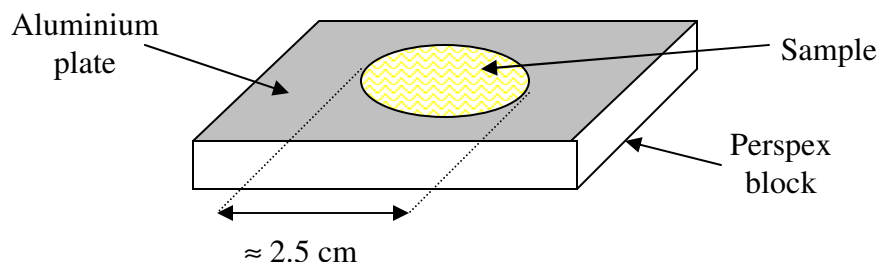


Fig. (5.1): XRD sample holder.

### *Interpretation of powder patterns*

In this study, Bruker software was used to label peaks, and identify (if any) crystalline phases present in the sample. This software labels peaks on the trace with their corresponding d-spacings. A CD-ROM database of diffraction patterns from the Joint Committee on Powder Diffraction Standards (JCPDS) was searched for each trace. The elements thought to be present in the powdered sample were entered in to the software, which finds all patterns available with any combination of these elements. These patterns can be compared with the recorded trace, enabling the identification of the composition and structure of the powdered sample. Usually, the three or four most intense peaks are used to identify unknown crystals, as no two crystalline materials have identical d-spacings and relative intensities [1].

#### **5.1.1.2. Theory of operation**

The structure of a crystal can be identified using radiation of a wavelength comparable to the interplanar spacings in the material. The interplanar spacings in most crystals are in

the range of 1 to 10 Å ( $10^{-10}$  to  $10^{-9}$  m) which corresponds to the wavelength of the X-ray part of the electromagnetic spectrum. When this X-ray radiation impinges on a material, two effects are observed: absorption and scattering [1]. Absorption results in excitation of inner orbital electrons of the atoms of the material which Auger electron spectroscopy (AES) and X-ray fluorescence (XRF) utilise for chemical analysis [1].

When X-rays are scattered by a material their wavelength is either changed (incoherent scattering) or their wavelength remains unchanged (coherent scattering) [1]. The coherent X-rays scattered from different electrons of the same atom lead to interference effects. These effects are more likely for X-rays coherently scattered by atoms of the same or adjacent planes [1]. This phenomena, known as X-ray diffraction, is analogous to the diffraction of light from an optical grating. The closely spaced lines of the grating are the two-dimensional equivalent of the atomic planes in a crystal. Once the diffraction pattern is obtained the atomic structure can be calculated [1].

The scattering of X-rays was first treated by von Laue [2]. He considered a row of atoms periodically spaced, scattering a parallel set of rays, which are only observable if they are travelling in phase. This means the path difference between each of the scattered rays should be an integral multiple of the wavelength,  $\lambda$  (i.e.  $n\lambda$ , where  $n$  = an integer 1, 2, 3 etc.).

W.L. Bragg found that beams of diffracted X-rays can be treated in terms of 'reflections' from the lattice planes of crystals [3]. Fig. (5.2) illustrates the diffraction of incident X-rays from parallel rows of atoms in a crystalline lattice, described below.

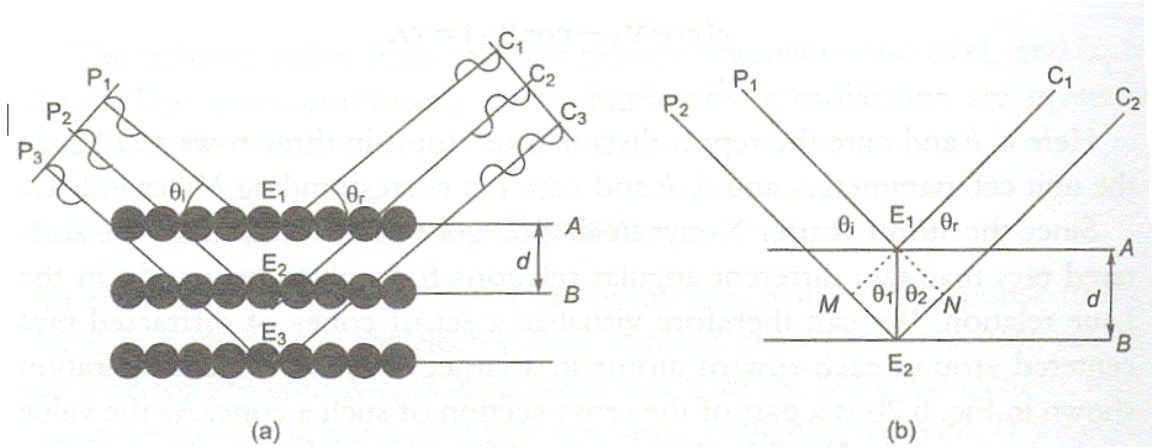


Fig. (5.2): Diffraction of incident X-rays from parallel rows of atoms in a crystalline lattice (see text for definitions of terms) [1].

Consider two sets of planes A and B, with interplanar spacing  $d$ . If a wavefront of in-phase X-rays,  $p_1p_2p_3$ , is incident on these planes with an angle  $\theta_i$ , this gives rise to ‘reflected’ beams  $c_1, c_2$  and  $c_3$  with an angle of  $\theta_r$ . The rays  $p_1E_1c_1$  and  $p_2E_2c_2$  should arrive at the same time at  $c_1c_2c_3$  only if they are in phase. This means the path difference between  $p_1E_1c_1$  and  $p_2E_2c_2$  should be given by equation (5.1).

$$n\lambda = ME_2 + NE_2 \quad (5.1)$$

If we consider the two right angle triangles,  $E_1ME_2$  and  $E_1NE_2$ , shown in fig. (5.2b):

$$\sin \theta_i = \frac{E_2M}{E_2E_1} = \frac{E_2M}{d} \quad (5.2)$$

Therefore:

$$E_2M = d \sin \theta_1 \quad (5.3)$$

and

$$E_2N = d \sin \theta_2 \quad (5.4)$$

Hence, the total path difference equals  $2d \sin \theta$  which should be integral multiples of  $\lambda$ :

$$n\lambda = 2d \sin \theta \quad (5.5)$$

This is known as the Bragg equation.

#### *The powder diffractometer*

Originally powder-XRD was performed using the powder photographic method, where the whole diffraction pattern is recorded simultaneously on a photographic film. This method was tedious as the film had to be exposed to the X-ray beam for long times, and there were problems associated with developing the film [1]. This has been overcome by the powder diffractometer technique. The diffractometer has the advantage of higher resolution by recording small ranges of  $2\theta$  on an expanded scale. The diffraction pattern is scanned by a counter device (Geiger proportional or scintillation counter) or a solid

state semiconductor detector. The counter / detector registers the diffracted beam intensity in successive stages away from the direct beam [1].

The sample is mounted at the centre of a goniometer, and a motor rotates the goniometer and substrate by an angle of  $\theta$ , and the X-ray detector is coupled to move  $2\theta$  [1]. The signal is recorded by data logging software attached to the instrument. Each  $hkl$  (Miller indices) reflection recorded appears as a peak on the trace, with a height depending on the intensity of the diffracted beam. The range of  $2\theta$  values, scan speed and step size can be varied to achieve the desired resolution [1].  $2\theta$  angles corresponding to the peaks on the traces can be converted d-spacings using the Bragg equation (equation (5.5)) [3].

## 5.2. Results

### 5.2.1. XRD

#### 5.2.1.1. XRD of batch materials

XRD was performed on batch materials to assess phase purity. Fig. (5.3) shows an XRD trace of the 99.9995%  $\text{TeO}_2$  obtained from Alfa Aesar. It can be seen from this trace, that the  $\text{TeO}_2$  powder used in this study was phase pure, resulting in a match to JCPDS card number 78-1714:  $\text{TeO}_2$ , tetragonal, space group  $P4_32_12$ . Table (5.1) shows the ten most intense peaks with corresponding  $2\theta$  (observed and theoretical) and Miller indices.

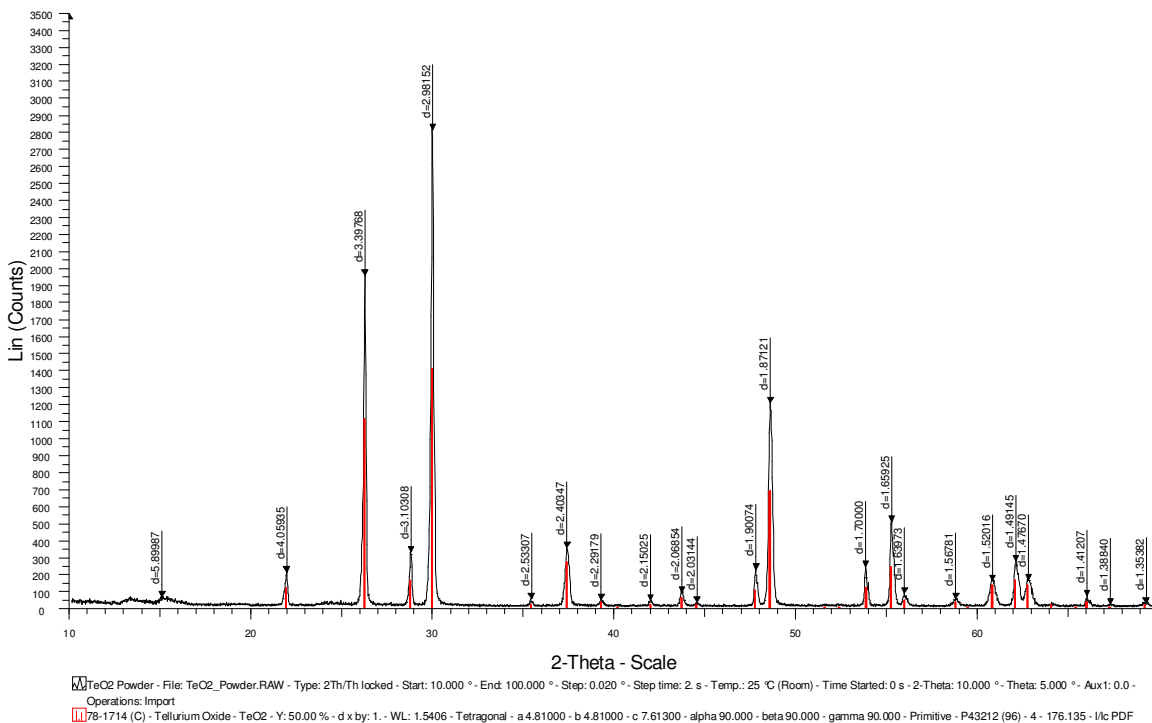


Fig. (5.3): XRD trace of 99.9995% TeO<sub>2</sub> powder, sourced from Alfa Aesar (— JCPDS card number 78-1714: TeO<sub>2</sub>, tetragonal, P4<sub>3</sub>2<sub>1</sub>2).

Table (5.1): Ten most intense peaks with corresponding  $2\theta$  (observed and theoretical) and Miller indices for 99.9995% TeO<sub>2</sub> powder, sourced from Alfa Aesar.

Observed $2\theta / ^\circ$	Observed intensity / %	Theoretical $2\theta / ^\circ$	Theoretical intensity / %	hkl	JCPDS Card
21.89281	7.3	21.85456	8	101	78-1714
26.22334	69.5	26.19589	79	110	"
28.76178	11.6	28.74014	11	111	"
29.95996	100.0	29.92528	100	102	"
37.38807	12.6	37.36348	19	200	"
47.76061	7.8	47.69421	7	004	"
48.55619	42.8	48.51403	49	212	"
53.76324	8.5	53.74333	8	220	"
55.17628	17.8	55.11794	17	114 / 221	"
61.90285	9.7	61.85775	11	204 / 311	"

Fig (5.4) shows an XRD trace of the 99.9995% ZnO powder sourced from Alfa Aesar.

Table (5.2) shows the ten most intense peaks with corresponding  $2\theta$  (observed and theoretical) and Miller indices.

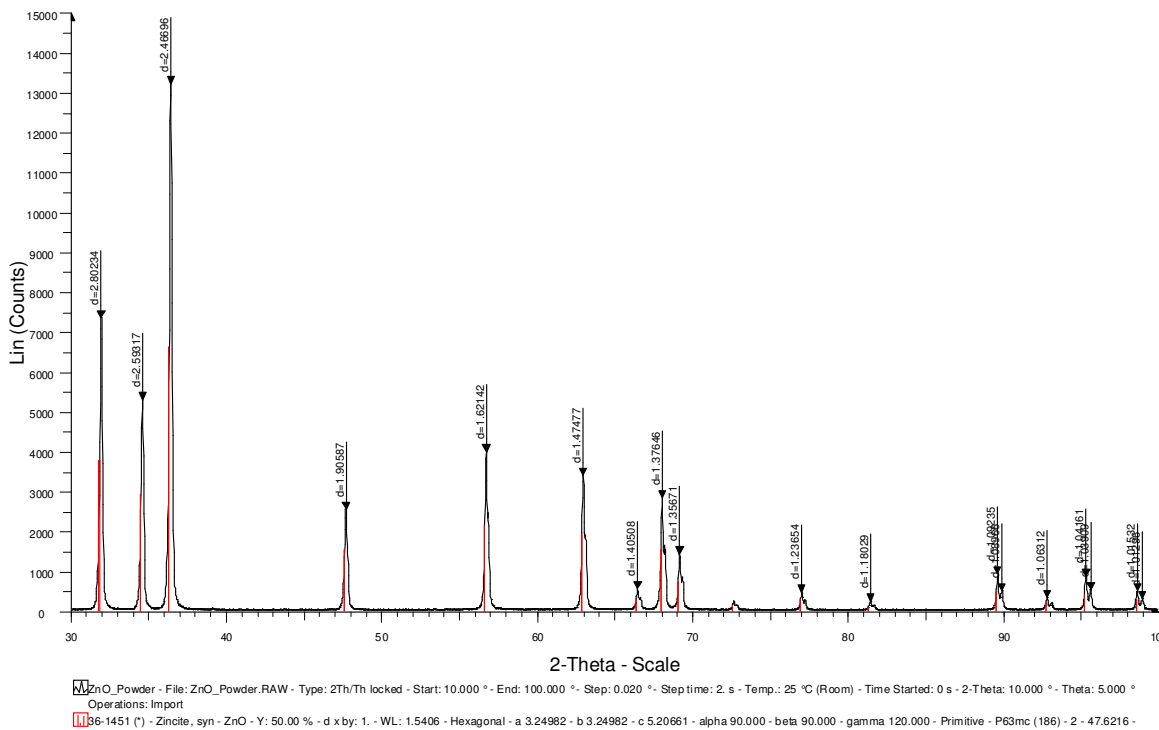


Fig. (5.4): XRD trace of 99.9995% ZnO powder, sourced from Alfa Aesar (— JCPDS card number 36-1451: ZnO, hexagonal, P<sub>63</sub>mc).

It can be seen from this trace, that the ZnO powder used in this study was phase pure, resulting in a match to JCPDS card number 36-1451: ZnO, hexagonal, space group P<sub>63</sub>mc.

Table (5.2): Ten most intense peaks with corresponding  $2\theta$  (observed and theoretical) and Miller indices for 99.9995% ZnO powder, sourced from Alfa Aesar.

Observed $2\theta / ^\circ$	Observed intensity / %	Theoretical $2\theta / ^\circ$	Theoretical intensity / %	hkl	JCPDS Card
31.92226	55.6	31.78322	57	100	36-1451
34.56988	40.0	34.43117	44	002	"
36.39434	100.0	36.25840	100	101	"
47.62511	19.3	47.48672	23	102	"
56.55821	30.2	56.43483	32	110	"
62.66531	25.7	62.55672	29	103	"
67.58624	21.3	67.49327	23	112	"
67.77897	11.8	-	-	-	-
68.67315	10.8	68.58710	11	201	36-1451
92.76702	6.6	92.69898	6	211	"

Fig (5.5) shows an XRD trace of the 99.997%  $\text{Na}_2\text{CO}_3$  powder sourced from Alfa Aesar.

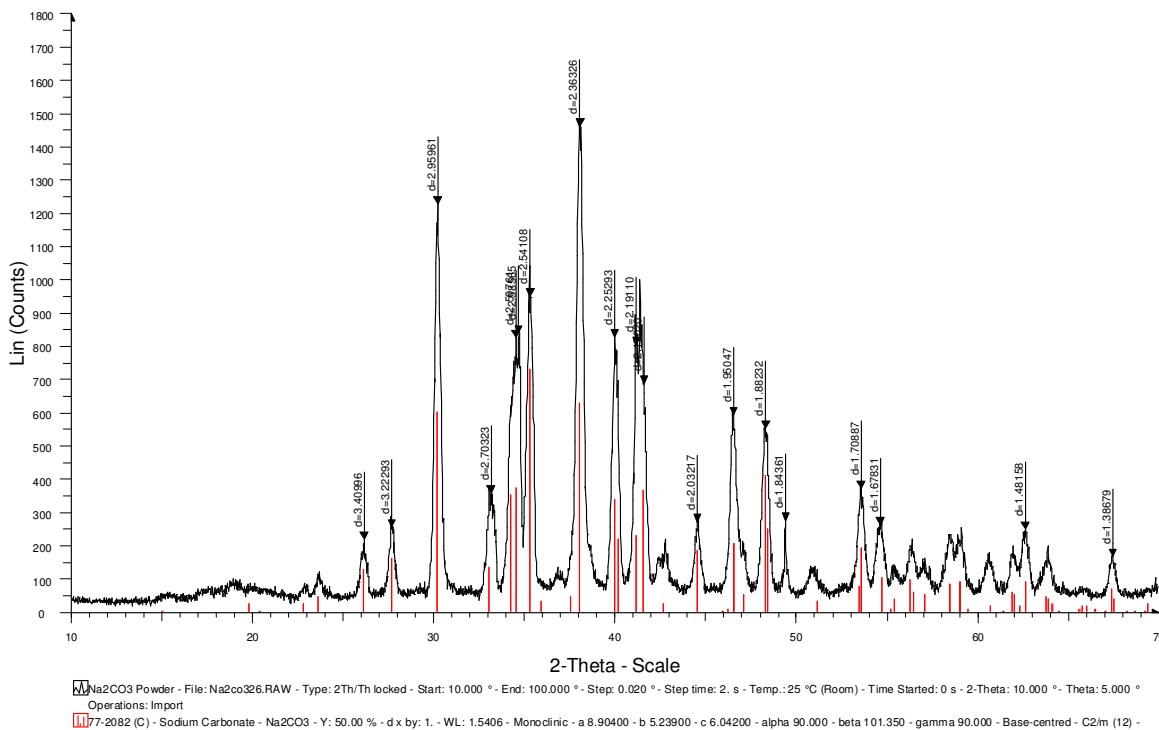


Fig. (5.5): XRD trace of 99.997%  $\text{Na}_2\text{CO}_3$  powder, sourced from Alfa Aesar (— JCPDS card number 77-2082:  $\text{Na}_2\text{CO}_3$ , monoclinic, C2/m).

It can be seen from this trace, that the  $\text{Na}_2\text{CO}_3$  powder used in this study was phase pure, resulting in a match to JCPDS card number 77-2082:  $\text{Na}_2\text{CO}_3$ , monoclinic, space group C2/m. Table (5.3) shows the ten most intense peaks with corresponding  $2\theta$  (observed and theoretical) and Miller indices.

Table (5.3): Ten most intense peaks with corresponding  $2\theta$  (observed and theoretical) and Miller indices for 99.997%  $\text{Na}_2\text{CO}_3$  powder, sourced from Alfa Aesar.

Observed $2\theta / ^\circ$	Observed intensity / %	Theoretical $2\theta / ^\circ$	Theoretical intensity / %	hkl	JCPDS Card
30.18673	84.1	30.16265	82	002	77-2082
34.22958	42.4	34.21237	48	020	"
34.50906	56.4	34.52329	51	$\bar{1}12$	"
34.67337	57.3	-	-	-	-
35.29993	65.0	35.25989	100	310	77-2082
38.04644	100.0	38.01481	86	112	"
39.98021	56.5	39.9697	46	202	"
41.15397	54.9	41.12349	31	$\bar{4}01$	"
41.37077	68.3	-	-	-	-
41.56676	46.9	41.48214	50	$\bar{2}21$	77-2082

Fig. (5.6) shows an XRD trace of the 99.995%  $\text{ZnF}_2$  sourced from Alfa Aesar [4]. It can be seen from this trace, that the  $\text{ZnF}_2$  powder used in this study was not phase pure, resulting in a matches to JCPDS card numbers - 74-1816:  $\text{Zn}(\text{OH})\text{F}$ , orthorhombic, and JCPDS card number 07-0214:  $\text{ZnF}_2$ , tetragonal, space group  $\text{P4}_2/\text{mm}$ . Table (5.4) shows the ten most intense peaks with corresponding  $2\theta$  (observed and theoretical), phases and Miller indices.

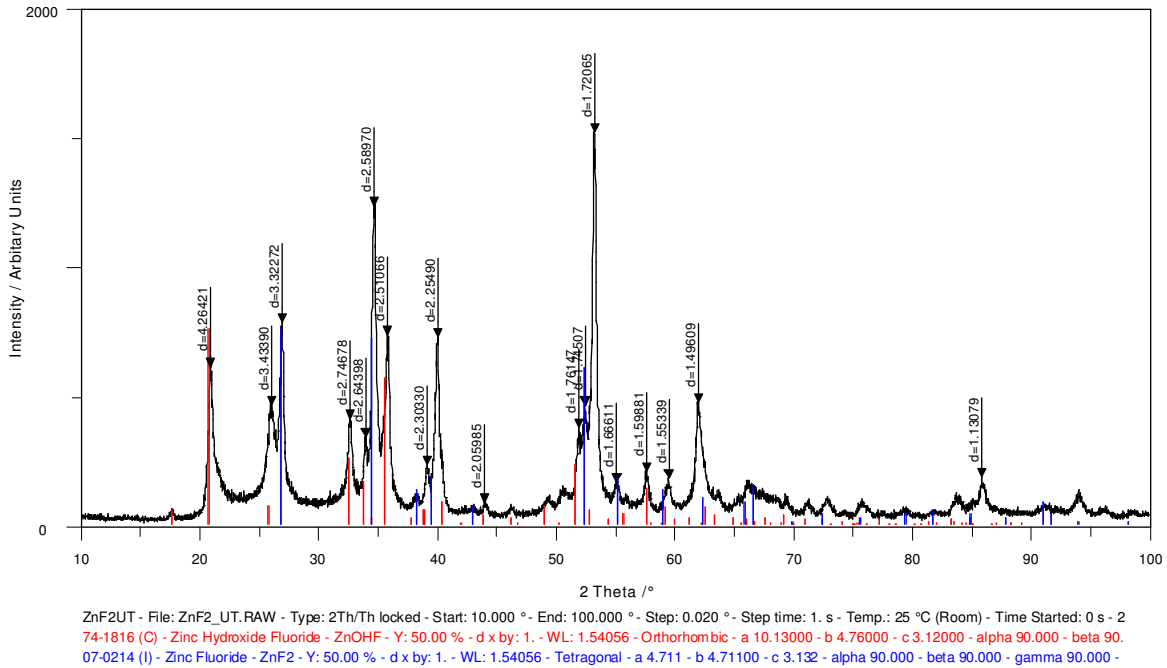


Fig. (5.6): XRD trace of 99.995%  $\text{ZnF}_2$  powder, sourced from Alfa Aesar (— JCPDS card number 74-1816:  $\text{Zn(OH)F}$ , orthorhombic; — JCPDS card number 07-0214:  $\text{ZnF}_2$ , tetragonal,  $P4_2/mnm$ ) [4].

Table (5.4): Ten most intense peaks with corresponding  $2\theta$  (observed and theoretical), phases and Miller indices for 99.995%  $\text{ZnF}_2$  powder, sourced from Alfa Aesar.

Observed $2\theta / ^\circ$	Observed intensity / %	Theoretical $2\theta / ^\circ$	Theoretical intensity / %	Phase	hkl	JCPDS Card
20.82932	40.3	20.61490	100	$\text{Zn(OH)F}$	100	74-1816
25.94209	30.5	25.67798	10	$\text{Zn(OH)F}$	210	"
26.82540	51.6	26.76571	100	$\text{ZnF}_2$	110	07-0214
32.58467	26.9	32.49605	34	$\text{Zn(OH)F}$	310	74-1816
34.61756	81.2	34.36759	95	$\text{ZnF}_2$	101	07-0214
35.74092	48.3	35.50382	75	$\text{Zn(OH)F}$	111	74-1816
39.94393	47.7	39.39781	25	$\text{ZnF}_2$	111	07-0214
52.28445	30.4	52.19120	80	$\text{ZnF}_2$	211	"
53.07517	100.0	52.62954	8	$\text{Zn(OH)F}$	420	74-1816
61.69414	31.3	61.96837	14	$\text{ZnF}_2$	310	07-0214

The presence of a hydroxide phase in the batch materials is problematic as it could lead to a significant amount of OH in the final glass. This would result in absorption bands in the

infrared, which must be avoided to produce low loss infrared transmitting optical fibre.

Fig. (5.7) shows the XRD trace of the 99.995%  $\text{ZnF}_2$  sourced from Alfa Aesar, after it had been treated by fluorination, as described in section 3.4 [4].

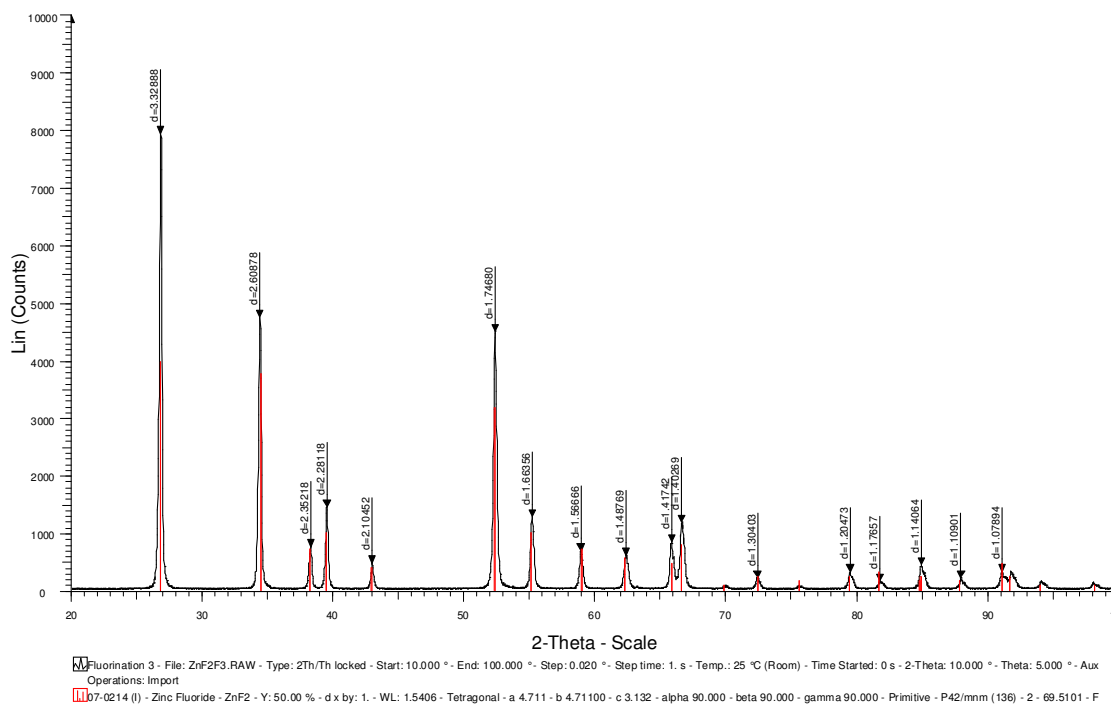


Fig. (5.7): XRD trace of 99.995%  $\text{ZnF}_2$  powder, sourced from Alfa Aesar (— JCPDS card number: 07-0214,  $\text{ZnF}_2$ , tetragonal,  $P4_2/mmm$ ) [4].

It can be seen that this treatment was highly effective, producing a phase pure powder, resulting in matches to JCPDS card number: 07-0214,  $\text{ZnF}_2$  tetragonal, space group  $P4_2/mmm$ . Table (5.5) shows the ten most intense peaks with corresponding  $2\theta$  (observed and theoretical) and Miller indices.

Table (5.5): Ten most intense peaks with corresponding  $2\theta$  (observed and theoretical) and Miller indices for 99.995%  $\text{ZnF}_2$  powder after fluorination, sourced from Alfa Aesar.

Observed $2\theta / ^\circ$	Observed intensity / %	Theoretical $2\theta / ^\circ$	Theoretical intensity / %	hkl	JCPDS Card
26.77487	100.0	26.76571	100	110	07-0214
34.35702	59.8	34.36759	95	101	"
38.23202	9.5	38.16783	18	200	"
39.46628	18.3	39.39781	25	111	"
52.22935	56.8	52.19120	80	211	"
55.02323	16.1	54.93697	25	220	"
58.68978	8.6	58.75698	18	002	"
62.07305	7.6	61.96837	14	310	"
65.44186	10.6	65.45300	12	112	"
66.19661	14.9	66.13394	20	301	"

### 5.2.1.2. XRD of deposits from glass melting and fluorination

#### *Fluorination*

During fluorination of  $\text{ZnF}_2$  (see section 3.4), HF,  $\text{H}_2\text{O}$ ,  $\text{NH}_3$  and possibly some  $\text{ZnF}_2$  were given off by the batch. The deposit left on the silica lid of the silica liner which contained the platinum crucible and batch in the glovebox was collected for analysis. Fig. (5.8) shows the XRD trace of this deposit. Two phases were clearly identified - JCPDS card number 74-0944 triammonium silicon fluoride  $(\text{NH}_4)_3\text{SiF}_6\text{F}$ , tetragonal, and JCPDS card number 35-0758 ammonium fluoride  $\text{NH}_4\text{F}$ , hexagonal, space group  $\text{P6}_3\text{mc}$ . Table (5.6) shows the ten most intense peaks with corresponding  $2\theta$  (observed and theoretical), phases and Miller indices.

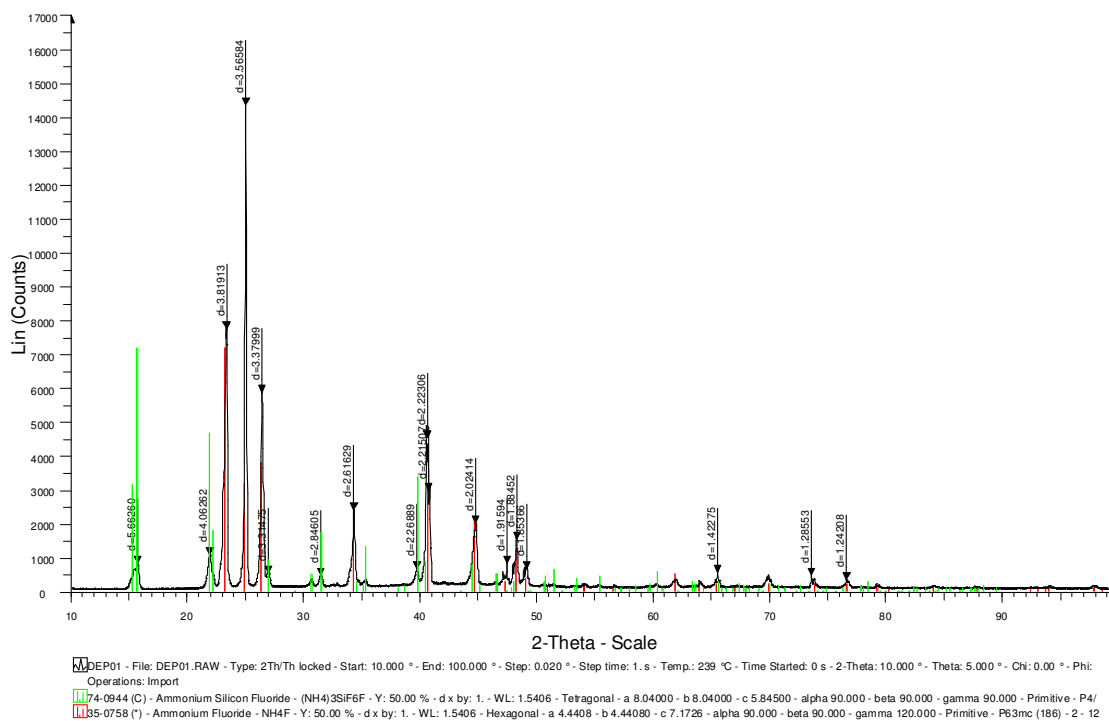


Fig. (5.8): Deposit from fluorination on silica liner lid in glovebox (— JCPDS card number 74-0944 (NH<sub>4</sub>)<sub>3</sub>SiF<sub>6</sub>F, tetragonal; — JCPDS card number 35-0758 NH<sub>4</sub>F, hexagonal, P6<sub>3</sub>mc).

Table (5.6): Ten most intense peaks with corresponding  $2\theta$  (observed and theoretical) and Miller indices for deposit from fluorination on silica liner lid in glovebox.

Observed $2\theta / ^\circ$	Observed intensity / %	Theoretical $2\theta / ^\circ$	Theoretical intensity / %	Phase	hkl	JCPDS Card
15.64860	5.7	15.58618	100	(NH <sub>4</sub> ) <sub>3</sub> SiF <sub>6</sub> F	110	74-0944
21.87498	7.5	21.80589	65	(NH <sub>4</sub> ) <sub>3</sub> SiF <sub>6</sub> F	111	"
23.28796	54.0	23.11875	100	NH <sub>4</sub> F	100	35-0758
24.96701	100.0	24.81206	44	NH <sub>4</sub> F	002	"
26.36295	40.8	26.27801	53	NH <sub>4</sub> F	101	"
34.25556	16.7	34.16474	22	NH <sub>4</sub> F	102	"
40.53863	31.6	40.56329	42	NH <sub>4</sub> F	110	"
40.69070	20.6	40.40954	12	(NH <sub>4</sub> ) <sub>3</sub> SiF <sub>6</sub> F	320	74-0944
44.70528	14.0	44.57491	30	NH <sub>4</sub> F	103	35-0758
48.19427	10.7	48.11534	17	NH <sub>4</sub> F	112	"

### Glass melting

During glass melting the melt volatilised, particularly for the fluorotellurite melts, due to the presence of volatile fluoride compounds. The deposit left on the silica liner and lid was collected after melting glass MOF005 (70TeO<sub>2</sub>-10Na<sub>2</sub>O-20ZnF<sub>2</sub>, mol. %) for 12 hours at 800°C in the glovebox under nitrogen. Fig. (5.9) shows the XRD trace of this deposit.

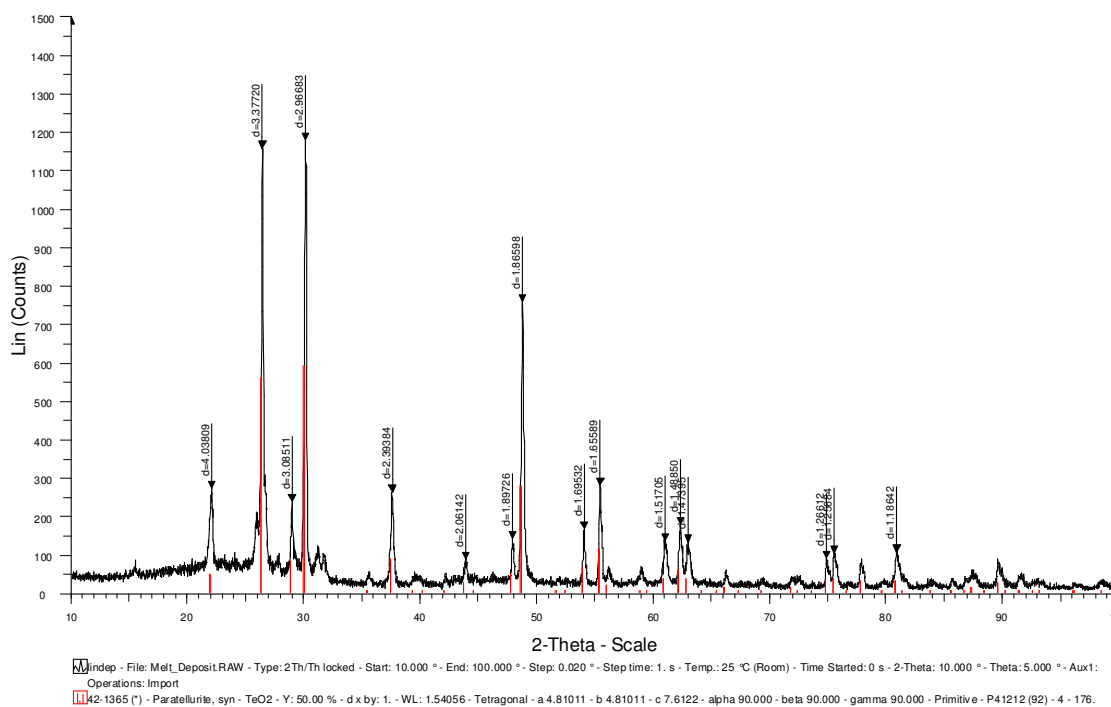


Fig (5.9): XRD trace of deposit left on the silica liner and lid after melting glass MOF005 (70TeO<sub>2</sub>-10Na<sub>2</sub>O-20ZnF<sub>2</sub>, mol. %) for 12 hours at 800°C in glovebox under nitrogen (— JCPDS card number 42-1365: TeO<sub>2</sub>, tetragonal, P4<sub>1</sub>2<sub>1</sub>2).

The deposit was identified using JCPDS card number 42-1365: TeO<sub>2</sub>, tetragonal, space group P4<sub>1</sub>2<sub>1</sub>2. Table (5.7) shows the ten most intense peaks with corresponding 2θ (observed and theoretical) and Miller indices.

Table (5.7): Ten most intense peaks with corresponding  $2\theta$  (observed and theoretical) and Miller indices for deposit left on the silica liner and lid after melting glass MOF005 (70TeO<sub>2</sub>-10Na<sub>2</sub>O-20ZnF<sub>2</sub>, mol. %) for 12 hours at 800°C in glovebox.

Observed $2\theta / ^\circ$	Observed intensity / %	Theoretical $2\theta / ^\circ$	Theoretical intensity / %	hkl	JCPDS Card
22.00947	23.0	21.86131	8	101	42-1365
25.90481	17.8	-	-	-	-
26.38511	98.1	26.20208	95	110	42-1365
26.67667	22.3	-	-	-	-
28.93278	20.1	28.75441	14	111	42-1365
30.11162	100.0	29.94866	100	102	"
37.54363	22.2	37.36155	15	200	"
48.69993	64.3	48.52443	47	212	"
55.29621	23.7	55.12931	19	114 / 221	"
62.03630	15.1	61.85459	10	204 / 311	"

### 5.2.1.3. XRD of glasses which crystallised during processing or characterisation

#### *During melting*

A batch of glass MOF001 (65TeO<sub>2</sub>-10Na<sub>2</sub>O-25ZnF<sub>2</sub>, mol. %) was melted in the fume cupboard, with fluorinating agent (see section 3.4) added to dry the batch further (1 g of (NH<sub>4</sub>)HF<sub>2</sub> to 1 g of batch). However, after melting a 10g batch for 5 hours in a platinum crucible at 800°C, and dropping to 700°C to cast, most of the melt had volatilised, leaving behind around 5g of a white solid deposit in the crucible. Fig. (5.10) shows the XRD trace of this deposit. It can be seen from this trace, that a glass-ceramic has resulted from this treatment. An amorphous 'halo' can be seen at around 30°  $2\theta$ , and the presence of crystalline material. The closest match to the crystalline peaks was JCPDS card number: 20-1182: sodium zinc fluoride NaZnF<sub>3</sub>, orthorhombic, space group Pbnm. Table

(5.8) shows the ten most intense peaks with corresponding  $2\theta$  (observed and theoretical), Miller indices were not available.

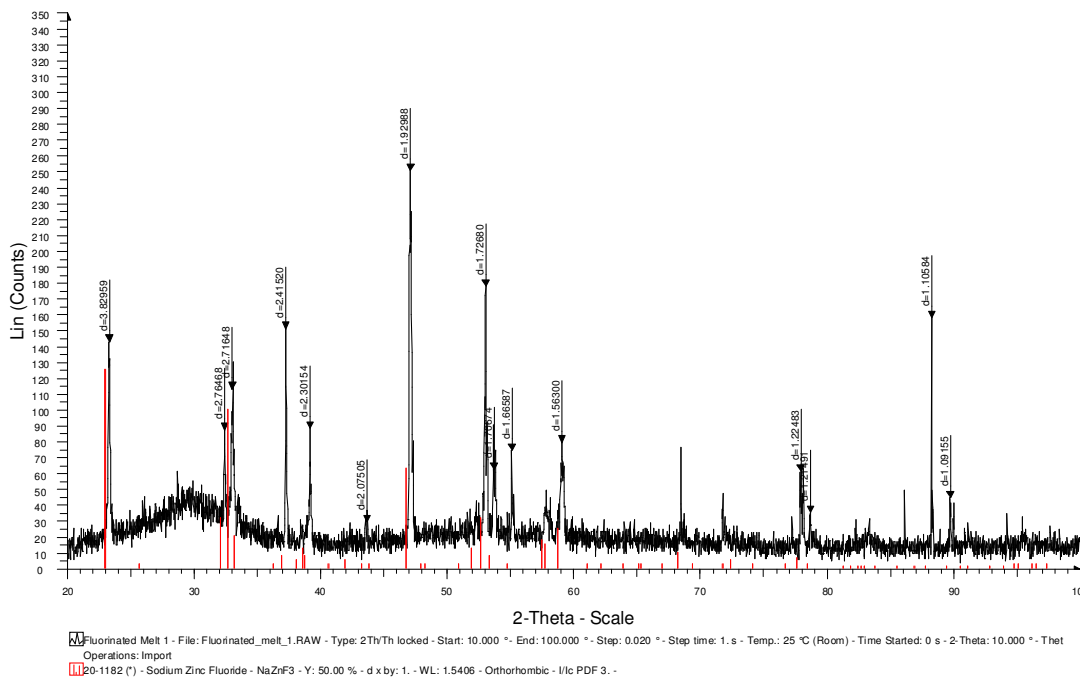


Fig. (5.10): Deposit which resulted from melting a 10g batch of glass MOF001 (65TeO<sub>2</sub>-10Na<sub>2</sub>O-25ZnF<sub>2</sub>, mol. %) for 5 hours in a platinum crucible at 800°C, and dropping to 700°C to cast, with fluorinating agent added (— JCPDS card number 20-1182: NaZnF<sub>3</sub>, orthorhombic, Pbnm).

Table (5.8): Ten most intense peaks with corresponding  $2\theta$  (observed and theoretical), Miller indices not available for JCPDS card number: 20-1182: NaZnF<sub>3</sub>. Deposit which resulted from melting a 10g batch of glass MOF001 (65TeO<sub>2</sub>-10Na<sub>2</sub>O-25ZnF<sub>2</sub>, mol. %) for 5 hours in a platinum crucible at 800°C, and dropping to 700°C to cast, with fluorinating agent added.

Observed $2\theta / ^\circ$	Observed intensity / %	Theoretical $2\theta / ^\circ$	Theoretical intensity / %	JCPDS Card
23.22349	57.0	22.88104	100	20-1182
32.36824	34.7	32.04241	25	"
32.95778	45.0	32.58016	80	"
37.20035	60.2	36.86213	6	"
39.10413	35.1	38.47392	10	"
47.00123	100.0	46.64207	50	"
52.87373	70.9	52.46974	25	"
58.83817	31.5	58.50879	20	"
67.95478	30.3	67.69251	8	"
86.51300	62.9	86.08170	1	"

Although the XRD trace and JCPDS card 20-1182 do not provide a perfect match, this was the closest fit. Miller indices were not available for this compound ( $\text{NaZnF}_3$ ).

### *During characterisation*

Whilst performing viscosity measurements in the TMA (see chapter 8), glass MOF005 ( $70\text{TeO}_2\text{-}10\text{Na}_2\text{O}\text{-}20\text{ZnF}_2$ , mol. %) crystallised at  $400^\circ\text{C}$ , at a heating rate of  $10^\circ\text{C}\cdot\text{min}^{-1}$ , under a helium atmosphere, with an applied load of 250 mN. Fig. (5.11) shows the XRD trace of this sample.

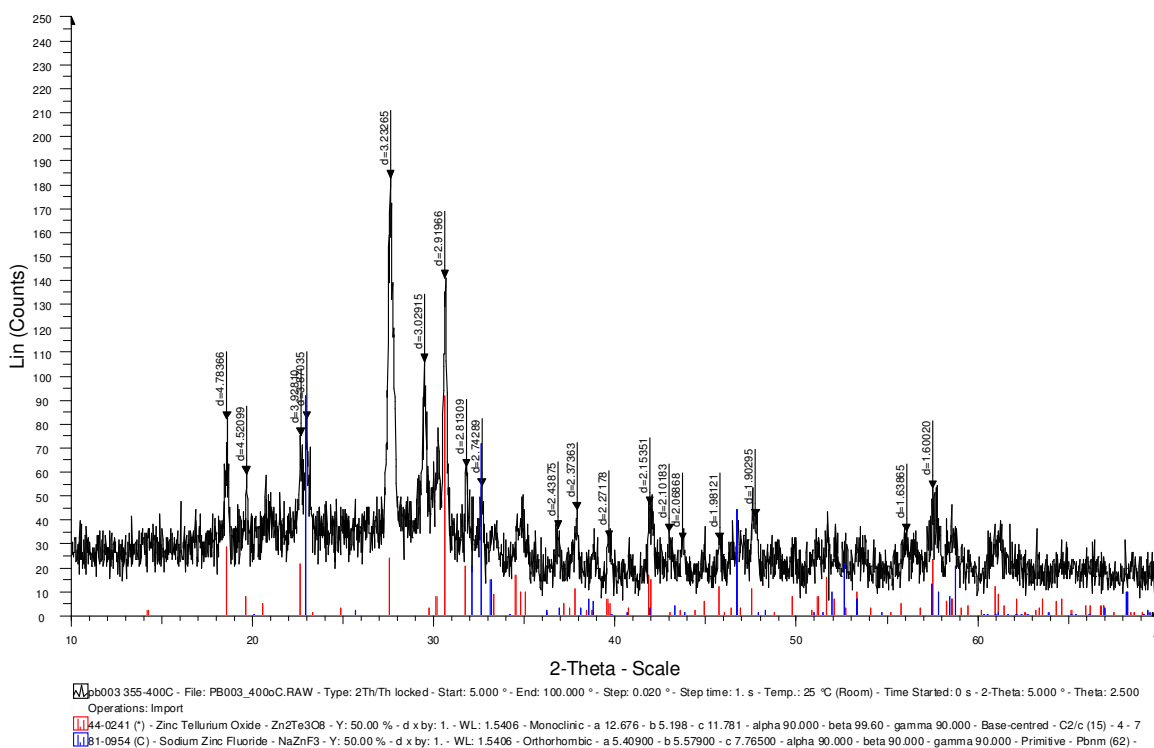


Fig. (5.11): XRD trace of glass MOF005 ( $70\text{TeO}_2\text{-}10\text{Na}_2\text{O}\text{-}20\text{ZnF}_2$ , mol. %) which crystallised at  $400^\circ\text{C}$  in TMA (— JCPDS card number 44-0241,  $\text{Zn}_2\text{Te}_3\text{O}_8$ , monoclinic, C2/c; — JCPDS card number 81-0954,  $\text{NaZnF}_3$ , orthorhombic, Pbnm).

Despite the presence of a noisy background signal, probably due to an amorphous component to the sample, peaks were matched to: JCPDS card number 44-0241, dizinc tritellurium oxide  $\text{Zn}_2\text{Te}_3\text{O}_8$ , monoclinic, space group  $C2/c$ ; and 81-0954, sodium zinc fluoride  $\text{NaZnF}_3$ , orthorhombic, space group  $Pbnm$ . Table (5.9) shows the ten most intense peaks with corresponding  $2\theta$  (observed and theoretical), phases and Miller indices.

Table (5.9): Ten most intense peaks with corresponding  $2\theta$  (observed and theoretical) and Miller indices for glass MOF005 ( $70\text{TeO}_2$ - $10\text{Na}_2\text{O}$ - $20\text{ZnF}_2$ , mol. %) which crystallised at  $400^\circ\text{C}$  in TMA, at a heating rate of  $10^\circ\text{C}.\text{min}^{-1}$ , under a helium atmosphere, with an applied load of 250 mN..

Observed $2\theta/^\circ$	Observed intensity / %	Theoretical $2\theta/^\circ$	Theoretical intensity / %	Phase	hkl	JCPDS Card
18.54678	44.8	18.50869	31	$\text{Zn}_2\text{Te}_3\text{O}_8$	110	44-0241
19.63449	32.2	19.56929	8	$\text{Zn}_2\text{Te}_3\text{O}_8$	$11\bar{1}$	"
22.63353	41.0	22.58055	23	$\text{Zn}_2\text{Te}_3\text{O}_8$	202	"
22.97567	44.8	22.89715	100	$\text{NaZnF}_3$	110 / 002	81-0954
27.58675	100.0	27.52083	26	$\text{Zn}_2\text{Te}_3\text{O}_8$	$31\bar{1}$	44-0241
29.47867	57.9	29.70982	3	$\text{Zn}_2\text{Te}_3\text{O}_8$	$31\bar{2}$	"
30.60927	77.0	30.56920	100	$\text{Zn}_2\text{Te}_3\text{O}_8$	113	"
31.79723	33.9	31.72810	22	$\text{Zn}_2\text{Te}_3\text{O}_8$	$20\bar{4}$	"
32.63209	29.5	32.59806	78	$\text{NaZnF}_3$	112	81-0954
57.36503	29.0	57.34960	25	$\text{Zn}_2\text{Te}_3\text{O}_8$	$42\bar{5}$	44-0241

#### 5.2.1.4. Heat treated $\text{Er}^{+3}$ -doped compositions

Glass MOF017 ( $69.86\text{TeO}_2$ - $9.98\text{Na}_2\text{O}$ - $19.96\text{ZnF}_2$ - $0.2\text{ErF}_3$  mol. %) was heat treated to attempt to grow  $\text{Er}^{+3}$ -rich nano-crystals. Fig. (5.12) shows an XRD trace of the glass before any heat treatment.

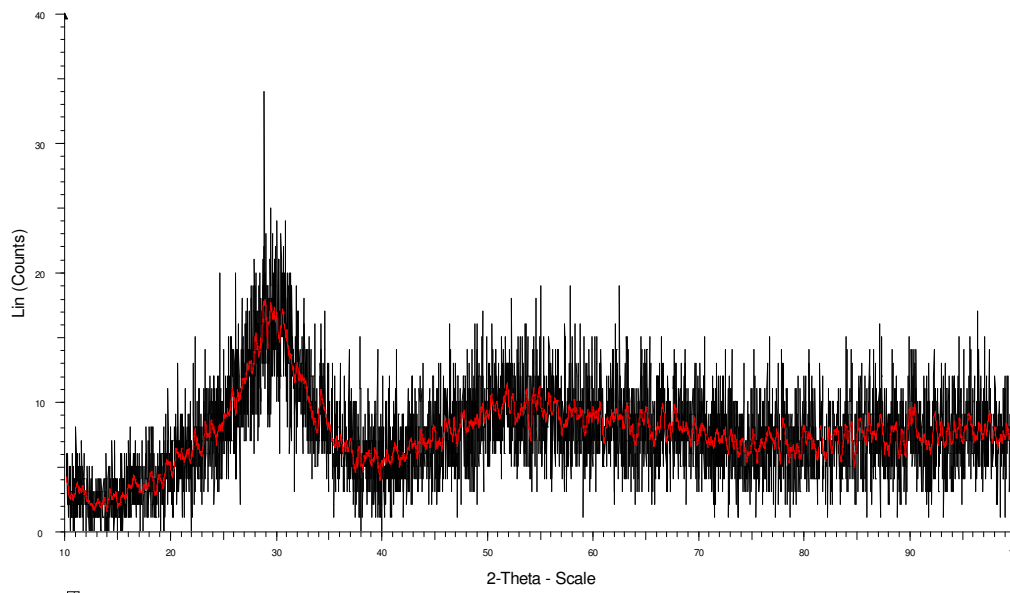


Fig. (5.12): XRD trace of glass MOF017 (69.86TeO<sub>2</sub>-9.98Na<sub>2</sub>O-19.96ZnF<sub>2</sub>-0.2ErF<sub>3</sub> mol. %) before heat treatment.

This trace shows the characteristic amorphous halo for a glassy material. Fig. (5.13) shows an XRD trace of the glass after a 1 hr. heat treatment at 275°C. The sample was completely opaque.

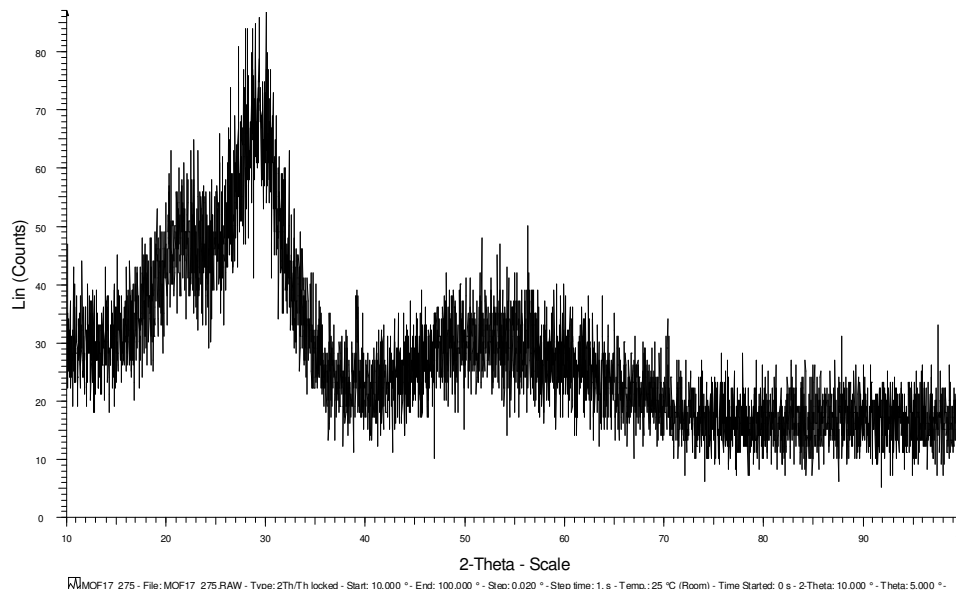


Fig. (5.13): XRD trace of glass MOF017 (69.86TeO<sub>2</sub>-9.98Na<sub>2</sub>O-19.96ZnF<sub>2</sub>-0.2ErF<sub>3</sub> mol. %) after heat treatment for 1 hr. at 275°C.

The trace does not contain any clearly discernable crystalline peaks. However the amorphous halo is higher in intensity, and has developed a shoulder of lower intensity at around  $23^\circ 2\theta$ .

## 5.3. Discussion

### 5.3.1. XRD

#### 5.3.1.1. XRD of batch materials

##### *TeO<sub>2</sub>*

Fig. (5.3) shows an XRD trace of the TeO<sub>2</sub> used in this study, sourced from Alfa Aesar. The powder was shown to be phase pure ( $\alpha$ -TeO<sub>2</sub>, tetragonal, space group P4<sub>3</sub>2<sub>1</sub>2), in accordance with the stated high grade (Puratronic, 99.9995%).  $\alpha$ -TeO<sub>2</sub> or paratellurite, consists of a tellurium atom four coordinated to oxygen, with the tellurium lone pair of electrons occupying the oxygen free corner of the trigonal bipyramid (tbp). Chapter 2 discusses the structures of TeO<sub>2</sub> in more detail.

##### *ZnO*

Fig. (5.4) shows an XRD trace of the ZnO powder used in this study, sourced from Alfa Aesar. Again, the powder was shown to be phase pure as suggested by the stated grade

(Puratronic, 99.9995%). The crystal structure is hexagonal, space group  $P6_3mc$ , analogous to wurtzite ( $ZnS$ ). Oxygen anions are hexagonally close packed (hcp) with alternate tetrahedral voids filled with zinc cations [1]. Both zinc and oxygen are four coordinated to one another, therefore the structure can be thought of as interpenetrating hcp sublattices of Zn and O [1].

### *Na<sub>2</sub>CO<sub>3</sub>*

Fig. (5.5) shows an XRD trace of the  $Na_2CO_3$  powder used in this study sourced from Alfa Aesar (Puratronic, 99.997%). There was relatively high background noise on the XRD trace, most likely due to the low atomic weight of the atoms in the powder (Na, C and O,  $Z = 11, 6$  and  $8$  respectively). This will result in less scattering of the incident X-rays compared to heavier compounds (e.g.  $TeO_2$  and  $ZnF_2$ ), and hence less X-ray counts at the detector for the hkl reflections of the  $NaCO_3$  crystals. However, the pattern matched that of pure  $Na_2CO_3$ , crystal structure monoclinic, space group  $C2/m$ .  $Na_2CO_3$  decomposes in the glass melt to  $Na_2O$ , therefore, the crystal structure of the carbonate is unrelated to the final state of the oxide in the glass.

### *As-received ZnF<sub>2</sub>*

Fig. (5.6) shows an XRD trace of the  $ZnF_2$  powder used in this study, sourced from Alfa Aesar. Although the quoted purity was high (Puratronic, 99.995%) there was a significant

amount of  $\text{Zn(OH)F}$ , an orthorhombic phase, present (fig. (5.6)) [4]. Only cationic impurities were quoted on the assay sheet, therefore anionic impurities such as  $\text{OH}^-$  were not included by Alfa Aesar for calculating purity.  $\text{OH}^-$  can readily substitute for  $\text{F}^-$  in many inorganic compounds and minerals, due to their similar ionic radius and electronegativity. There was some tetragonal  $\text{ZnF}_2$  present (space group  $\text{P4}_2/\text{mnm}$ ) in the powder which was identified on the trace.

#### *Fluorinated $\text{ZnF}_2$*

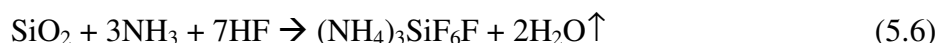
The XRD trace of the purified  $\text{ZnF}_2$  powder (fig. (5.7)), shows that the fluorination process was highly effective, removing a high proportion of the hydroxide phase from the batch [4] (see X-ray photoelectron spectroscopy (XPS) spectra in chapter 7 for quantification). The tetragonal phase  $\text{ZnF}_2$  (space group  $\text{P4}_2/\text{mnm}$ ) has an analogous structure to rutile ( $\text{TiO}_2$ ). The zinc cations sit in octahedral holes, between the fluorine anions. Each zinc ion is surrounded by six fluorine ions, with each fluorine surrounded by three zinc ions [1].

#### **5.3.1.2. XRD of deposits from melting and fluorination**

##### *Fluorination*

Fig. (5.8) shows an XRD trace of the deposit left from fluorination of  $\text{ZnF}_2$  with  $(\text{NH}_4)\text{HF}_2$ , on the silica liner lid in glovebox. Two crystalline phases can clearly be

identified: tetragonal triammonium silicon fluoride  $(\text{NH}_4)_3\text{SiF}_6\text{F}$  and hexagonal ammonium fluoride  $\text{NH}_4\text{F}$  (space group  $\text{P6}_3\text{mc}$ , analogous to  $\text{ZnO}$ ). It is probable that the by-products of the fluorination reaction (see section 3.4),  $\text{NH}_3$  and  $\text{HF}$ , reacted with the underside of the silica lid of the melting liner, to form the crystalline phase:  $(\text{NH}_4)_3\text{SiF}_6\text{F}$ . A likely chemical reaction proposed by this author is given by equation (5.6).



If this reaction occurs during fluorination (and possibly melting),  $\text{SiO}_2$  containment therefore produces water, which could be reintroduced into the batch material / melt, due to the vapour pressure of  $\text{H}_2\text{O}$  generated inside the liner as the  $\text{SiO}_2$  degrades. Therefore, complete OH removal from batch / melt may not be possible using silica containment. The  $\text{NH}_4\text{F}$  deposited on the silica lid was probably formed by the recombination of the  $\text{HF}$  and  $\text{NH}_3$  volatiles from the batch, as shown by equation (5.7).



Further addition of  $\text{HF}$  and  $\text{NH}_3$  to the  $\text{NH}_4\text{F}$  already deposited in the silica lid, could cause a subsequent reaction to form  $(\text{NH}_4)_3\text{SiF}_6\text{F}$  as shown by equation (5.8).



Ammonium fluoride could therefore be an intermediate product, which attacks the liner producing triammonium silicon fluoride.

### *Melting*

Fig. (5.9) shows an XRD trace of the deposit left on the silica liner and lid after melting glass MOF005 (70TeO<sub>2</sub>-10Na<sub>2</sub>O-20ZnF<sub>2</sub>, mol. %) for 12 hours at 800°C in the glovebox. The material can be clearly identified as tetragonal TeO<sub>2</sub> (space group P4<sub>1</sub>2<sub>1</sub>2), or α-TeO<sub>2</sub>. It was expected that any volatilisation and deposit left on the silica containment would be a fluoride compound, such as ZnF<sub>2</sub> (melting point = 872°C and boiling point = 1500°C [5]), due to the marked difference in volatilisation between oxide tellurite and fluorotellurite glasses (see tables (3.5) and (3.6)). However, TeO<sub>2</sub> has slightly lower melting and boiling points (733 and 1245°C respectively [5]) than ZnF<sub>2</sub>, and may react in the melt (e.g. TeO<sub>2</sub> + 3ZnF<sub>2</sub> → TeF<sub>4</sub>↑ + 2ZnO) forming more volatile fluoride compounds such as TeF<sub>6</sub> and TeF<sub>4</sub> (which sublime at -39 and 194°C respectively, with the latter forming TeF<sub>6</sub> on sublimation [5]). The gaseous fluoride would then most likely react with oxygen in the liner atmosphere and deposit as TeO<sub>2</sub> on the silica (e.g. TeF<sub>4</sub> + O<sub>2</sub> → TeO<sub>2</sub> + 2F<sub>2</sub>↑).

### 5.3.1.3. XRD of glasses which crystallised during processing or characterisation

#### *During melting*

Fig. (5.10) shows an XRD trace of the deposit which resulted from melting a 10g batch of glass MOF001 (65TeO<sub>2</sub>-10Na<sub>2</sub>O-25ZnF<sub>2</sub>, mol. %) in the laboratory atmosphere for 5 hours in a platinum crucible at 800°C, and dropping to 700°C to cast, with fluorinating agent (NH<sub>4</sub>HF<sub>2</sub>) added (see fig (3.2) for set-up). Most of the melt had volatilised, leaving behind around 5g of a white solid deposit. This deposit was identified by means of XRD (fig. (5.10)) as orthorhombic NaZnF<sub>3</sub> (space group Pbnm). An amorphous halo can also be seen on the trace. Any TeO<sub>2</sub> left is likely to be found within the glassy fraction of the sample, as TeO<sub>2</sub> glasses can be formed with the addition of a few mol. % of a second oxide or halide component [6]. As the fluorinating agent ((NH<sub>4</sub>)HF<sub>2</sub>) broke down into NH<sub>3</sub> and HF, it has reacted with the batch, and some of the products of this reaction volatilised. The fluorinating agent could have promoted the formation of the volatile tellurium fluoride compounds (TeF<sub>4</sub> and TeF<sub>6</sub>) discussed in section 5.3.1.2.. Another possibility is that the reactions due to the decomposition of (NH<sub>4</sub>)HF<sub>2</sub>, and between the batch and (NH<sub>4</sub>)HF<sub>2</sub> were sufficiently exothermic, in addition to the melt temperature, to result in the volatilisation of components from the batch which are normally relatively stable at 800°C, such as TeO<sub>2</sub> which boils at 1245°C [5]. This would have changed the chemistry of the batch, and destabilised the composition, increasing the likelihood of crystallisation. Therefore, adding (NH<sub>4</sub>)HF<sub>2</sub> directly to the glass batch was not pursued further, as treating the ZnF<sub>2</sub> directly before melting appeared to result in effective drying.

*During characterisation*

Fig. (5.11) shows an XRD trace of glass MOF005 (70TeO<sub>2</sub>-10Na<sub>2</sub>O-20ZnF<sub>2</sub>, mol. %) which crystallised at 400°C in the TMA instrument whilst performing viscosity measurements. The phases identified by XRD (fig. (5.11)) were monoclinic Zn<sub>2</sub>Te<sub>3</sub>O<sub>8</sub> (space group C2/c) and orthorhombic NaZnF<sub>3</sub> (space group Pbnm) [4]. Fig. (5.14) shows the Gaussian deconvolution of the crystallisation peak from DTA of this glass composition. The peak is clearly asymmetric with a high temperature shoulder. Two crystallisation peaks can be resolved from this trace with maximums at:  $x_1 = 410^\circ\text{C}$  and  $x_2 = 421^\circ\text{C}$ . At 400°C the first crystallisation event ( $x_1$ ) is near its maximum and a second phase ( $x_2$ ) has also clearly begun to form. Therefore, it would be reasonable to assign the crystalline phases Zn<sub>2</sub>Te<sub>3</sub>O<sub>8</sub> and NaZnF<sub>3</sub> to these peaks. EDX analysis from optical fibre which was pulled at around 300°C of this composition showed crystals present around 1 to 2 μm in diameter (see chapter 8). These crystals were fluorine and sodium rich, and oxygen and tellurium deficient, suggesting the first crystalline product above  $T_g$  to be NaZnF<sub>3</sub>. Therefore, the DTA peak at 410°C is likely to be NaZnF<sub>3</sub> crystallising, and the peak at 421°C due to the formation of Zn<sub>2</sub>Te<sub>3</sub>O<sub>8</sub>. As the glass is quenched from the melt, oxide nuclei may form, providing homogeneous nucleation sites for the fluoride phase to form on heating. Fig. (5.14) illustrates these temperatures, with a dashed line at 400°C where the glass crystallised in the TMA [4].

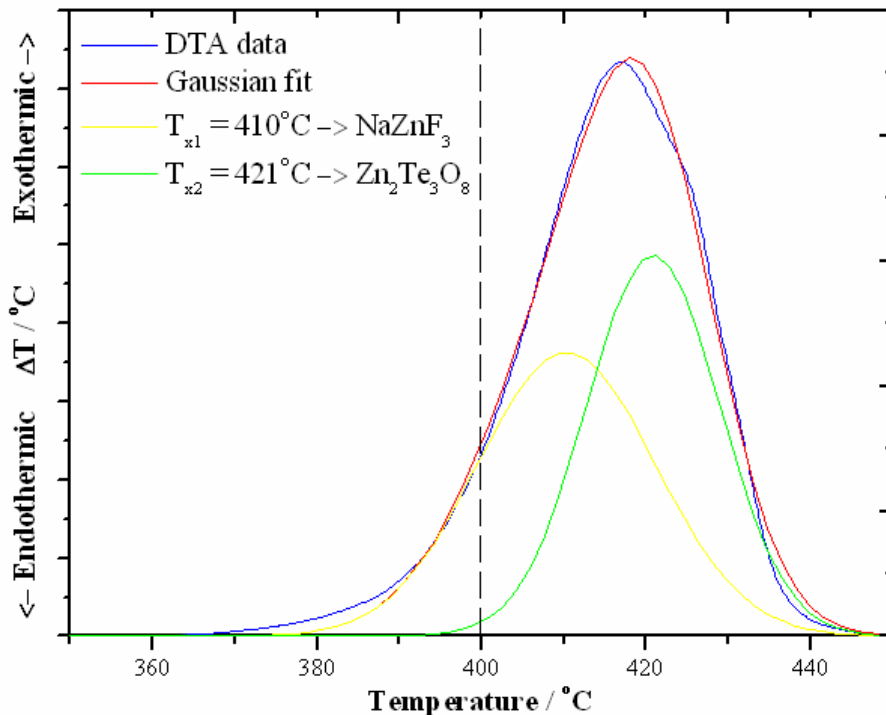


Fig. (5.14): DTA trace of glass MOF005 (70TeO<sub>2</sub>-10Na<sub>2</sub>O-20ZnF<sub>2</sub> (mol. %)), showing crystallisation peaks with background removed and Gaussian deconvolution [4].

Nukui *et al.* [7] have shown that glasses in the binary system TeO<sub>2</sub>-ZnO devitrify into two phases: ZnTeO<sub>3</sub> and Zn<sub>2</sub>Te<sub>3</sub>O<sub>8</sub>. For low ZnO compositions (10 mol. %), ZnTeO<sub>3</sub> forms at a lower temperatures ( $\approx 380^{\circ}\text{C}$ ) than Zn<sub>2</sub>Te<sub>3</sub>O<sub>8</sub> ( $\approx 480^{\circ}\text{C}$ ). As the ZnO content in the glass is increased to 30 mol. %, the Zn<sub>2</sub>Te<sub>3</sub>O<sub>8</sub> phase field opens up, and the phase crystallises from around  $440^{\circ}\text{C}$  (i.e. from a lower temperature). The ZnTeO<sub>3</sub> phase field remains approximately the same size, but moves to higher temperatures [7]. For the ternary glass system used in this study, TeO<sub>2</sub>-Na<sub>2</sub>O-ZnF<sub>2</sub>, the addition of fluorine and sodium to the composition lower the initial temperature of crystallisation for the Zn<sub>2</sub>Te<sub>3</sub>O<sub>8</sub> phase further, and no ZnTeO<sub>3</sub> was seen in the sample which crystallised at  $400^{\circ}\text{C}$ . This phase may be stable at a higher temperature, or the fluoride phase (NaZnF<sub>3</sub>) is more stable and crystallises in preference.

#### 5.3.1.4. Heat treated Er<sup>+3</sup>-doped compositions

Fig. (5.12) and (5.13) show XRD traces of glass MOF017 (69.86TeO<sub>2</sub>-9.98Na<sub>2</sub>O-19.96ZnF<sub>2</sub>-0.2ErF<sub>3</sub> mol. %) before and after a heat treatment for 1 hr. at 275°C respectively. Although the heat treated sample was opaque, no distinct crystalline phase was identified by XRD, indicating either liquid / liquid phase separation, which could result in opacity and lack of crystallites shown by fig. (5.13), or that the crystals are too small to be resolved by the diffractometer, but still contribute to scattering. As crystal size decreases, Debye diffraction rings, and hence peaks broaden [8]. If crystal size is sufficiently small (of the order of nm), peaks can become indistinguishable from the amorphous halo. The untreated glass exhibits the characteristic halo at around 30° 2θ, with a lower intensity broader halo centered at around 55° 2θ. After the heat treatment the main halos shape has developed a lower angle shoulder at around 23° 2θ and there is possibly a peak developing at around 40° 2θ. Kukkonen [9] and Beggiora [10] *et al.* studied the crystallisation of SiO<sub>2</sub>-Al<sub>2</sub>O<sub>3</sub>-CdF<sub>2</sub>-PbF<sub>2</sub>-ZnF<sub>2</sub>-YF<sub>3</sub>-ErF<sub>3</sub> glass-ceramics. Erbium (III) was found to preferentially partition to PbF<sub>x</sub> nano-crystals. Crystalline peaks appeared from the amorphous halo of the untreated glass with increasing time and temperature. In the TeO<sub>2</sub>-Na<sub>2</sub>O-ZnF<sub>2</sub>-ErF<sub>3</sub> system, Er<sup>+3</sup> could preferentially partition to one of the phases, possibly the lower temperature fluoride phase (NaZnF<sub>3</sub>).

## 5.4. Summary

Fluoride batch materials ( $\text{ZnF}_2$ ) were shown by XRD to be significantly 'wet' in the form of  $\text{Zn}(\text{OH})\text{F}$ . This as-received powder was treated with a fluorinating agent,  $(\text{NH}_4)\text{HF}_2$ , resulting in increased purity (confirmed by XRD and XPS) [4]. Addition of this fluorinating agent directly to the batch of a fluorotellurite melt caused  $\approx 50$  wt. % volatilisation, and therefore was not pursued further. The fluorination of the precursors resulted in volatiles ( $\text{NH}_3$  and  $\text{HF}$ ) which attacked the silica containment vessel. These chemical reactions formed solid deposits ( $(\text{NH}_4)_3\text{SiF}_6\text{F}$  and  $\text{NH}_4\text{F}$ ) which reintroduced molecular water into the atmosphere, and possibly to the  $\text{ZnF}_2$ .

Two crystalline phases were identified (by XRD, energy dispersive X-ray (EDX) analysis and DTA) to crystallise from the  $70\text{TeO}_2\text{-}10\text{Na}_2\text{O-}20\text{ZnF}_2$  mol. % glass at  $400^\circ\text{C}$ :  $\text{NaZnF}_3$ , and  $\text{Zn}_2\text{Te}_3\text{O}_8$  [4]. It is possible that the competition between these two phases stabilises the glass as it approaches the eutectic composition with  $\text{ZnF}_2$  addition.

$\text{Er}^{+3}$ -doped  $70\text{TeO}_2\text{-}10\text{Na}_2\text{O-}20\text{ZnF}_2$  mol. % glasses which were heat treated, did not show sharply defined XRD peaks, although the amorphous halo was modified. This lack of observable crystallinity, even in opaque samples could be due to the small size of crystallites.

## 5.5. References

- [1] J. A. K. Tareen and T. R. N. Kutty, *A basic course in crystallography*. Bangalore: Universities Press, 2001.

- [2] W. Friedrich, P. Knipping, and M. Laue, "Interference phenomena with Rontgen rays," *Munch. Ber.*, June 1912.
- [3] W. L. Bragg, "The diffraction of short electromagnetic waves by a crystal," *Proceedings of the Cambridge Philosophical Society*, vol. 17, 1912.
- [4] M. D. O'Donnell, D. Furniss, V. K. Tikhomirov, and A. B. Seddon, "Low loss infrared fluorotellurite optical fibre," *Physics and Chemistry of Glasses*, in press.
- [5] N. N. Greenwood and A. Earnshaw, *Chemistry of the elements*. Oxford: Butterworth-Heinemann, 1995.
- [6] W. Vogel, *Glass chemistry*, 2nd ed. New York: Springer-Verlag, 1994.
- [7] A. Nukui, T. Taniguchi, and M. Miyata, "In situ high-temperature X-ray observation of structural changes of tellurite glasses with p-block oxides; ZnO-TeO<sub>2</sub> glasses," *Journal of Non-Crystalline Solids*, vol. 293, pp. 255-260, 2001.
- [8] B. D. Cullity, *Elements of X-ray diffraction*. London: Addison-Wesley, 1959.
- [9] L. L. Kukkonen, I. M. Reaney, D. Furniss, M. G. Pellatt, and A. B. Seddon, "Nucleation and crystallisation of transparent, erbium III-doped, oxyfluoride glass-ceramics," *Journal of Non-Crystalline Solids*, vol. 290, pp. 25-31, 2001.
- [10] M. Beggiora, I. M. Reaney, A. B. Seddon, D. Furniss, and S. A. Tikhomirov, "Phase evolution in oxy-fluoride glass ceramics," *Journal of Non-Crystalline Solids*, vol. 326&327, pp. 476-483, 2003.

## 6. Optical Properties

The aims of this part of the study were to assess the effect of composition and processing route on glass optical properties (infrared (IR) absorption and refractive indices). After investigation of these properties, glasses which had the best prospects for achieving a low-loss, wide transmission window in the IR were selected for possible core / clad pairs. Structural units in the glasses, and loss mechanisms were also identified where possible.

### 6.1. Experimental

#### 6.1.1. Infrared (IR) absorption spectroscopy

##### 6.1.1.1. Method and instrumentation

Fourier-transform-infrared (FTIR) spectroscopy was performed using a Bruker IFS 66/S FTIR spectrometer. A glow-lamp was used as the source in the near and mid-IR (1,500 to 7,000  $\text{cm}^{-1}$ , 1.43 to 6.67  $\mu\text{m}$ ) and the detector material used was DTGS (deuterated triglycine sulphate). The raw absorbance data were then divided by the glass optical path length ( $\approx 3$  mm) so maximum absorption peak heights could be easily compared. Fresnel reflection losses (see equation (6.20) and (6.21)) were not subtracted from the spectra, but contributed to around 17.8 to 27.0 % of the background loss (depending on refractive index). The gas prior to entry to the spectrometer chamber, was passed through a Parker

75-52-12VDC FT-IR Purge Gas Generator. Due to the sensitivity of the FTIR, a small amount of moisture was still present after this drying and an absorption band was observed in some of the spectra at around  $3600\text{ cm}^{-1}$  ( $2.78\text{ }\mu\text{m}$ ) due to atmospheric water [1]. Later in the work more careful purging was carried out on the sample chamber and the atmospheric water could be removed. A band observed around  $2800\text{ cm}^{-1}$  ( $3.57\text{ }\mu\text{m}$ ) was attributed to CH, CH<sub>2</sub> or CH<sub>3</sub> also [1] which is an artefact from the polishing process due to mounting wax and / or polishing oil, because this band was not present in the fibre loss spectra (see chapter 8). To prepare bulk glass samples, opposite sides were ground flat and parallel using SiC powder in an oil suspension. The samples were then polished using diamond paste to a  $1\text{ }\mu\text{m}$  finish, resulting in a sample of around 3 mm thickness, washing in between stages with acetone (Fisher). The raw absorption data from the spectrometer was divided by sample thickness (in cm) to give the absorption coefficient in  $\text{cm}^{-1}$ . Background loss was therefore not meaningful. Absorption bands, which were believed to be made up of a number of overlapping bands, were Gaussian deconvoluted using the method described in section 4.1.1.3 in Microcal Origin software.

#### **6.1.1.2. Theory of operation**

Spectroscopy is a group of techniques which measure the interaction of electromagnetic radiation with matter. The infrared (IR) region of the electromagnetic spectrum ( $100\text{-}5000\text{ cm}^{-1}$ ) has sufficient energy to excite molecular vibrations or phonons [2]. Absorption bands in infrared spectra can therefore be used to identify structural units and organic groups in a material. Absorption spectroscopy measures the total absorption of a

sample for near monochromatic radiation over a range of wavelengths. The energy,  $E$ , of the incident radiation is given by equation (6.1) [3].

$$E = hf \quad (6.1)$$

where  $h = \text{Planck's constant} = 6.62608 \times 10^{-34} \text{ J.s}$  and  $f = \text{frequency of the incident radiation}$ . The wavelength,  $\lambda$ , of the radiation is given by equation (6.2) [3].

$$\lambda = \frac{c}{f} \quad (6.2)$$

where  $c = \text{the speed of light in a vacuum} = 2.99792458 \times 10^8 \text{ m.s}^{-1}$ . Spectroscopists often express the  $x$ -axis of spectra in wavenumbers,  $\tilde{f}$ , which are usually measured in reciprocal centimetres ( $\text{cm}^{-1}$ ). This is convenient, as wavenumbers are directly proportional to energy. Equation (6.3) shows the relation between wavenumbers and equation (6.1) and (6.2) [3].

$$\tilde{f} = \frac{f}{c} = \frac{1}{\lambda} = \frac{E}{hc} \quad (6.3)$$

Fig. (6.1) shows the setup of a typical dual beam absorption spectrometer [3].

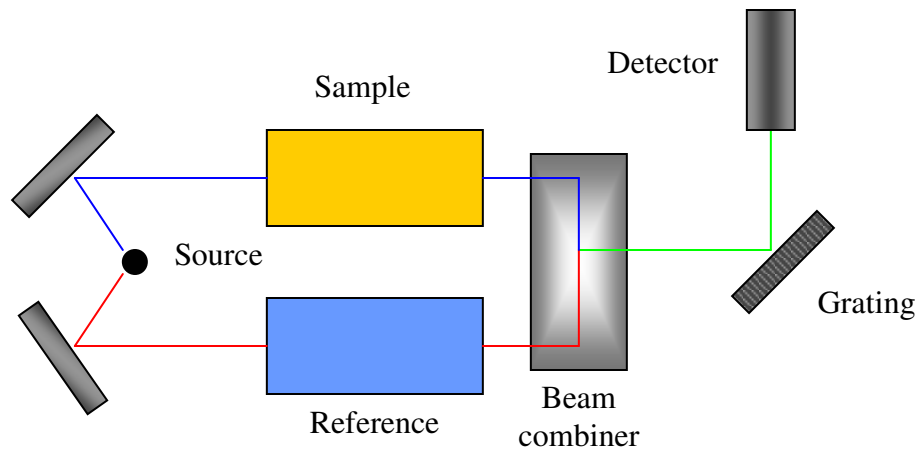


Fig. (6.1): Setup of a typical dual beam absorption spectrometer [3].

The spectrometer consists of a source of radiation with a beamsplitter, a sample and a detector [3].

#### *Radiation sources*

In the far-infrared (FIR), a mercury arc inside a quartz envelope is used. In the near-infrared (NIR), a Nernst filament is used. This consists of a heated ceramic element, doped with rare-earth oxides [3].

#### *Dispersing element*

The dispersing element separates various frequencies into different spatial directions to record the change in absorption with frequency. The simplest component to use is a

quartz / glass prism. As refractive index increases with frequency, high frequency radiation is deflected to a higher degree as it passes through the prism [3]. Problems associated with passing the beam through a material (such as absorption) can be avoided by using a diffraction grating. This device consists of a glass or ceramic plate with fine parallel grooves of the order of the wavelength of light ( $\approx 1 \mu\text{m}$ ). The grating is covered in a reflective coating (aluminium). Reflection from the grating results in interference, which is constructive at certain angles, depending on the wavelength of the light. The intensity of the diffracted beam is enhanced by shaping the grating in a certain way, resulting in blazing [3].

#### *Fourier transform (FT)*

The spectrometer used in this study operated by a Fourier transform (FT) method. The Fourier transform infrared (FTIR) spectrometer used a Michelson interferometer to analyse the individual frequencies present in a composite signal. The Michelson interferometer operated by splitting the beam from the sample into two, then introduced a path difference,  $\delta$ , into one of them, which was varied. The two beams were then recombined, and interfered constructively or destructively, depending on  $\delta$ . The intensity of the signal from the sample,  $I$ , varied according to equation (6.4) [3].

$$I(\delta) = I(\tilde{f})(1 + \cos 2\pi\tilde{f}\delta) \quad (6.4)$$

In reality the signal consisted of a range of frequencies, therefore the total intensity at the detector is given by equation (6.5) [3].

$$I(\delta) = \int_0^{\infty} I(\tilde{f})(1 + \cos 2\pi\tilde{f}\delta)d\tilde{f} \quad (6.5)$$

To provide a useful spectrum, the variation in intensity with wavenumber,  $I(\tilde{f})$ , must be found. This was obtained by a Fourier transform integration step shown by equation (6.6) [3].

$$I(\tilde{f}) = 4 \int_0^{\infty} [I(\delta) - \frac{1}{2}I(0)] \cos(2\pi\tilde{f}\delta) d\delta \quad (6.6)$$

This integration was performed here by the FTIR spectrometer computer, which displayed the output,  $I(\tilde{f})$  against  $\tilde{f}$ , which formed the spectra of the sample.

The major advantage of the FTIR spectrometer is that all of the radiation detected from the sample is continuously monitored. Therefore, the FTIR is highly sensitive and fast compared to spectrometers where a monochromator discards most of the radiation.

The resolution,  $\Delta\tilde{f}$ , is defined by equation (6.7) [3].

$$\Delta\tilde{f} = \frac{1}{2\delta_{\max}} \quad (6.7)$$

where  $\delta_{max}$  = maximum pathlength difference of the interferometer. Therefore, a resolution of  $0.2 \text{ cm}^{-1}$ , gives  $\delta_{max} = 2.5 \text{ cm}$ .

### *Detectors*

The detector in a spectrometer converts the incident radiation received from the sample into an electronic signal to be processed. Much like the source, the detector type depends on the region of the electromagnetic spectrum being investigated. However, semiconductor detectors are commonly used in the ultraviolet (UV), visible and IR. One popular type of semiconductor detector is known as a charge coupled device (CCD) [3]. In higher frequency regions, such as the visible and UV, a photomultiplier is alternatively used. This photomultiplier works by releasing an electron from a photosensitive screen each time it is struck by an incident photon. This electron is accelerated by a current, striking further screens creating a cascade effect, resulting in an amplified signal. Although semiconductor devices are becoming more frequently used, thermocouple detectors are sometimes used for the IR [3].

### *Intensities of absorption bands and the Beer-Lambert law*

An empirical equation, known as the Beer-Lambert law, can be used to calculate the intensity of absorption,  $I$ , with sample thickness,  $l$ . This is shown by equation (6.8) [3].

$$\log \frac{I}{I_0} = -\epsilon[J]l \quad (6.8)$$

where  $I_0$  = incident intensity,  $[J]$  = molar concentration of absorbing species  $J$ , and  $\epsilon$  = extinction coefficient or molar absorption coefficient.  $\epsilon$  has units  $\text{mol}^{-1}\text{cm}^{-1}$ , therefore the product of  $\epsilon[J]l$  is dimensionless, and known as absorbance,  $\gamma$ . Transmittance,  $\phi$ , of the sample is given by  $I/I_0$ . The relation between transmittance and equation (6.8) is shown by equation (6.9) [3].

$$\log \phi = -\gamma \quad (6.9)$$

The absorbance of the sample can be easily obtained by determining  $I$  and  $I_0$  (and hence  $\phi$ ) experimentally. As equation (6.8) implies, sample absorption decreases exponentially with sample thickness,  $l$ , and concentration,  $[J]$  [3].

#### *Molecular explanation of vibrational spectroscopy*

If a molecule possesses a permanent electric dipole moment,  $P$ , with particles of charges  $+e$  and  $-e$  separated by distance  $r$ , shown by equation (6.10) [2].

$$P = er \quad (6.10)$$

A heteronuclear diatomic molecule above absolute 0K vibrates at a particular frequency. The molecular dipole also vibrates about its equilibrium position. This dipole can only absorb energy from an electric field (i.e. incident IR radiation) if the dipole oscillates at the same frequency. A resonant energy transfer occurs, for example, between the net

negative charge from the dipole on one end of the molecule, and the negative sign of the electromagnetic field [2].

A dipole moment,  $P_{ind}$ , will be induced in a molecule placed in an electric field,  $\mathbf{E}$ . This is due to the attraction of the nuclei to the negative pole of the field, and the electrons to the positive.  $P_{ind}$  is given by equation (6.11) [2].

$$P_{ind} = \pi_{ion}\mathbf{E} \quad (6.11)$$

where  $\pi_{ion}$  is known as the polarisability of the molecule, and is a constant for a given atom or molecule and typically has units  $\text{\AA}^3$  ( $10^{-10} \text{ m}^3$ ) [2].

#### *The harmonic oscillator*

A simple model for the vibration of a diatomic molecule can be formed by considering Hooke's law, which gives the restoring force,  $F$ , on a spring (i.e. a bond between two nuclei). This is illustrated by equation (6.12) and fig. (6.2) [2].

$$F = -kq \quad (6.12)$$

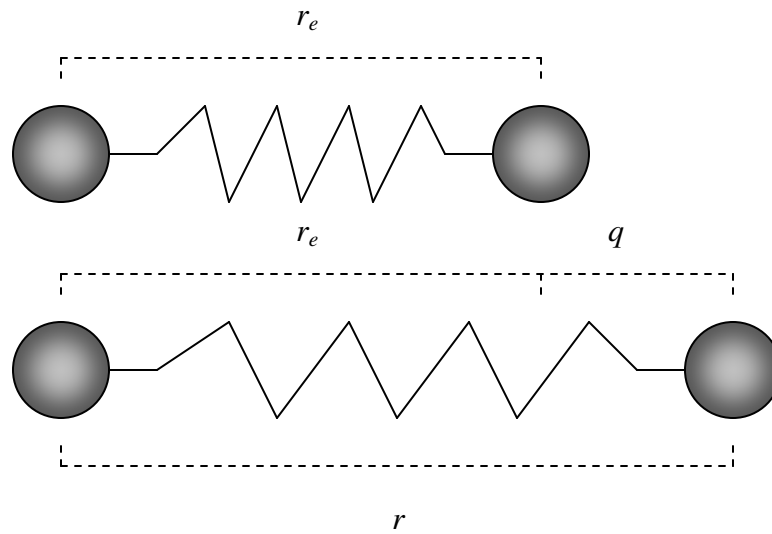


Fig. (6.2): Harmonic oscillation of two nuclei [2].

where  $q$  is the distance the 'spring' has stretched from its equilibrium position,  $r_e$ , and  $k$  is the force constant, measured in  $\text{N}\cdot\text{m}^{-1}$ . The potential energy of the bond,  $E_p$ , is given by equation (6.13) [2].

$$dE_p = -Fdq = kq dq \quad \therefore E_p = \frac{1}{2}kq^2 \quad (6.13)$$

Fig. (6.3) shows the variation in potential energy with distance between two nuclei, using the harmonic oscillator model [2].

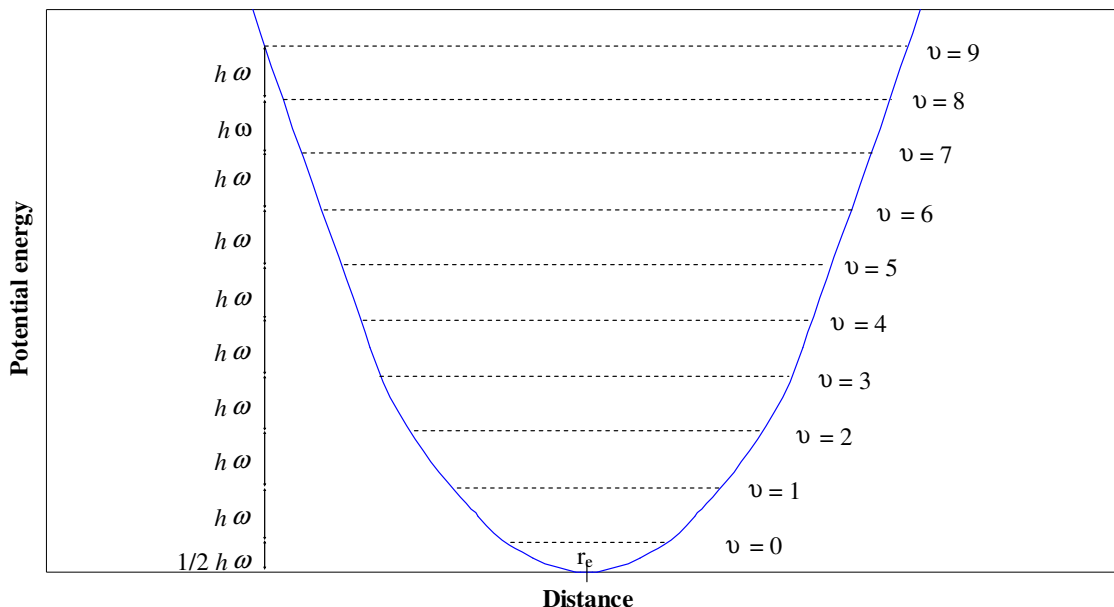


Fig. (6.3): Variation in potential energy with distance between two nuclei, using the harmonic oscillator model [2].

Quantum mechanical theory states that the molecule can only occupy discrete energy levels, given by the quantum number,  $v$  (an integer). The energy of a particular level is given by equation (6.14) [2].

$$E_v = \left(v + \frac{1}{2}\right) \frac{h}{2\pi} \sqrt{\frac{k}{\mu}} \equiv \left(v + \frac{1}{2}\right) h\omega \quad (6.14)$$

where  $\mu =$  reduced mass  $= \frac{m_1 m_2}{m_1 + m_2}$ ,  $m_i =$  mass of atom  $i$ , and  $\omega = \frac{1}{2\pi} \sqrt{\frac{k}{\mu}}$ . At the lowest

vibrational energy ( $v = 0$ ), the molecule still has energy,  $E_0 = \frac{1}{2} h\omega$ . Higher energy

levels (1, 2, 3...), are separated by energy  $h\omega$  [2]. For diatomic molecules, the force constant of the bond can be calculated relatively easily from vibrational spectra.

Absorption results from the excitation of the molecule from  $v = 0$  to  $v = 1$ , and so on, by the incident radiation. This gives  $\Delta E = h\omega$ , and  $k$  can be obtained by rearranging equation (6.14) [2].

### *The anharmonic oscillator*

The parabolic potential well shown by equation (6.13) and fig. (6.3) is not an accurate model of the variation in force experienced by a diatomic molecule. Equation (6.13) represents a symmetric potential well, whereas in reality it would be asymmetric [2]. As the nuclei come together, they repel each other and the potential energy will rise exponentially, similar to the harmonic oscillator. However, as the nuclei are pulled apart, the potential energy will level off as dissociation occurs, resulting in an asymmetric potential well. An empirical equation known as the Morse potential, can be used to model this behaviour. This is shown by equation (6.15) [2].

$$E_p = E_d(1 - e^{-\kappa x})^2 \quad (6.15)$$

where  $E_d$  = depth of the potential well, and  $\kappa$  = curvature of bottom of the potential well.

This is graphically illustrated in fig. (6.4).

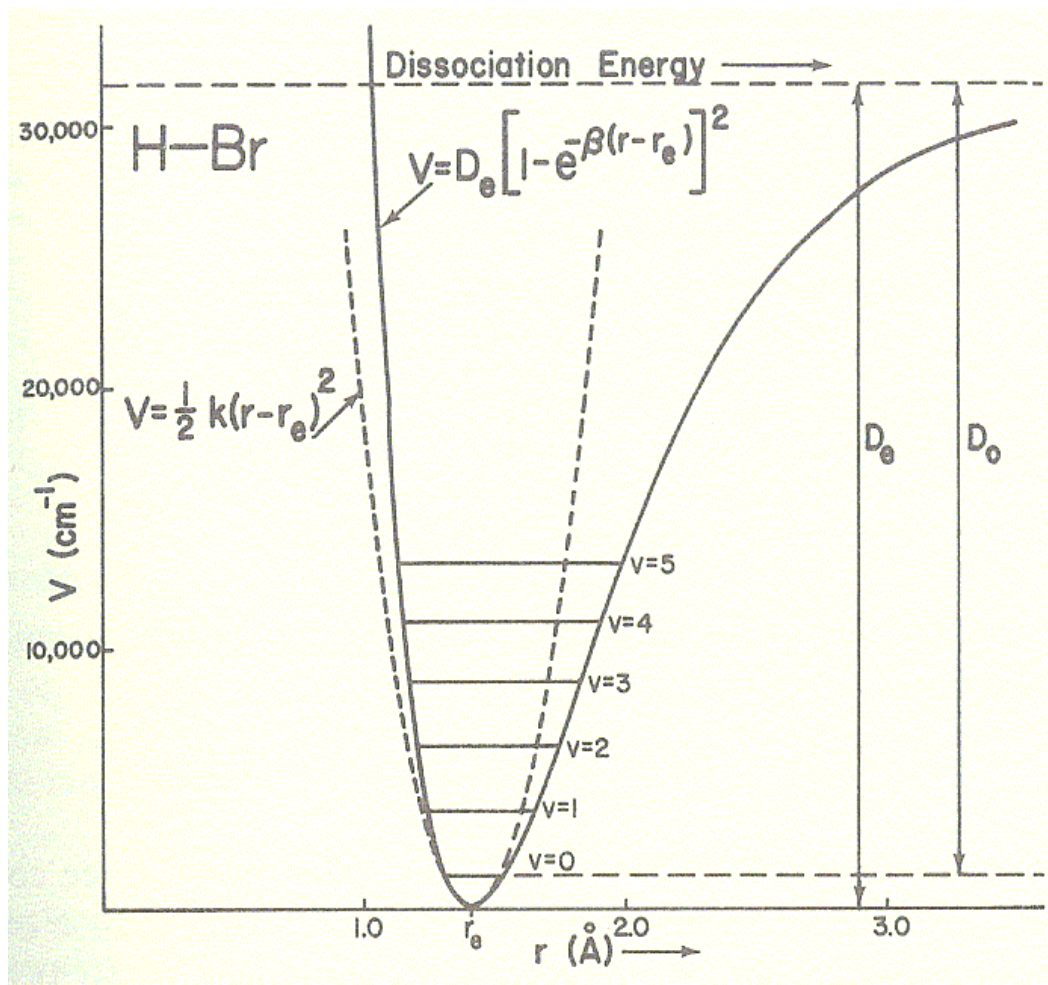


Fig. (6.4): Variation in potential energy with distance between two nuclei (H and Br), using the anharmonic oscillator model [2].

Allowed energy levels are given by equation (6.16) [2].

$$\bar{E}_v = \bar{\omega}_e \left( v + \frac{1}{2} \right) - \bar{\omega}_e x_e \left( v + \frac{1}{2} \right)^2 \quad (6.16)$$

where  $\bar{\omega}_e = \frac{\omega}{100c}$  and has units  $\text{cm}^{-1}$  and  $x_e$  is a small anharmonic correction.  $\bar{\omega}_e$  and  $x_e$

are experimentally determined constants, from which  $E_d$  and  $\kappa$  can be derived [2]. The

energy of transitions from the ground state ( $\nu = 0$ ), to higher levels is given by equation (6.17) [2].

$$\Delta\bar{E} = \bar{E}_\nu - \bar{E}_0 = \bar{\omega}_e \nu - \bar{\omega}_e x_e \nu(\nu+1) \quad (6.17)$$

The transition between levels  $\nu = 0$  to  $\nu = 1$  for a molecule is known as the fundamental transition, and is seen on vibrational spectra as the fundamental frequency. Higher transitions, which are approximate multiples of the fundamental frequency, are known as the first overtone ( $\nu = 0$  to  $\nu = 2$ ), second overtone ( $\nu = 0$  to  $\nu = 3$ ) etc. [2].

The harmonic model predicts equally spaced overtones, when in fact this spacing decreases slightly with increasing energy level [2]. The disassociation energy of the molecule,  $\bar{D}_e$ , is not equal to  $\bar{E}_d$ , but shown by equation (6.18) [2].

$$\bar{D}_e = \bar{E}_d - \bar{E}_0 = \bar{E}_d - \frac{1}{2}\bar{\omega}_e + \frac{1}{4}\bar{\omega}_e x_e \quad (6.18)$$

$\bar{\omega}_e$  is related to  $k_e$ , the anharmonic force constant and is a better representation of bond strength than  $k$  obtained from the harmonic model [2].

### *Selection rules*

The general selection rule for infrared vibration of a molecule is that the dipole of the molecule must change with the atomic displacement. This process can occur as the

molecule's vibration can resist the electromagnetic field by changing its dipole moment [3]. The molecule does not need to have a permanent dipole for a vibration to be stimulated, just a change in dipole moment needs to occur. Some vibrations will not be affected by the incident radiation, and are known as infrared inactive [3].

### *Vibrations of polyatomic molecules*

For diatomic molecules, there is only one mode of vibration, the bond stretch. In polyatomic molecules, a number of modes exist, stretching and bending [3]. Nonlinear molecules with  $N$  atoms have  $(3N - 6)$  modes, and linear molecules with  $N$  atoms have  $(3N - 5)$  modes. Water ( $\text{H}_2\text{O}$ ), for example, has  $[(3 \times 3) - 6] = 3$  modes: (i) symmetric stretch, (ii) asymmetric stretch, and (iii) bending modes. Fundamental and overtone frequencies of these modes make up vibrational infrared spectra of molecules such as  $\text{H}_2\text{O}$  [3]. The symmetric stretch of  $\text{CO}_2$  leaves the net dipole moment unchanged, therefore this mode is infrared inactive. However, the asymmetric stretch is infrared active, as the dipole moment changes on vibration [3]. For a more detailed treatment of infrared transmission, and multiphonon absorption in glass, see section 2.4.2.

## 6.1.2. Ellipsometry

### 6.1.2.1. Method and instrumentation

Refractive index measurements were performed using a Rudolph Research AutoEL<sup>R</sup>-II automatic ellipsometer at 632.8 nm. The ellipsometer was calibrated using a Rudolph Research standard silica sample on a silicon substrate (part no. A9291, serial no. 1772) with a stated refractive index of 1.460; the measured index of the standard lay within  $1.460 \pm 0.002$ . Samples were prepared by the same method described in section 6.1.1.1. When a large population of measurements were made for a particular sample (e.g. 15 or 25), 3 to 5 measurements were taken at one point, and then the same number taken from other points over the samples surface.

### 6.1.2.2. Theory of operation

Ellipsometry is typically used to measure the thickness and optical constants (such as  $n$ , refractive index) of thin films. However, it can also be used to measure the refractive index of bulk glass samples. Monochromatic light (633 nm in this study) of an angle between 0 and 90° is reflected from the surface of a sample, and its polarisation analysed. The change in polarisation is expressed as two functions,  $\Psi$ , which is a complex dielectric function relating to the ellipticity of the reflected light, and  $\Delta$ , which is related to the phase of the reflected light. Equation (6.19) shows the relationship between these

functions, and the ratio of the Fresnel reflection coefficients,  $R_p$  and  $R_s$ , of the  $p$  and  $s$  polarised light.

$$\tan(\Psi)e^{i\Delta} = \frac{R_p}{R_s} \quad (6.19)$$

Fig. (6.5) shows the geometry of the ellipsometry experiment.

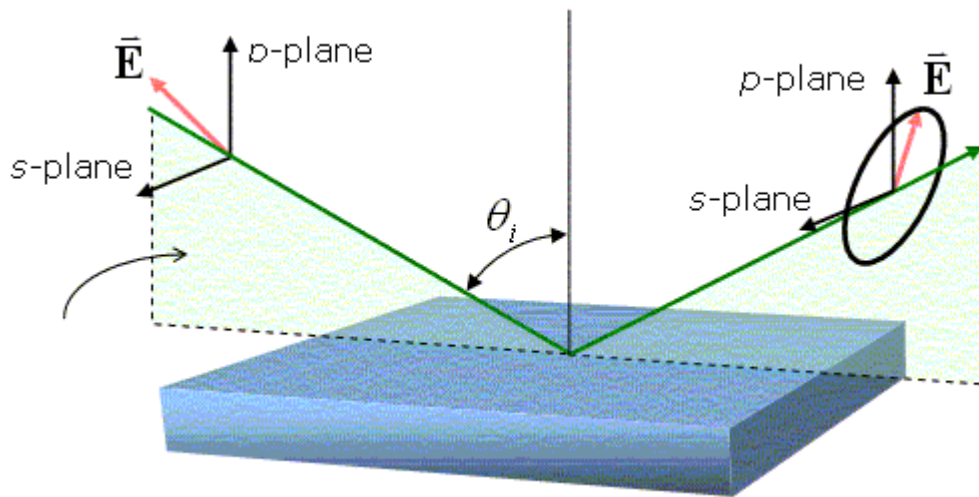


Fig. (6.5): Geometry of the ellipsometry experiment.

It can be seen, the incident linearly polarised beam is converted to an elliptically polarised beam, due to the change in polarisation of the  $s$  and  $p$  components of the beam on reflection. Fresnel reflection is the reflection of a portion of the incident light at an interface between two substances with different refractive indices. The Fresnel reflection coefficient,  $R_f$ , is given by equation (6.20) [4].

$$R_f = \frac{(n_1 - n_2)^2}{(n_1 + n_2)^2} \quad (6.20)$$

where  $n_i$  is the refractive index of substance  $i$ . For an air-glass interface, such as that seen in the ellipsometry experiment,  $n_2$  (refractive index of air) is assumed unity in equation (6.20), as shown by equation (6.21).

$$R_f = \frac{(n-1)^2}{(n+1)^2} \quad (6.21)$$

A circular spot of light from the instruments source is focused onto the sample surface by viewing through a microscope eyepiece, to ensure the incident light is focused onto the sample surface region (i.e. the sample height is adjusted). The sample orientation is then adjusted to be flat relative to the microscope eyepiece using a second circular spot, by moving the sample stage (i.e. the angle of sample can be adjusted in two planes). The ellipsometer obtains values  $\Psi$  and  $\Delta$ , by analysing the polarisation of the reflected light, and displays these values on a screen built into the instrument. These are recorded, and subsequently input into a program which uses equation (6.21) and (6.19) to calculate  $n$  for the sample, from values of  $\Psi$  and  $\Delta$ .

There are a number of advantages to ellipsometry. The technique is accurate and reproducible, as it measures the ratio between two values of  $R$  (the  $s$  and  $p$  component of the reflected beam). No reference is needed, except to calibrate the equipment for accuracy, and sample preparation is simple. This is because a flat surface is needed for the measurement rather than a prism. The technique is not sensitive to scatter and

fluctuations in source intensity and atmospheric absorption, but of course would be affected by imperfections in the glass.

## 6.2. Results

This section presents the infrared absorption spectra of oxide tellurite and fluorotellurite glasses studied. These are followed by emission spectra of previously heat treated  $\text{Er}^{+3}$ -doped fluorotellurite glasses. Refractive indices of oxide tellurite and fluorotellurite glasses are then presented.

### 6.2.1. Infrared spectroscopy

#### 6.2.1.1. Infrared spectroscopy of oxide tellurite glasses

*Infrared spectroscopy of glasses of the series  $(80-x)\text{TeO}_2-10\text{Na}_2\text{O}-10\text{ZnO}-x\text{MO}$  mol. %, where MO is PbO or  $\text{GeO}_2$*

Fig. (6.6) shows infrared spectra of glasses in the series  $(80-x)\text{TeO}_2-10\text{Na}_2\text{O}-10\text{ZnO}-x\text{MO}$  mol. %, where MO was PbO or  $\text{GeO}_2$ , for MOD006 ( $x = 3$  mol. % PbO), MOD010 ( $x = 5$  mol. % PbO) and MOD012 ( $x = 5$  mol. %  $\text{GeO}_2$ ).

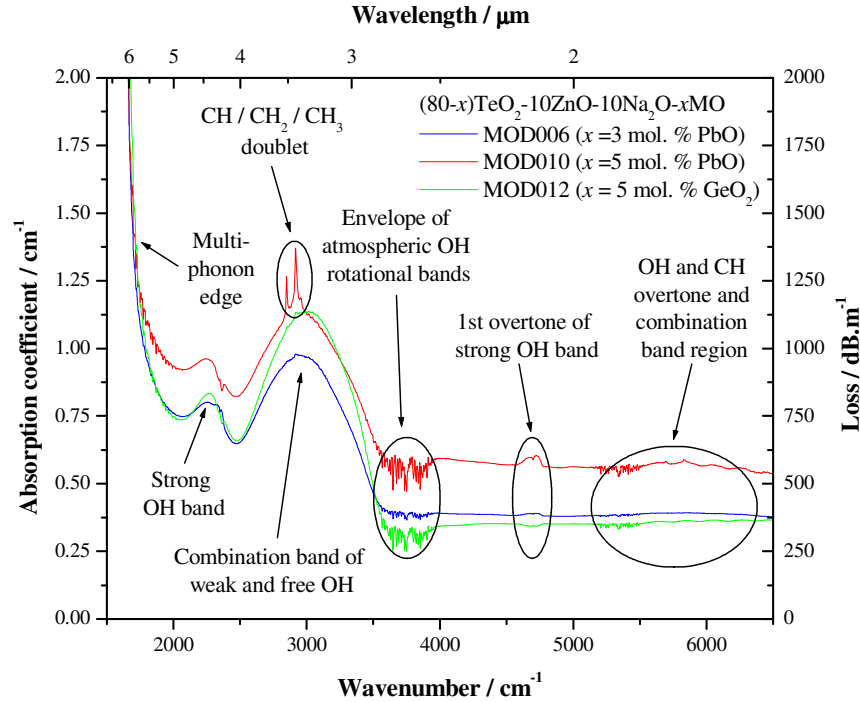


Fig. (6.6): Infrared spectra of glasses in the series  $(80-x)\text{TeO}_2-10\text{Na}_2\text{O}-10\text{ZnO}-x\text{MO}$ , where MO is PbO or  $\text{GeO}_2$ , for MOD006 ( $x = 3$  mol. % PbO), MOD010 ( $x = 5$  mol. % PbO) and MOD012 ( $x = 5$  mol. %  $\text{GeO}_2$ ). Strongly hydrogen bonded OH = strong OH and weakly hydrogen bonded OH = weak OH.

It can be seen the multiphonon edge (taken from the  $x$ -axis where the absorption coefficient reaches  $2 \text{ cm}^{-1}$ ) for these glasses occurred at around  $1667 \text{ cm}^{-1}$  ( $6 \mu\text{m}$ ). All three glasses exhibited absorption bands in the infrared region due to hydroxide (OH) groups in the glass. Three OH bands were seen, the positions depending on the degree of hydrogen bonding of the OH in the glass: strongly hydrogen bonded OH (strong OH), weakly hydrogen bonded OH (weak OH), and free OH. A higher intensity asymmetric band was seen at around  $3000 \text{ cm}^{-1}$  ( $3.33 \mu\text{m}$ ). This band was identified as a combination band of weakly H-bonded OH and free OH. The lower intensity band at around  $2270 \text{ cm}^{-1}$  ( $4.41 \mu\text{m}$ ) was due to strongly H-bonded OH in the glass. The doublet which appeared at around  $2800 \text{ cm}^{-1}$  ( $3.57 \mu\text{m}$ ) for glass MOD010 was identified as CH /  $\text{CH}_2$  /

CH<sub>3</sub> (artefacts from polishing process) groups. The noisy band at around 3600 cm<sup>-1</sup> (2.78 μm) for all three glasses was identified as the envelope of the rotational bands of atmospheric water [2]. The bands in the 4500 to 6500 cm<sup>-1</sup> (1.54 to 2.22 μm) region were identified as overtones and combinations of CH and OH groups.

Fig. (6.7) shows the multiphonon edge of glasses in the series (80-*x*)TeO<sub>2</sub>-10Na<sub>2</sub>O-10ZnO-*x*MO, where MO is PbO or GeO<sub>2</sub>, for MOD006 (*x* = 3 mol. % PbO), MOD010 (*x* = 5 mol. % PbO) and MOD012 (*x* = 5 mol. % GeO<sub>2</sub>).

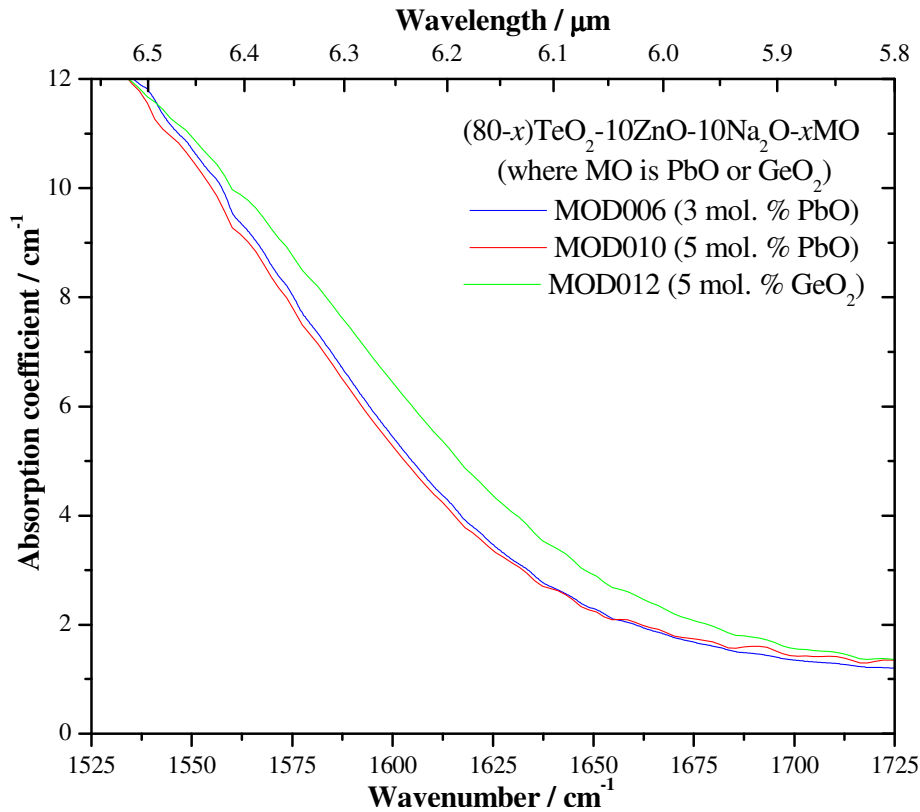


Fig. (6.7): Multiphonon edge of glasses in the series (80-*x*)TeO<sub>2</sub>-10Na<sub>2</sub>O-10ZnO-*x*MO, where MO is PbO or GeO<sub>2</sub>, for MOD006 (*x* = 3 mol. % PbO), MOD010 (*x* = 5 mol. % PbO) and MOD012 (*x* = 5 mol. % GeO<sub>2</sub>).

Fig. (6.8) to (6.10) show Gaussian deconvolution of the OH bands in glasses MOD006 (77TeO<sub>2</sub>-10Na<sub>2</sub>O-10ZnO-3PbO mol. %), MOD010 (75TeO<sub>2</sub>-10Na<sub>2</sub>O-10ZnO-5PbO mol.

%), and MOD012 (75TeO<sub>2</sub>-10Na<sub>2</sub>O-10ZnO-5GeO<sub>2</sub> mol. %). The background absorption, and multiphonon edge were subtracted in each case from the spectra by fitting a curve of the form  $y = \left(\frac{A}{x}\right)^4 + B$  to the data, where  $A$  and  $B$  are constants, and  $x$  is the wavenumber, and  $y$  the absorption coefficient. This form of equation gave a reasonable fit to the background in each case. This equation and the peak data from deconvolution are shown on the spectra, where  $x_i$  is the position of peak  $i$ ,  $w_i$  the half width of peak  $i$ ,  $A_i$  the area of peak  $i$ .  $\chi^2$  (is related to the iteration calculation performed by the software) and  $R^2$  (is the square of the correlation coefficient) indicate the degree of fit between the generated peaks and the data (the closer  $\chi^2$  is to 0 and  $R^2$  to 1, the better the Gaussian fit correlates with the data).

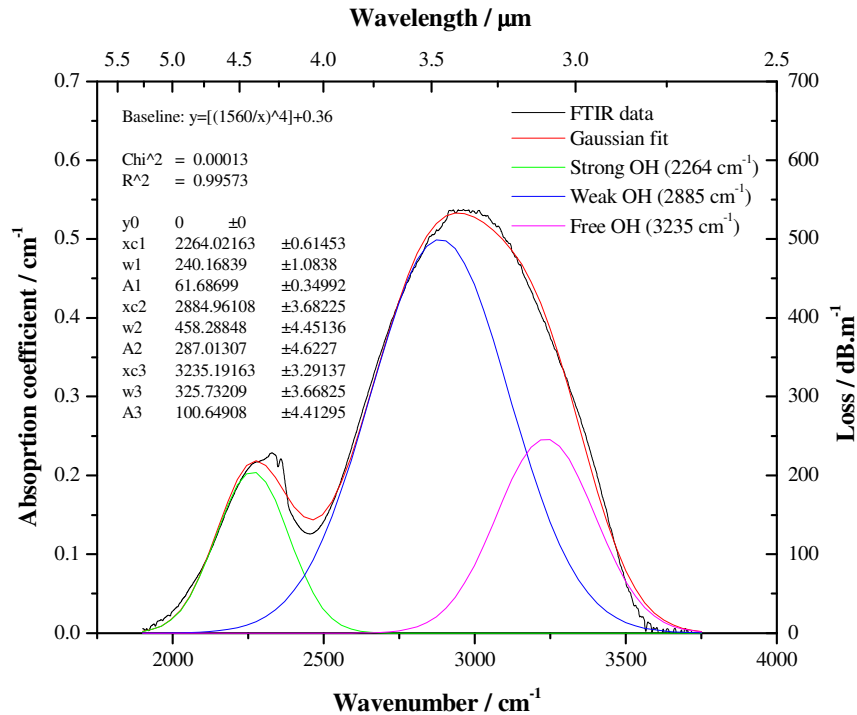


Fig. (6.8): Gaussian deconvolution of OH bands in glass MOD006 (77TeO<sub>2</sub>-10Na<sub>2</sub>O-10ZnO-3PbO mol. %).

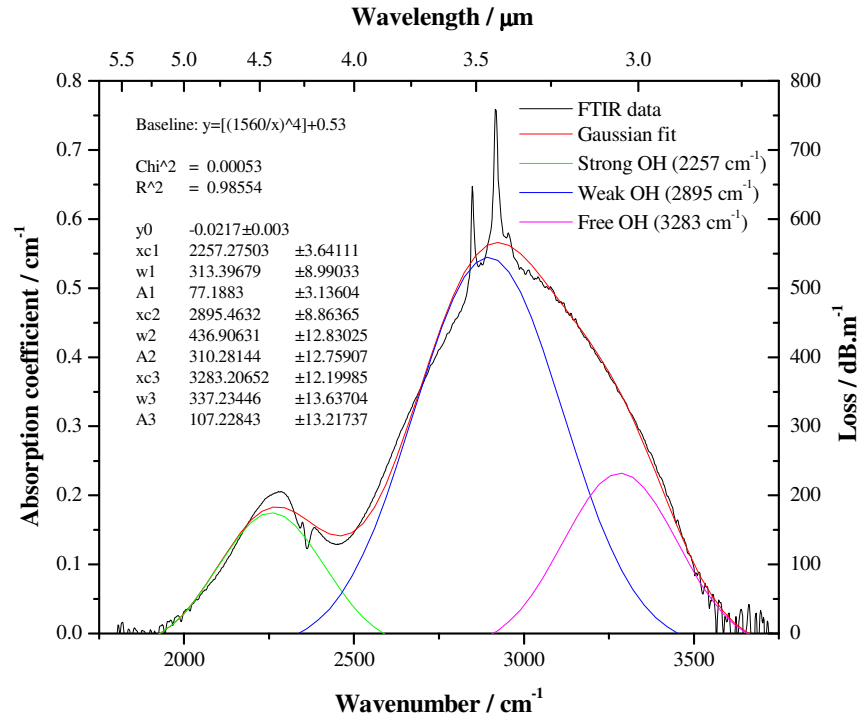


Fig. (6.9): Gaussian deconvolution of OH bands in glass MOD010 (75TeO<sub>2</sub>-10Na<sub>2</sub>O-10ZnO-5PbO mol. %).

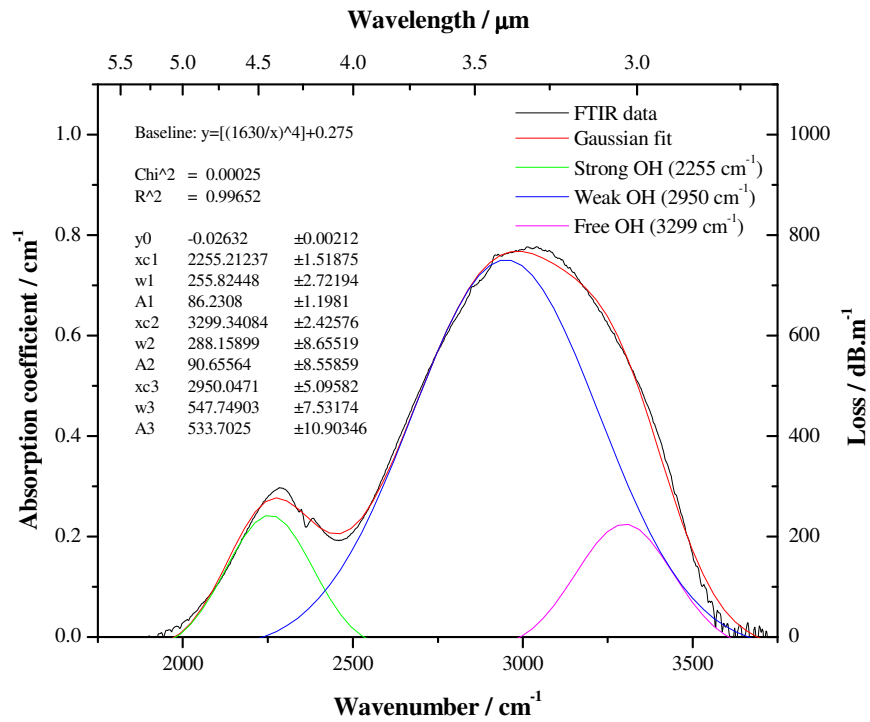


Fig. (6.10): Gaussian deconvolution of OH bands in glass MOD012 (75TeO<sub>2</sub>-10Na<sub>2</sub>O-10ZnO-5GeO<sub>2</sub> mol. %).

Table (6.1) summarises the positions (P), half-widths (W), and areas (A) of these bands.

Table (6.1): Position (P), half-widths (W), and areas (A) of OH groups for glass series  $(80-x)\text{TeO}_2-10\text{Na}_2\text{O}-10\text{ZnO}-x\text{MO}$ , where MO is PbO or  $\text{GeO}_2$ , for MOD006 ( $x = 3$  mol. % PbO), MOD010 ( $x = 5$  mol. % PbO) and MOD012 ( $x = 5$  mol. %  $\text{GeO}_2$ ).

Glass MOD ID	Strong OH			Weak OH			Free OH		
	P / $\text{cm}^{-1}$	W / $\text{cm}^{-1}$	A / $(\text{cm}^{-1})^2$	P / $\text{cm}^{-1}$	W / $\text{cm}^{-1}$	A / $(\text{cm}^{-1})^2$	P / $\text{cm}^{-1}$	W / $\text{cm}^{-1}$	A / $(\text{cm}^{-1})^2$
<b>006</b>	2264	240	62	2885	458	287	3235	326	101
<b>010</b>	2257	313	77	2895	437	310	3283	337	107
<b>012</b>	2255	256	86	2950	548	534	3299	288	91

From table (6.1), the area of each band is proportional to the concentration of the absorbing species in the glass. Therefore, the areas can be used to calculate the fraction of each type of OH present in the glass, assuming each type has approximately equal extinction coefficients. Table (6.2) and fig. (6.11) summarise this.

Table (6.2): Percentage of OH groups in glass series  $(80-x)\text{TeO}_2-10\text{Na}_2\text{O}-10\text{ZnO}-x\text{MO}$ , where MO is PbO or  $\text{GeO}_2$ , for MOD006 ( $x = 3$  mol. % PbO), MOD010 ( $x = 5$  mol. % PbO) and MOD012 ( $x = 5$  mol. %  $\text{GeO}_2$ ).

Glass MOD ID	Strong OH / %	Weak OH / %	Free OH / %
<b>006</b>	14	64	22
<b>010</b>	16	63	22
<b>012</b>	12	75	13

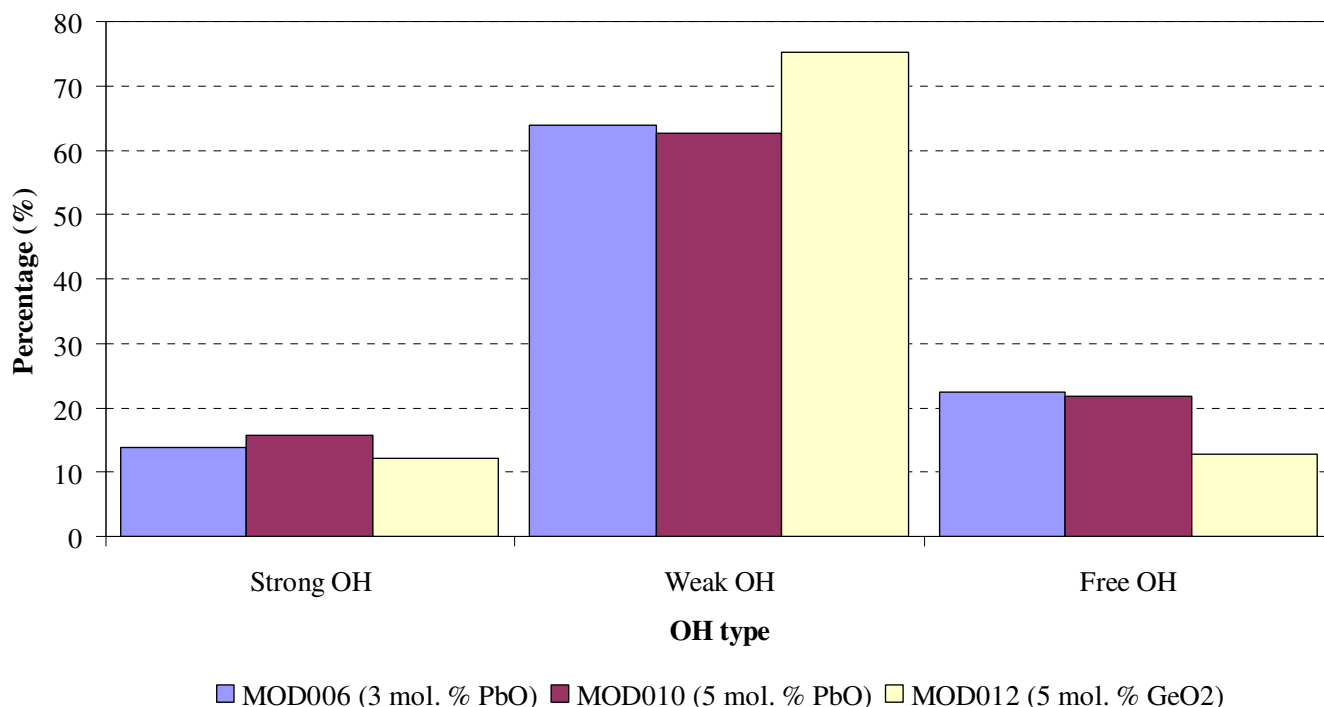


Fig (6.11): Percentage of OH groups in glass series  $(80-x)\text{TeO}_2-10\text{Na}_2\text{O}-10\text{ZnO}-x\text{MO}$ , where MO is PbO or  $\text{GeO}_2$ , for MOD006 ( $x = 3$  mol. % PbO), MOD010 ( $x = 5$  mol. % PbO) and MOD012 ( $x = 5$  mol. %  $\text{GeO}_2$ ).

It can be seen that the percentage of strongly H-bonded OH in all three glasses was approximately the same,  $\approx 14\%$ . The percentage of weakly H-bonded OH and free OH in the PbO containing glasses was approximately the same ( $\approx 63$  and  $22\%$  respectively). However, the percentage of weakly H-bonded OH and free OH was lower in the  $\text{GeO}_2$  containing glass than the PbO containing glasses ( $\approx 75$  and  $13\%$  respectively).

#### *Infrared spectroscopy of glasses of the series $(90-x)\text{TeO}_2-10\text{Na}_2\text{O}-x\text{ZnO}$*

Fig. (6.12) shows infrared spectra of glass of the series  $(90-x)\text{TeO}_2-10\text{Na}_2\text{O}-x\text{ZnO}$ , for  $x = 12$  mol. % (MOD007) and  $x = 10$  mol. % (MOD013).

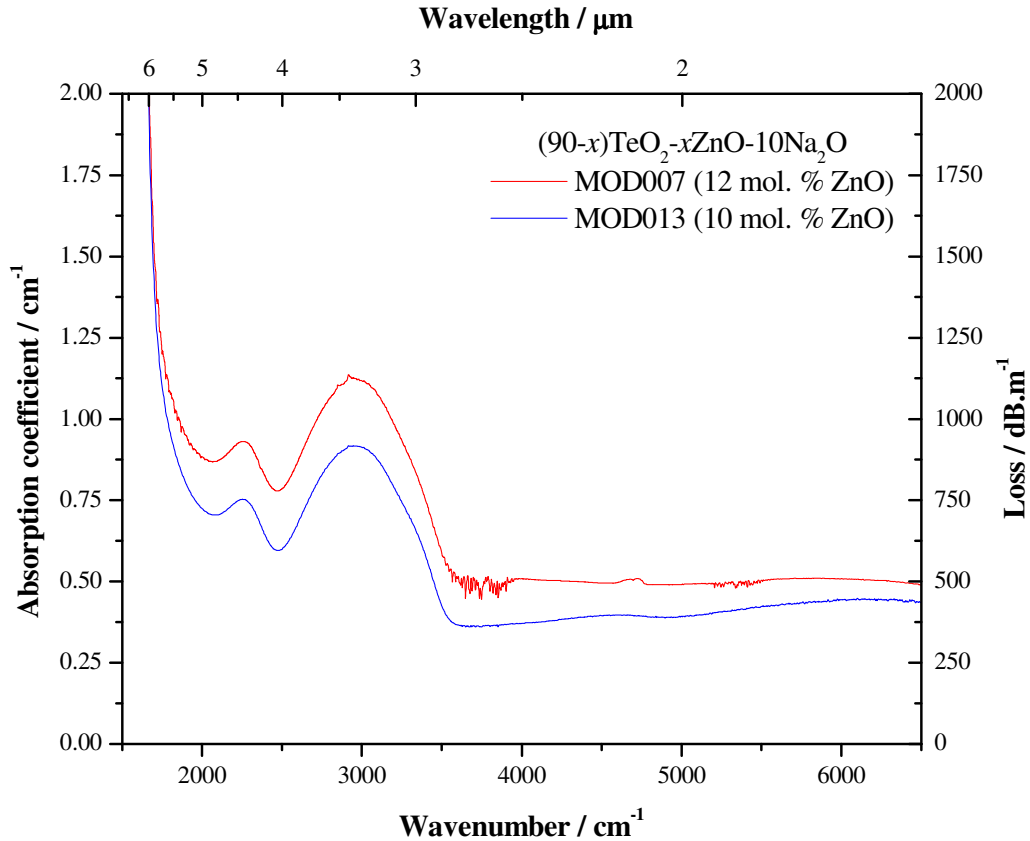


Fig. (6.12): Infrared spectra of glass of the series  $(90-x)\text{TeO}_2-10\text{Na}_2\text{O}-x\text{ZnO}$ , for  $x = 12$  mol. % (MOD007) and  $x = 10$  mol. % (MOD013).

Again, the multiphonon edge for these glasses occurred at around  $1667\text{ cm}^{-1}$  ( $6\text{ }\mu\text{m}$ ) and hydroxide (OH) bands occurred at around  $3000\text{ cm}^{-1}$  ( $3.33\text{ }\mu\text{m}$ ) and  $2270\text{ cm}^{-1}$  ( $4.41\text{ }\mu\text{m}$ ).

Fig. (6.13) shows the infrared spectra in the mid- and far-infrared regions for glasses of composition  $80\text{TeO}_2-10\text{Na}_2\text{O}-10\text{ZnO}$  mol. %, performed on samples of varying thickness *viz.* 2.98, 0.50 and 0.20 mm. Due to the high extinction coefficients of fundamental absorption bands, thin samples were used to make these more distinguishable.

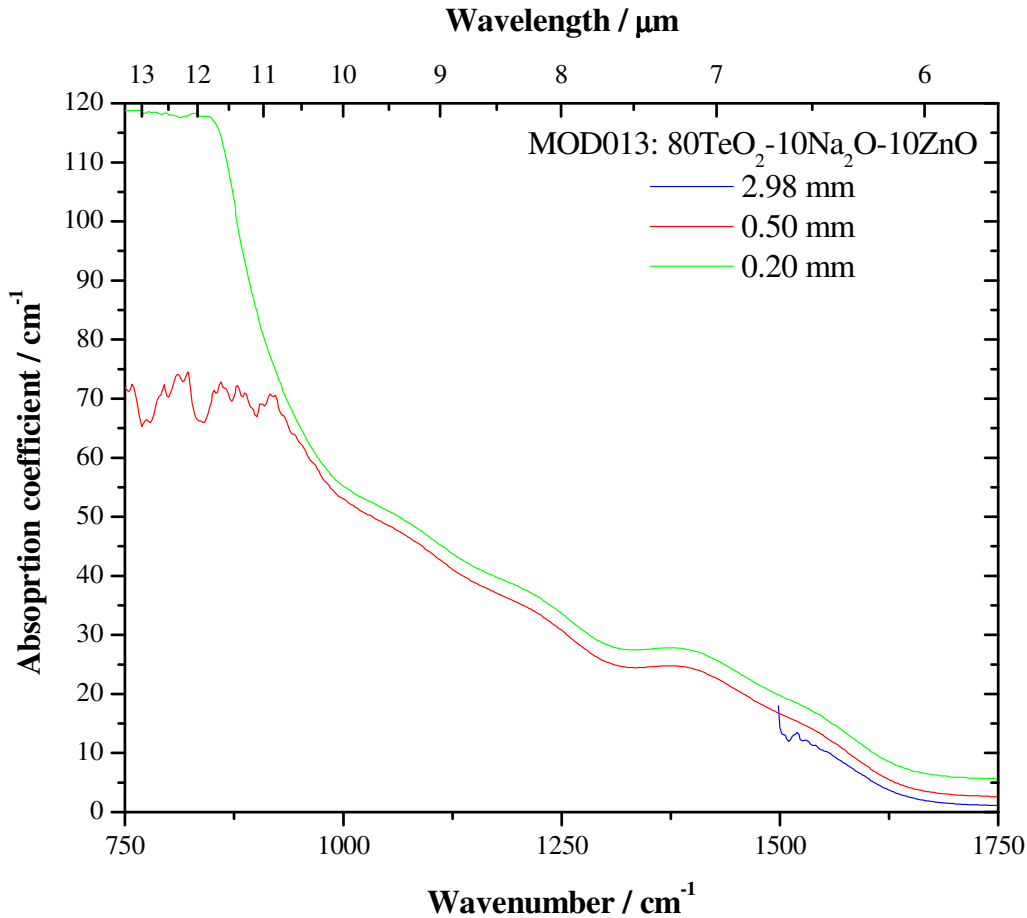


Fig. (6.13): Infrared spectra in the mid- and far-infrared regions for glasses of composition MOD013 (80TeO<sub>2</sub>-10Na<sub>2</sub>O-10ZnO mol. %), performed on samples of thickness, 2.98, 0.50 and 0.20 mm.

From fig. (6.13), it can be seen that the region where spectra were to be collected before the signal become too noisy (i.e. the detector was underloaded), was extended with decreasing thickness of the sample. For the 2.98 mm sample the spectra extended to around 1520 cm<sup>-1</sup> (6.58  $\mu\text{m}$ ), for 0.50 mm to around 920 cm<sup>-1</sup> (10.87  $\mu\text{m}$ ), and for 0.20 mm to around 850 cm<sup>-1</sup> (11.76  $\mu\text{m}$ ). Absorption bands within the multiphonon edge become more easily discernable with decreasing thickness of sample. Fig. (6.14), the bands seen in the multiphonon edge are seen for the 0.20 mm sample.

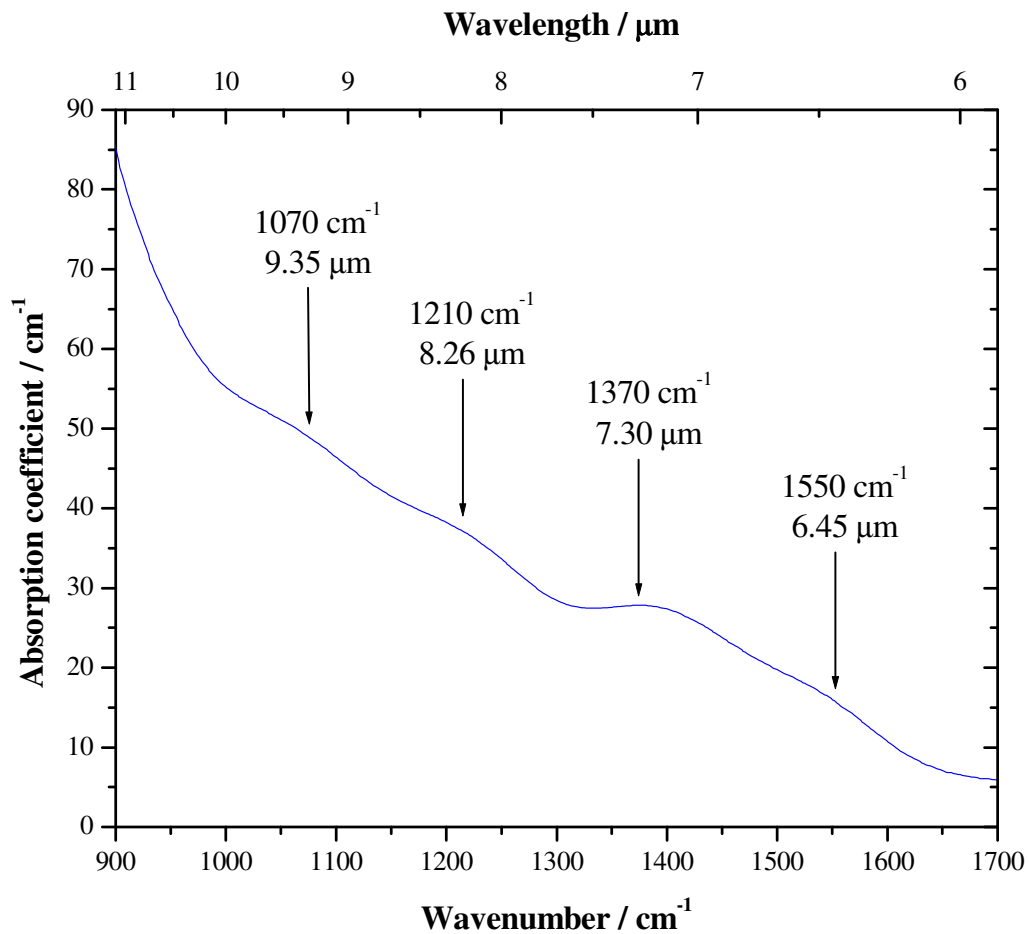


Fig. (6.14): Absorption bands seen in multiphonon edge for 0.20 mm thick sample of glass MOD013 (80TeO<sub>2</sub>-10Na<sub>2</sub>O-10ZnO mol. %).

Fig. (6.15) shows the infrared spectra of the mid- and near-infrared regions for glasses of composition 80TeO<sub>2</sub>-10Na<sub>2</sub>O-10ZnO mol. %, performed on samples of varying thickness (2.98, 0.50 and 0.20 mm).

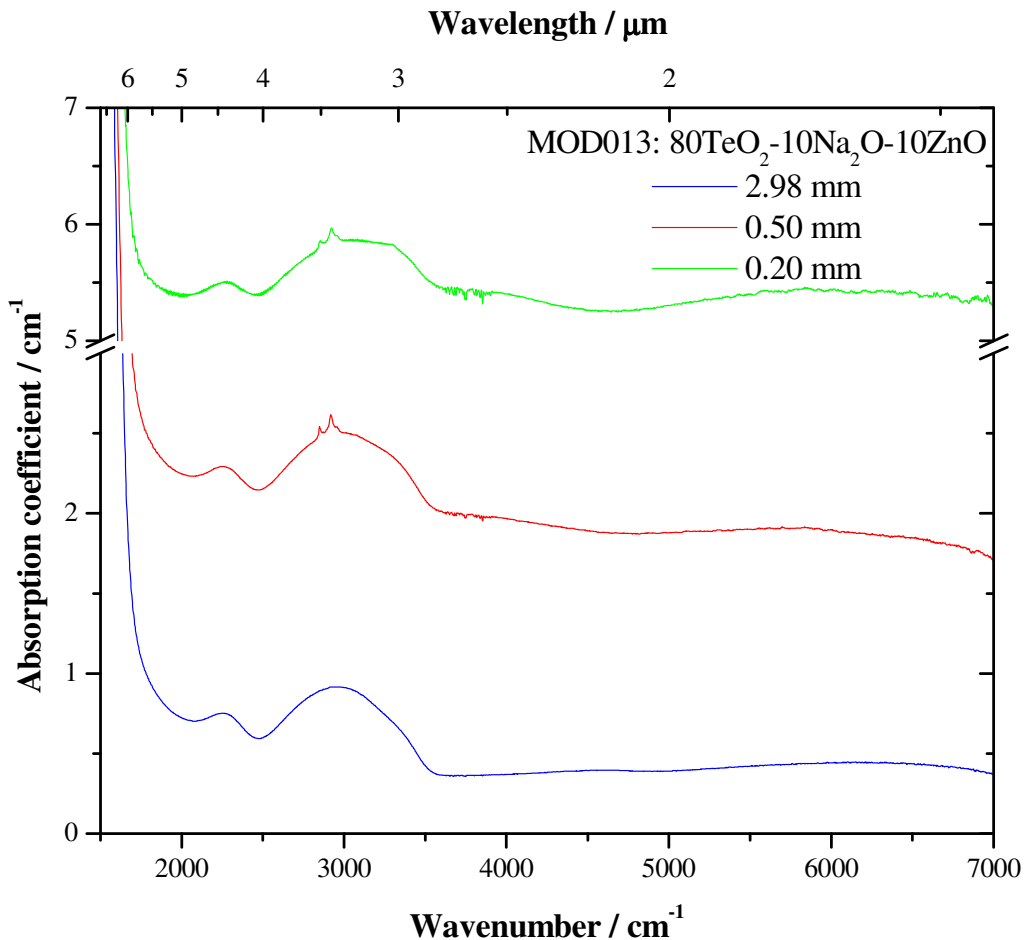


Fig. (6.15): Infrared spectra of the mid- and near-infrared regions for glasses of composition MOD013 80TeO<sub>2</sub>-10Na<sub>2</sub>O-10ZnO mol. %, performed on samples of thickness, 2.98, 0.50 and 0.20 mm.

It can be seen that the glasses background loss increased with decreasing sample thickness. This was likely to be due to deflection of the beam in the spectrometer, arising from the difficulty in making thin samples. The asymmetry of the higher intensity OH band at around 3000 cm<sup>-1</sup> became more prominent with decreasing thickness.

Figs. (6.16) and (6.17) show the Gaussian deconvolution of OH bands in glass MOD007 (78TeO<sub>2</sub>-10Na<sub>2</sub>O-12ZnO mol. %) and MOD013 (80TeO<sub>2</sub>-10Na<sub>2</sub>O-10ZnO mol. %).

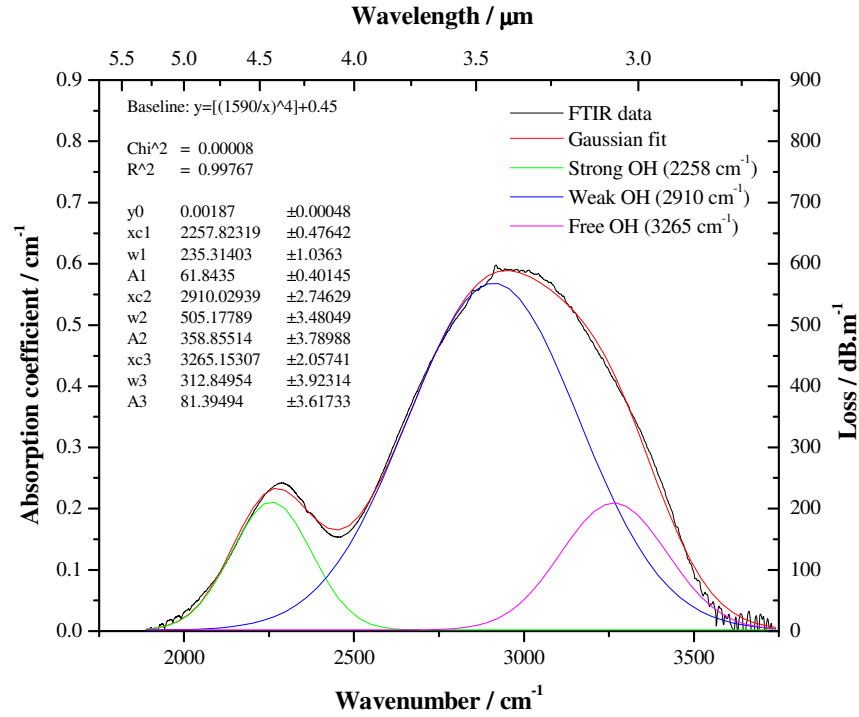


Fig. (6.16): Gaussian deconvolution of OH bands in glass MOD007 (78TeO<sub>2</sub>-10Na<sub>2</sub>O-12ZnO mol. %).

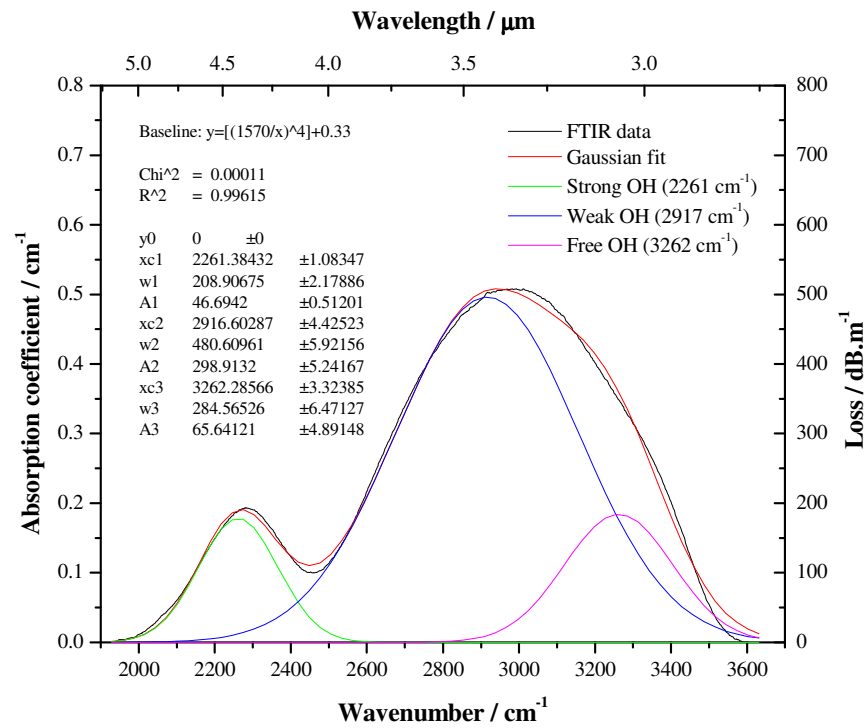


Fig. (6.17): Gaussian deconvolution of OH bands in glass MOD013 (80TeO<sub>2</sub>-10Na<sub>2</sub>O-10ZnO mol. %), thickness 2.98 mm.

Table (6.3) summarises the positions (P), half-widths (W), and areas (A) of these bands.

Table (6.3): Position (P), half-widths (W), and areas (A) of OH bands for glass series  $(90-x)\text{TeO}_2-10\text{Na}_2\text{O}-x\text{ZnO}$  for MOD007 ( $x = 12$  mol. % ZnO), MOD013 ( $x = 10$  mol. % ZnO).

Glass MOD ID	Strong OH			Weak OH			Free OH		
	P / $\text{cm}^{-1}$	W / $\text{cm}^{-1}$	A / $(\text{cm}^{-1})^2$	P / $\text{cm}^{-1}$	W / $\text{cm}^{-1}$	A / $(\text{cm}^{-1})^2$	P / $\text{cm}^{-1}$	W / $\text{cm}^{-1}$	A / $(\text{cm}^{-1})^2$
<b>007</b>	2258	235	62	2910	505	359	3265	313	81
<b>013</b>	2261	209	47	2917	481	299	3262	285	66

Table (6.4) and fig. (6.18) summarise the areas of these bands.

Table (6.4): Percentage of OH groups in glass series  $(90-x)\text{TeO}_2-10\text{Na}_2\text{O}-x\text{ZnO}$  mol. %, for MOD007 ( $x = 12$  mol. % ZnO), MOD013 ( $x = 10$  mol. % ZnO).

Glass MOD ID	Strong OH / %	Weak OH / %	Free OH / %
<b>007</b>	12	71	16
<b>013</b>	11	73	16

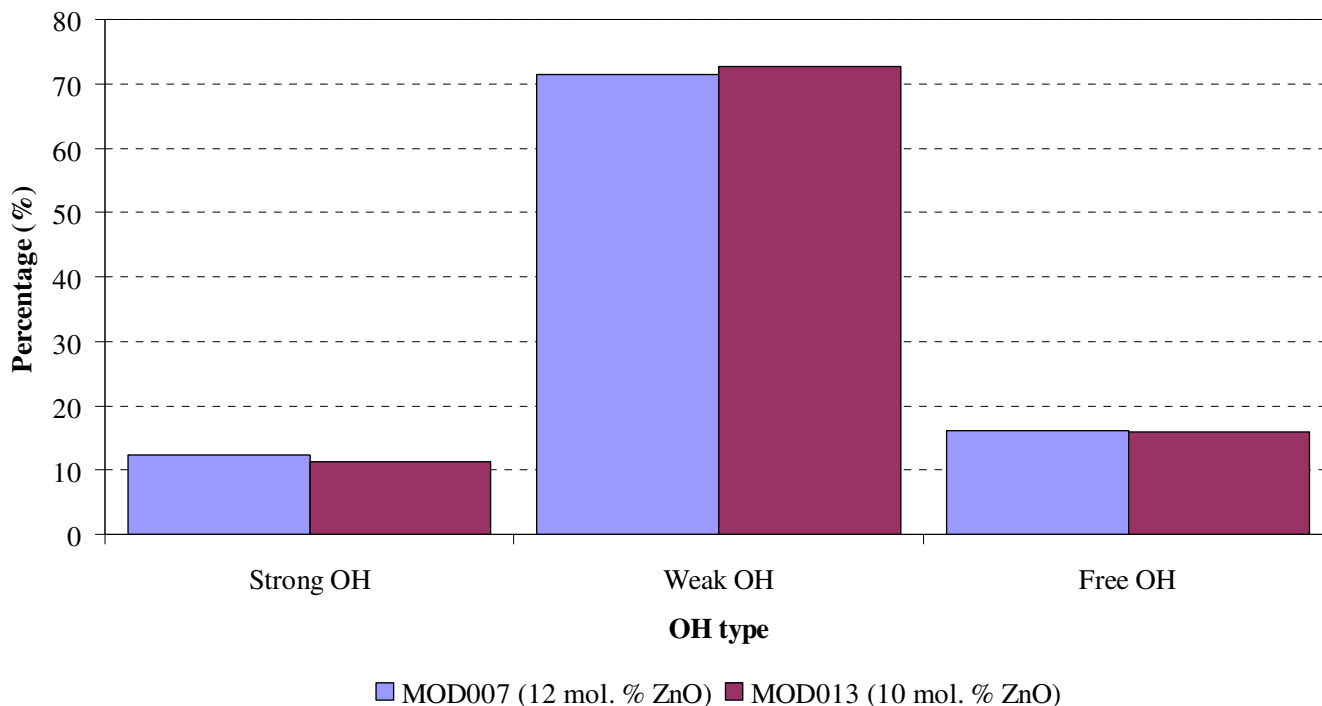


Fig. (6.18): Percentage of OH groups in glass series  $(90-x)\text{TeO}_2-10\text{Na}_2\text{O}-x\text{ZnO}$  mol. %, for MOD007 ( $x = 12$  mol. % ZnO), MOD013 ( $x = 10$  mol. % ZnO).

It can be seen that the amount of each type of OH in glass MOD007 (12 mol. % ZnO) and 2.98 mm MOD013 (10 mol. % ZnO) is approximately the same.

#### *Infrared spectroscopy of $\text{WO}_3$ containing glasses*

Fig. (6.19) shows infrared spectra of glasses MOD014 ( $90\text{TeO}_2-5\text{WO}_3-5\text{Nb}_2\text{O}_5$  mol. %), MOD015 ( $82.5\text{TeO}_2-7.5\text{WO}_3-10\text{Nb}_2\text{O}_5$  mol. %), and MOD016 ( $70\text{TeO}_2-25\text{WO}_3-5\text{Bi}_2\text{O}_3$  mol. %). It can be seen that the multiphonon-edge moves to a higher wavenumber with increasing  $\text{WO}_3$  content. The edge also develops an absorption band which increases in intensity with increasing  $\text{WO}_3$ . Fig. (6.20) shows the multiphonon-edges in detail.

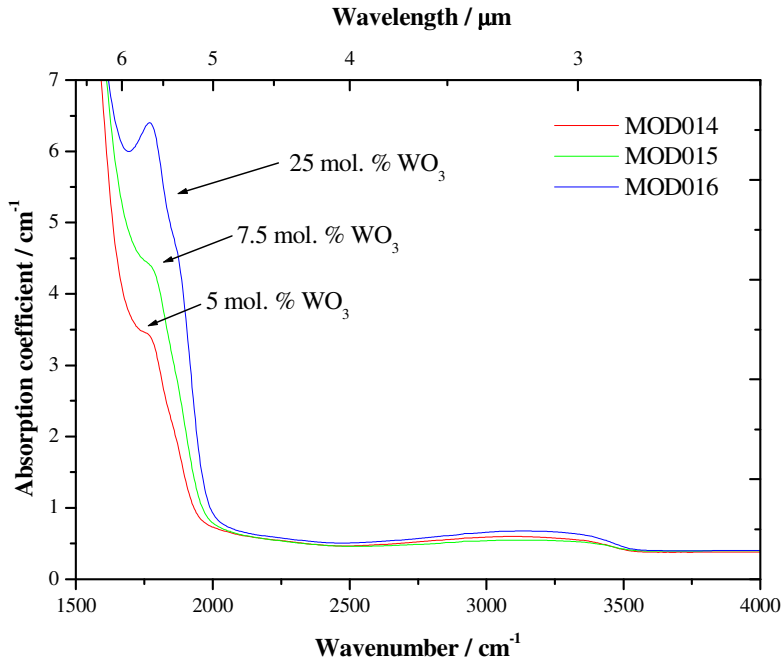


Fig. (6.19): Infrared spectra of glasses MOD014 (90 $\text{TeO}_2$ -5 $\text{WO}_3$ -5 $\text{Nb}_2\text{O}_5$  mol. %), MOD015 (82.5 $\text{TeO}_2$ -7.5 $\text{WO}_3$ -10 $\text{Nb}_2\text{O}_5$  mol. %), and MOD016 (70 $\text{TeO}_2$ -25 $\text{WO}_3$ -5 $\text{Bi}_2\text{O}_3$  mol. %).

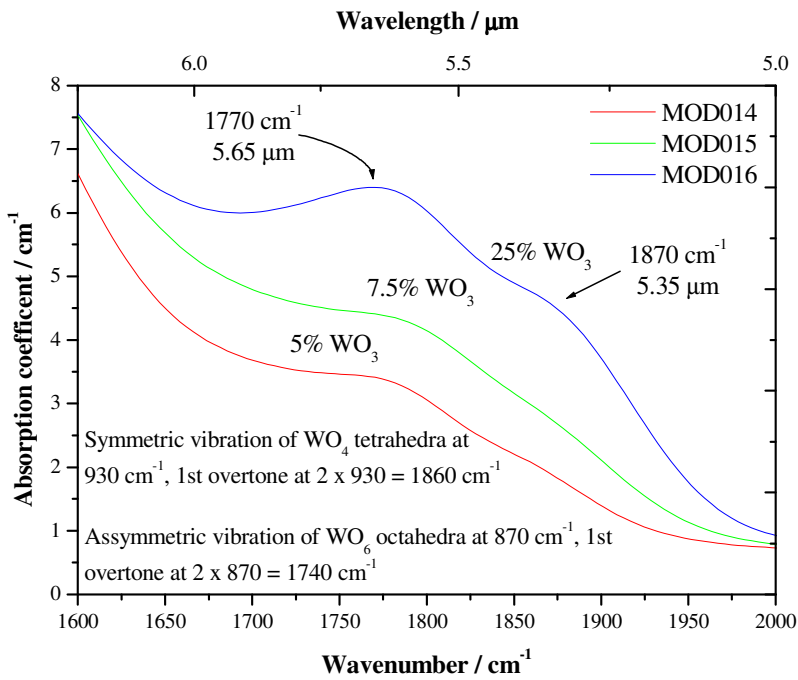


Fig. (6.20): Multiphonon-edges of glasses MOD014 (90 $\text{TeO}_2$ -5 $\text{WO}_3$ -5 $\text{Nb}_2\text{O}_5$  mol. %), MOD015 (82.5 $\text{TeO}_2$ -7.5 $\text{WO}_3$ -10 $\text{Nb}_2\text{O}_5$  mol. %), and MOD016 (70 $\text{TeO}_2$ -25 $\text{WO}_3$ -5 $\text{Bi}_2\text{O}_3$  mol. %).

Fig. (6.21) gives the OH absorption bands for these glasses.

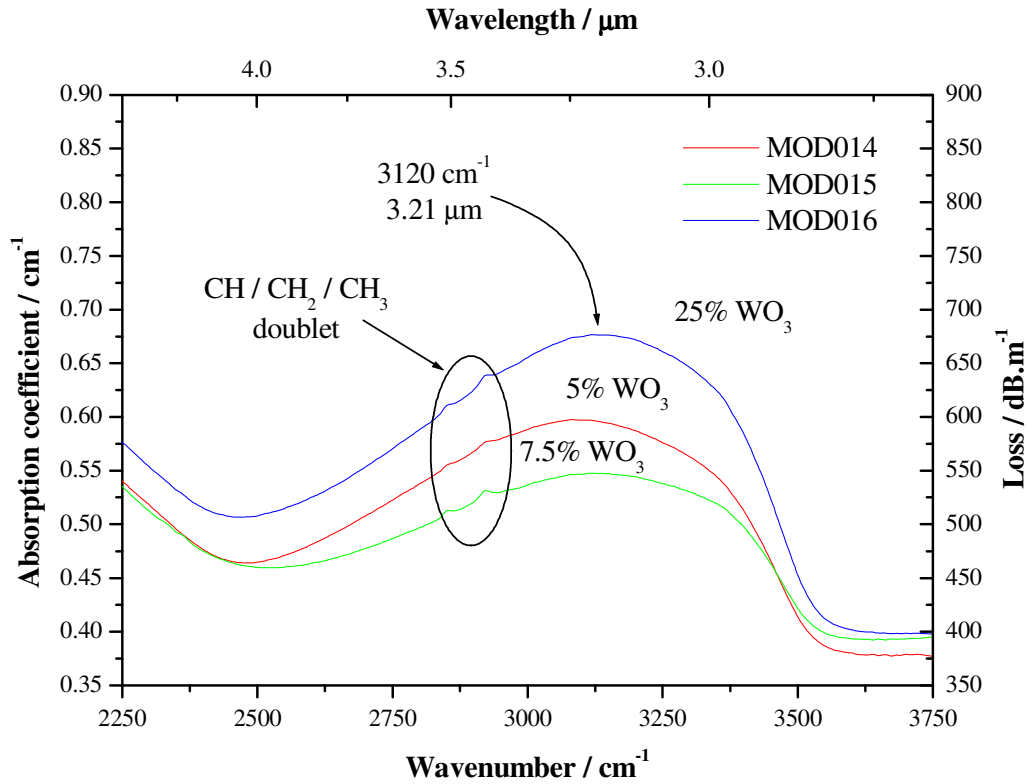


Fig. (6.21): OH absorption bands of glasses MOD014 (90TeO<sub>2</sub>-5WO<sub>3</sub>-5Nb<sub>2</sub>O<sub>5</sub> mol. %), MOD015 (82.5TeO<sub>2</sub>-7.5WO<sub>3</sub>-10Nb<sub>2</sub>O<sub>5</sub> mol. %), and MOD016 (70TeO<sub>2</sub>-25WO<sub>3</sub>-5Bi<sub>2</sub>O<sub>3</sub> mol. %).

Fig. (6.22) to (6.24) show the Gaussian deconvolution of the OH bands of glasses MOD014 (90TeO<sub>2</sub>-5WO<sub>3</sub>-5Nb<sub>2</sub>O<sub>5</sub> mol. %), MOD015 (82.5TeO<sub>2</sub>-7.5WO<sub>3</sub>-10Nb<sub>2</sub>O<sub>5</sub> mol. %), and MOD016 (70TeO<sub>2</sub>-25WO<sub>3</sub>-5Bi<sub>2</sub>O<sub>3</sub> mol. %).

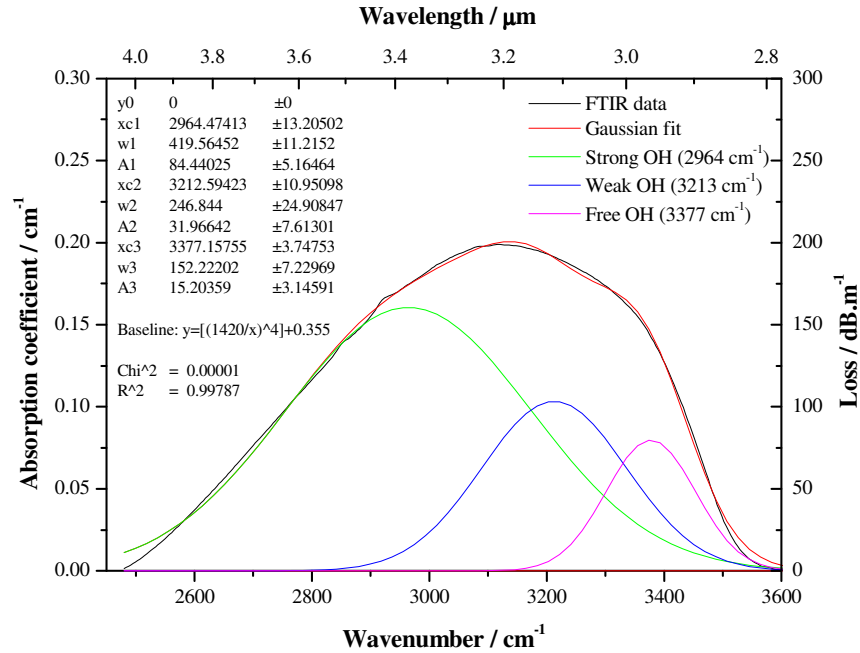


Fig. (6.22): Gaussian deconvolution of the OH bands of glass MOD014 (90TeO<sub>2</sub>-5WO<sub>3</sub>-5Nb<sub>2</sub>O<sub>5</sub> mol. %).

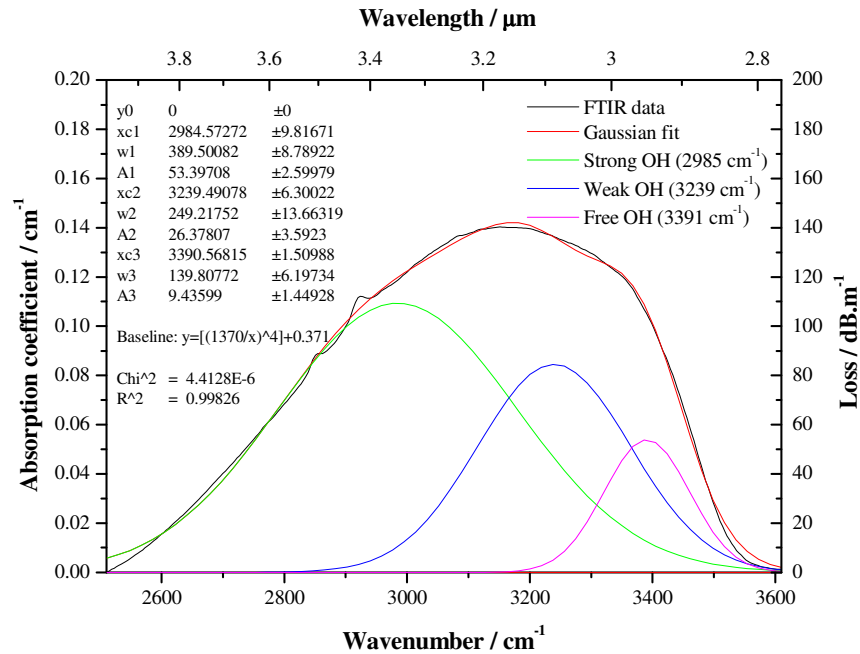


Fig. (6.23): Gaussian deconvolution of the OH bands of glass MOD015 (82.5TeO<sub>2</sub>-7.5WO<sub>3</sub>-10Nb<sub>2</sub>O<sub>5</sub> mol. %).

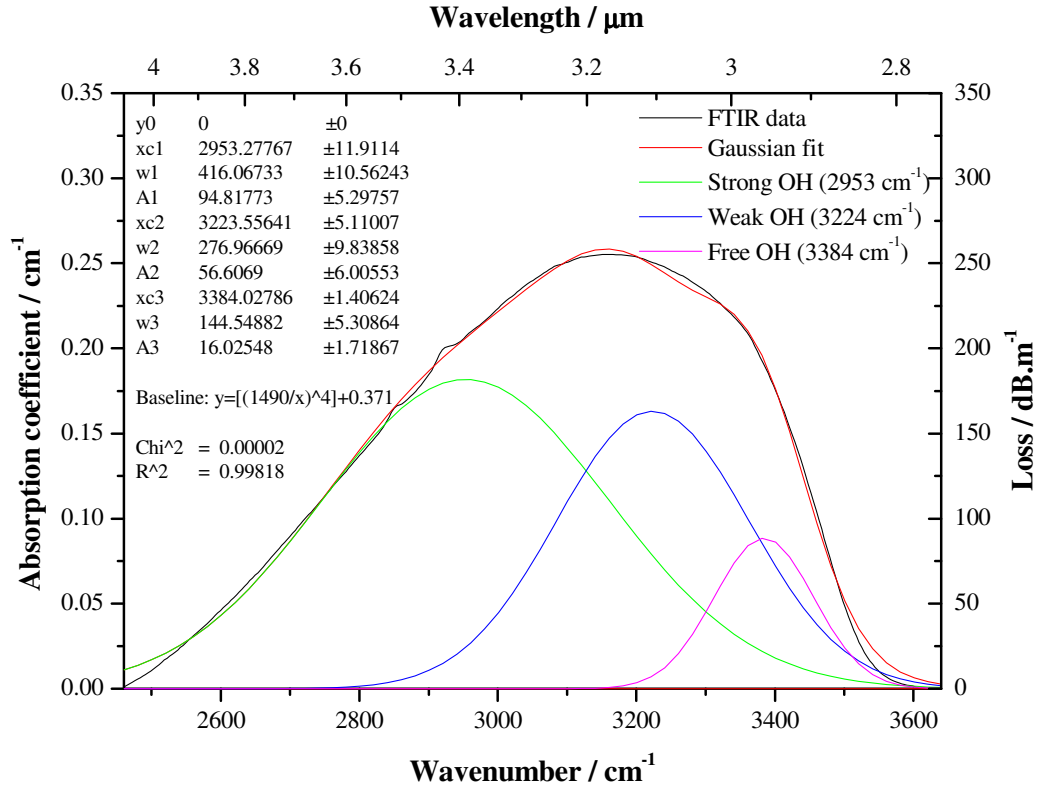


Fig. (6.24): Gaussian deconvolution of the OH bands of glass MOD016 (70TeO<sub>2</sub>-25WO<sub>3</sub>-5Bi<sub>2</sub>O<sub>3</sub> mol. %).

Table (6.5) summarises the positions (P), half-widths (W), and areas (A) of these bands.

Table (6.5): Positions (P), half-widths (W), and areas (A) of OH bands for glasses MOD014 (90TeO<sub>2</sub>-5WO<sub>3</sub>-5Nb<sub>2</sub>O<sub>5</sub> mol. %), MOD015 (82.5TeO<sub>2</sub>-7.5WO<sub>3</sub>-10Nb<sub>2</sub>O<sub>5</sub> mol. %), and MOD016 (70TeO<sub>2</sub>-25WO<sub>3</sub>-5Bi<sub>2</sub>O<sub>3</sub> mol. %).

Glass MOD ID	Strong OH			Weak OH			Free OH		
	P / cm <sup>-1</sup>	W / cm <sup>-1</sup>	A / (cm <sup>-1</sup> ) <sup>2</sup>	P / cm <sup>-1</sup>	W / cm <sup>-1</sup>	A / (cm <sup>-1</sup> ) <sup>2</sup>	P / cm <sup>-1</sup>	W / cm <sup>-1</sup>	A / (cm <sup>-1</sup> ) <sup>2</sup>
<b>014</b>	2964	420	84.44	3213	247	31.97	3377	152	15.20
<b>015</b>	2985	390	53.40	3239	249	26.38	3391	140	9.44
<b>016</b>	2953	416	94.82	3224	277	56.61	3384	145	16.03

Table (6.6) and fig. (6.25) summarise the areas of these bands.

Table (6.5): Percentage of OH groups for glasses MOD014 (90TeO<sub>2</sub>-5WO<sub>3</sub>-5Nb<sub>2</sub>O<sub>5</sub> mol. %), MOD015 (82.5TeO<sub>2</sub>-7.5WO<sub>3</sub>-10Nb<sub>2</sub>O<sub>5</sub> mol. %), and MOD016 (70TeO<sub>2</sub>-25WO<sub>3</sub>-5Bi<sub>2</sub>O<sub>3</sub> mol. %).

Glass MOD ID	Strong OH / %	Weak OH / %	Free OH / %
014	64	24	12
015	60	30	11
016	57	34	10

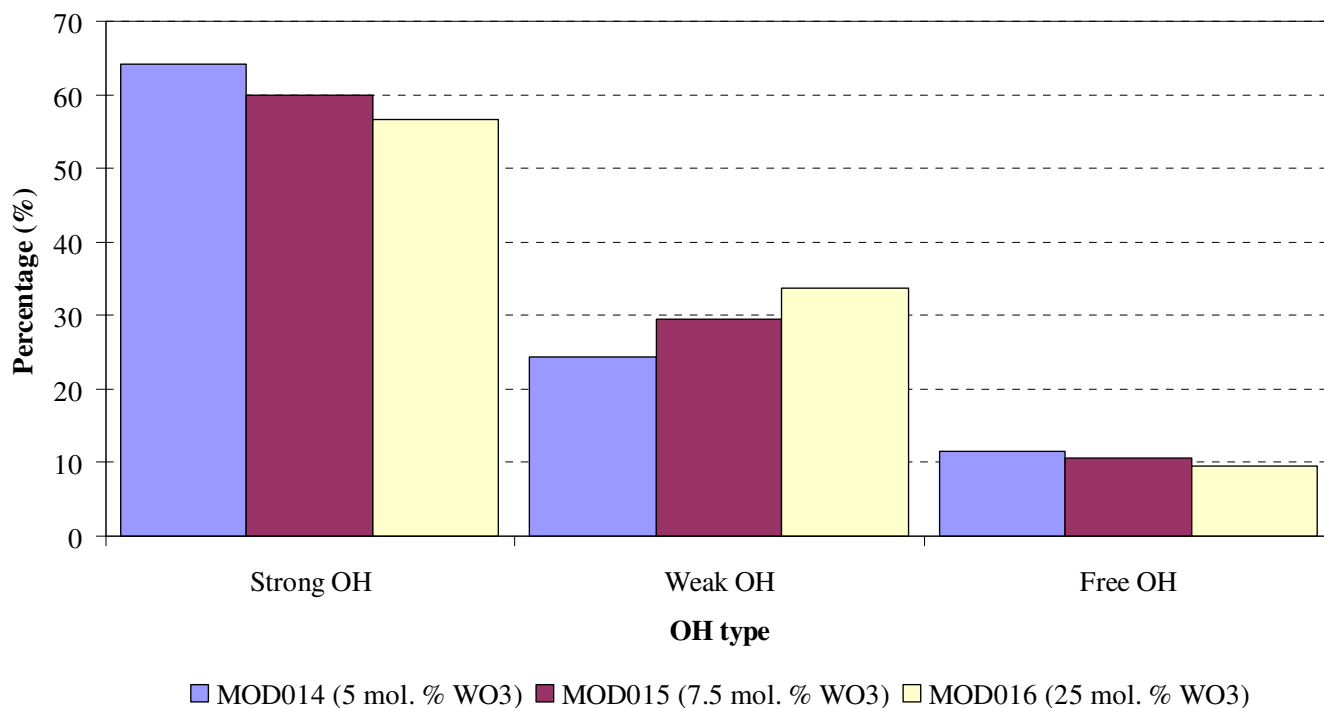


Fig. (6.25): Percentage of OH groups for glasses MOD014 (90TeO<sub>2</sub>-5WO<sub>3</sub>-5Nb<sub>2</sub>O<sub>5</sub> mol. %), MOD015 (82.5TeO<sub>2</sub>-7.5WO<sub>3</sub>-10Nb<sub>2</sub>O<sub>5</sub> mol. %), and MOD016 (70TeO<sub>2</sub>-25WO<sub>3</sub>-5Bi<sub>2</sub>O<sub>3</sub> mol. %).

From table (6.5) and fig. (6.25), it can be seen that the amount of strong and free OH tended to fall with increasing WO<sub>3</sub> content. However, the weakly H-bonded OH did not follow this trend, and increased with WO<sub>3</sub>. These variations may however be smaller than the error introduced from Gaussian fitting the bands.

### 6.2.1.2. Infrared spectroscopy of fluorotellurite glasses

*Infrared spectroscopy of series  $(90-x)\text{TeO}_2-10\text{Na}_2\text{O}-x\text{ZnF}_2$  mol. %, for  $5 \leq x \leq 30$  mol. %*

Fig. (6.26) shows the infrared spectra of glasses of the series  $(90-x)\text{TeO}_2-10\text{Na}_2\text{O}-x\text{ZnF}_2$ , mol. %, for  $5 \leq x \leq 30$  mol. % (glasses MOF001, 004 to 008). Glass MOD013 ( $80\text{TeO}_2-10\text{Na}_2\text{O}-10\text{ZnO}$  mol. %) was also plotted for comparison. The y-axis was splayed, for presentation purposes and hence the numbers on the y-axis only apply to the 30 mol. %  $\text{ZnF}_2$  glass. [5].

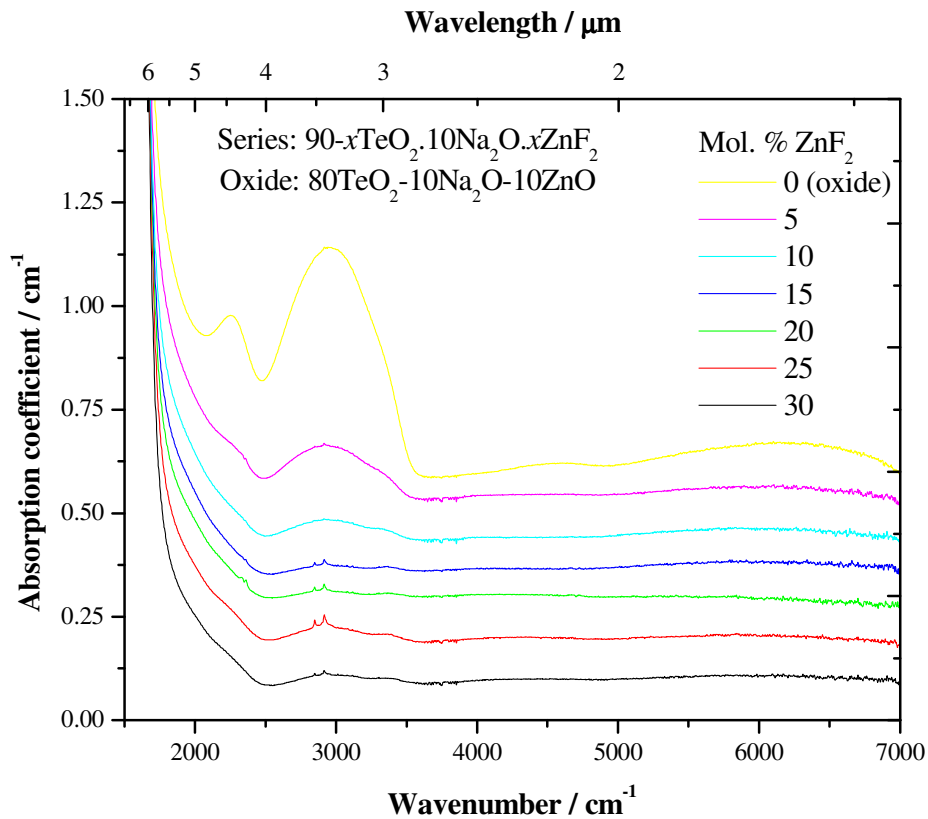


Fig. (6.26): Infrared spectra of glasses of the series  $(90-x)\text{TeO}_2-10\text{Na}_2\text{O}-x\text{ZnF}_2$ , mol. %, for  $5 \leq x \leq 30$  mol. % (glasses MOF001, 004 to 008). Glass MOD013 ( $80\text{TeO}_2-10\text{Na}_2\text{O}-10\text{ZnO}$  mol. %) plotted for comparison [5].

It can be seen there was no lower wavenumber strongly H-bonded OH band for the fluorotellurite glasses at around  $2300\text{ cm}^{-1}$ , or it was enveloped by the multiphonon edge.

It can be seen that the OH absorption bands decrease significantly with increasing  $\text{ZnF}_2$  content. Fig. (6.27) illustrates this trend [5].

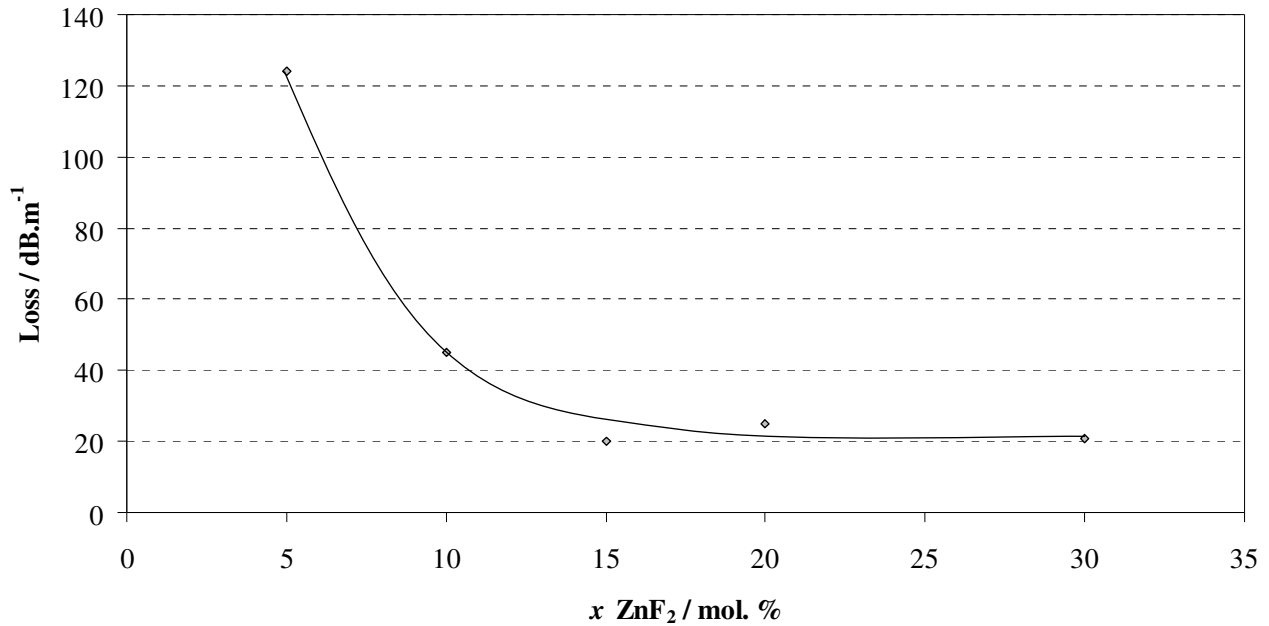


Fig. (6.27): Variation of OH band height peak absorbance at  $2900\text{ cm}^{-1}$  with increasing  $\text{ZnF}_2$  content for glass series  $(90-x)\text{TeO}_2-10\text{Na}_2\text{O}-x\text{ZnF}_2$ , mol. %, for  $5 \leq x \leq 30$  mol. % (glasses MOF001, 004 to 008, with background loss removed) [5].

It can be seen that absorption due to the OH band decreased with increasing  $\text{ZnF}_2$  in the glass, reaching a minimum of around  $20\text{ dB.m}^{-1}$  for glasses containing  $> 15$  mol. %  $\text{ZnF}_2$ .

Fig. (6.28) shows the variation in this band with melting time for glass MOF001 ( $65\text{TeO}_2-10\text{Na}_2\text{O}-25\text{ZnF}_2$  mol. %).

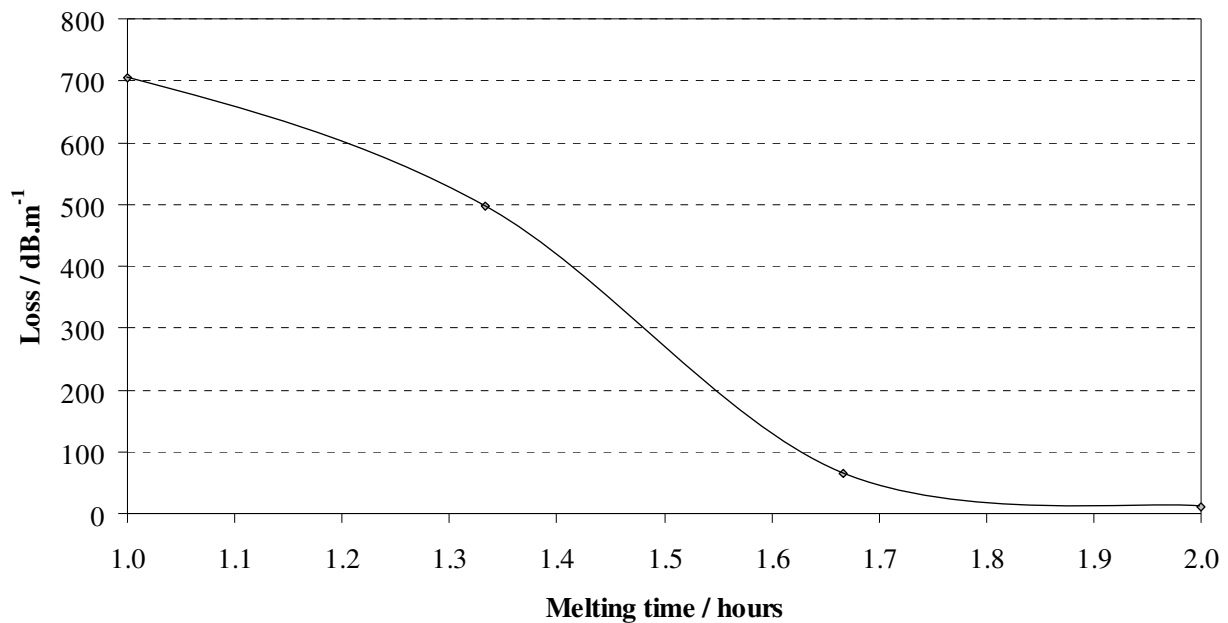


Fig. (6.28): Variation of OH band height at around  $2900\text{ cm}^{-1}$  with increasing melting time for glass MOF001 ( $65\text{TeO}_2\text{-}10\text{Na}_2\text{O-}25\text{ZnF}_2$  mol. %) [5].

It can be seen that absorption due to OH bands in the glass decreased with increasing melting time, and were as low as  $10\text{ dB.m}^{-1}$  after 2 hours, around seven times lower than for 1 hour of melting ( $705\text{ dB.m}^{-1}$ ).

Fig. (6.29) to (6.34) show the Gaussian deconvolution of the OH bands for glasses of the series  $(90-x)\text{TeO}_2\text{-}10\text{Na}_2\text{O-}x\text{ZnF}_2$ , mol. %, for  $5 \leq x \leq 30$  mol. % (glasses MOF001, 004 to 008).

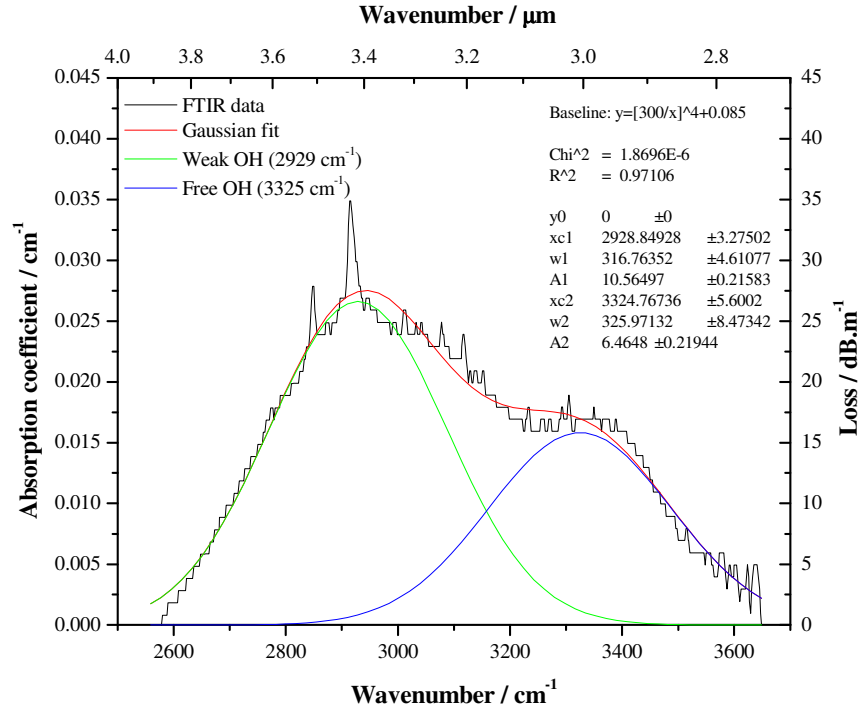


Fig. (6.29) shows the Gaussian deconvolution of the OH bands for glass MOF004 ( $60\text{TeO}_2\text{-}10\text{Na}_2\text{O-}30\text{ZnF}_2$  mol. %).

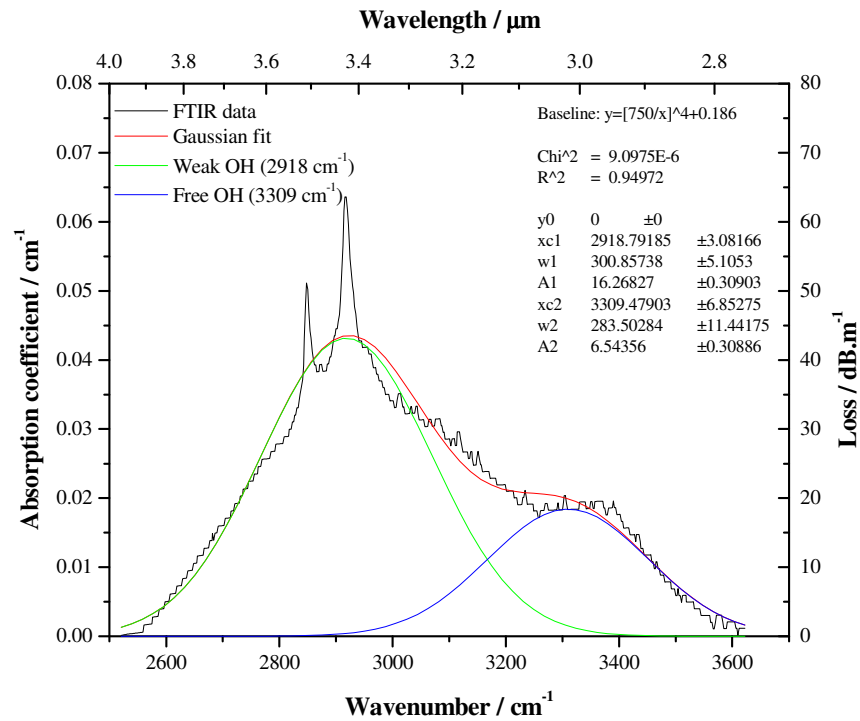


Fig. (6.30) shows the Gaussian deconvolution of the OH bands for glass MOF001 ( $65\text{TeO}_2\text{-}10\text{Na}_2\text{O-}25\text{ZnF}_2$  mol. %).

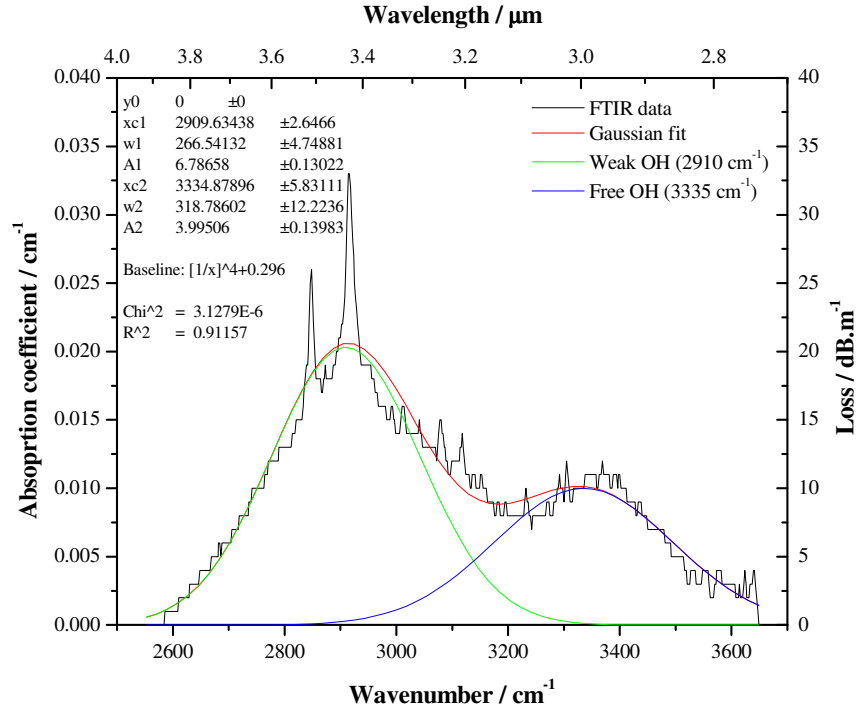


Fig. (6.31): Gaussian deconvolution of the OH bands for glass MOF005 (70TeO<sub>2</sub>-10Na<sub>2</sub>O-20ZnF<sub>2</sub> mol. %).

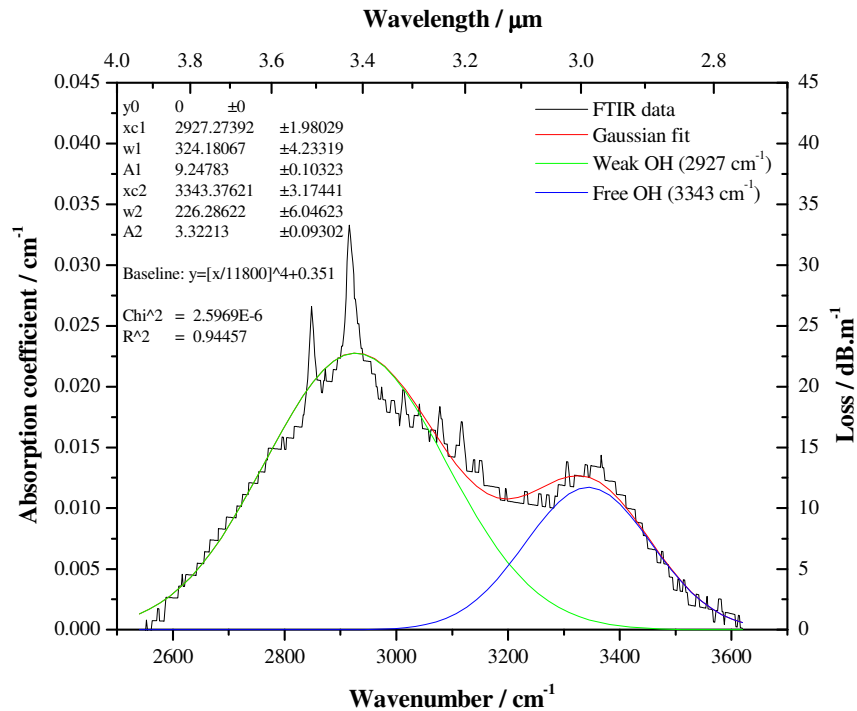


Fig. (6.32) shows the Gaussian deconvolution of the OH bands for glass MOF006 (75TeO<sub>2</sub>-10Na<sub>2</sub>O-15ZnF<sub>2</sub> mol. %).

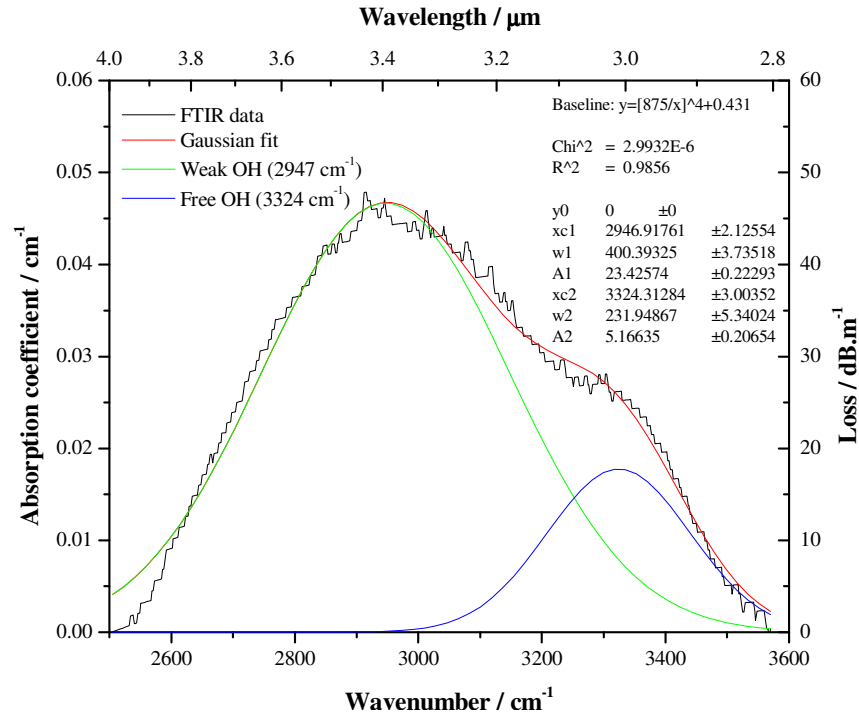


Fig. (6.33): Gaussian deconvolution of the OH bands for glass MOF007 (80TeO<sub>2</sub>-10Na<sub>2</sub>O-10ZnF<sub>2</sub> mol. %).

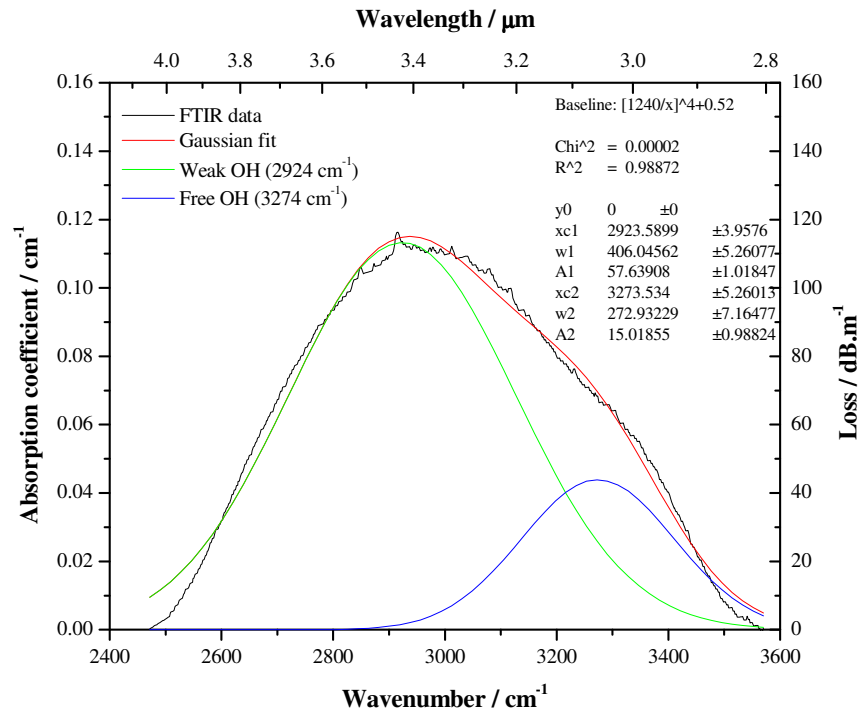


Fig. (6.34): Gaussian deconvolution of the OH bands for glass MOF008 (85TeO<sub>2</sub>-10Na<sub>2</sub>O-5ZnF<sub>2</sub> mol. %).

Table (6.7) summarises the positions (P), half-widths (W), and areas (A) of these bands.

Table (6.7): Positions (P), half-widths (W), and areas (A) of OH bands for glasses of the series  $(90-x)\text{TeO}_2-10\text{Na}_2\text{O}-x\text{ZnF}_2$ , mol. %, for  $5 \leq x \leq 30$  mol. % (glasses MOF001, 004 to 008).

Glass MOF ID	$x \text{ ZnF}_2 / \text{mol. \%}$	Weak OH			Free OH		
		P / $\text{cm}^{-1}$	W / $\text{cm}^{-1}$	A / $(\text{cm}^{-1})^2$	P / $\text{cm}^{-1}$	W / $\text{cm}^{-1}$	A / $(\text{cm}^{-1})^2$
<b>004</b>	30	2929	317	11	3325	326	6
<b>001</b>	25	2919	301	16	3309	284	7
<b>005</b>	20	2910	267	7	3335	319	4
<b>006</b>	15	2927	324	9	3343	226	3
<b>007</b>	10	2947	400	23	3324	232	5
<b>008</b>	5	2924	406	58	3274	273	15

Table (6.8) and fig. (6.35) summarise the areas of these bands.

Table (6.8): Percentage of OH groups for glasses of the series  $(90-x)\text{TeO}_2-10\text{Na}_2\text{O}-x\text{ZnF}_2$ , mol. %, for  $5 \leq x \leq 30$  mol. % (glasses MOF001, 004 to 008).

Glass MOF ID	$x \text{ ZnF}_2 / \text{mol. \%}$	Weak OH / %	Free OH / %
<b>004</b>	30	62	38
<b>001</b>	25	71	29
<b>005</b>	20	63	37
<b>006</b>	15	74	26
<b>007</b>	10	82	18
<b>008</b>	5	79	21

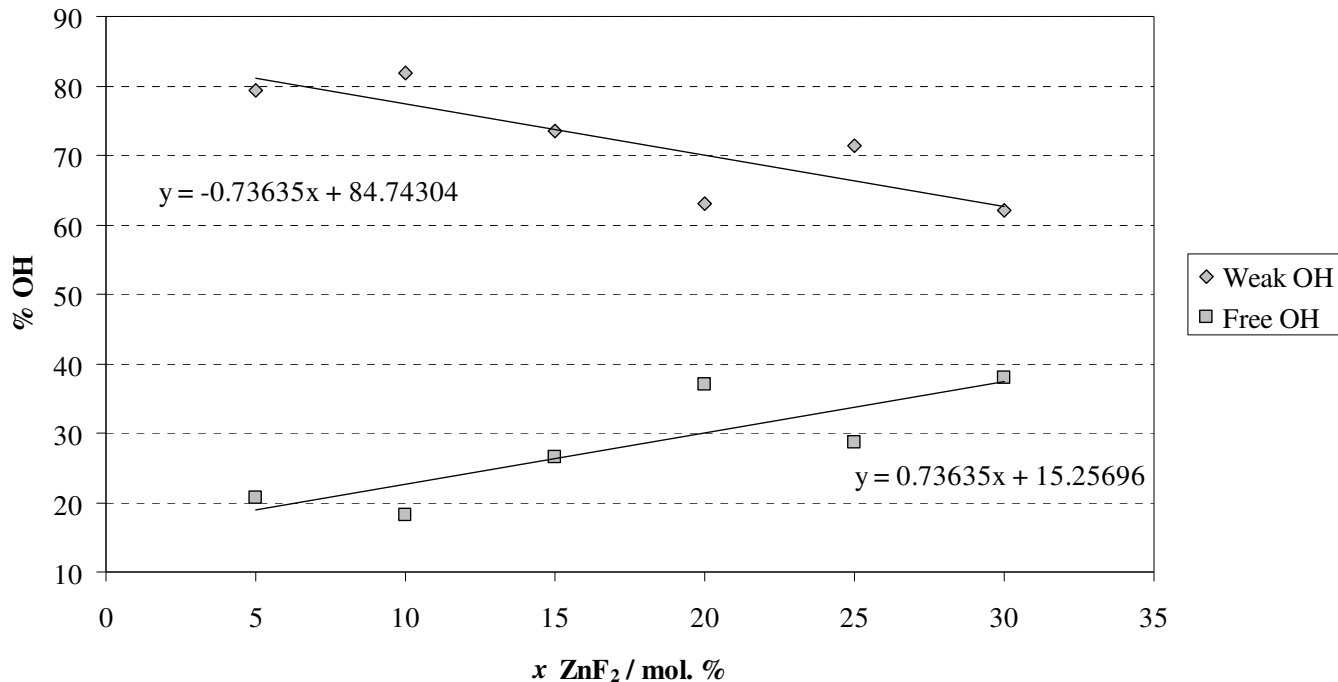


Fig. (6.35): Percentage of weakly H-bonded OH and free OH groups for glasses of the series  $(90-x)\text{TeO}_2-10\text{Na}_2\text{O}-x\text{ZnF}_2$ , mol. %, for  $5 \leq x \leq 30$  mol. % (MOF001, 004 to 008).

It can be seen there was a general decrease in weak and an increase in free OH with increasing  $\text{ZnF}_2$  content.

*Infrared spectroscopy of series 65 mol. %, for  $5 \leq x \leq 30$  mol. %*

Fig. (6.36) shows the infrared spectra of glasses MOF009 to 013 which were part of the series  $65\text{TeO}_2-(25-x)\text{ZnF}_2-x\text{ZnO}-10\text{Na}_2\text{O}$  mol. %, for  $5 \leq x \leq 25$  mol. %. The y-axis was splayed for display purposes, hence numbers on the y-axis refer only to the spectrum of the  $x = 5$  glass, but the divisions on the y-axis apply to all.

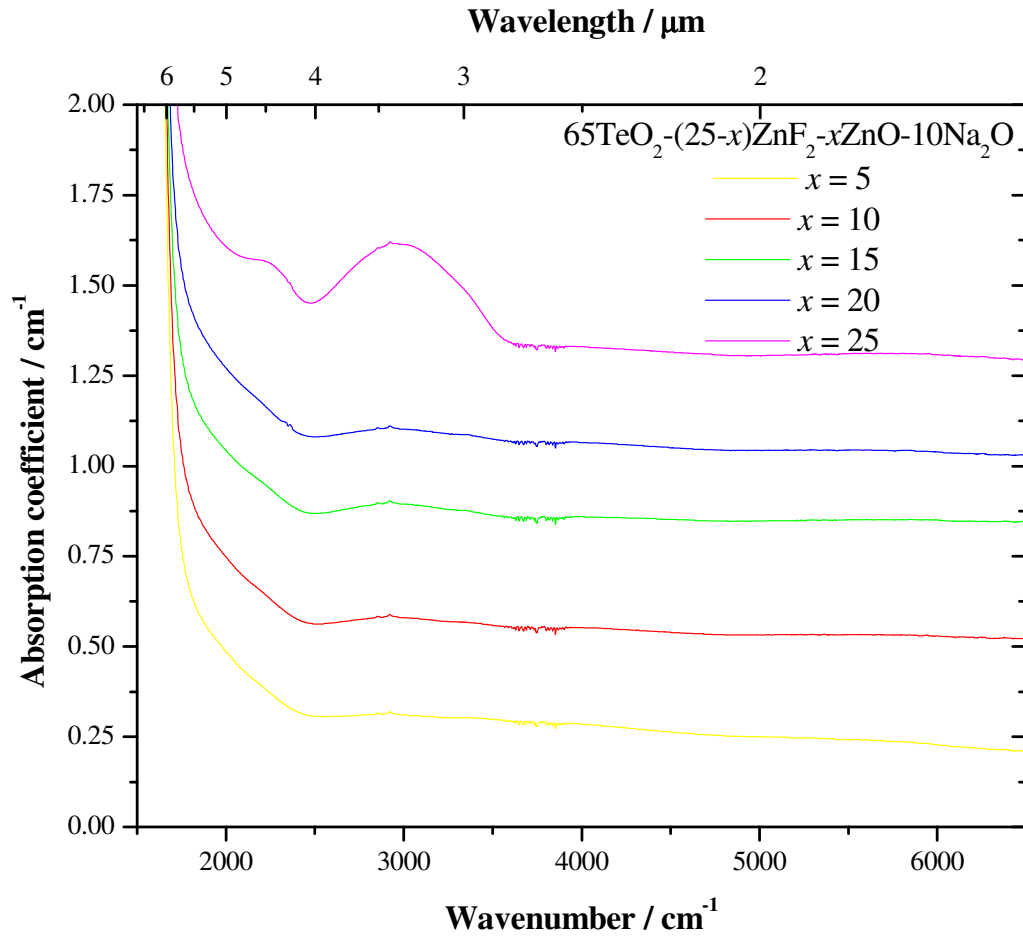


Fig. (6.36): Infrared spectra of glasses MOF009 to 013 of series  $65\text{TeO}_2-(25-x)\text{ZnF}_2-x\text{ZnO}-10\text{Na}_2\text{O}$  mol. %, for  $5 \leq x \leq 25$  mol. %.

Fig. (6.37) to (4.41) show the Gaussian deconvolution of the OH bands in glasses MOF009 to 013 which were part of the series  $65\text{TeO}_2-(25-x)\text{ZnF}_2-x\text{ZnO}-10\text{Na}_2\text{O}$  mol. %, for  $5 \leq x \leq 25$  mol. %..

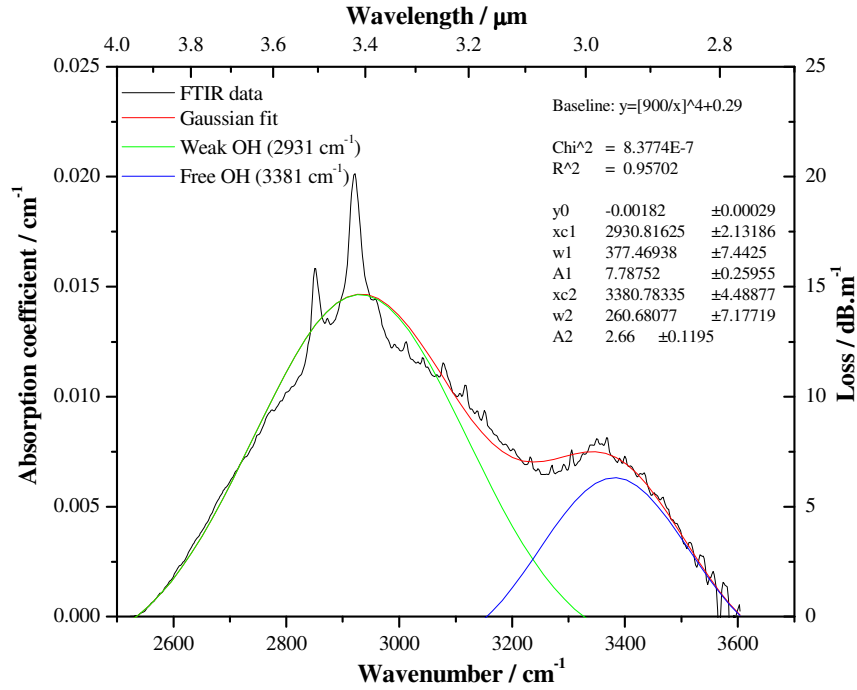


Fig. (6.37): Gaussian deconvolution of the OH bands in glass MOF009 (65TeO<sub>2</sub>-20ZnF<sub>2</sub>-5ZnO-10Na<sub>2</sub>O mol. %).

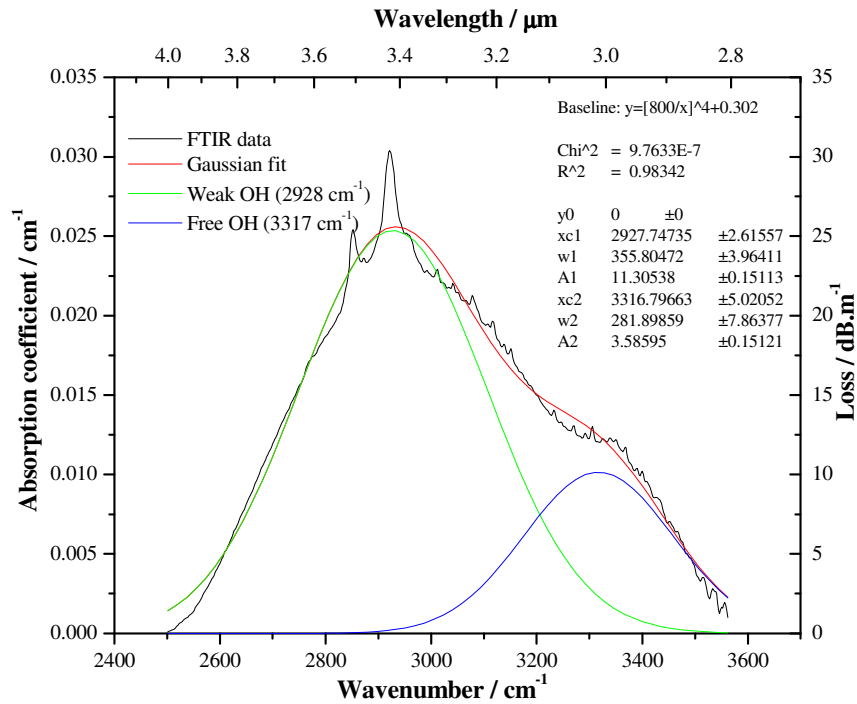


Fig. (6.38): Gaussian deconvolution of OH bands in glass MOF010 (65TeO<sub>2</sub>-15ZnF<sub>2</sub>-10ZnO-10Na<sub>2</sub>O mol. %).

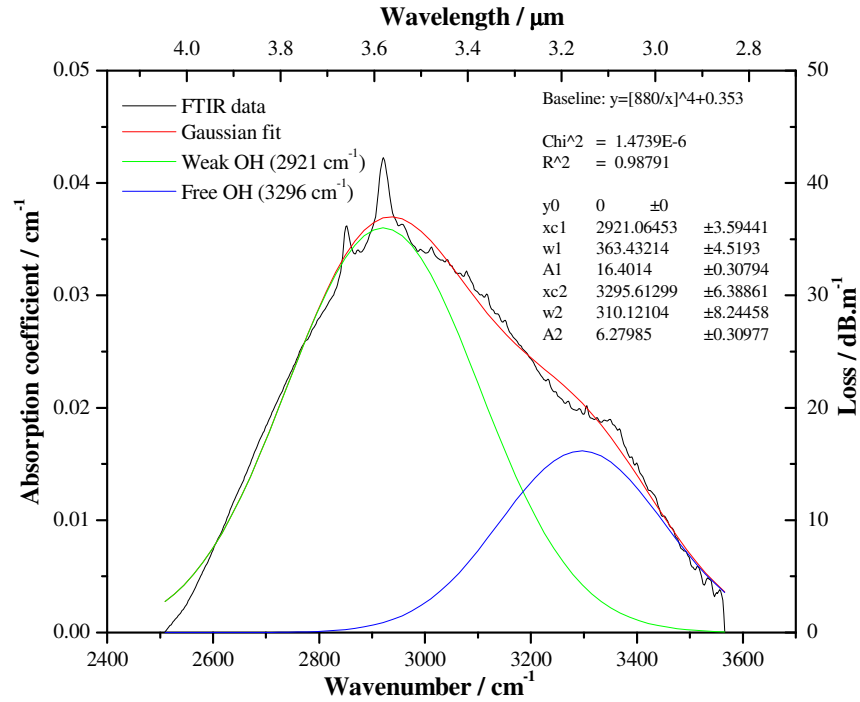


Fig. (6.39): Gaussian deconvolution of OH bands in glass MOF011 ( $65\text{TeO}_2\text{-}10\text{ZnF}_2\text{-}15\text{ZnO-}10\text{Na}_2\text{O}$  mol. %).

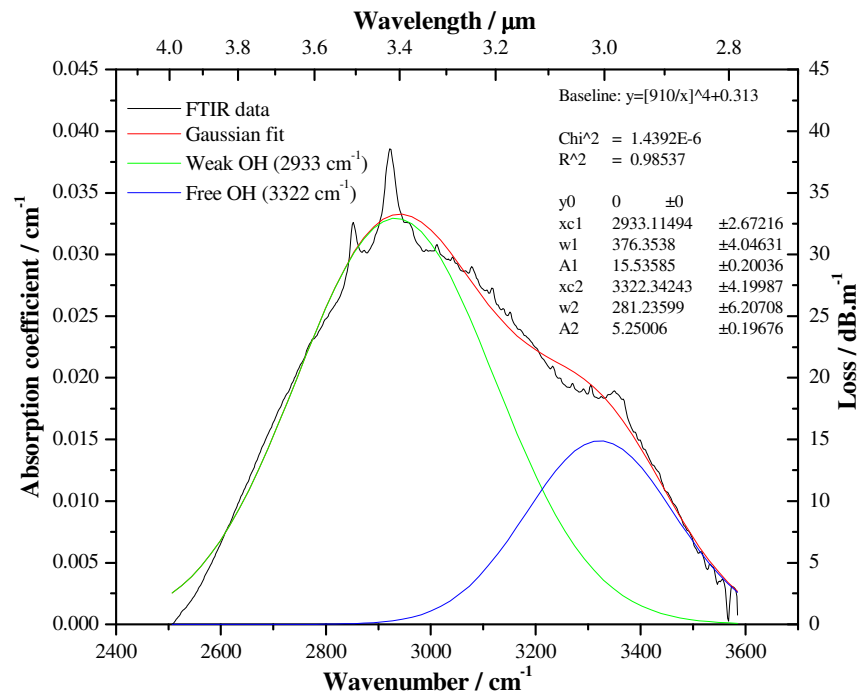


Fig. (6.40): Gaussian deconvolution of OH bands in glass MOF012 ( $65\text{TeO}_2\text{-}5\text{ZnF}_2\text{-}20\text{ZnO-}10\text{Na}_2\text{O}$  mol. %).

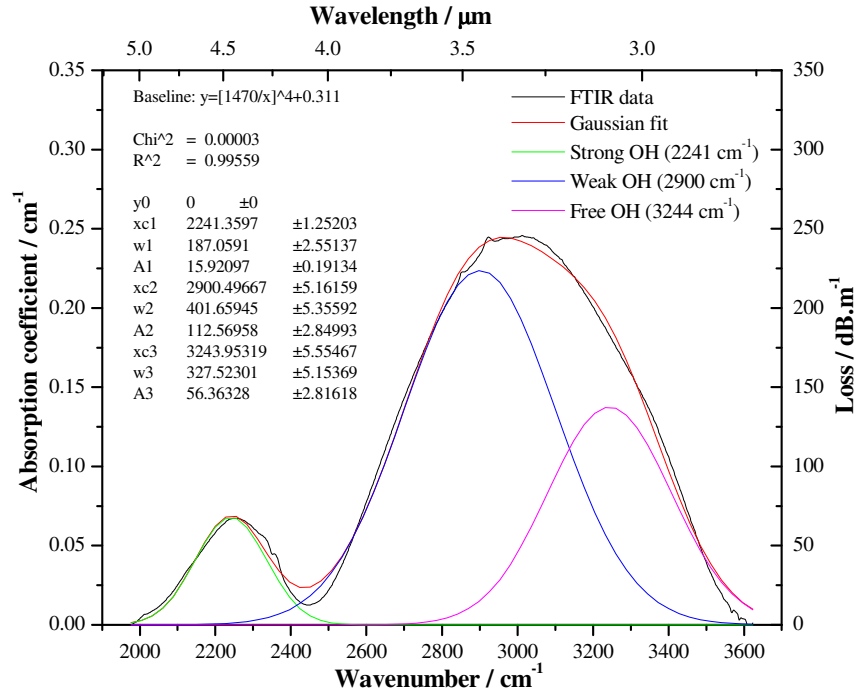


Fig. (6.41) shows the Gaussian deconvolution of the OH bands in glass MOF013 (65TeO<sub>2</sub>-25ZnO-10Na<sub>2</sub>O mol. %).

It can be seen that the ZnF<sub>2</sub> containing glasses (fig. (6.37) to (6.40)) did not exhibit a strongly H-bonded OH band, whereas the oxide glasses did (fig. (6.41)).

Fig. (6.42) shows the variation of OH band height peak absorbance at around 2900 cm<sup>-1</sup> (weakly H-bonded OH) with increasing ZnO / ZnF<sub>2</sub> ratio. Table (6.9) summarises the positions (P), half-widths (W), and areas (A) of these bands.

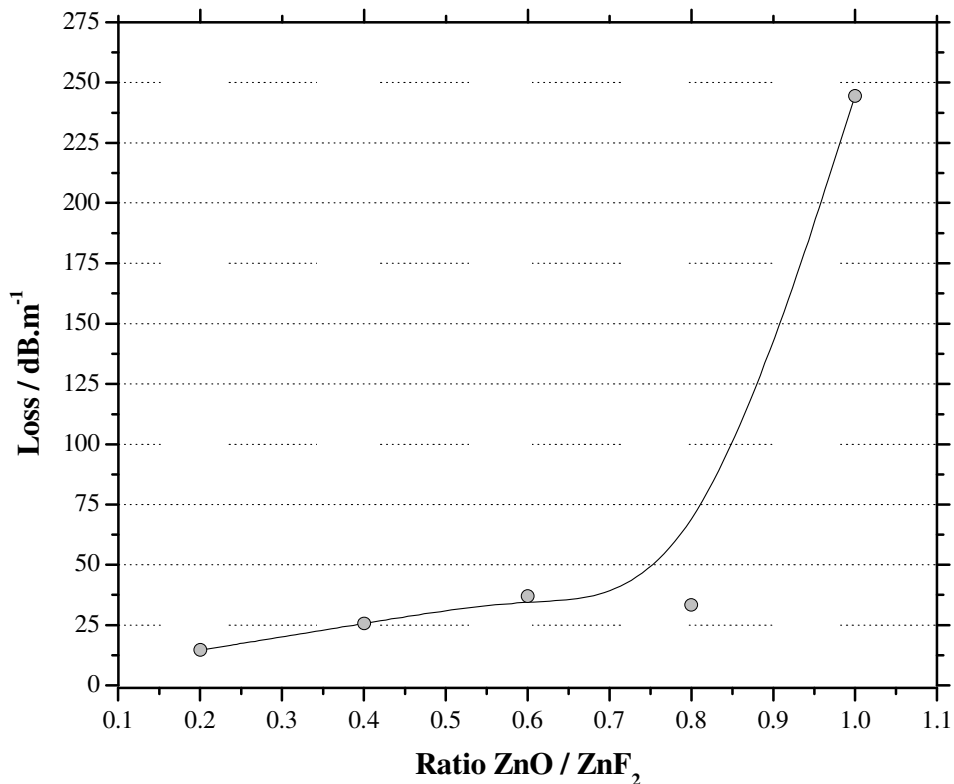


Fig. (6.42): Variation of OH band height peak absorbance at around  $2900\text{ cm}^{-1}$  with increasing ZnO / ZnF<sub>2</sub> ratio for glasses of the series  $65\text{TeO}_2-(25-x)\text{ZnF}_2-x\text{ZnO}-10\text{Na}_2\text{O}$  mol. %, for  $5 \leq x \leq 25$  mol. % (MOF009 to 013).

Table (6.9): Positions (P), half-widths (W), and areas (A) of OH bands of the series  $65\text{TeO}_2-(25-x)\text{ZnF}_2-x\text{ZnO}-10\text{Na}_2\text{O}$  mol. %, for  $5 \leq x \leq 25$  mol. % (MOF009 to 013).

Glass MOF ID	ZnO / ZnF <sub>2</sub> ratio	Weak OH			Free OH		
		P / cm <sup>-1</sup>	W / cm <sup>-1</sup>	A / (cm <sup>-1</sup> ) <sup>2</sup>	P / cm <sup>-1</sup>	W / cm <sup>-1</sup>	A / (cm <sup>-1</sup> ) <sup>2</sup>
<b>009</b>	0.2	2931	377	8	3381	261	3
<b>010</b>	0.4	2928	356	11	3317	282	4
<b>011</b>	0.6	2921	363	16	3296	310	6
<b>012</b>	0.8	2933	376	16	3322	281	5
<b>013</b>	1.0	2900	402	113	3244	328	56

Fig. (6.43) and table (6.10) summarises these areas.

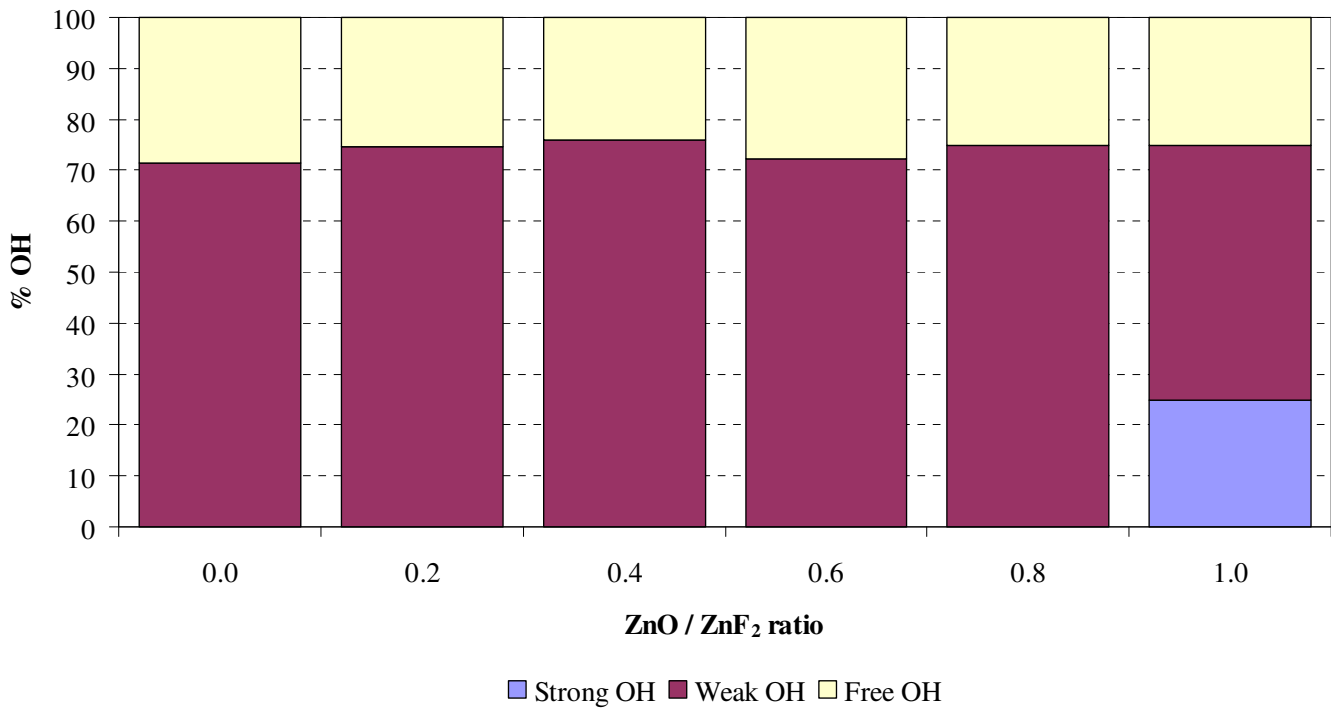


Fig. (6.43): Percentage of OH groups for glasses of the series  $65\text{TeO}_2-(25-x)\text{ZnF}_2-x\text{ZnO}-10\text{Na}_2\text{O}$  mol. %, for  $5 \leq x \leq 25$  mol. % (MOF009 to 013).

Table (6.10): Percentage of OH groups for glasses of the series  $65\text{TeO}_2-(25-x)\text{ZnF}_2-x\text{ZnO}-10\text{Na}_2\text{O}$  mol. %, for  $5 \leq x \leq 25$  mol. % (MOF009 to 013).

Glass MOF ID	ZnO / ZnF <sub>2</sub> ratio	Strong OH / %	Weak OH / %	Free OH / %
<b>001</b>	0.0	-	71	29
<b>009</b>	0.2	-	75	25
<b>010</b>	0.4	-	76	24
<b>011</b>	0.6	-	72	28
<b>012</b>	0.8	-	75	25
<b>013</b>	1.0	25	50	25

### 6.2.1.3. Spectroscopy of $\text{Er}^{+3}$ -doped composition

When a glass host which transmits in the NIR region is doped with erbium, emission bands are seen in this region (around  $1.5 \mu\text{m}$ ) due to the large number of energy levels of the  $\text{Er}^{+3}$  ion (such as  ${}^4\text{I}_{15/2} \rightarrow {}^4\text{I}_{13/2}$ ). This phenomenon can be used to amplify signals carried by the glass in this important telecommunications window. Doping of fluorotellurite glass compositions was investigated here. The glasses were heat treated to investigate possible modification of the erbium bands with time and temperature.

Fig. (6.44) shows the near-IR spectra of glass MOF017 ( $69.86\text{TeO}_2\text{-}9.98\text{Na}_2\text{O-}19.96\text{ZnF}_2\text{-}0.20\text{ErF}_3$  mol. %) as-annealed, and heat treated for 1 hour at 245, 255, 265 and 275°C.

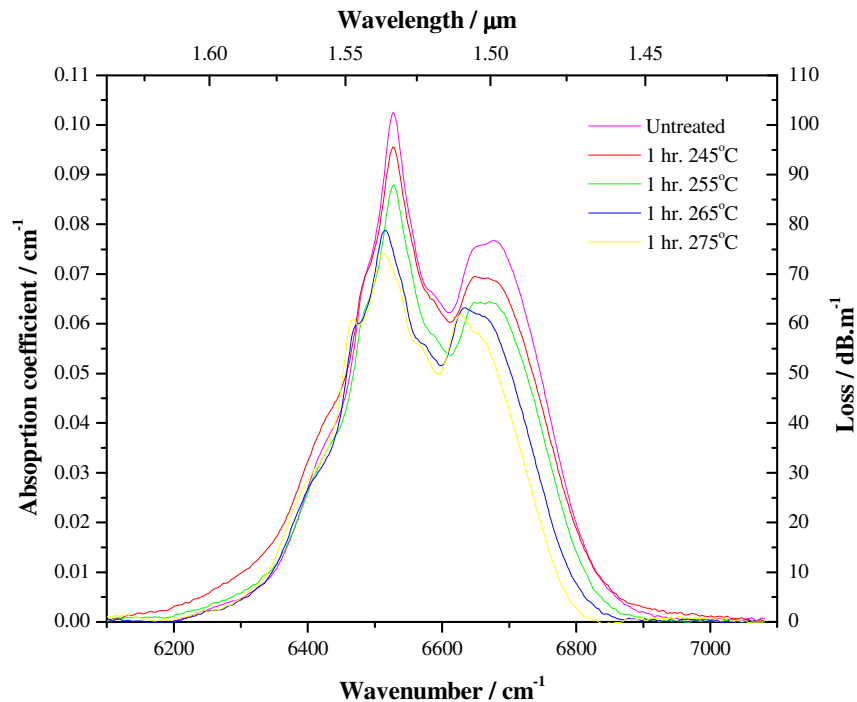


Fig. (6.44): Near-IR spectra of glass MOF017 ( $69.86\text{TeO}_2\text{-}9.98\text{Na}_2\text{O-}19.96\text{ZnF}_2\text{-}0.20\text{ErF}_3$  mol. %) untreated, and heat treated for 1 hour at 245, 255, 265 and 275°C.

It can be seen that the bands due to  $\text{Er}^{+3}$  shifted to lower wavenumber with increasing temperature. The underlying structure of the bands also became more distinct with increasing temperature.

Fig. (6.45) shows the near-IR spectra of glass MOF017 ( $69.86\text{TeO}_2\text{-}9.98\text{Na}_2\text{O-}19.96\text{ZnF}_2\text{-}0.20\text{ErF}_3$  mol. %) heat treated for 1, 5 and 11 hours at  $240^\circ\text{C}$ .

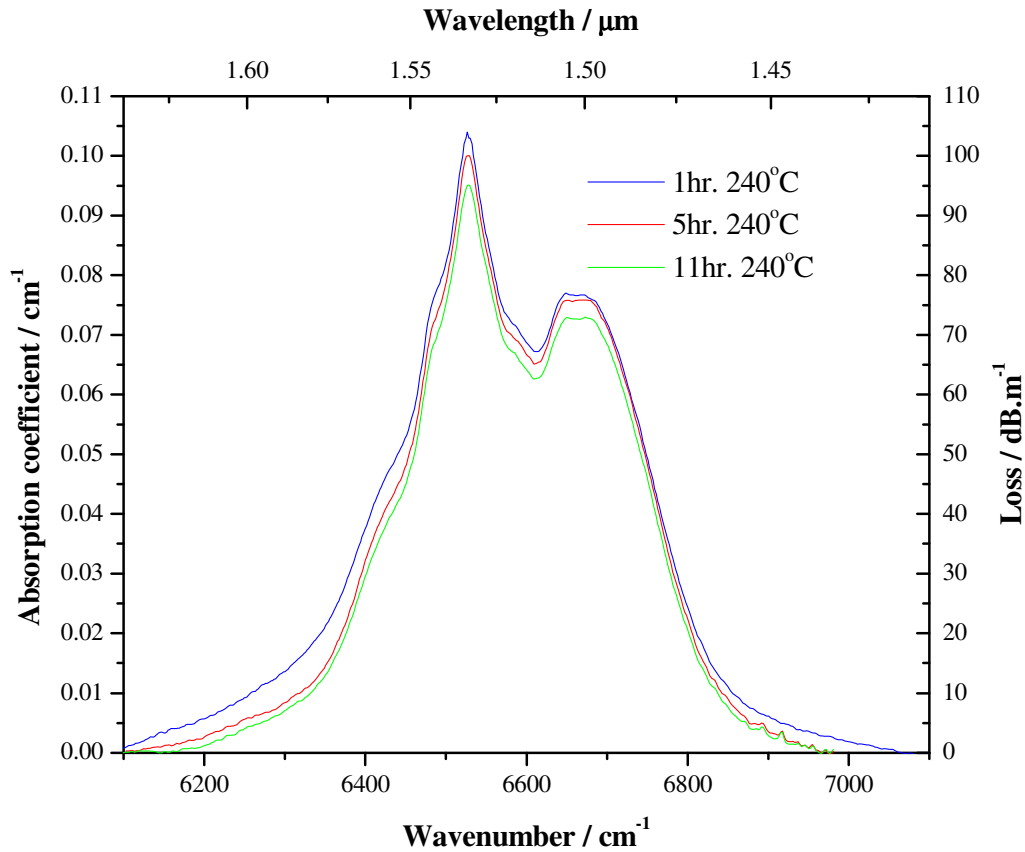


Fig. (6.45): Near-IR spectra of glass MOF017 ( $69.86\text{TeO}_2\text{-}9.98\text{Na}_2\text{O-}19.96\text{ZnF}_2\text{-}0.20\text{ErF}_3$  mol. %) heat treated for 1, 5 and 11 hours at  $240^\circ\text{C}$ .

It can be seen that the band intensity decreased with increasing temperature, however the shape did not change significantly.

Fig. (6.46) shows the visible spectra of glass MOF017 ( $69.86\text{TeO}_2\text{-}9.98\text{Na}_2\text{O-}19.96\text{ZnF}_2\text{-}0.20\text{ErF}_3$  mol. %), untreated, and heat treated 1 hour at  $245$  and  $255^\circ\text{C}$ .

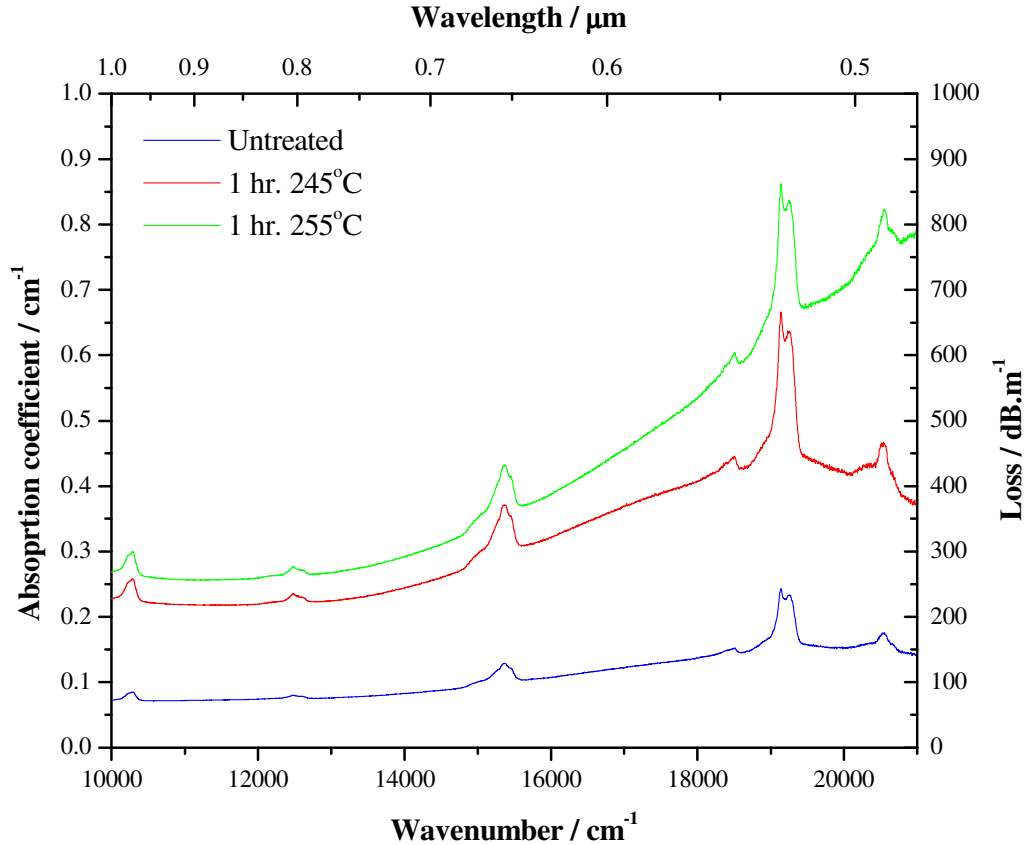


Fig. (6.46): Visible spectra of glass MOF017 ( $69.86\text{TeO}_2\text{-}9.98\text{Na}_2\text{O-}19.96\text{ZnF}_2\text{-}0.20\text{ErF}_3$  mol. %), untreated, and heat treated 1 hour at 245 and 255°C.

It can be seen that the intensity of the absorption bands increased with increasing heat treatment temperature; also the slope on the background loss increased more at shorter wavelength – a phenomenon associated with increased scattering loss.

Fig. (6.47) shows the visible spectra of glass MOF017 ( $69.86\text{TeO}_2\text{-}9.98\text{Na}_2\text{O-}19.96\text{ZnF}_2\text{-}0.20\text{ErF}_3$  mol. %), heat treated for 1, 5 and 11 hours at 240°C.

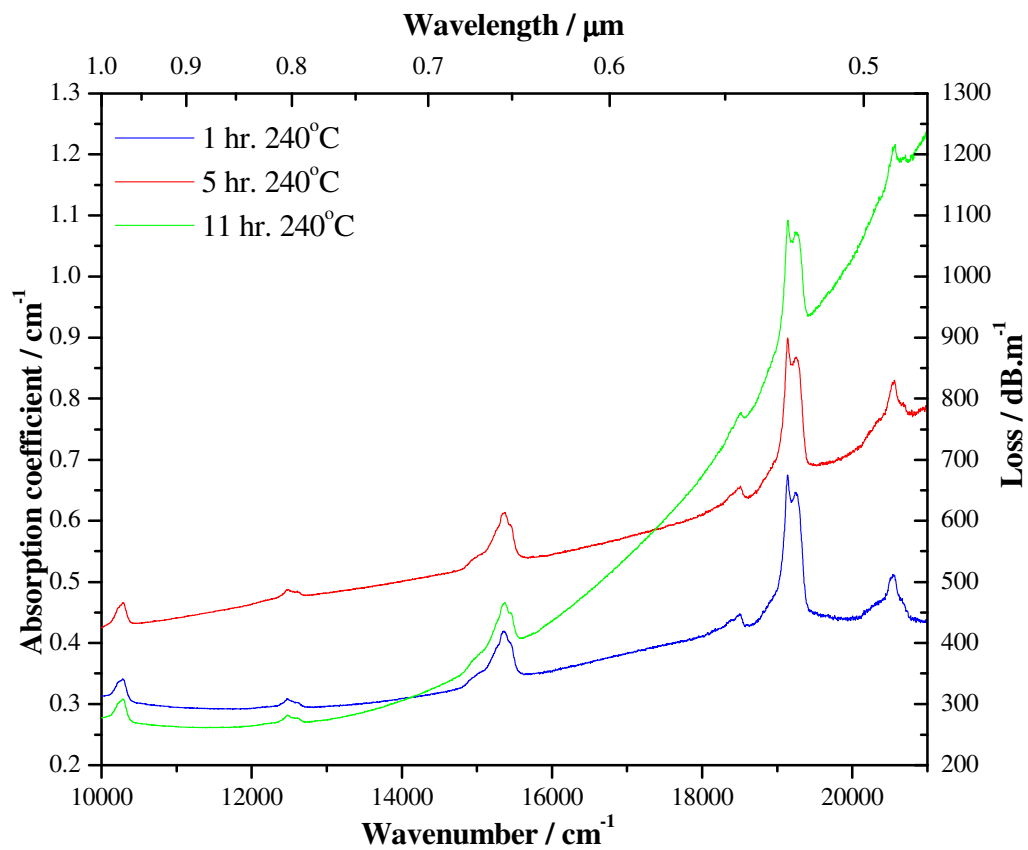


Fig. (6.47): Visible spectra of glass MOF017 ( $69.86\text{TeO}_2\text{-}9.98\text{Na}_2\text{O-}19.96\text{ZnF}_2\text{-}0.20\text{ErF}_3$  mol. %), heat treated for 1, 5 and 11 hours at  $240^\circ\text{C}$ .

It can be seen that the background absorption increased with increasing heat treatment time, due to scattering particularly at shorter wavelength.

## 6.2.2. Refractive index (ellipsometry)

### 6.2.2.1. Refractive index of oxide tellurite glasses

Table (6.11) shows the mean refractive index measured by ellipsometer, at 632.8 nm, the number of times measured (population), and standard deviation (SD) for oxide tellurite glasses studied.

Table (6.11): Mean refractive index measured by ellipsometer, at 632.8 nm, number of times measured (population), and standard deviation (SD) for oxide tellurite glasses (see table (3.1)).

<b>MOD glass ID</b>	<b>Refractive index, <i>n</i>, at 632.8 nm</b>	<b>Population</b>	<b>SD</b>
<b>007</b>	2.02093	15	0.00144
<b>010</b>	2.02364	25	0.00298
<b>012</b>	1.99160	15	0.01344
<b>014</b>	2.14687	15	0.00828
<b>015</b>	2.15160	15	0.01007
<b>016</b>	2.15693	15	0.00825

Variability in the refractive indices can result from a number of factors such as inhomogeneity in the sample, surface degradation, and quality of the polish. Rare-earth doping can also result in disparate data due to complex polarisation and absorption behaviour.

### 6.2.2.2. Refractive index of fluorotellurite glasses

Table (6.12) shows the mean refractive index measured by ellipsometer, at 632.8 nm, number of times measured (population), and standard deviation (SD) for fluorotellurite glasses studied.

Table (6.12): Mean refractive index at measured by ellipsometer, 632.8 nm, number of times measured (population), and standard deviation (SD) for fluorotellurite glasses (see table (3.2)).

MOF Glass ID	Refractive index, $n$ , at 632.8 nm	Population	SD
004	1.85020	5	0.00179
001	1.88740	5	0.00195
005	1.91440	5	0.00195
006	1.94660	5	0.00152
007	1.99040	5	0.00134
008	2.02040	5	0.00207
009	1.91500	3	0.00200
010	1.91200	3	0.00265
011	1.92367	3	0.00115
012	1.95200	3	0.00361
013	1.95167	3	0.00153

Variability in values was less for these glasses compared to the oxide compositions (table (6.11)). Glasses MOF001, 004 to 008 were part of the series  $(90-x)\text{TeO}_2\text{-}10\text{Na}_2\text{O-}x\text{ZnF}_2$  mol. %, for  $5 \leq x \leq 30$  mol. %. Fig. (6.48) shows the variation in refractive index at 633 nm with  $\text{ZnF}_2$  content [5]. The error bars represent  $\pm 3\sigma$  (i.e. 99.7 % confidence intervals).

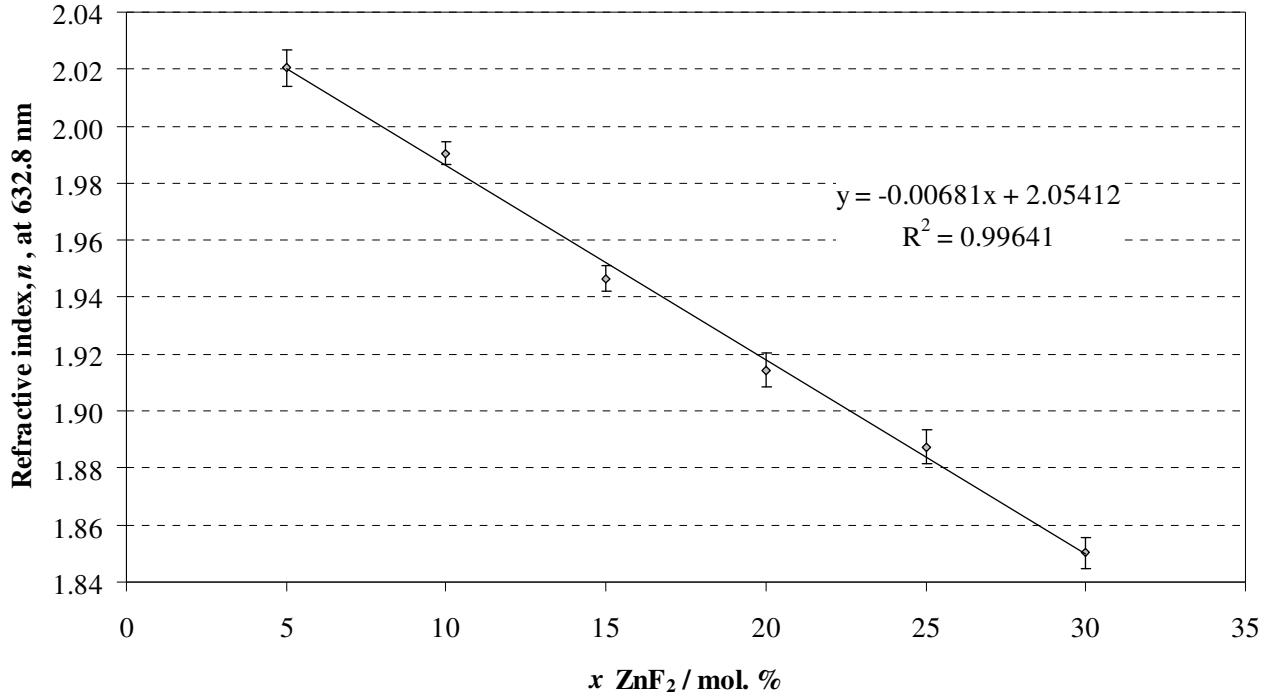


Fig. (6.48): Variation in refractive index at 633 nm with ZnF<sub>2</sub> content, for glass series (90-x)TeO<sub>2</sub>-10Na<sub>2</sub>O-xZnF<sub>2</sub> mol. %, for 5 ≤ x ≤ 30 mol. % (MOF001, 004 to 008) [5].

It can be seen,  $n$  decreased with increasing ZnF<sub>2</sub>.

Glass MOF009 to 013 were part of the series 65TeO<sub>2</sub>-(25-x)ZnF<sub>2</sub>-xZnO-10Na<sub>2</sub>O mol. %, for 5 ≤ x ≤ 25 mol. %. Fig. (6.49) shows the variation of refractive index at 633 nm with increasing oxide to fluoride ratio. Glass MOF001 (65TeO<sub>2</sub>-25ZnF<sub>2</sub>-10Na<sub>2</sub>O mol. %) was used for oxide / fluoride = 0, as this composition complied with the formula 65TeO<sub>2</sub>-(25-x)ZnF<sub>2</sub>-xZnO-10Na<sub>2</sub>O mol. %, x = 0. The error bars represent ±3σ (i.e. 99.7 % confidence intervals).

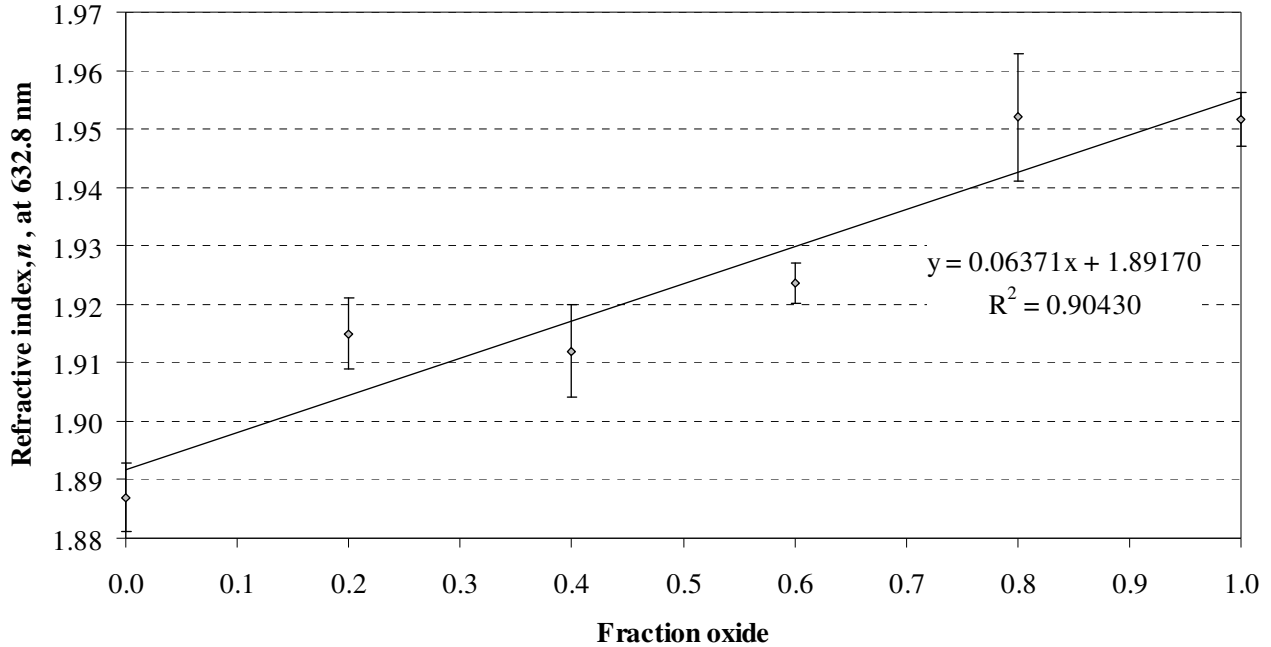


Fig. (6.49): Variation of refractive index at 633 nm with increasing oxide to fluoride ratio of glasses in the series  $65\text{TeO}_2-(25-x)\text{ZnF}_2-x\text{ZnO}-10\text{Na}_2\text{O}$  mol. %, for  $5 \leq x \leq 25$  mol. % (MOF009 to 013). Glass MOF001 ( $65\text{TeO}_2-25\text{ZnF}_2-10\text{Na}_2\text{O}$  mol. %) used for oxide / fluoride = 0.

It can be seen that refractive index increased with increasing ZnO content, however variation was greater than the series shown in fig. (6.48).

### 6.3. Discussion

The results presented in the previous section (6.2) are discussed here in the same order, starting with the infrared absorption spectra of oxide tellurite and fluorotellurite glasses. These are followed by the emission spectra of heat treated  $\text{Er}^{+3}$ -doped fluorotellurite glasses. Refractive indices of oxide tellurite and fluorotellurite glasses are then discussed. To conclude, a core / clad pair is selected for fibre drawing, based on properties discussed in this chapter, and chapter 4.

### 6.3.1. Infrared spectroscopy

#### 6.31.1. Infrared spectroscopy of oxide tellurite glasses

*Infrared spectroscopy of glasses of the series  $(80-x)\text{TeO}_2-10\text{Na}_2\text{O}-10\text{ZnO}-x\text{MO}$ , where MO is PbO or  $\text{GeO}_2$*

Fig. (6.6) shows infrared spectra of glasses in the series  $(80-x)\text{TeO}_2-10\text{Na}_2\text{O}-10\text{ZnO}-x\text{MO}$ , where MO is PbO or  $\text{GeO}_2$ , for MOD006 ( $x = 3$  mol. % PbO), MOD010 ( $x = 5$  mol. % PbO) and MOD012 ( $x = 5$  mol. %  $\text{GeO}_2$ ). Fig. (6.7) shows the multiphonon edge of these glasses. The 3 and 5 mol. % PbO glasses had approximately the same multiphonon edge (the edge of the 3 mol. % glass was at a slightly higher wavenumber). The edge for the  $\text{GeO}_2$  containing glass was found to be at a higher wavenumber than the PbO glasses. This is probably due to a combination of: (i) Ge is of a lower atomic mass than Pb, and (ii) the Pb-O bond ( $382.0 \text{ kJ}\cdot\text{mol}^{-1}$ ) is weaker than the Ge-O bond ( $659.4 \text{ kJ}\cdot\text{mol}^{-1}$ ) [6]. Applying the Szigeti equation (2.8), the multiphonon edge will tend to be shifted to a higher wavenumber if  $\text{GeO}_2$  is substituted for PbO, as  $\mu$  (reduced mass) will decrease, and  $k$  (related to bond strength) will increase. The edge will also tend to shift to higher wavenumbers from 5 to 3 mol. % PbO, as PbO was substituted for  $\text{TeO}_2$ , and is much heavier ( $Z = 82$  and  $52$ , respectively). Using the Szigeti equation (2.8),  $\mu$  will decrease with decreasing PbO content, which will tend to shift the multiphonon edge to higher frequencies.

Stanworth [7] studied the optical spectra of a number of PbO-containing tellurite glasses; however these were melted in ceramic (silica, alumina and zirconia) crucibles, and therefore would probably have been contaminated. Feng *et al.* [8, 9] studied the spectral properties of glasses of the system  $\text{TeO}_2\text{-Na}_2\text{O-ZnO-GeO}_2\text{-Y}_2\text{O}_3\text{-Er}_2\text{O}_3$ . This group added  $\text{GeO}_2$  to the ternary system  $\text{TeO}_2\text{-Na}_2\text{O-ZnO}$  [10] with the potential to increase the viscosity at fibre drawing temperatures, and therefore inhibit crystallisation [9].  $\text{Er}_2\text{O}_3$  was added for luminescence at  $1.5\ \mu\text{m}$  with potential for all-optical amplification, and stability after work by Wang *et al.* [10].  $\text{Y}_2\text{O}_3$  was hoped to have a similar stabilising effect to  $\text{Er}_2\text{O}_3$  [9]. This work showed glass stability to increase with  $\text{GeO}_2$  and  $\text{Y}_2\text{O}_3$  addition [9].

The aim of synthesising bulk glasses in this study was a precursor to producing low optical loss fibre. The position of the multiphonon edge is important for a wide mid-IR transmission window. However, the tellurite glasses reported by Feng *et al.* [8, 9] were found to contain significant absorption bands in the infrared due to hydroxyl groups, also seen in this study in figs. (6.8) to (6.10). Reactive atmosphere processing (RAP) by this group [8] (bubbling  $\text{CCl}_4$  through the melt) did reduce these bands, but not significantly (see fig. (2.12)). It is interesting to note that the glasses prepared by Feng *et al.* exhibited OH bands with an intensity of around  $3\ \text{cm}^{-1}$  ( $3000\ \text{dB}\cdot\text{m}^{-1}$ ) before RAP, and around  $2\ \text{cm}^{-1}$  ( $2000\ \text{dB}\cdot\text{m}^{-1}$ ) after RAP [8]. The  $\text{GeO}_2$  containing glass melted in this study (MOD012) exhibited OH bands of around  $0.8\ \text{cm}^{-1}$  ( $800\ \text{dB}\cdot\text{m}^{-1}$ ) without RAP, and are therefore relatively dry by comparison. The  $\text{TeO}_2\text{-ZnO-Na}_2\text{O-PbO}$  glasses melted in this study were even dryer, with OH band intensities of around  $0.55\ \text{cm}^{-1}$  ( $550\ \text{dB}\cdot\text{m}^{-1}$ ).

Absorption bands due to OH in glasses, and the solubility of water in glasses has been studied extensively in the literature [11-21]. Adams found that association of OH groups through hydrogen-bonding in silicate glasses produces three effects on infrared OH absorption bands [11]:

1. decrease of the frequency of asymmetric stretching bands;
2. enhancement of the integrated intensity and
3. broadening of the contour of absorption bands.

In general, multiple hydrogen-bonded OH absorption bands are found for silicate glasses only when modifiers ( $\text{Na}^+$ ,  $\text{K}^+$ ) and / or intermediates ( $\text{Ca}^{2+}$ ,  $\text{Pb}^{2+}$ ) are present, as the electronic structure of the oxygen atom changes, the field strength increases and the greater negative charge on the oxygen atom results in greater affinity for hydrolysis to occur [11]. Scholze [17] identified a number of vibrational absorption bands for silicate glasses which will be discussed in more detail later in this section, in relation to tellurite and fluorotellurite glasses. He found that vitreous silica possessed a single absorption band around  $3675 \text{ cm}^{-1}$  attributed to 'free-OH', which exhibits no hydrogen-bonding. Like Adams, Scholze found by adding alkali metal oxides such as  $\text{Na}_2\text{O}$  that this band gradually shifted to longer wavelengths eventually overlapping with a band around  $3000 \text{ cm}^{-1}$  not present in the spectrum of vitreous silica. This band, and another at around  $2300 \text{ cm}^{-1}$ , was attributed to OH in the glass, which participates in hydrogen bonding of varying bond-strength and length [17]. Zarubin [19] has recently challenged this model by suggesting the bands around  $3000$ ,  $2300$  and a further band at  $1800 \text{ cm}^{-1}$  are the result

of an ABC triplet due to a single type of hydrogen-bonded-OH, and not variation of OH bond distances / strength in the network.

The glasses shown in fig. (6.6), of the series  $(80-x)\text{TeO}_2-10\text{Na}_2\text{O}-10\text{ZnO}-x\text{MO}$ , where MO is PbO or  $\text{GeO}_2$ , for MOD006 ( $x = 3$  mol. % PbO), MOD010 ( $x = 5$  mol. % PbO) and MOD012 ( $x = 5$  mol. %  $\text{GeO}_2$ ), exhibited two bands in the mid-infrared attributed to OH species. The presence of OH in the glass indicated the batch materials may have been contaminated with hydroxide (see chapter 5), and entrapped water, and / or water entered the glass via the furnace atmosphere and hydrolysed the glass melt producing hydroxide. The lower frequency band at around  $2300\text{ cm}^{-1}$  ( $4.5\text{ }\mu\text{m}$ ) has previously in the literature been attributed to H-bonded OH [8]. The more intense band around  $3000\text{ cm}^{-1}$  ( $3.5\text{ }\mu\text{m}$ ) has previously been attributed to free-OH [8] and appears here to incorporate a higher wavenumber shoulder at around  $3300\text{ cm}^{-1}$  ( $3.0\text{ }\mu\text{m}$ ). It has been shown in alkali and alkaline earth silicates that the analogous band can be deconvoluted into several Gaussian spectral components [20], and similar behaviour has been observed here as shown by fig. (6.8) to (6.10). For the tellurite glasses in this study, the lower frequency band (strongly H-bonded OH) at  $\approx 2300\text{ cm}^{-1}$  was found to be lower in intensity, and sharper than the higher frequency band (free OH) at  $\approx 3000\text{ cm}^{-1}$ ; these intensities are the converse of the effects observed by Adams [11]. One possibility is that the tellurite glasses are relatively dry, therefore the OH in the bulk of the glass has fewer OH groups nearby for hydrogen-bonding to occur [5], although H-bonding will still occur with other oxygens in the glass network. This disparate trend in OH band intensities compared to silicates could be due to the equilibration of charge distributions in bridging, and non-bridging oxygens in

tellurite glasses (see chapter 7). The exact nature of these OH bands will be discussed later in this section.

Fig (6.11) shows the relative percentage of absorption by the different types of OH groups in the glass series  $(80-x)\text{TeO}_2-10\text{Na}_2\text{O}-10\text{ZnO}-x\text{MO}$ , where MO is PbO or  $\text{GeO}_2$ , for MOD006 ( $x = 3$  mol. % PbO), MOD010 ( $x = 5$  mol. % PbO) and MOD012 ( $x = 5$  mol. %  $\text{GeO}_2$ ). The PbO glasses contained relatively more free-OH and strongly hydrogen bonded OH (strong-OH), and less weakly hydrogen bonded OH (weak-OH) than the  $\text{GeO}_2$  glass. Germanium has a lower electronegativity than lead (2.01 and 2.33 respectively), which may have promoted the formation of weak-OH. This latter type of OH hydrogen-bonding exhibited the largest absorption bands in these glasses, indicating it is the most energetically favourable state for OH in the glass, assuming that the extinction coefficients of the different types of OH are relatively similar. Therefore, adding a cation of relatively high electronegativity to the glass (lead), may have interfered with the hydrogen bonding of the OH, which tends to form due the permanent dipole on the OH groups (due to the large difference in electronegativity between oxygen, 3.44, and hydrogen, 2.20).

*Infrared spectroscopy of glasses of the series  $(90-x)\text{TeO}_2-10\text{Na}_2\text{O}-x\text{ZnO}$*

Fig. (6.12) shows infrared spectra of glass of the series  $(90-x)\text{TeO}_2-10\text{Na}_2\text{O}-x\text{ZnO}$ , for  $x = 12$  mol. % (MOD007) and  $x = 10$  mol. % (MOD013). An increase in ZnO (from 10 to 12 mol. %) shifts the multiphonon edge to higher wavenumbers. Zinc is lighter than tellurium ( $Z = 30$  and 52 respectively), therefore, substituting ZnO for  $\text{TeO}_2$  will result in

a change in the multiphonon edge. Tellurium also has a higher charge than zinc, therefore also has a higher lattice energy. Using equation (2.8), addition of zinc will result in a decrease in  $\mu$  (reduced mass), causing the edge to shift to higher frequencies.

Fig. (6.13) shows the multiphonon edges of glass of composition  $80\text{TeO}_2\text{-}10\text{Na}_2\text{O-}20\text{ZnO}$  mol. % (MOD013) with thickness *viz.* 2.98, 0.50 and 0.20 mm. The multiphonon edge was enhanced with decreasing thickness due to an increasing amount of signal reaching the detector. Ernsberger [14] has shown that by using very thin silicate glass samples it was possible to 'extend the useful spectrum [of silicates] to  $\approx 1,300\text{cm}^{-1}$ ' i.e. enable us to see more clearly bands that were indistinguishable before. This is also true for tellurite glasses as fig. (6.14) and (6.15) show [5]. In the spectrum of thin (0.20 mm) glass, of composition  $80\text{TeO}_2.10\text{ZnO}.10\text{Na}_2\text{O}$  (mol. %), the higher wavenumber shoulder of the  $3060\text{ cm}^{-1}$  band can be more clearly discerned than in the spectra of the longer optical pathlength specimens (fig. (6.15)), and at least four bands thought to be related to structural units in the glass network (see below) can be seen within the multi-phonon absorption edge (fig. (6.14)). Fig. (6.16) to (6.17) show the Gaussian deconvolution of these OH bands in the longer optical pathlength samples.

Scholze [17] identified a band around  $3500\text{ cm}^{-1}$  for alkali metal silicate glasses and attributed this to the stretching mode of the free Si-OH groups. Ryskin [22, 23] also identified a band around  $3500\text{ cm}^{-1}$  for hydrated crystalline silicates and attributed this to a stretching mode of the water molecule. It is therefore proposed that the band around  $3300\text{ cm}^{-1}$  in fig. (6.17) (which is a shoulder of the  $3060\text{ cm}^{-1}$  band) be attributed to free Te-OH groups or molecular water (or a combination of both) [5]. By exposing thin glass films to a high a vapour pressure of water (i.e. steam) Ernsberger [14] entrapped

molecular water in alkali-silicate glasses, evidenced by the characteristic absorption band at  $1600\text{ cm}^{-1}$  (fundamental H-O-H bending mode) and a broader band around  $3600\text{ cm}^{-1}$  which occurred for the water vapour treated glasses. Two equilibria must be taken into account when considering hydrolysis of a glass melt [20] (where R is the main glass forming cation e.g.  $\text{Si}^{4+}$  or  $\text{Te}^{4+}$ ):

- (i) Water vapour entering the melt as molecular water (i.e.  $[\text{H}_2\text{O}]_{\text{vapour}} \leftrightarrow [\text{H}_2\text{O}]_{\text{melt}}$ ).
- (ii) Molecular water in the melt hydrolysing the molten network (i.e.  $[\text{R-O-R}]_{\text{melt}} + [\text{H}_2\text{O}]_{\text{melt}} \leftrightarrow 2[\text{R-OH}]_{\text{melt}}$ ).

Therefore the coexistence of these two equilibria in the melt seems to suggest the probable non-zero concentration of molecular water in any glass with a non-zero water content [20].

Scholze [17] identified a band around  $2800\text{ cm}^{-1}$  for alkali metal silicate glasses and attributed this to the stretching mode of the Si-OH group that forms the weaker hydrogen bonding with the non-bridging oxygens (NBO's) of the  $\text{Q}^2$  or  $\text{Q}^3$  tetrahedron (where  $\text{Q}^n$  is a  $\text{SiO}_4$  tetrahedron with  $n$  bridging oxygen bonds to the surrounding network). Ryskin [22, 23] also identified a stretching mode of the hydrogen-bonded Si-OH groups around  $2800\text{ cm}^{-1}$  in crystalline hydrated silicates. It is proposed in the current study that the band, which occurs around  $3060\text{ cm}^{-1}$  for tellurite and fluorotellurite glasses (fig. (6.17)) be attributed to the stretching mode of the weakly hydrogen-bonded Te-OH groups [5].

Scholze [17] identified a band around  $2350\text{ cm}^{-1}$  for alkali metal silicate glasses and assigned this to the stretching mode of Si-OH groups which form the strongest hydrogen bonding with the NBO's of the isolated  $\text{SiO}_4$  tetrahedron  $Q^0$  (i.e. isolated  $\text{SiO}_4$  group with no bridging oxygens). Ryskin [22, 23] also identified a band attributed to a stretching mode of the hydrogen-bonded Si-OH groups around  $2350\text{ cm}^{-1}$  for crystalline hydrated silicates. It is proposed that the band, which occurs around  $2290\text{ cm}^{-1}$  for tellurite glasses (fig. (6.17)) be attributed to the stretching mode of the strongly hydrogen-bonded Te-OH groups [5].

Ryskin [22, 23] identified a band at *circa*  $1700\text{ cm}^{-1}$  attributed to a stretching mode of the hydrogen-bonded Si-OH groups and band at *circa*  $1650\text{ cm}^{-1}$  assigned to the bending mode of the water molecule in crystalline hydrated silicates. However, this former band would contradict Scholze [17] who stated the strongest hydrogen bonded Si-OH stretching band for multi-component silicate glasses occurs around  $2350\text{ cm}^{-1}$ , meaning there are no more stretching modes for hydrogen-bonded R-OH groups at lower wavenumbers than  $2350\text{ cm}^{-1}$ . Bands around  $1650$  and  $1700\text{ cm}^{-1}$  were not seen in this study.

Fuxi [24] has reported Raman or infrared active fundamental lattice vibrations of tellurite glasses. Fuxi [24] identified the fundamental symmetric stretch of O-Te-O at  $790\text{ cm}^{-1}$ . It is propose that the band which occurs around  $1550\text{ cm}^{-1}$  in fig. (6.14) corresponds to the first overtone of the  $790\text{ cm}^{-1}$  fundamental ( $2 \times 790\text{ cm}^{-1} = 1580\text{ cm}^{-1}$ ) or the bending mode of molecular water identified by Ryskin (or a convolution of both) [5].

Fuxi [24] identified the fundamental asymmetric stretch of O-Te-O or Te-O<sup>-</sup> at  $710\text{ cm}^{-1}$  and the group vibration of  $[\text{TeO}_6]$  at  $610\text{ cm}^{-1}$ . It is proposed that the band which

occurs at  $1370\text{ cm}^{-1}$  in fig. (6.14) be attributed to the combination of these two fundamental bands ( $730 + 610 = 1340\text{ cm}^{-1}$ ) [5]. The current author would assign the band which occurs at  $1210\text{ cm}^{-1}$  in fig. (6.14) to the first overtone of the aforementioned  $610\text{ cm}^{-1}$  band due to the vibration of the  $[\text{TeO}_6]$  group ( $2 \times 610\text{ cm}^{-1} = 1220\text{ cm}^{-1}$ ). The band which occurs at  $1070\text{ cm}^{-1}$  in fig. (6.14) could be attributed to the first overtone of the  $[\text{TeO}_6]$  band at  $490\text{ cm}^{-1}$  ( $2 \times 490\text{ cm}^{-1} = 980\text{ cm}^{-1}$ ), however this is unlikely as the fundamental absorption is weak (and the overtone would be even weaker) and the difference between theoretical and experimental band positions is too large ( $90\text{ cm}^{-1}$ ) [5].

The assignment of these bands is summarised in table (6.13) below.

Table (6.13): Assignment of absorption bands from fig. (6.14) and (6.15) for a 0.2 mm sample of glass MOD013:  $80\text{TeO}_2\text{-}10\text{Na}_2\text{O-}10\text{ZnO}$  (mol. %) [5].

Band / $\text{cm}^{-1}$	Comments	Ref.
$\approx 3300$	Stretching mode of free Te-OH groups and/or stretching mode of molecular water	[14, 17, 22, 23]
$\approx 3060$	Stretching mode of weak hydrogen-bonded Te-OH groups	[17, 22, 23]
$\approx 2290$	Stretching mode of strong hydrogen-bonded Te-OH groups	[17, 22, 23]
$\approx 1550$	1 <sup>st</sup> overtone of O-Te-O symmetric stretch ( $2 \times 790 = 1580\text{ cm}^{-1}$ ) and/or bending mode of molecular water	[14, 22-24]
$\approx 1370$	Combination of asymmetric stretch of O-Te-O or Te-O <sup>-</sup> and $[\text{TeO}_6]$ group vibration ( $730 + 610 = 1340\text{ cm}^{-1}$ )	[24]
$\approx 1210$	1 <sup>st</sup> overtone of $[\text{TeO}_6]$ group ( $2 \times 610 = 1220\text{ cm}^{-1}$ )	[24]
$\approx 1070$	Unidentified, possibly 1 <sup>st</sup> overtone of $[\text{TeO}_6]$ group vibration ( $2 \times 490 = 980\text{ cm}^{-1}$ )	[24]

The proposed identification of the multiphonon absorption bands shown in table (6.13) assumed that combination bands and overtones of fundamental Raman and infrared Te-O

bands both result in active modes in the infrared. In reality it is not this simple, because Raman and IR have different quantum mechanical selection rules (for IR, mode is only active if incident radiation stimulates a change in dipole moment); however this serves as a good first approximation [25].

### *Infrared spectroscopy of WO<sub>3</sub> containing glasses*

Fig. (6.19) shows infrared spectra of glasses MOD014 (90TeO<sub>2</sub>-5WO<sub>3</sub>-5Nb<sub>2</sub>O<sub>5</sub> mol. %), MOD015 (82.5TeO<sub>2</sub>-7.5WO<sub>3</sub>-10Nb<sub>2</sub>O<sub>5</sub> mol. %), and MOD016 (70TeO<sub>2</sub>-25WO<sub>3</sub>-5Bi<sub>2</sub>O<sub>3</sub> mol. %). The multiphonon edge shifted to higher wavenumbers and developed a shoulder with increasing WO<sub>3</sub> content. WO<sub>3</sub> is highly refractory (TeO<sub>2</sub>  $T_m = 733^\circ\text{C}$ , WO<sub>3</sub>  $T_m = 1473^\circ\text{C}$ , and Nb<sub>2</sub>O<sub>5</sub>  $T_m = 1460^\circ\text{C}$ ) and therefore has a much higher bond strength W-O (672 kJ.mol<sup>-1</sup>) compared to Te-O (376.1 kJ.mol<sup>-1</sup>) [6]. Using the Szigeti equation (2.8), substituting WO<sub>3</sub> for TeO<sub>2</sub> will increase  $k$  (the bond force constant), shifting the multiphonon edge to higher frequencies.

A number of studies has been performed on the structure of tungsten-tellurite glass systems [26-29]. The bands which developed, in the multiphonon edge, which increased in intensity with increasing WO<sub>3</sub> content, can be clearly seen in fig. (6.19) and (6.20). This author would propose the band which occurred at around 1770 cm<sup>-1</sup> (5.65 μm) can be attributed to the first overtone of the asymmetric vibrations of the [WO<sub>6</sub>] octahedra ( $2 \times 870 \text{ cm}^{-1} = 1740 \text{ cm}^{-1}$ ) [26, 28, 29]. This author would propose that the band which occurred at around 1870 cm<sup>-1</sup> (5.35 μm) can be attributed to the first overtone of the symmetric vibrations of the [WO<sub>4</sub>] tetrahedra ( $2 \times 930 \text{ cm}^{-1} = 1860 \text{ cm}^{-1}$ ) [26, 28, 29].

The band at around  $1870\text{ cm}^{-1}$  ( $5.35\text{ }\mu\text{m}$ ) attributed to  $[\text{WO}_4]$  tetrahedra appeared to grow with increasing  $\text{WO}_3$ . Shalout *et al.* [28] found that the number of  $[\text{WO}_4]$  tetrahedra increased in binary  $\text{TeO}_2\text{-WO}_3$  glasses with increasing  $\text{WO}_3$ , up to around 30 mol. %  $\text{WO}_3$ . All the  $\text{WO}_3$  glasses prepared in this study contained between 5 and 25 mol %  $\text{WO}_3$ , therefore it would be reasonable to assume the bands growing out of the multiphonon edge were due to equilibrium between  $[\text{WO}_6]_{\text{oct}} \leftrightarrow [\text{WO}_4]_{\text{tet}}$  in the glass with varying  $\text{WO}_3$  content.

Fig. (6.21) shows the OH band envelope of the  $\text{WO}_3$  containing glasses, and fig. (6.22) to (6.24) show the associated Gaussian deconvolution. It is interesting to note that these glasses exhibit very different shaped OH bands from the  $\text{TeO}_2\text{-Na}_2\text{O-ZnO}$  containing glasses discussed earlier in this section (fig. (6.17) for example). Much like silicate glasses, the OH bands for tungsten-tellurite glasses show a decrease in frequency (and wavenumber), and an increase in intensity and width, with the increasing degree of hydrogen bonding [11]; i.e. free-OH  $\rightarrow$  weakly H-bonded OH  $\rightarrow$  strongly H-bonded OH. Fig. (6.25) illustrates this. This similar trend to silicates could be due to similarities in the bonding in the tungsten-tellurite glasses. Like the Si-O bond ( $799.6\text{ kJ.mol}^{-1}$ ), the W-O ( $672\text{ kJ.mol}^{-1}$ ) and Nb-O ( $771\text{ kJ.mol}^{-1}$ ) bonds are very strong compared to Zn-O ( $159\text{ kJ.mol}^{-1}$ ), Pb-O ( $382.0\text{ kJ.mol}^{-1}$ ) and Te-O ( $376.1\text{ kJ.mol}^{-1}$ ) [6]. This change in bonding environment could affect the population of states of the OH groups in the glass, favouring strongly hydrogen bonded OH, as opposed to weakly bonded OH in the  $\text{TeO}_2\text{-Na}_2\text{O-ZnO}$  containing glasses. The cations in the tungsten tellurite glasses were also high in valence ( $\text{Te}^{+4}$ ,  $\text{W}^{+6}$ ,  $\text{Nb}^{+5}$  and  $\text{Bi}^{+3}$ ) compared to the earlier compositions ( $\text{Te}^{+4}$ ,  $\text{Zn}^{+2}$ ,  $\text{Na}^+$ ,  $\text{Pb}^{+2}$  and  $\text{Ge}^{+4}$ ). This could also alter the bonding environment and population of OH types.

*Comparison of infrared spectra of oxide tellurite glasses with a view to the manufacture of low optical loss mid-infrared fibre*

Glasses in the ternary system  $\text{TeO}_2\text{-ZnO-Na}_2\text{O}$  exhibited transmission to around  $1667\text{ cm}^{-1}$  ( $6\text{ }\mu\text{m}$ ) with OH absorption bands of around  $0.6\text{ cm}^{-1}$  ( $600\text{ dB.m}^{-1}$ ) in intensity. The addition of a few mol. %  $\text{GeO}_2$ ,  $\text{PbO}$ , or varying the  $\text{ZnO}$  content of these glasses did not dramatically alter the multiphonon edge, or intensity of the OH bands. The OH bands in the tungsten-tellurite glasses were less intense than the  $\text{TeO}_2\text{-ZnO-Na}_2\text{O}$  glasses, at around  $0.2\text{ cm}^{-1}$  ( $200\text{ dB.m}^{-1}$ ). However, these glasses did not transmit as far into the infrared, and addition of tungsten significantly shifted the multiphonon edge to higher wavenumbers: 5 mol. %  $\text{WO}_3$   $1862\text{ cm}^{-1}$  ( $5.37\text{ }\mu\text{m}$ ), 7.5 mol. %  $\text{WO}_3$   $1905\text{ cm}^{-1}$  ( $5.25\text{ }\mu\text{m}$ ), and 25 mol. %  $\text{WO}_3$   $1946\text{ cm}^{-1}$  ( $5.14\text{ }\mu\text{m}$ ). For low loss fibre in the 2 to  $5\text{ }\mu\text{m}$  region, the tungsten-tellurite glasses would be more suitable than the  $\text{TeO}_2\text{-ZnO-Na}_2\text{O}$  glasses, due to the lower intensity OH bands seen, although reflection losses would be higher due to higher refractive indices. Because of the refractory nature of the compounds in the tungsten-tellurite glasses ( $\text{WO}_3$  and  $\text{Nb}_2\text{O}_5$ ), fibre pulled from these materials would have better environmental durability than the  $\text{TeO}_2\text{-ZnO-Na}_2\text{O}$  based glasses. However, processing such as fibre drawing would have to be carried out at higher temperatures as the fibre drawing viscosity ( $\approx 10^{4.5}\text{ Pa.s}$ ) would occur at higher temperatures for the tungsten-tellurite glasses compared to the  $\text{TeO}_2\text{-ZnO-Na}_2\text{O}$  glass. If transmission is required to  $6\text{ }\mu\text{m}$ , the  $\text{TeO}_2\text{-ZnO-Na}_2\text{O}$  based glasses would be more suitable, and have the advantage of altering the refractive index for a core / clad pair with

addition of PbO or GeO<sub>2</sub>, without significantly affecting the multiphonon edge, although OH bands were more intense.

### 6.3.1.2. Infrared spectroscopy of fluorotellurite glasses

*Infrared spectroscopy of series (90-x)TeO<sub>2</sub>-10Na<sub>2</sub>O-xZnF<sub>2</sub> mol. %, for 5 ≤ x ≤ 30 mol. %*

Fig. (6.26) shows the infrared spectra of glasses of the series (90-x)TeO<sub>2</sub>-10Na<sub>2</sub>O-xZnF<sub>2</sub>, mol. %, for 5 ≤ x ≤ 30 mol. % (glasses MOF001, 004 to 008). Glass MOD013 (80TeO<sub>2</sub>-10Na<sub>2</sub>O-10ZnO mol. %) was also plotted for comparison. As expected the intensity of the OH spectral absorptions decrease with increasing ZnF<sub>2</sub> content and melting time as the glass is dried *in situ* (see section 3). Fig. (6.27) illustrates this, by plotting the loss in dB.m<sup>-1</sup> attributed to the free-OH at 2900 cm<sup>-1</sup> with increasing ZnF<sub>2</sub> content, which plateaux to a minimum loss of around 20 dB.m<sup>-1</sup> at compositions containing more than 15 mol. % ZnF<sub>2</sub>. The drying effect was significant, as the 5 mol. % ZnF<sub>2</sub> glass showed an optical loss of around 120 dB.m<sup>-1</sup> at 2900 cm<sup>-1</sup> [5]. Fig. (6.28) shows the effect of melting time of glass MOF001 (65TeO<sub>2</sub>,25ZnF<sub>2</sub>,10Na<sub>2</sub>O mol. %), on the loss caused by spectral absorption of the OH band around 2900 cm<sup>-1</sup>. After 1 hour of melting the optical loss of the finished glass MOF001 (65TeO<sub>2</sub>-10Na<sub>2</sub>O-25ZnF<sub>2</sub> mol. %) was relatively high (comparable to the pure oxide glass MOD013 - 80TeO<sub>2</sub>-10Na<sub>2</sub>O-10ZnO mol. %), however after 2 hours of melting the loss had decreased by almost two orders of magnitude (from 705 to 10 dB.m<sup>-1</sup>) showing the importance of melting time for the drying process [5].

Glass MOF004 (30 mol. %  $\text{ZnF}_2$  melted for 2 hours) still has hydroxide present, as addition of zinc fluoride caused volatilisation during melting resulting in a decrease in the hydroxyl concentration in the final glass. This is favourable for fabrication of fibre as the loss attributed to OH absorption was significantly reduced with increasing fluoride: 526  $\text{dB.m}^{-1}$  for MOD013 (0 mol. %  $\text{ZnF}_2$ ), is decreased to 21  $\text{dB.m}^{-1}$  for MOF004 (30% mol.  $\text{ZnF}_2$ ), over 20 times less. However, as fig. (6.27) shows, the optical loss due to fluoride content plateaux above 15 mol. % indicating using the current melting procedure (i.e. melting for 2 hours in a fume cupboard with dry air) all of the OH cannot be completely removed, although it can be reduced to a large extent [5].

A number of other groups has studied the drying effect of addition of  $\text{ZnF}_2$  or  $\text{PbF}_2$  to tellurite glasses [7, 30-33]. Nazabel *et al.* [33] showed absorption of around  $0.5 \text{ cm}^{-1}$  (500  $\text{dB.m}^{-1}$ ) for the band at  $2900 \text{ cm}^{-1}$  for a glass of composition  $61\text{TeO}_2\text{-}12\text{ZnO}\text{-}27\text{ZnF}_2$  melted for 20 min. between  $650$  and  $800^\circ\text{C}$ . Glass MOF001 (25 mol. %  $\text{ZnF}_2$ , fig. (6.30)) and MOF004 (30 mol. %  $\text{ZnF}_2$ , fig. (6.29)) showed absorption lower than 0.05 and  $0.03 \text{ cm}^{-1}$  respectively (50 and 30  $\text{dB.m}^{-1}$ ) at around  $2900 \text{ cm}^{-1}$ . The OH absorption bands in spectra of the fluorotellurite glasses prepared in this study, such as MOF001 and MOF004, are one order of magnitude lower (in absorption coefficient and  $\text{dB.m}^{-1}$ ) than the glasses melted by Nazabel *et al.* [33].

Fig. (6.29) to (6.34) show the Gaussian deconvolution of OH bands in spectra of glasses in the series  $(90-x)\text{TeO}_2\text{-}10\text{Na}_2\text{O}\text{-}x\text{ZnF}_2$ , mol. %, for  $5 \leq x \leq 30$  mol. % (glasses MOF001, 004 to 008). These fluorotellurite glasses did not exhibit a strongly H-bonded OH band at around  $2300 \text{ cm}^{-1}$ , which was seen in the spectra of the oxide glasses (this band was no longer present for  $\text{ZnF}_2$  containing glasses in fig. (6.26), which also shows

an oxide glass for comparison). This strongly H-bonded OH band could have been masked by the fluorotellurite multiphonon edge, or the presence of fluoride in the glass could have actually prevented the formation of strongly H-bonded OH bonds. As the number of OH groups in the glass decreased with increasing  $\text{ZnF}_2$  and / or melting time, there would have been less chance of neighbouring OH groups to hydrogen bond to. Also, hydrogen-bonding will occur between OH and F in these glasses (e.g.  $-\text{F}-----\text{OH}-$ ), possibly explaining the difference in OH band structure seen in the IR for the fluorotellurite glasses compared to the oxide tellurite glasses. If ZnO is substituted for  $\text{ZnF}_2$ , the multiphonon edge will tend to shift to a higher wavenumber (see fig. (6.26)). The Zn-F bond ( $368 \text{ kJ}\cdot\text{mol}^{-1}$ ) is stronger than the ZnO bond ( $159 \text{ kJ}\cdot\text{mol}^{-1}$ ) [6], therefore, applying the Szigeti equation (2.8), this will result in an increase in  $k$ , shifting the multiphonon edge to higher frequencies.

Fig. (6.35) shows that the number of weakly H-bonded OH groups in the glass tended to decrease with increasing  $\text{ZnF}_2$ , and the number of free-OH increased. This is possibly due to the decreasing number of OH groups present with increasing fluoride, which promotes the formation of free-OH due to the lack of close proximity OH groups to hydrogen bond to, however  $-\text{F}-----\text{HO}-$  type H-bonds will form in these glasses.

Bulk fluorotellurite glass was prepared with the fluorinated  $\text{ZnF}_2$  described in section 3.4. However, spectra of bulk samples did not show any reduction in OH band intensity. Effect of fluorination on the optical loss of fluorotellurite fibre is reported in chapter 8.

*Infrared spectroscopy of series 65 TeO<sub>2</sub>-(25-x)ZnF<sub>2</sub>-xZnO-10Na<sub>2</sub>O, for 5 ≤ x ≤ 30 mol. %*

Fig. (6.36) shows the infrared spectra of glasses MOF009 to 013 which were part of the series 65TeO<sub>2</sub>-(25-x)ZnF<sub>2</sub>-xZnO-10Na<sub>2</sub>O mol. %, for 5 ≤ x ≤ 25 mol. %. The OH bands grew in intensity with increasing ZnO in these glasses. Fig. (6.37) to (6.41) shows the Gaussian deconvolution of these glasses. It is interesting to note that the ZnF<sub>2</sub> containing glasses (MOF009 to MOF012, x = 5 to 20 mol. % ZnO) did not exhibit strongly H-bonded OH, and only exhibited weakly H-bonded OH and free-OH bands. Only the oxide glass, MOF013 (x = 25 mol. % ZnO), exhibited a strongly H-bonded OH band in addition to the weakly H-bonded OH and free-OH. Fig. (6.42) shows the variation in intensity of the OH band at around 2900 cm<sup>-1</sup> with ZnO / ZnF<sub>2</sub> ratio. For ZnO / ZnF<sub>2</sub> = 0.2 (20 % mol. ZnF<sub>2</sub>) the loss was around 15 dB.m<sup>-1</sup>, which increased to around 240 dB.m<sup>-1</sup> for ZnO / ZnF<sub>2</sub> = 1 (0 % mol. ZnF<sub>2</sub>). Fig. (6.43) shows all glasses had around the same relative amount of free-OH (25 %). All fluoride containing glasses (MOF009 to MOF012) contained around 75 % weakly H-bonded OH. The oxide glass (MOF013) contained around 50 % weakly H-bonded OH and 25 % strongly H-bonded OH.

*Comparison of infrared spectra of fluorotellurite glasses with a view to the manufacture of low optical loss mid-infrared fibre*

Glasses of the series (90-x)TeO<sub>2</sub>-10Na<sub>2</sub>O-xZnF<sub>2</sub> mol. %, for 5 ≤ x ≤ 30 mol. % (MOF001, 004 to 008) transmitted to around 6 μm, and when melted for 2 hours exhibited OH absorption bands at 2900 cm<sup>-1</sup> of around 0.02 cm<sup>-1</sup> (20 dB.m<sup>-1</sup>) for x = 15 to

30 mol. %  $\text{ZnF}_2$  (over 20 times less than the  $\text{TeO}_2\text{-Na}_2\text{O-ZnO}$  based glasses. The multiphonon edge did not shift significantly with  $\text{ZnF}_2$  addition. For glasses of the series 65  $\text{TeO}_2\text{-(25-x)ZnF}_2\text{-xZnO-10Na}_2\text{O}$ , for  $5 \leq x \leq 30$  mol. %, increasing the ZnO content did not significantly shift the multiphonon edge at around  $6 \mu\text{m}$ , however it did increase the intensity of the OH absorption bands at around  $2900 \text{ cm}^{-1}$  (from around  $25 \text{ dB.m}^{-1}$  for  $\text{ZnO/ZnF}_2 = 0.4$ , to around  $40 \text{ dB.m}^{-1}$  for  $\text{ZnO/ZnF}_2 = 0.6$ ). Therefore, for low optical loss mid-infrared fibre the glasses of the series  $(90-x)\text{TeO}_2\text{-10Na}_2\text{O-xZnF}_2$  mol. % would be more suitable. The composition of these glasses can be altered over a wider range (15 to 30 mol. %  $\text{ZnF}_2$ ) than the 65  $\text{TeO}_2\text{-(25-x)ZnF}_2\text{-xZnO-10Na}_2\text{O}$  mol. % series without significantly shifting the multiphonon edge or OH absorption band intensities. This would enable a larger refractive index difference in a core / clad pair, without compromising other optical properties.

### 6.3.1.3. Spectroscopy of $\text{Er}^{+3}$ -doped composition

The effect of heat treatment on the emission bands of erbium, particularly at around  $1.55 \mu\text{m}$  is discussed here. These heat treatments were performed in the hope of producing transparent glass ceramics, analogous to the fluoroaluminosilicate based materials produced by Kukkonen and Beggiara *et al.* [34, 35]. In this work, the heat treatments resulted in the precipitation of a nano-crystalline erbium rich phase, which enhanced the optical properties and broadened the emission bands of  $\text{Er}^{+3}$ .

Fig. (6.44) shows the near-IR spectra of glass MOF017 ( $69.86\text{TeO}_2\text{-9.98Na}_2\text{O-19.96ZnF}_2\text{-0.20ErF}_3$  mol. %) untreated, and heat treated for 1 hour at 245, 255, 265 and

275°C. The erbium (III) band centered at 1.5  $\mu\text{m}$  consists of two main peaks, both with some degree of asymmetry. The peak intensity decreased with increasing temperature. The asymmetry of the bands became more distinct with increasing temperature, making additional bands more visible. The bands also shifted to lower wavenumbers with increasing temperature.

Jha and Shen *et al.* [36, 37] observed an enhancement (i.e. broadening) of this  $\text{Er}^{+3}$  band with increasing  $\text{Er}^{+3}$  concentration in  $\text{TeO}_2\text{-ZnO-Na}_2\text{O}$  glasses. This was thought to be due to a number of reasons:

- i. The range of structural units present in the glass ( $[\text{TeO}_4]$ ,  $[\text{TeO}_3]$  and  $[\text{TeO}_{3+1}]$ ). This results in a range of Te-O bond lengths in the equatorial and axial directions. Addition of  $\text{Er}_2\text{O}_3$  will therefore change the ion host field strength as it changes the range of polyhedra present [36].
- ii. The interaction between the  $\text{Te}^{+4}$  lone electron pair and other cations ( $\text{Zn}^{+2}$  and  $\text{Na}^+$ ) will change with  $\text{Er}_2\text{O}_3$  addition [36].
- iii.  $\text{Er}^{+3}$  coordination changes with increasing concentration [36].

Hirano *et al.* [38] also observed broadening of the  $\text{Er}^{+3}$  bands after heat treatment of  $\text{Er}^{+3}$  doped  $\text{TeO}_2\text{-K}_2\text{O-Nb}_2\text{O}_5$  glass. This indicated that the environment surrounding the erbium ion in glass MOF017 (69.86 $\text{TeO}_2\text{-9.98Na}_2\text{O-19.96ZnF}_2\text{-0.20ErF}_3$  mol. %) had changed with increasing heat treatment temperature. The erbium (III) could have been preferentially segregating into the crystalline phase [34, 35], resulting in the enhancement of the bands.

Fig. (6.45) shows the near-IR spectra of glass MOF017 (69.86TeO<sub>2</sub>-9.98Na<sub>2</sub>O-19.96ZnF<sub>2</sub>-0.20ErF<sub>3</sub> mol. %) heat treated at 240°C for 1, 5 and 11 hours. The peak intensity decreased slightly with time, however the shape or positions of the bands did not change significantly.

Fig. (6.46) shows the visible spectra of glass MOF017 (69.86TeO<sub>2</sub>-9.98Na<sub>2</sub>O-19.96ZnF<sub>2</sub>-0.20ErF<sub>3</sub> mol. %), untreated, and heat treated for 1 hour at 245 and 255°C. It can be seen scattering losses increased with increasing temperature of heat treatment towards the ultraviolet region, as scattering losses are proportional to  $\frac{1}{\lambda^n}$  ( $n = 4$  for Rayleigh scattering (nano-particulate), and  $n = 2$  for Mie scattering (micro-particulate)). As heat treatment temperature increases, more crystalline phase will be present for a given time of heat treatment. This will result in more scattering centres. Fig. (6.47) shows a similar trend with increasing time of heat treatment (240°C for 1, 5 and 11 hours). As time of heat treatment increases, the number of crystal and hence scattering centers will increase.

However, no further work was done to investigate the nature of the phase crystallising, and whether Er<sup>+3</sup> partitioned to nano-crystals. The preliminary work reported here suggests further work should be done, particularly in compositional development.

### 6.3.2. Refractive index (ellipsometry)

#### 6.3.2.1. Refractive index of oxide tellurite glasses

Table (6.11) shows the refractive index of a selection of the oxide tellurite glasses melted in this study. Glass MOD007 (78TeO<sub>2</sub>-12ZnO-10Na<sub>2</sub>O mol. %) had a lower refractive index ( $n = 2.021$ ) than glass MOD010 (75TeO<sub>2</sub>-10ZnO-10Na<sub>2</sub>O-5PbO mol. %,  $n = 2.024$ ). This is a result of the large polarisability of PbO (3.45 Å<sup>3</sup>) compared to ZnO (2.612 Å<sup>3</sup>) [39]. The index of glass MOD012 (75TeO<sub>2</sub>-10ZnO-10Na<sub>2</sub>O-5GeO<sub>2</sub> mol. %,  $n = 1.992$ ) was lower than MOD007 and MOD010. This is due to the low polarisability of GeO<sub>2</sub> (1.72 Å<sup>3</sup>) compared to ZnO and PbO [39]. MOD014 (90TeO<sub>2</sub>-5WO<sub>3</sub>-5Nb<sub>2</sub>O<sub>5</sub> mol. %), MOD015 (82.5TeO<sub>2</sub>-7.5WO<sub>3</sub>-10Nb<sub>2</sub>O<sub>5</sub> mol. %), and MOD016 (70TeO<sub>2</sub>-25WO<sub>3</sub>-5Bi<sub>2</sub>O<sub>3</sub> mol. %) had much higher indices ( $n = 2.147$ , 2.152 and 2.157 respectively) than the ZnO, PbO and GeO<sub>2</sub> containing glasses. These glasses contained WO<sub>3</sub>, Bi<sub>2</sub>O<sub>3</sub> and Nb<sub>2</sub>O<sub>5</sub> which have high polarisabilities (2.677, 3.507 and 2.679 Å<sup>3</sup> respectively) [39], resulting in high refractive indices.

#### 6.3.2.2. Refractive index of fluorotellurite glasses

Fig. (6.48) shows the variation in refractive index with increasing ZnF<sub>2</sub> batch content for the glass series (90- $x$ )TeO<sub>2</sub>-10Na<sub>2</sub>O- $x$ ZnF<sub>2</sub> mol. %, for  $5 \leq x \leq 30$  mol. % (MOF001, 004 to 008). The index decreases linearly (with a correlation coefficient of 0.99641) from 2.02 (5 mol. % ZnF<sub>2</sub>) to 1.85 (30 mol. % ZnF<sub>2</sub>). This is to be expected as the fluoride and

zinc species are less polarisable than oxygen and tellurium [40], respectively, so the index decreases with  $\text{ZnF}_2$  replacement of  $\text{TeO}_2$ .

Fig. (6.49) shows the variation in refractive index at 633 nm with increasing oxide to fluoride ratio of glasses in the series  $65\text{TeO}_2-(25-x)\text{ZnF}_2-x\text{ZnO}-10\text{Na}_2\text{O}$  mol. %, for  $5 \leq x \leq 25$  mol. % (MOF009 to 013). Glass MOF001 ( $65\text{TeO}_2-25\text{ZnF}_2-10\text{Na}_2\text{O}$  mol. %) used for oxide / fluoride = 0. The index increased linearly (with a correlation coefficient 0.90430) from 1.88740 ( $\text{ZnO} / \text{ZnF}_2 = 0$ ) to 1.95167 ( $\text{ZnO} / \text{ZnF}_2 = 1$ ). This is to be expected as fluorine is less polarisable than oxygen [40], therefore the index increased as ZnO replaced  $\text{ZnF}_2$ .

## 6.4. Summary

### *Core / clad choices for oxide tellurite and fluorotellurite compositions*

For fibre fabrication from tungsten-tellurite glasses studied here, a possible core / clad pair would be MOD014 ( $90\text{TeO}_2-5\text{WO}_3-5\text{Nb}_2\text{O}_5$  mol. %) for the cladding ( $n = 2.147$ ), and MOD016 ( $70\text{TeO}_2-25\text{WO}_3-5\text{Bi}_2\text{O}_3$  mol. %) for the core ( $n = 2.157$ ). Using equation (2.5) the numerical aperture,  $NA = 0.21$ , and acceptance angle,  $\theta = 12^\circ$ , for guiding light at 632.8 nm was calculated. However, this is a rather small acceptance angle and may be problematic when attempting to launch light into the fibre. The index difference for glasses MOD010 ( $75\text{TeO}_2-10\text{ZnO}-10\text{Na}_2\text{O}-5\text{PbO}$  mol. %,  $n = 2.024$ ) and MOD012 ( $75\text{TeO}_2-10\text{ZnO}-10\text{Na}_2\text{O}-5\text{GeO}_2$  mol. %,  $n = 1.992$ ) was higher, and therefore would be more suitable for an oxide core / clad pair. Using equation (2.5), this gives  $NA = 0.34$ ,

and  $\theta = 20^\circ$ . These glasses also transmitted to around 6  $\mu\text{m}$ , whereas the tungsten-tellurite glasses only transmitted to around 5.25  $\mu\text{m}$ .

A suitable core / clad pair for a fluorotellurite multimode optical fibre operating at 632.8 nm would be MOF001 (25 mol. %  $\text{ZnF}_2$ ) as the clad ( $n_2 = 1.887$ ) and MOF005 (20 mol. %  $\text{ZnF}_2$ ) as the core ( $n_1 = 1.914$ ). Using equation (2.5), this gives  $NA = 0.32$ , and  $\theta = 19^\circ$ , an intermediate  $NA$  and acceptance angle compared to the oxide core / clad pairs suggested above. Both glasses were relatively thermally stable on reheating, with a high  $T_x - T_g$  (161°C for MOF001 and 153°C for MOF005). They also had similar glass transition temperatures (237°C for MOF004 and 241°C for MOF005), and hence probably minimal thermal expansion ( $TEC$ ) mismatch (important for making strong fibre) as the product  $TEC/T_g$  tends to be constant across a particular limited range of glass compositions. These compositions also showed low intensity OH absorption bands at 2900  $\text{cm}^{-1}$  (20  $\text{dB}\cdot\text{m}^{-1}$ ), and transmitted to around 6  $\mu\text{m}$ . Therefore the fluorotellurite glasses would probably be a better core / clad pair than the oxide glasses in terms of thermal and optical properties.

## 6.5. References

- [1] S. F. Dyke, A. J. Floyd, M. Sainsbury, and R. S. Theobald, *Organic Spectroscopy an Introduction*. London: Longman, 1978.
- [2] D. C. Harris and M. D. Bertolucci, *Symmetry and spectroscopy: An introduction to vibrational and electronic spectroscopy*. New York: Dover, 1989.
- [3] P. W. Atkins, *Physical chemistry*, 5th ed. Oxford: Oxford University Press, 1994.

- [4] P. M. Fishbane, S. Gasiorowicz, and S. T. Thornton, *Physics for scientists and engineers*, 2nd ed. London: Prentice-Hall, 1996.
- [5] M. D. O'Donnell, C. A. Miller, D. Furniss, V. K. Tikhomirov, and A. B. Seddon, "Fluorotellurite glasses with improved mid-infrared transmission," *Journal of Non-Crystalline Solids*, vol. 331, pp. 48-57, 2003.
- [6] J. A. Kerr, *CRC Handbook of Chemistry and Physics*, 81st ed. Florida: CRC Press, 2000.
- [7] J. E. Stanworth, "Tellurite glasses," *Journal of the Society of Glass Technology*, vol. 36, pp. 217-241, 1952.
- [8] X. Feng, S. Tanabe, and T. Hanada, "Hydroxyl groups in erbium-doped germanotellurite glasses," *Journal of Non-Crystalline Solids*, vol. 281, pp. 48-54, 2001.
- [9] X. Feng, S. Tanabe, and T. Hanada, "Spectroscopic properties and thermal stability of Er<sup>3+</sup>-doped germanotellurite glasses for broadband fiber amplifiers," *Journal of the American Ceramic Society*, vol. 84, pp. 165-171, 2001.
- [10] J. Wang, E. Vogel, and E. Snitzer, "Tellurite glass: a new candidate for fiber devices," *Optical Materials*, vol. 3, pp. 187-203, 1994.
- [11] R. Adams, "Infra-red absorption due to water in glasses," *Physics and Chemistry of Glasses*, vol. 2, pp. 39-49, 1961.
- [12] R. Adams, "Some experiments on the removal of water from glasses," *Physics and Chemistry of Glasses*, vol. 2, pp. 50-54, 1961.
- [13] R. F. Bartholomew, "High-Water Containing Glasses," *Journal of Non-Crystalline Solids*, vol. 56, pp. 331-342, 1983.
- [14] F. M. Ernsberger, "Molecular water in glass," *Journal of the American Ceramic Society*, vol. 60, pp. 91-92, 1977.
- [15] C. R. Kurkjian and L. E. Russell, "Solubility of water in molten alkali silicates," *Journal of the Society of Glass Technology*, vol. 42, pp. 130-144, 1958.
- [16] L. E. Russell, "Solubility of water in molten glass," *Journal of the Society of Glass Technology*, vol. 41, pp. 304-317, 1957.
- [17] H. Scholze, "Gases and water in glass part two," *The Glass Industry*, vol. 43, pp. 622-628, 1966.
- [18] M. Tomozawa, "Water in Glass," *Journal of Non-Crystalline Solids*, vol. 73, pp. 197-204, 1985.

- [19] D. P. Zarubin, "Infrared spectra of hydrogen bonded hydroxyl groups in silicate glasses. A re-interpretation," *Physics and Chemistry of Glasses*, vol. 40, pp. 184-192, 1999.
- [20] A. M. Efimov, T. G. Kostyreva, and G. A. Sycheva, "Water-related IR absorption spectra for alkali zinc pyrophosphate glasses," *Journal of Non-Crystalline Solids*, vol. 238, pp. 124-142, 1998.
- [21] A. M. Efimov and V. G. Pogareva, "Water-related IR absorption spectra for some phosphate and silicate glasses," *Journal of Non-Crystalline Solids*, vol. 275, pp. 189-198, 2000.
- [22] Y. I. Ryskin, *Opt. Spektrosk.*, vol. 8, pp. 606, 1960.
- [23] Y. I. Ryskin, *Neorgan. Mater.*, vol. 7, pp. 375, 1971.
- [24] G. Fuxi, *Optical and Spectroscopic Properties of Glass*, First ed. London: Springer-Verlag, 1992.
- [25] C. N. Banwell, *Fundamentals of Molecular Spectroscopy*. London: McGraw-Hill, 1966.
- [26] P. Charton, L. Gengembre, and P. Armand, "TeO<sub>2</sub>-WO<sub>3</sub> glasses: Infrared, XPS and XANES structural characterizations," *Journal of Solid State Chemistry*, vol. 168, pp. 175-183, 2002.
- [27] N. Ford and D. Holland, "Optical and Physical-Properties of Glasses in the Systems GeO<sub>2</sub>- Bi<sub>2</sub>O<sub>3</sub>-PbO and TeO<sub>2</sub>-Bi<sub>2</sub>O<sub>3</sub>-WO<sub>3</sub>," *Glass Technology*, vol. 28, pp. 106-113, 1987.
- [28] I. Shaltout, Y. Tang, R. Braunstein, and A. M. Abuelazm, "Structural studies of tungstate tellurite glasses by Raman-spectroscopy and differential scanning calorimetry," *Journal of Physics and Chemistry of Solids*, vol. 56, pp. 141-150, 1995.
- [29] I. Shaltout, Y. Tang, R. Braunstein, and E. E. Shaisha, "FTIR spectra and some optical properties of tungstate-tellurite glasses," *Journal of Physics and Chemistry of Solids*, vol. 57, pp. 1223-1230, 1996.
- [30] K. Kobayashi, "Development of infrared transmitting glasses," *Journal of Non-Crystalline Solids*, vol. 316, pp. 403-406, 2003.
- [31] K. Kobayashi and H. Sasaki, "Visible rays cutoff and infrared transmission properties of TeO<sub>2</sub>-GeO<sub>2</sub>-V<sub>2</sub>O<sub>5</sub>-PbF<sub>2</sub> glass systems," *Journal of the European Ceramic Society*, vol. 19, pp. 637-639, 1999.

- [32] H. Burger, W. Vogel, and V. Kozhukharov, "IR transmission and properties of glasses in the  $\text{TeO}_2\text{-R}_n\text{O}_m, \text{R}_n\text{X}_m, \text{R}_n(\text{SO}_4)_m, \text{R}_n(\text{PO}_3)_m$  and  $\text{B}_2\text{O}_3$  systems," *Infrared Physics*, vol. 25, pp. 395-409, 1985.
- [33] V. Nazabal, S. Todoroki, S. Inoue, T. Matsumoto, S. Suehara, T. Hondo, T. Araki, and T. Cardinal, "Spectral properties of  $\text{Er}^{3+}$  doped oxyfluoride tellurite glasses," *Journal of Non-Crystalline Solids*, vol. 326-327, pp. 359-363, 2003.
- [34] M. Beggiora, I. M. Reaney, A. B. Seddon, D. Furniss, and S. A. Tikhomirov, "Phase evolution in oxy-fluoride glass ceramics," *Journal of Non-Crystalline Solids*, vol. 326&327, pp. 476-483, 2003.
- [35] L. L. Kukkonen, I. M. Reaney, D. Furniss, M. G. Pellatt, and A. B. Seddon, "Nucleation and crystallisation of transparent, erbium III-doped, oxyfluoride glass-ceramics," *Journal of Non-Crystalline Solids*, vol. 290, pp. 25-31, 2001.
- [36] A. Jha, S. Shen, and M. Naftaly, "Structural origin of spectral broadening of 1.5 micron emission in  $\text{Er}^{3+}$ -doped tellurite glasses," *Physical Review B*, vol. 62, pp. 6215-6227, 2000.
- [37] S. X. Shen, A. Jha, X. B. Liu, M. Naftaly, K. Bindra, H. J. Bookey, and A. K. Kar, "Tellurite glasses for broadband amplifiers and integrated optics," *Journal of the American Ceramic Society*, vol. 85, pp. 1391-1395, 2002.
- [38] K. Hirano, Y. Benino, and T. Komatsu, "Rare earth doping into optical nonlinear nanocrystalline phase in transparent  $\text{TeO}_2$ -based glass-ceramics," *Journal of Physics and Chemistry of Solids*, vol. 62, pp. 2075-2082, 2001.
- [39] V. Dimitrov and T. Komatsu, "Classification of simple oxides: A polarizability approach," *Journal of Solid State Chemistry*, vol. 163, pp. 100-112, 2002.
- [40] K. Aida, T. Komatsu, and V. Dimitrov, "Thermal stability, electronic polarisability and optical basicity of ternary tellurite glasses," *Physics and Chemistry of Glasses*, vol. 42, pp. 103-111, 2001.

## 7. Surface properties

In this chapter are collected together various studies involving the surface properties of a number of selected oxide tellurite and fluorotellurite compositions. Specifically: X-ray photoelectron spectroscopy (XPS), chemical durability to water, acids and alkalis, and ion exchange. XPS was performed: (i) to assess the effect of fluorination on batch materials, and (ii) on polished and cleaved bulk tungsten-tellurite and fluorotellurite glass surfaces for semi-quantitative elemental analysis, to quantify the effect of melt time on composition of the later system.

Chemical durability was investigated, to choose a possible etchant to ‘clean’ up the preform surface prior to fibre drawing. The ideal etchant would etch congruently, to leave a topologically smooth, and non-contaminated surface. Some of this etching was quantitative by a simple weight loss method, and other results qualitative, describing the quality of the etch. Environmental durability was also studied as any fibre device will inevitably come into contact with water. Therefore, it was important to assess the sensitivity of the glass to water, as the degree of degradation would determine if materials properties (e.g. mechanical and optical) were significantly affected.

Two methods of ion exchange were investigated for an oxide tellurite composition, in both cases  $\text{Ag}^+$  for  $\text{Na}^+$  exchange was attempted. This was undertaken to study the possible manufacture of planar waveguide devices containing a silver rich surface layer with a potentially higher refractive index than the bulk glass, due to the increased polarisability of  $\text{Ag}^+$  compared to  $\text{Na}^+$ , 2.40 and 0.41  $\text{\AA}^3$  ( $1 \text{\AA}^3 = 1 \times 10^{-3} \text{ nm}^3 = 1 \times 10^6 \text{ pm}^3$ ) respectively [1].

## 7.1. Experimental

### 7.1.1. X-ray photoelectron spectroscopy (XPS)

X-ray photoelectron spectroscopy (XPS) is a technique which can be used to probe the surface structure of materials, as the signal obtained is typically from a few nm of the surface of the material. The radiation which is incident on the sample is of high enough energy to result in the ejection of inner shell electrons, with a binding energy characteristic of the atom the electron originated from. The bonding state of species present in a material can result in a shift in the binding energies compared with those expected from the pure element. These peaks can consist of an underlying structure if an atom (such as oxygen) is bonded to more than one type of cation in the material.

#### 7.1.1.1. Method and instrumentation

XPS was performed in this study using two spectrometers due to the availability of equipment.

Powdered ZnF<sub>2</sub> samples were analysed in their as-received and fluorinated states (i.e. powder was not separated by mesh size), using a VG Scientific Escalab Mark II X-ray photoelectron spectrometer, with unmonochromated AlK<sub>α</sub> X-rays operating at an anode potential of 10kV, and a filament emission current of 20 mA. Samples were attached to a metal substrate with carbon tape. The electron spectrometer comprised a hemispherical analyser and was operated in the constant energy mode (CAE) at electron pass energies

of 10 eV and 50 eV for the high-resolution peak scans and survey scans respectively. The vacuum in the analysis chamber was typically better than  $4 \times 10^{-9}$  mbar ( $4 \times 10^{-7}$  Pa). The electron take-off angle used was 90 degrees and the area analysed approximately  $1 \times 1$  cm. The XPS was calibrated monthly with a silver standard.

Glass samples were analysed using a Kratos AXIS ULTRA XPS (under the direction of Prof. D. Briggs), with a mono-chromated  $\text{AlK}_{\alpha}$  source (1486.6 eV) operating at 10 mA emission current, and 10 kV anode potential. This XPS was used in fixed analyser transmission (FAT) mode, with pass energy of 160 eV for wide scans, and 10 eV for high resolution scans. The magnetic immersion lens system used a slot aperture of  $300 \times 700$   $\mu\text{m}$  for wide and high resolution scans. The take-off angle the photoelectron analyser was  $90^{\circ}$ , and acceptance angle  $30^{\circ}$  (in magnetic lens mode). The analysis chamber pressure was typically better than  $1.3 \times 10^{-9}$  mbar ( $1.3 \times 10^{-7}$  Pa). Bulk glass samples were analysed on polished and cleaved surfaces (see chapter 6.1.1.1 for description of polishing process). Surfaces were cleaved in the laboratory atmosphere with a SiC glass cleaver, immediately prior to analysis, as contamination on the sample surface such as hydrolysis, fingerprints, residue from organic solvents (e.g. acetone), silicone release agents from sample bags, and artefacts from polishing (mounting wax and polishing oil), can mask the signal from the sample. As XPS is a surface technique, cleaving the sample should result in spectra which give a better representation of bulk glass composition; however some degree of hydrolysis will be inevitable when cleaved in the laboratory atmosphere. Therefore, any quantitative analysis relating to hydroxide groups in the glass had to be treated carefully.

For both machines (i.e. all samples), a survey scan spectrum in the 0 to 1100 eV binding energy (BE) range was collected, in addition to high resolution scans of regions of interest (e.g. C1s, F1s, Zn2p, Te3d, and O1s regions). A Shirley background model was used to subtract the background; individual peaks were fitted with a Gaussian / Lorentz ratio of 70 / 30. Background removal, peak fitting and peak area determination were performed using CasaXPS software. Semi-quantitative data (i.e. atomic % determination) of survey spectra were derived using modified Scofield elemental sensitivity factors for the ZnF<sub>2</sub> powders, and Kratos elemental sensitivity factors for glass samples. The entire spectra were calibrated (i.e. shifted) to the C1s binding energy of 285 eV. Both X-ray photoelectron spectrometers described above produce semi-quantitative elemental analysis of similar accuracy, however the Kratos machine produces spectra of higher resolution.

#### 7.1.1.2. Theory of operation

The photoelectric effect, conceived by Einstein [2], showed there was a threshold in frequency of incident radiation on a metal's surface, below which no electrons were ejected, regardless of the intensity of the radiation [3]. This is a direct consequence of the fact light is quantised, with energy given by equation (6.1). This threshold in frequency,  $f_c$ , is directly proportional to the minimum energy,  $e\Gamma$ , required to eject these photoelectrons, shown by equation (7.1) [3].

$$e\Gamma = hf_c \tag{7.1}$$

where  $e$  is the charge on an electron ( $1.6022 \times 10^{-19}$  C),  $\Gamma$  = work function of the material, which is the lowest energy at which an electron can escape, and  $h$  = Planck's constant ( $6.62608 \times 10^{-34}$  J.s). At higher incident frequency, photoelectrons are created with a maximum kinetic energy,  $E_{kin}^{max}$ , reflecting the excess energy of the incident photons over the work function [3].

$$E_{kin}^{max} = hf - e\Gamma \quad (7.2)$$

$E_{kin}^{max}$  is associated with electrons from around the Fermi level, i.e. the highest lying occupied energy levels (valence band). The energy of electrons emitted from below the conduction band,  $E_{kin}$ , is given by equation (7.3) [3].

$$E_{kin} = hf - E_B - e\Gamma \quad (7.3)$$

where  $E_B$  is the binding energy of the ejected electron. If the incident radiation is of much greater energy than the work function of the material, the resulting energy spectrum will be directly related to the electronic structure of the sample [3]; this is the basic premise of X-ray photoelectron spectroscopy (XPS).

A wide scan XPS spectrum (i.e. low resolution or survey scan) provides instant chemical identification of species present in a sample, as core electron binding energies are unique to a particular element [3]. High resolution spectra of regions identified from the wide scan can reveal chemical shifts, multiplet peaks, and satellites. This fine detail

can then be used to determine changes in chemical bonding in the sample [3], such as valence and ionicity.

Absorption of X-rays is typically  $10^3$  to  $10^4$  Å ( $10^2$  to  $10^3$  nm, i.e. up to 1 µm) deep into the sample. However, the mean free path of photoelectrons emitted due to an incident beam of  $\approx 1.5$  keV (the energy from an  $\text{AlK}_\alpha$  source) is only 15 Å (1.5 nm) [3]. Therefore, XPS is confined to gathering information from the immediate surface of the sample. Because most of the photoelectrons created are inelastically scattered before emerging from the material, the peaks in a photoelectron spectrum are very sharp. The main peak is a result of photoelectrons from only a few atomic layers. Those from deeper in the sample produce a broad structure, or loss tail, extending to higher binding energies, due to inelastic scattering [3].

The kinetic energy of emitted photoelectrons in the XPS is typically measured by electromagnetic deflection. For optimum resolution, the deflection elements operate at a constant, and low pass energy (e.g. 10 eV for high resolution scans), and utilise variable retardation before photoelectrons enter the electrostatic analyser [3].

The loss tail of a characteristic peak consists of interband transitions<sup>1</sup>, and the summation of excitations from the valence band, known as plasmons. Extrinsic plasmons are a result of excitations after the photoelectric process; intrinsic plasmons occur during photoemission. Extrinsic and intrinsic plasmons are indistinguishable from one another in the spectra [3]. The number of intrinsic plasmons excited during photoemission from a sample is an important consideration, which is used for semi-

---

<sup>1</sup> e.g. shake-up satellites, which are due to intra-atomic relaxation, as an outer-shell electron fills the hole of the core ejected electron.

quantitative elemental analysis, but is difficult to obtain accurately, particularly for multi-component materials (see below).

Photoemission from electronic levels with a non-zero orbital angular momentum ( $j$ ), i.e. for electronic levels higher in energy than the  $s$  level, such as  $p$ ,  $d$ ,  $f$ , etc., results in a spin-orbit doublet [3]. For degenerate  $p$  sub-shells, the ratio of the XPS peak areas of sub-shells is  $1/2$  (e.g. Zn2p<sub>1/2</sub> and Zn2p<sub>3/2</sub>),  $2/3$  for  $d$  sub-shells (e.g. Te3d<sub>3/2</sub> and Te3d<sub>5/2</sub>),  $3/4$  for  $f$  sub-shells (e.g. W4f<sub>5/2</sub> and W4f<sub>7/2</sub>) etc. A multicomponent glass for example, containing  $d$ - and  $f$ -block elements such as zinc, tellurium, and tungsten, as well as lighter elements, such as sodium, fluorine and oxygen, will result in a complex XPS spectrum with multiple peaks, corresponding to the  $s$ ,  $p$ ,  $d$ , and  $f$  levels of the elements present, as well as their loss tails and associated features.

In general, the photoelectron cross-section increases with increasing angular momentum of the orbital; therefore the electron with the largest  $j$  value (e.g. Te3d) of a given core shell results in the most intense XPS peak, and is most appropriate for semi-quantitative chemical analysis [3]. The positions, widths, and areas of the peaks can then be measured from wide and high resolution scans, and semi-quantitative analysis performed with the appropriate sensitivity factors (which vary from spectrometer to spectrometer). Overlapping peaks can be deconvoluted with Gaussian-Lorentzian fitting, and attributed to different chemical species in the sample.

Peak areas are used to calculate the relative concentrations of species in the sample. The ratio in atomic concentration of species A, and species B is given by equation (7.4).

$$\frac{[A]}{[B]} = \frac{\sigma_b \zeta_b \lambda_b \eta_b I_a}{\sigma_a \zeta_a \lambda_a \eta_a I_b} \quad (7.4)$$

where  $\sigma$  is the photoelectric cross-section,  $\zeta$  the fraction of photoelectric events which take place without intrinsic plasmon excitation,  $\lambda$  the mean free-path in the sample,  $\eta$  the kinetic energy dependent spectrometer transmission, and  $I$  the area of the peak [3]. Cross-sections are well known from theoretical calculations by Scofield [4], the mean free path can be estimated from a universal curve, which depends on the energy of the incident beam, not the atomic number of the sample, and  $\eta$  is inversely proportional to the kinetic energy. Due to the superimposition of intrinsic and extrinsic plasmon events,  $\zeta$  is difficult to estimate. Often the entire loss tail is assigned to extrinsic events, i.e.  $\zeta = 1$ . This can introduce in significant errors into quantification, as  $\zeta$  is not necessarily the same for two individual elements in a compound [3].

## **7.1.2. Chemical and environmental durability**

### **7.1.2.1. Method**

For the chemical durability etching studies glass samples (of dimensions  $3 \times 5 \times 5$  mm, polished as described in section 6.1.1.1.) were immersed in a solution of 50 ml of the etchant, in a Pyrex beaker (250 ml capacity). For samples etched at 15 or 21°C, the beaker containing the etchant was surrounded by a constant temperature water bath, and the experiment begun (i.e. the sample was immersed) when the etchant had reached the appropriate temperature, measured with a mercury thermometer. For some samples (where stated) these were removed from the water bath to a sonic bath and agitated ultrasonically at room temperature (measured), to ensure homogeneous etching on all

sides of the sample. For etchants based on HF, the experiments were carried out in a fume cupboard at room temperature in polyethylene containers.

The environmental durability studies were performed on fluorotellurite glass samples of dimension  $3 \times 5 \times 5$  mm (see section 6.1.1.1. for polishing details), in a polypropylene sealed container with 50 ml distilled water (filled to capacity). The experiment at  $60^\circ\text{C}$  was carried out in an oven.

Samples were removed from the etchant / water with polyethylene tweezers after the appropriate time (measured by a stopwatch) and immediately placed in a 250 ml beaker containing 50 ml acetone (Fisher analytical reagent grade), and dried to constant weight using a hotplate at  $70^\circ\text{C}$ . The mass difference after treatment was measured on electronic scales (Sartorius BP211D), which nominally read to five decimal places (i.e. to the nearest  $1 \times 10^{-5}$  g).

The volume of acid or alkali,  $V_A$ , required to produce the total volume of etchant,  $V_{total}$ , of concentration  $[A]_{final}$ , is given by equation (7.5).

$$V_A = V_{total} \times \frac{[A]_{final}}{[A]_{initial}} \quad (7.5)$$

where  $[A]_{initial}$  is the initial concentration of the undiluted acid or alkali. The acid or alkali was made up to the volume  $V_{total}$  with distilled water, i.e.  $V_{total} = V_A + V_{dw}$ , where  $V_{dw}$  = volume of distilled water. For example, to make up a 1000 ml solution of 1M  $\text{H}_2\text{SO}_4$ , from 18M undiluted sulphuric acid, 55.56 ml (1000/18) was added to a 1000 ml container, and made up to 1000 ml with distilled water. Table (7.1) summarises the

etchants used in this study, with molarity for HCl (the number of moles of acid / alkali per litre of solution), and molality (number of moles of acid / alkali per kg of solvent, i.e. water), calculated from the grade (weight %) of acid / alkali.

Table (7.1): Etchants used in this study.

Etchant	Chemical formula	Source	Grade <sup>2</sup> / wt. %	Molarity <sup>3</sup> / mol.l <sup>-1</sup>	Molality / mol.kg <sup>-1</sup>
Sodium hydroxide	NaOH	Fisher	50.0	-	25.0
Sulphuric acid	H <sub>2</sub> SO <sub>4</sub>	"	50.0	-	10.2
Hydrochloric acid	HCl	"	30.5	12.0	-
Hydrofluoric acid	HF	"	50.0	-	50.0
Nitric acid	HNO <sub>3</sub>	"	70.0	-	37.0
Ortho-phosphoric acid	H <sub>3</sub> PO <sub>4</sub>	"	85.0	-	57.8
Glacial acetic acid	CH <sub>3</sub> COOH	"	99.8	-	8309.2

Optical microscopy was performed using a Nikon Optiphot with a Nikon DMX1200F digital camera. Scales on the micrographs were digitally created using a micrograph of a graticule at the same magnification as the sample micrograph.

### 7.1.3. Ion exchange

#### 7.1.3.1. Method and instrumentation

Glasses melted at Nottingham University (see chapter 3) were sent to Prof. G. Rigini's group at CNR in Florence, Italy. These glasses, were polished flat and parallel on

<sup>2</sup> Residual was water

<sup>3</sup> At standard temperature and pressure

opposite sides (see section 6.1.1.1), and treated with silver ion-exchange, as described in table (7.2).

Table (7.2): Ion-exchange methods used on tellurite glasses.

Sample ID	Composition / mol. %	T / °C	t / hr.	Treatment
T08	80TeO <sub>2</sub> -9ZnO-10Na <sub>2</sub> O-1Er <sub>2</sub> O <sub>3</sub>	285	12	Evaporated silver layer on both flat sides (100 and 300 μm), followed by heat treatment under an inert atmosphere (argon).
ST08	79TeO <sub>2</sub> -5ZnO-10Na <sub>2</sub> O-5PbO-1Yb <sub>2</sub> O <sub>3</sub>	270	5	Dipped one flat side into a molten salt solution of 2AgNO <sub>3</sub> -49NaNO <sub>3</sub> -49KNO <sub>3</sub> (mol. %).

These glasses were then annealed to reduce stresses introduced by the ion-exchange process, and mounted in epoxy resin and cross-sectioned for EDX analysis in the electron microscope.

### 7.1.3.2. Environmental scanning electron microscopy (ESEM)

The concentration profile of the silver ions in the glass was mapped using electron dispersive X-ray (EDX) analysis in an environmental scanning electron microscope (ESEM), using a FEI XL30 FEG-ESEM. This instrument was used in auxiliary mode, with the chamber filled with nitrogen (BOC). This mode enabled the sample to be imaged and analysed without coating the sample. In standard SEM operating under a vacuum, insulating samples must be sputtered with a conductive coating such as carbon or gold. Aperture size, accelerating voltage and scales are displayed on all electron micrographs.

Elemental analyses on EDX traces were performed using the ESEM software. The column aperture diameter was 100  $\mu\text{m}$  for EDX analysis and 30  $\mu\text{m}$  for imaging.

### *Theory of operation*

Images are formed in the SEM by a scanning method. The SEM uses a beam of electrons to image the sample. Fig. (7.1) illustrates a typical SEM setup.

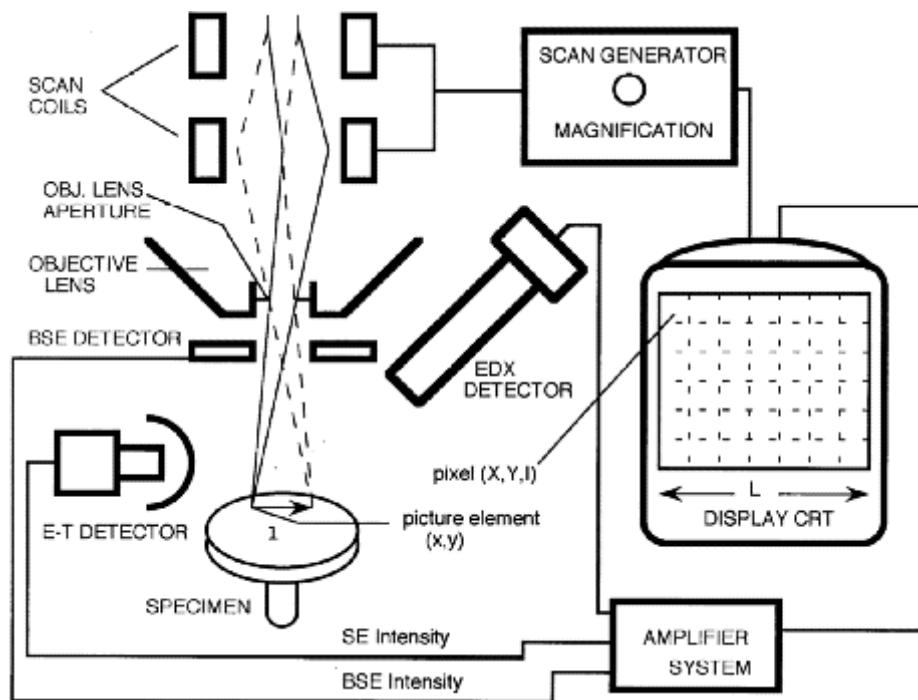


Fig. (7.1): Schematic of typical SEM setup, where SE = secondary electron, BSE = backscattered electron, CRT = cathode ray tube, and E-T = Everhart-Thornley [5].

Electrons are produced by thermionic emission from a tungsten filament, and are accelerated to energies of the range 20-40 keV. The beam is focused onto the surface of the sample by a number of magnetic lenses, where the beam diameter is typically 2-10 nm [5]. The electron beam is scanned across the sample surface by the scan coils, and a

detector counts the number of low energy secondary electrons (SE), and other radiation from each point. Simultaneously, the spot of a cathode ray tube (CRT) is scanned across the microscope screen, and its brightness modulated by the amplified current from the detector. The electron beam and CRT spot are scanned in a similar way to a television, in a rectangular array of straight lines known as a raster [5]. The magnification of the microscope is the ratio of the CRT screen dimensions, to the area being scanned on the sample; e.g. if the beam scans an area  $50 \times 50 \mu\text{m}$ , displayed on a screen  $10 \times 10 \text{ cm}$ , magnification =  $10 \times 10^{-2} / 50 \times 10^{-6} = 2000$ .

#### *Beam interaction with sample*

As the electron beam interacts with the sample, the energy of the incident electrons is reduced, resulting in a number of secondary, backscattered and other emissions. Fig. (7.2) summarises the radiation emitted from a sample surface exposed to the electron beam in an SEM.

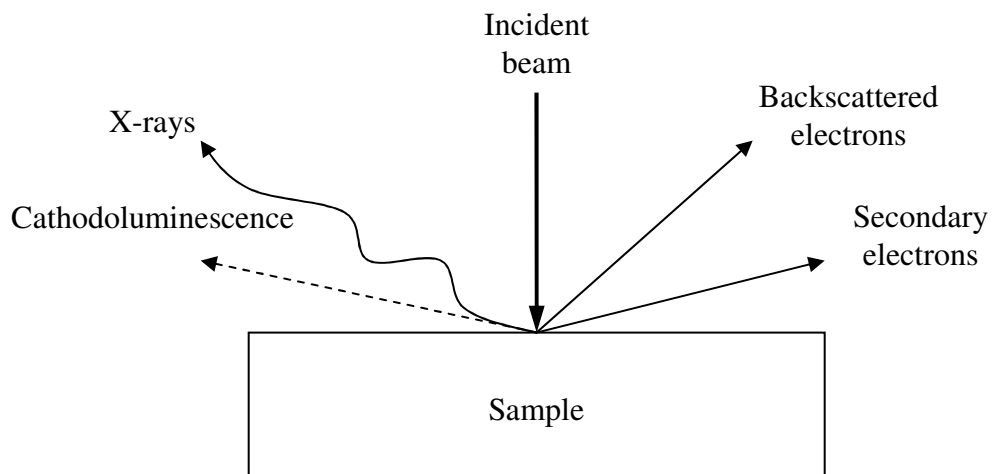


Fig. (7.2): Radiation emitted from a surface exposed to the electron beam in an SEM [5].

All SEMs have facilities for detecting SEs and backscattered electrons (BSEs); either can be used for imaging on the CRT, but each provides different information about the sample. X-rays are generally used for chemical analysis, and will be discussed later. The different types of radiation generated are a result of inelastic scattering. Only radiation generated which escapes the sample will be detected. X-rays are not absorbed easily, therefore most will escape from the sample and the volume of the material contributing to X-rays (the sampling volume) is almost equivalent to the interaction volume [5].

Electrons which are backscattered will not escape the sample if they are generated at depths greater than around 1  $\mu\text{m}$ , resulting in a smaller region that the backscattered signal is gathered from. The actual sampling volume is around 0.1  $\mu\text{m}$  into the sample, for materials of medium atomic weight, as low energy BSEs originate too far from the incident beam to be detected [5]. A small number of SEs are generated from escaping BSEs, but most are from electrons in the incident beam which enter the sample. Because of this, the SE signal originates from a region slightly larger than the diameter of the incident beam [5].

### *Electron detection*

SEs are detected using an Everhart-Thornley detector, which is based on a scintillator-photomultiplier system. For flat samples, this type of detectors is highly efficient, collecting virtually all the SEs [5]. It should be noted, BSEs travelling at the appropriate angle, will strike the Everhart-Thornley detector, although the number of BSEs is negligible. The two most common types of BSE detectors are scintillator-photomultiplier

or solid-state types. The former tend to be bulky, but respond quickly to high scan rates, and the later consist of a thin plate mounted on the base of the objective, but are slow to respond [5].

### *Optics of the SEM*

The probe size (diameter of the electron beam on the sample surface) is controlled by the strength of the condenser lens; increasing the lens strength decreases the probe diameter. If the strength is kept constant, the diameter can be decreased by reducing the distance between the objective aperture and the sample (i.e. the working distance). To minimise spherical aberration, an objective aperture of diameter  $r$  is used, which restricts entry of the electrons into the objective aperture. Because of this, not all the beam which has passed through the condenser lens can enter the objective lens. If the semi-angle of the beam leaving the condenser lens is  $\phi_0$ , and the semi-angle of the beam entering the objective lens is  $\phi_1$ , then the current in the probe striking the sample surface ( $C_1$ ) is given by equation (7.6).

$$C_1 = C_0 \times \left( \frac{\phi_1}{\phi_0} \right)^2 \quad (7.6)$$

where  $C_0$  is the current of the monochromatic beam of electrons leaving the tungsten filament. Therefore, the beam current striking the sample surface decreases as the condenser lens strength is increased (and hence probe diameter decreases) and as  $r$

becomes smaller. Probe size and current are very important in determining the ultimate resolution of the SEM.

### *Pixels and depth of field*

To understand fully image formation in the SEM, which is entirely different to that of an optical and transmission electron microscope (TEM), pixels (picture elements) must be considered. The amplified signal from the detector is transferred to the CRT with a diameter of around 0.1 mm. Therefore, a CRT 10 × 10 cm displays  $1000 \times 1000 = 10^5$  pixels [5]. These units are the smallest element of the image, 0.1 × 0.1 mm square of uniform intensity. As the electron beam mimics the movement of the CRT, there is a corresponding pixel on the sample for each one on the screen. The size of the pixel, *PS*, on the sample is given by equation (7.7) [5].

$$PS = \frac{100}{m_g} \mu\text{m} \quad (7.7)$$

where  $m_g$  is magnification. To resolve two features in the image, they must occupy separate pixels. Therefore, the working resolution of the SEM is limited by the sample pixel size [5]. If the electron beam is larger than the pixel size, then the signal from adjacent pixels will be merged, and this will degrade the signal. If the beam size is smaller than the pixel size, the signal will be weak and noisy. To achieve optimum performance in the SEM, the beam diameter should be equal to the pixel size, which will vary with magnification [5].

The SEM has a much higher depth of field as well as spatial resolution. Depth of field,  $DOF$ , in the SEM is given by equation (7.8).

$$DOF = \frac{0.2W_d}{r \times m_g} \text{ mm} \quad (7.8)$$

where  $W_d$  is the working distance. A typical value of  $DOF$  in the SEM is 40  $\mu\text{m}$  compared to 1  $\mu\text{m}$  for an optical microscope [5].

#### *Ultimate resolution*

The best resolution the SEM can achieve is given by the sample pixel size,  $PS$ , which in turn depends on the magnification. This resolution is only achieved if the sampling volume is no bigger than  $PS$ . For X-rays, this volume can be of the order of microns, and for SEs, of the order of the beam diameter. Therefore, spatial resolution better than this cannot be achieved [5]. Lowering the beam current reduces the beam diameter, and hence sampling volume, but this may result in insufficient signal. Ultimate resolution can therefore be defined as the smallest probe diameter which provides a useable signal from the sample [5].

#### *Energy dispersive X-ray (EDX) analysis*

When electrons with energy of the order of a few keV strike a sample, X-rays are produced. These X-rays are characteristic of the atoms within the sample, and can

provide information regarding chemical composition [5]. The different types of elements present (qualitative) can be identified by the energy (and hence wavelength) of the X-rays emitted, and the amount of each element present (quantitative) can be obtained by the number of X-rays of a particular energy detected per unit time [5].

$K_{\alpha 1}$  and  $K_{\alpha 2}$  X-rays (the K-doublet) are around eight times more intense than  $K_{\beta}$  X-rays, and are therefore used to identify lighter elements. For atoms heavier than tin ( $Z = 50$ ), electrons with an energy greater than 25 keV are needed to excite K lines, therefore L lines (or M lines for very heavy elements) provide a suitable signal for identification [5]. All elements have at least one strong X-ray line of energy  $< 10$  keV. The most efficient production of X-rays occurs when the bombarding electrons have around three times the energy. Therefore an incident electron beam of energy 25-30 keV should produce suitable X-rays from the sample for chemical analysis [5].

The relative amounts of characteristic X-rays emitted from elements of similar atomic number may be affected by a phenomenon known as fluorescence. This occurs when X-rays travelling through the sample excite other atoms, which emit X-rays of slightly lower energy. Even though the process is not particularly efficient, it can lead to complications when trying to accurately quantify the amount of each element present in a sample which contains elements of similar atomic number [5].

The size of the X-ray sampling volume is virtually identical to the interaction volume. Therefore, the smallest volume which can be analysed is typically  $1 \mu\text{m}^3$ . Reducing this volume would require reducing the beam energy, which in turn would result in an insufficient amount of X-rays emitted for analysis [5]. Therefore, accurate quantitative analysis is complex [5].

The X-ray detector (see fig. (7.1)) consists of a reverse-biased silicon p-i-n junction coated with gold. X-rays strike the detector, resulting in excitation of electrons into the conduction band, leaving positive holes. The number of electron-hole pairs generated is proportional to the energy of the X-ray detected [5]. As the detector is reverse-biased, a current will flow each time an X-ray strikes the detector. In pure silicon this current would be negligible compared to the applied voltage. Therefore, the resistivity of the detector is increased by doping the silicon with lithium, and cooling the detector with liquid nitrogen to around 77 K. Now, when an X-ray enters the detector, the current is much larger relative to the applied voltage, making detection, amplification, and recording easier [5]. The detector is protected by a beryllium window (7-8  $\mu\text{m}$  thick) to prevent condensation of contaminants onto the cold detector. However, this means X-rays from elements lighter than Be ( $Z \leq 4$ ) cannot be detected [5].

The current generated by the X-rays lasts  $< 1 \mu\text{s}$ , and is known as a pulse. The pulse is amplified and transmitted to a multi-channel analyser (MCA). The MCA consists of thousands of channels corresponding to different X-ray energies [5]. The MCA collects the energies of the X-rays detected, and plots a histogram of energy against number of counts. A suitable spectra can be obtained in 1 to 2 minutes, however if the counts per second (cps) exceed 1000, some of the pulses will be rejected by the MCA [5]. This information is displayed on the PC linked to the SEM. The software can then assign elements to the peaks, and quantify the amount of each element present by integrating the peaks.

There are a number of limitations of the EDX system. Elements lighter than beryllium cannot be detected due to the presence of the Be-window. Fluorescence from samples

containing elements of similar atomic number can result in misleading quantitative analysis [5]. To reduce noise in the spectra, the detector must be kept at 77K which can be difficult to achieve at all times. X-ray peaks are poorly resolved (typically 100-200 keV wide), rather than sharply defined. As all peaks occupy a number of channels in the MCA, this reduces the peak heights [5].

### *ESEM*

One of the main limitations of the conventional SEM is that insulated materials must be coated (typically with carbon or gold) to avoid sample charging. This can interfere with imaging fine surface features and chemical analysis. Also, 'wet' samples require lengthy preparation due to the high vacuum needed in the sample chamber [6]. In the ESEM, by using pressure limiting apertures (PLAs), the electron gun can be kept at high vacuum, whilst the sample can be kept at relatively high pressures: 13 to 27 mbar (1.3 to 2.7 kPa). A number of PLAs are placed down the ESEM column, with a pressure differential maintained across each one [6]. Fig. (7.3) illustrates the ESEM column and sample stage.

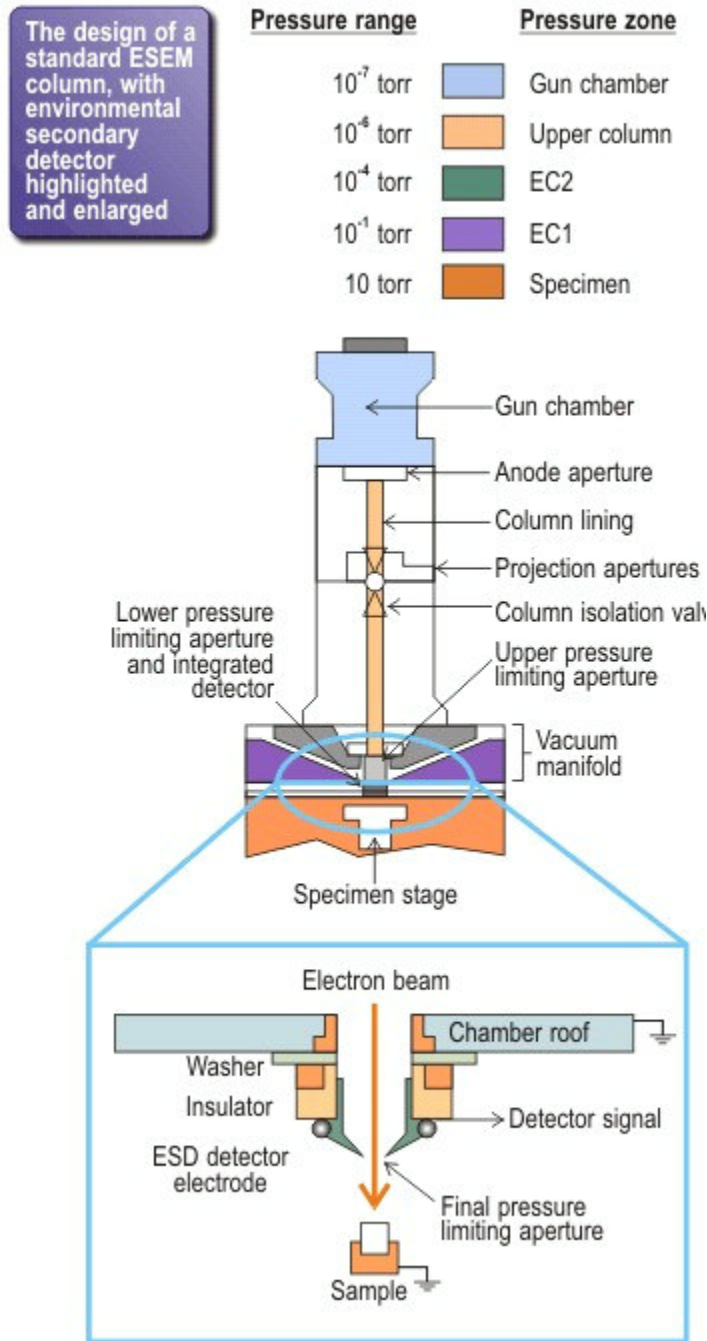


Fig. (7.3): ESEM column and sample stage [6].

LaB<sub>6</sub> and field emission guns can also be used at these low pressures for high quality imaging [6]. Due to the presence of water (wet-mode), or a gas<sup>(4)</sup> (auxiliary-mode), in the sample chamber, the conventional Everhart-Thornley detector mentioned earlier, cannot be used to detect SEs in the ESEM. The environmental SE detector was developed to work at pressures in excess of 13 mbar (1.3 kPa) [6].

Scattering of the electron beam between the gun and sample must be considered, due to the large number of atoms / molecules present in the sample chamber. High resolution can be achieved if the distance between the final PLA and sample is kept relatively small ( $\approx 50$  cm) and the pressure low ( $\approx 16$  mbar  $\equiv 1.6$  kPa) [6]. With these conditions, a 20 keV electron beam will result in a well defined probe on the sample surface, with a weak background scatter extending tens of microns. A resolution of 5 nm can be obtained using a LaB<sub>6</sub> filament operating at low enough pressure [6].

SEs and BSEs emitted from the sample surface collide with atoms / molecules in the chamber. This invariably will lead to ionization of the gas (particularly with SEs) [6]. Each ionization results in the emission of a daughter electron, which in turn ionizes another gas molecule, causing a cascade effect in the gap between the sample and the detector [6]. Fig. (7.4) illustrates this.

---

<sup>(4)</sup> typically nitrogen

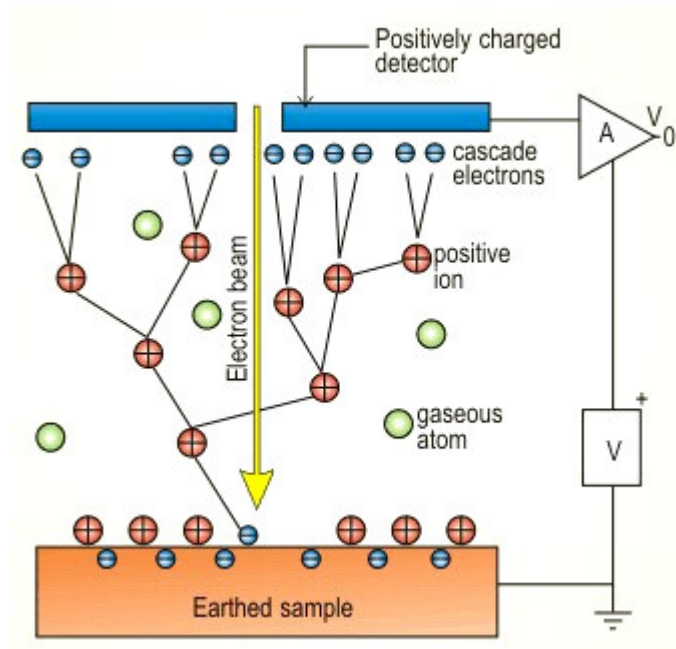


Fig. (7.4): Process for electron detection in the ESEM chamber [6].

The overall cascade process results in considerable signal amplification. The net amplification depends on gas type and pressure, detector bias, and the energy and number of electrons leaving the sample [6].

## 7.2. Results

### 7.2.1. X-ray photoelectron spectroscopy (XPS)

#### 7.2.1.1. XPS of ZnF<sub>2</sub> powder

Fig. (7.5) shows a low resolution XPS scan of the as received Alfa Aesar 99.995 % ZnF<sub>2</sub> powder [7]. Fig. (7.6) shows a low resolution XPS scan of the ZnF<sub>2</sub> powder after fluorination [7].

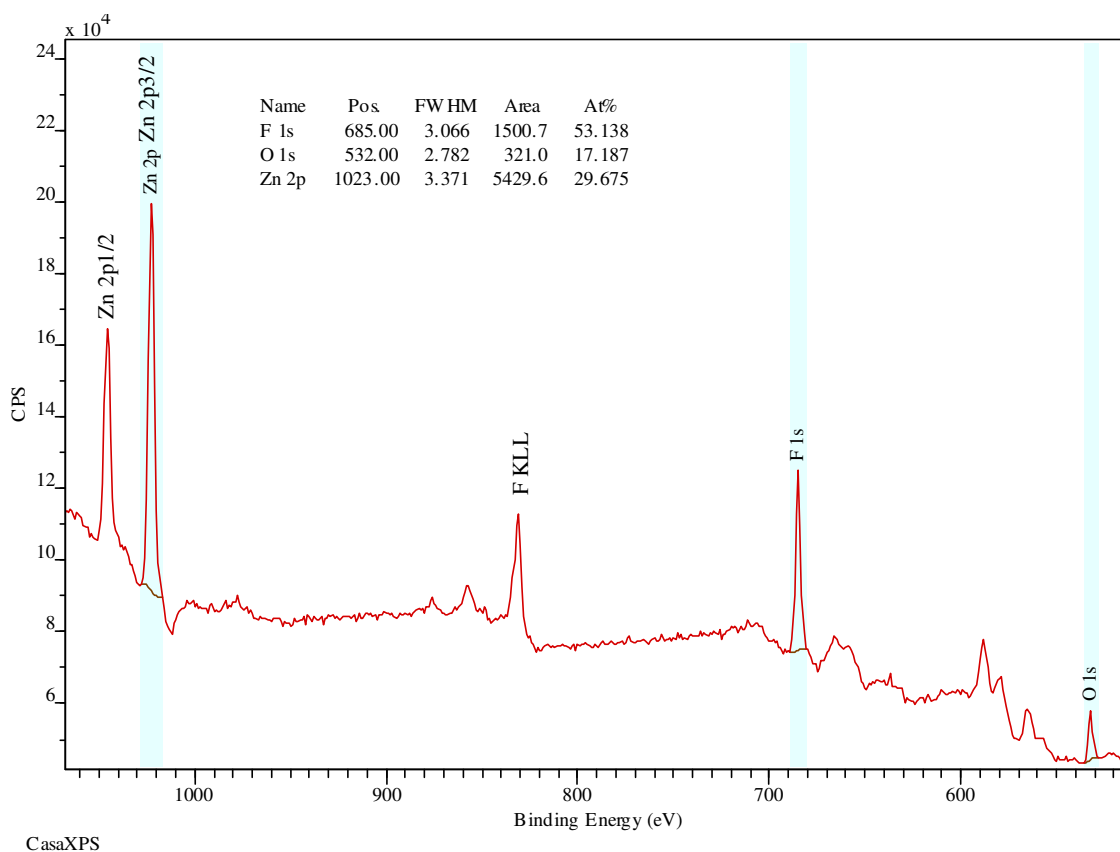


Fig. (7.5): Wide scan XPS spectrum of the as-received ZnF<sub>2</sub> powder [7].

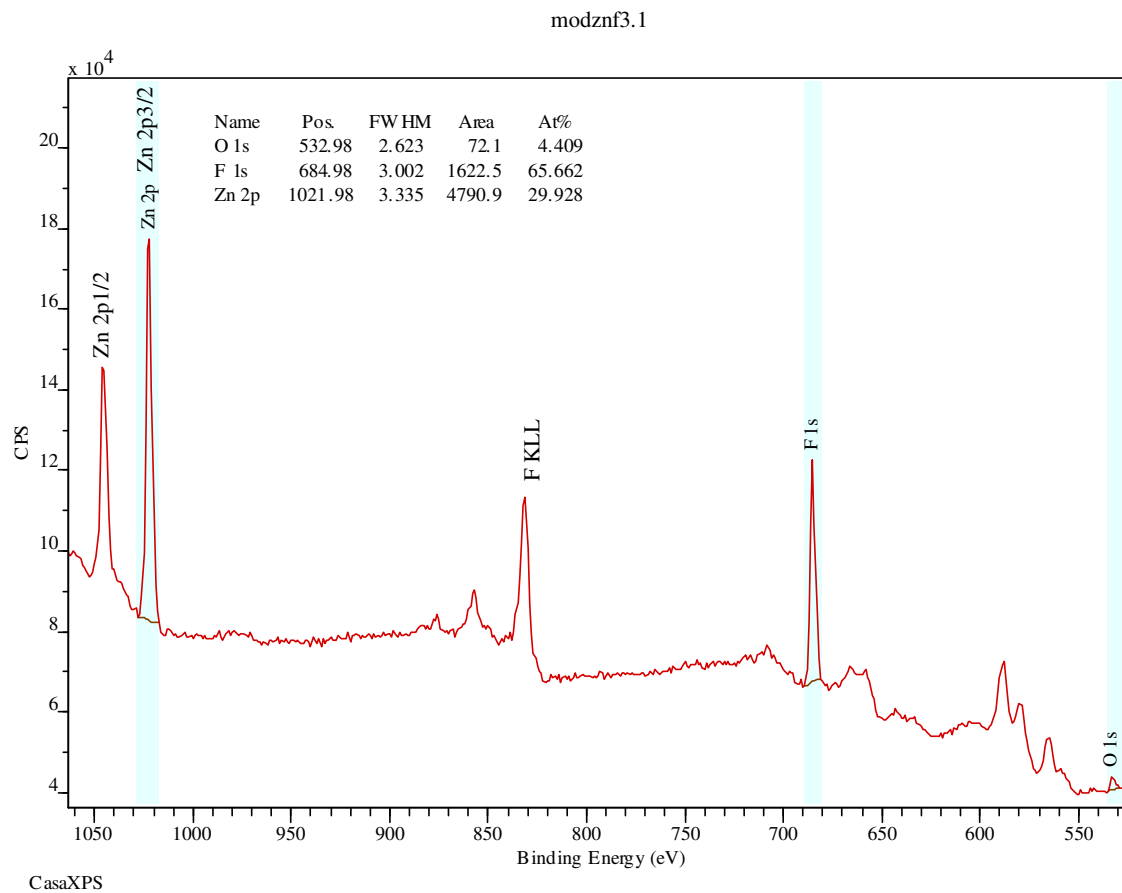


Fig. (7.6): Wide scan XPS spectrum of the fluorinated  $\text{ZnF}_2$  powder [7].

It can be seen by comparing fig. (7.5) and (7.6) that the O1s peak has been significantly reduced by fluorination. Table (7.3) summarises the most intense fluorine (1s), zinc ( $2p_{3/2}$ ), and oxygen (1s) peaks, from the high resolution XPS scans of the as-received and fluorinated  $\text{ZnF}_2$ , with atomic and mass compositions of the powders, and theoretical value from the NIST (National Institute of Standards and Technology) XPS database for  $\text{ZnF}_2$  ( $\text{Zn}2p_{3/2}$  and F1s) and  $\text{ZnO}$  (O1s) [7].

Table (7.3): Positions of most intense fluorine (1s), zinc ( $2p_{3/2}$ ), and oxygen (1s) peaks, from high resolutions XPS scans of as-received and fluorinated  $ZnF_2$ , with atomic and mass compositions of the powders [7].

XPS peak	Peak / eV	As received			Fluorinated		
		Position / eV	Wt. %	At. %	Position / eV	Wt. %	At. %
F 1s	684.8	685.2	22.82	45.40	685.1	29.78	57.95
Zn $2p_{3/2}$	1022.5	1022.8	71.58	41.38	1022.5	68.87	38.93
O 1s	530.4	532.0	5.60	13.22	531.7	1.35	3.12

These values from the high resolution scans differ significantly from the low resolution quantitative analysis shown on fig. (7.5) and (7.6). The F1s peak shifted -0.1 eV on fluorination, the Zn $2p_{3/2}$  peak -0.3 eV, and the O1s peak -0.3 eV. The position of the Zn $2p_{3/2}$  peak was identical to the theoretical value after fluorination (1022.5 eV), and the F1s peak shifted 0.1 eV closer to the theoretical value (684.8 eV).

#### 7.2.1.2. XPS of oxide tellurite glasses

Fig. (7.7) shows a wide scan XPS spectrum on a cleaved surface of glass MOD015 ( $82.5TeO_2-7.5WO_3-10Nb_2O_5$  mol. %, see chapter 3 for melting and annealing details).

The C1s peak can be seen at around 285 eV (due to contamination on sample surface).

Fig. (7.8) shows the high resolution O1s spectrum for cleaved glass MOD015.

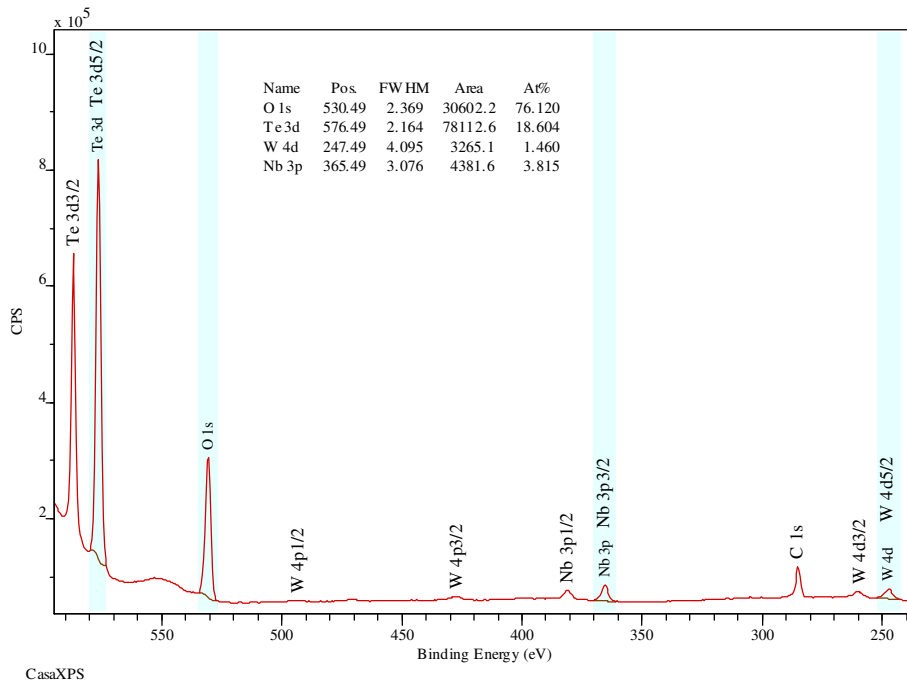


Fig. (7.7): Wide scan XPS spectrum on a cleaved surface of glass MOD015 ( $82.5\text{TeO}_2$ - $7.5\text{WO}_3$ - $10\text{Nb}_2\text{O}_5$  mol. %).

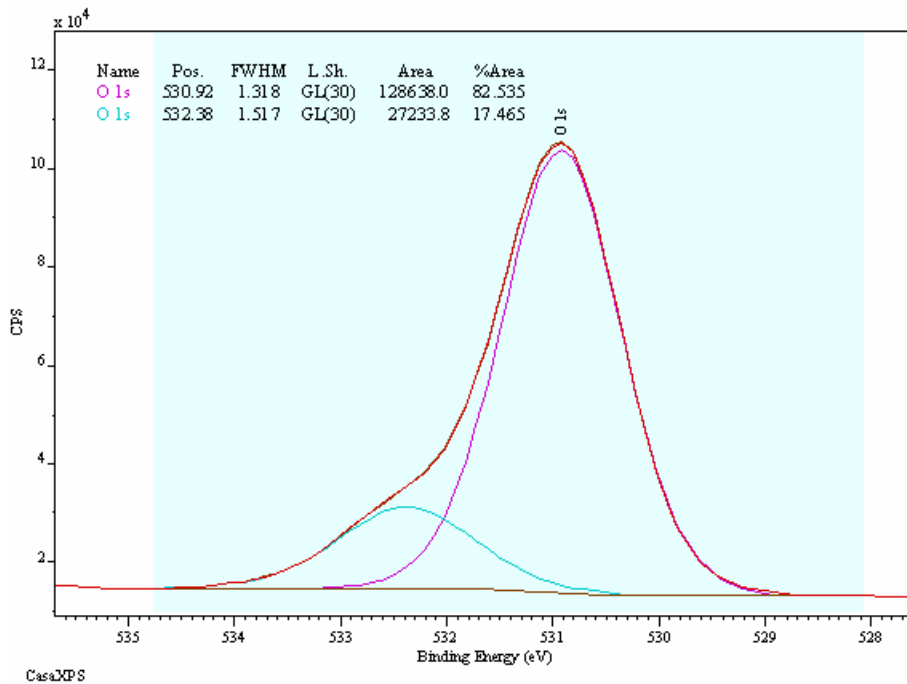


Fig. (7.8): High resolution O1s XPS spectrum on a cleaved surface of glass MOD015 ( $82.5\text{TeO}_2$ - $7.5\text{WO}_3$ - $10\text{Nb}_2\text{O}_5$  mol. %), with deconvoluted components due to: bridging and non-bridging oxygens (O1s) and OH (O1s).

This peak was asymmetric, with a higher bonding energy shoulder at 532.4 eV (17.5 %), to the main peak at 530.9 eV (82.5 %). Table (7.4) summarises the quantitative analysis for this glass from the high resolution scans.

Table (7.4): Quantitative analysis from high resolution XPS scans of cleaved glass MOD015 (82.5TeO<sub>2</sub>-7.5WO<sub>3</sub>-10Nb<sub>2</sub>O<sub>5</sub> mol. %), and theoretical peak positions and atomic % batched.

XPS peak	Theoretical		High resolution XPS scan		
	Peak / eV	At. %	Peak / eV	At. %	Wt. %
O 1s	530.4	68.35	530.9	66.67	20.49
Te 3d <sub>5/2</sub>	576.2	23.74	576.8	25.15	61.66
W 4d <sub>5/2</sub>	248.0	2.16	247.6	1.86	6.56
Nd 3d <sub>5/2</sub>	207.6	5.76	207.5	6.33	11.29

It can be seen that the at. % quantitative analysis were very close to the as-batched values (varying 2.5 to 13.9 %). For comparison, fig. (7.9) shows the wide scan of the polished surface of glass MOD015. The intense peak at around 285 eV was due to C1s, i.e. organic contamination at the surface. Fig. (7.10) shows the high resolution O1s scan from the polished surface (see section 6.1.1.1) of glass MOD015,

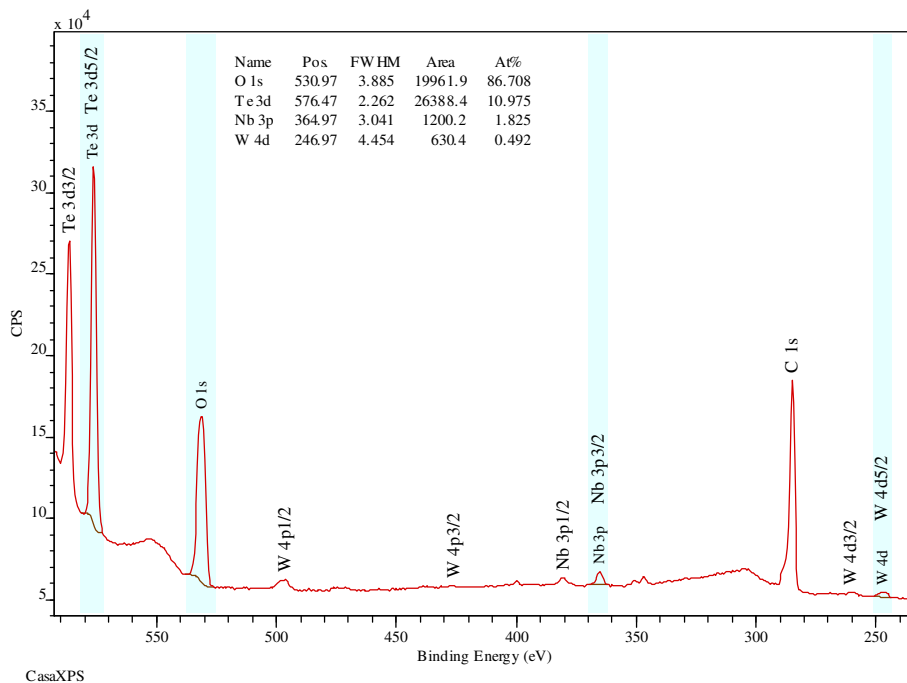


Fig. (7.9): Wide scan XPS spectrum on a polished surface of glass MOD015 (82.5TeO<sub>2</sub>-7.5WO<sub>3</sub>-10Nb<sub>2</sub>O<sub>5</sub> mol. %).

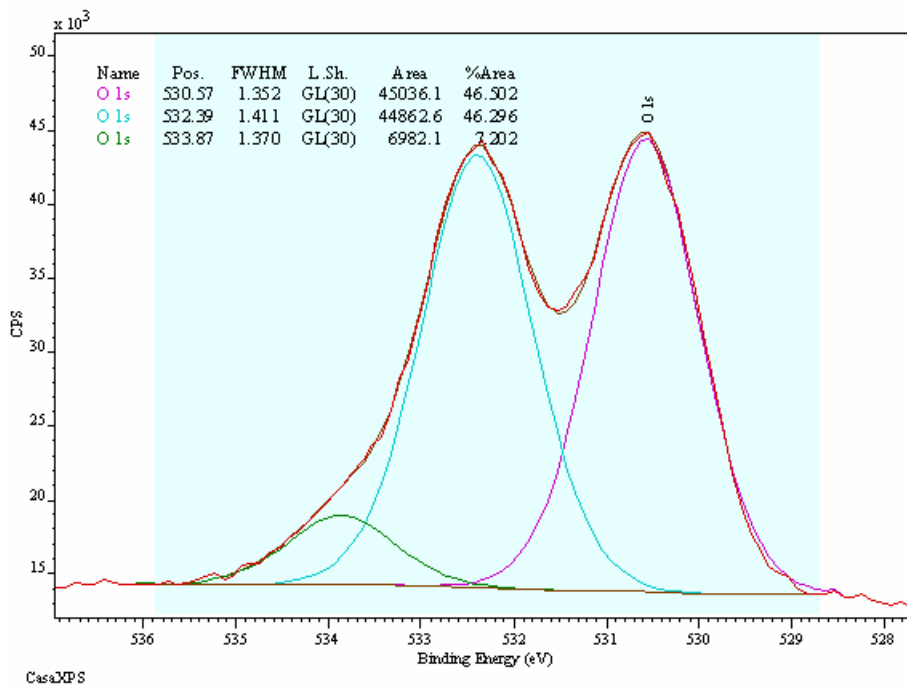


Fig. (7.10): High resolution O1s XPS spectrum on a polished surface of glass MOD015, (82.5TeO<sub>2</sub>-7.5WO<sub>3</sub>-10Nb<sub>2</sub>O<sub>5</sub> mol. %), with deconvoluted components due to: bridging and non-bridging oxygens (○1s), OH (○1s) and M=O species (○1s).

It can be seen that the peak is highly asymmetric, incorporating higher energy shoulders at 532.4 eV (46.3 %), and 533.9 eV (7.2 %), to the main peak at 530.6 eV (46.5 %). This peak was asymmetric, with a higher bonding energy shoulder at 532.4 eV (17.5 %), to the main peak at 530.9 eV (82.5 %). Table (7.5) summarises the quantitative analysis for this glass from the high resolution scans.

Table (7.5): Quantitative analysis from high resolution XPS scans of polished glass MOD015 (82.5TeO<sub>2</sub>-7.5WO<sub>3</sub>-10Nb<sub>2</sub>O<sub>5</sub> mol. %), and theoretical peak positions and atomic % batched.

XPS peak	Theoretical		High resolution XPS scan		
	Peak / eV	At. %	Peak / eV	At. %	Wt. %
O 1s	530.4	68.35	530.5	78.52	32.23
Te 3d <sub>5/2</sub>	576.2	23.74	576.4	16.65	54.51
W 4d <sub>5/2</sub>	248.0	2.16	247.1	0.75	3.55
Nd 3d <sub>5/2</sub>	207.6	5.76	207.1	4.08	9.71

It can be seen by comparing table (7.4) and (7.5), for the polished surface and cleave respectively, that the polished glass surface was relatively oxygen rich, and tellurium and tungsten deficient, compared to the batched and cleaved compositions (14.9 to 65.1 % variation from batched values).

### 7.2.1.3. XPS of fluorotellurite glasses

XPS spectra of two fluorotellurite glasses will be shown here, with varying melting time. The effect of this processing should be manifested in the ratio of F1s / O1s peaks in the XPS spectra.

Fig. (7.11) shows a wide scan XPS spectrum of a cleaved surface of glass MOF001\_iii ( $65\text{TeO}_2\text{-}10\text{Na}_2\text{O-}25\text{ZnF}_2$  mol. %), which was melted for 1.75 hours, with un-fluorinated  $\text{ZnF}_2$  (see chapter 3 for further details).

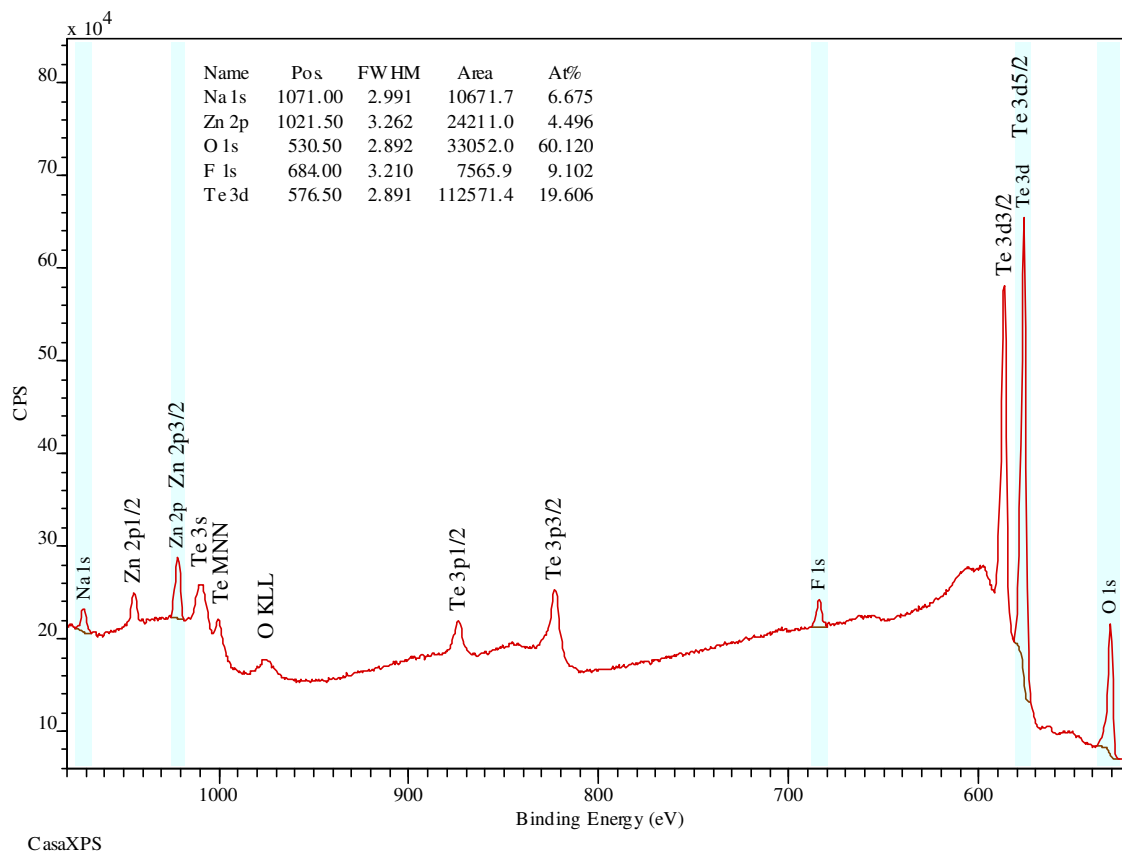


Fig. (7.11): Wide scan XPS spectrum of cleaved surface of glass MOF001\_iii ( $65\text{TeO}_2\text{-}10\text{Na}_2\text{O-}25\text{ZnF}_2$  mol. %).

Fig. (7.12) shows the high resolution XPS scan of the F1s peak, which was asymmetric, from a cleaved surface of glass MOF001\_iii ( $65\text{TeO}_2\text{-}10\text{Na}_2\text{O-}25\text{ZnF}_2$  mol. %), melted for 1.75 hours. The O1s peak was also asymmetric as shown in fig. (7.13).

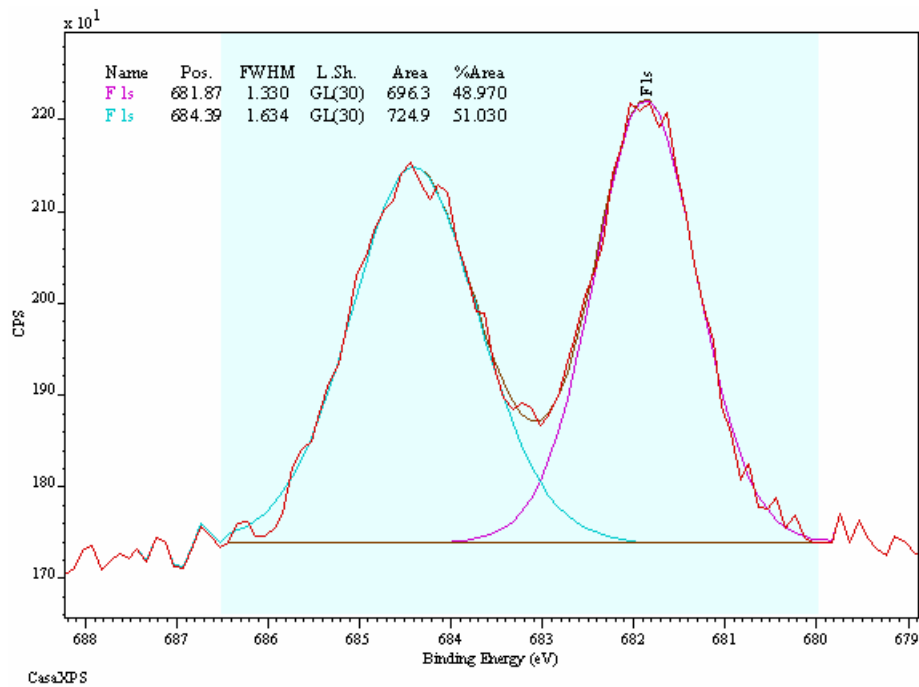


Fig. (7.12): High resolution XPS spectrum of F1s peak from cleaved surface of glass MOF001\_iii (65TeO<sub>2</sub>-10Na<sub>2</sub>O-25ZnF<sub>2</sub> mol. %), with deconvoluted components due to: M-F (F1s) and M'-F (F1s).

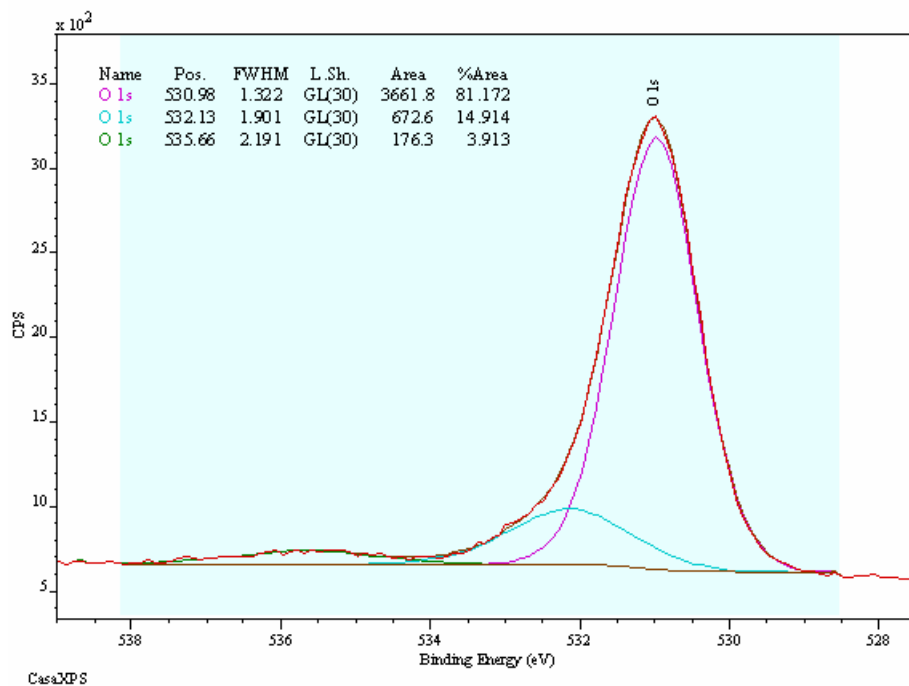


Fig. (7.13): High resolution XPS scan of O1s spectrum from cleaved surface of glass MOF001\_iii (65TeO<sub>2</sub>-10Na<sub>2</sub>O-25ZnF<sub>2</sub> mol. %), with deconvoluted components due to: bridging and non-bridging oxygens (O1s), OH (O1s) and M=O species (O1s).

All other high resolution peaks scanned (Na1s, Zn2p, and Te3d) were reasonably symmetric (with a residual standard deviation between the XPS data and Gaussian / Lorentz fit typically < 3.09). Table (7.6) summarises the quantitative analysis from the high resolution scans, and for comparison, the actual atomic % batched and theoretical peak positions from the NIST XPS database.

Table (7.6): Quantitative analysis from high resolution XPS scans of cleaved glass MOF001\_iii (65TeO<sub>2</sub>-10Na<sub>2</sub>O-25ZnF<sub>2</sub> mol. %), and theoretical peak positions and atomic % batched.

XPS peak	Theoretical		High resolution XPS scan		
	Peak / eV	At. %	Peak / eV	At. %	Wt. %
Te 3d <sub>5/2</sub>	576.2	21.67	576.8	24.47	66.50
O 1s	530.4	46.67	531.0	52.15	17.77
Na 1s	1072.5	6.67	1071.2	6.18	3.02
Zn 2p <sub>3/2</sub>	1022.5	8.33	1021.9	5.82	8.10
F 1s	684.8	16.67	681.8	11.39	4.61

It can be seen from this table, that the quantitative analysis is again relatively accurate, giving atomic % values much closer to the batched composition than the wide scan values show in fig. (7.11).

Fig. (7.14) shows a wide scan XPS spectrum of a cleaved surface of glass MOF001\_v (65TeO<sub>2</sub>-10Na<sub>2</sub>O-25ZnF<sub>2</sub> mol. %), which was melted for 2 hours with fluorinated ZnF<sub>2</sub>. Fig. (7.15) shows the Na1s peak for the cleaved surface of glass MOF001\_v (65TeO<sub>2</sub>-10Na<sub>2</sub>O-25ZnF<sub>2</sub> mol. %), which was melted for 2 hours with fluorinated ZnF<sub>2</sub> (all high resolution scans will be shown for this glass, regardless of symmetry, for completeness).

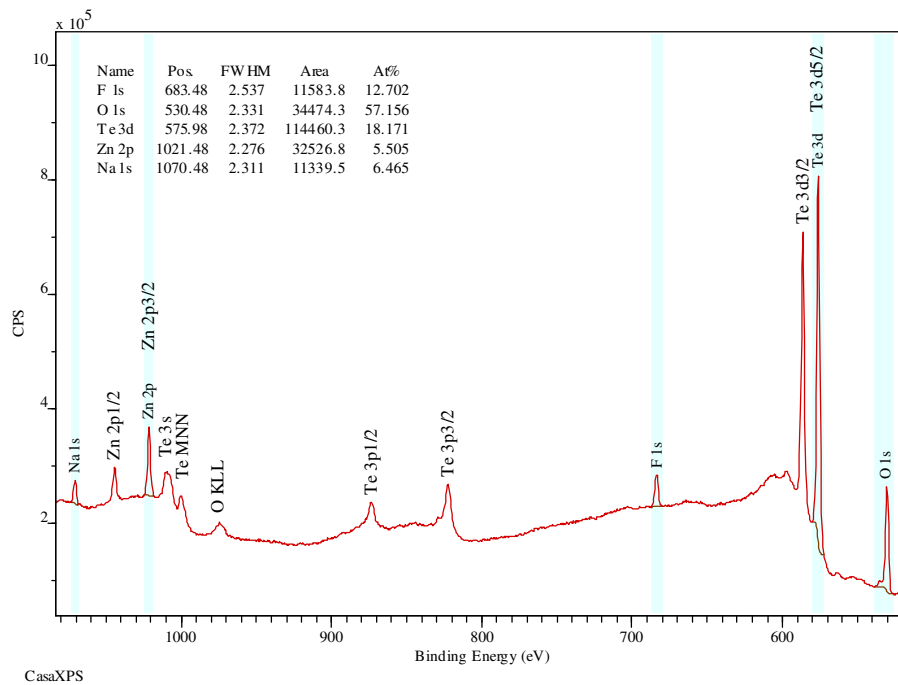


Fig. (7.14): Wide scan XPS spectrum of cleaved surface of glass MOF001\_v (65TeO<sub>2</sub>-10Na<sub>2</sub>O-25ZnF<sub>2</sub> mol. %).

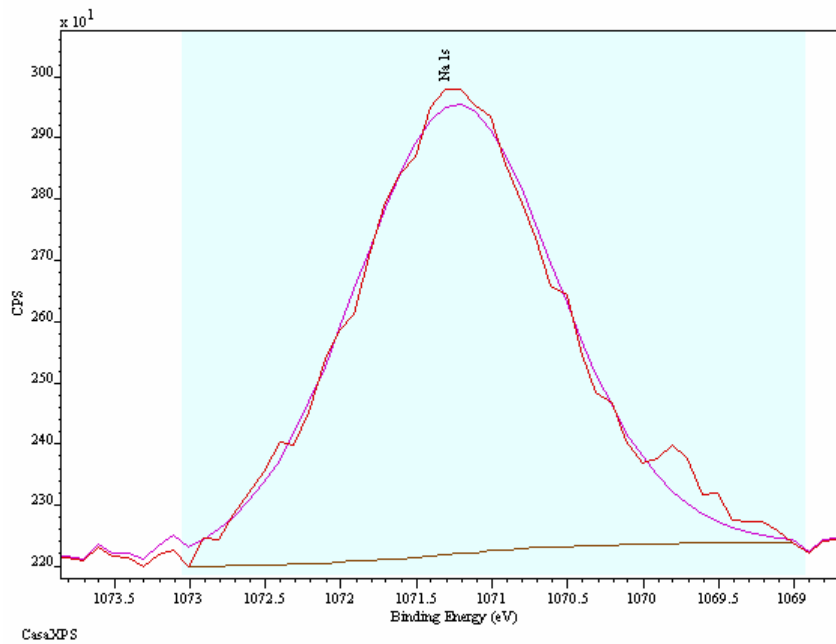


Fig. (7.15): High resolution XPS spectrum of Na 1s peak from cleaved surface of glass MOF001\_v (65TeO<sub>2</sub>-10Na<sub>2</sub>O-25ZnF<sub>2</sub> mol. %), melted for 2 hours with fluorinated ZnF<sub>2</sub>.

Fig. (7.16) shows the  $Zn2p_{1/2}$  and  $Zn2p_{3/2}$  peaks for the cleaved surface of glass MOF001\_v ( $65TeO_2-10Na_2O-25ZnF_2$  mol. %), which was melted for 2 hours with fluorinated  $ZnF_2$ .

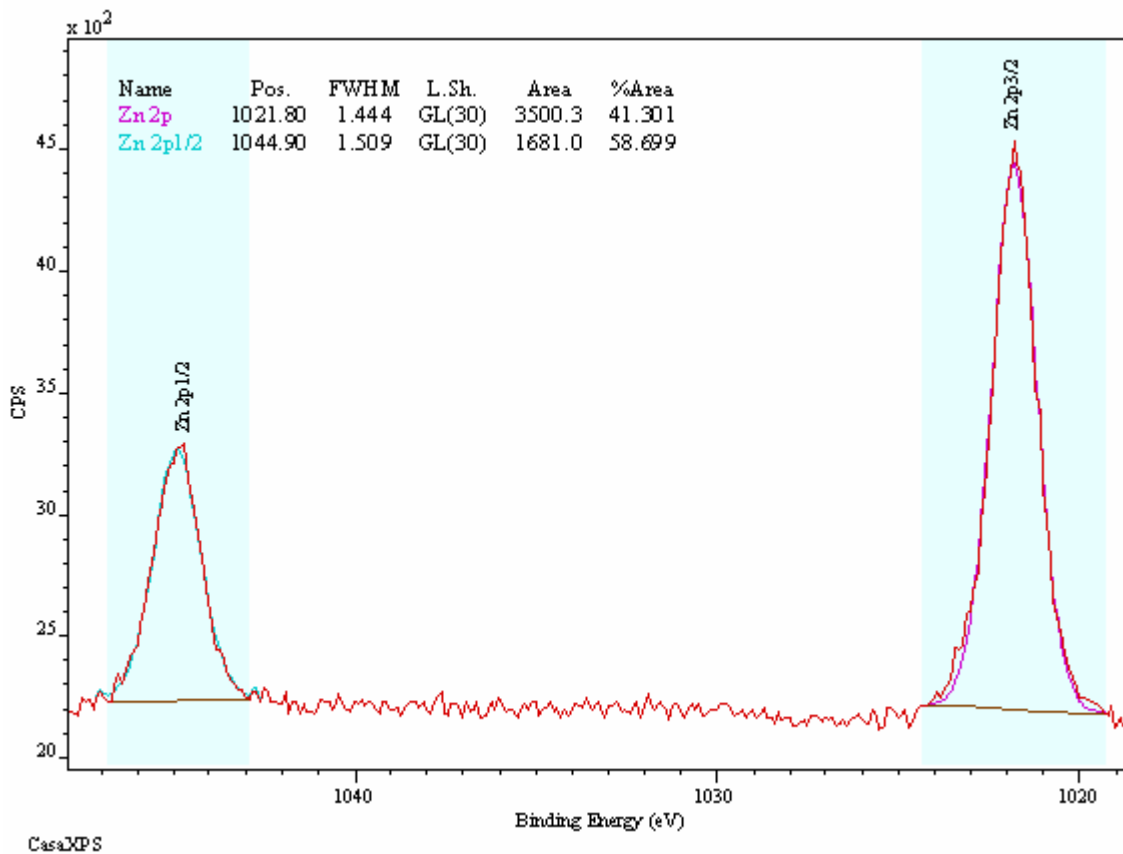


Fig. (7.16): High resolution XPS spectrum of  $Zn2p_{1/2}$  and  $Zn2p_{3/2}$  peaks from cleaved surface of glass MOF001\_v ( $65TeO_2-10Na_2O-25ZnF_2$  mol. %), melted for 2 hours with fluorinated  $ZnF_2$ .

Fig. (7.17) shows the F1s peak for the cleaved surface of glass MOF001\_v ( $65TeO_2-10Na_2O-25ZnF_2$  mol. %), which was melted for 2 hours with fluorinated  $ZnF_2$ . Fig. (7.18) shows the  $Te3d_{3/2}$  and  $Te3d_{5/2}$  peaks for the cleaved surface of glass MOF001\_v ( $65TeO_2-10Na_2O-25ZnF_2$  mol. %), which was melted for 2 hours with fluorinated  $ZnF_2$ .

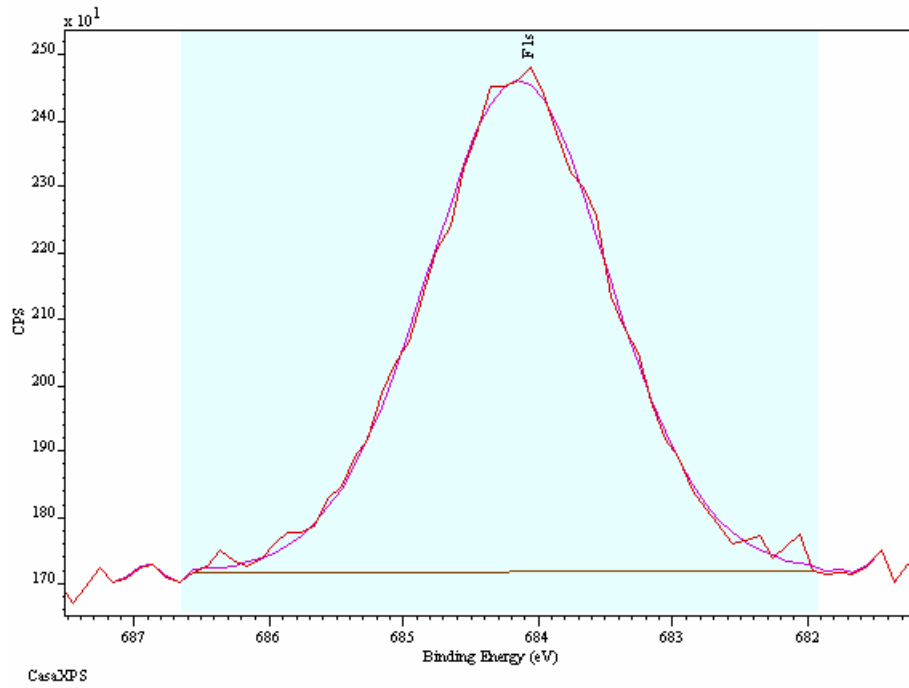


Fig. (7.17): High resolution XPS spectrum of F1s peak from cleaved surface of glass MOF001\_v (65TeO<sub>2</sub>-10Na<sub>2</sub>O-25ZnF<sub>2</sub> mol. %), melted for 2 hours with fluorinated ZnF<sub>2</sub>.

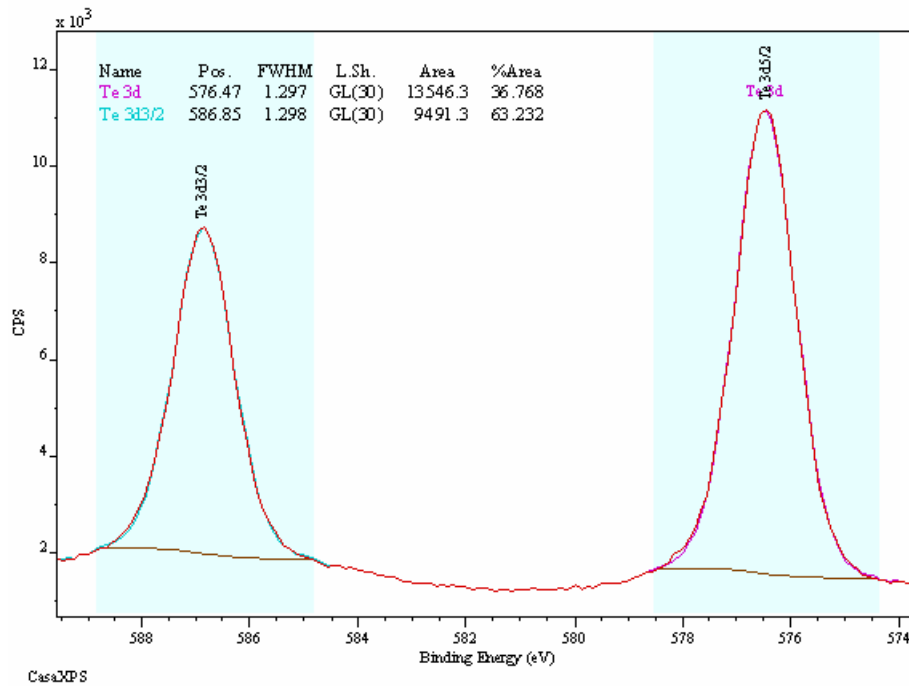


Fig. (7.18): High resolution XPS spectrum of Te3d<sub>3/2</sub> and Te3d<sub>5/2</sub> peaks from cleaved surface of glass MOF001\_v (65TeO<sub>2</sub>-10Na<sub>2</sub>O-25ZnF<sub>2</sub> mol. %), melted for 2 hours with fluorinated ZnF<sub>2</sub>.

Fig. (7.19) shows the high resolution scan of the O1s peak, which was asymmetric, of glass MOF001\_v (65TeO<sub>2</sub>-10Na<sub>2</sub>O-25ZnF<sub>2</sub> mol. %), which was melted for 2 hours with fluorinated ZnF<sub>2</sub>.

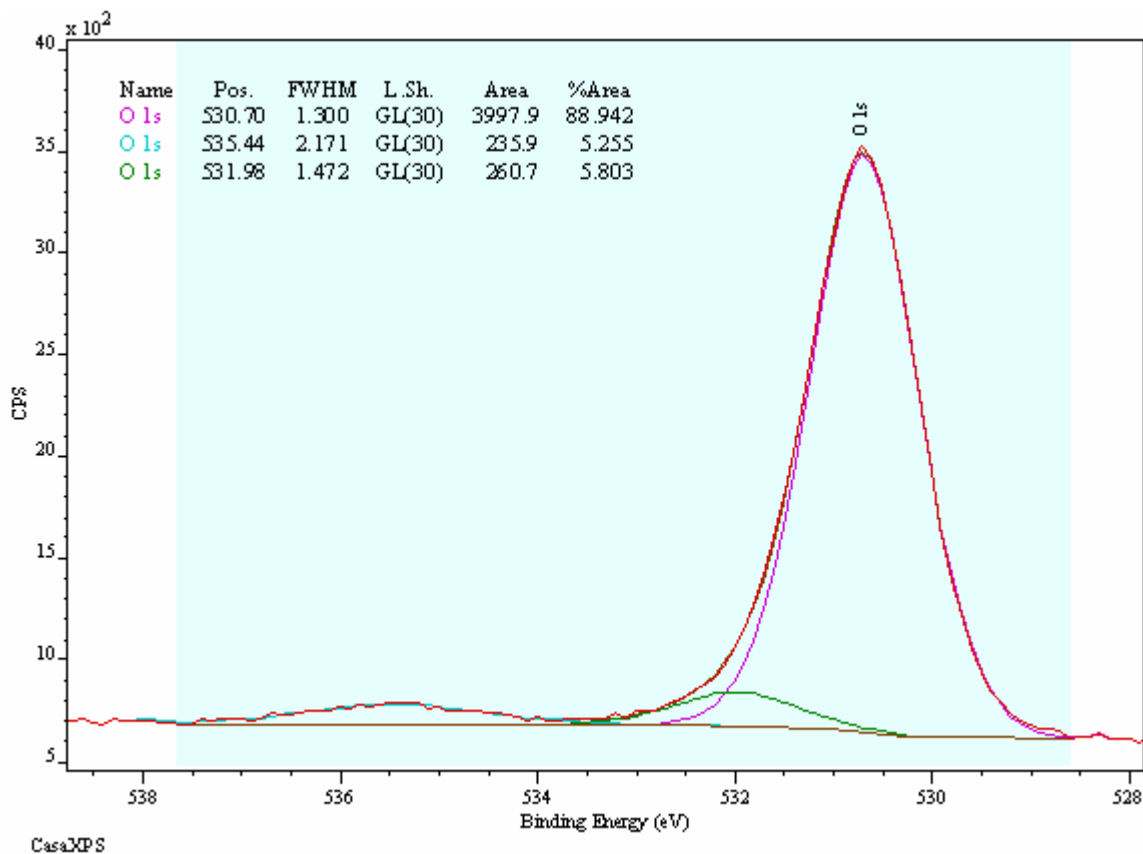


Fig. (7.19): High resolution XPS spectrum of O1s peak from cleaved surface of glass MOF001\_v (65TeO<sub>2</sub>-10Na<sub>2</sub>O-25ZnF<sub>2</sub> mol. %), with deconvoluted components due to: bridging and non-bridging oxygens (O 1s), OH (O 1s) and M=O species (O 1s).

Table (7.7) summarises the quantitative analysis from the high resolution scans, and for comparison, the actual atomic % batched and theoretical peak positions from the NIST XPS database.

Table (7.7): Quantitative analysis from high resolution XPS scans of cleaved glass MOF001\_v (65TeO<sub>2</sub>-10Na<sub>2</sub>O-25ZnF<sub>2</sub> mol. %), and theoretical peak positions and atomic % batched.

XPS peak	Theoretical		High resolution XPS scan		
	Peak / eV	At. %	Peak / eV	At. %	Wt. %
Te 3d <sub>5/2</sub>	576.2	21.67	576.5	25.55	66.46
O 1s	530.4	46.67	530.7	50.42	16.44
Na 1s	1072.5	6.67	1071.3	6.25	2.93
Zn 2p <sub>3/2</sub>	1022.5	8.33	1021.8	7.71	10.28
F 1s	684.8	16.67	684.1	10.07	3.90

It can be seen from this table, that the quantitative analysis is once again relatively close to the batched composition compared to the wide scan values show in fig. (7.14).

Fig. (7.20) shows the XPS wide scan of the polished surface (i.e. un-cleaved) of glass MOF001\_v (65TeO<sub>2</sub>-10Na<sub>2</sub>O-25ZnF<sub>2</sub> mol. %), which was melted for 2 hours with fluorinated ZnF<sub>2</sub>, for comparison.

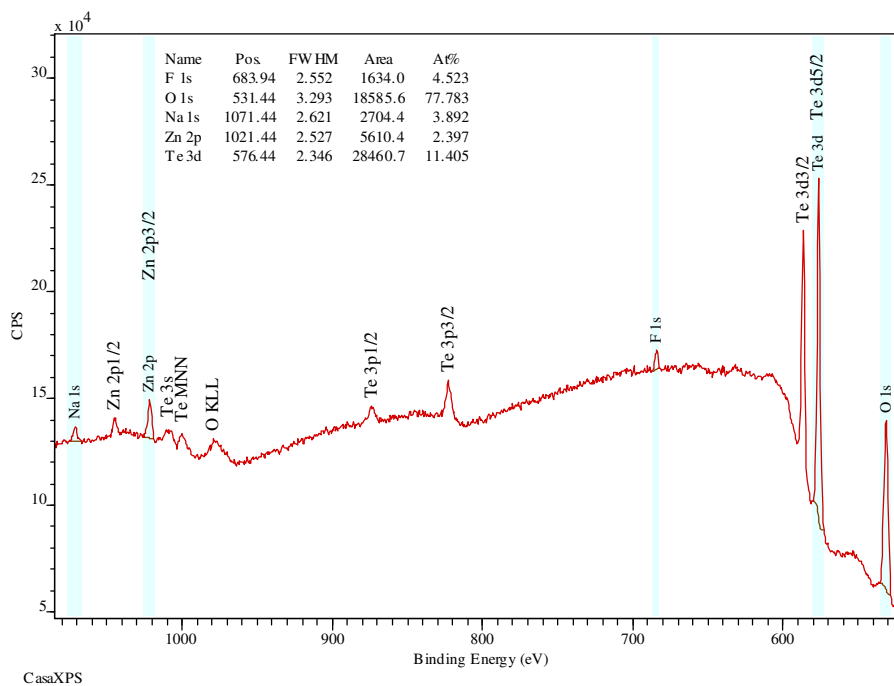


Fig. (7.20): Wide scan XPS spectrum of polished surface of glass MOF001\_v (65TeO<sub>2</sub>-10Na<sub>2</sub>O-25ZnF<sub>2</sub> mol. %).

Fig. (7.21) shows the O1s peak of the polished surface (i.e. un-cleaved) of glass MOF001\_v (65TeO<sub>2</sub>-10Na<sub>2</sub>O-25ZnF<sub>2</sub> mol. %), which was melted for 2 hours with fluorinated ZnF<sub>2</sub>.

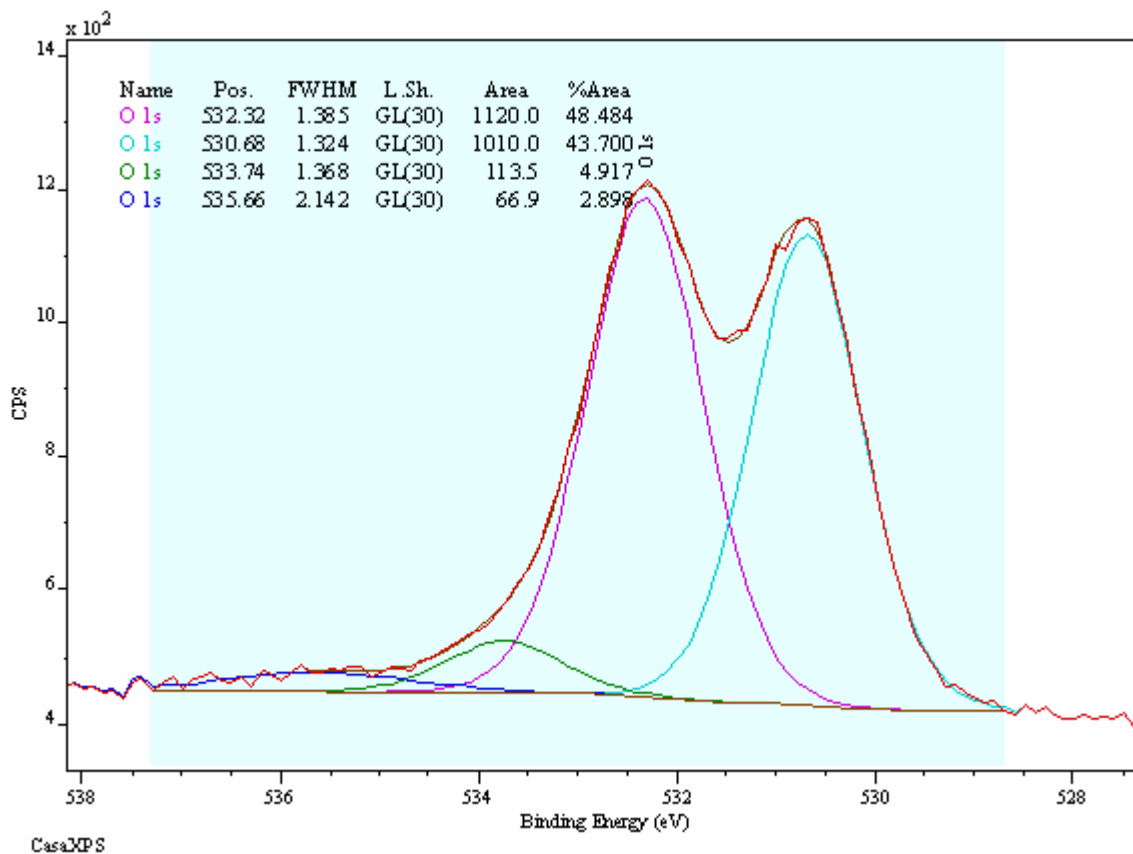


Fig. (7.21): High resolution XPS spectrum of O1s peak from polished surface of glass MOF001\_v (65TeO<sub>2</sub>-10Na<sub>2</sub>O-25ZnF<sub>2</sub> mol. %), with deconvoluted components due to: bridging and non-bridging oxygens (○1s), OH (○1s), M=O species (○1s) and organic (○1s).

This kind of doublet structure to the O1s peak was seen for all fluorotellurite glass surfaces which were polished; therefore this O1s structure would seem to be indicative of fluorotellurite glass surface chemistry. No other peaks were asymmetric for the polished

sample (with a residual standard deviation between the XPS data and Gaussian / Lorentz fit typically < 1.61).

Table (7.8) summarises the quantitative analysis from the high resolution scans, and for comparison, the actual atomic % batched and theoretical peak positions from the NIST XPS database.

Table (7.8): Quantitative analysis from high resolution XPS scans of polished glass MOF001\_v (65TeO<sub>2</sub>-10Na<sub>2</sub>O-25ZnF<sub>2</sub> mol. %), and theoretical peak positions and atomic % batched.

XPS peak	Theoretical		High resolution XPS scan		
	Peak / eV	At. %	Peak / eV	At. %	Wt. %
Te 3d <sub>5/2</sub>	576.2	21.67	576.3	16.29	57.35
O 1s	530.4	46.67	532.3	71.48	31.55
Na 1s	1072.5	6.67	1071.7	2.90	1.84
Zn 2p <sub>3/2</sub>	1022.5	8.33	1022.0	3.41	6.15
F 1s	684.8	16.67	684.6	5.92	3.11

It can be seen by comparing table (7.8) with table (7.7) that the surface composition of the glass was significantly different to the bulk (which can be approximately represented by the cleaved sample analysis in table (7.7)). The oxygen level at the surface was around 25 at. % more than the as-batched composition (71 and 47 at. % respectively), and the fluorine level around 11 at. % less (6 and 17 at. % respectively), which corresponds to around 67 % less fluorine than in the bulk glass.

Fig. (7.22) summarises the atomic % composition of the batched (i.e. theoretical), cleaved, and polished glass surface, of composition MOF001\_v (65TeO<sub>2</sub>-10Na<sub>2</sub>O-25ZnF<sub>2</sub> mol. %), which was melted for 2 hours with fluorinated ZnF<sub>2</sub>.

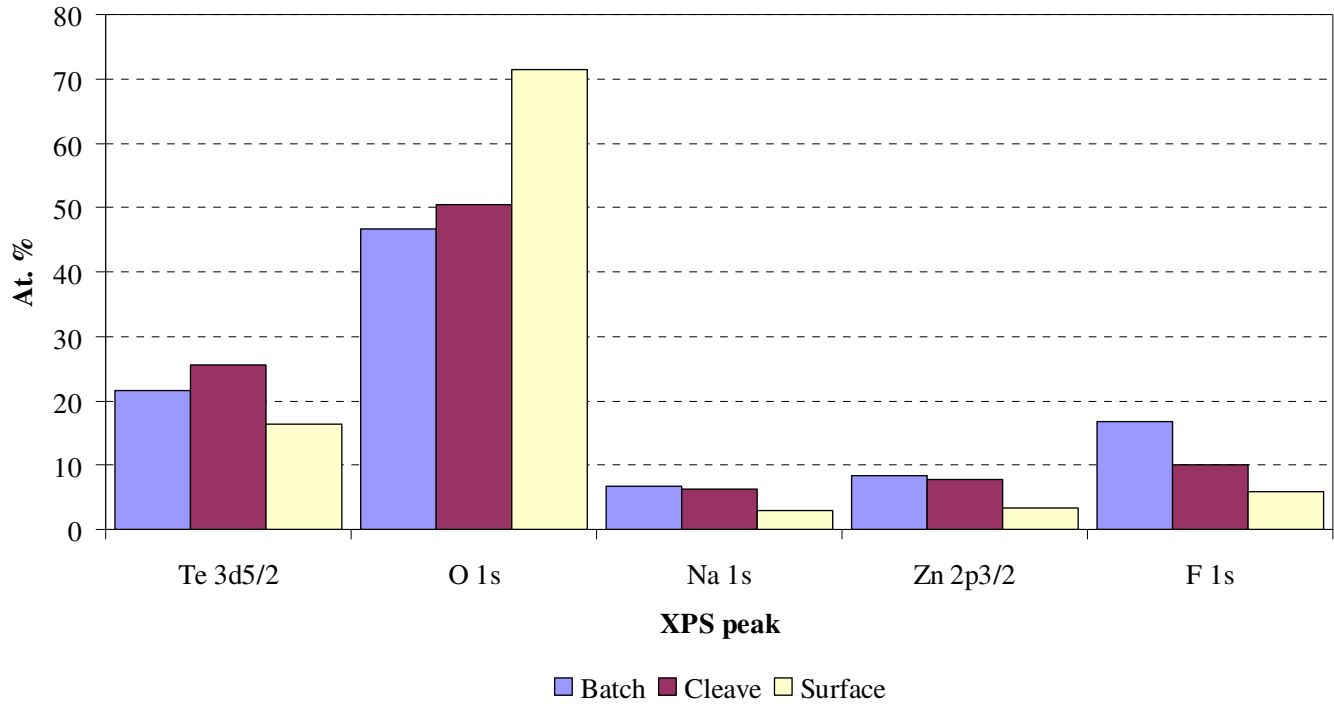


Fig. (7.22): Atomic % composition of batched, cleaved and polished glass MOF001\_v ( $65\text{TeO}_2$ - $10\text{Na}_2\text{O}$ - $25\text{ZnF}_2$  mol. %).

## 7.2.2. Chemical and environmental durability

### 7.2.2.1. Durability of oxide tellurite glasses

Fig. (7.23) shows optical micrographs of glass MOD009 ( $77\text{TeO}_2$ - $12\text{ZnO}$ - $10\text{Na}_2\text{O}$ - $1\text{Yb}_2\text{O}_3$  mol. %) before, and after 60, 120, and 180 sec. immersion in a 1M solution of NaOH at  $21^\circ\text{C}$  (see section 7.1.2.1 for further experimental details).

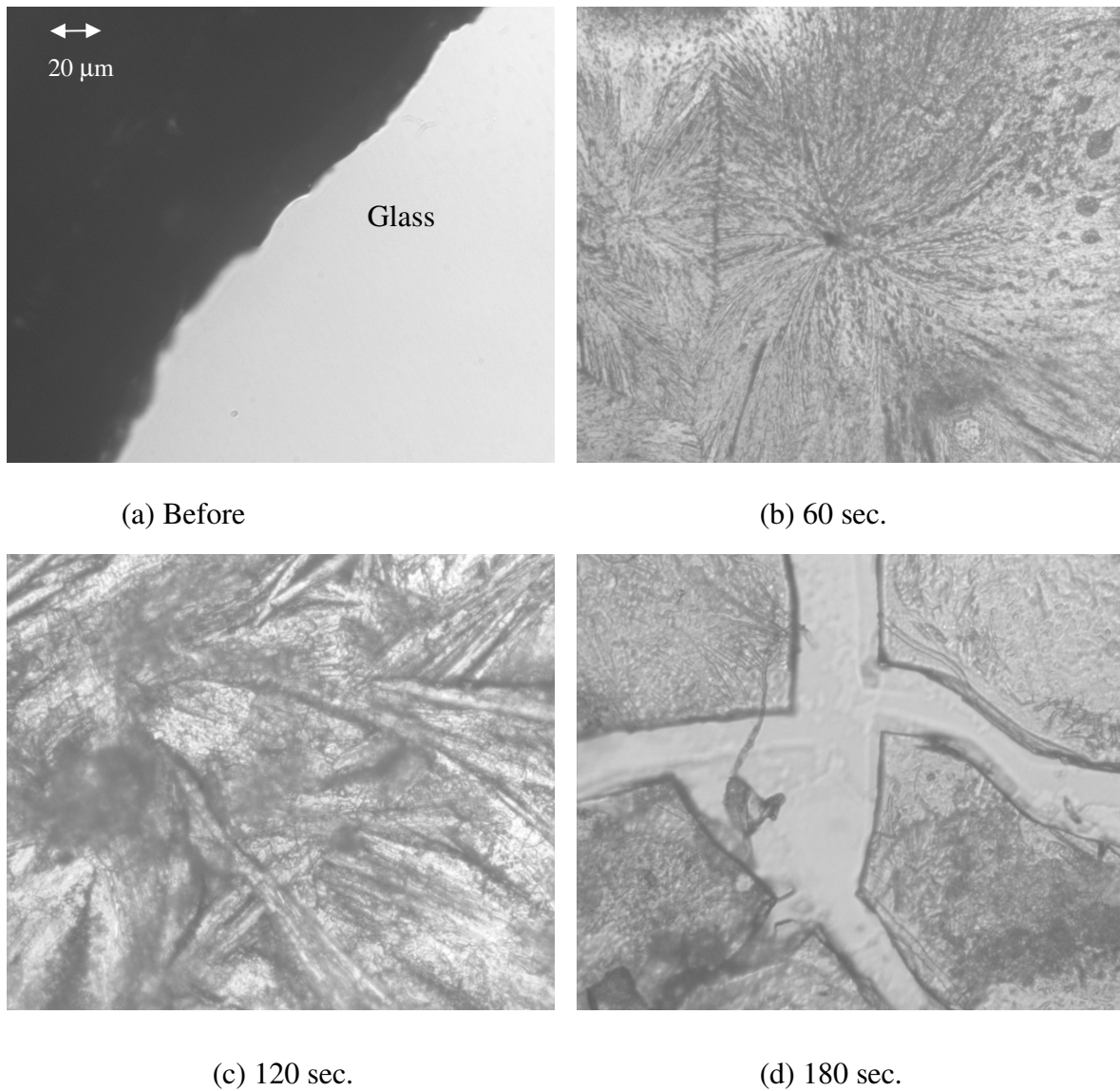


Fig. (7.23): Optical micrographs of glass MOD009 ( $77\text{TeO}_2$ - $12\text{ZnO}$ - $10\text{Na}_2\text{O}$ - $1\text{Yb}_2\text{O}_3$  mol. %) (a) before, and after (b) 60, (c) 120, and (d) 180 sec. immersion in a 1M solution of NaOH at  $21^\circ\text{C}$  (all micrographs the same scale).

It can be seen that the surface quality progressively deteriorated, with etch time, indicating NaOH was an unsuitable etchant. After 180 sec., it can be seen that the layer which formed at the surface of the glass began to break up, exposing glass beneath. It can also be seen from the 60 and 120 sec. micrographs that the glass exhibited ridges and pits, indicating the NaOH had attacked the glass incongruently. Fig. (7.24) shows the etch rate

of glass MOD009 (77TeO<sub>2</sub>-12ZnO-10Na<sub>2</sub>O-1Yb<sub>2</sub>O<sub>3</sub> mol. %) immersed in a 1M solution of NaOH at 21°C.

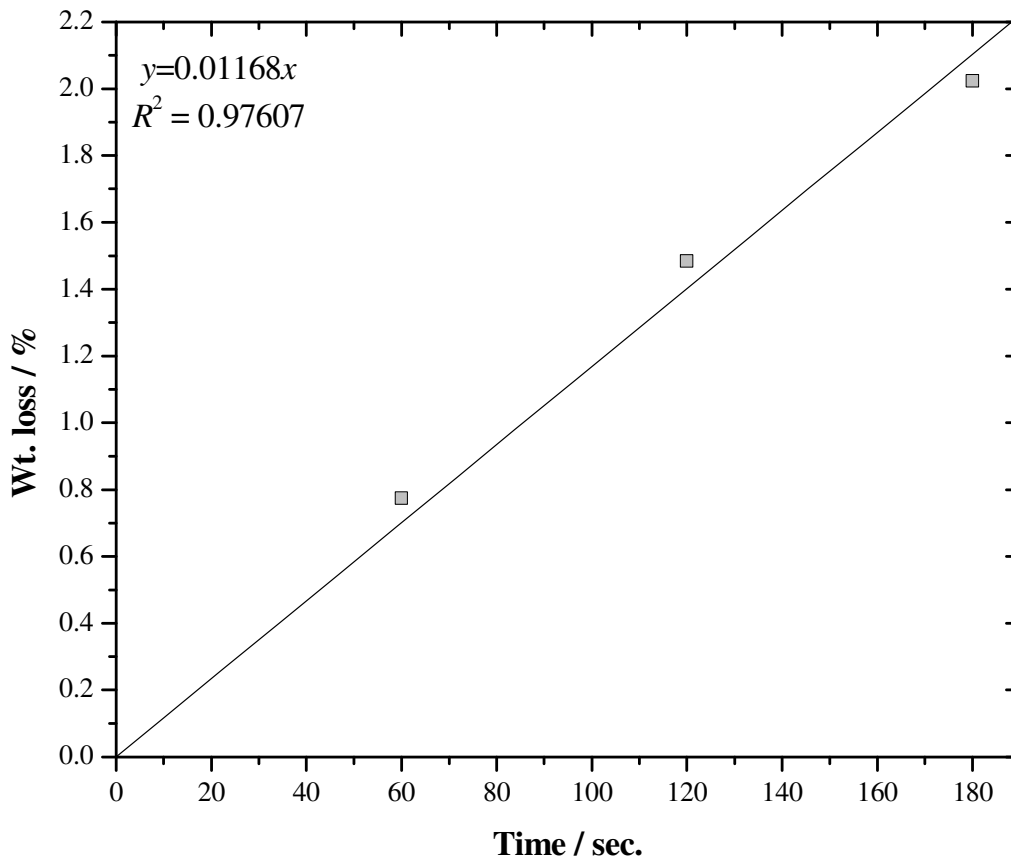


Fig. (7.24): Etch rate of glass MOD009 (77TeO<sub>2</sub>-12ZnO-10Na<sub>2</sub>O-1Yb<sub>2</sub>O<sub>3</sub> mol. %) immersed in a 1M solution of NaOH at 21°C.

The glass appeared to exhibit a linear etch rate (correlation coefficient  $\approx 0.976$ ), of around 0.012 wt. % per second.

Fig. (7.25) shows optical micrographs of glass MOD012 (75TeO<sub>2</sub>-10ZnO-10Na<sub>2</sub>O-5GeO<sub>2</sub> mol. %), after 60, 120, 180, and 240 sec. immersion in a 3M solution of H<sub>2</sub>SO<sub>4</sub> at 15°C (see section 7.1.2.1 for further experimental details).

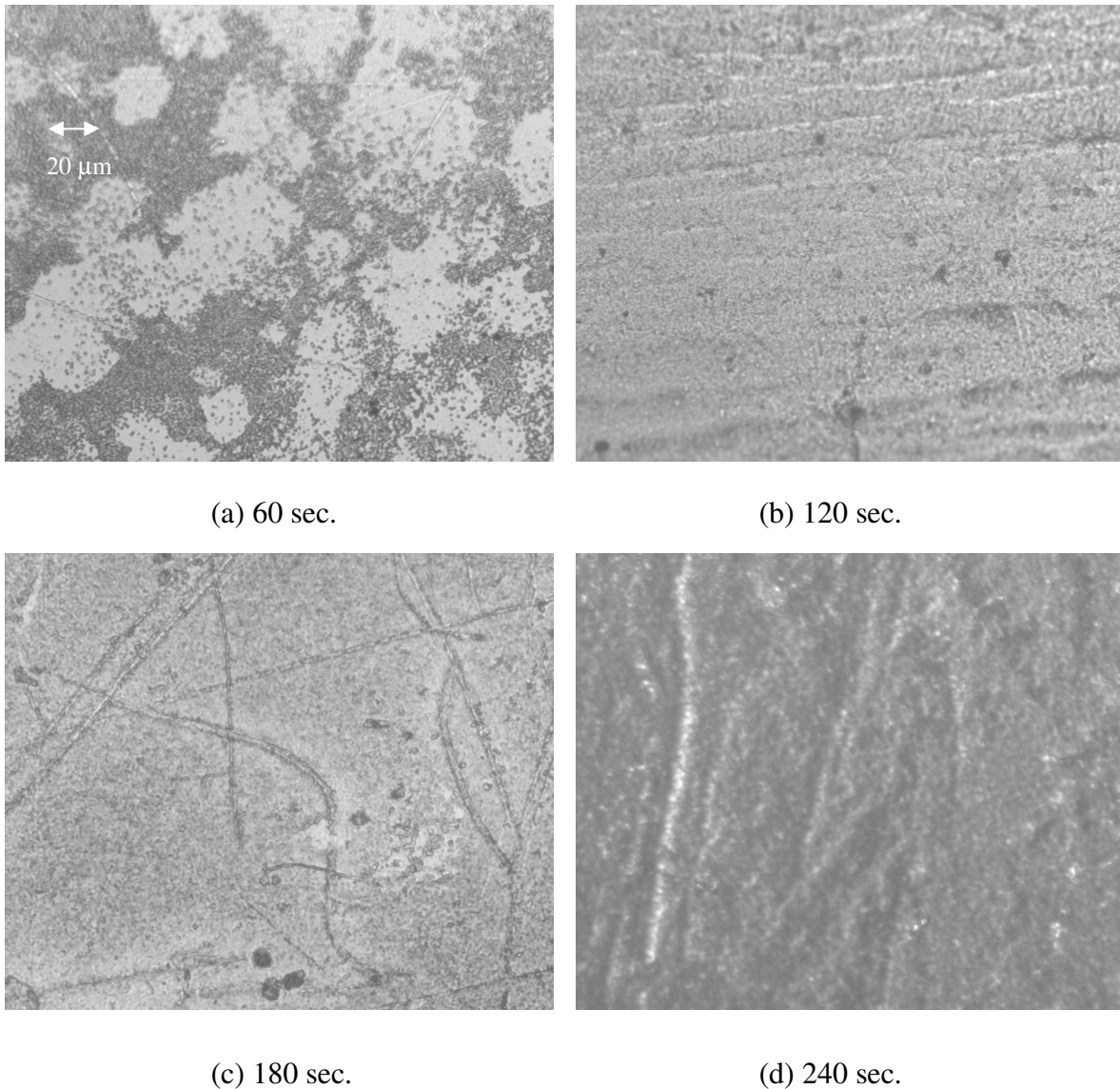


Fig. (7.25): Optical micrographs of glass MOD012 ( $75\text{TeO}_2$ - $10\text{ZnO}$ - $10\text{Na}_2\text{O}$ - $5\text{GeO}_2$  mol. %), after (a) 60, (b) 120, (c) 180, and (d) 240 sec. immersion in a 3M solution of  $\text{H}_2\text{SO}_4$  at  $15^\circ\text{C}$  (all micrographs the same scale).

Again, this etchant ( $\text{H}_2\text{SO}_4$ ) was poor; however the etch was not as severe as the  $\text{NaOH}$ .

Fig. (7.26) shows optical micrographs of glass MOD012 ( $75\text{TeO}_2$ - $10\text{ZnO}$ - $10\text{Na}_2\text{O}$ - $5\text{GeO}_2$  mol. %), after 60, 120, 180, and 240 sec. immersion in a 1M solution of  $\text{HCl}$  at  $15^\circ\text{C}$  (see section 7.1.2.1 for further experimental details).

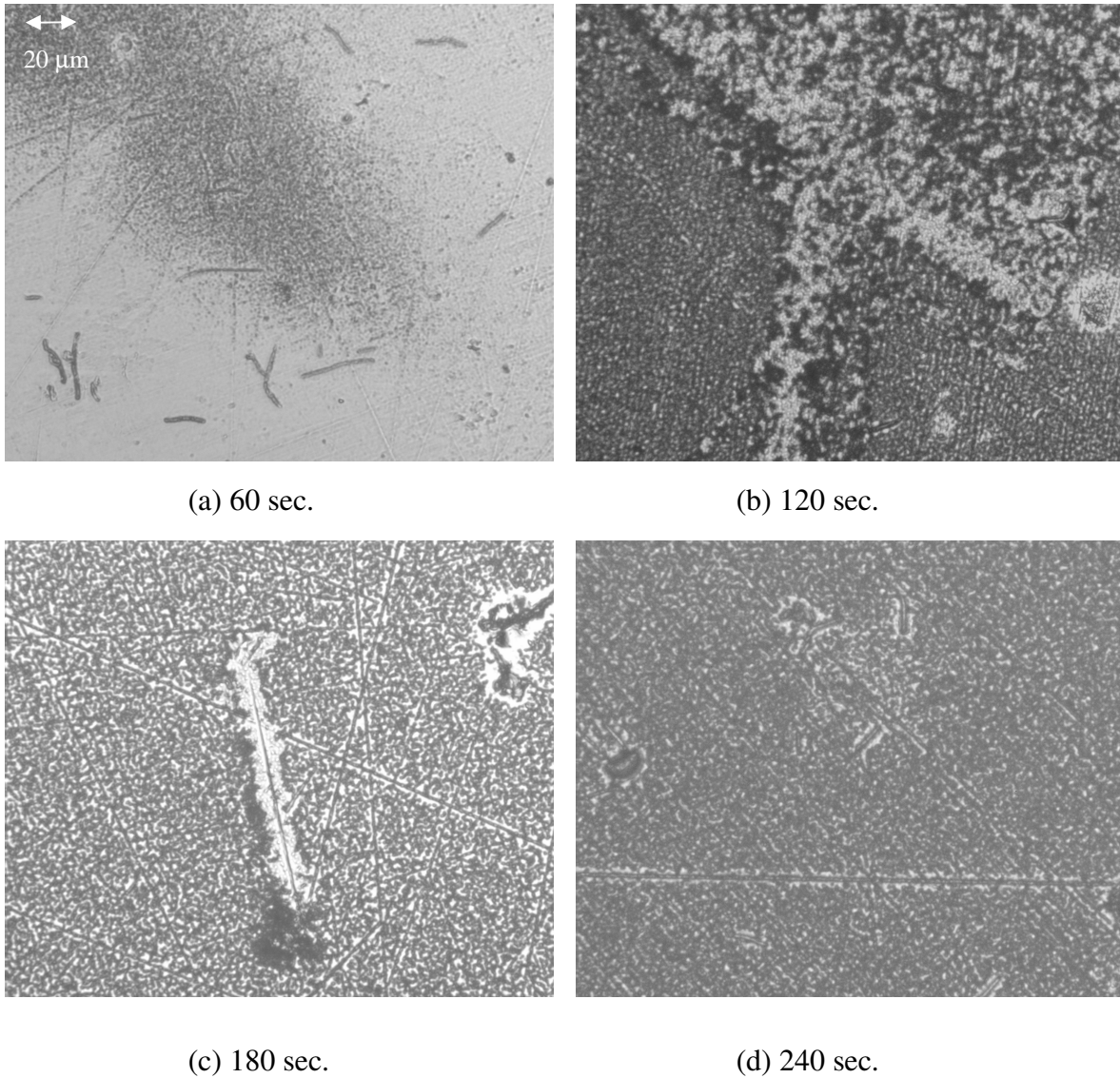


Fig. (7.26): Optical micrographs of glass MOD012 (75TeO<sub>2</sub>-10ZnO-10Na<sub>2</sub>O-5GeO<sub>2</sub> mol. %), after (a) 60, (b) 120, (c) 180, and (d) 240 sec. immersion in a 1M solution of HCl at 15°C (all micrographs the same scale).

Fig. (7.27) shows the etch rates of glass MOD012 (75TeO<sub>2</sub>-10ZnO-10Na<sub>2</sub>O-5GeO<sub>2</sub> mol. %), immersed in 1M HCl, and 3M H<sub>2</sub>SO<sub>4</sub> at 15°C.

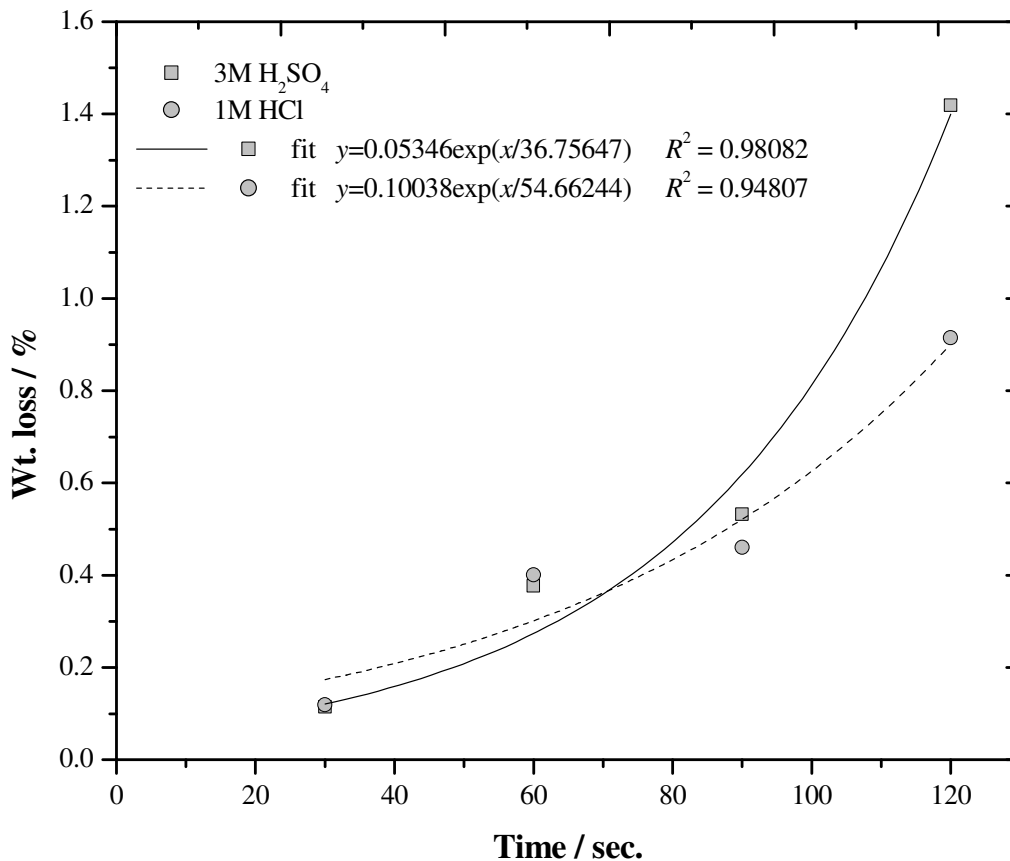
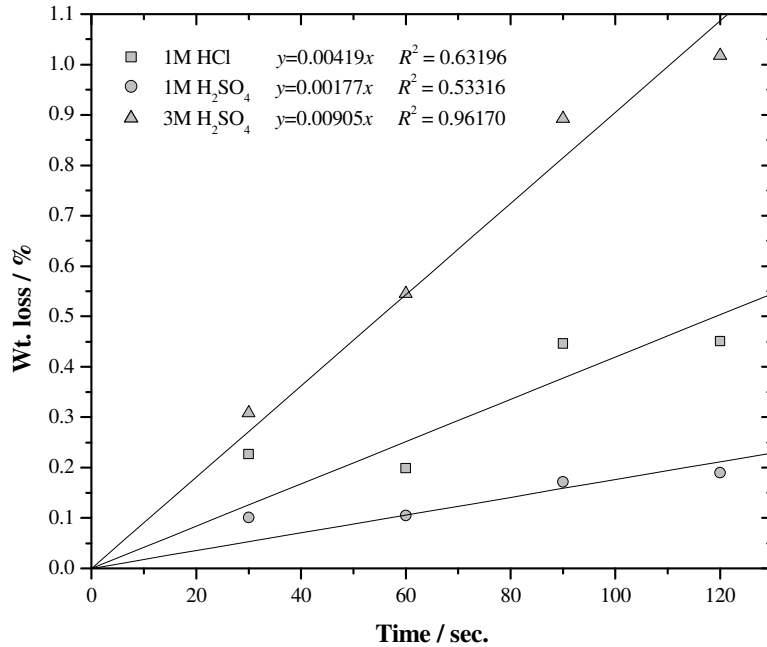


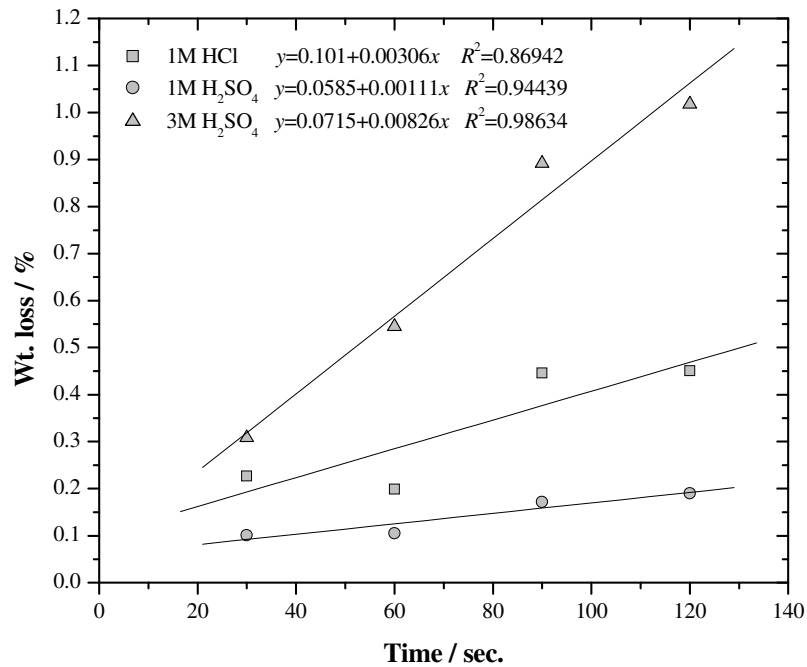
Fig. (7.27): Etch rate of glass MOD012 (75TeO<sub>2</sub>-10ZnO-10Na<sub>2</sub>O-5GeO<sub>2</sub> mol. %), immersed in 1M HCl (●), and 3M H<sub>2</sub>SO<sub>4</sub> (■) at 15°C.

It can be seen that the both solutions resulted in an approximately exponential growth etch rate. The 3M H<sub>2</sub>SO<sub>4</sub> etch initially showed a similar etch rate to the 1M HCl, but was increased at longer times.

Fig. (7.28) shows the etch rates of glass MOD012 (75TeO<sub>2</sub>-10ZnO-10Na<sub>2</sub>O-5GeO<sub>2</sub> mol. %), immersed in 1M HCl, 1M H<sub>2</sub>SO<sub>4</sub>, and 3M H<sub>2</sub>SO<sub>4</sub> at 21°C (see section 7.1.2.1 for further experimental details).



(a)



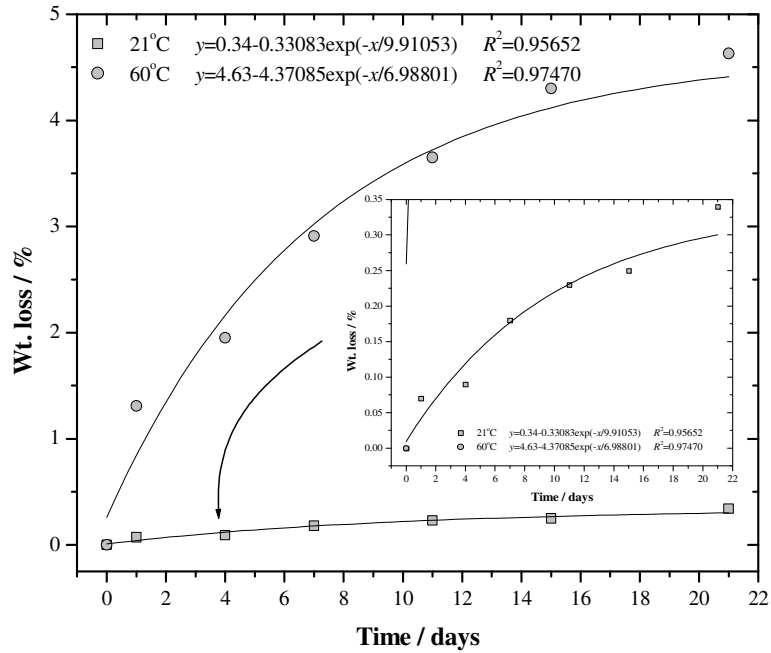
(b)

Fig. (7.28): Etch rates of glass MOD012 (75TeO<sub>2</sub>-10ZnO-10Na<sub>2</sub>O-5GeO<sub>2</sub> mol. %), immersed in 1M HCl (■), 1M H<sub>2</sub>SO<sub>4</sub> (●), and 3M H<sub>2</sub>SO<sub>4</sub> (▲) at 21°C, with linear fits (a) forced through zero, and (b) not forced through zero.

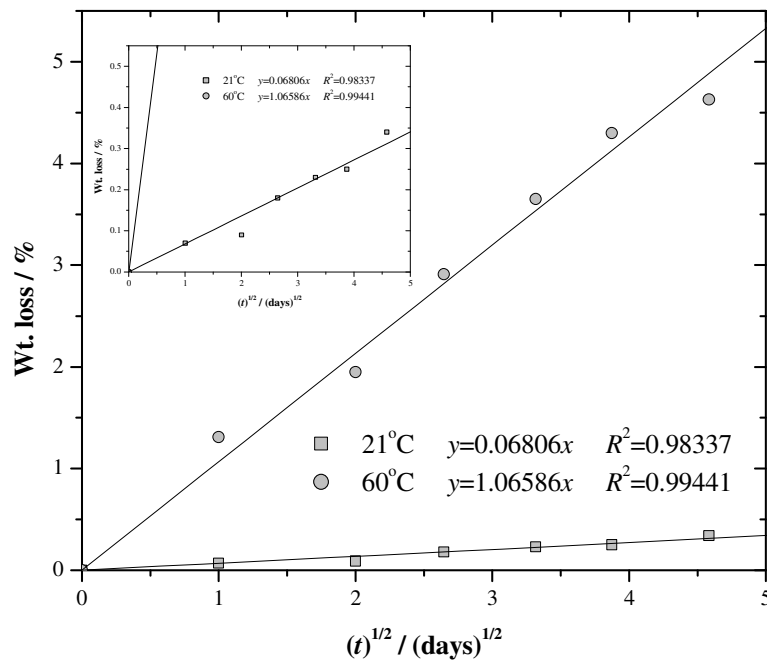
It can be seen the 3M H<sub>2</sub>SO<sub>4</sub> etch rates was approximately linear (correlation coefficient  $\approx 0.96$ ), however the correlation coefficients for the HCl and H<sub>2</sub>SO<sub>4</sub> 1M solutions were low ( $\approx 0.53$  and  $0.63$  for H<sub>2</sub>SO<sub>4</sub> and HCl respectively), as a result of forcing the fits to pass through zero. The linear fits which were not made to pass through zero showed higher correlation coefficients (all  $> 0.87$ ). The 3M H<sub>2</sub>SO<sub>4</sub> solution showed the highest etch rate ( $\approx 0.008$  wt. % per second), followed by 1M HCl ( $\approx 0.0035$  wt. % per second), then lastly 1M H<sub>2</sub>SO<sub>4</sub> ( $\approx 0.0015$  wt. % per second).

#### 7.2.2.2. Durability of fluorotellurite glasses

Fig. (7.29) shows the weight loss of glass MOF001 (65TeO<sub>2</sub>-10Na<sub>2</sub>O-25ZnF<sub>2</sub> mol. %) after immersion in distilled water at 21 and 60°C (see section 7.1.2.1 for further experimental details). Both sets of data were best fitted with an exponential decay (fig. (7.29a)). As expected, the overall weight loss of the 60°C sample was higher than the 21°C sample after 21 days (4.63 and 0.34 wt % respectively). The plot of wt. % loss vs.  $(t)^{1/2}$  (fig. (7.29b)) was linear, indicating the attack mechanism was diffusion controlled. Glasses immersed in water at both temperatures (21 and 60°C) exhibited frosted surfaces, and were opaque to the eye after 21 days treatment.



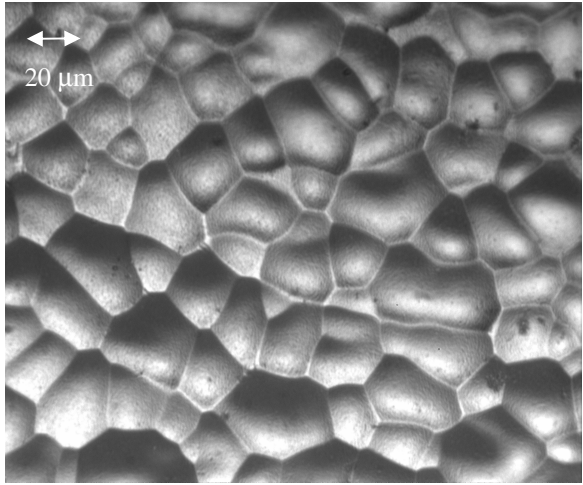
(a)



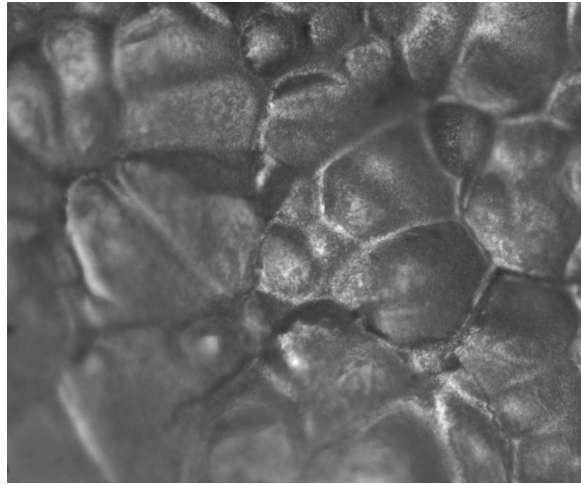
(b)

Fig. (7.29): Weight loss of glass MOF001 (65TeO<sub>2</sub>-10Na<sub>2</sub>O-25ZnF<sub>2</sub> mol. %) after immersion in distilled water at 21 (■) and 60°C (●), plotted against: (a) time, and (b)  $(\text{time})^{1/2}$ .

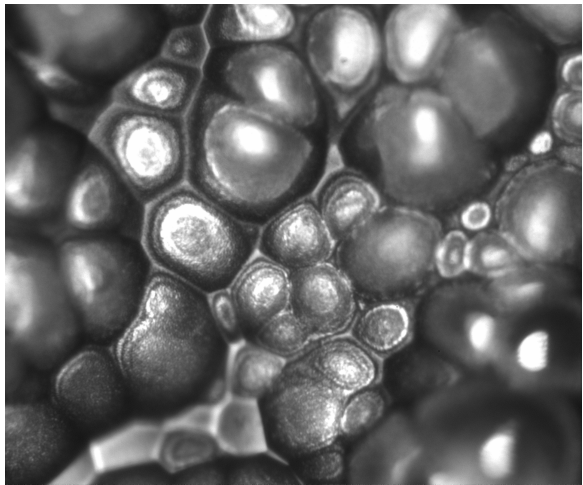
Fig. (7.30) shows optical micrographs of glass MOF001 ( $65\text{TeO}_2\text{-}10\text{Na}_2\text{O-}25\text{ZnF}_2$  mol. %) after etching in 3M HCl at  $21^\circ\text{C}$  whilst agitated in an ultrasonic bath (see section 7.1.2.1 for further experimental details).



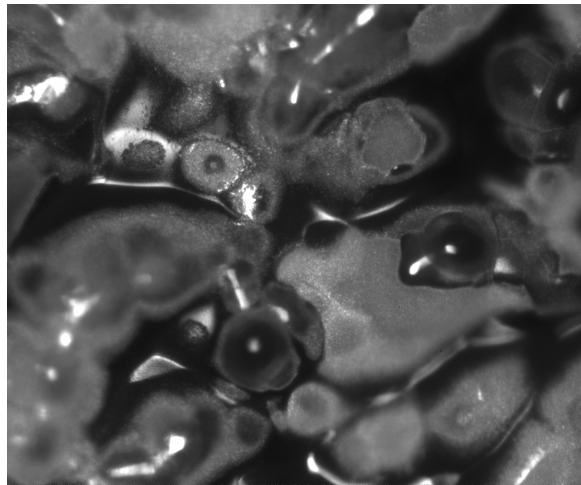
(a) 30 sec.



(b) 1 min.



(c) 2 min.



(d) 5 min.

Fig. (7.30): Optical micrographs of glass MOF001 ( $65\text{TeO}_2\text{-}10\text{Na}_2\text{O-}25\text{ZnF}_2$  mol. %) after etching in 3M HCl at  $21^\circ\text{C}$  whilst agitated (all micrographs the same scale).

Again, 3M HCl was a poor etchant, producing heavy pitting. Fig. (7.31) shows the etch rates of glasses MOF001 ( $65\text{TeO}_2\text{-}10\text{Na}_2\text{O-}25\text{ZnF}_2$  mol. %) in 3M HCl and MOF005 ( $70\text{TeO}_2\text{-}10\text{Na}_2\text{O-}20\text{ZnF}_2$  mol. %) in 1M HCl, both at  $21^\circ\text{C}$  whilst agitated.

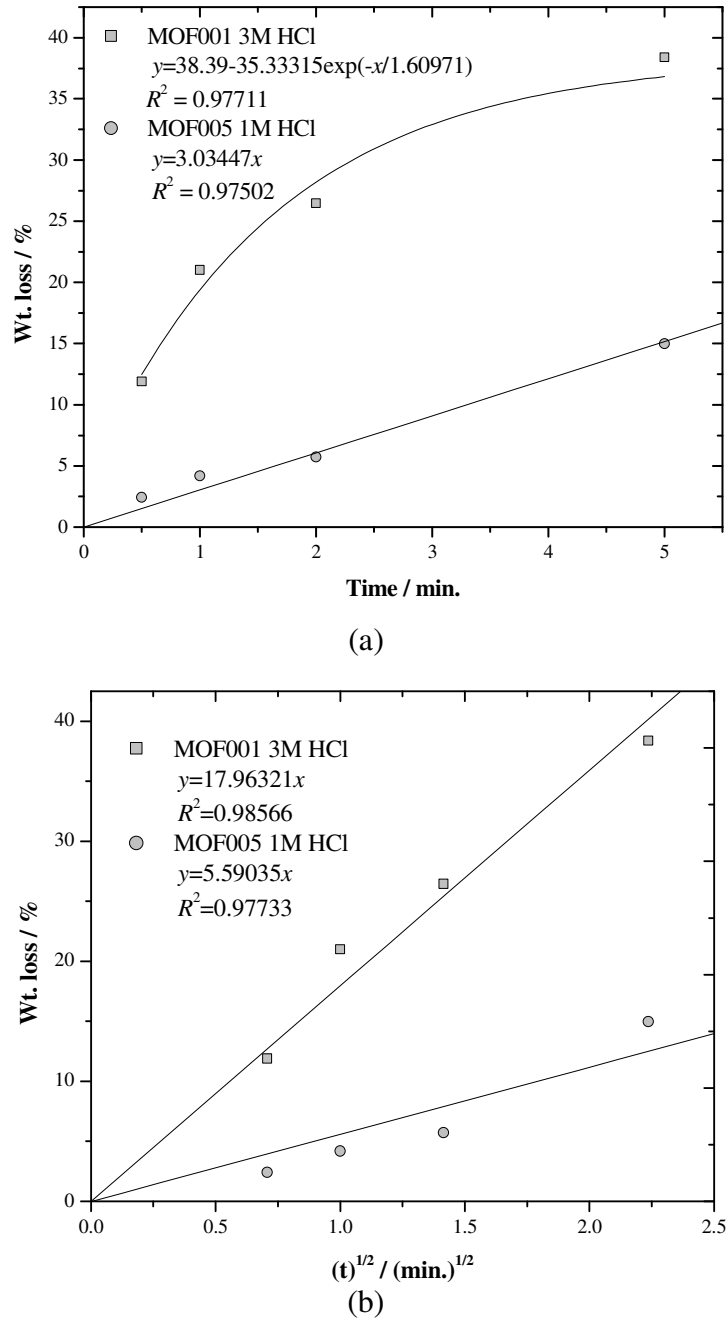
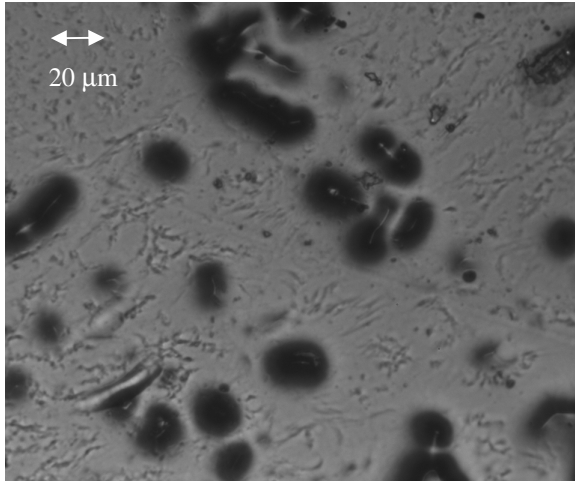


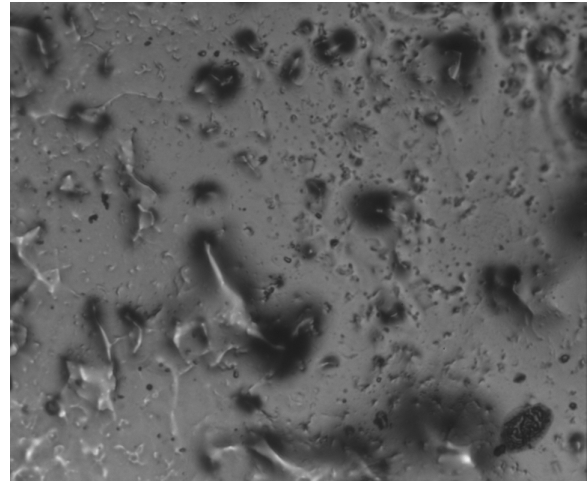
Fig. (7.31): Etch rates of glasses MOF001 ( $65\text{TeO}_2\text{-}10\text{Na}_2\text{O-}25\text{ZnF}_2$  mol. %) in 3M HCl (■) and MOF005 ( $70\text{TeO}_2\text{-}10\text{Na}_2\text{O-}20\text{ZnF}_2$  mol. %) in 1M HCl (●), both at  $21^\circ\text{C}$  whilst agitated, plotted against: (a) time, and (b)  $(\text{time})^{1/2}$ .

The 3M HCl solution attack resulted in a weight loss versus time with an exponential decay fit, and the 1M HCl solution gave a linear fit, with an etch rate of around 3.0 wt. % per minute (fig (7.31a)). Linear fits also correlated highly (correlation coefficients > 0.97) when wt. % loss was plotted against  $(t)^{1/2}$  illustrated in fig. (7.31b), indicating attack was diffusion controlled.

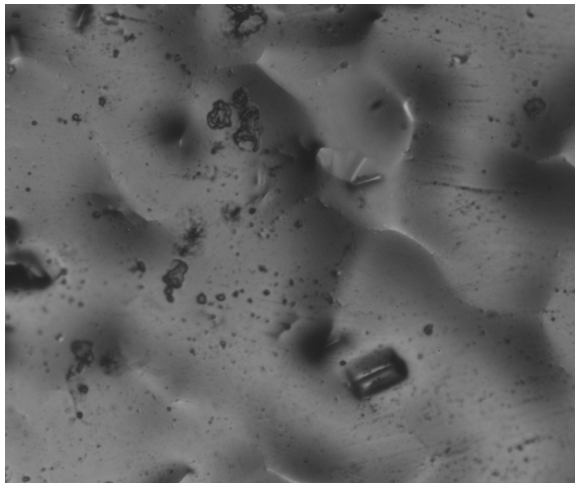
Fig. (7.32) shows optical micrographs of glass MOF001 (65TeO<sub>2</sub>-10Na<sub>2</sub>O-25ZnF<sub>2</sub> mol. %) after etching in 40 % HF at 21°C (see section 7.1.2.1 for further experimental details). HF was clearly a better etchant than NaOH, HCl and H<sub>2</sub>SO<sub>4</sub>. Although the etch formed some ridges after long exposure times, there was no opaque layer formed at the glass surface, as seen with all other etchants shown in fig. (7.23) to (7.31). Fig. (7.33) shows the etch rate of 4 % HF at 21°C on this glass. This glass followed an approximately linear etch rate of 0.92 wt. % per minute (correlation coefficient of around 0.91). Fig. (7.34) shows infrared spectra of the unetched glass (MOF001), and glass of this composition immersed in 4% HF at 21°C for 2 and 10 min. It can be seen from fig. (7.34) that the OH bands increased significantly with increasing etching time.



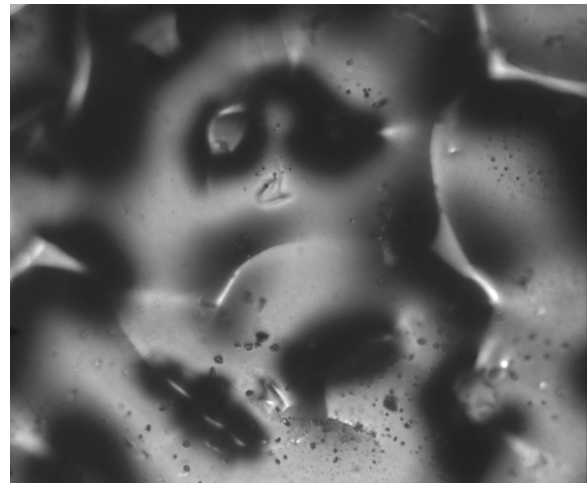
(a) 2 min.



(b) 5 min.



(c) 10 min.



(c) 30 min.

Fig. (7.32): Optical micrographs of glass MOF001 ( $65\text{TeO}_2$ - $10\text{Na}_2\text{O}$ - $25\text{ZnF}_2$  mol. %) after etching in 40% HF at  $21^\circ\text{C}$  (all micrographs the same scale).

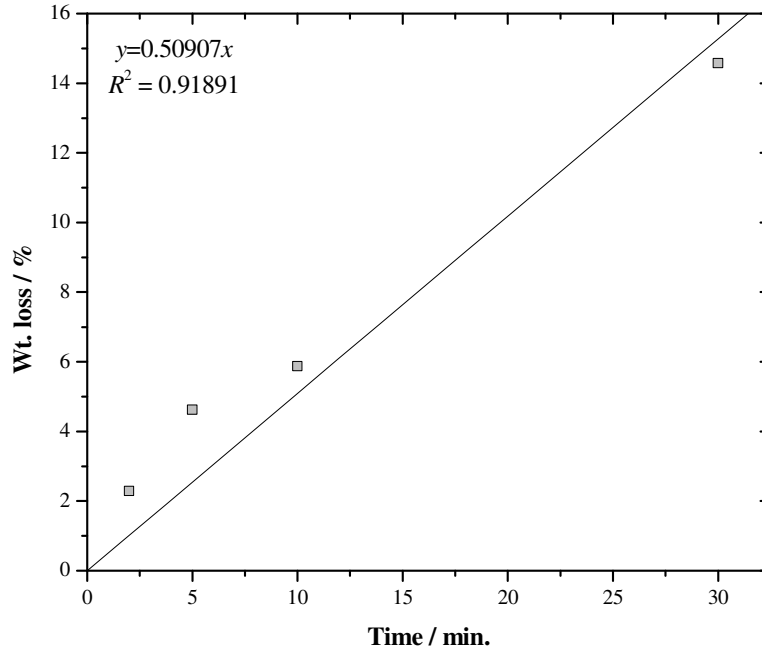


Fig. (7.33): Etch rate of glass MOF001 ( $65\text{TeO}_2\text{-}10\text{Na}_2\text{O-}25\text{ZnF}_2$  mol. %) in 4% HF at  $21^\circ\text{C}$ .

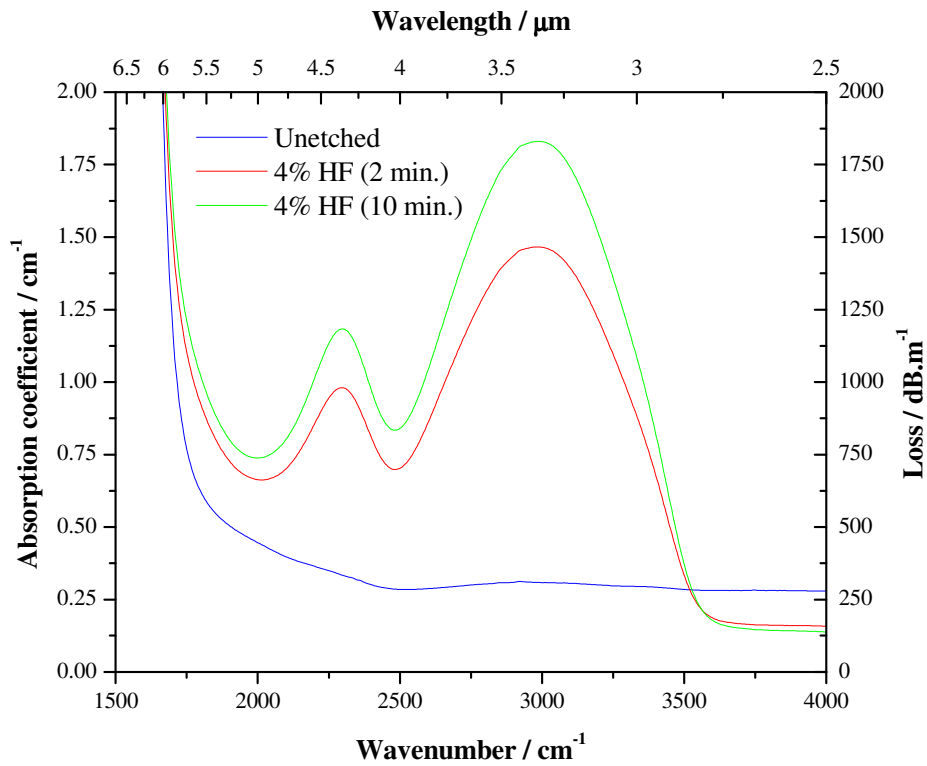


Fig. (7.34): Infrared spectra of the unetched glass, and glasses immersed in 4% HF at  $21^\circ\text{C}$  for 2 and 10 min of composition MOF001 ( $65\text{TeO}_2\text{-}10\text{Na}_2\text{O-}25\text{ZnF}_2$  mol. %).

Fig. (7.35) shows optical micrographs of glass MOF005 ( $70\text{TeO}_2\text{-}10\text{Na}_2\text{O-}20\text{ZnF}_2$  mol. %), treated for 1 min. in various solutions: 4% HF, 7%  $\text{HNO}_3$ , 8.5%  $\text{H}_3\text{PO}_4$ , and 10%  $\text{CH}_3\text{COOH}$ . These solutions were made by diluting the corresponding concentrated acid listed in table (7.1) in a 1:10 volume ratio with distilled water making a 100 ml solution. (see section 7.1.2.1 for further experimental details).

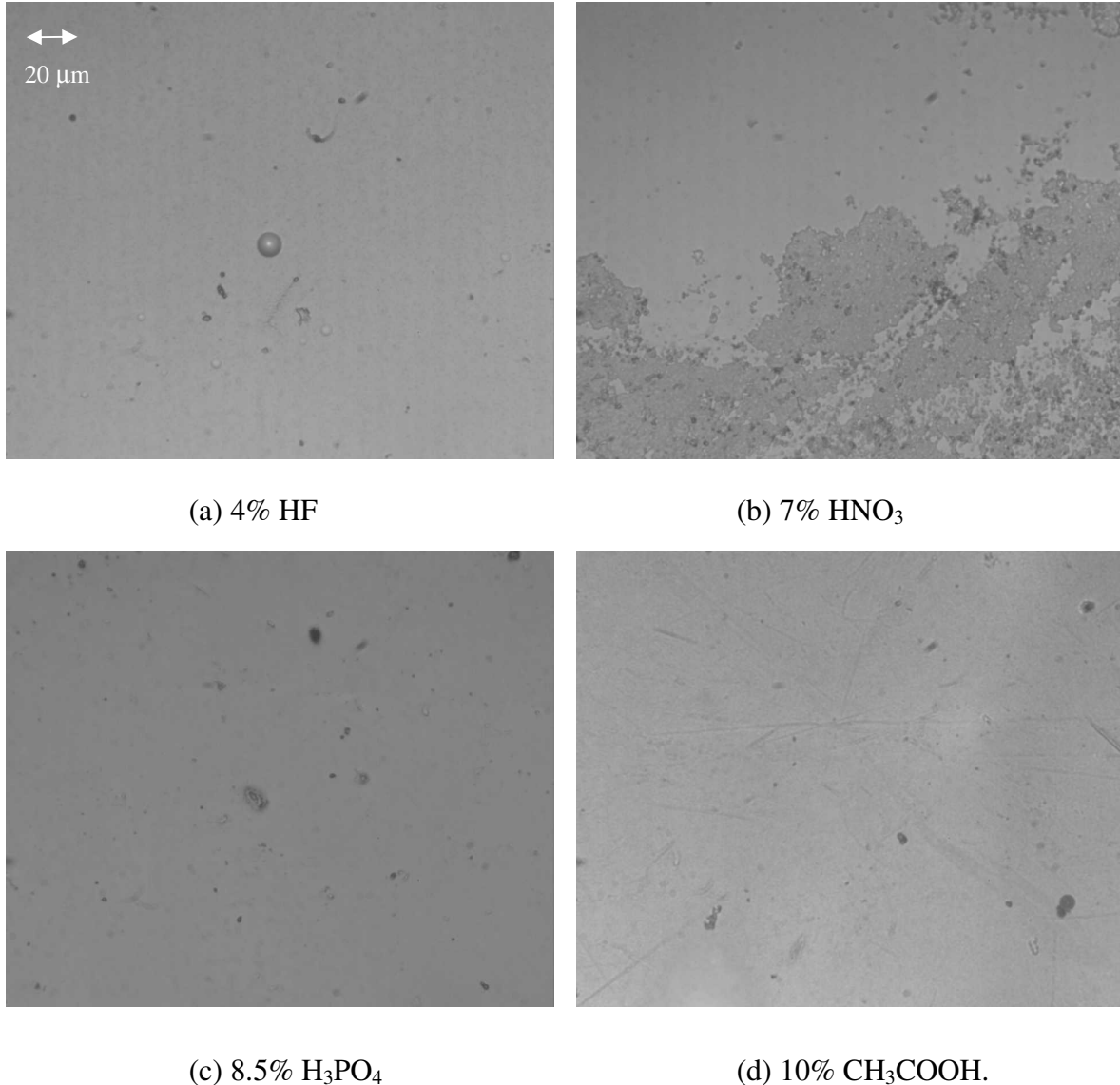


Fig. (7.35): Optical micrographs of glass MOF005 ( $70\text{TeO}_2\text{-}10\text{Na}_2\text{O-}20\text{ZnF}_2$  mol. %), treated for 1 min. in: (a) 4% HF, (b) 7%  $\text{HNO}_3$ , (c) 8.5%  $\text{H}_3\text{PO}_4$ , and (d) 10%  $\text{CH}_3\text{COOH}$  (all micrographs the same scale).

All four etchants from fig. (7.35) produced reasonable etches (i.e. no visible opaque layer, except nitric acid) compared to 1 and 3M NaOH, HCl and H<sub>2</sub>SO<sub>4</sub>. On inspection, the phosphoric and acetic acids produced an etch of similar quality to HF (no opaque layer or pitting), and should be investigated further. Weight loss was not measured due to lack of availability of an electronic balance.

### 7.2.3. Ion exchange

Fig. (7.36) shows the EDX analysis of glass T08 (80TeO<sub>2</sub>-9ZnO-10Na<sub>2</sub>O-1Er<sub>2</sub>O<sub>3</sub> mol. %), which had a silver layer evaporated on both polished sides (100 and 300 μm), followed by heat treatment at 285°C for 12 hours under inert atmosphere (argon). The concentration profile of the 100 μm side was best fitted with an exponential decay curve, and the 300 μm side by a third order polynomial. The depth of silver was recorded until the peak was indistinguishable from the EDX spectrum background.

Fig. (7.37) shows the EDX analysis of glass ST08 (79TeO<sub>2</sub>-5ZnO-10Na<sub>2</sub>O-5PbO-1Yb<sub>2</sub>O<sub>3</sub> mol. %), for which one flat side was dipped into a molten salt solution (2AgNO<sub>3</sub>-49NaNO<sub>3</sub>-49KNO<sub>3</sub> mol. %) at 270°C for 5 hours.

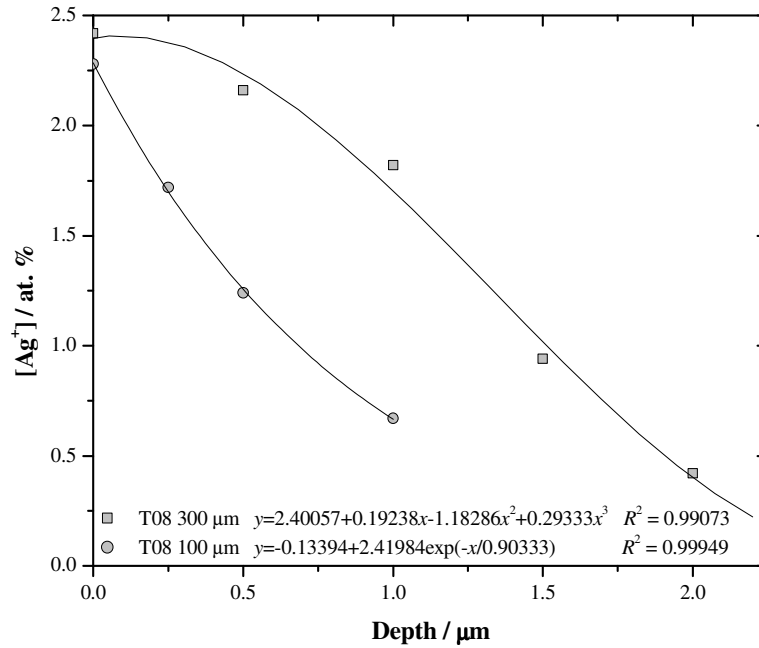


Fig. (7.36): EDX analysis of glass T08 (80TeO<sub>2</sub>-9ZnO-10Na<sub>2</sub>O-1Er<sub>2</sub>O<sub>3</sub> mol. %), with silver layer evaporated on both sides (100 (●) and 300 μm (■)), followed by heat treatment at 285°C for 12 hours.

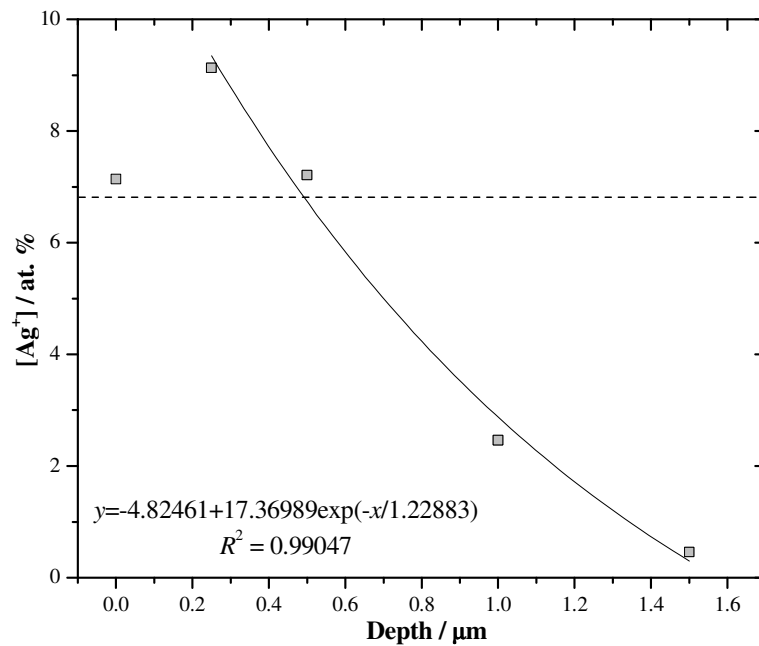


Fig. (7.37): EDX analysis of glass ST08 (79TeO<sub>2</sub>-5ZnO-10Na<sub>2</sub>O-5PbO-1Yb<sub>2</sub>O<sub>3</sub> mol. %), with one flat side dipped into molten salt solution (2AgNO<sub>3</sub>-49NaNO<sub>3</sub>-49KNO<sub>3</sub> mol. %) at 270°C for 5 hours (dashed line is the batched sodium level (6.8 at. %) in the glass).

The first point was left out of the exponential decay fit, as this lower at. % silver value at 0  $\mu\text{m}$  was most likely due to the presence of the surface attack from the molten salt, resulting in many voids, and heavy pitting (ridges spaced around 0.5 mm) at the glass surface, producing a spurious value.

### 7.3. Discussion

#### 7.3.1. X-ray photoelectron spectroscopy (XPS)

##### 7.3.1.1. XPS of $\text{ZnF}_2$ powder

Fig. (7.5) and (7.6) show the low resolution XPS spectra of  $\text{ZnF}_2$  powder used in this study before and after fluorination. As expected, the oxygen levels were significantly reduced by this treatment [7]. This can be seen from table (7.3), which summarises the quantitative analysis from the high resolution scans. If it is assumed that all of the oxygen in the powders was within the  $\text{Zn(OH)F}$  phase identified by XRD in chapter 5, it is possible to calculate the proportion of  $\text{Zn(OH)F}$  and  $\text{ZnF}_2$  in the powders before and after fluorination.  $\text{Zn(OH)F}$  is composed of 33.33 at. % zinc, 33.33 at. % OH (i.e. oxygen), and 33.33 at. % fluorine.  $\text{ZnF}_2$  is composed of 33.33 at. % zinc, and 66.67 at. % fluorine. Therefore, 13.22 at % O1s XPS peak from table (7.3), results from 39.67 mol. %  $\text{Zn(OH)F}$  and 60.33 mol. %  $\text{ZnF}_2$ . For the fluorinated sample, the 3.12 at. % O1s XPS peak from table (7.3), results from 9.35 mol. %  $\text{Zn(OH)F}$  and 90.65 mol. %  $\text{ZnF}_2$ . This is

over four times less than the as-received powder, and will be further reduced by self drying during melting. Table (7.8) summarises these proportions [7].

Table (7.8): Proportion of Zn(OH)F and ZnF<sub>2</sub> in untreated and fluorinated ZnF<sub>2</sub> powder, calculated from O1s XPS peaks [7].

Species	Untreated / at. %		Fluorinated / at. %	
	Zn(OH)F	ZnF <sub>2</sub>	Zn(OH)F	ZnF <sub>2</sub>
Zn	13.22	20.11	3.12	30.22
OH	13.22	-	3.12	-
F	13.22	40.22	3.12	60.43
<b>Total / mol. %</b>	39.66	60.33	9.36	90.65

The proportion of Zn(OH)F in the untreated ZnF<sub>2</sub> was less than the 50 mol. % value assumed in the fluorination batch calculations (see section 3.4), therefore excess (NH<sub>4</sub>)HF<sub>2</sub> was used. Fig. (7.38) shows the mol. % of ZnF<sub>2</sub> and Zn(OH)F before and after fluorination graphically. After fluorination, the Zn2p<sub>3/2</sub> peak position was identical to the value for ZnF<sub>2</sub> from the NIST XPS database (1022.8 eV). The F1s peak also shifted towards the value for ZnF<sub>2</sub> (684.8 eV). This is to be expected as the powder contained over 90 mol. % ZnF<sub>2</sub> after fluorination, compared to around 60 mol. % before. A double fluorination of ZnF<sub>2</sub> may reduce the oxygen content further, and should be investigated.

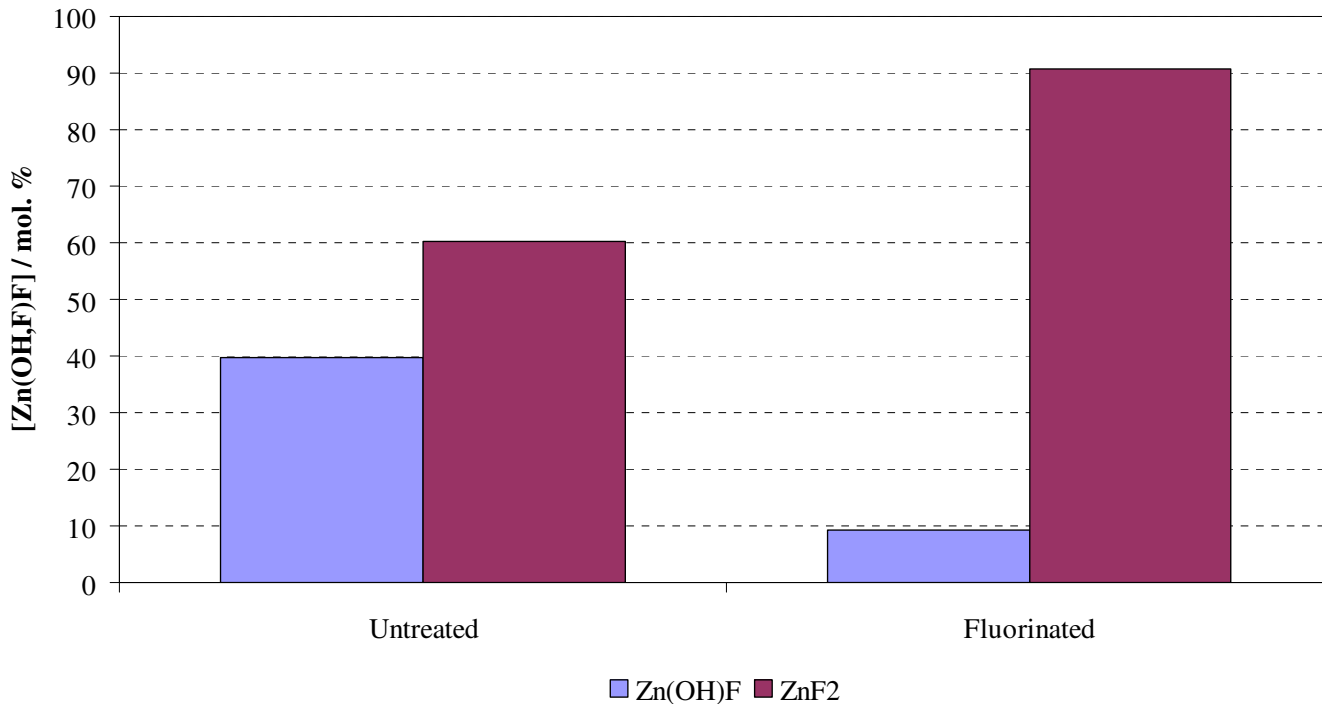


Fig. (7.38): Mol. % of ZnF<sub>2</sub> and Zn(OH)F before and after fluorination .

### 7.3.1.2. XPS of oxide tellurite glasses

A number of studies have been performed on the XPS spectra of tellurite glasses [8-19]. Fig. (7.7) to (7.10) show the XPS spectra of glass MOD015 (82.5TeO<sub>2</sub>-7.5WO<sub>3</sub>-10Nb<sub>2</sub>O<sub>5</sub> mol. %). Fig. (7.8) shows the asymmetry of the high resolution scan of the O1s peak. Himei *et al.* [8] studied the XPS spectra of alkali-tellurite glasses, and only observed O1s peak asymmetry in uncleaved samples, and attributed this high energy shoulder to OH groups on the glass surface (O1s binding energy around 533 eV for Al(OH)<sub>3</sub>). As glass MOD015 was cleaved in the laboratory atmosphere, some hydrolysis would have occurred in addition to the OH contained in the bulk of the glass, indicating this peak at

532.4 eV (7.5 %) in fig. (7.8) can be attributed to the O1s level in OH groups at the cleaved glass surface.

The [TeO<sub>4</sub>] tbp has a lone pair of electrons at one of the equatorial sites of the Te sp<sup>3</sup>d hybrid orbitals, and the [TeO<sub>3</sub>] tp also has a lone pair at one of the Te sp<sup>3</sup> hybrid orbitals (see fig. (2.2)). Himei *et al.* [8] showed that the O1s and Te3d<sub>5/2</sub> binding energies decreased with increasing Na<sub>2</sub>O. Tellurite glasses have lower O1s binding energies than silicates due to the higher electron density of tellurium compared to silicon. Some of the electrons from the lone pair on the Te atom in [TeO<sub>n</sub>] polyhedra are donated to the ligand oxide ions through Te-O σ bonds. In alkali silicates two peaks are seen in the XPS spectra: one for bridging oxygens (BO) and one for non-bridging (NBO). However in alkali tellurites, this is not the case, only one peak is observed. Himei *et al.* [8] propose that this is due to the fact that the electron density of the valence shell of BO atoms is almost equal to that of NBO atoms. This can be explained by electrons of the NBO atoms in [TeO<sub>n</sub>] being back donated to Te atoms and the electrons delocalised through pπ-dπ bonds between O2p and empty Te5d orbitals. As a result the electronic density of the valence shell between BO and NBO atoms is equalised to give one component of the O1s peak. In this study, the main O1s peak could not be resolved into two similar sized peaks close in energy (fig. (7.8)), as in the work of Chowdari *et al.* [15-20], who deconvoluted the main O1s peak into two components. These two components were attributed to non-bridging oxygens (531.1 eV) and bridging oxygens (533.0 eV), with the NBO peak growing at the expense of the BO peak with increasing modifier (Ag<sup>+</sup>) content. The NBO peak was found at a lower energy than the BO peak as in the NBOs, the electron density is higher around the oxygen atom, resulting in a lower nuclear potential and hence

binding energy [19]. Intermediates in the glass such as  $Zn^{+2}$  can also result in termination of the glass network in places, much like  $Na^+$ , but weakly link it in others [21]. Therefore, the main O1s peak at around 530.9 eV (82.5 %) eV is a combination of the binding energies of oxygens within BOs and NBOs in the glass.

The spectrum from the polished surface of glass MOD015 (fig. (7.10)) clearly shows that the O1s peak attributed to OH at 532.4 eV (46.3 %) has clearly grown, due to hydrolysis at the exposed glass surface, in addition to the main peak at 530.6 eV (46.5 %). An additional peak can be seen at 533.9 eV (7.2 %), most likely to be due to organic groups (C-O / C=O) at the glass surface.

### 7.3.1.3. XPS of fluorotellurite glasses

No XPS studies, to this author's knowledge, have been performed on fluorotellurite glasses. However, Chowdari *et al.* performed XPS studies on CuI containing  $TeO_2$  glasses [20].

Fig. (7.11) shows the wide scan XPS spectra of glass MOF001\_iii (65 $TeO_2$ -10 $Na_2O$ -25 $ZnF_2$  mol. %), which was melted for 1.75 hours with un-fluorinated  $ZnF_2$ . Na1s, Zn2p, F1s, Te3d, and O1s peaks were identified and quantification is shown. Quantification from the wide scan gives a rough estimate of composition, however the high resolution peaks give more accurate values. The F1s peak (fig. (7.12)) was asymmetric, the higher energy shoulder at 684.4 eV now almost a separate peak of similar area to the peak at 681.9 eV (51.0 and 49.0 % respectively). This multipeak structure is to be expected, as although fluorine enters the glass in  $ZnF_2$ , it will probably bond to other cations in the

network. NaF is a stable compound, and fluorides of tellurium exist, but are not as stable as  $\text{ZnF}_2$  and NaF.  $\text{TeF}_4$  is a colorless, hygroscopic solid, which decomposes above  $190^\circ\text{C}$ , forming gaseous  $\text{TeF}_6$  (sublimes at  $-39^\circ\text{C}$ ), also hydrolysing completely after 1 day at room temperature [22]. A number of oxyfluorides of tellurium exist, but all are liquids at room temperature, and form from  $\text{Te}^{+6}$ , these include:  $\text{Te}_2\text{O}_2\text{F}_8$ ,  $\text{Te}_2\text{OF}_{10}$ ,  $\text{Te}_3\text{O}_2\text{F}_{14}$ , and  $\text{Te}_6\text{O}_5\text{F}_{26}$ . However, the Te-F bond may be more stable in the solid state when contained within the glass network, but also may result in volatilisation of tellurium fluorides, as discussed in chapter 5. Asymmetry in the XPS peaks of tellurite and fluorotellurite glasses may be as a result of the high degree of asymmetry of the structural units in the glass. Unlike the  $[\text{SiO}_4]$  unit which forms highly symmetric tetrahedra, the  $\text{TeO}_2$  structural units are trigonal bipyramidal (tbp),  $[\text{TeO}_4]$ , and trigonal pyramidal (tp),  $[\text{TeO}_3]$ , in structure, with a lone pair of electrons from tellurium in the corner of the polyhedra not occupied by an oxygen atom [23]. This lone pair of electrons will inevitably affect the distribution of electrons (and as a consequence the bonding) of any atoms in close proximity, such as fluorine which is highly electronegative. The asymmetry could also be due to fluorine associated with  $\text{ZnF}_2$ , and  $\text{Zn}(\text{OH})\text{F}$  derived structural units in the bulk glass. This impurity ( $\text{Zn}(\text{OH})\text{F}$ ) would also shift the F1s peak in the glass away from the value for  $\text{ZnF}_2$ .

The O1s peak for this glass was also asymmetric, as shown by fig. (7.13), which shows the O1s peak deconvoluted into three main components, at 531.0 eV (81.2 %  $\rightarrow$  BOs and NBOs), 532.1 eV (14.9 %  $\rightarrow$  OH), and 535.7 eV (3.9 %). The peak at around 535.7 eV could be due to C-O and / or C=O groups from hydrocarbons used in the vacuum system of the XPS; however this peak was not seen in the XPS spectra of the

ZnF<sub>2</sub> powders or cleaved tungsten-tellurite glasses, indicating that the peak is associated with oxygens within, or on the surface of the fluorotellurite glasses. The peak observed at 535.7 eV in this study was also seen in the spectra of sodium-tellurite glasses by Himei *et al.* but not commented on. The O1s peak for urea ((NH<sub>2</sub>)<sub>2</sub>C=O) from the NIST XPS database occurs at 535 eV indicating the C=O bond increases the O1s binding energy compared to singly bonded oxygen. Te=O bonds are present in some of the tellurite polyhedra such as the isolated unit [TeO<sub>3</sub>], which contains three non-bridging oxygens, one of which is doubly bonded to the tellurium atom, and the remaining two carry a single negative charge [24]. This structural unit is common in alkali-tellurite glasses. Therefore, this peak at around 535.7 eV, not seen in the ZnF<sub>2</sub> powders could be due to the Te=O bond in the glass or other M=O species.

Table (7.6) shows the peak positions from the NIST XPS database of TeO<sub>2</sub>, (Te3d<sub>3/2</sub> and O1s), Na<sub>2</sub>O (Na1s), and ZnF<sub>2</sub> (Zn2p<sub>3/2</sub> and F1s), batched at. %, and the quantitative analysis (peak positions, at. and wt. %) of the corresponding high resolution peaks for glass MOF001\_iii, which was melted for 1.75 hours. The actual at. % values were very close to the batched values, and as expected, the fluorine levels were lower than batched, and oxygen higher due to volatilisation of fluorides from the melt. Fluorine, which volatilises from the glass as species such as HF, F<sub>2</sub> and MF<sub>x</sub> (where M is a cation), will be replaced by oxygen in the vicinity of the melt surface, to ensure charge neutrality. There will inevitably be a small error in these values, as the Shirley background model was fitted manually. Sensitivity factors used by CasaXPS to calculate the quantitative analysis will also be for pure crystalline elements / compounds, not multicomponent vitreous solids. However, these errors will be small.

Fig. (7.15) to (7.19) show the wide scan, and high resolution Na1s, Zn2p, F1s, Te3d, and O1s XPS spectra respectively, for glass MOF001\_v (65TeO<sub>2</sub>-10Na<sub>2</sub>O-25ZnF<sub>2</sub> mol. %), melted for 2 hours with fluorinated ZnF<sub>2</sub>. The quantitative analysis from the high resolution scans for this glass are shown in table (7.7). Only the O1s peak was asymmetric for this glass (see fig. (7.19)), with three peaks at 330.7 eV (88.9 % → BOs and NBOs combined), 532.0 eV (5.8 % → OH), and 535.4 eV (5.3 % Te=O). The F1s peak was symmetric for this glass, perhaps an indication of batch purity, as the ZnF<sub>2</sub> was fluorinated (far fewer F-Zn-OH species). From table (7.7), the fluorine levels were even lower for this glass, melted for 2 hours (10.1 at. %), compared to the 1.75 hour melt (11.4 at. %), as a result of volatilisation. The O1s peak (50.4 at. %) was lower than the 1.75 melt by 1.8 at. %. This could be due to experimental error. Fig. (6.28) shows optical loss plateaus to a minimum of around 10 dB.m<sup>-1</sup> at 2900 cm<sup>-1</sup> for melting times > 1.75 hours for glass MOF001. This indicates that self-drying whilst melting has reached equilibrium, i.e. most of the OH has been eliminated from the glass, therefore fluorine volatilisation will not proceed as rapidly. If ± a few at. % error is considered, the values of oxygen and fluorine in glass MOF001\_v from the XPS spectra are consistent with the optical loss measurements of this glass series from chapter 6.

For comparison, fig. (7.20) and (7.21) show the wide scan and high resolution O1s spectra for glass MOF001\_v (65TeO<sub>2</sub>-10Na<sub>2</sub>O-25ZnF<sub>2</sub> mol. %) un-cleaved surface. From the O1s spectrum (fig. (7.21)), the OH peak at around 532.3 eV (OH) has grown compared to the cleaved sample (fig. (7.19)). In addition to the peaks seen in the cleaved sample, a fourth peak at 533.7 eV can be seen. This is likely to be organic (e.g. singly bonded C-O). The OH peak has grown due to longer exposure to moisture of the un-

cleaved surface, during sample synthesis and preparation. As expected, the oxygen levels were higher on this polished sample compared to the cleaved glass (71.5 and 50.4 at. % respectively), most likely due to hydrolysis, with OH groups replacing fluorine, which was lower at the surface than the cleave (5.9 and 10.1 at. % respectively). Sodium was also lower (6.3 to 2.9 at. %), as this is easily leached from the glass after contact with atmospheric moisture. Fig. (7.22) shows these trends graphically.

### 7.3.2. Chemical and environmental durability

#### 7.3.2.1. Durability of oxide tellurite glasses

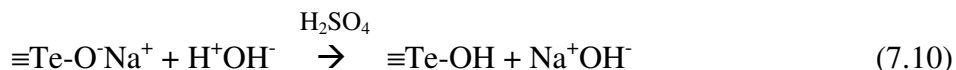
Fig. (7.23) shows the surface quality of glass MOF009 (77TeO<sub>2</sub>-12ZnO-10Na<sub>2</sub>O-1Yb<sub>2</sub>O<sub>3</sub> mol. %) before, and after 60, 120, and 180 sec. immersion in a 1M solution of NaOH at 21°C. An uneven surface layer formed, indicating preferential attack of components in the glass. Initially all component of the glass will be attacked by the alkali and taken into solution, such as ZnO (2NaOH + ZnO → Zn(OH)<sub>2</sub> + Na<sub>2</sub>O) and TeO<sub>2</sub> (2NaOH + TeO<sub>2</sub> → Na<sub>2</sub>TeO<sub>3</sub> + H<sub>2</sub>O) [22]. However, it is attack of the glass network by OH which will strongly degrade mechanical and optical properties, as illustrated by equation (7.9).



After 180 seconds, the surface has begun to break up, exposing fresh glass below. This indicates the hydrolysed layer was not mechanically rigid, or had been attacked by the

solution which would have decreased in alkalinity with increasing time. The linear etch rate of this solution (fig. (7.24)) was around 0.012 wt. % glass per second. It would appear NaOH is an unsuitable etchant for cleaning the surface (e.g. preform) of oxide tellurite glass.

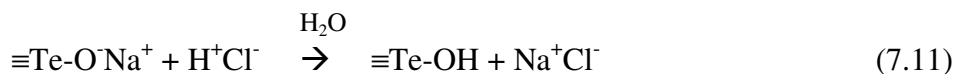
Fig. (7.25) shows optical micrographs of glass MOD012 (75TeO<sub>2</sub>-10ZnO-10Na<sub>2</sub>O-5GeO<sub>2</sub> mol. %) after immersion in 3M H<sub>2</sub>SO<sub>4</sub> at 15°C for 60, 120, 180, and 240 seconds. Qualitatively, the surface was not attacked as severely as by the NaOH at 21°C, however this 3M H<sub>2</sub>SO<sub>4</sub> etch was performed at a lower temperature. TeO<sub>2</sub> has also been shown to be completely insoluble in concentrated (100%) H<sub>2</sub>SO<sub>4</sub> [25]. The Na<sub>2</sub>O in the glass would be more readily attacked in this glass when in contact with an acidic solution, and Zn<sup>+2</sup> also leached into solution (ZnO + H<sub>2</sub>SO<sub>4</sub> → ZnSO<sub>4</sub> + H<sub>2</sub>O). Again this solution will hydrolyse the glass network as shown by equation (7.10).



If the sodium was leached from the glass, and the solution donated a proton (H<sup>+</sup>) to the oxygen ion attached to Te, this would have formed OH at the glass surface. This reaction would have proceeded, increasing the pH of the solution. Hydrolysis of bridging oxygens, shown by equation (7.9), probably also occurred. The etchant was again poor, due to severe surface hydrolysis forming an opaque surface layer.

Fig. (7.26) shows the surface of the glass from fig. (7.25) immersed in 1M HCl at 15°C for 60, 120, 180 and 240 sec. Surface quality was again poor. Sodium ions will

have been leached from the glass, and the solution again probably donated a proton to the oxygen ion.



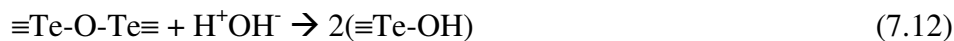
Hydrolysis of bridging oxygens, and attack of ZnO [22] are likely to also to have occurred with HCl. Fig. (7.27) shows the etch rates of the glass from fig. (7.25) and (7.26), which were best fitted by exponential curves. The solutions initially showed similar etch rates, however the rate of the 3M H<sub>2</sub>SO<sub>4</sub> solution was higher after 120 sec.

Fig. (7.28a) shows the etch rates of glass MOD012 (75TeO<sub>2</sub>-10ZnO-10Na<sub>2</sub>O-5GeO<sub>2</sub> mol. %), immersed in 1M HCl, 1M H<sub>2</sub>SO<sub>4</sub>, and 3M H<sub>2</sub>SO<sub>4</sub> at 21°C. All were best fitted linearly, however the correlation between the data and fits for the 1M solutions were lower than the 3M solution. This was partially due to forcing the fit to pass through zero. Fig. (7.28b) shows better correlation when the linear fitting was not forced through zero. It can be seen that the etch rates for this glass were of the order 3M H<sub>2</sub>SO<sub>4</sub> > 1M HCl > 1M H<sub>2</sub>SO<sub>4</sub>. This is to be expected, the 3M H<sub>2</sub>SO<sub>4</sub> will have more protons available to attack the glass than the 1M HCl, however; HCl is a 'stronger' acid (or proton donor) than H<sub>2</sub>SO<sub>4</sub>, therefore the 1M solution etches more rapidly than the 1M H<sub>2</sub>SO<sub>4</sub>.

### 7.3.2.2. Durability of fluorotellurite glasses

Fig. (7.29a) shows the degradation of glass MOF001 (65TeO<sub>2</sub>-10Na<sub>2</sub>O-25ZnF<sub>2</sub> mol. %) after immersion in distilled water at 21 and 60°C. The weight loss was best fitted

exponentially for both temperatures. As expected, the 60°C glass degraded more rapidly, as water more readily dissociates into H<sup>+</sup> and OH<sup>-</sup> at higher temperatures. This will result in the severance of bridging bonds, and hydrolysis.



OH will also replace fluorine in the glass due to their similar ionic radii and electronegativities, and sodium ions probably leached into solution as described above. The glass treated at room temperature, showed relatively low weight loss, 0.34 wt. %, over the 21 day period. This may indicate two different temperature regimes of water attack. At lower temperatures (21°C), very few cationic species (Te<sup>+4</sup>, Na<sup>+</sup> and Zn<sup>+2</sup>) were leached into solution (based on overall weight loss), and severance of bridging bonds by hydrolysis, was also low. The replacement of fluorine with OH is common, resulting in a smaller net weight loss over time; fluoride was taken into solution, with RAM = 19.9 g.mol<sup>-1</sup>, and OH added, with RMM = 17.0 g.mol<sup>-1</sup>, a 2.9 g.mol<sup>-1</sup> difference. At higher temperatures (60°C), cationic species were leached into solution more readily, bridging bonds were severed by hydrolysis, along with the attack occurring at lower temperatures, which will have resulted in a higher weight loss over time, as shown by fig. (7.29a). The severance of bridging bonds will have resulted in a gain in weight (H<sub>2</sub>O RMM = 18.0 g.mol<sup>-1</sup>), and leaching of species, a loss, the weight depending on the cation leached (RAM<sub>Na</sub> = 23.0 g.mol<sup>-1</sup>, RAM<sub>Zn</sub> = 65.4 g.mol<sup>-1</sup>, and RAM<sub>Te</sub> = 127.6 g.mol<sup>-1</sup>). Table (7.8) summarises these reactions.

Table (7.8): Proposed regimes of water attack on fluorotellurite glasses.

Temperature regime		Main reactions	Comments
High $T$ ( $\approx 60^\circ\text{C}$ )	Low $T$ ( $\approx 21^\circ\text{C}$ )	$-\text{Zn}^+\text{F}^- + \text{H}^+\text{OH}^- \rightarrow -\text{Zn}-\text{OH} + \text{H}^+\text{F}^-$	$\text{F}^- / \text{OH}^-$ exchange
		$\equiv\text{Te}-\text{O}-\text{Te}\equiv + \text{H}^+\text{OH}^- \rightarrow 2(\equiv\text{Te}-\text{OH})$	Bridging bond severance
		$\equiv\text{Te}-\text{O}-\text{Na}^+ + \text{H}^+\text{OH}^- \rightarrow \equiv\text{Te}-\text{OH} + \text{Na}^+\text{OH}^-$	Cationic leaching

The leaching of sodium ions and severance of Te-O-Te bonds could take place at around a 1:1 ratio at lower temperatures and the weight loss and gain would approximately cancel each other out ( $\text{RAM}_{\text{Na}} = 23.0 \text{ g.mol}^{-1}$ , and  $\text{RMM}_{\text{H}_2\text{O}} = 18.0 \text{ g.mol}^{-1}$ ), with little effect seen on the durability curve, fig. (7.29a). If this was the case, higher temperature leaching also occurs with sodium ions, as well as heavier cations, i.e. tellurium and zinc. The durability curves levelled out eventually, perhaps as an impermeable hydroxide layer will form, protecting the material away from the surface hydrolysing further. Fig. (7.29b) shows the weight loss from (fig. 7.29a) plotted against  $(t)^{1/2}$ . For both temperatures, 21 and  $60^\circ\text{C}$ , the plot was highly linear, suggesting diffusion controlled attack of the fluorotellurite glass by the water.

Fig. (7.30) shows the surface quality of glass MOF001 ( $65\text{TeO}_2$ - $10\text{Na}_2\text{O}$ - $25\text{ZnF}_2$  mol. %) after immersion in 3M HCl, with agitation at  $21^\circ\text{C}$ . These glasses exhibited different surface morphology after etching to the oxide glasses reported in the previous section. Initially (30 sec.) the spherical pitting was relatively smooth, but after 1 min. the surface quality became very poor. Fig. (7.31a) shows the exponential etch rate of this solution, and the linear etch rate ( $\approx 3 \text{ wt. \%}$  per min.) of the 1M solution on glass MOF005 ( $70\text{TeO}_2$ - $10\text{Na}_2\text{O}$ - $20\text{ZnF}_2$  mol. %). This pronounced pitting may be due to the preferential attack of  $\text{TeO}_2 / \text{Na}_2\text{O} / \text{ZnO}$ , leaving more fluoride material, etched at a

lower rate by the HCl. Fig. (7.31a) shows the wt. % loss versus  $(t)^{1/2}$  for the glasses shown in fig. (7.31a), with linear fitting, again indicating diffusion controlled attack.

Fig. (7.32) shows micrographs of glass MOF001 (65TeO<sub>2</sub>-10Na<sub>2</sub>O-25ZnF<sub>2</sub> mol. %) after etching with 40% HF at 21°C. It can be clearly seen, that although this etchant produced some pitting, (preferential attack), the acid solution did not appear to deposit any kind of surface layer, leaving fluorotellurite glass at the surface even after 30 min. This would seem to indicate hydrolysis was avoided, compared to other etchants studied. Fig. (7.33) shows the linear etch rate for 4% HF at 21°C on glass MOF005 (70TeO<sub>2</sub>-10Na<sub>2</sub>O-20ZnF<sub>2</sub> mol. %) on this glass (MOF001), which also left a clean surface (see fig. (7.34)). The linear etch rate was around 0.5 wt. % per min. This rate is reasonable to perform a controlled etch on the glass. Fig. (7.34) shows the effect of this treatment on the infrared spectra. It can be seen, that the OH bands increased significantly with etching time. The strongly H-bonded OH band can also be seen, which was not apparent in the bulk polished ZnF<sub>2</sub> containing samples (see chapter 6), indicating these latter glasses were very dry. Therefore, any wet etching techniques may not be suitable for fluorotellurite preform preparation, as this OH content, presumable concentrated near the glass surface, may introduce stresses, and crystal nucleation sites in the preform, as well as exhibiting dissimilar rheological behaviour to the 'dry' glass.

Fig. (7.35) shows a micrographs of the effect of various etchants on a similar glass to MOF001, of composition MOF005 (70TeO<sub>2</sub>-10Na<sub>2</sub>O-20ZnF<sub>2</sub> mol. %). Hydrofluoric, acetic and phosphoric acids produced good surface finishes and the latter two acids should be investigated further, as weight loss was not measured, and would need to be

quantified to determine if any material was removed. Nitric acid, however produced a relatively poor etch.

From these initial studies HF appeared to be the best etchant for fluorotellurite glasses, however over short times introduced a significant amount of OH into the glass. If this OH was confined to the glass surface, it may not greatly affect the optical loss of a clad preform; however, it may detrimentally alter the fibre drawing process. Therefore, high concentration HF (e.g. 40 %), for short times, at 21°C would seem to be the best choice of etchant to try to minimise surface degradation.

### 7.3.3. Ion exchange

The general phenomena of ion-exchange in glasses has been long studied [26], and specifically  $\text{Ag}^+/\text{Na}^+$  ion-exchange for waveguides in silicates [1, 27] and tellurites [28] also. Fig. (7.36) shows the diffusion profile of glass T08 (80TeO<sub>2</sub>-9ZnO-10Na<sub>2</sub>O-1Er<sub>2</sub>O<sub>3</sub> mol. %), which had a silver layer evaporated on both polished sides (100 and 300 μm), followed by heat treatment at 285°C for 12 hours under inert atmosphere (argon). The thicker silver layer (300 μm) resulted in deeper penetration (at least 2 μm) into the glass, compared to the 100 μm layer ( $\approx 1 \mu\text{m}$ ). However, large errors may be involved due to the similarity between: the errors of the EDX experiment ( $\pm 1$  at. %) and the silver levels measured (for heat treated samples particularly), and the depth of penetration of silver (1 to 2 μm) and the electron beam interaction volume ( $\approx 1 \mu\text{m}^3$ ). At the surface the silver content was around 2.3 and 2.5 at. % for the 100 and 300 μm layers respectively, and the sodium content of the glass was 6.8 at. % batched; therefore total replacement of  $\text{Na}^+$

with  $\text{Ag}^+$  did not occur. The content decreased to 0.7 at. % at 1  $\mu\text{m}$  depth for the 100  $\mu\text{m}$  layer, and 0.4 at. % at 2  $\mu\text{m}$  depth for the 300  $\mu\text{m}$  layer. Silver ions ‘exchange’ with  $\text{Na}^+$  ions in the glass due to their similar ionic radii (114 and 113 pm respectively in four-fold coordination), and both are monovalent, ensuring charge neutrality. At room temperature, the ion exchange of the silver layer will be kinetically inhibited. However, at elevated temperatures, the exchange becomes thermodynamically and kinetically more favourable, and due to the concentration difference at the silver / glass interface,  $\text{Ag}^+/\text{Na}^+$  ion-exchange takes place. Equation (7.13) shows Fick’s second law.

$$\frac{\partial N}{\partial t} = D \frac{\partial^2 N}{\partial x^2} \quad (7.13)$$

where  $N$  is the exchanged ion concentration (i.e. silver),  $t$  is time,  $x$  the depth of exchange into the material, and  $D$  the diffusion coefficient of the ion. Solving this equation results in a concentration profile shown by equation (7.14). Flux of sodium ions out of the glass results in a more complex profile, with the silver content levelling off initially, before decreasing according to an erfc function.

$$N(x,t) = N_0 \operatorname{erfc} \left[ \frac{x}{2(Dt)^{0.5}} \right] \quad (7.14)$$

where  $N_0$  is the surface concentration [1], and erfc is the complementary error function defined by equation (7.15).

$$\operatorname{erfc}(z) \equiv 1 - \operatorname{erf}(z) = \frac{2}{\sqrt{\pi}} \int_z^{\infty} e^{-u^2} du \quad (7.15)$$

Using equation (7.14), the diffusion profiles of the glasses studied were modelled using Mathcad software. For each glass,  $N_0$  values from EDX were used (or generated if not known). Times ( $t$ ) of the experiments were known and constant, and  $D$  was iterated to give  $N$  values equal to EDX values at the maximum depth into the glass recorded for each glass. For the 300  $\mu\text{m}$  side of glass T08,  $N_0 = 0.0242$  (2.41 at. %),  $t = 43200$  seconds (i.e. 12 hours), and  $D = 25.21 \times 10^{-6} \text{ m}^2 \cdot \text{s}^{-1}$  (using constraint: silver fraction =  $4.244 \times 10^{-3}$  (0.42 at. %) at  $x = 2 \mu\text{m}$ ). Fig. (7.39) shows the EDX data, and the modelling for glass T08 ( $80\text{TeO}_2\text{-}9\text{ZnO-}10\text{Na}_2\text{O-}1\text{Er}_2\text{O}_3$  mol. %), with 300  $\mu\text{m}$  silver layer evaporated on one side, followed by heat treatment at  $285^\circ\text{C}$  for 12 hours.

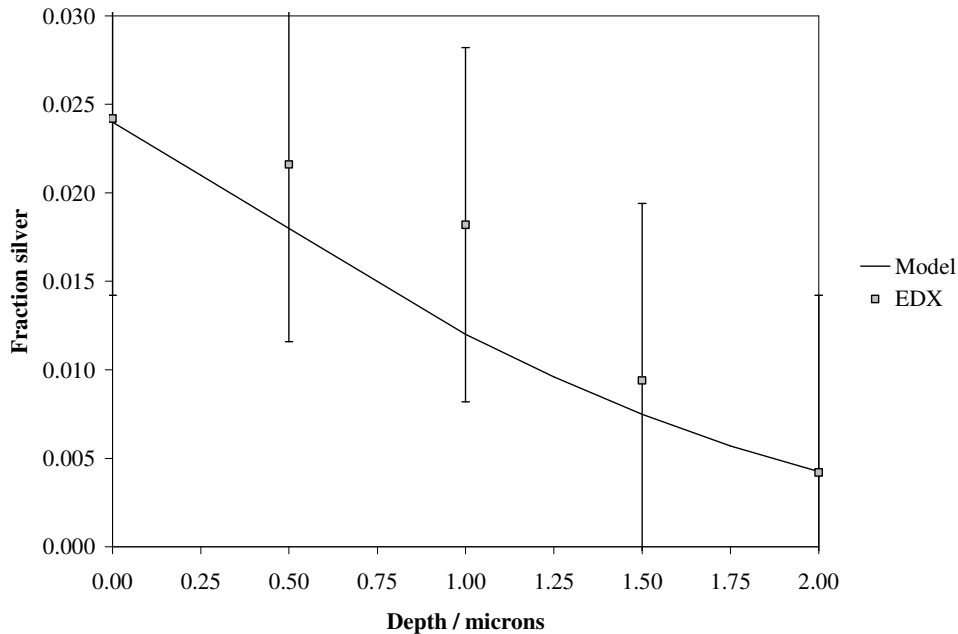


Fig. (7.39): Silver concentration profile (EDX data and model) for glass T08 ( $80\text{TeO}_2\text{-}9\text{ZnO-}10\text{Na}_2\text{O-}1\text{Er}_2\text{O}_3$  mol. %), with 300  $\mu\text{m}$  silver layer evaporated on one side, followed by heat treatment at  $285^\circ\text{C}$  for 12 hours (error bars  $\pm 1$  at. %).

It can be seen the model fitted the data reasonably well, although errors were potentially large. This disparity between the data points and the fit could be due to EDX experimental error, inhomogeneity in the glass and / or temperature of the experiment, resulting in non-equilibrium ion-exchange, or a more complex diffusion profile (see above). For the 100  $\mu\text{m}$  side of glass T08,  $N_0 = 0.0229$  (2.3 at. %),  $t = 43200$  seconds (i.e. 12 hours), and  $D = 10.58 \times 10^{-6} \text{ m}^2 \cdot \text{s}^{-1}$  (using constraint: silver fraction =  $6.769 \times 10^{-3}$  at  $x = 1 \mu\text{m}$ ). Fig. (7.40) shows the EDX data, and the modelling for glass T08 (80TeO<sub>2</sub>-9ZnO-10Na<sub>2</sub>O-1Er<sub>2</sub>O<sub>3</sub> mol. %), with 100  $\mu\text{m}$  silver layer evaporated on one side, followed by heat treatment at 285°C for 12 hours.

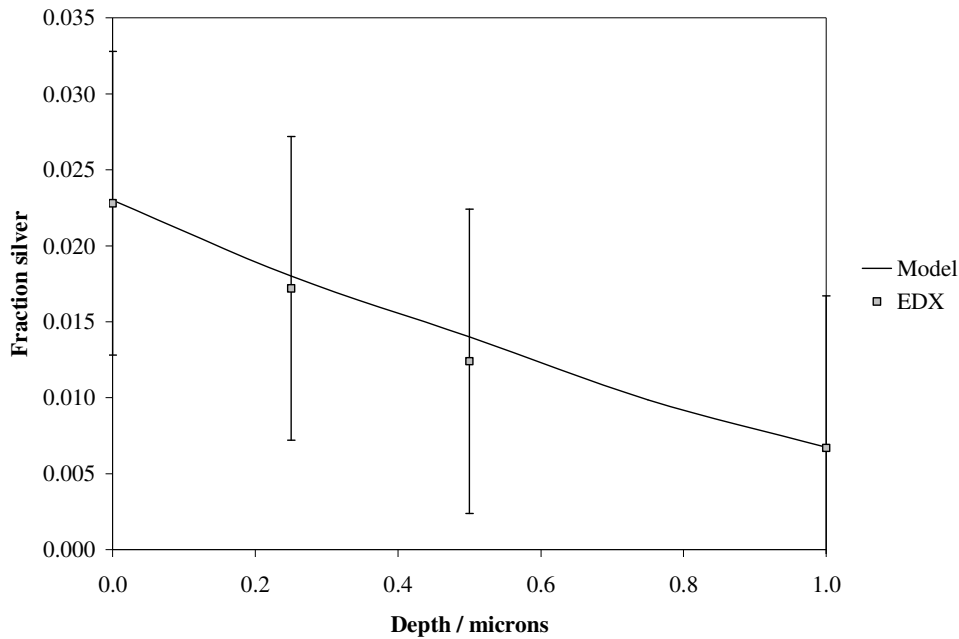


Fig. (7.40): Silver concentration profile (EDX data and model) for glass T08 (80TeO<sub>2</sub>-9ZnO-10Na<sub>2</sub>O-1Er<sub>2</sub>O<sub>3</sub> mol. %), with 100  $\mu\text{m}$  silver layer evaporated on one side, followed by heat treatment at 285°C for 12 hours (error bars  $\pm 1$  at. %).

This provided a reasonable fit for the EDX data, with all points lying within the error bars ( $\pm 1$  at. %).

Fig. (7.37) shows the diffusion profile of  $\text{Ag}^+$  for glass ST08 ( $79\text{TeO}_2$ - $5\text{ZnO}$ - $10\text{Na}_2\text{O}$ - $5\text{PbO}$ - $1\text{Yb}_2\text{O}_3$  mol. %), for which one flat side was dipped into a molten salt solution ( $2\text{AgNO}_3$ - $49\text{NaNO}_3$ - $49\text{KNO}_3$  mol. %) at  $270^\circ\text{C}$  for 5 hours. A much higher silver content was incorporated into the glass, around 9.1 at. % at  $0.25\ \mu\text{m}$ , and 0.5 at. %  $1.5\ \mu\text{m}$ , although the depth of diffusion was not greater than the heat treated sample. This high level over shorter time of treatment is to be expected, as the molten salt solution will result in a more vigorous exchange, and higher refractive index contrast in the exchanged region compared to the bulk glass. The first data point at  $0\ \mu\text{m}$  was not included in the exponential decay fit. The surface contained some pitting from the molten salt, therefore the electron beam will sample some of these voids when performing EDX analysis, lowering the overall silver content. However, if the sodium exchanged for the silver 1:1, this would result in 6.8 at. % at the surface, similar to the value seen in fig. (7.37) at  $0\ \mu\text{m}$ . Around 7 at. % silver was also seen at  $0.5\ \mu\text{m}$  depth, possibly indicating the measurement at  $0.25\ \mu\text{m}$  was incorrect, and the ion-exchange followed a more complex profile than shown by equation (7.14).

For this glass  $N_0 = 0.125$  ( $N = 0.091$  (9.1 at. %) at  $x = 0.25\ \mu\text{m}$  was used as a constraint, due to the spurious EDX value at  $x = 0\ \mu\text{m}$ ),  $t = 18000$  seconds (i.e. 5 hours), and  $D = 14.38 \times 10^{-6}\ \text{m}^2 \cdot \text{s}^{-1}$  (using constraint: silver fraction =  $4.636 \times 10^{-3}$  (0.46 at. %) at  $x = 1.5\ \mu\text{m}$ ). Fig. (7.41) shows the EDX data and modelling for glass ST08 ( $79\text{TeO}_2$ - $5\text{ZnO}$ - $10\text{Na}_2\text{O}$ - $5\text{PbO}$ - $1\text{Yb}_2\text{O}_3$  mol. %), where one flat side was dipped into a molten salt solution ( $2\text{AgNO}_3$ - $49\text{NaNO}_3$ - $49\text{KNO}_3$  mol. %) at  $270^\circ\text{C}$  for 5 hours.

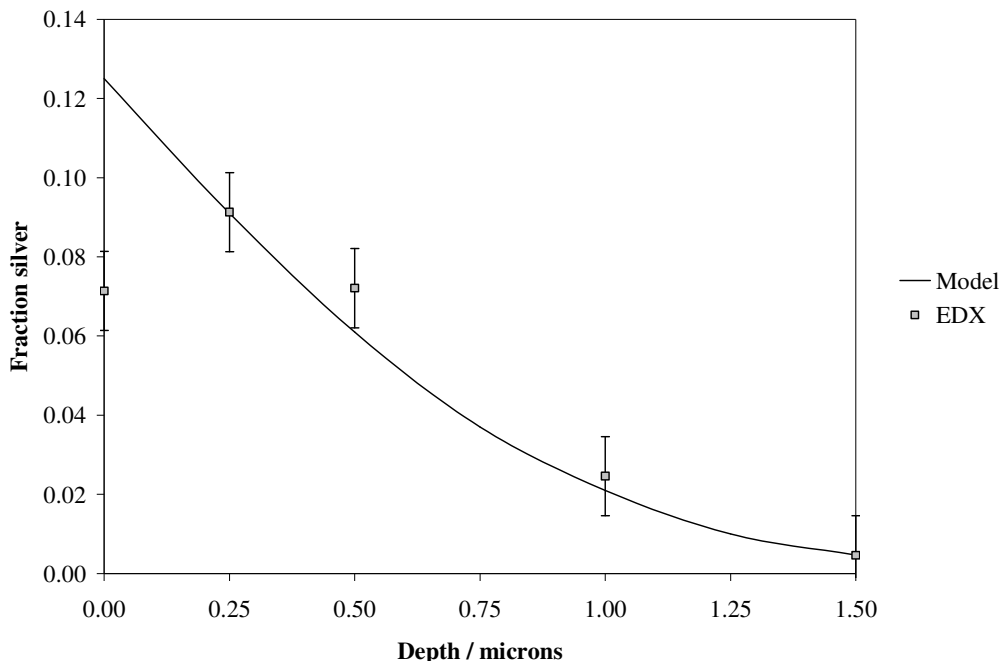


Fig. (7.41): Silver concentration profile (EDX data and model) modelling for glass ST08 (79TeO<sub>2</sub>-5ZnO-10Na<sub>2</sub>O-5PbO-1Yb<sub>2</sub>O<sub>3</sub> mol. %), where one flat side was dipped into a molten salt solution (2AgNO<sub>3</sub>-49NaNO<sub>3</sub>-49KNO<sub>3</sub> mol. %) at 270°C for 5 hours (error bars  $\pm 1$  at. %).

This provided a relatively good fit. It is interesting to note that by this method of ion-exchange around three times the amount of silver was incorporated into the glass near the surface, compared to the heat treated samples. However, at 1.5  $\mu\text{m}$  depth, the level of silver was approximately equal to the heat treated samples at 1 and 2  $\mu\text{m}$  for the 100 and 300  $\mu\text{m}$  layers respectively, i.e. this treatment produced a steeper silver concentration profile. The heat treated samples would have reached thermal equilibrium across the whole of the sample relatively quickly during treatment (i.e. no temperature gradient) relative to the time scale of the experiment (12 hours). The surface of the sample treated with molten salt was dipped into the melt, creating a sharper temperature gradient, as the atmosphere around the bulk of the glass would have been at a lower temperature.

Therefore, the glass would probably not reach thermal equilibrium during the duration of the experiment, to the extent of the samples heat treated in a furnace. This could result in the sharper diffusion profile seen in fig. (7.41).

Table (7.9) summarises the parameters from equation (7.14) for all three ion-exchange models.

Table (7.9): Parameters for ion-exchange models, where  $N_0$  = fraction of silver at glass surface (from EDX data),  $t$  = time of experiment, and  $D$  = diffusion coefficient.

Parameter	Glass		
	T08 300 $\mu\text{m}$	T08 100 $\mu\text{m}$	ST08 molten salt
$N_0$	0.0242	0.0228	0.1250
$t / \times 10^4 \text{ sec.}$	4.32	4.32	1.80
$D / \times 10^{-6} \text{ m}^2 \cdot \text{s}^{-1}$	25.21	10.58	14.38

## 7.4. Summary

XPS of as-received and fluorinated  $\text{ZnF}_2$  powders showed ‘oxygen’ levels were reduced from around 13 to 3 at. %, and the level of  $\text{Zn(OH)F}$  from around 40 to 9 mol. % on fluorination [7]. The level of  $\text{Zn(OH)F}$  may be lower if molecular water and organic contaminants were present.

XPS of tungsten-tellurite, and fluorotellurite glasses showed a multi-peak structure to the O1s peak, thought to be due to the following with increasing binding energy: BOs / NBOs, OH, C-O, and M=O species. The OH component was relatively small on spectra from cleaved glass surfaces, however this grew significantly on optically polished surfaces, due to degradation on exposure to atmospheric moisture. This degradation also

resulted in lower at. % of cationic constituents of the glass at the polished surfaces. Semi-quantitative analysis of cleaved surfaces showed good agreement with batched at. % values, with only fluorine differing significantly due to melt volatilisation.

NaOH, H<sub>2</sub>SO<sub>4</sub>, HCl, and nitric acid were poor etchants for the TeO<sub>2</sub>-Na<sub>2</sub>O-ZnO and TeO<sub>2</sub>-Na<sub>2</sub>O-ZnF<sub>2</sub> glasses due to severe hydrolysis at the glass surface. HF, acetic and phosphoric acid did not produce this poor visible surface layer on TeO<sub>2</sub>-Na<sub>2</sub>O-ZnF<sub>2</sub> glasses, however infrared spectra of 4% HF glasses showed a significant increase in OH bands, which may have an undesirable effect on fibre drawing of preforms treated this way. A hydrolysed layer could potentially result in stresses, crystal nucleation sites, and contrasting viscosity to the bulk glass in a preform. After these initial studies HF seems the best etchant for fluorotellurite glasses, however any water containing solution will introduce some degree of OH to the glass surface; therefore exposure to high concentration acids for short times would be recommended.

Ag<sup>+</sup>/Na<sup>+</sup> ion-exchange of TeO<sub>2</sub>-Na<sub>2</sub>O-ZnO glasses by two methods (immersion in molten salt and heat treated Ag-layer) produced measurable silver content (by EDX) in the glasses, with the molten salt incorporating higher silver content, and the heat treatment lower content, but with no chemical erosion of the treated surface. These Ag<sup>+</sup> concentration profiles were modelled using erfc function, and diffusion parameters were obtained.

## 7.5. References

- [1] T. Findakly, "Glass waveguides by ion exchange: a review," *Optical Engineering*, vol. 24, pp. 244-250, 1985.

- [2] A. Einstein, "Über einen die erzeugung und verwandlung des liches betreffenden heuristischen gesichtspunkt / On a heuristic point of view about the creation and conversion of light," *Annalen der Physik*, vol. 17, pp. 132, 1905.
- [3] G. K. Wertheim, "X-ray photoelectron spectroscopy and related methods," in *Solid state chemistry techniques*, A. K. Cheetham and P. Day, Eds. Oxford: Oxford University Press, 1991, pp. 84-121.
- [4] J. Scofield, "Hartree-Slater subshell photoionization cross-sections at 1254 and 1487eV," *Journal of Electron Spectroscopy and Related Phenomena*, vol. 8, pp. 129-137, 1976.
- [5] P. J. Goodhew and F. J. Humphreys, *Electron microscopy and analysis*. London: Taylor & Francis, 1988.
- [6] A. M. McDonald, "Environmental scanning electron microscopy - ESEM," *Materials World*, vol. 6, pp. 399-401, 1998.
- [7] M. D. O'Donnell, D. Furniss, V. K. Tikhomirov, and A. B. Seddon, "Low loss infrared fluorotellurite optical fibre," *Physics and Chemistry of Glasses*, in press.
- [8] Y. Himei, Y. Miura, T. Nanba, and A. Osaka, "X-ray photoelectron spectroscopy of alkali tellurite glasses," *Journal of Non-Crystalline Solids*, vol. 211, pp. 64-71, 1997.
- [9] G. D. Khattak and M. A. Salim, "X-ray photoelectron spectroscopic studies of zinc-tellurite glasses," *Journal of Electron Spectroscopy and Related Phenomena*, vol. 123, pp. 47-55, 2002.
- [10] V. Dimitrov and T. Komatsu, "Electronic polarizability, optical basicity and non-linear optical properties of oxide glasses," *Journal of Non-Crystalline Solids*, vol. 249, pp. 160-179, 1999.
- [11] V. Dimitrov and T. Komatsu, "Classification of simple oxides: A polarizability approach," *Journal of Solid State Chemistry*, vol. 163, pp. 100-112, 2002.
- [12] P. Charton, L. Gengembre, and P. Armand, "TeO<sub>2</sub>-WO<sub>3</sub> glasses: Infrared, XPS and XANES structural characterizations," *Journal of Solid State Chemistry*, vol. 168, pp. 175-183, 2002.
- [13] M. A. Salim, G. D. Khattak, N. Tabet, and L. E. Wenger, "X-ray photoelectron spectroscopy (XPS) studies of copper-sodium tellurite glasses," *Journal of Electron Spectroscopy and Related Phenomena*, vol. 128, pp. 75-83, 2003.
- [14] G. D. Khattak, A. Mekki, and L. E. Wenger, "Local structure and redox state of copper in tellurite glasses," *Journal of Non-Crystalline Solids*, vol. 337, pp. 174-181, 2004.

- [15] B. V. R. Chowdari and P. Pramoda Kumari, "Studies on  $\text{Ag}_2\text{O}\cdot\text{M}_x\text{O}_y\cdot\text{TeO}_2$  ( $\text{M}_x\text{O}_y=\text{WO}_3, \text{MoO}_3, \text{P}_2\text{O}_5$  and  $\text{B}_2\text{O}_3$ ) ionic conducting glasses," *Solid State Ionics*, vol. 113-115, pp. 665-675, 1998.
- [16] B. V. R. Chowdari, K. L. Tan, and L. Fang, "Synthesis and characterization of  $x\text{Cu}_2\text{O}\cdot y\text{TeO}_2\cdot(1-x-y)\text{MoO}_3$  glass system," *Solid State Ionics*, vol. 113-115, pp. 711-721, 1998.
- [17] B. V. R. Chowdari and P. Pramoda Kumari, "Effect of mixed glass-formers in  $\text{Ag}_2\text{O}\cdot\text{MoO}_3\cdot\text{TeO}_2$  system," *Journal of Physics and Chemistry of Solids*, vol. 58, pp. 515-525, 1997.
- [18] B. V. R. Chowdari and P. Pramoda Kumari, "Synthesis and characterization of silver borotellurite glasses," *Solid State Ionics*, vol. 86-88, pp. 521-526, 1996.
- [19] B. V. R. Chowdari and P. Pramoda Kumari, "Thermal, electrical and XPS studies of  $\text{Ag}_2\text{O}\cdot\text{TeO}_2\cdot\text{P}_2\text{O}_5$  glasses," *Journal of Non-Crystalline Solids*, vol. 197, pp. 31-40, 1996.
- [20] B. V. R. Chowdari, K. L. Tan, and L. Fang, "Synthesis and characterisation of  $\text{CuI}\cdot\text{Cu}_2\text{O}\cdot\text{TeO}_2\cdot\text{MO}_3$  ( $\text{M}=\text{Mo}$  or  $\text{W}$ ) glass systems," *Solid State Ionics*, vol. 136-137, pp. 1101-1109, 2000.
- [21] V. Kozhukharov, H. Burger, S. Neov, and B. Sidzhimov, "Atomic arrangement of a zinc-tellurite glass," *Polyhedron*, vol. 5, pp. 771-777, 1986.
- [22] N. N. Greenwood and A. Earnshaw, *Chemistry of the elements*. Oxford: Butterworth-Heinemann, 1995.
- [23] W. Vogel, *Glass chemistry*, 2nd ed. New York: Springer-Verlag, 1994.
- [24] S. Sakida, S. Hayakawa, and T. Yoko, "Part 1. Te-125 NMR study of tellurite crystals," *Journal of Non-Crystalline Solids*, vol. 243, pp. 1-12, 1999.
- [25] K. W. Bagnall, *The chemistry of selenium, tellurium and polonium*. London: Elsevier, 1966.
- [26] R. H. Doremus, "Ion exchange in glasses," in *Ion exchange - a series of advances*, vol. 2, J. A. Marinsky, Ed. New York: Marcel Dekker, 1969, pp. 1-42.
- [27] R. V. Ramaswamy and R. Srivastava, "Ion-exchanged glass wave-guides - a review," *Journal of Lightwave Technology*, vol. 6, pp. 984-1002, 1988.
- [28] Y. Ding, S. Jiang, T. Luo, Y. Hu, and N. Peyghambarian, "Optical waveguides prepared in  $\text{Er}^{3+}$ -doped tellurite glass by  $\text{Ag}^+\text{-Na}^+$  ion-exchange," *Proceedings of SPIE*, vol. 4282, pp. 23-30, 2001.

## 8. Fibre drawing

The properties most significant to fibre drawing (glass viscosity and the stress in a core / clad fibre) are reported here. The fibre drawing parameters are shown for preforms fibreised. The defects present in, and optical loss of pulled fibres will then be discussed. Recommendations for the possibility of reducing the optical loss in fluorotellurite fibre further in future work will then be given.

### 8.1. Experimental

#### 8.1.1. Thermal mechanical analysis (TMA)

A Perkin Elmer TMA7 was used to obtain viscosity and thermal expansion data in this study, using the parallel plate viscometry method [1]. This method was validated with a standard sample (National Bureau of Standards sample no. 710) over the  $10^5$  to  $10^{7.5}$  Pa.s viscosity range (the region close to the glass transition temperature,  $T_g$ , and the fibre drawing temperature,  $T_\eta$ ). The instrument consisted of a sample chamber, inside a furnace, with an articulated silica pushrod. The sample dimensions were a disc of diameter 5 mm, and thickness ( $h$ ) 2 to 3 mm. A stainless steel foot was attached to the pushrod, and the sample was placed on a stainless steel base in the sample chamber. A force of 250 mN was applied to the pushrod, which was calibrated using electronic scales. This force, and the force of the steel foot were recorded, giving the total force,  $F$ ,

applied to the sample. The sample was then heated at  $10^{\circ}\text{C}\cdot\text{min}^{-1}$  under a helium atmosphere to above its softening temperature. The change in sample height ( $h_s$ ), with time ( $t$ ), was recorded, and the viscosity in Pa.s,  $\eta$ , calculated using equation (8.1).

$$\eta = \frac{2\pi F h_s^5}{3V \frac{dh_s}{dt} (2\pi h_s^3 + V)} \quad (8.1)$$

where  $V$  = sample volume. The viscosity data obtained was modelled using a number of equations, shown in table (8.1), where parameters  $A$ ,  $B$ , and  $C$  are materials constants, and  $T$  is temperature. The meaning of  $T_0$  depends on the equation used, and will be discussed later.

Table (8.1): Viscosity models used in this study, where parameters  $A$ ,  $B$ ,  $C$  and  $T_0$  are materials constants, and  $T$  is temperature.

Model	Equation	Reference
Arrhenius	$\log \eta = A + B \cdot \frac{1}{T}$	[2]
Vogel-Fulcher-Tamman	$\log \eta = A + \frac{B}{T - T_0}$	[3]
Cohen-Grest	$\log \eta = A + \frac{2 \cdot B}{\left\{ (T - T_0) + \left[ (T - T_0)^2 + 4 \cdot C \cdot T \right]^{0.5} \right\}}$	[4]
Macedo-Litovitz	$\log \eta = A + \frac{B}{T} + \frac{C}{T - T_0}$	[5]

The data obtained was fitted to these models using least squares analysis, followed by the iterative Solver function in Microsoft Excel, and parameters  $A$ ,  $B$ ,  $C$  and  $T_0$  were then obtained. Initial values were used from the study by Braglia *et al.* [6].

### 8.1.2. Preform manufacture

Unstructured preforms (no cladding layer) were manufactured by casting around 30 g of glass into the cylindrical brass (CB) mould described and pictured in section (3.3). Early oxide structured preforms (core / clad) were manufactured using rotational casting [7] equipment shown in fig. (8.1), however fibre drawing of these preforms was not successful due to severe surface hydrolysis.

The glass preform was manufactured by the process shown in fig. (8.1a). The crucible of molten core glass was put in either one of the crucible holder and the cladding glass in the other, and the chamber evacuated (no additional heating is provided by the rotational casting equipment). The preheated mould ( $\approx 250^\circ\text{C}$ ) was placed into the holder, and the core glass was poured into the mould (1), which was then rotated horizontally and spun at 1000 rpm for 10 seconds (2) by which time it had cooled to around the mould temperature ( $\approx T_g$ ) and solidified into a tube of homogeneous thickness. The mould was then rotated to its original vertical position and the cladding glass poured in (3). This preform was then annealed for an hour at around  $T_g - 10^\circ\text{C}$  and left to cool slowly to room temperature. Fibres which result from preforms manufactured by this method potentially have lower loss compared to fibre from preforms manufactured by the rod-in-

tube method, due to a potentially superior core-cladding boundary. Table (8.2) shows the parameters associated with the unstructured preforms made in this study.

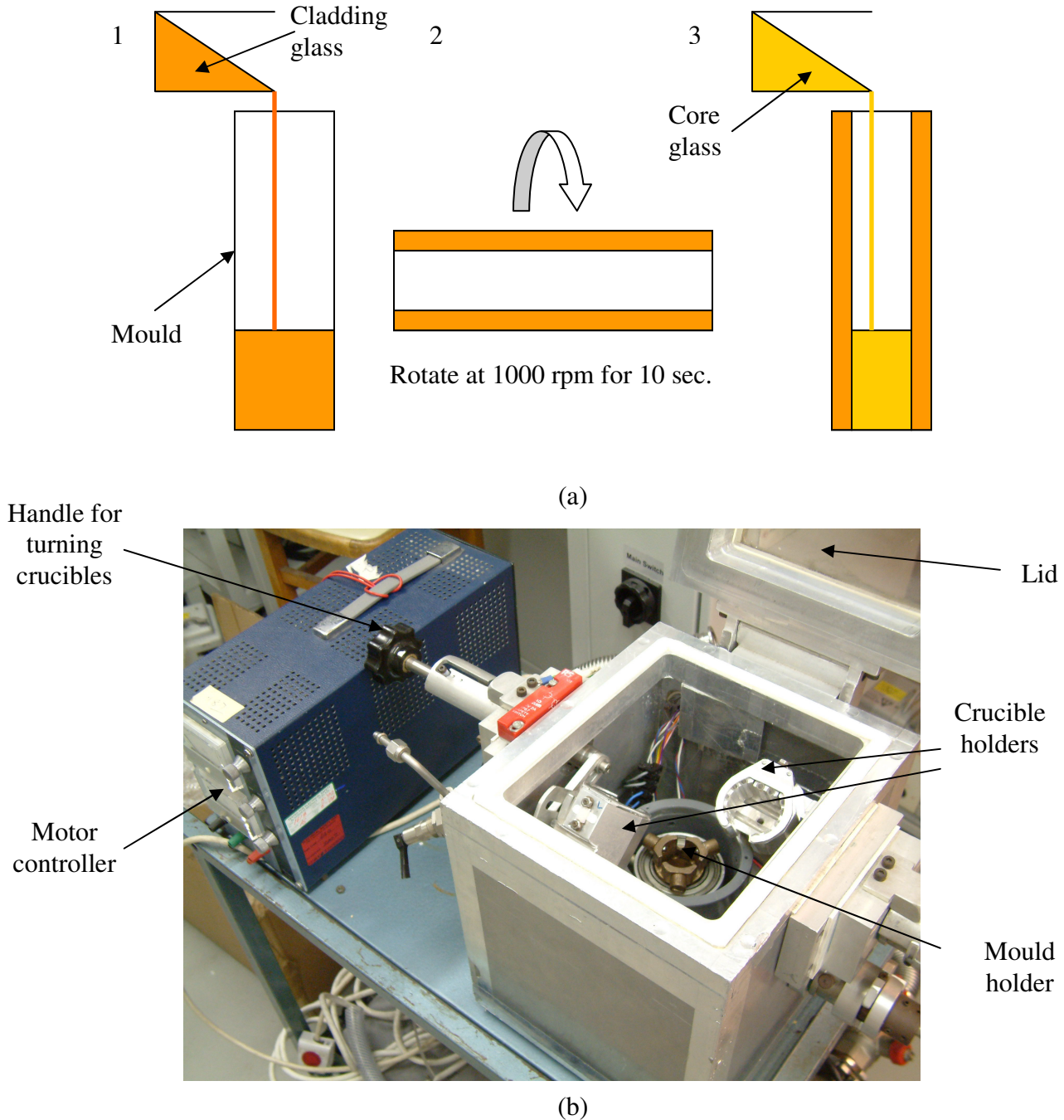


Fig. (8.1): (a) Schematic illustration of rotational casting process; (b) photograph of rotational casting equipment.

Table (8.2): Parameters relating to unstructured tellurite and fluorotellurite preform manufacture: preform ID, composition, melting time and temperature, crucible and mould (CB = cylindrical brass, CA = cylindrical aluminium) used, and comments on preform / fibre quality relating to melting / casting process, all made from 30 g batches, of 1 cm diameter.

Preform ID	Composition / mol. %	T / °C	t / hr.	Crucible	Mould	Comments
MOD010_i	75TeO <sub>2</sub> -10Na <sub>2</sub> O-10ZnO-5PbO	800	2.0	Pt	CB	Contained small bubbles, and after drawing, fibre poor surface
MOF004_iv	60TeO <sub>2</sub> -10Na <sub>2</sub> O-30ZnF <sub>2</sub>	800 670	1.5 1.5	"	"	Surface frosted, poor fibre when drawn with N <sub>2</sub> atmosphere
MOF005_ii	70TeO <sub>2</sub> -10Na <sub>2</sub> O-20ZnF <sub>2</sub>	800 670	1.0 1.0	"	"	Good glass, homogeneous, and no bubbles, however fibre drawing not steady or dimensionally consistent, producing weak fibre
MOF005_iii	"	800 670	1.0 1.0	"	"	
MOF005_iv	"	800 670	1.5 1.5	"	"	
MOF005_v	"	800 670	2.0 2.0	Au	"	
MOF005_vi	"	800 <sup>1</sup> 670	2.5 2.5	"	"	Good glass, resulting in strong pristine fibre
MOF005_vii	"	800 <sup>1</sup> 670	5.0 5.0	"	"	Some striations, but produced good fibre and drew steadily
MOF005_viii	"	800 <sup>1</sup> 670	6.0 6.0	"	"	Good glass, resulting in strong pristine fibre
MOF005_ix <sub>2</sub>	"	800 <sup>1</sup>	12.0	"	CA	Discoloured surface
MOF005_x <sup>2</sup>	"	800 <sup>1</sup>	12.0	"	"	

It can be seen that the use of Au crucibles resulted in good quality fibre, however the melting atmosphere was also altered for preforms MOF005\_iv to MOF005\_x (see table (8.3) in the next section for further details), and also had a significant effect on the control of fibre drawing. Using an aluminium mould in a nitrogen rich glovebox atmosphere caused preform surface discolouration, most likely due to the reduction of the

<sup>1</sup> Used fluorinated ZnF<sub>2</sub>

<sup>2</sup> Melted in glovebox with 2:1 ratio dry N<sub>2</sub>:O<sub>2</sub>

glass surface when it came into contact with the aluminium (e.g.  $1\frac{1}{2}\text{TeO}_2 + 2\text{Al}^{+3} \rightarrow \text{Al}_2\text{O}_3 + 1\frac{1}{2}\text{Te}^{+4}$ ) at temperatures around its melting point (660°C [8]). Aluminium is only protected by an  $\text{Al}_2\text{O}_3$  layer of the order of nm, and the oxyfluoride melt would be relatively reactive, on casting in the 670 to 800°C region.

### 8.1.3. Fibre drawing

Fibre was pulled from glass preforms of 1 cm diameter using a Heathway Soft Glass Research Tower, in a class 10,000 cleanroom. Fig. (8.2) shows this fibre drawing tower. Glass preforms were lowered into the hot zone of the furnace, and held there until the glass softened and necked down. At this point the fibre was pulled manually onto the drum and attached with tape. The preform was then fed, and the drum rotated and traversed automatically pulling fibre until most of the preform had been used. Table (8.3) summarises the draw parameters used for preforms in this study.

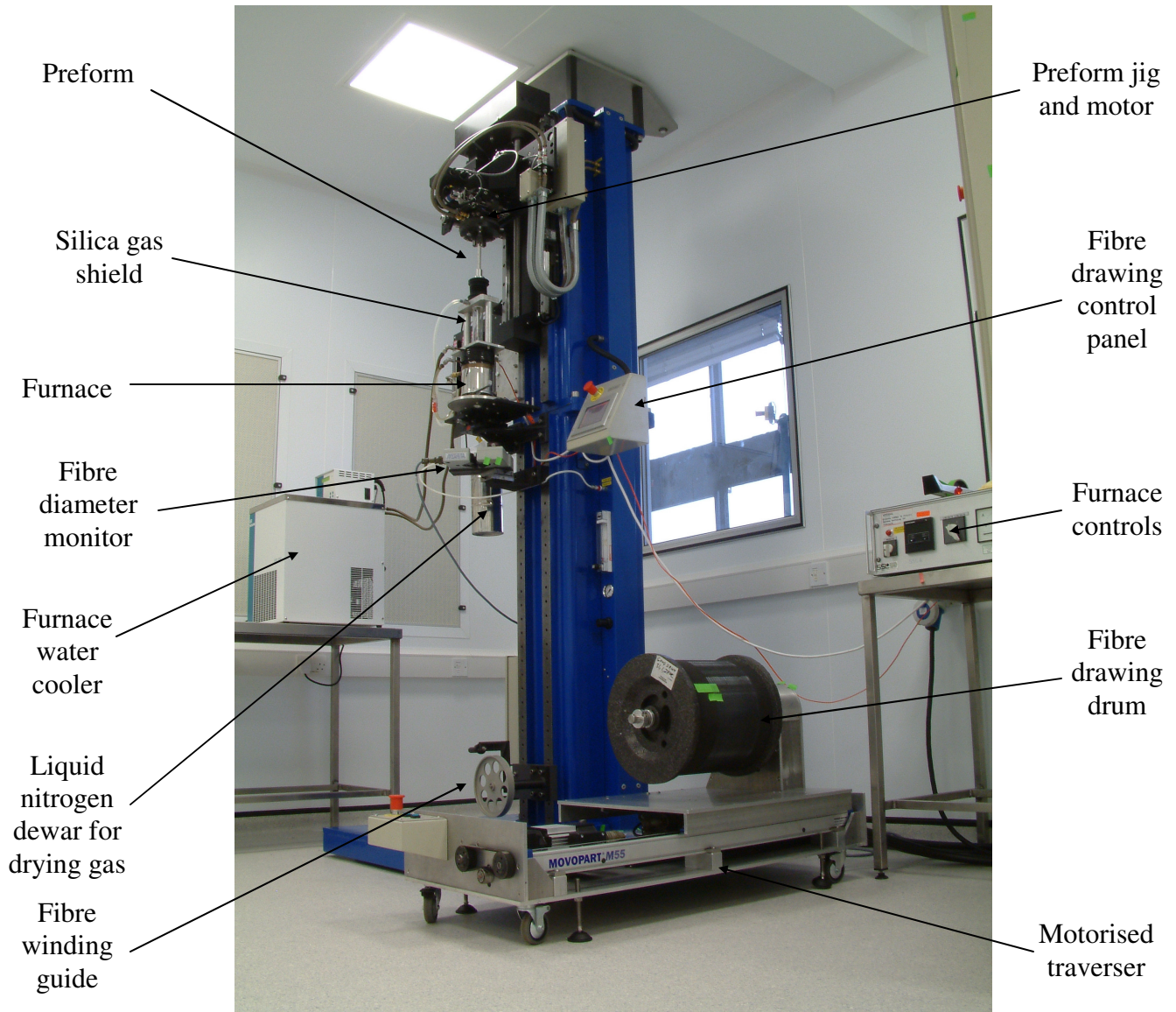


Fig. (8.2): Tower used for fibre drawing in this study.

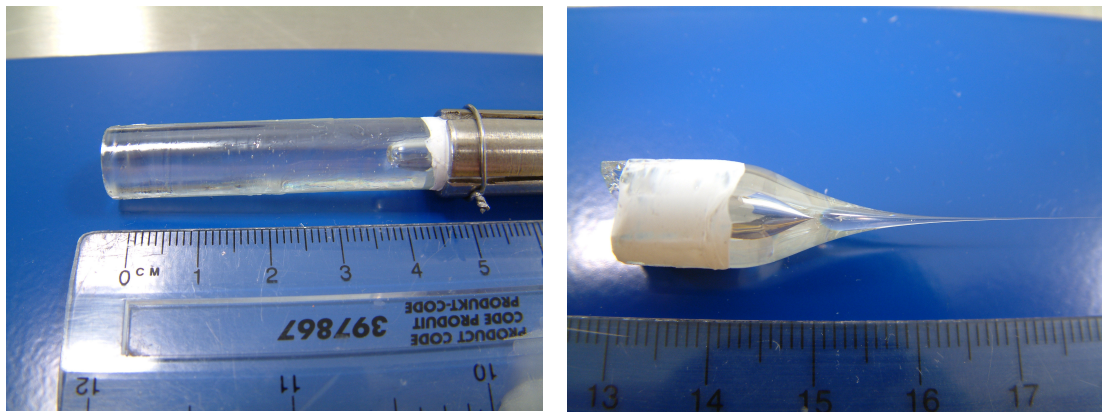
Table (8.3): Fibre drawing parameters for glasses melted in this study (all from cast unstructured preforms of diameter 10 mm),  $T_{nd}$  = neck down temperature,  $T_{ss}$  = steady state draw temperature, and  $d_f$  = fibre diameter.

Preform ID	Gas	Rate / ml / min.	$T_{nd}$ / °C	$T_{ss}$ / °C	$d_f$ / $\mu\text{m}$	Preform feed in / mm/min.	Draw speed / m/min.	Surface quality <sup>3</sup>	Crystals <sup>4</sup>	Comments
MOD010_i	Air	300	350	284	100 $\pm 50$	4	20	P	N	-
MOF004_iv	N <sub>2</sub>	50	285	285	150 $\pm 50$	"	"	"	Y	Better with air
MOF005_ii	N <sub>2</sub>	50	290	275	150 $\pm 50$	"	"	"	"	-
MOF005_iii	N <sub>2</sub>	50	290	280	150 $\pm 50$	"	"	"	"	-
MOF005_iv	Air	300	270	285	100	"	"	"	N	Passed gas mixture through a liquid nitrogen dewar to remove water
MOF005_v	Air / N <sub>2</sub>	15 / 30	295	290	85 $\pm 35$	"	"	G	"	
MOF005_vi	Air / N <sub>2</sub>	5 / 15	310	290	150 $\pm 5$	2	5-10	"	"	
MOF005_vii	Air / N <sub>2</sub>	15 / 30	315	305	150 $\pm 5$	"	"	"	"	
MOF005_viii	Air / N <sub>2</sub>	5 / 10	310	290-295	150 $\pm 10$	"	8	"	"	
MOF005_ix	Air / N <sub>2</sub>	5 / 10	300	277	180 $\pm 20$	"	6	"	"	
MOF005_x	Air / N <sub>2</sub>	5 / 5	305	276	160 $\pm 20$	"	5	"	"	

This table demonstrates that gas quality (i.e. amount of moisture) during drawing was significant for producing pristine, stronger fibres. The preforms were unstructured in this initial study which eliminated losses from core / cladding boundary imperfections, but losses may have been incurred at the glass / air interface. From table (8.2) and (8.3) it can be seen, for fluorotellurite preforms, using fluorinated ZnF<sub>2</sub>, melted in Au crucibles, cast in brass moulds, drawn with a dry air/N<sub>2</sub> atmosphere generally resulted in good quality fibre. Fig. (8.3) shows fluorotellurite optical fibre preforms (a) before, and (b) after fibre drawing.

<sup>3</sup> P = poor, G = good

<sup>4</sup> N = no, Y = yes



(a)

(b)

Fig. (8.3): Fluorotellurite glass preforms (a) before, and (b) after fibre drawing, with non-adhesive white tape to protect glass surface from damage from grip of metal clamp.

#### 8.1.4. Optical loss measurements – cut-back method

Fibre optical loss measurements were performed using, the FTIR set-up described in section 6.1.1, and the cut-back method. The loss over a length of fibre (typically 1 m) was measured. The fibre was then cut-back a number of times (e.g. in 20 cm segments) and the loss measured each time. A number of spectra were then obtained, and an average taken. A defect at one point in the fibre would result in high loss over a 1 m length. Therefore, if this section of the fibre was cut-back, the loss of the remaining defect free glass was measured. This method also can allow the characterisation of defects, in combination with microscopy. Light was brought out of the spectrometer from a tungsten lamp and focused into the fibre using a parabolic aluminium mirror. The InSb detector was cooled with liquid nitrogen.

## 8.2. Results

### 8.2.1. Viscosity (TMA)

Fig. (8.4) shows the viscosity / temperature behaviour of glasses MOF001 (65TeO<sub>2</sub>-10Na<sub>2</sub>O-25ZnF<sub>2</sub> mol. %) and MOF005 (70TeO<sub>2</sub>-10Na<sub>2</sub>O-20ZnF<sub>2</sub> mol. %) [9].

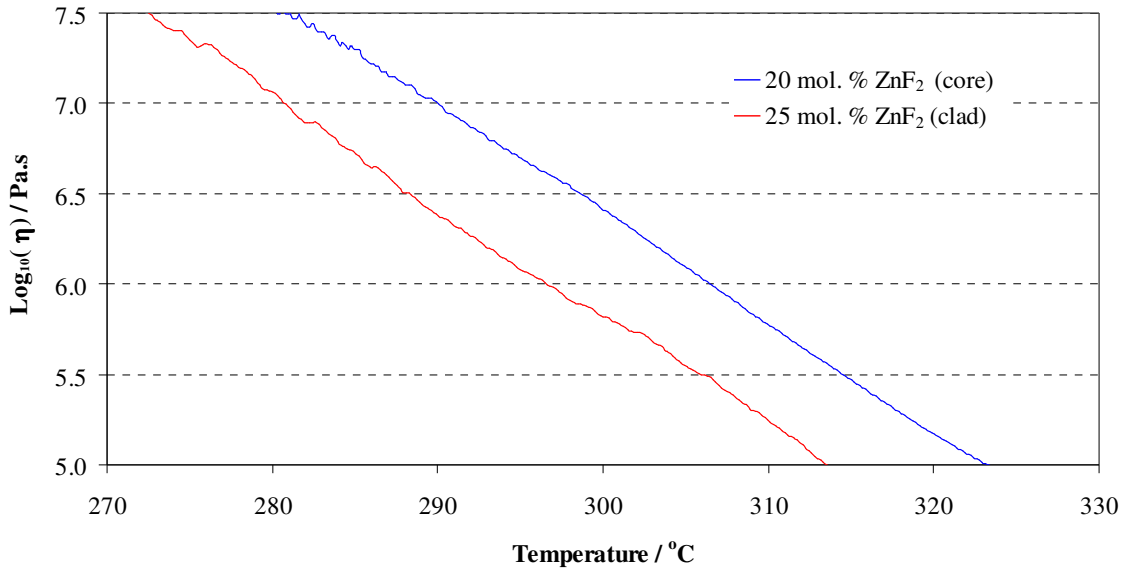


Fig. (8.4): Viscosity / temperature behaviour of glasses MOF001 (65TeO<sub>2</sub>-10Na<sub>2</sub>O-25ZnF<sub>2</sub> mol. %) and MOF005 ((70TeO<sub>2</sub>-10Na<sub>2</sub>O-20ZnF<sub>2</sub> mol. %) [9].

It can be seen the viscosity decreased for a given temperature with increasing batched ZnF<sub>2</sub> in the glass. Fig. (8.5) and (8.6) shows the modelling for these glasses. The dashed lines show  $T_g$  measured by DTA (see table (4.2)), and the fibre drawing viscosity ( $10^{4.5}$  Pa.s) [9].

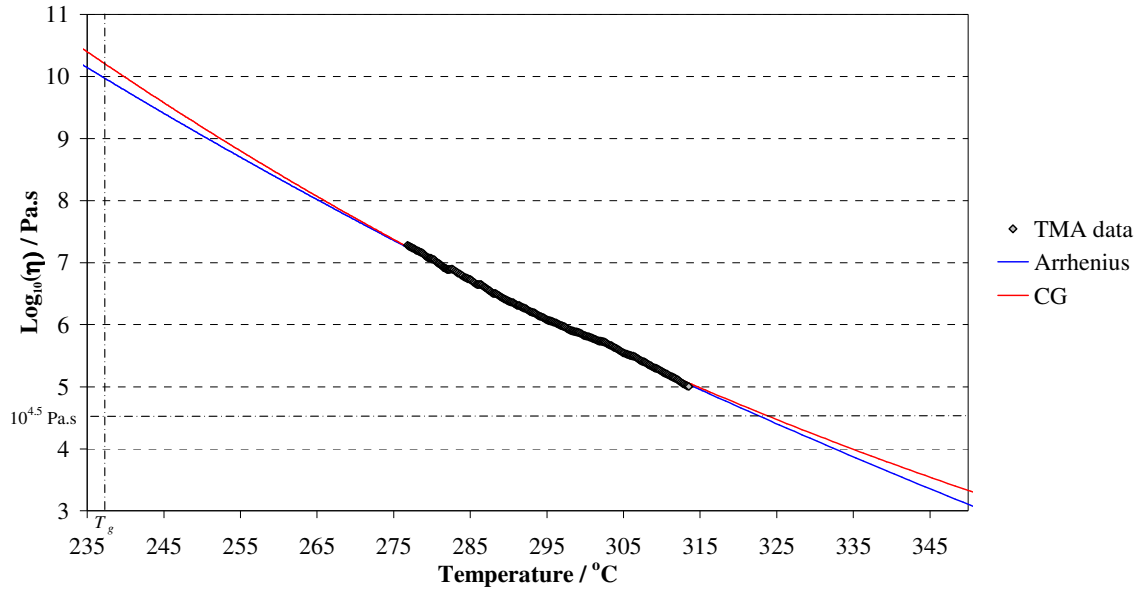


Fig. (8.5): Viscosity / temperature modelling for cladding glass MOF001 (65TeO<sub>2</sub>-10Na<sub>2</sub>O-25ZnF<sub>2</sub> mol. %) [9].

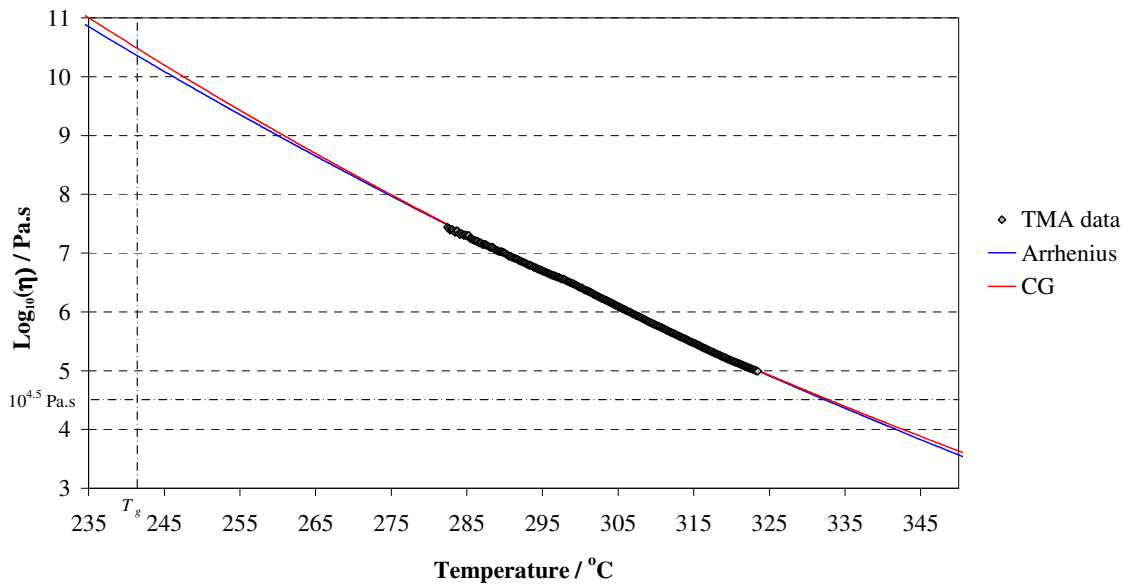


Fig. (8.6): Viscosity / temperature modelling for core glass MOF005 (70TeO<sub>2</sub>-10Na<sub>2</sub>O-20ZnF<sub>2</sub> mol. %) [9].

Table (8.4) summarises the parameters obtained from the models from table (8.1) for both glasses and predicted temperatures of fibre drawing from the models.

Table (8.4): Parameters of viscosity models for glasses MOF001 (65TeO<sub>2</sub>-10Na<sub>2</sub>O-25ZnF<sub>2</sub> mol. %) and MOF005 ((70TeO<sub>2</sub>-10Na<sub>2</sub>O-20ZnF<sub>2</sub> mol. %), and predicted fibre drawing temperatures ( $T_{\eta=5}$ ).

Glass	Model	A	B	C	$T_0 / ^\circ\text{K}$	$T_{\eta=5} / ^\circ\text{C}$
MOF001 clad (25 mol. % ZnF <sub>2</sub> )	Arrhenius	-27.98	$1.94 \times 10^4$	-	-	324
	VFT	-7.39	$3.06 \times 10^3$	-	341.28	
	CG	-4.32	737.22	18.68	647.41	
	ML	-7.98	902.96	$2.75 \times 10^3$	347.64	
MOF005 core (20 mol. % ZnF <sub>2</sub> )	Arrhenius	-28.61	$2.00 \times 10^4$	-	-	333
	VFT	-29.94	$2.16 \times 10^4$	-	-22.04	
	CG	-6.73	753.71	25.05	764.87	
	ML	-36.73	$3.52 \times 10^3$	$2.72 \times 10^4$	-162.67	

The VFT and ML models were not used to predict fibre drawing viscosities, as they generated nonsensical parameters for the core glass, such as negative Kelvin values for  $T_0$ .

### 8.2.3. Crystals in drawn fibre

The ESEM (environmental scanning electron microscopy) and EDX (energy dispersive X-ray) analysis techniques are described in section 7.1.3.1. Fibre of composition MOF005ii (70TeO<sub>2</sub>-10Na<sub>2</sub>O-20ZnF<sub>2</sub> mol. %), which crystallised on drawing is reported here (i.e. all ESEM micrographs shown were taken from one drum of fibre), and EDX results of fibre MOF005ii (70TeO<sub>2</sub>-10Na<sub>2</sub>O-20ZnF<sub>2</sub> mol. %) are also tabulated.

Fig. (8.7) shows an ESEM micrograph of triangular shaped crystals near the surface in unstructured glass fibre of composition MOF005ii (70TeO<sub>2</sub>-10Na<sub>2</sub>O-20ZnF<sub>2</sub> mol. %), diameter around 200  $\mu\text{m}$ . The fibre was mounted length-ways in epoxy resin, and cross-

sectioned by grinding and polishing (see section 6.1.1.1). The glass was pulled into fibre at around 310°C, under a nitrogen atmosphere (see table (8.2) and (8.3)).

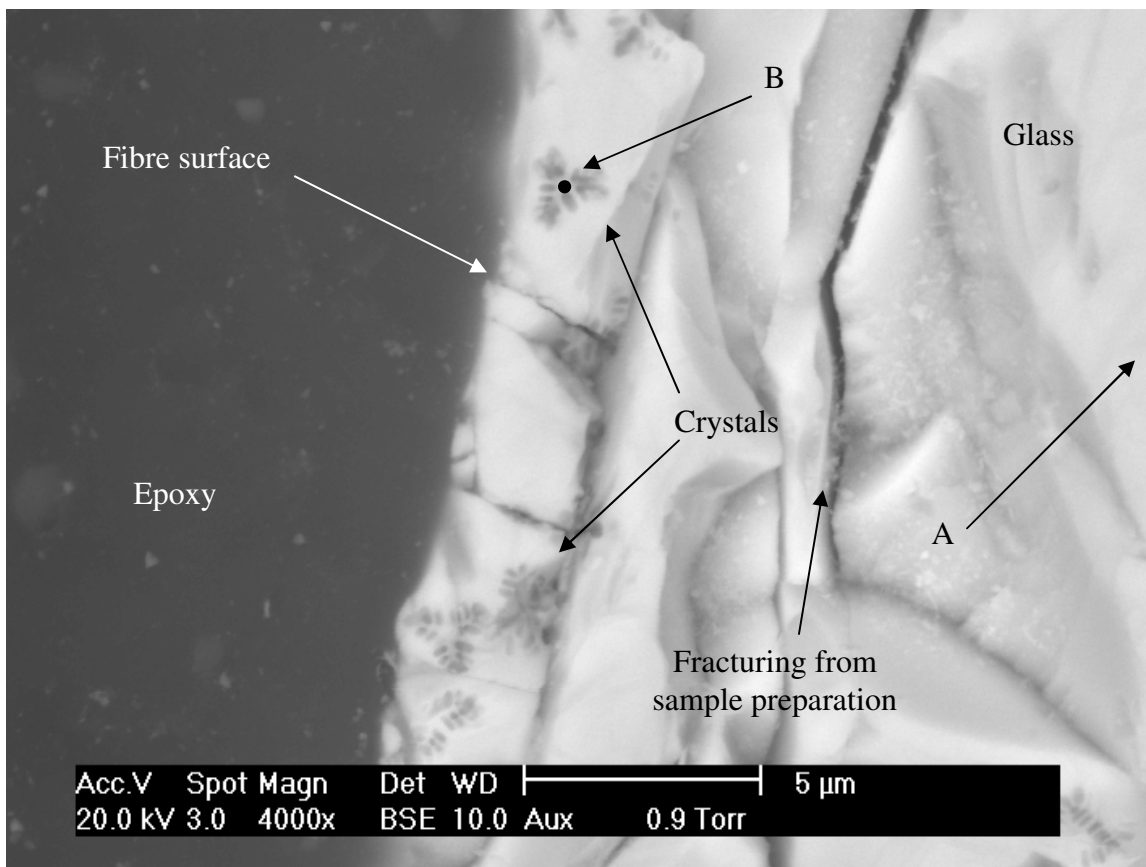


Fig. (8.7): ESEM micrograph of triangular shaped crystals near the surface in the glass fibre of composition MOF005ii (70TeO<sub>2</sub>-10Na<sub>2</sub>O-20ZnF<sub>2</sub> mol. %), mounted length-ways in epoxy resin, and cross-sectioned.

EDX analysis was performed at points A (glass) and B (crystal) and is tabulated later in this section (table (8.5)). The carbon peaks, assumed due to the presence of epoxy, were ignored when performing quantitative elemental analysis.

Fig. (8.8) shows an ESEM micrograph of a dendritic snowflake shaped crystal in the glass fibre of composition MOF005ii (70TeO<sub>2</sub>-10Na<sub>2</sub>O-20ZnF<sub>2</sub> mol. %), around 50 µm away from the surface. The fibre was mounted length-ways in epoxy resin, and cross-sectioned.

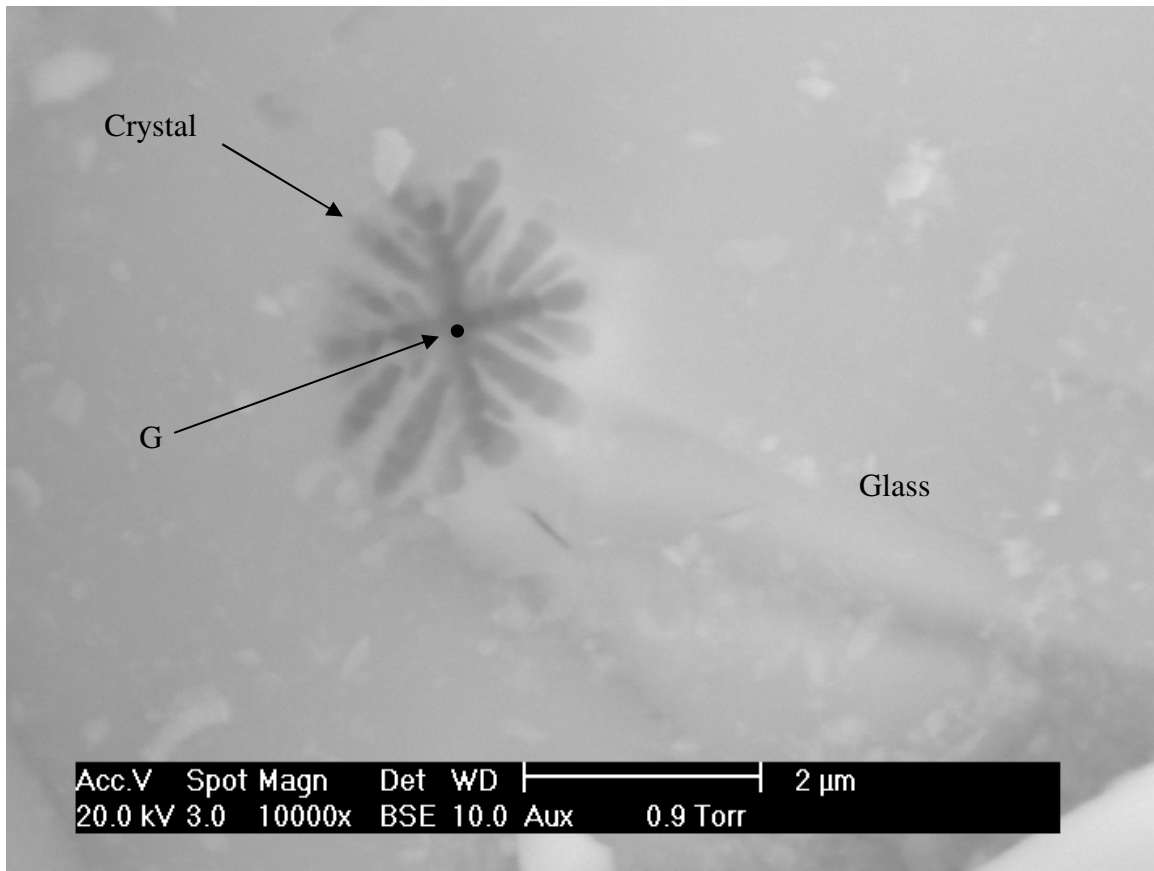


Fig. (8.8): ESEM micrograph of a snowflake shaped crystal in the glass fibre of composition MOF005ii ( $70\text{TeO}_2\text{-}10\text{Na}_2\text{O-}20\text{ZnF}_2$  mol. %), mounted length-ways in epoxy resin, and cross-sectioned.

EDX analysis was performed at point G (crystal) on fig. (8.8) (see table (8.5)).

Fig. (8.9) shows an ESEM micrograph of crystals in 10  $\mu\text{m}$  region near the surface in glass fibre of composition MOF005ii ( $70\text{TeO}_2\text{-}10\text{Na}_2\text{O-}20\text{ZnF}_2$  mol. %). The fibre was mounted length-ways in epoxy resin, and cross-sectioned.

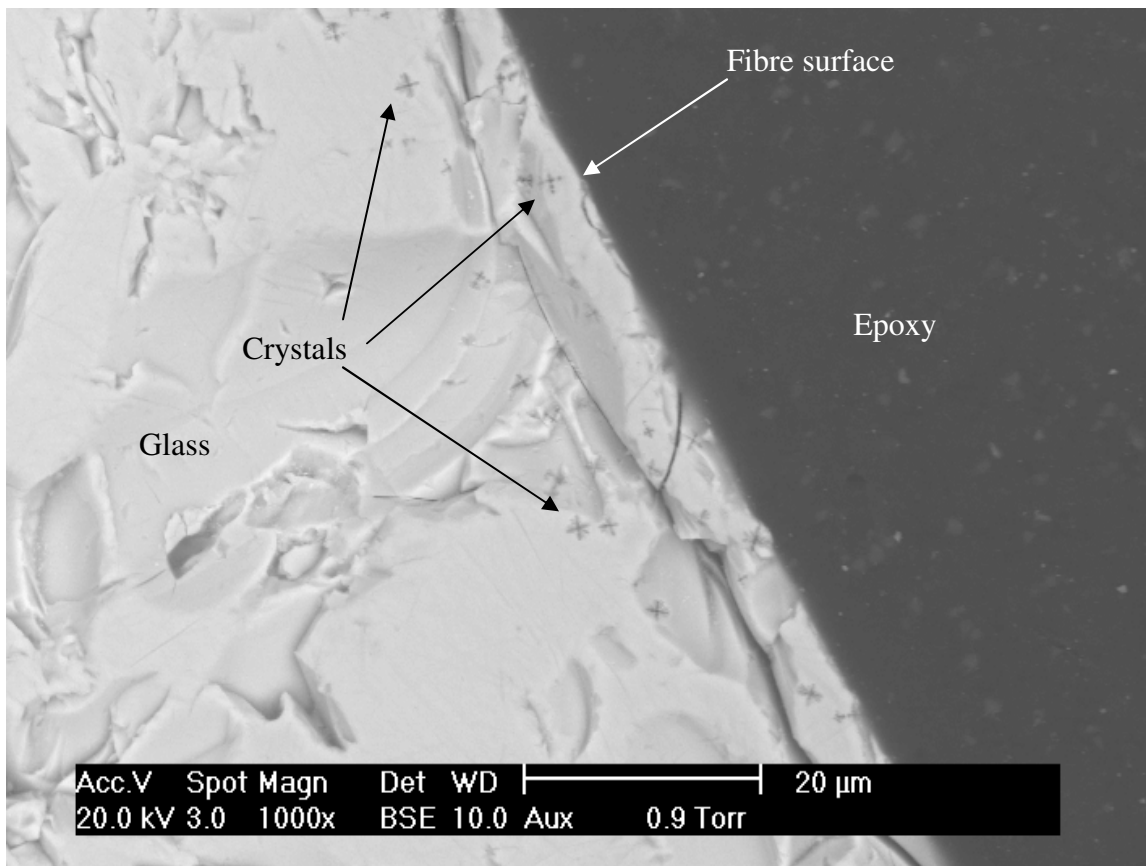


Fig. (8.9): ESEM micrograph of crystals near the surface in glass fibre of composition MOF005ii (70TeO<sub>2</sub>-10Na<sub>2</sub>O-20ZnF<sub>2</sub> mol. %), mounted length-ways in epoxy resin, and cross-sectioned.

It can be seen from this figure that most of the crystals were 10-20 µm from the fibre surface, and around 2 µm in diameter. There appears to have been three types of crystals present in the glass: (i) triangular, (ii) snowflake, and (iii) cross (can be more clearly seen in later figures). These could have been different crystalline phases, or the same, but different morphologies have arisen by artifact, thus after polishing, and this can give a false idea of orientation of the crystals in the glass.

Fig. (8.10) shows an ESEM micrograph of the surface of the glass fibre of composition MOF005ii (70TeO<sub>2</sub>-10Na<sub>2</sub>O-20ZnF<sub>2</sub> mol. %). The fibre was mounted on a carbon tab.

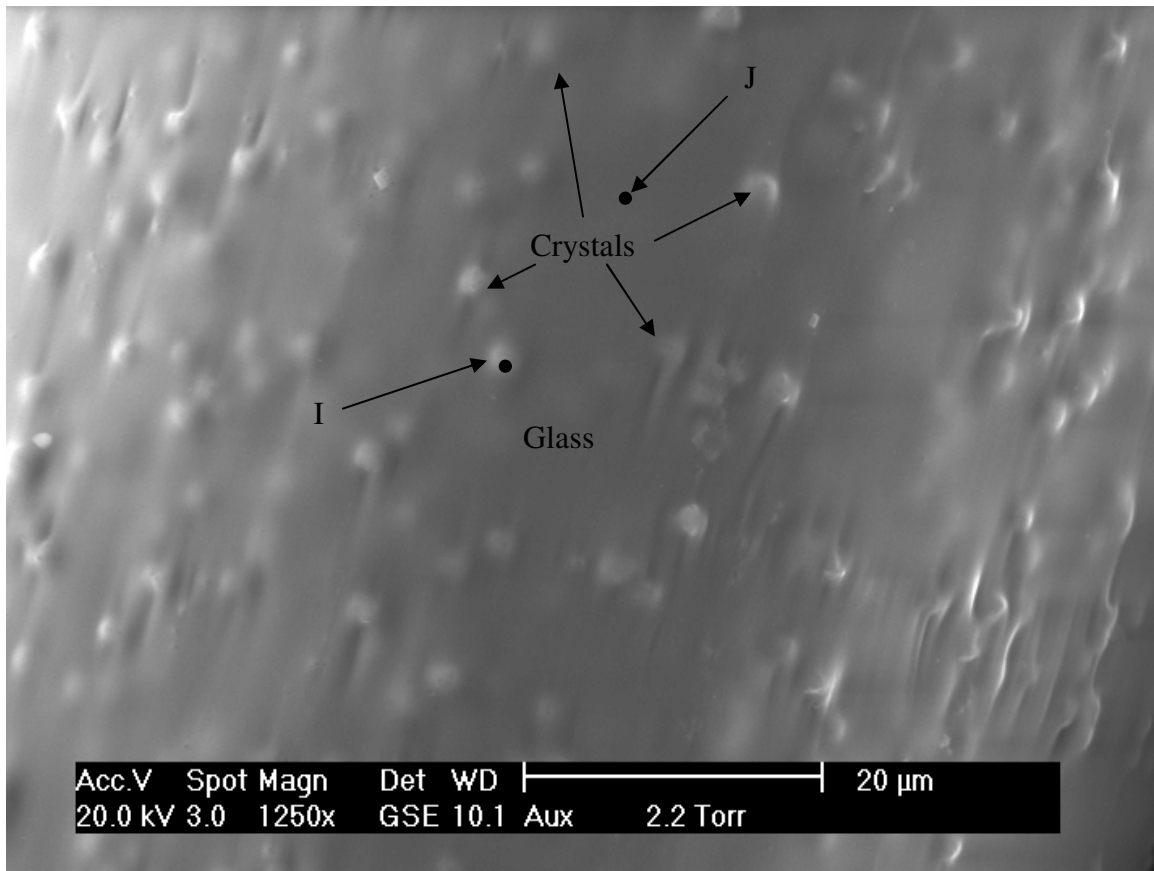


Fig. (8.10): ESEM micrograph of the surface of glass fibre of composition MOF005ii ( $70\text{TeO}_2\text{-}10\text{Na}_2\text{O-}20\text{ZnF}_2$  mol. %), mounted on a carbon tab.

It is tentatively concluded from observing the surface structure that the undercooled glass melt has crystallised at, or near the surface, and the melt has subsequently flowed around the crystals. EDX analysis was performed at point I (crystal) and J (glass) on fig. (8.10).

Fig. (8.11) shows an ESEM micrograph of the surface of the glass fibre of composition MOF005ii ( $70\text{TeO}_2\text{-}10\text{Na}_2\text{O-}20\text{ZnF}_2$  mol. %). The fibre was mounted on a carbon tab.

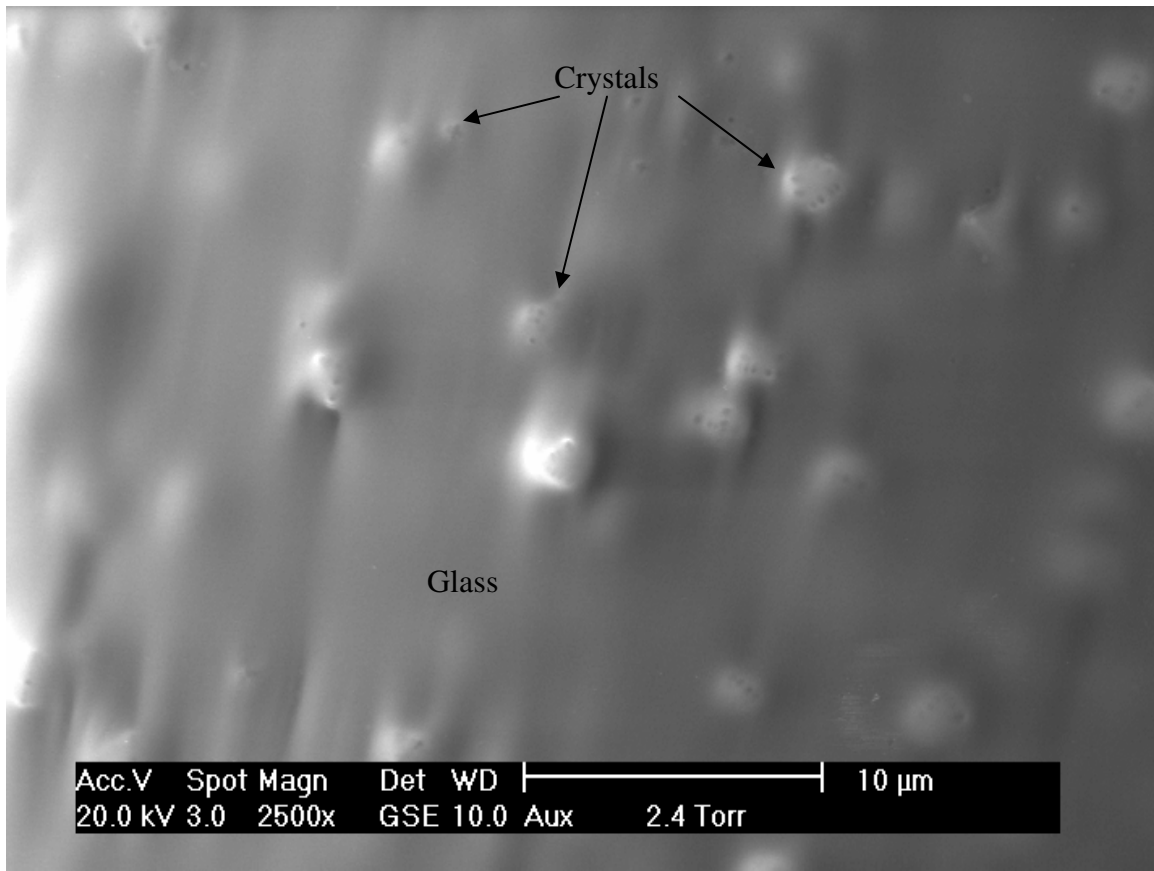


Fig. (8.11): ESEM micrograph of the surface of glass fibre of composition MOF005ii (70TeO<sub>2</sub>-10Na<sub>2</sub>O-20ZnF<sub>2</sub> mol. %), mounted on a carbon tab.

These crystals, which are nodular when imaged on the surface of the fibre, are of the same order of magnitude ( $\approx 2 \mu\text{m}$ ) as the crystals seen in cross-section (figs. (8.7) to (8.10)).

Fig. (8.12) shows an ESEM micrograph of a snowflake shaped crystal away from the surface in the glass fibre of composition MOF005ii (70TeO<sub>2</sub>-10Na<sub>2</sub>O-20ZnF<sub>2</sub> mol. %). The fibre was mounted end on in epoxy resin, and polished back.

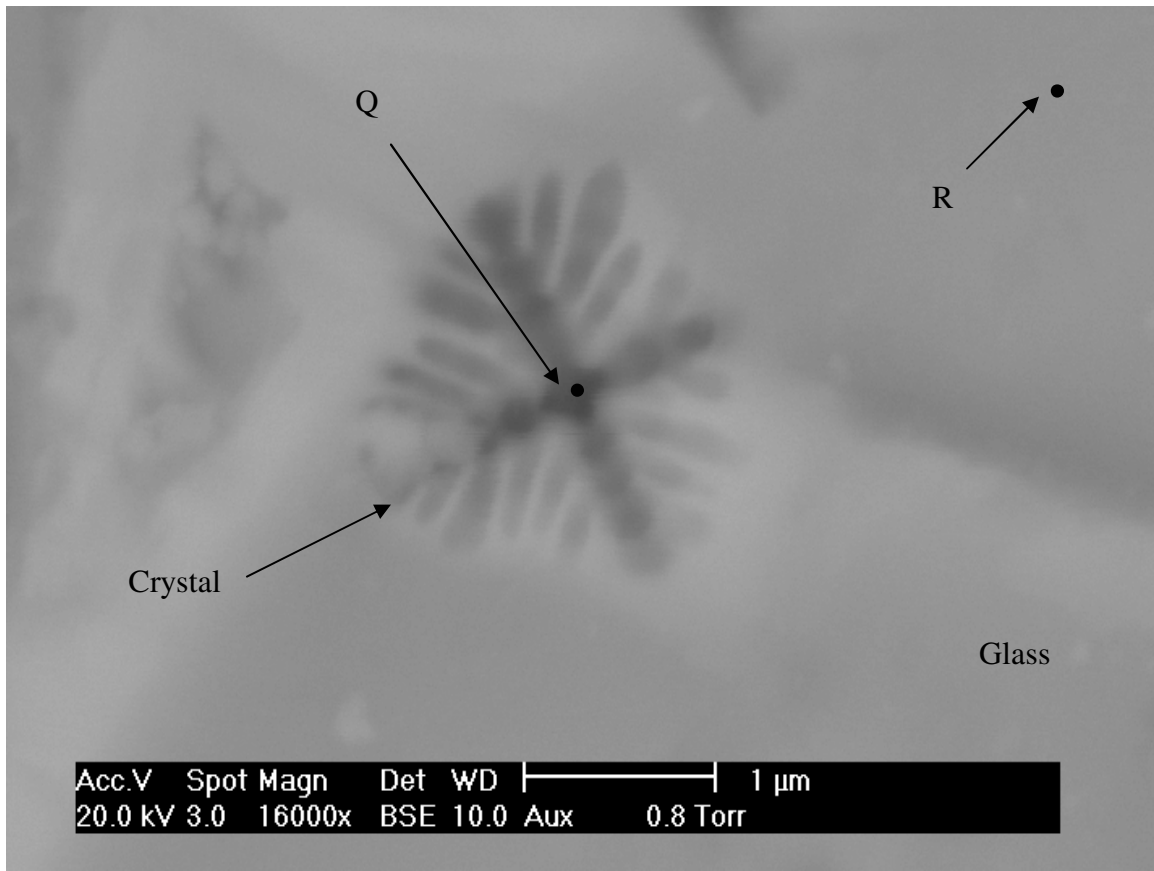


Fig. (8.12): ESEM micrograph of a snowflake shaped crystal in the glass fibre of composition MOF005ii ( $70\text{TeO}_2$ - $10\text{Na}_2\text{O}$ - $20\text{ZnF}_2$  mol. %), mounted end on in epoxy resin, and polished back.

EDX analysis was performed at point Q (crystal) and R (glass) on fig. (8.12). Fig. (8.13) shows the EDX spectra from points Q and R.

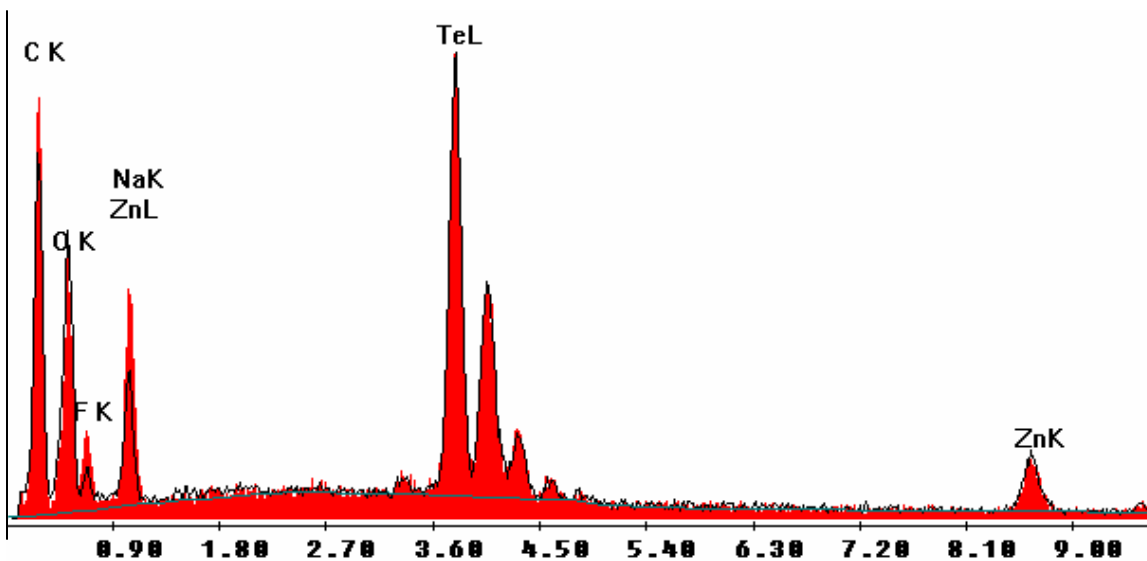


Fig. (8.13): EDX spectra from points Q (— crystal) and R (— glass) from fig. (8.12).

It can be seen from these EDX spectra (fig. (8.13)) that the crystal contains less oxygen and tellurium, and more fluorine and sodium than the glass. The amount of zinc is approximately the same in both the crystal and the glass. The EDX technique will sample an area similar to the diameter of the beam (10  $\mu\text{m}$ ). The crystal in fig. (8.12) is around 2  $\mu\text{m}$  in diameter, therefore, inevitably some glass will also have been sampled. The quantification from EDX in cases such as this therefore can only be used to obtain relative amounts of elements present, i.e. the crystalline phase is fluorine and sodium rich, and oxygen and tellurium deficient, compared to the glass.

Fig. (8.14) shows an ESEM micrograph of four crystals in the glass fibre of composition MOF005ii (70TeO<sub>2</sub>-10Na<sub>2</sub>O-20ZnF<sub>2</sub> mol. %). The fibre was mounted end-on in epoxy resin, and polished back.

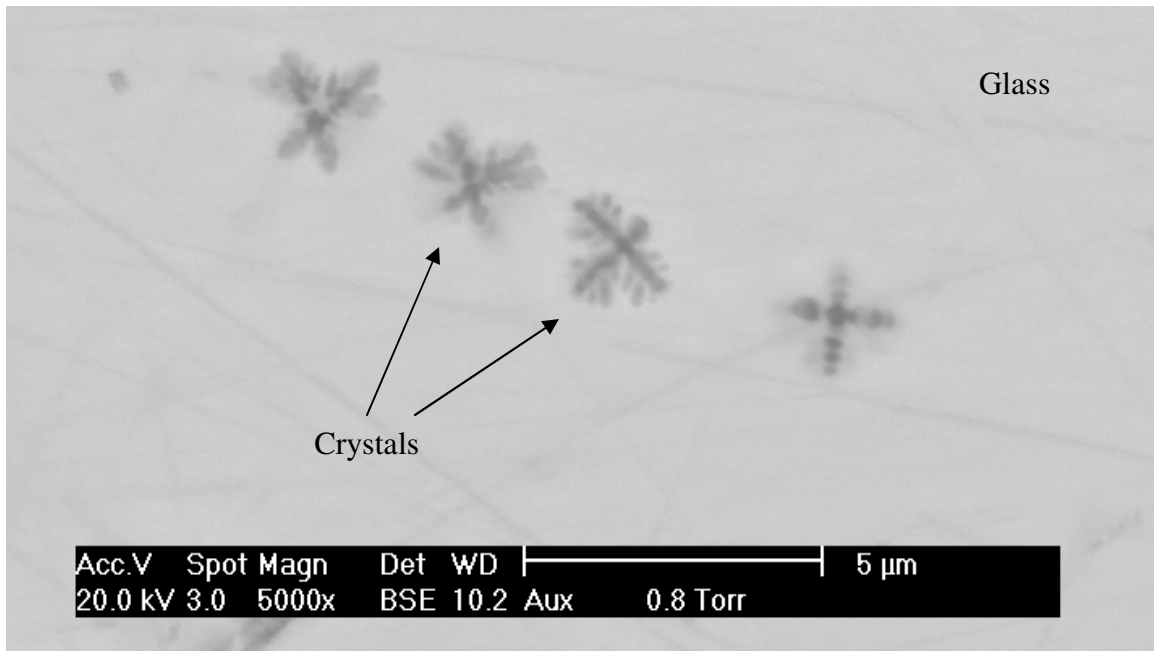


Fig. (8.14): ESEM micrograph of four crystals in glass fibre of composition MOF005ii ( $70\text{TeO}_2$ - $10\text{Na}_2\text{O}$ - $20\text{ZnF}_2$  mol. %), mounted end-on in epoxy resin, and polished back.

Fig. (8.15) shows an ESEM micrograph of crystals near the surface in the glass fibre of composition MOF005ii ( $70\text{TeO}_2$ - $10\text{Na}_2\text{O}$ - $20\text{ZnF}_2$  mol. %). The fibre was mounted end-on in epoxy resin, and polished back.

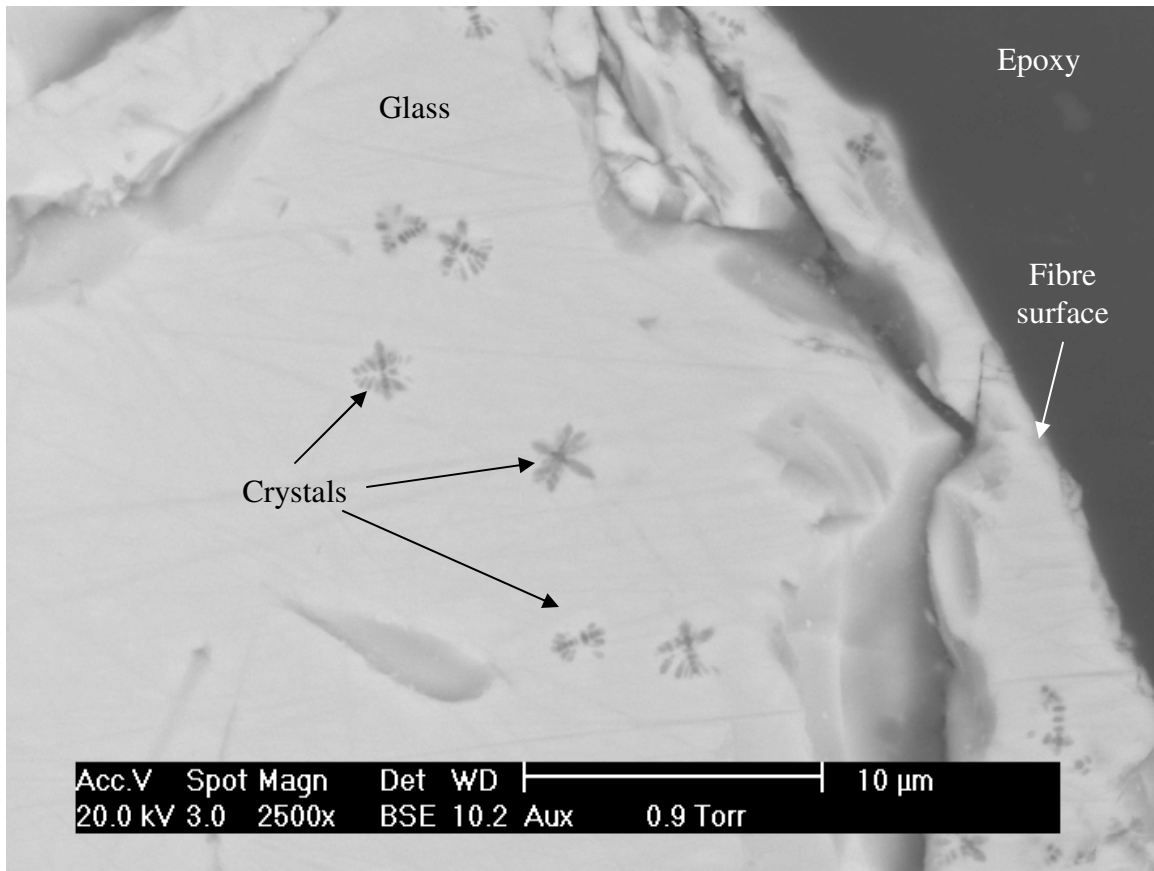


Fig. (8.15): ESEM micrograph of crystals near surface in glass fibre of composition MOF005ii ( $70\text{TeO}_2\text{-}10\text{Na}_2\text{O-}20\text{ZnF}_2$  mol. %), mounted end-on in epoxy resin, and polished back.

Table (8.5) summarises the EDX analysis from samples of composition MOF005ii and iii ( $70\text{TeO}_2\text{-}10\text{Na}_2\text{O-}20\text{ZnF}_2$  mol. %).

Table (8.5): EDX analysis of fibre drawing samples of composition MOF005 (70TeO<sub>2</sub>-10Na<sub>2</sub>O-20ZnF<sub>2</sub> mol. %).

EDX spectra <sup>5</sup>	Comments	Atomic %				
		O	F	Na	Te	Zn
<i>MOF005ii: fibre mounted in epoxy length ways and cross-sectioned:</i>						
A	Bulk glass $\approx$ 10 $\mu$ m from fibre edge	44.02	10.26	4.74	27.81	13.17
B	Triangular crystal $\approx$ 1 $\mu$ m from fibre surface	30.03	22.01	20.37	18.63	8.96
C	Triangular crystal	34.39	10.88	16.20	25.48	13.05
D	Edge of snowflake crystal	34.70	12.55	11.54	27.58	13.63
E	Cross crystal $\approx$ 1 $\mu$ m from fibre surface	26.21	22.92	24.78	17.17	8.91
F	Cross crystal	20.89	28.12	26.47	16.81	7.72
G	Centre of snowflake crystal	26.00	20.46	23.48	20.15	9.92
H <sup>6</sup>	Light particle on surface at centre of fibre	45.56	9.64	3.55	26.91	13.07
<i>MOF005ii: fibre surface mounted on a carbon tab:</i>						
I	Light crystal protruding from fibre surface	38.15	13.36	13.25	24.33	10.91
J	Dark bulk glass on fibre surface	39.02	9.62	10.54	27.58	13.24
K	Light crystal protruding from fibre surface	36.39	11.02	10.98	28.53	13.08
L	Light crystal protruding from fibre surface	28.95	18.10	24.18	19.34	9.44
M	Light crystal protruding from fibre surface	35.48	11.29	13.61	27.08	12.54
<i>MOF005ii: fibre mounted end on in epoxy, and polished back:</i>						
N	Bulk glass at centre of fibre	43.31	11.39	6.03	26.30	12.98
O	Centre of snowflake crystal	25.99	21.26	23.63	19.48	9.64
P	Edge of triangular crystal	28.66	19.52	22.77	19.44	9.61
Q	Centre of snowflake crystal	24.08	21.93	22.96	20.75	10.28
R	Bulk glass at centre of fibre	43.22	9.77	9.65	25.33	12.02
<i>MOF005iii: neck down piece of glass mounted in epoxy and cross-sectioned</i>						
S	Bulk glass	43.06	14.63	2.25	27.27	12.79
T	Cross crystal	36.10	17.26	7.81	26.77	12.06
U	Bulk glass at centre of fibre	41.96	17.45	4.91	24.17	11.51
V	Cross crystal	35.84	15.11	7.57	28.24	13.24
W	Bulk glass	42.46	16.54	3.44	25.50	12.06
X	Bulk glass	42.22	15.86	3.40	25.87	12.65
Y	Cross crystal	31.79	18.00	12.10	25.53	12.57

<sup>5</sup> Batched glass: 47.62 at. % O, 15.87 at. % F, 6.35 at. % Na, 22.22 at. % Te, and 7.94 at. % Zn.<sup>6</sup> 1.28 at. % Si

### 8.2.4. Optical loss of fluorotellurite fibre

Fig. (8.16) shows the optical loss of fibre of composition MOF005 ( $70\text{TeO}_2$ - $10\text{Na}_2\text{O}$ - $20\text{ZnF}_2$  mol. %) with various melting times (3, 4, 5 and 10 hours) [9].

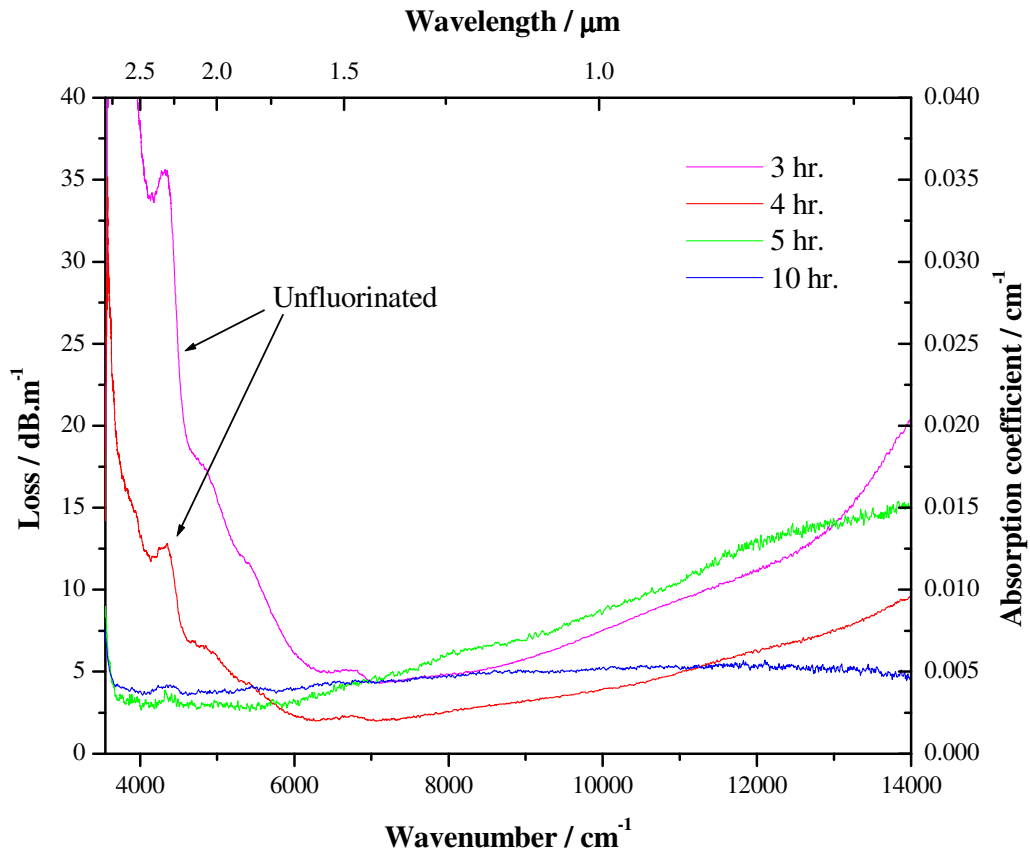


Fig. (8.16): Optical loss of fibre of composition MOF005 ( $70\text{TeO}_2$ - $10\text{Na}_2\text{O}$ - $20\text{ZnF}_2$  mol. %) with various melting times (3, 4, 5 and 10 hours) [9].

It can be seen that optical loss was significantly reduced with increasing melting time. Table (8.6) shows the losses at 4000 ( $2.5\ \mu\text{m}$ ), 6452 ( $1.55\ \mu\text{m}$ ), 7634 ( $1.31\ \mu\text{m}$ ), 10000 ( $1\ \mu\text{m}$ ), and  $14000\ \text{cm}^{-1}$  ( $714\ \text{nm}$ ) with increasing melting time for glass MOF005 ( $70\text{TeO}_2$ - $10\text{Na}_2\text{O}$ - $20\text{ZnF}_2$  mol. %) [9].

Table (8.6): Optical loss of unstructured fibre of composition MOF005 - 70TeO<sub>2</sub>-10Na<sub>2</sub>O-20ZnF<sub>2</sub> (mol. %), with increasing melting time [9].

Melting time / hr.	Loss / dB.m <sup>-1</sup>				
	4000 cm <sup>-1</sup> 2.5 μm	6452 cm <sup>-1</sup> 1.55 μm	7634 cm <sup>-1</sup> 1.31 μm	10000 cm <sup>-1</sup> 1 μm	14000 cm <sup>-1</sup> 714 nm
3	38.25	5.02	4.64	7.52	20.55
4	13.22	2.14	2.25	3.92	9.46
5	2.89	3.63	5.46	8.58	14.90
10	3.82	4.21	4.68	5.25	4.71

This shows a general decrease in loss with melting time. The OH absorption band at 2.5 μm was removed with fluorination, and scattering significantly reduced in the 10 hour melt.

### 8.3. Discussion

#### 8.3.1. Stress in a proposed core / clad pair

Different thermal expansion coefficients are inevitable in a core / clad pair, therefore, stresses will be generated in the resulting fibre. Table (8.7) summarises some thermal and mechanical properties for a possible core / clad optical fibre pair [9].

Table (8.7): Thermal and mechanical properties of a possible core / clad pair, where  $T_g$  = onset of glass transition temperature,  $TEC$  = thermal expansion coefficient,  $Y$  = Young's modulus,  $r_{of}$  = outer fibre / preform diameter (5 mm),  $r_{co}$  = core diameter (2.5 mm),  $\mu_p$  = Poisson's ratio, and  $K_b$  = bulk modulus [10]. Subscripts 1 and 2 denote core and cladding respectively, and \*, properties just above  $T_g$  [9].

Composition / mol. %	$T_g / ^\circ\text{C}$	$TEC / \times 10^{-6} \text{ } ^\circ\text{C}^{-1}$	$TEC^* / \times 10^{-6} \text{ } ^\circ\text{C}^{-1}$	$Y / \text{GPa}$	$\mu_p$	$K_b / \text{GPa}$	$K_b^* / \text{GPa}$	$r / \text{mm}$
65TeO <sub>2</sub> -10Na <sub>2</sub> O-25ZnF <sub>2</sub> (clad)	237	49.6	-	-	-	-	-	5.0
70TeO <sub>2</sub> -10Na <sub>2</sub> O-20ZnF <sub>2</sub> (core)	241	47.7	83.9	42.1	0.289	32.5	16.3	2.5

Thermal expansion coefficients ( $TEC$ ) were measured at 225°C (just below  $T_g$ ) for both glasses, and  $TEC^*$  at 250°C. Values of  $Y$ ,  $\mu_p$ ,  $K_b$  are from a study on 80TeO<sub>2</sub>-20ZnCl<sub>2</sub> mol. % glass [10] (assuming  $K_{b1} \approx K_{b2}$ , and bulk modulus above  $T_g$  is 0.5 times that below [11]). Close  $TEC$ , will mean minimal thermal expansion mismatch in the fibre. Below  $T_g$ , on cooling, the cladding will contract more than the core (higher  $TEC$ ), putting the core in compression, and the cladding in tension of equal and opposing magnitude. Tensile stress in the cladding would tend to open up Griffith flaws at the fibre surface, therefore coating would be necessary. The stress,  $\sigma$ , in the fibre can be calculated using equation (8.2) [11, 12].

$$\sigma = \frac{(TEC_1 - TEC_2)(T - T_{g1})Y}{(r_{of}^2 / r_{co}^2)(1 - \mu_p)} + \frac{(TEC_1^* - TEC_2)(T_{g2} - T_{g1})}{((1 - r_{of}^2 / r_{co}^2) / 3K_{b1}^*) - (1 / (3K_{b2}))} \quad (8.2)$$

where  $T = 21^{\circ}\text{C}$ . Using values from table (8.7), gives stress in the fibre made from this core / clad pair around 72 MPa, which is relatively low [9]. Cherbanov *et al.* have reported 170  $\mu\text{m}$   $\text{TeO}_2\text{-WO}_3$  fibre with tensile strength as high as 5.8 GPa [13].

### 8.3.2 Viscosity (TMA)

The viscosity / temperature curves of both glasses was studied using TMA. Modelling was performed to extrapolate the viscosity over a small temperature range either side of the validated TMA data, to predict the temperature at which fibre drawing should occur ( $10^{4.5}$  Pa.s). These models are generally useful over a narrow compositional and temperature range. Fig. (8.4) shows the TMA data for core and clad compositions. For a given temperature, the viscosity increases with decreasing  $\text{ZnF}_2$  content.  $\text{ZnF}_2$  breaks up the  $\text{TeO}_2$  network, enabling the glass to flow more easily at lower temperatures [9]. This is desirable for fibre drawing, as stability increases with  $\text{ZnF}_2$  content. Figure (8.5) shows the viscosity modelling for the clad glass. The Cohen-Grest model is shown [4], with the Arrhenius [2] for comparison. Moynihan showed the Cohen-Grest equation models the viscosity / temperature behaviour of fluorozirconate glasses (fragile and non-Arrhenian, see [14]) more accurately. Stronger glass formers (such as silicates and phosphates [15, 16]) exhibit Arrhenian behaviour, and are better modelled by the Vogel-Fulcher-Tamman equation [3, 17]. On heating above  $T_g$ , structural break down is more rapid for fragile glass formers due their ionic nature, resulting in a steeper viscosity / temperature curve. The presence of oxygen and fluorine in these glasses, will result in a fragility somewhere in between oxide tellurite glasses (stronger), and fluorozirconates (more fragile). This is

confirmed by viscosity data reported by Wang *et al.* [18], which shows TeO<sub>2</sub>-Na<sub>2</sub>O-ZnO and ZBLAL viscosity of 10<sup>6</sup> Pa.s to occur at 352 and 295°C respectively. From fig. (8.4) it can be seen the viscosity of 10<sup>6</sup> Pa.s occurs at 296 and 306°C for the 25 and 20 mol. % ZnF<sub>2</sub> glasses respectively, closer in fragility to fluorozirconate glasses, but slightly stronger. The models predict the fibre drawing viscosity (10<sup>4.5</sup> Pa.s) of the clad glass to occur around 324°C, 74°C below  $T_x$ . Figure (8.6) shows the modelling for the core glass. As expected, the predicted fibre drawing viscosity occurred at a higher temperature than the value for the clad glass, at 333°C, 61°C below  $T_x$ . Table (8.4) shows the parameters from the viscosity models for both glasses, and predicted fibre drawing temperatures. These values indicate successful fibre drawing is possible without devitrification.

The VFT and ML models generated negative Kelvin values for  $T_0$  in these models for the core (MOF005) glass, therefore these models were not used on the plots shown in fig. (8.5) and (8.6). In the VFT model,  $T_0$  is believed to correspond to an ideal glass transition temperature below  $T_g$ , where the free volume of the glass tends to zero [19]. Therefore, some researchers have suggested this justifies the theoretical basis for an otherwise empirically derived equation. However, as this equation models the viscosity-temperature behaviour of strong glass formers, such as silicates, more accurately, it will not be considered further here. The CG model was also developed by the considering the free volume of the glass [4], although  $T_0$  takes on a different meaning. Here it represents the transition between high and low temperature behaviour, and below the transition certain relaxation modes in the glass are no longer active. For high (h) and low (l) regions, different values of  $T_0$  exist, with the free volume proportional to  $T-T_{0l}$  and  $T-T_{0h}$ . At high temperatures, the CG model approximates VFT behaviour (i.e. when  $(T-T_0)^2 \gg 4CT$ ),

and low temperatures ( $T < T_0$ ) the behaviour is more Arrhenian [20]. As  $T$  approaches  $T_0$ , the viscosity is proportional to  $T^{1/2}$ , and therefore non-linear in this region. If  $T_0$  is close to  $T_g$  the viscosity behaviour around the transformation range will be non-Arrhenian, and linear over a small region ( $\approx 60^\circ\text{C}$  above  $T_g$ ). This modelling has been shown to yield  $T_0$  values  $> T_g$  for fluoride glasses [20], which was also seen in this study (see table (8.4)). The CG model has been shown to fit the behaviour of fluoride melts where  $T_0$  was close to the liquidus temperature [19].  $T_0$  for both glasses from table (8.4) is  $> T_g$ , and closer to the melting temperatures than  $T_g$  in both samples.

Fig. (8.16) shows a fragility plot ( $\eta$  versus  $T_g / T$ ) for glass MOF001 (25 % mol.  $\text{ZnF}_2$ ) and for a hypothetical strong glass former such as a silicate or phosphate. The plot for the fluorotellurite glass was generated using the CG parameters in table (8.4), and the hypothetical plot for a strong glass was generated using a linear relationship. It can be seen the viscosity-temperature behaviour of a fragile glass is significantly different to a strong glass, with almost linear behaviour for  $T_g / T > 0.6$ . However this linear behaviour still deviates from the strong glass former, with viscosity decreasing at a higher rate with increasing temperature. For  $T_g / T < 0.6$  (approaching the melting temperature), the viscosity-temperature behaviour begins to plateau, and tends towards stronger behaviour. At these high temperatures ( $T_g / T \rightarrow 0$ ), there will be sufficient thermal energy for virtually complete structural breakdown of the glass regardless of fragility, resulting in very low viscosities.

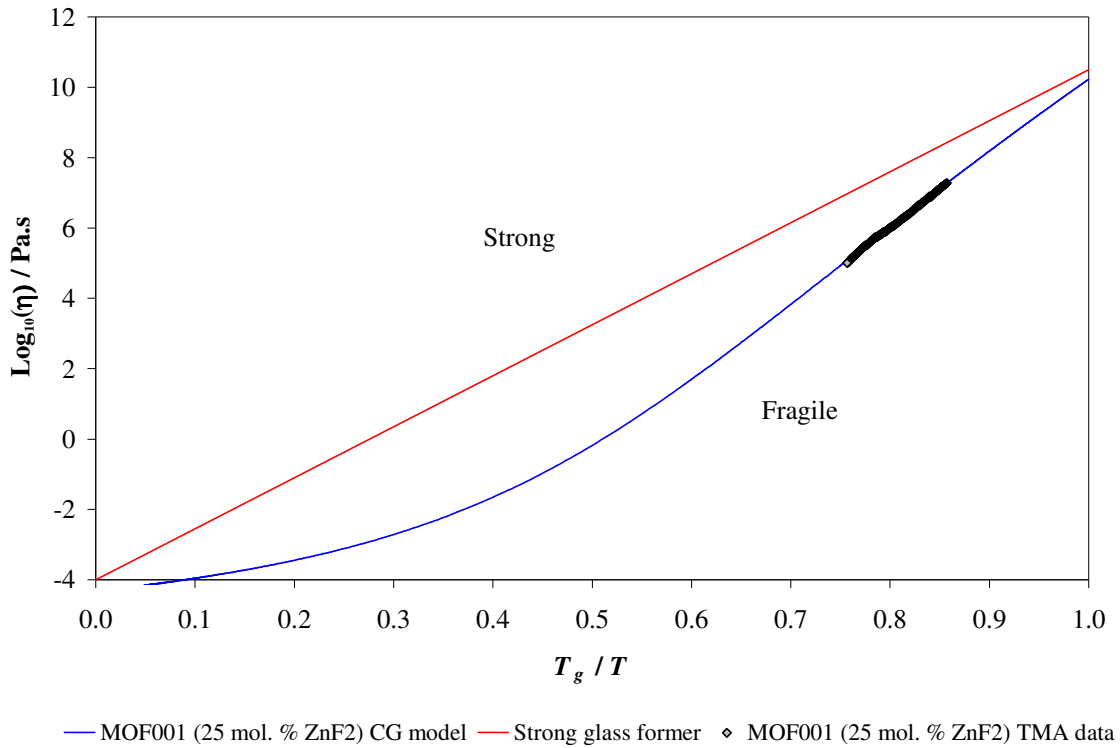


Fig. (8.16): Fragility plot of glass MOF001 (25 % mol. ZnF<sub>2</sub>) and a hypothetical strong glass former for comparison.

Komatsu *et al.* [21-23] have shown that TeO<sub>2</sub> based glasses fall into the category of fragile glasses (but stronger than fluorozirconates), due to their steep viscosity-temperature profile, and large heat capacity change ( $\Delta C_p$ ) at  $T_g$ . A discrepancy has been shown by this group in tellurite glasses between the activation energy for viscous flow,  $E_\eta$ , and the enthalpy of relaxation,  $\Delta H$ , around  $T_g$ . This is thought to be due to decoupling between the activation energies for enthalpy relaxation and viscous flow in the glass transition region [21].

Watanabe *et al.* [24] related the Vicker's hardness of tellurite glasses to fragility and relaxation processes in the glass. There are two types of relaxation processes in glasses:  $\alpha$ -relaxation which is observed above  $T_g$  due to atomic displacement / rearrangement, and

$\beta$ -relaxation which occurs mainly below  $T_g$ , possibly due to non-cooperative atom movements. The Vicker's hardness of fragile glasses such as  $\text{TeO}_2$ - and  $\text{Bi}_2\text{O}_3$ -based systems, was shown to decrease rapidly at around  $T/T_g = 0.9$  to  $1.0$  (i.e. just below  $T_g$ ). For stronger glass formers based on  $\text{P}_2\text{O}_5$  and  $\text{SiO}_2$ , this behaviour was observed at  $T/T_g = 1.0$  to  $1.1$  (i.e. just above  $T_g$ ). This is thought to be due to  $\beta$ -relaxation processes playing a greater role in the rheological properties of fragile glasses, whereas  $\alpha$ -relaxation is more prominent in the stronger glasses [24].

The slope at any point of fig. (8.16) is equal to the activation energy for viscous flow [25]. Fig. (8.17) shows the differential curve of the fragility plot of glass MOF001 (25 mol. %  $\text{ZnF}_2$ ).

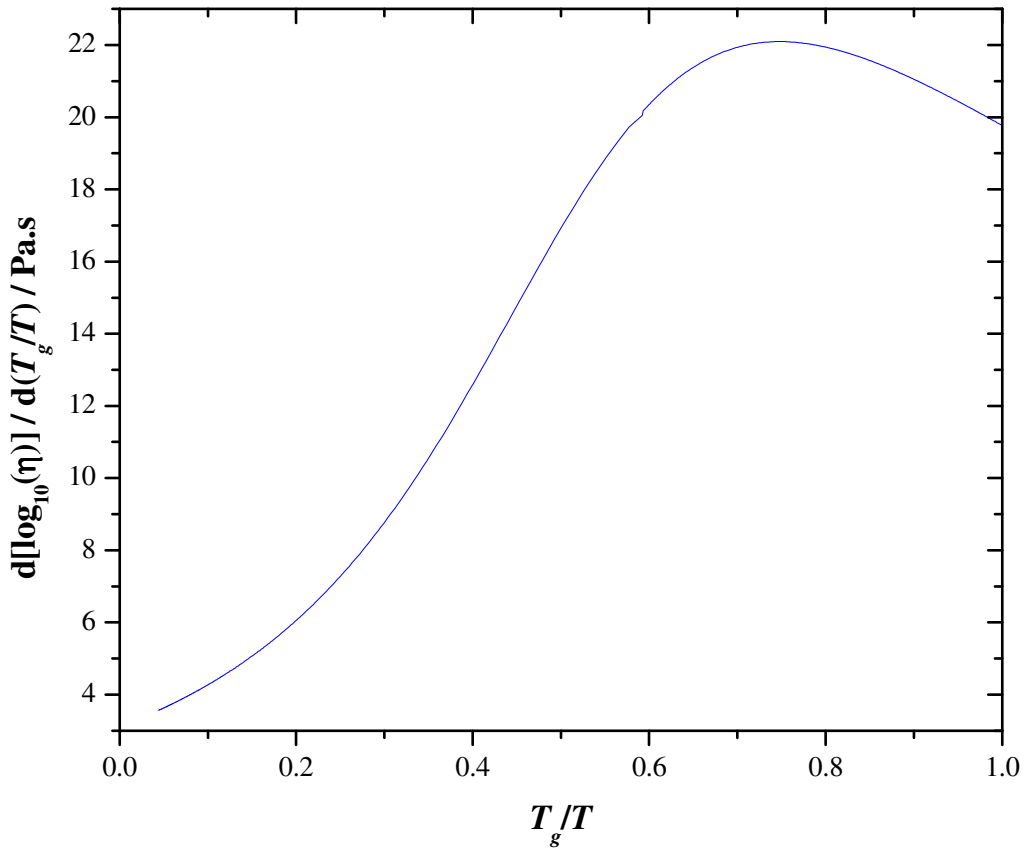


Fig. (8.17): Differential of fragility plot for glass MOF001 (25 mol. %  $\text{ZnF}_2$ ).

It can be seen the activation energy for viscous flow generally increases as  $T_g$  is approached, as expected.

Braglia *et al.* [6] showed  $\text{TeO}_2\text{-Na}_2\text{O-ZnO}$  glasses behave in a Newtonian manner (i.e. viscosity-temperature behaviour independent of the applied force). This is advantageous for fibre drawing, as the viscosity will only depend on temperature, rather than also draw speed, as seen with fluorozirconates and chalcogenides.

### 8.3.3. ESEM of crystallised fibres

Fig. (8.7) shows an electron micrograph of triangular shaped crystals near the surface (10 to 20  $\mu\text{m}$ ) of the glass fibre of composition MOF005ii (70 $\text{TeO}_2$ -10 $\text{Na}_2\text{O}$ -20 $\text{ZnF}_2$  mol. %), mounted length-ways in epoxy resin, and cross-sectioned. These crystals have grown close to the fibre surface, and are around 2  $\mu\text{m}$  in diameter. This surface crystallisation, could be due to degradation of the fibre surface during heating in the fibre drawing tower. The nitrogen atmosphere in the fibre drawing furnace was not passed through a liquid nitrogen dewar for preform MOF005ii. Therefore, there could have been sufficient water vapour present in the atmosphere to attack and degrade the surface of the fibre, and provide sites for crystal nucleation. OH groups lower the local viscosity of the glass [26], increasing the likelihood of atomic rearrangement, and crystallisation. Physical volatilisation from the fibre surface, could have changed the surface composition, destabilising the glass and causing local crystallisation. Organic contaminants (from the internal surface of the brass mould or preform handling) also could have been present on

the preform surface, altering the surface chemistry, to provide nucleation sites, and also making reducing conditions. The EDX spectra which were performed at point A (glass) and B (crystal) on fig. (8.7) show the oxygen content of the crystal was lower than of the glass (44 and 30 atomic % respectively). The fluorine content of the crystal was over double that of the glass (22 and 10 atomic % respectively). The sodium content of the crystal was around four times that of the glass (20 and 5 atomic % respectively). The tellurium and zinc contents were slightly lower of the crystal (19 and 9 atomic % respectively) than those of the glass (28 and 13 atomic % respectively). As the electron beam will have sampled a volume greater than the crystals (around 10  $\mu\text{m}$  compared to 1 to 2  $\mu\text{m}$  respectively), and glass will be inevitably present in the areas between the dendrites of the crystals, these values of elemental analysis cannot be used to calculate stoichiometry of phases. However, they can provide an estimate of the composition of crystalline phases identified (i.e. relative amounts). The crystal shown in fig. (8.7) was Na and F rich, and Te and O deficient compared to the glass, with Zn approximately the same. Therefore, it would be reasonable to assume this crystal was the orthorhombic phase,  $\text{NaZnF}_3$ , indexed in fig. (5.11).

Fig. (8.8) shows an electron micrograph of a snowflake shaped crystal in the glass fibre of composition MOF005ii (70 $\text{TeO}_2$ -10 $\text{Na}_2\text{O}$ -20 $\text{ZnF}_2$  mol. %), mounted length-ways in epoxy resin, and cross-sectioned. Again, this crystal had higher atomic % Na and F, and lower Zn, Te and O than the bulk glass. This type of dendritic or skeleton crystallite has been reported in a number of glass systems such as silicates and fluorides [27]. These crystals often bear little resemblance to their mineralogical counterparts. If a sphere is cut out of a cubic crystal and introduced into a saturated solution (i.e. a glass melt or

undercooled glass), and allowed to grow, certain directions will grow preferentially. Fig. (8.18) illustrates this [27].

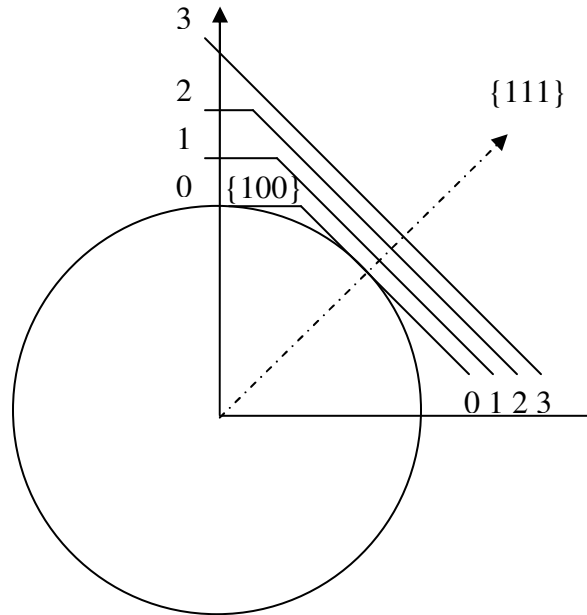


Fig. (8.18): Growth of a sphere cut out of a cubic crystal in a saturated solution [27].

The cubic  $\{001\}$  and octahedral  $\{111\}$  planes will grow primarily, but not uniformly (as illustrated by steps 0 to 3 in fig. (8.18)). This is due to different rates of plane growth. Initially the cubic  $\{001\}$  plane grows most rapidly, growing smaller until it merges, and is enveloped by the octahedral  $\{111\}$  plane. Less material is deposited at the octahedral  $\{111\}$  plane, therefore it moves at a slower rate. As a consequence, the corners and edges of crystals can be defined as the planes with the highest rates of growth [27]. In a glass melt or undercooled glass, due to the high viscosity, diffusion is slow. Crystallisation will occur in preferred directions which are typically those with the highest growth rates, and a dendritic / skeleton structure will result. These directions of preferred growth can be

altered by external factors such as impurities, pressure, temperature and rate of cooling [27].

It is interesting to note, that these snowflake shaped crystals (see fig. (8.8)) initially grow to form a cross shapes, possibly due to a similar mechanism shown in fig. (8.18). Then from the primary cross-shaped dendrites, secondary dendrites grow diagonally (in the  $\{110\}$  direction). This is likely to be due to a similar mechanism described above for a cubic crystal. In orthorhombic  $\text{NaZnF}_3$ , first the cubic  $\{001\}$  plane grows forming a cross shaped dendritic structure. Eventually, the  $\{001\}$  plane is enveloped by the slower moving  $\{110\}$  plane and secondary dendrites grow from the primary structure. The triangular shaped crystals seen in fig. (8.7) are likely to be due to an orientation effect from the polishing process. Fig. (8.19) shows a possible model for crystallisation of the snowflake shaped orthorhombic  $\text{NaZnF}_3$  crystals in glass MOF005 (70 $\text{TeO}_2$ -10 $\text{Na}_2\text{O}$ -20 $\text{ZnF}_2$  mol. %) and similar compositions.

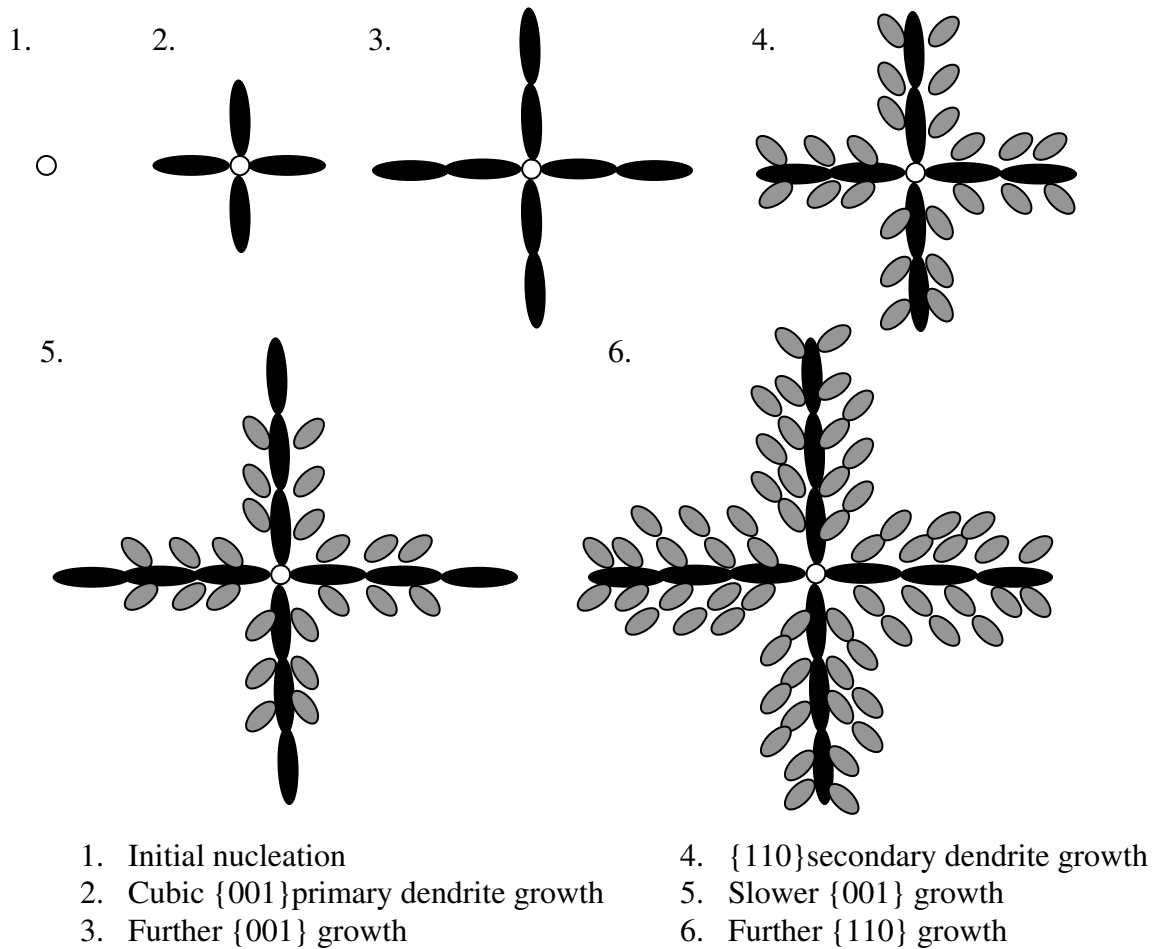


Fig. (8.19): Possible model for crystallisation of the snowflake shaped orthorhombic  $\text{NaZnF}_3$  crystals in glass MOF005 (70 $\text{TeO}_2$ -10 $\text{Na}_2\text{O}$ -20 $\text{ZnF}_2$  mol. %).

Öveçoğlu *et al.* [28] studied the crystallisation of glasses in the system  $(1-x)\text{TeO}_2-x\text{LiCl}$  ( $x = 0.4-0.6$  mol. %). Fig. (8.20) illustrates one of these crystals, which are similar in shape to the snowflake shaped crystals seen in this study.

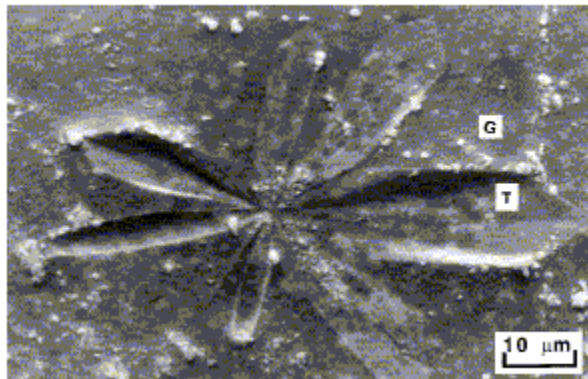


Fig. (8.20): Crystal grown at 435°C in TeO<sub>2</sub>-LiCl glass [28].

These crystals in fig. (8.20) were an order of magnitude larger than those seen in the fluorotellurite fibre (40 μm compared to 2 μm), and occurred at the surface of the glass (4 to 9 μm deep). The crystal shown in fig. (8.20) was identified by EDX analysis and XRD to be tetragonal α-TeO<sub>2</sub> (paratellurite) [28].

Fig. (8.9) shows an electron micrograph of crystals near the surface (10 to 20 μm) of the glass fibre of composition MOF005ii (70TeO<sub>2</sub>-10Na<sub>2</sub>O-20ZnF<sub>2</sub> mol. %), mounted length-ways in epoxy resin, and cross-sectioned. It can be seen that most of the crystals were found around 10 μm from the fibre surface. The fibre was around 200 μm in diameter, pulled from a preform 10 mm in diameter. Therefore, this region corresponds to the outer 0.5 mm of the preform (due to a 50 times reduction in diameter). This surface crystallisation phenomenon could be due to changes in surface chemistry mentioned earlier in this section. It could also be due to excess heating at the preform / fibre surface. The surface of the glass will inevitably be hotter than the interior, which may be enough to nucleate and grow crystals in this region. This local heating could also lead to degradation of the fibre, also destabilising the glass. These crystals seem to be primarily

cross-shaped, indicating that the fibre was not held for sufficient time or temperature to promote the growth of secondary dendrites described above.

Fig. (8.10) and (8.11) show electron micrographs of crystals near the surface of the glass fibre of composition MOF005ii ( $70\text{TeO}_2\text{-}10\text{Na}_2\text{O-}20\text{ZnF}_2$  mol. % ) as drawn. Crystals can be clearly seen protruding from the fibre surface. The glass appears to have flowed around the crystals during fibre drawing. The nodular crystals have darker regions. These 'holes' are filled by glass or voids. This is likely to be due to preferential growth described earlier in this section. The rounded edges are possibly the result of re-dissolution of any sharply defined edges by the flowing glass during the fibre drawing process. Therefore, it is reasonable to propose that the crystals grew on the neckdown region of the preform, and the reflow occurred at the tip of the preform as the fibre drew.

Fig. (8.12) depicts an electron micrograph of a snowflake shaped crystal in the glass fibre of composition MOF005ii ( $70\text{TeO}_2\text{-}10\text{Na}_2\text{O-}20\text{ZnF}_2$  mol. %). The fibre was mounted end-on in epoxy resin, and polished-back to reveal the transverse plane to the fibre axis, i.e. cross-section. Again, this type of crystal showed the primary and secondary dendrite structure described above. Fig. (8.13) displays the EDX analysis from points Q and R in fig. (8.12). The crystal contained significantly more Na and F than the bulk glass and less O. This indicates once more that it is the orthorhombic  $\text{NaZnF}_3$  phase.

Fig. (8.14) and (8.15) present electron micrographs of a crystals 10-20  $\mu\text{m}$  from the surface in the glass fibre of composition MOF005ii ( $70\text{TeO}_2\text{-}10\text{Na}_2\text{O-}20\text{ZnF}_2$  mol. %). The fibre was mounted end on in epoxy resin, and polished-back. A number of different crystal shapes were observed. This is likely to be due to orientation from polishing and different stages in the growth of the crystals.

### 8.3.4. Optical loss of fluorotellurite fibre

Fig. (8.16) shows the optical loss of fibre of composition MOF005 (70TeO<sub>2</sub>-10Na<sub>2</sub>O-20ZnF<sub>2</sub> mol. %) with various melting times (3, 4, 5 and 10 hours). After 3 hours of melting, the fibre exhibited a minimum loss at around 6000 cm<sup>-1</sup> (1.67 μm) of around 5 dB.m<sup>-1</sup>. From this minimum, the loss increased in the infrared to over 35 dB.m<sup>-1</sup> at around 4200 cm<sup>-1</sup> (2.38 μm). The loss also increased into the visible region (beyond 14000 cm<sup>-1</sup> → 714 nm) to over 20 dB.m<sup>-1</sup>, likely to be due to scattering (proportional to  $\frac{1}{\lambda^4}$ ). After 4 hours of melting, the fibre showed minimum loss at around 6000 cm<sup>-1</sup> (1.67 μm) of about 2.5 dB.m<sup>-1</sup>. From this minimum, the loss increased into the infrared to over 12 dB.m<sup>-1</sup> at around 4200 cm<sup>-1</sup> (2.38 μm). The loss also increased into the visible region (beyond 14000 cm<sup>-1</sup> → 714 nm) to over 10 dB.m<sup>-1</sup>, again likely to be due to scattering. For the glass melted for 5 hours the minimum loss of around 3 dB.m<sup>-1</sup> occurred at around 4000 cm<sup>-1</sup> (2.5 μm) and increased to over 15 dB.m<sup>-1</sup> into the visible region. The glass melted for 10 hours showed a minimum loss of around 4 dB.m<sup>-1</sup> at around 4000 cm<sup>-1</sup> (2.5 μm) and stayed at 5 dB.m<sup>-1</sup> or below over the entire 700 nm to 2.5 μm region [9]. It is interesting to note, the fibre made using fluorinated ZnF<sub>2</sub> (5 and 10 hr. melts) does not exhibit the intense band around 2.5 μm attributed to the first overtone of strongly hydrogen bonded OH in the glass. This is to be expected, as fluorination and longer melting times will significantly reduce the amount of OH in the glass, resulting in few nearest neighbours for remaining OH groups to H-bond to.

A small number of studies have been performed on oxide tellurite fibres [18, 29-32], but none to the authors knowledge on fluoride containing tellurite fibres. Wallenberger *et al.* [32] reported transmission between 50 and 70 % (1.5 to 3.0 dB.m<sup>-1</sup> by this authors calculations, however this would depend of the method used to obtain transmission in this study) in the 500 nm to 2.5 μm region for TeO<sub>2</sub>-Al<sub>2</sub>O<sub>3</sub> fibre. Wang *et al.* [18] reported losses of 1.0 to 1.5 dB.km<sup>-1</sup> for the 1 to 1.6 μm region for TeO<sub>2</sub>-ZnO-Na<sub>2</sub>O fibre, but losses increased significantly beyond this band. Kim *et al.* [30] reported transmission of around 75 % in the 500 to 700 nm region for TeO<sub>2</sub>-Na<sub>2</sub>O-Li<sub>2</sub>O glass fibre doped with LiNbO<sub>3</sub>. Burger *et al.* [29] reported optical loss for bulk TeO<sub>2</sub>-ZnO-PbO-PbF<sub>2</sub>-Nb<sub>2</sub>O<sub>5</sub>-La<sub>2</sub>O<sub>3</sub> glasses of around 0.2 dB.m<sup>-1</sup> at 6800 cm<sup>-1</sup> (1.47 μm), but this increased significantly into the visible and infrared regions. Fluorotellurite fibre was pulled in the Burger *et al.* [29] study, but was too lossy to measure the attenuation. Shen *et al.* [31] reported loss of around 0.5 dB.m<sup>-1</sup> at around 1.3 μm for TeO<sub>2</sub>-Na<sub>2</sub>O-ZnO glass fibre, but this loss increased exponentially to lower and higher wavelengths (see section 2.5.1.1.). Therefore, the fibre pulled in this study is the lowest loss fluorotellurite fibre to date (5 dB.m<sup>-1</sup>) over a wide wavelength range (700 nm to 2.5 μm). Fig. (8.21) shows the fluorotellurite fibre pulled in this study (MOF005) guiding light.

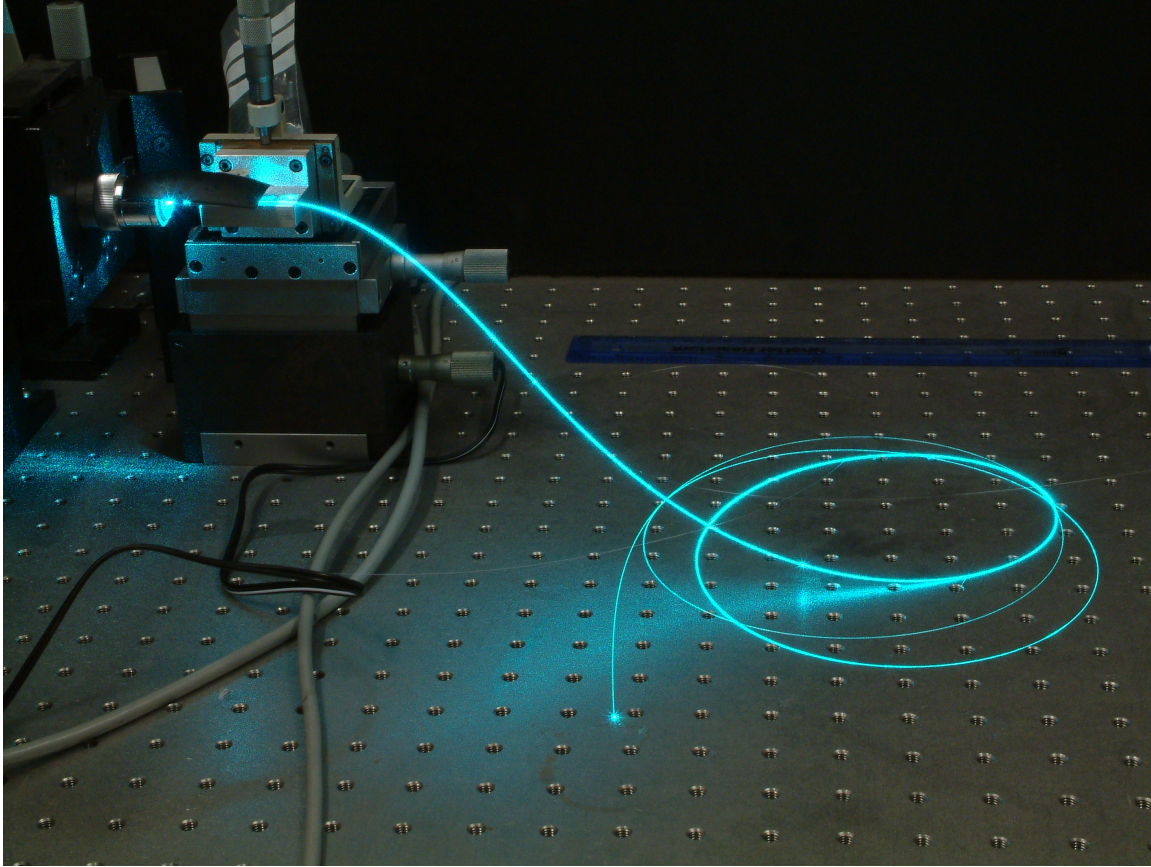


Fig. (8.21): Fluorotellurite fibre (MOF005) pulled in this study guiding light.

Wang *et al.* [18] predicted a minimum loss of around  $3.6 \times 10^{-3}$  dB.km<sup>-1</sup> at 3.02  $\mu$ m for TeO<sub>2</sub>-Na<sub>2</sub>O-ZnO glass (see section 2.5.1.1.). This is shifted to  $1.8 \times 10^{-2}$  dB.km<sup>-1</sup> at 1.9  $\mu$ m with OH present. Losses are much higher in the pulled fluorotellurite fibre most likely due to the lack of cladding, cationic impurities, crucible contamination, and other nano- and micro-inhomogeneities. Cherbanov *et al.* [13] have reported around  $10^5$  to  $10^6$  cm<sup>3</sup> nano-inhomogeneities in a number of oxide tellurite compositions, including air bubbles, Pt particles (52 ppm), and crystals, the size and population depending on processing. These particles ranged in size from 70 to 170 nm. All the fibres from fig. (8.16), except the 10 hour melt, show an increase in loss into the visible region, where these types of

particles would contribute to losses due to the similarity in their dimensions to the wavelength of the light. These nano-particles will result in Rayleigh scattering proportional to  $1/\lambda^4$ . Larger micro-particles give rise to Mie scattering, proportional to  $1/\lambda^2$ . The 10 hour melt does not seem to exhibit significant scattering losses, due to the increased refining of the glass due to longer melting time.

Ryder *et al.* [33] showed a decrease in overall visible transmittance (400 to 750 nm) with increasing Pt content in phosphate glasses, although around seven absorption bands occur in the 200 to 333 nm region [34]. Therefore, the remaining background absorption seen in fig. (8.16) for the 10 hour melt is likely to be due to losses from the unclad fibre surface, and to noble metal (Au / Pt) absorption. Producing fibre by rotational casting [7], should result in fluorotellurite fibre of lower loss than the rod-in-tube TZN fibre reported by Wang *et al.* ( $0.9 \text{ dB.m}^{-1}$  at  $1.35 \mu\text{m}$ ) [18]. Gold is known to stay in solution better than platinum, although both can precipitate as tiny particles in the glass. These metals are taken into the melt by a number of processes: vapour phase transport above the melt surface, mechanical abrasion, and reaction with the melting batch [35]. Metallic particle inclusions can result in severe failure in laser glasses, therefore solid solution is preferred. These particles can absorb laser energy, until melting, resulting in cracking of the glass. Precipitation is encouraged under reducing conditions, whilst solubility increased under oxidising conditions for platinum [35]. Noble metals also impart a yellow colour to tellurite glasses, in greater severity for Pt than Au.

Increasing melting times reduces OH absorption and scattering due to inhomogeneity. However longer melting times will inevitably increase noble metal dissolution into the glass. Therefore, an acceptable balance must be struck between processing times and

temperatures giving sufficient OH reduction and melt refining, as well as minimal noble metal incorporation into the glass.

## 8.4. Summary

Stresses in a proposed core / clad fluorotellurite optical fibre pair (20 / 25 mol. %  $\text{ZnF}_2$ ) due to thermal expansion mismatch were calculated to be relatively low (72 MPa). The viscosity / temperature behaviour of this pair was obtained (by TMA) and modelled enabling the prediction of the fibre drawing temperatures ( $\approx 330^\circ\text{C} \rightarrow$  at least  $60^\circ\text{C}$  below  $T_x$ ) and fragilities (stronger than fluorozirconates, and more fragile than oxide tellurite glasses) [9].

Snowflake shaped crystals were identified in fibres pulled under ‘wet’ atmosphere, due to degradation and destabilisation at the fibre surface. These  $\text{NaZnF}_3$  crystals (characterised by DTA, EDX and XRD) were thought to grow initially in a cross orientation when viewed cross-sectionally, with later secondary dendrite growth, giving this snowflake appearance. Other parameters important for producing pristine fibre include: gold melting crucibles, brass annealing moulds, and fluorinated  $\text{ZnF}_2$ .

Optical loss of  $70\text{TeO}_2\text{-}10\text{Na}_2\text{O-}20\text{ZnF}_2$  mol. % fibre decreased with increasing melting time, and fluorinated  $\text{ZnF}_2$ , with flat loss spectra ( $\leq 5 \text{ dB.m}^{-1}$ ) over the 700 nm to  $2.5 \mu\text{m}$  region for the 10hr. melt [9]. Structured preforms manufactured by rotational casting should result in even lower losses.

## 8.5. References

- [1] E. H. Fontana, "A versatile parallel-plate viscometer for glass viscosity measurements to 1000°C," *American Ceramic Society Bulletin*, vol. 49, pp. 594-597, 1970.
- [2] A. K. Doolittle, "Studies in Newtonian flow. II. The dependence of the viscosity of liquids on free-space," *Journal of Applied Physics*, vol. 22, pp. 1471-1475, 1951.
- [3] G. S. Fulcher, "Analysis of recent measurements of the viscosity of glasses," *Journal of the American Ceramic Society*, vol. 8, pp. 339-355, 1925.
- [4] M. H. Cohen and G. S. Grest, "Liquid-glass transition, a free-volume approach," *Physical Review B*, vol. 20, pp. 1077-1098, 1979.
- [5] P. B. Macedo and T. A. Litovitz, "On the relative roles of free volume and activation energy in the viscosity of liquids," *The Journal of Chemical Physics*, vol. 42, pp. 245-256, 1965.
- [6] M. Braglia, S. Mosso, G. Dai, E. Billi, L. Bonelli, M. Baricco, and L. Battezzati, "Rheology of tellurite glasses," *Materials Research Bulletin*, vol. 35, pp. 2343-2351, 2000.
- [7] D. C. Tran, C. F. Fisher, and G. H. Sigel, "Fluoride glass preforms prepared by a rotational casting process," *Electronics Letters*, vol. 18, pp. 657-658, 1982.
- [8] N. N. Greenwood and A. Earnshaw, *Chemistry of the elements*. Oxford: Butterworth-Heinemann, 1995.
- [9] M. D. O'Donnell, D. Furniss, V. K. Tikhomirov, and A. B. Seddon, "Low loss infrared fluorotellurite optical fibre," *Physics and Chemistry of Glasses*, in press.
- [10] R. El-Mallawany, "Tellurite glasses - Part 1. Elastic properties," *Materials Chemistry and Physics*, vol. 53, pp. 93-120, 1998.
- [11] D. A. Krohn, "Determination of axial stress in clad glass fibers," *Journal of the American Ceramic Society*, vol. 53, pp. 505, 1970.
- [12] D. Furniss, J. D. Shephard, and A. B. Seddon, "A novel approach for drawing optical fibers from disparate core / clad glasses," *Journal of Non-Crystalline Solids*, vol. 213&214, pp. 141-146, 1997.
- [13] M. Churbanov, E. Zorin, I. Grishin, and T. Petrova, "Investigation into micro-inhomogeneity of tellurite glasses," presented at Glass and Optical Materials Fall

- 2004 Meeting incorporating the XIVth International Symposium on Non-Oxide and Novel Optical Glasses, Cape Canaveral, Florida, USA, 2004.
- [14] K. Ito, C. T. Moynihan, and C. A. Angell, "Thermodynamic determination of fragility in liquids and a fragile-to-strong liquid transition in water," *Nature*, vol. 398, pp. 492-495, 1999.
- [15] C. A. Angell, "Spectroscopy simulation and scattering, and the medium range order problem in glass," *Journal of Non-Crystalline Solids*, vol. 73, pp. 1-17, 1985.
- [16] S. W. Martin and C. A. Angell, "On the glass transition and viscosity of P<sub>2</sub>O<sub>5</sub>," *Journal of Physical Chemistry*, vol. 90, pp. 6736-6740, 1986.
- [17] S. English, "The effect of various constituents on the viscosity of glass near its annealing temperature," *Journal of the Society of Glass Technology*, vol. 7, pp. 25-45, 1923.
- [18] J. Wang, E. Vogel, and E. Snitzer, "Tellurite glass: a new candidate for fiber devices," *Optical Materials*, vol. 3, pp. 187-203, 1994.
- [19] M. Braglia, "Viscosity of halide glasses," in *Properties, processing and applications of glass and rare earth-doped glasses for optical fibres*, D. Hewak, Ed. Exeter: INSPEC, 1988, pp. 194-201.
- [20] A. Jha and J. M. Parker, "Viscosity models for fluorozirconate and fluoroaluminate glasses," *Physics and Chemistry of Glasses*, vol. 30, pp. 220-228, 1989.
- [21] T. Komatsu, K. Aida, T. Honma, Y. Benino, and R. Sato, "Decoupling between enthalpy relaxation and viscous flow and its structural origin in fragile oxide glass-forming liquids," *Journal of the American Ceramic Society*, vol. 85, pp. 193-199, 2002.
- [22] T. Komatsu, R. Ike, R. Sato, and K. Matusita, "Mixed-alkali effect in tellurite glasses and change in fragility," *Physics and Chemistry of Glasses*, vol. 36, pp. 216-221, 1995.
- [23] T. Kosuge, Y. Benino, V. Dimitrov, R. Sato, and T. Komatsu, "Thermal stability and heat capacity changes at the glass transition in K<sub>2</sub>O-WO<sub>3</sub>-TeO<sub>2</sub> glasses," *Journal of Non-Crystalline Solids*, vol. 242, pp. 154-164, 1998.
- [24] T. Watanabe, Y. Benino, and T. Komatsu, "Change in Vickers hardness at the glass transition region for fragile and strong glasses," *Journal of Non-Crystalline Solids*, vol. 286, pp. 141-145, 2001.

- [25] D. M. Zhu, C. S. Ray, W. C. Zhou, and D. E. Day, "Glass transition and fragility of  $\text{Na}_2\text{O}-\text{TeO}_2$  glasses," *Journal of Non-Crystalline Solids*, vol. 319, pp. 247-256, 2003.
- [26] J. E. Shelby, *Introduction to glass science and technology*. Cambridge: RSC Paperbacks, 1997.
- [27] W. Vogel, *Glass chemistry*, 2nd ed. New York: Springer-Verlag, 1994.
- [28] M. L. Ovecoglu, G. Ozen, B. Demirata, and A. Genc, "Microstructural characterization and crystallization kinetics of  $(1-x)\text{TeO}_2-x\text{LiCl}$  ( $x=0.6-0.4$  mol) glasses," *Journal of the European Ceramic Society*, vol. 21, pp. 177-183, 2001.
- [29] H. Burger, I. Gugov, U. Grunke, J. Kraus, and B. Manzanares-Taylor, "Preforms for large optical bandwidth amplifier fibres," *Glass Science and Technology*, vol. 75, pp. 261-264, 2002.
- [30] H. G. Kim, T. Komatsu, R. Sato, and K. Matusita, "Fiber drawing of  $\text{LiNbO}_3$ -doped mixed-alkali tellurite glasses," *Journal of the Ceramic Society of Japan*, vol. 103, pp. 1073-1076, 1995.
- [31] S. Shen, A. Jha, E. Zhang, and S. J. Wilson, "Compositional effects and spectroscopy of rare earths ( $\text{Er}^{3+}$ ,  $\text{Tm}^{3+}$ , and  $\text{Nd}^{3+}$ ) in tellurite glasses," *Comptes Rendus Chimie*, vol. 5, pp. 921-938, 2002.
- [32] F. T. Wallenberger, N. E. Weston, and D. B. Sherman, "Infrared optical tellurite glass fibers," *Journal of Non-Crystalline Solids*, vol. 144, pp. 107-110, 1992.
- [33] R. J. Ryder and G. E. Rindone, "Color and light scattering of platinum in some lead glasses," *Journal of the American Ceramic Society*, vol. 41, pp. 415-422, 1958.
- [34] A. Paul and A. N. Tiwari, "Optical absorption of platinum(IV) in  $\text{Na}_2\text{O}-\text{B}_2\text{O}_3$  and  $\text{Na}_2\text{O}-\text{NaCl}-\text{B}_2\text{O}_3$  glasses," *Physics and Chemistry of Glasses*, vol. 14, pp. 69-72, 1973.
- [35] M. Karabulut, G. K. Marasinghe, C. A. Click, E. Metwalli, R. K. Brow, C. H. Booth, J. J. Bucher, D. K. Shuh, T. I. Suratwala, and J. H. Campbell, "XAFS investigation of platinum impurities in phosphate glasses," *Journal of the American Ceramic Society*, vol. 85, pp. 1093-1099, 2002.

## 9. Conclusions

This chapter will summarise the main points from the discussions of chapters 4 to 8 inclusive.

### 9.1. Thermal properties and glass stability (Chapter 4)

- Characteristic temperatures of a number of oxide tellurite and fluorotellurite glasses were studied by differential thermal analysis (DTA).

#### *Oxide tellurite glasses*

- Addition of PbO ( $> \approx 5$  mol. %) to the ternary TeO<sub>2</sub>-Na<sub>2</sub>O-ZnO (TZN) reduced glass stability ( $T_x - T_g$ ) for compositions 79TeO<sub>2</sub>-10Na<sub>2</sub>O-10PbO-1Yb<sub>2</sub>O<sub>3</sub> and 78.21TeO<sub>2</sub>-4.95ZnO-9.9Na<sub>2</sub>O-4.95PbO-0.99Yb<sub>2</sub>O<sub>3</sub>-0.99Er<sub>2</sub>O<sub>3</sub> mol. %, however rare-earth (Er<sup>+3</sup> and Yb<sup>+3</sup>) and GeO<sub>2</sub> addition did not adversely affect stability, for compositions 74TeO<sub>2</sub>-12ZnO-10Na<sub>2</sub>O-3PbO-1Yb<sub>2</sub>O<sub>3</sub>, 77TeO<sub>2</sub>-12ZnO-10Na<sub>2</sub>O-1Yb<sub>2</sub>O<sub>3</sub>, and 75TeO<sub>2</sub>-10ZnO-10Na<sub>2</sub>O-5GeO<sub>2</sub> mol. %).
- The stability of the TZN glasses (with  $T_g \approx 280^\circ\text{C}$ ) could be due to the large amount of polyhedra present providing a sufficient energy barrier to devitrification [1-3], and the interaction of oxides of high (Na<sub>2</sub>O), and low (ZnO)

optical basicity in the glass suppressing movement of  $\text{Na}^+$  and  $\text{Zn}^{2+}$ , particularly for molar  $\text{Na}_2\text{O}:\text{ZnO}$  ratio = 1 [4].

- The tungsten-tellurite glasses ( $90\text{TeO}_2\text{-}5\text{WO}_3\text{-}5\text{Nb}_2\text{O}_5$ ,  $82.5\text{TeO}_2\text{-}7.5\text{WO}_3\text{-}10\text{Nb}_2\text{O}_5$ ,  $70\text{TeO}_2\text{-}25\text{WO}_3\text{-}5\text{Bi}_2\text{O}_3$  mol. %, with  $T_g \approx 350^\circ\text{C}$ ) exhibited  $T_x\text{-}T_g > 110^\circ\text{C}$ . Glass stability has been shown to reach a maximum at 27.5 mol. %  $\text{WO}_3$  where  $[\text{WO}_4]$  tetrahedra content was highest for the binary  $\text{TeO}_2\text{-}\text{WO}_3$ . Above this mol. % stability decreased and the amount of  $[\text{WO}_6]$  octahedra increased [5].
- Unlike the TZN glasses, the tungsten-tellurite compositions were shown to form high stability glasses with molar  $\text{MO}_x:\text{WO}_3$  ratio = 1, and molar  $\text{MO}_x:\text{WO}_3$  ratio  $\neq 1$ , i.e. glass formation occurs over a wider range than the TZN glasses.

#### *Fluorotellurite glasses*

- Glass formation was shown for the first time in the ternary system  $\text{TeO}_2\text{-}\text{Na}_2\text{O}\text{-}\text{ZnF}_2$  [6].
- For the series  $(90\text{-}x)\text{TeO}_2\text{-}10\text{Na}_2\text{O}\text{-}x\text{ZnF}_2$ ,  $5 \leq x \leq 30$  mol. %,  $T_g$  decreased with  $\text{ZnF}_2$  content from  $273^\circ\text{C}$  ( $x = 5$  mol. %) to  $235^\circ\text{C}$  ( $x = 30$  mol. %), due to depolymerisation of the  $\text{TeO}_2$  network with fluoride addition [6].
- Glass stability ( $T_x\text{-}T_g$ ) was shown to increase with  $\text{ZnF}_2$  addition, reaching a plateau of around  $161^\circ\text{C}$  at  $x = 25$  mol. %. This could be due to competition of various phases to crystallise, and as the eutectic is approached with fluoride addition [6].

- These glasses are the most stable  $\text{ZnF}_2$  containing tellurite compositions reported to date to the author's knowledge, with  $T_x - T_g > 160^\circ\text{C}$  [6].
- Addition of  $\text{PbF}_2$  ( $70\text{TeO}_2\text{-}10\text{Na}_2\text{O-}10\text{ZnF}_2\text{-}10\text{PbF}_2$  and  $65\text{TeO}_2\text{-}10\text{Na}_2\text{O-}20\text{ZnF}_2\text{-}5\text{PbF}_2$  mol. %) to the  $\text{TeO}_2\text{-Na}_2\text{O-ZnF}_2$  compositions listed above reduced glass stability, although  $T_x - T_g$  gaps were  $> 100^\circ\text{C}$ .
- Replacement of  $\text{Na}_2\text{O}$  with  $\text{WO}_3$  in the glass  $65\text{TeO}_2\text{-}10\text{Na}_2\text{O-}25\text{ZnF}_2$  mol. % ( $65\text{TeO}_2\text{-}10\text{WO}_3\text{-}25\text{ZnF}_2$  mol. %) resulted in a glass of high stability.
- $65\text{TeO}_2\text{-}10\text{Na}_2\text{O-}x\text{ZnF}_2\text{-(}25\text{-}x\text{)ZnO}$ ,  $0 \leq x \leq 20$  mol. %, glasses showed a different stability trend to the  $\text{TeO}_2\text{-Na}_2\text{O-ZnF}_2$  glasses:  $T_x - T_g$  increased to  $168^\circ\text{C}$  for molar  $\text{ZnO}:\text{ZnF}_2$  ratio = 0.55, then decreased with molar  $\text{ZnO}:\text{ZnF}_2$  ratio  $> 0.6$ .  $T_g$  increased with molar  $\text{ZnO}:\text{ZnF}_2$  ratio, with a marked increase at molar  $\text{ZnO}:\text{ZnF}_2$  ratio  $\approx 0.6$ , indicating a structural change in the glass at this point, possibly  $\text{Zn}^{+2}$  coordination.

## 9.2. Crystallisation studies (Chapter 5)

### *Batch materials*

- Batch materials  $\text{TeO}_2$ ,  $\text{ZnO}$ , and  $\text{Na}_2\text{CO}_3$  were shown to be phase pure using X-ray diffraction (XRD).
- However, the as-received  $\text{ZnF}_2$  was shown to contain a significant proportion (see section 9.4) of  $\text{Zn(OH)F}$  [7].

- The as-received  $\text{ZnF}_2$  was fluorinated with  $(\text{NH}_4)\text{HF}_2$  [8, 9], which produced a highly phase pure powder [7].

#### *Fluorination deposit*

- Deposits on the silica liner after fluorination of  $\text{ZnF}_2$  were identified as  $(\text{NH}_4)_3\text{SiF}_6\text{F}$  and  $\text{NH}_4\text{F}$  by XRD.
- A likely attack mechanism of the  $\text{SiO}_2$ , is the initial deposit of  $\text{NH}_4\text{F}$  from the volatilised  $\text{NH}_3$  and  $\text{HF}$ , which then reacts with the liner to produce  $(\text{NH}_4)_3\text{SiF}_6\text{F}$ .
- It is probable that these reactions create 2 moles of  $\text{H}_2\text{O}$  per mole of  $(\text{NH}_4)_3\text{SiF}_6\text{F}$  produced, which may then re-enter the batch as OH.

#### *Melt deposit*

- The deposit on the silica liner after melting a  $\text{TeO}_2\text{-Na}_2\text{O-ZnF}_2$  glass in the glovebox, under a dry, nitrogen rich atmosphere, was identified as  $\text{TeO}_2$ , probably due to the volatile nature of tellurium fluoride species.

#### *Fluorinated melt*

- When  $(\text{NH}_4)\text{HF}_2$  was added to a 10 g batch of  $\text{TeO}_2$ ,  $\text{Na}_2\text{CO}_3$ , and  $\text{ZnF}_2$ , and melted at  $800^\circ\text{C}$ , around 50 wt. % of the batch volatilised, leaving a deposit of partially amorphous and partially crystalline  $(\text{NaZnF}_3)$  phases, identified by XRD.

- This was possibly due to reaction of the  $(\text{NH}_4)\text{HF}_2$  with the batch, producing volatile compounds ( $\text{TeF}_4$  and  $\text{TeF}_6$ ), or the reaction was sufficiently exothermic to decompose the melt. This drying route was not pursued further.

#### *Fluorotellurite crystallisation*

- Two crystalline phases were identified by XRD from glass 70TeO<sub>2</sub>-10Na<sub>2</sub>O-20ZnF<sub>2</sub> mol. % heat treated at 400°C, which were Zn<sub>2</sub>Te<sub>3</sub>O<sub>8</sub> and NaZnF<sub>3</sub> [7].
- The asymmetric DTA crystallisation exotherm was Gaussian deconvoluted into two peaks at 410°C (NaZnF<sub>3</sub>) and 421°C (Zn<sub>2</sub>Te<sub>3</sub>O<sub>8</sub>) [7]. The lower temperature phase was confirmed to be fluorine and sodium rich by EDX analysis, possibly growing from oxide homogeneous nucleation sites which formed on quenching.

#### *Heat treated Er<sup>+3</sup>-doped fluorotellurite glasses*

- No crystalline phases were identified in the Er<sup>+3</sup>-doped 70TeO<sub>2</sub>-10Na<sub>2</sub>O-20ZnF<sub>2</sub> mol. % glasses, heat treated at various temperatures and times.
- Even opaque samples exhibited the characteristic amorphous halo, however the shape of this halo was modified with heat treatment, developing a shoulder, and growing in intensity, indicating a structural change. However, the crystallites may have been too small to detect by powder diffraction.

### 9.3. Optical properties (Chapter 6)

#### *Infrared spectroscopy*

- Infrared spectra of oxide tellurite and fluorotellurite glasses were studied, and refractive indices obtained by ellipsometry.
- Addition of PbO and GeO<sub>2</sub> to TeO<sub>2</sub>-Na<sub>2</sub>O-ZnO glasses shifts the multiphonon edge (at  $\approx 6 \mu\text{m}$ ) to lower and higher wavenumbers respectively, due to bond strength and the masses of the cations (as predicted by the Szigeti equation [10]).
- Addition of ZnO to TeO<sub>2</sub>-Na<sub>2</sub>O-ZnO compositions shifts the multiphonon edge to higher wavenumbers.
- A number of absorption bands in the infrared were identified in the TeO<sub>2</sub>-Na<sub>2</sub>O-ZnO glasses due to intrinsic lattice vibrations (visible in a 0.2 mm sample), and extrinsic impurities [6]:
  - Free OH / molecular water stretching mode ( $\approx 3.0 \mu\text{m} \equiv 3300 \text{ cm}^{-1}$ ).
  - Weakly hydrogen-bonded OH stretching mode ( $\approx 3.3 \mu\text{m} \equiv 3060 \text{ cm}^{-1}$ ).
  - Strongly hydrogen-bonded OH stretching mode ( $\approx 4.8 \mu\text{m} \equiv 2090 \text{ cm}^{-1}$ ).
  - 1<sup>st</sup> overtone of O-Te-O symmetric stretch / bending mode of molecular water ( $\approx 6.5 \mu\text{m} \equiv 1550 \text{ cm}^{-1}$ ).
  - Combination of asymmetric stretch of O-Te-O or Te-O<sup>-</sup> and [TeO<sub>6</sub>] group vibration ( $\approx 7.3 \mu\text{m} \equiv 1370 \text{ cm}^{-1}$ ).
  - 1<sup>st</sup> overtone of [TeO<sub>6</sub>] group ( $\approx 8.3 \mu\text{m} \equiv 1210 \text{ cm}^{-1}$ ).

- Unidentified, possibly 1<sup>st</sup> overtone of [TeO<sub>6</sub>] group vibration ( $\approx 9.3 \mu\text{m} \equiv 1070 \text{ cm}^{-1}$ ).
- The areas of the deconvoluted OH bands of the TeO<sub>2</sub>-Na<sub>2</sub>O-ZnO glasses generally decreased in relative area, and therefore percentage OH (assuming approximately equal extinction coefficients) by: weakly hydrogen-bonded OH > free OH > strongly hydrogen-bonded OH.
- This difference in OH band intensities compared to silicates could be due to charge equalisation of bridging and non-bridging oxygens.
- The multiphonon edge of the tungsten-tellurite glasses (TeO<sub>2</sub>-WO<sub>3</sub>-MO, where MO = Bi<sub>2</sub>O<sub>3</sub> or Nb<sub>2</sub>O<sub>5</sub>) shifted to a higher wavenumber (due to strength of W-O bond), and developed features within the multiphonon edge with WO<sub>3</sub> addition.
- The band at around  $1770 \text{ cm}^{-1}$  ( $5.65 \mu\text{m}$ ) which grew with WO<sub>3</sub> content was attributed to the first overtone of the asymmetric vibrations of the [WO<sub>6</sub>] octahedra ( $2 \times 870 \text{ cm}^{-1} = 1740 \text{ cm}^{-1}$ ) [5, 11, 12].
- The band which occurred at around  $1870 \text{ cm}^{-1}$  ( $5.35 \mu\text{m}$ ) was attributed to the first overtone of the symmetric vibrations of the [WO<sub>4</sub>] tetrahedra ( $2 \times 930 \text{ cm}^{-1} = 1860 \text{ cm}^{-1}$ ) [5, 11, 12].
- The relative areas of the OH bands in the tungsten-tellurite glasses did not resemble the TeO<sub>2</sub>-Na<sub>2</sub>O-ZnO glasses, with areas in the following order: strongly hydrogen-bonded OH > weakly hydrogen-bonded OH > free OH, signifying a different structure.
- These overall areas of these OH bands in the tungsten-tellurite glasses were less than the TeO<sub>2</sub>-Na<sub>2</sub>O-ZnO glasses, indicating dryer glasses.

- For fibre drawing, the  $\text{TeO}_2\text{-Na}_2\text{O-ZnO}$  glasses would be more suitable than the tungsten-tellurite compositions, as they can be worked at lower temperatures ( $T_g \approx 280$  and  $350^\circ\text{C}$  respectively), and transmit further into the infrared ( $\approx 6$  and  $5.25 \mu\text{m}$  respectively), even though OH bands were more intense, which could be potentially reduced with reactive atmosphere processing (RAP).
- For the series  $(90-x)\text{TeO}_2\text{-}10\text{Na}_2\text{O-}x\text{ZnF}_2$ , mol. %,  $5 \leq x \leq 30$  mol. % melted for 2 hours, OH bands at  $2900 \text{ cm}^{-1}$  were reduced in intensity with  $\text{ZnF}_2$  addition due to self drying of the melt, from around  $120 \text{ dB.m}^{-1}$  ( $x = 5$  mol. %) to  $20 \text{ dB.m}^{-1}$  ( $x \geq 15$  mol. %) [6].
- Melting time also had a significant effect on drying of this series, with the loss at  $2900 \text{ cm}^{-1}$  reduced by two orders of magnitude when increased from 1 hour ( $705 \text{ dB.m}^{-1}$ ) to 2 hours ( $10 \text{ dB.m}^{-1}$ ) [6].
- The OH bands of this series did not exhibit strongly-hydrogen bonded OH, possibly obscured by the multiphonon edge, or more likely, very little was present due to the low OH content of the glass, resulting in weakly hydrogen-bonded OH and free OH statistically and energetically more favourable, however -F-----HO-type bonds will exist.
- The  $65\text{TeO}_2\text{-(}25\text{-}x\text{)ZnF}_2\text{-}x\text{ZnO-}10\text{Na}_2\text{O}$  mol. %,  $5 \leq x \leq 25$  mol. % glasses showed an increase in OH bands with molar  $\text{ZnO}:\text{ZnF}_2$  ratio, and again the  $\text{ZnF}_2$  containing glasses did not exhibit strongly-hydrogen bonded OH bands.
- Glass  $69.86\text{TeO}_2\text{-}9.98\text{Na}_2\text{O-}19.96\text{ZnF}_2\text{-}0.20\text{ErF}_3$  mol. % was heat treated, with varying times and temperatures above  $T_g$ , and enhancement of the  $\text{Er}^{+3}$  bands in the visible and near-IR was seen with increasing treatment. This is likely to be

due to the change in the chemical environment surrounding the erbium (III) ion, possibly due to preferential segregation of  $\text{Er}^{+3}$  to the crystallites.

### *Refractive indices*

- PbO addition to  $\text{TeO}_2\text{-Na}_2\text{O-ZnO}$  glasses resulted in an increase in refractive index, and  $\text{GeO}_2$  caused a decrease, due to the high and low polarisability respectively compared to  $\text{TeO}_2$  [13].
- $\text{TeO}_2$  glasses which contained  $\text{WO}_3$ ,  $\text{Bi}_2\text{O}_3$ , and  $\text{Nb}_2\text{O}_5$  had higher refractive indices than the  $\text{TeO}_2\text{-Na}_2\text{O-ZnO}$  glasses, due to the high polarisability of all components [13].
- Refractive index of the series  $(90-x)\text{TeO}_2\text{-}10\text{Na}_2\text{O-xZnF}_2$ , mol. %,  $5 \leq x \leq 30$  mol. % decreased linearly with  $\text{ZnF}_2$  addition, from 2.02 ( $x = 5$  mol. %) to 1.85 ( $x = 30$  mol. %), as the fluoride and zinc are less polarisable than oxygen and tellurium [6].
- Glasses in the series  $65\text{TeO}_2\text{-(}25\text{-}x\text{)ZnF}_2\text{-}x\text{ZnO-}10\text{Na}_2\text{O}$  mol. %, for  $5 \leq x \leq 25$  mol. % showed a linear increase refractive index with oxide / fluoride ratio, from 1.887 ( $\text{ZnO} / \text{ZnF}_2 = 0$ ) to 1.952 ( $\text{ZnO} / \text{ZnF}_2 = 1$ ).

### *Core / clad choice*

- For the series  $(90-x)\text{TeO}_2\text{-}10\text{Na}_2\text{O-xZnF}_2$ , mol. %,  $5 \leq x \leq 30$  mol. %, stable glasses can be formed ( $T_x\text{-}T_g > 110^\circ\text{C}$ ), with only a small shift in the multiphonon

edge across the series, with low softening points ( $T_g \approx 240^\circ\text{C}$ ),  $\Delta n = 0.17$  for 5 to 30 mol. %  $\text{ZnF}_2$ , and decreasing OH content with  $\text{ZnF}_2$  addition.

- Therefore, this series offers enhanced potential for low loss infrared transmitting fibres compared to the  $\text{TeO}_2\text{-Na}_2\text{O-ZnO}$  glasses, with a prospective core / clad pair of glasses 65 $\text{TeO}_2\text{-25ZnF}_2\text{-10Na}_2\text{O}$  mol. % (clad,  $n = 1.887$ ), and 70 $\text{TeO}_2\text{-20ZnF}_2\text{-10Na}_2\text{O}$  mol. % (core,  $n = 1.914$ ) giving a numerical aperture of 0.32 and  $\theta = 19^\circ$  [7].

## 9.4. Surface properties (Chapter 7)

### *X-ray photoelectron spectroscopy (XPS)*

- X-ray photoelectron spectroscopy (XPS) of the as-received and fluorinated  $\text{ZnF}_2$  powder confirmed the effectiveness of the treatment, with O1s peak decreasing from 13.2 to 3.1 at. % after fluorination [7].
- By calculation from the O1s values, the proportion of  $\text{Zn(OH)F}$  was reduced in the powders from 39.7 to 9.4 mol. % [7].
- These values were likely to be lower, due to the presence of molecular water, organic contaminants, and experimental error [7].
- XPS of the cleaved surface of glass MOD015 82.5 $\text{TeO}_2\text{-7.5WO}_3\text{-10Nb}_2\text{O}_5$  mol. % showed two components to the O1s peaks, with increasing binding energy (and intensity), the main peak attributed to bridging / non-bridging oxygens (BOs and

NBOs respectively) in the glass (82.5 % → equalised at 530.9 eV), and a smaller asymmetric shoulder due to OH groups at the cleave surface (7.5 % → 532.4 eV).

- The semi-quantitative analysis of this glass produced at. % values close to the batched values (2.5 to 13.9 % variation).
- XPS of the polished surface of this glass showed a large increase in the OH peak intensity as expected, and larger variation in the at. % values from the batched values (14.9 to 65.1 % variation), due to degradation and contamination at the glass surface. The surface was oxygen rich, and tellurium and tungsten depleted.
- In addition to the OH, BO and NBOs O1s peaks, a component was seen at around 533.9 eV, possibly due to M=O species (e.g. Te=O, C=O).
- There were two components to the F1s peak of the cleaved surface of glass MOF001\_iii (65TeO<sub>2</sub>-10Na<sub>2</sub>O-25ZnF<sub>2</sub> mol. %), which was melted for 1.75 hours with un-fluorinated ZnF<sub>2</sub>, possibly due to different bonding environments surrounding the fluorine anion, most likely Na-F, F-Zn-F, and O-Zn-F.
- Like the tungsten-tellurite glass, the O1s peak of this ZnF<sub>2</sub> containing glass contained a BO / NBO, and OH component. A small higher binding energy component was also seen, as with the polished surface of the tungsten-tellurite glass, though to be due to M=O species.
- Semi-quantitative analysis of the cleaved surface of this glass produced at. % values close to the batched values, with only fluorine significantly lower. This is to be expected, as fluoride species (e.g TeF<sub>x</sub>) would be the most volatile species in these glasses.

- For glass MOF001\_v (65TeO<sub>2</sub>-10Na<sub>2</sub>O-25ZnF<sub>2</sub> mol. %), which was melted for 2 hours with fluorinated ZnF<sub>2</sub> the O1s peak contained NBO / BO, OH, and M=O components, however the F1s peak consisted of a single symmetric component compared to the unfluorinated 1.75 hour melt. This is possible due to the reduced number of F-Zn-OH species in the glass.
- Again, the OH content of the polished glass surface was greater than the cleaved surface, and a fourth higher binding energy O1s component was seen possibly due to C-O contamination.
- Oxygen levels were higher at the polished surface compared to the cleave, and all other elements lower than batched (particularly F), which were leached on contact with moisture.

#### *Environmental and chemical durability*

- NaOH, H<sub>2</sub>SO<sub>4</sub>, and HCl solutions produced poor etches for TeO<sub>2</sub>-Na<sub>2</sub>O-ZnO based glasses at various concentrations (1 and 3M), and temperatures (15 and 21°C).
- Glass 65TeO<sub>2</sub>-10Na<sub>2</sub>O-25ZnF<sub>2</sub> mol. % was relatively durable to 21°C distilled water, with only 0.34 wt. % loss after 21 days immersion.
- As expected, weight loss for this glass was higher when immersed in 60°C distilled water, with around 4.5 wt. % loss after 21 days.
- This author proposes that the main regimes for water attack of these glasses (TeO<sub>2</sub>-Na<sub>2</sub>O-ZnF<sub>2</sub>) were F/OH<sup>-</sup> exchange at lower temperatures (≈ 21°C), and

higher temperatures ( $\approx 60^\circ\text{C}$ ), and bridging bond severance ( $\text{Te-O-Te} + \text{H}_2\text{O} \rightarrow 2[\text{Te-OH}]$ ), and cationic leaching ( $\text{Na}^+$ ,  $\text{Te}^{+4}$ , and  $\text{Zn}^{+2}$ ) at higher temperatures ( $\approx 60^\circ\text{C}$ ).

- HCl showed a different etched surface morphology after attack of the  $\text{TeO}_2$ - $\text{Na}_2\text{O}$ - $\text{ZnF}_2$  glasses, possibly due to the preferential etching of the oxide components of the glass by this halide containing acid.
- HF, acetic, and phosphoric acids produced good etched surfaces for the  $\text{TeO}_2$ - $\text{Na}_2\text{O}$ - $\text{ZnF}_2$  glasses, and the later two should be investigated further.
- Infrared spectroscopy showed the 4% HF etch introduced significant OH content into the 65 $\text{TeO}_2$ -10 $\text{Na}_2\text{O}$ -25 $\text{ZnF}_2$  mol. % glass. If this method was used to clean preforms, it could introduce a high OH surface ‘skin’ to the preform, with disparate viscosity behaviour to the ‘dry’ glass, unwanted stresses, and crystal nucleation sites. Therefore, if a ‘wet’ method must be used to clean preform surfaces, high concentration HF (e.g. 40 %) for short times should be used.

### *Ion-exchange*

- $\text{Ag}^+/\text{Na}^+$  ion-exchange of  $\text{TeO}_2$ - $\text{Na}_2\text{O}$ - $\text{ZnO}$  based glasses using molten salt, and Ag-layer heat treatments routes resulted in measurable silver contents (by EDX) in the glasses to around 1 to 2  $\mu\text{m}$  depth.
- Around 2.5 at. %  $\text{Ag}^+$  was incorporated into the glasses heat treated at the surfaces, and around 10 at. % at 0.25  $\mu\text{m}$  depth for the glass dipped in the molten salt, which was quite heavily pitted (6.8 at. % batched sodium in both glasses).

- The  $\text{Ag}^+$  concentration profiles were modelled by erfc equations using Mathcad software, and diffusion parameters obtained (surface concentrations,  $N_0$ , and diffusion coefficients,  $D$ ) if not already known.

## 9.5. Fibre drawing (Chapter 8)

### *Stress in fluorotellurite fibre*

- Stresses in a proposed core / clad fluorotellurite pair (20 and 25 mol. %  $\text{ZnF}_2$ ) due to thermal expansion mismatch were calculated to be around 72 MPa, relatively low compared to the tensile strength of the fibre [7].

### *Viscosity-temperature behaviour*

- The viscosity-temperature behaviour of this fluorotellurite core / clad pair was obtained using thermal mechanical analysis (TMA), and modelled using various equations [7].
- For a given temperature, the viscosity of the glass increased with decreasing  $\text{ZnF}_2$ , due to depolymerisation of the  $\text{TeO}_2$  network with  $\text{ZnF}_2$  addition [7].
- The Cohen-Grest model showed the best fit and parameters for the viscosity-temperature behaviour of these glasses, due to their fragile nature [7].
- The fragility of these glasses falls somewhere between fluorozirconate (more fragile) and oxide tellurite (stronger) glasses [7, 14].

- These models were used to predict the fibre drawing temperature ( $T_{\eta} \approx 330^{\circ}\text{C}$  corresponding to a viscosity of  $10^{4.5}$  Pa.s) of the fluorotellurite core / clad pair, occurring at least  $60^{\circ}\text{C} < T_x$  [7].

### *Crystals in fibre*

- Dendritic snowflake shaped crystals were seen in optical fibres of composition 70TeO<sub>2</sub>-10Na<sub>2</sub>O-20ZnF<sub>2</sub> mol. % pulled at around 300°C under a 'wet' atmosphere.
- These Na, and F rich, and Te and O (most likely NaZnF<sub>3</sub>) deficient crystals were seen near the surface of the fibre indicating that degradation due to moisture at elevated temperatures has promoted their nucleation and growth. Fibre drawn under dryer conditions did not devitrify.
- A proposed growth mechanism for these crystals is initial primary cross shaped dendrites (in the 2-dimensional plane), followed by secondary dendrites growing along a different crystallographic plane from these primary dendrites.

### *Optical loss of fluorotellurite fibre*

- The following melting, casting and fibre drawing parameters resulted in the best quality final fibre (strength, appearance, and optical loss) for fluorotellurite glasses:  $\geq 10$  hr. melting time, a dry oxidising melting atmosphere, fluorinated ZnF<sub>2</sub>, gold crucible, brass mould, and dry air / N<sub>2</sub> fibre drawing atmosphere.

- Increasing melting time and fluorination resulted in a significant decrease in OH bands in the 700 nm to 2.5  $\mu\text{m}$  region for unstructured 70TeO<sub>2</sub>-10Na<sub>2</sub>O-20ZnF<sub>2</sub> mol. % fibre, from around 40 to 4 dB.m<sup>-1</sup> at 2.5  $\mu\text{m}$  as melting time was increased from 3 to 10 hours [7].
- Loss for the 10 hour melt was relatively flat ( $\leq 5$  dB.m<sup>-1</sup>) over the entire 700 nm to 2.5  $\mu\text{m}$  region [7].
- This remaining loss is likely to be a combination of reflection, residual OH, crucible (Au / Pt) impurities, scattering centres, and scattering from the unclad fibre surface.

## 9.6. Overall conclusions and recommendations

The aims of this study were to investigate suitable compositions and fabricate low loss optical fibre from TeO<sub>2</sub>-based glasses. Processing routes were carefully controlled, which ultimately manifested as lower optical loss in drawn fibres. Attenuation in the initial fibre drawn from fluorotellurite glasses in this study was too high to measure; this was reduced considerably due to a number of factors, primarily: OH reduction in the batch materials by fluorination, increasing melting times (self-drying) and drying of the processing atmosphere (melting and drawing). Control of these factors minimised the number of scattering and absorbing species in the glasses, resulting in fibre which transmitted in the 700 nm to 2.5  $\mu\text{m}$  region with losses of around 5 dB.m<sup>-1</sup>.

Fluorotellurite (TeO<sub>2</sub>-Na<sub>2</sub>O-ZnF<sub>2</sub>) glasses provide an attractive alternative to other candidate infrared fibreoptic materials such as fluorides and chalcogenides due to ease of

manufacture, durability, low  $T_g$ , high refractive index (for high power and non-linear applications) and low OH content. However, the nature of the structural units and hydrogen bonding in these oxyfluoride glasses should be investigated further to provide a more detailed understanding of structure-property relationships in these systems. Identification of products of volatilisation during melting should also be performed (e.g. by TGA-mass spectrometry [15]) as the melt composition on casting determines properties and is an important consideration for glass formation.

Losses in these fibres must be reduced below  $1 \text{ dB}\cdot\text{m}^{-1}$  in the near- and mid-infrared regions (around 700 nm to 5  $\mu\text{m}$ ) for short path length applications such as sensors (e.g. military threat detection) and power delivery (e.g. surgical lasers). Double fluorination, reactive atmosphere processing (RAP) and batching / melting inside a glovebox are a number of possible routes for reducing extrinsic impurities, particularly hydroxyl groups, in fluorotellurite glasses and optical fibres.

## 9.7. References

- [1] J. W. Zwanziger, J. C. McLaughlin, and S. L. Tagg, "Sodium distribution in sodium tellurite glasses probed with spin-echo NMR," *Physical Review B*, vol. 56, pp. 5243-5249, 1997.
- [2] J. C. McLaughlin, S. L. Tagg, and J. W. Zwanziger, "The structure of alkali tellurite glasses," *Journal of Physical Chemistry B*, vol. 105, pp. 67-75, 2001.
- [3] J. C. McLaughlin, S. L. Tagg, J. W. Zwanziger, D. R. Haeffner, and S. D. Shastri, "The structure of tellurite glass: a combined NMR, neutron diffraction, and X-ray diffraction study," *Journal of Non-Crystalline Solids*, vol. 274, pp. 1-8, 2000.
- [4] K. Aida, T. Komatsu, and V. Dimitrov, "Thermal stability, electronic polarisability and optical basicity of ternary tellurite glasses," *Physics and Chemistry of Glasses*, vol. 42, pp. 103-111, 2001.

- [5] I. Shaltout, Y. Tang, R. Braunstein, and A. M. Abuelazm, "Structural studies of tungstate tellurite glasses by Raman-spectroscopy and differential scanning calorimetry," *Journal of Physics and Chemistry of Solids*, vol. 56, pp. 141-150, 1995.
- [6] M. D. O'Donnell, C. A. Miller, D. Furniss, V. K. Tikhomirov, and A. B. Seddon, "Fluorotellurite glasses with improved mid-infrared transmission," *Journal of Non-Crystalline Solids*, vol. 331, pp. 48-57, 2003.
- [7] M. D. O'Donnell, D. Furniss, V. K. Tikhomirov, and A. B. Seddon, "Low loss infrared fluorotellurite optical fibre," *Physics and Chemistry of Glasses*, in press.
- [8] K. J. Ewing, J. S. Sanghera, R. E. Miklos, M. G. Sachon, L. Peitersen, P. Hart, and I. Aggarwal, "Reaction of zirconium fluoride monohydrate and ammonium bifluoride - its effect on fluoride glass preparation and quality," *Journal of the American Ceramic Society*, vol. 72, pp. 1441-1443, 1989.
- [9] J. S. Sanghera, P. Hart, M. G. Sachon, K. J. Ewing, and I. Aggarwal, "New fluorination reactions of ammonium bifluoride," *Journal of the American Ceramic Society*, vol. 73, pp. 1339-1346, 1990.
- [10] J. M. Parker and A. B. Seddon, "Infrared-transmitting optical fibres," in *High-Performance Glasses*, M. Cable and J. M. Parker, Eds. London: Blackie, 1992, pp. 252-286.
- [11] P. Charton, L. Gengembre, and P. Armand, "TeO<sub>2</sub>-WO<sub>3</sub> glasses: Infrared, XPS and XANES structural characterizations," *Journal of Solid State Chemistry*, vol. 168, pp. 175-183, 2002.
- [12] I. Shaltout, Y. Tang, R. Braunstein, and E. E. Shaisha, "FTIR spectra and some optical properties of tungstate-tellurite glasses," *Journal of Physics and Chemistry of Solids*, vol. 57, pp. 1223-1230, 1996.
- [13] V. Dimitrov and T. Komatsu, "Classification of simple oxides: A polarizability approach," *Journal of Solid State Chemistry*, vol. 163, pp. 100-112, 2002.
- [14] J. Wang, E. Vogel, and E. Snitzer, "Tellurite glass: a new candidate for fiber devices," *Optical Materials*, vol. 3, pp. 187-203, 1994.
- [15] M. Kamruddin, P. K. Ajikumar, S. Dash, A. K. Tyagi, and B. Raj, "Thermogravimetry-evolved gas analysis-mass spectrometry system for materials research," *Bulletin of Materials Science*, vol. 26, pp. 449-461, 2003.

## 10. Future work

- Raman spectroscopy / Raman gain measurements of fluorotellurite glasses ( $\text{TeO}_2\text{-Na}_2\text{O-ZnF}_2$ ) in collaboration with Dr. K. Richardson's group at the University of Central Florida [1].
- Mechanical strength measurements fluorotellurites ( $\text{TeO}_2\text{-Na}_2\text{O-ZnF}_2$ ):
  - Hardness / microhardness of bulk glass / glass-ceramics.
  - Tensile strength of fibres.
  - 2-point bend test of fibres.
- Further compositional development of  $\text{Er}^{+3}$ -doped  $\text{TeO}_2\text{-Na}_2\text{O-ZnF}_2$  glasses to identify phase field where ceraming process can be controlled for optimum emission band enhancement.
- Development of fibre-on-glass (FOG, invented by Prof. P. Sewell) devices using  $\text{TeO}_2\text{-Na}_2\text{O-ZnF}_2$  glasses, with Profs T. Benson and P. Sewell's modelling group at Nottingham University. These comprise of unstructured fibres 'pressed' into a slightly lower refractive index substrate (using TMA). Early investigations have shown light guiding is possible [2]. Fig. (10.1) shows this device under the ESEM, (10.2) the modelling of the device, and (10.3) the device guiding laser light.

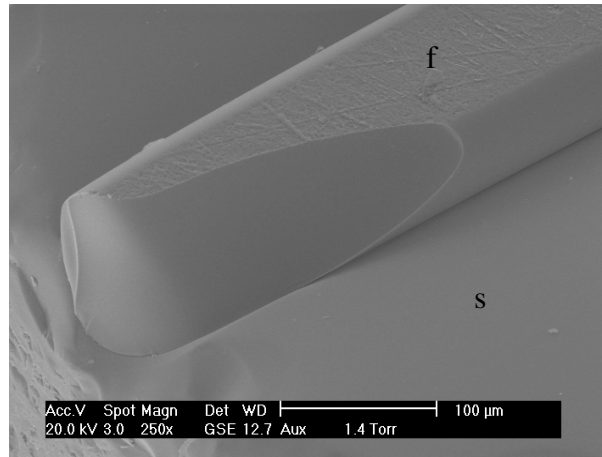
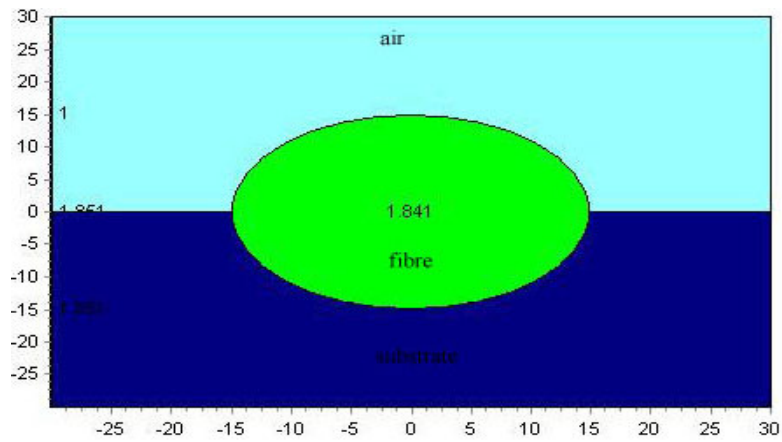
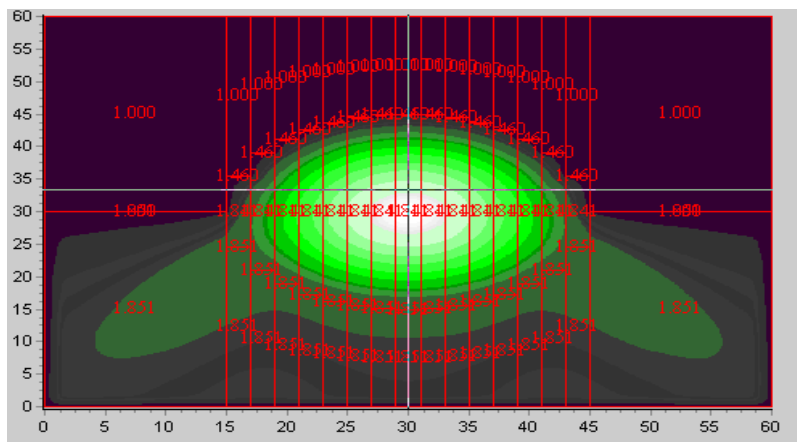


Fig. (10.1): ESEM micrograph of FOG device made from substrate (s):  $65\text{TeO}_2\text{-}10\text{Na}_2\text{O-}25\text{ZnF}_2$  mol. % and fibre (f):  $70\text{TeO}_2\text{-}10\text{Na}_2\text{O-}20\text{ZnF}_2$  [2].

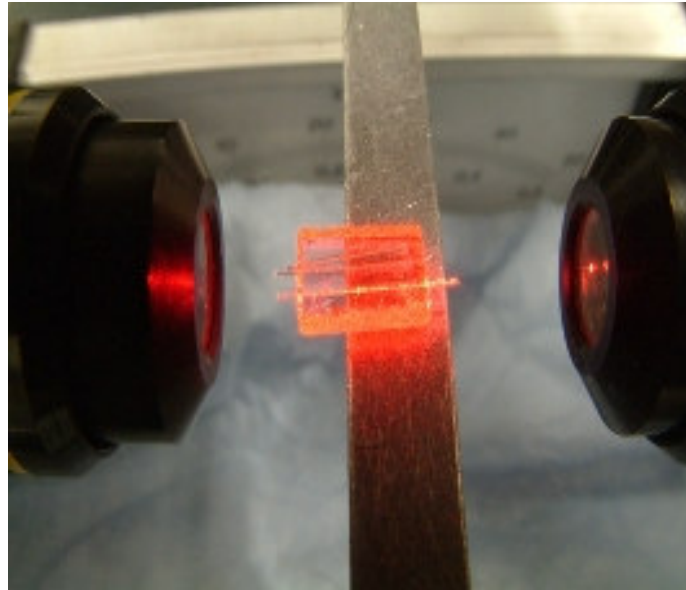


(a)



(b)

Fig. (10.2): (a) Boundary conditions, and (b) finite difference guided mode modelling, of FOG device [2].



(a)



(b)

Fig. (10.3): (a) FOG device guiding light (632.8 nm), and (b) near field image of FOG output guiding multimode [2].

- $\text{Ag}^+/\text{Na}^+$  ion-exchange of  $\text{TeO}_2\text{-Na}_2\text{O-ZnF}_2$  glasses.
- Measure non-linear properties of  $\text{TeO}_2\text{-Na}_2\text{O-ZnF}_2$  glasses:
  - Induced second harmonic generation.

- Non-linear refractive index.
- Construct time-temperature-transformation (TTT) diagrams of  $\text{TeO}_2\text{-Na}_2\text{O-ZnF}_2$  glasses using an oxidising atmosphere in differential scanning calorimeter (DSC). Fig. (10.4) shows measurements made in sealed gold pans with a nitrogen atmosphere on  $\text{TeO}_2\text{-Na}_2\text{O-ZnF}_2$  glasses, and nose of TTT diagram appeared to reside at  $t = 0$ , indicating glass formation not possible under inert / reducing conditions. Possibly due to higher volatilisation under these conditions (see section 5.3.1.2.).

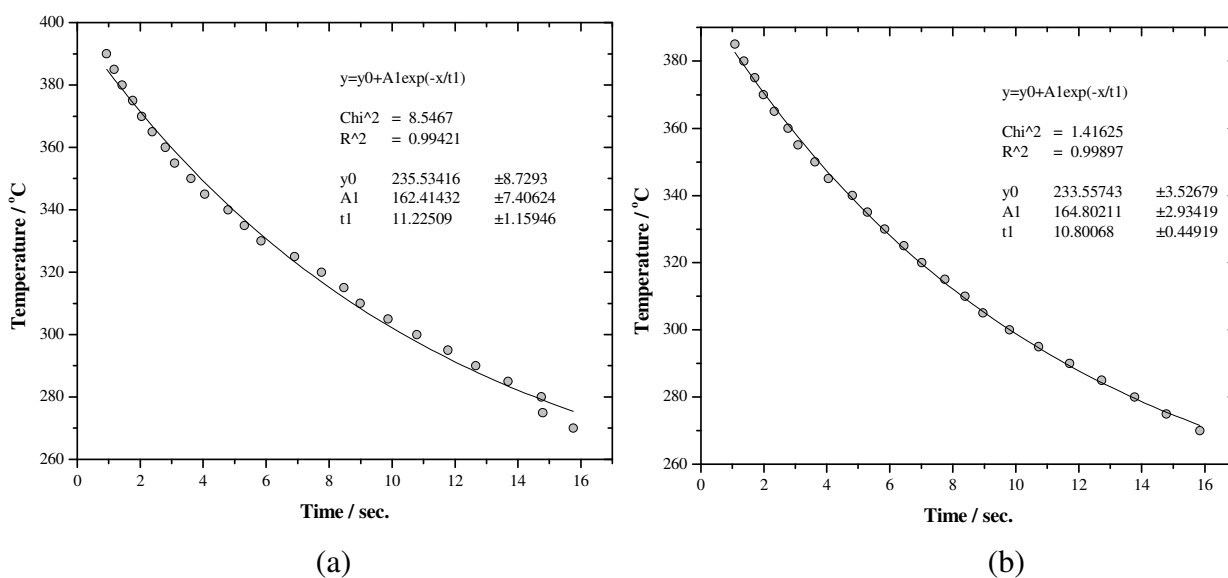


Fig. (10.4): Time-temperature-transformation (TTT) diagrams of (a) cladding 65TeO<sub>2</sub>-10Na<sub>2</sub>O-25ZnF<sub>2</sub> mol. % and (b) core 70TeO<sub>2</sub>-10Na<sub>2</sub>O-20ZnF<sub>2</sub> mol. % glasses, using DSC in gold pans sealed under a nitrogen atmosphere.

- Manufacture structured  $\text{TeO}_2\text{-Na}_2\text{O-ZnF}_2$  fibre using rotational casting / rod-in-tube methods.
- Further X-ray photoelectron spectroscopy (XPS) studies, relating these to FTIR and Raman measurements of structure.

- Heat capacity ( $C_p$ ) measurements in DTA / DSC to thermodynamically compare  $\text{TeO}_2\text{-Na}_2\text{O-ZnF}_2$  fragility to oxide tellurite and fluorozirconate glasses.
- Further crystallisation studies of  $\text{TeO}_2\text{-Na}_2\text{O-ZnF}_2$  glasses to determine the phase fields of  $\text{NaZnF}_3$  and  $\text{Zn}_2\text{Te}_3\text{O}_8$ , and relate this to glass stability.
- Further etching of  $\text{TeO}_2\text{-Na}_2\text{O-ZnF}_2$  glasses, concentrating on HF, acetic, and phosphoric acids, with the etched surfaces characterized by XPS.
- TGA-mass spectrometry [3] of fluorotellurite glass melt volatilisation.

## 10.1. References

- [1] R. Stegeman, L. Jankovic, H. Kim, C. Rivero, G. Stegeman, K. Richardson, and P. Delfyett, "Tellurite glasses with peak absolute Raman gain coefficients up to 30 times that of fused silica," *Optics Letters*, vol. 28, pp. 1126-1128, 2003.
- [2] T. M. Benson, A. Vukovic, P. Sewell, D. Zhang, M. D. O'Donnell, J. Lousteau, D. Furniss, and A. B. Seddon, "Fibre on glass (FOG): a novel concept for planar photonics," presented at 6th International Conference on Transparent Optical Networks (ICTON), Wroclaw, Poland, 2004.
- [3] M. Kamruddin, P. K. Ajikumar, S. Dash, A. K. Tyagi, and B. Raj, "Thermogravimetry-evolved gas analysis–mass spectrometry system for materials research," *Bulletin of Materials Science*, vol. 26, pp. 449-461, 2003.